Lattice Dynamics

observed with x-ray diffraction

JAN-ETIENNE PUDELL

Universität
Potsdam
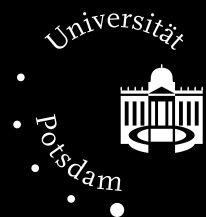
Lattice Dynamics

observed with x-ray diffraction

Jan-Etienne Pudell

zur Erlangung des akademischen Grades
doctor rerum naturalium (Dr. rer. nat.)
in der Wissenschaftsdisziplin: Experimentalphysik

The cover and the front page illustrate the coherent and incoherent strain evolution in a heterostructure (Al_2O_3, 50 nm MgO, 16 nm Ni, 50 nm MgO, Al_2O_3) after laser excitation, where the Ni layer (spine of the cover) absorbs the energy of the optical excitation. The spatial coordinate is horizontal, the temporal coordinate is vertical and the excitation occurs at the bottom. Blue colors indicate compressive strain and gray colors indicate expansive strain.

There are many variables, but it can succeed.

Seven of Nine

Abstract

In this thesis I summarize my contribution to the research field of ultrafast structural dynamics in condensend matter. It consists of 17 publications that cover the complex interplay between electron, magnon, and phonon subsystems in solid materials and the resulting lattice dynamics after ultrafast photoexcitation. The investigation of such dynamics is necessary for the physical understanding of the processes in materials that might become important in the future as functional materials for technological applications, for example in data storage applications, information processing, sensors, or energy harvesting.

In this work I present ultrafast x-ray diffraction (UXRD) experiments based on the optical pump – x-ray probe technique revealing the time-resolved lattice strain. To study these dynamics the samples (mainly thin film heterostructures) are excited by femtosecond near-infrared or visible light pulses. The induced strain dynamics caused by stresses of the excited subsystems are measured in a pump-probe scheme with x-ray diffraction (XRD) as a probe. The UXRD setups used during my thesis are a laser-driven table-top x-ray source and large-scale synchrotron facilities with dedicated time-resolved diffraction setups. The UXRD experiments provide quantitative access to heat reservoirs in nanometric layers and monitor the transient responses of these layers with coupled electron, magnon, and phonon subsystems. In contrast to optical probes, UXRD allows accessing the material-specific information, which is unavailable for optical light due to the detection of multiple indistinguishable layers in the range of the penetration depth.

In addition, UXRD facilitates a layer-specific probe for layers buried opaque heterostructures to study the energy flow. I extended this UXRD technique to obtain the driving stress profile by measuring the strain dynamics in the unexcited buried layer after excitation of the adjacent absorbing layers with femtosecond laser pulses. This enables the study of negative thermal expansion (NTE) in magnetic materials, which occurs due to the loss of the magnetic order. Part of this work is the investigation of stress profiles which are the source of coherent acoustic phonon wave packets (hypersound waves). The spatiotemporal shape of these stress profiles depends on the energy distribution profile and the ability of the involved subsystems to produce stress. The evaluation of the UXRD data of rare-earth metals yields a stress profile that closely matches the optical penetration profile: In the paramagnetic (PM) phase the photoexcitation results in a quasi-instantaneous expansive stress of the metallic layer whereas in the antiferromagnetic (AFM) phase a quasi-instantaneous contractive stress and a second contractive stress contribution rising on a 10 ps time scale adds to the PM contribution. These two time scales are characteristic for the magnetic contribution and are in agreement with related studies of the magnetization dynamics of rare-earth materials.

Several publications in this thesis demonstrate the scientific progress in the field of active strain control to drive a second excitation or engineer an ultrafast switch. These applications of ultrafast dynamics are necessary to enable control of functional material properties via strain on ultrafast time scales.

For this thesis I implemented upgrades of the existing laser-driven table-top UXRD setup in order to achieve an enhancement of x-ray flux to resolve single digit nanometer thick layers. Furthermore, I developed and built a new in-situ time-resolved magneto-optic Kerr effect (MOKE) and optical reflectivity setup at the laser-driven table-top UXRD setup to measure the dynamics of lattice, electrons and magnons under the same excitation conditions.

Kurzdarstellung

In dieser Doktoarbeit sind meine Beiträge zum Forschungsgebiet der ultraschnellen Strukturdynamik in kondensierter Materie zusammegefasst. Sie besteht aus 17 Publikationen, welche die Wechselwirkung zwischen Elektron-, Magnon- und Phononsystem in Festkörpern, sowie die dadurch verursachte Gitterdynamik nach ultraschneller optischer Anregung diskutieren. Die Untersuchung dieser Dynamik ist erforderlich für das physikalische Verständnis der Prozesse in Materialien, die in Zukunft als Funktionsmaterialien für technologische Anwendungen, z.B. in der Datenspeicherung und Informationsverarbeitung, sowie bei Sensoren und der Energiegewinnung, wichtig werden könnten.

In dieser Arbeit präsentiere ich Experimente, welche ultraschneller Röntgenbeugung (UXRD) als Technik nutzen. Sie basiert auf der Anrege-Abfrage-Technik: Die Dynamik in der Probe (hauptsächlich Dünnfilm-Heterostrukturen) wird durch Femtosekunden-Lichtpulse im nahen Infrarot oder im sichtbaren Bereich angeregt. Die Dehnung des Materials, welche die Spannung (Druck) der angeregten Teilsysteme hervorruft, wird mit Röntgenbeugung als Abfrage gemessen. Während meiner Doktorandentätigkeit habe ich zwei Arten von Aufbauten zur UXRD genutzt: lasergetriebene laborbasierte Röntgenquellen und Synchrotronstrahlungsquellen mit zugehörigen zeitaufgelösten Messinstrumenten. Mit den UXRD-Experimenten kann die gespeicherte Energie unterschiedlicher gekoppelter Teilsysteme, wie Elektronen, Mangonen und Phononen, einer nur wenige Nanometer dicken Schicht gemessen werden. Im Vergleich zu optischen Messtechniken bietet UXRD den Zugriff auf materialspezifische Informationen, die für optisches Licht aufgrund der Detektion mehrerer nicht unterscheidbarer Schichten im Bereich der Eindringtiefe nicht zur Verfügung steht.

Darüber hinaus lässt sich mit UXRD eine für optische Detektion verdeckte Schicht als schichtspezifische Sonde nutzen, um den Energietransport zu untersuchen. Dieses Prinzip wurde dazu genutzt, um das treibende Spannungsprofil mittels der Dehnungsdynamik in einer angrenzenden, optisch nicht angeregten Schicht zu messen. Dies ermöglichte die Untersuchung der Dichteanomalie in magnetischen Materialen, die durch den Verlust der magnetischen Ordnung entsteht. Ebenfalls Teil dieser Arbeit ist die Untersuchung von Spannungsprofilen als Quelle von kohärenten akustischen Phononen (Hyperschallwellen). Das raumzeitliche Profil des Spannungsprofils hängt von der Energieverteilung innerhalb der Teilsysteme und ihrer Fähigkeit ab, Energie in Dehnung umzusetzen. Die Auswertung von UXRD Experimenten an Metallen der Seltenen Erden ergab ein Spannungsprofil, dass dem Absorptionsprofil der optischen Anregung entsprach: In der paramagnetischen Phase erzeugte es einen instantanen expansiven Druck, wohingegen in der antiferromagnetischen Phase ein instantaner und ein auf einer $10\,\mathrm{ps}$ Zeitskala ansteigender kontrahierender Druck zusätzlich auftritt. Die beiden charakteristischen Zeitskalen in der antiferromagnetischen Phase sind in Übereinstimmung mit verschiedenen Studien der Demagnetisierungsdynamik in den Metallen der Seltenen Erden.

Einige Publikationen dieser Arbeit beschäftigen sich mit Feld der aktiven Dehnungskontrolle. Dies ermöglich die Kontrolle von Funktionsmaterialen via Dehnung auf ultraschnellen Zeitskalen.

Im Rahmen meiner Doktorandentätigkeit habe ich den lasergetriebenen UXRD Aufbau optimiert, um mit dem hohen Röntgenfluss Experimente mit nur einigen Nanometer dicken Schichten zu ermöglichen. Diese Maschine habe ich um einen zeitaufgelösten Aufbau zur in situ Messung der Reflektivität und Magnetisierungsdynamik mittels magnetooptischem Kerr-Effekt ergänzt. Dies ermöglicht die gleichzeitige Messung von Gitter-, Elektronen- und Magnonendynamik unter derselben Anregebedingung.

Table of Contents

Abbrevations

1D	one-dimensional
3D	three-dimensional
AFM	antiferromagnetic
Al_2O_3	sapphire
BBO	beta-barium borate
BESSY	Berliner Elektronenspeicherring-Gesellschaft für Synchrotronstrahlung
Bi:YIG	bismuth-substituted yttrium iron garnet
CAD	computer-aided design
cf.	confer
CW	continuous wave
e.g.	exempli gratia
ESRF	European Synchrotron Radiation Facility
etc.	et cetera
FePt	iron platinum
HAMR	heat-assisted magnetic recording
HHG	high-order harmonic generation
Ho	holmium
i.e.	id est
LCM	linear chain model
MAMR	microwave-assisted magnetic recording
MgO	magnesium oxide
MOKE	magneto-optic Kerr effect
Nb	niobium
Ni	nickel
NTE	negative thermal expansion
NTM	N-temperature model
PEC	pulse energy change
PM	paramagnetic
PXS	plasma x-ray source
SAW	surface acoustic wave
SSLW	surface skimming longitudinal wave
$TbFe_2$	terbium iron
TR-XRR	time-resolved x-ray reflectivity
UXRD	ultrafast x-ray diffraction
XFEL	x-ray free-electron laser
XRD	x-ray diffraction
XRR	x-ray reflectivity
Y	yttrium

Introduction

FUNCTIONAL materials are the basis of our current live. Without them, computers, smartphones and other electronic devices would not exist. The intrinsic properties such as (anti-)ferromagnetism, ferroelectricity, or superconductivity make these materials useful for different technological applications. These properties can be enhanced or suppressed by changing the geometrical shape or the local environment of these materials, which allows engineering them for certain application [1–5]. Fundamental developments in this field lead to a huge progress e.g. in data storage and communication, sensors, and energy harvesting [6–11].

The understanding of the underlying properties of functional materials are important for the development of new technological applications. Especially for the optimization of data processing and storage speed, the transient response of materials becomes more and more important. In many cases, the physical properties are closely connected to the structural and chemical properties of the materials. This makes scattering techniques using electrons, neutrons, or x-rays useful and sensitive probes of structural details [12–14].

Since their discovery in 1895 by Röntgen [15], x-rays offer insights in the structure of materials and help to understand their nature. Their impact on science is reflected by 25 Nobel Prizes involving x-rays in physics, chemistry, and medicine [14]. The penetrating capabilities of x-rays with short wavelengths give access to x-ray imaging. Monochromatic x-ray radiation provides an element-specific study of the atomic configuration of a material, which allows to infer structural quality, orbital order, magnetic properties, and recently even phonon properties [13, 16–19].

Recent advances in ultrafast X-ray sources allow investigating the transient non-equilibrium atomic configuration after ultrashort photoexcitation of the sample with an ultrafast laser pulse. Therefore, a duration of the probe pulse which is on the order of time scales comparable with atomic motion is required [14]. Synchrotron based sources generate x-ray radiation by acceleration of relativistic electrons and have a typical pulse duration of 100 ps. Special modes (low-alpha) of operating the storage ring provide less than 10 ps pulse durations. Due to the high x-ray flux and the good beam quality, synchrotron sources have been the work-horse of the time-resolved x-ray community. The field of laboratory based ultrafast x-ray sources has two successful approaches using high-power ultrafast lasers: high-order harmonic generation (HHG) sources for generating coherent attosecond x-rays pulse trains in the soft x-ray range [20, 21] and plasma x-ray sources (PXSs) for generating incoherent hard x-ray pulses in the femtosecond regime [14, 22–27]. The advantage of laser-driven x-ray sources is a lack of timing jitter due to the same laser pulse used for both photoexcitation of the sample and for producing x-ray pulses [26–30].

Other methods used for further shortening the x-ray pulses are to manipulate the relativistic electron beam in the synchrotron facilities [31–33], laser-driven x-ray switches based on the acoustic response of a sample after photoexcitation [34, 35] and the transient surface modulations induced by ultrafast

excitation [36, 37]. In the last decade x-ray free-electron lasers (XFELs) have been realized to generate tunable x-ray pulses, orders of magnitudes brighter than synchrotrons with a pulse duration of several femtoseconds and even less [38, 39].

Using any of these sources allow for studying the non-equilibrium dynamics of materials including their coupling between electrons, magnons, phonons and their resulting structural dynamics, which determine the main properties and the possible functions of materials [14, 24, 40–44]. Most of the time-resolved experiments rely on the pump-probe technique: The material is excited from a defined state into a non-equilibrium state with a pump pulse typically delivered by a femtosecond laser system. The sample response is detected with a delayed x-ray probe pulse. Repeating the this procedure with different delays from the same defined initial state reveals the complete dynamics with this stroboscopic technique.

In this work the ultrafast structural response of nanoscale metal multilayers is investigated in order to understand the ultrafast energy flow between and within the layers due to conduction and interaction of the subsystems in the sample. The energy flow in nanoscale heterostructures is of huge interest for further improvements of functional materials. Especially the heat flow in magnetic materials is important for the evolution of the materials' magnetic state, which is highly relevant in technological applications based on magnetic properties.

The energy flow and the resulting energy distribution inside the material becomes accessible because of different contributions to the total lattice response depending on the Grüneisen coefficient. The Grüneisen coefficient describes the efficiency of a system to produce stress from the deposited energy density. This makes it possible to track the energy flux after excitation through different subsystems of the heterostructure. For magnetic and ferroelectric materials or certain phonon modes negative Grüneisen coefficients are observed [45–52]. Depending on the time-scale of the excitation and the coupling of the subsystems, the induced lattice stress can generate coherent acoustic phonon dynamics, in particular in multilayer structures. The analysis of these characteristic signals allows extracting the driving stress profiles. The various interaction channels of the strain with optic [53], electronic [54], and magnetic [55–58] degrees of freedom suggest functions in materials can be engineered to be triggered by coherent strain as selective excitation. However, this requires control of the temporal and spatial shape, frequency, lifetime, etc. of the strain wave. Several publications in this thesis show different realizations for generating and controlling strain and use this as selective excitation for phonons and surface modes. Furthermore, the use of controlled strain excitations as devices, i.e. ultrafast switches, is demonstrated.

The thesis consists of the following chapters: In chapter 2 a list of my articles is given. Chapter 3 presents the main theoretical concepts that are the basis of these articles. In chapter 4 the experimental concepts are briefly discussed and details of the ultrafast x-ray diffraction (UXRD) setup are presented including various modifications, which I add step-by-step between different measurement series. This includes a magneto-optic Kerr effect (MOKE) and optical reflectivity setup to measure the response of electronic, phononic and magnetic systems under the same excitation conditions after ultrafast photoexcitation. The scientific progress developed during my doctoral studies is presented in form of 17 published and unpublished articles in chapter 5. At the end a short conclusion is given in chapter 6.

List of Articles

D URING my doctoral studies in the group ULTRAFAST DYNAMICS IN CONDENSED MATTER headed by Matias Bargheer at the Institute of Physics and Astronomy at the University of Potsdam I (co-)authored 17 published and unpublished articles. These articles are sorted by content in the following list of articles. A short summary of the contents and descriptions of these articles is given including my contribution for each manuscript.

The first three articles focus on heat transport in nano-structures: x-ray diffraction (XRD) experiments provide access to the lattice temperature under equilibrium conditions and/or to the deposited energy in non-equilibrium conditions. The depth sensitivity and chemical selectivity of XRD allows measuring heat and energy transport across nanometer thin layers as well as buried layers capped with opaque layers. In article I the structural response and the energy flow in the ultra-thin gold/nickel double-layer system is discussed. The observed heat transport is two orders of magnitude slower than predicted by the conventional heat transport equation. A modified two-temperature model is introduced to describe the energy flow dictated by electron–phonon coupling. In article II the heat transfer by electrons through a 100 nm copper layer in and out of equilibrium with the lattice is observed and modeled. Electron and phonon pressures impose stresses scaled by the respective Grüneisen constants and the speed of the energy flow between these subsystems is determined by the electron–phonon coupling constants. In article III this behavior is used to measure the electron–phonon coupling constant of gold nanotriangles. Furthermore, the thermal interface conductance between the gold nonotriangles and the substrate is inferred. Such nanoparticles facilitate chemical reactions by illumination with high intensity laser-light. In article IV the thermal limitation is investigated. By varying the laser-spots on the sample from small to big spot sizes the heat transport changes its dimensionality from faster three-dimensional (3D) to slower one-dimensional (1D) transport. This increases the particle temperature up to the melting point.

Jan-Etienne Pudell, Alexei Maznev, Marc Herzog, Matthias Kronseder, Christian Back, Grégory Malinowski, Alexander von Reppert, and Matias Bargheer, *Nature Communications* 9, 3335 (2018)

I initiated the project and upgraded the plasma x-ray source (PXS) setup to achieve the necessary high photon counts on the sample and detector to make the experiments possible. I participated in processing and analysis of the experiments and also in performing the simulations and the modeling. I also contributed to the writing of the manuscript.

Jan-Etienne Pudell, Maximilian Mattern, Michel Hehn, Grégory Malinowski, Marc Herzog, and Matias Bargheer, *Advanced Functional Materials* 30, 2004555 (2020)

I performed the ultrafast x-ray diffraction (UXRD) experiments together with Maximilian Mattern. I analyzed the data and performed the simulations and modeling. Marc Herzog, Matias Bargheer and I led the interpretation of the experiments and prepared the manuscript.

Alexander von Reppert, Radwan Mohamed Sarhan, Felix Stete, **Jan-Etienne Pudell**, Natalia Del Fatti, Aurélien Crut, Joachim Koetz, Ferenz Liebig, Claudia Prietzel, and Matias Bargheer, *The Journal of Physical Chemistry C* 120, 28894-28899 (2016)

I performed the UXRD experiments and the raw data evaluation together with Alexander von Reppert. I commented on the manuscript.

Radwan Mohamed Sarhan, Wouter Koopman, **Jan-Etienne Pudell**, Felix Stete, Matthias Rössle, Marc Herzog, Clemens Nikolaus Zeno Schmitt, Ferenc Liebig, Joachim Koetz, and Matias Bargheer, *The Journal of Physical Chemistry C* 123, 9352-9357 (2019)

I and built the optical setup for the XRD measurements, which was installed on top of the goniometer in the experimental hutch of the KMC3-XPP beamline at the synchrotron facility BESSY II. I participated in the beamtime, performed the data analysis and interpreted the XRD data together with Matthias Rössle. I wrote parts of the manuscript.

In addition to electron and phonon subsystems, a significant part of energy can be stored in magnetic subsystems. The related lattice expansion/contraction can be described by the Grüneisen coefficient. The antiferromagnetic (AFM) rare-earth metals dysprosium and holmium have a large negative Grüneisen coefficient caused by magnetic order, which leads to negative thermal expansion (NTE) by increasing the magnetic entropy. In article V the energy distribution between magnetic and phononic systems and their cooling behavior is discussed. A slow energy transfer from the magnetic to the phononic subsystem after the loss of the AFM spin-order is observed. Around the Néel temperature the spin-order relaxation time is drastically decelerated and can be described by critical phenomena [59]. The coupling between lattice and magnetic order is not only relevant for remagnetization, but also for demagnetization: The magnetic stress generated by the photoexcitation of the magnetic system in holmium can be inferred from the transient strain pulse in the sample as explained in article VI. We found the same time scales for the stress generation process and the demagnetization process. A model considering the saturation of the magnetic energy reservoir is presented in article VII where the lattice dynamics of a dysprosium transducer is discussed as function of the excitation fluence and temperature. In article VIII strain pulses are tracked in a sample: The interaction of the strain pulses in the ferrimagnetic terbium iron ($TbFe_2$) layer is measured using UXRD and magneto-optic Kerr effect (MOKE) techniques.

Alexander von Reppert, **Jan-Etienne Pudell**, Azize Koç, Matthias Reinhardt, Wolfram Leitenberger, Karine Dumesnil, Flavio Zamponi, and Matias Bargheer, *Structural Dynamics* 3, 054302 (2016)

I conducted the XRD and UXRD measurements and raw data evaluation with Alexander von Reppert. I commented on the manuscript.

Jan-Etienne Pudell, Alexander von Reppert, Daniel Schick, Flavio Zamponi, Matthias Rössle, Marc Herzog, Hartmut Zabel, and M. Bargheer, *Physical Review B: Condensed Matter and Materials Physics* 99, 094304 (2019)

I performed the XRD and UXRD experiments and the raw data evaluation together with Alexander von Reppert. I generated the stress profile for the paramagnetic (PM) and AFM phases and used these models as input for the UDKM1DSIM toolbox to run the simulations. I developed most of the presented interpretations and contributed to the writing of the manuscript.

Alexander von Reppert, Maximilian Mattern, **Jan-Etienne Pudell**, Steffen Peer Zeuschner, Karine Dumesnil, and M. Bargheer, *Structural Dynamics* 7, 024303 (2020)

I performed the UXRD experiments together with Alexander von Reppert. I advised Maximalian Mattern on the modeling of the stress profile in the PM and AFM phase used as input for the UDKM1DSIM toolbox to run the simulations. I contributed to the writing of the manuscript.

Steffen Peer Zeuschner, Tymur Parpiiev, Thomas Pezeril, Arnaud Hillion, Karine Dumesnil, Abdelmadjid Anane, **Jan-Etienne Pudell**, Lisa Willig, Matthias Rössle, Marc Herzog, Alexander von Reppert, and Matias Bargheer, *Structural Dynamics* 6, 024302 (2019)

I performed the UXRD experiments and the data evaluation together with Alexander von Reppert. I helped to interpret the simulated spatiotemporal strain to identify the back reflections from the Nb-interface and commented on the manuscript.

In article IX we investigated iron platinum (FePt). As a granular film this material is used for next-generation hard disks: The granular samples have a good resistance against thermal fluctuations providing safe storage of the information. To gain write access to the magnetic structure heat-assisted magnetic recording (HAMR) or microwave-assisted magnetic recording (MAMR) schemes are used. Thus, the

saturation magnetization is reduced by heating of the material [9, 10]. With UXRD one can compare the different strain evolutions after laser excitations between granular and continuous thin films where clamping effects to the substrate play a decisive role. In article X a study of the magneto-elastic properties and the relevant time scales of the magnetic stress after excitation with multiple femtosecond laser pulses is presented.

Alexander von Reppert, Lisa Willig, **Jan-Etienne Pudell**, Matthias Rössle, Wolfram Leitenberger, Marc Herzog, Fabian Ganss, Olav Hellwig, and Matias Bargheer, *Applied Physics Letters* 113, 123101 (2018)

I performed the UXRD experiments and the raw data evaluation together with Alexander von Reppert and contributed to the writing of the manuscript.

Alexander von Reppert, Lisa Willig, **Jan-Etienne Pudell**, Steffen Peer Zeuschner, Gabriel Sellge, Fabian Ganss, Olav Hellwig, Jon Ander Arregi, Vojtěch Uhlíř, Aurélien Crut and Matias Bargheer, *Science Advances* 6, no. 28 (2020)

I performed the UXRD experiments and the raw data evaluation together with Alexander von Reppert and commented on the manuscript.

The excitation of higher-order standing spinwaves in insulating bismuth-substituted yttrium iron garnet (Bi:YIG) is possible with coherent and incoherent phonons [58]. In article XI we monitored the lattice strain after laser excitation and observe coherent and incoherent phonons in the form of propagating strain pulses and localized thermal expansion, respectively. Bi:YIG is excited with near-infrared light corresponding to an energy below its band gap. A quadratic dependence of the lattice strain on the excitation fluence is observed. The variation of the pump pulse duration yields an inverse proportional dependence of the lattice strain on the pulse duration.

Steffen Peer Zeuschner, **Jan-Etienne Pudell**, Alexander von Reppert, Marwan Deb, Elena Popova, Niels Keller, Matthias Rössle, Marc Herzog, and Matias Bargheer, *Physical Review Research* 2, 022013 (2020)

I performed the UXRD experiments and the raw data evaluation together with Steffen Peer Zeuschner. I interpreted the data and contributed to the writing of the manuscript.

The following publications are focused on coherent acoustic phonon wave packets (hypersound waves). These hypersound waves are generated due to displacive electron or phonon stresses with a shape given by the excitation profile as explained in article VI and article VIII. If the amplitude of such a strain wave is sufficiently large, non-linear properties of the medium become relevant: the shape, as well as the frequency spectrum of the hypersound wave changes with propagation. In article XII the second harmonic generation of monochromatic longitudinal acoustic phonon wave packets is observed with

optical methods and UXRD. In most cases solid optoacoustic transducers, typically metals or metallic oxides, are used for hypersound wave generation. For applications, polymer materials are appealing as optoacoustic transducers because of their cost-efficient non-invasive production. In article XIII the amplitude of the hypersound wave generated by an azobenzene optoacoustic transducer was characterized and quantified with UXRD. Due to the well-defined timings of such a hypersound wave with the involved lattice compression and expansion, the hypersound wave can be used as a switch to generate or shorten x-ray pulses as shown in article XIV.

XII   Second harmonic generation of nanoscale phonon wave packets **183**

André Bojahr, Matthias Gohlke, Wolfram Leitenberger, **Jan-Etienne Pudell**, Matthias Reinhardt, Alexander von Reppert, Matthias Rössle, Mathias Sander, Peter Gaal and Matias Bargheer, *Physical Review Letters* 115, 195502 (2015)

I participated in the UXRD experiments at the ID09 beamtime at the European Synchrotron Radiation Facility (ESRF).

XIII   Azobenzene–functionalized polyelectrolyte nanolayers as ultrafast optoacoustic transducers **197**

Elena Pavlenko, Mathias Sander, Steffen Mitzscherling, **Jan-Etienne Pudell**, Flavio Zamponi, Matthias Rössle, André Bojahr and Matias Bargheer, *Nanoscale* 8, 13297 (2016)

I added a setup for second harmonic generation of the laser pulses to the pump stage of the PXS setup for efficient photoexcitation of the azobenzene molecules. I performed the measurements at the PXS setup to quantify the generated strain of an azobenzene transducer and commented on the manuscript.

XIV   Characterization of an ultrafast Bragg-switch for shortening hard x-ray pulses **205**

Mathias Sander, Azize Koç, Christelle T. Kwamen, H. Michaels, Alexander von Reppert, **Jan-Etienne Pudell**, Flavio Zamponi, Matias Bargheer, Jan Sellmann, Jutta Schwarzkopf and Peter Gaal, *Journal of Applied Physics* 120, 193101 (2016)

I performed the UXRD experiments at the PXS to determine the switching time of the device.

In addition to the excitation of the hypersound waves that propagate perpendicular to the surface into a sample, sound waves traveling parallel to the surface can be excited by an ultrashort photoexcitation. In article XV time-resolved x-ray reflectivity (TR-XRR) is used to detect and quantify the absolute periodic surface distortion caused by the incoherent lattice expansion and coherent hypersound waves after laser excitation. Coherent control is applied to gate individual x-ray pulses from the synchrotron pulse pattern. The TR-XRR signal can disentangle multiple coherent modes and incoherent phonon excitation by frequency and wave vector as presented in article XVI. The coherent control technique is useful to enhance or suppress coherent and incoherent modes on ultrafast time scales. In article XVII the advantages of spatiotemporal coherent control are investigated and a detailed view on the setup, method, and data interpretation is presented.

XV   Spatiotemporal coherent control of thermal excitations in solids **215**

Mathias Sander, Marc Herzog, **Jan-Etienne Pudell**, Matias Bargheer, Norbert Weinkauf, Martin Pedersen, Gemma Elizabeth Newby, Jan Sellmann, Jutta Schwarzkopf, Valentin Besse, Vasily V. Temnov and Peter Gaal, *Physical Review Letters* 119, 075901 (2017)

I participated in the experiments at the ID09 beamlime at the ESRF. I prepared the optical setup and performed and evaluated the experiments. I commented on the manuscript.

XVI   Quantitative disentanglement of coherent and incoherent laser-induced surface defor-mations by time-resolved x-ray reflectivity **231**

Mathias Sander, **Jan-Etienne Pudell**, Marc Herzog, Matias Bargheer, Roman Bauer, Valentin Besse, Vasily V. Temnov and Peter Gaal, *Applied Physics Letters* 111, 261903 (2017)

I participated in the experiments at the ID09 beamlime at the ESRF. I prepared the optical setup and performed and evaluated the experiments. I participated in the interpretation of the data and contributed to the writing of the manuscript.

XVII Full spatiotemporal control of laser-excited periodic surface deformations **237**

Jan-Etienne Pudell, Mathias Sander, Roman Bauer, Matias Bargheer, Marc Herzog, and Peter Gaal, *Physical Review Applied* 12, 024036 (2019)

I constructed the setup for transient grating excitations with 3D CAD model. I participated in the experiments at the ID09 beamlime at the ESRF. I prepared the optical setup and performed and evaluated the experiments. I created the 2D numerical model to simulate the measured data. I interpreted the data and contributed to the writing of the manuscript.

During my thesis I developed and improved various setups. As already shown, I constructed an experimental setup for the laser excitation of gold nanoprisms at the KMC3-XPP beamline at the synchrotron facility BESSY II (article IV) and another for transient grating pump and x-ray probe experiments used for the experiments at the ID09-beamline at the ESRF (article XVII). I also helped to improve the setup at the KMC3-XPP beamline with a storage server, network infrastructure and a monitor and configuration setup for the pump beam. In a long-term project I improved the PXS setup step-by-step among the measurements in many aspects and performed a major upgrade to enable experiments that combine the time-resolved measurements of the response of individual subsystems such as the electronic, phononic and magnetic systems to ultrafast photoexcitation. These upgrades are presented in chapter 4 in detail.

Energy and Expansion

I N this chapter I introduce the basic physical concepts relevant for my publications. The experiments I performed are based on the pump-probe method: A sample is excited typically by an ultrashort laser pulse and the system response is tracked by a probe, either x-ray diffraction or optical transmission/reflection change.

In the first section 3.1 I describe how the electromagnetic energy of the laser light is absorbed in a material. An important factor is the spatial energy distribution directly after the laser excitation. Models such as the Bouguer–Lambert–Beer law give a simple exponential profile for the distribution in case of a linearly absorbing medium. If the sample consists of layers with different optical properties, this approach is not sufficient and a more complex transfer-matrix formalism, based on Maxwell's equations, yields a better description of the spatial energy distribution.

The laser excitation in my experiments typically deposits energy in the electronic degrees of freedom of the absorbing material. This energy density is subsequently redistributed inside the sample by two main mechanisms, which may or may not occur in parallel depending on the properties of the involved materials. On the one hand, the energy may be redistributed among distinct coupled energy reservoirs such as electrons, phonons and spins. On the other hand, spatial redistribution of energy may take place in either reservoir via thermal transport. A physical description of the coupling between these systems and their spatial transport is given in section 3.2.

The stored energy inside the reservoirs of the sample normally results in mechanical stress, which is balanced by bonding forces of the lattice resulting in lattice expansion. The amount of stress per energy density is specified by the Grüneisen parameter, which is introduced in section 3.3. Based on the thermodynamic Maxwell's relations between entropy, heat capacity, and pressure, i.e. stress, this parameter can describe not only positive but also negative stress that occurs in some solids, for example due to magnetic excitations, and results in a lattice contraction. A prominent example is Invar, a nickel-iron alloy known for its very small linear thermal expansion coefficient over a wide temperature range around room temperature. In this temperature range the regular lattice expansion due to phonon excitations and anharmonic phonon interactions is counterbalanced by the contractive stress originating from an entropy change in the magnetic system which results in a negative thermal expansion (NTE). I used the Grüneisen parameter approach to quantify the contraction of the rare earth material holmium in the antiferromagnetic (AFM) phase after laser excitation.

If the laser-excited stress sets in on time scales faster than the inverse phonon frequencies of the material, these phonon modes are coherently excited. Consequently, quasi-instantaneous stress triggers longitudinal acoustic (hypersonic) wavepackets that propagate across the layered structure of the sample. Due to the acoustic impedance mismatch of the individual layers of the sample, multiple reflections of the excited sound wave are created and can be observed by ultrafast x-ray diffraction (UXRD). An overview of the

basics of sound-wave propagation is given in section 3.4.

A spatially inhomogeneous excitation along the sample surface generates sound waves propagating on the sample surface, the so-called surface acoustic wave (SAW). In an experiment we used coherent control of these excitations to amplify or suppress the excited surface after the excitation. This technique can be used as ultra-fast switch, for example for x-rays or magnetization.

3.1 Absorption of Light

I N solid materials many excitations lead to the absorption of electromagnetic waves: electronic polarization given by intraband and interband excitations described by Drude–Lorentz oscillators having an imaginary part describing the absorption depending on the frequency. It may additionally result from surface plasmons, magnetic excitations, and more [60, 61]. These physical processes can be described in a macroscopic way by the complex refractive index $n(\omega)$ [60]. Experimental methods such as reflectivity, transmission and absorption spectroscopy or ellipsometry provide access to the frequency-dependent optical properties.

The distribution of absorbed energy inside a sample directly after the excitation of the material is given by the absorption profile. An efficient way to calculate this profile is the Bouguer–Lambert–Beer law as described in section 3.1.1. A more sophisticated way, which is also suitable for more complex sample structures, is given by Maxwell's equations and a matrix formalism. They describe the propagation of light including reflection, transmission, and absorption in materials with the complex refractive index n. In section 3.1.2 a closer view on energy-transfer from an electromagnetic wave to a macroscopic material is given. The propagation of an electromagnetic wave through different materials and the impact of the interface is described in section 3.1.3. To calculate the absorption of a stack of materials with different refractive indices including multiple reflections, a matrix formalism is described in section 3.1.4.

3.1.1 Bouguer–Lambert–Beer Law

A simple approach to describe the attenuation of light in a one-dimensional (1D) model is the Bouguer–Lambert–Beer law

$$\frac{\mathrm{d}I(z)}{\mathrm{d}z} = -\alpha I(z), \tag{3.1}$$

where $\mathrm{d}I$ is the change of the radiant flux due to an infinitesimal slice $\mathrm{d}z$ of the linear absorbing material with the attenuation coefficient α [62]. The 1D approach is substitutable for most pump-probe experiments. This is only valid within an infinite medium without any interfaces [63]. This means any changes of the refractive index n at interfaces, which scale the amplitude of the light flux and lead to reflections at these interfaces, are neglected. If the light is completely absorbed in the first layer of a sample and the reflection at the sample surface is known, the Bouguer–Lambert–Beer law gives the exponential absorption profile inside this layer.

This model can be extended to describe multi-photon absorption processes [61, 64], for example the two-photon attenuation

$$\frac{\mathrm{d}I(z)}{\mathrm{d}z} = -\alpha I(z) - \beta I^2(z), \tag{3.2}$$

with the two-photon attenuation coefficient β. In article XI this differential equation is used to describe the observed strain with a two-photon process in a bismuth-substituted yttrium iron garnet (Bi:YIG).

3.1.2 From Maxwell to an Absorption Profile

For multilayer structures, the Bouguer–Lambert–Beer law approach is not adequate due to different optical constants of the various materials that result in multiple internal reflections, which may interfere constructively or destructively [63, 65, 66]. To account for the interference of all reflections, a transfer-matrix formalism based on the Maxwell equations is used to calculate the absorption while considering the material-specific optical properties using the complex refractive index n [67–71].

The propagation of electromagnetic waves is described by the macroscopic Maxwell equations:

$$\nabla \cdot \mathbf{D} = \rho, \tag{3.3}$$

$$\nabla \cdot \mathbf{B} = 0, \tag{3.4}$$

$$\nabla \times \mathbf{E} + \frac{\partial \mathbf{B}}{\partial t} = 0, \tag{3.5}$$

$$\nabla \times \mathbf{H} - \frac{\partial \mathbf{D}}{\partial t} = \mathbf{j}, \tag{3.6}$$

with the electric induction $\mathbf{D}$, the electric field $\mathbf{E}$ averaged over microscopic regions, the magnetic induction $\mathbf{B}$ averaged over microscopic regions, and the macroscopic magnetic field $\mathbf{H}$. ρ represents the (free) charge density and $\mathbf{j}$ the current density. The spatial partial derivatives are represented by the three-dimensional (3D) vector differential operator nabla (∇). The effect of the material on the electromagnetic field is described by two vector fields: the electric induction $\mathbf{D}$ and magnetic field $\mathbf{H}$. These vector fields are related to the electric field $\mathbf{E}$ and magnetic induction $\mathbf{B}$ by two phenomenological equations:

$$\mathbf{D} = \varepsilon_0 \mathbf{E} + \mathbf{P} = \varepsilon \mathbf{E}, \tag{3.7}$$

$$\mathbf{H} = {}^1\!/\!\mu_0 \mathbf{B} - \mathbf{M} = {}^1\!/\!\mu \mathbf{B}, \tag{3.8}$$

where $\mathbf{P}$ is the dielectric polarization of the material and $\mathbf{M}$ the magnetization [72–74]. With the dielectric permittivity $\varepsilon = \varepsilon_0 \varepsilon_r$ and the magnetic permeability $\mu = \mu_0 \mu_r$ the linear response of the material is described. For isotopic materials ε and μ can be represented by scalars, however, if the material is anisotropic a tensor representation is necessary.

To describe electromagnetic waves in a macroscopic volume free of electric charges and currents the Maxwell equations (3.5, 3.6) are transformed into two wave equations for the electric field

$$\Delta \mathbf{E} - \varepsilon \mu \frac{\partial^2 \mathbf{E}}{\partial t^2} = 0 \tag{3.9}$$

and the magnetic field

$$\Delta \mathbf{H} - \varepsilon \mu \frac{\partial^2 \mathbf{H}}{\partial t^2} = 0 \tag{3.10}$$

using Maxwell's equations (3.3, 3.4) and the phenomenological equations (3.7,3.8) by elimination of $\mathbf{D}$ and $\mathbf{B}$ and conversion of the nabla operator (∇) to the Laplace operator (Δ) by an appropriate product rule. The propagation speed of the electromagnetic wave can be identified with $c = {}^1\!/\!\sqrt{\varepsilon\mu}$ and possible solutions of the wave equations (3.9, 3.10) are plane wave eigenmodes:

$$\mathbf{E}(\mathbf{x}, t) = \mathbf{E}_0 \, e^{-i(\omega t - \mathbf{k} \cdot \mathbf{x})}, \tag{3.11}$$

$$\mathbf{H}(\mathbf{x}, t) = \mathbf{H}_0 \, e^{-i(\omega t - \mathbf{k} \cdot \mathbf{x})} \tag{3.12}$$

with the angular frequency ω and the wave vector $\mathbf{k}$. The real part of the solutions (3.11) and (3.12)

represents the physical electromagnetic field. The electric and the magnetic field are connected by

$$\mathbf{k} \times \mathbf{E} = \omega \mu \mathbf{H},$$ (3.13)

$$\mathbf{k} \times \mathbf{H} = -\omega \varepsilon \mathbf{E}$$ (3.14)

resulting from equation (3.5) and equation (3.6), respectively. For their amplitude follows $\mu \mathbf{H}^2 = \varepsilon \mathbf{E}^2$. The relation between wave vector and the angular frequency is given by

$$\frac{\mathbf{k}^2}{\omega^2} = \varepsilon \mu = n^2$$ (3.15)

where n is the complex refractive index.

The energy flux of the electromagnetic wave is given by the Poynting vector [72, 73]

$$\mathbf{S} = \mathbf{E} \times \mathbf{H}.$$ (3.16)

The Poynting vector represents the instantaneous rate of energy flow through a reference area due to propagating electromagnetic waves. For the absorption the time-averaged energy flux $\langle \mathbf{S} \rangle_t$ is of interest in which the field oscillations are not considered. Separating the temporal evolution $\exp(-i\omega t)$ from equations (3.11) and (3.12) allows for averaging over a full period of $2\pi/\omega$ of the oscillation:

$$\langle \mathbf{S} \rangle_t = \int_0^{2\pi/\omega} \Re \left(\mathbf{E}(\mathbf{x}) e^{-i\omega t} \right) \times \Re \left(\mathbf{H}(\mathbf{x}) e^{-i\omega t} \right) dt$$

$$= \frac{1}{2} \Re \left(\mathbf{E}(\mathbf{x}) \times \mathbf{H}^*(\mathbf{x}) \right),$$ (3.17)

where * labels the complex conjugate. For the plane wave eigenmodes (3.11) and (3.12), the time-averaged Poynting vector (3.17) can be simplified to

$$\langle \mathbf{S} \rangle_t = \frac{1}{2} \Re \left(\frac{1}{\mu \omega} \left(\mathbf{E}(\mathbf{x}) \cdot \mathbf{E}^*(\mathbf{x}) \right) \mathbf{k} \right)$$

$$= \Re \left(\frac{\sqrt{\varepsilon \mu}}{\mu} \mathbf{E}_0 \cdot \mathbf{E}_0^* e^{-2\Im(\mathbf{k}) \cdot \mathbf{x}} \right) \mathbf{k}_{\mathrm{u}}$$ (3.18)

using equation (3.13). Note that the Poynting vector is parallel to the unit wave vector $\mathbf{k}_{\mathrm{u}}$ and perpendicular to the electric field $\mathbf{E}$ and the magnetic field $\mathbf{B}$.

The absorption profile $dA(z)$ is given by the spatial variation of $\langle \mathbf{S} \rangle_t$ along the sample depth z

$$dA(z) = -\frac{\partial}{\partial z} \langle \mathbf{S} \rangle_t = \Re \left(\frac{\sqrt{\varepsilon \mu}}{\mu} \Im(k_z) \mathbf{E}_0 \cdot \mathbf{E}_0^* e^{-2\Im(k_z) \cdot z} \right)$$

$$= \Re(n) \Im(k_z) I(z)$$ (3.19)

where $I(z) = \mathbf{E}_0 \cdot \mathbf{E}_0^* e^{-2\Im(k_z)z}$ is the intensity of the electromagnetic wave and k_z the z-component of the wave vector $\mathbf{k}$. At frequencies of optical light $\mu_r = 1$ is a good approximation in the macroscopic picture [72, 74, 75]. A different ansatz using Ohm's law shown in [60] gives a comparable result.

Comparing equation (3.19) with the solution of (3.1) the absorption coefficient is related to the refractive index as

$$\alpha = 2\Im(k_z) = 2\Im(n)k_{z0} = 2\Im(n) \frac{2\pi c_0}{\lambda}$$ (3.20)

where k_{z0} is the z-component of the wave vector $\mathbf{k}_0$ in vacuum and $\lambda = 2\pi c_0/\omega$ is the wavelength of the electromagnetic wave with the speed of light c_0 in vacuum.
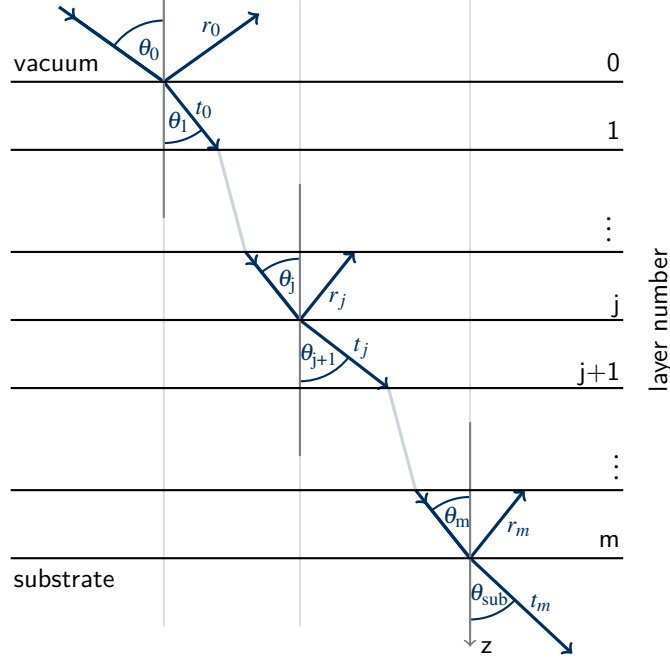
Figure 3.1

A multilayer thin film sample with m layers on top of a substrate: The light arrives under an angle θ_0 on the sample surface where part of the incoming light is reflected and the rest is transmitted into the first layer under an angle θ_1 given by Snell's law. In analogy to the first interface, the refractive angle θ_j can be calculated for every layer using this procedure. The amplitudes of the reflected and transmitted light are given by the Fresnel coefficients r_j and t_j for each interface as well as for the substrate.

3.1.3 Propagation of Electromagnetic Waves

Most of the investigated samples consist of more than one material. Often a capping layer is necessary to protect the sample from oxidation, also a substrate is necessary to handle the thin layers in a practicable way. In some cases the substrate or an additional layer controls sample properties for example by strain or other interface-driven effects like structural defects and the associated reordering of unit cells, or the screening of charges or spins. If the penetration depth extends over more than one material layer, the optical properties change at every interface. A sketch of a typical sample containing m layers and a substrate is shown in figure 3.1 with θ_0 incidence angle from the light to the sample and n_0 is the refractive index of the surrounding medium. Every interface dividing two layers will split an incoming light beam in a transmitted and reflected part. At every interface between different materials, the boundary condition of continuous electro-magnetic fields demands that the in-plane components of the wave vector must be the same for the incoming, reflected and transmitted wave. The propagation directions of the waves lie in one plane, i.e. the so-called plane of incidence (here the x, z plane). With equation (3.15) and the trigonometric relations for the wave vector components $k_{z,j} = |\mathbf{k}_j| \cos(\theta_j)$ and $k_{x,j} = |\mathbf{k}_j| \sin(\theta_j)$ it follows that the angle of the reflected beam to the surface is equal to the angle of the incident beam to the surface, which is given by the law of refraction (Snell's law):

$$\frac{\sin \theta_j}{\sin \theta_{j-1}} = \frac{n_{j-1}}{n_j}. \tag{3.21}$$

Note that the angle θ_j can generally be complex if the refractive index is complex.

In addition to the incidence and transmittance angle, the amplitude of the reflection and transmission is also relevant. In our measurement geometry we use parallel polarized light that means the electric field **E** of the pump light oscillates parallel to the plane of incidence (p-polarized). Thus, the magnetic field **H** of

the electromagnetic wave is perpendicular to the plane of incidence, the xz-plane. The boundary conditions require continuity of H_y and E_x. Hence, the magnetic field amplitude in the first medium j, which is the sum of the incident and reflected field, matches the amplitude of the transmitted field: $H_{i,y} + H_{r,y} = H_{t,y}$, i.e. $\mathbf{H}_i + \mathbf{H}_r = \mathbf{H}_t$. With the amplitude relations between magnetic and electric field resulting from equations (3.13) and (3.14) we obtain for the electric field $\sqrt{\varepsilon_j/\mu}\,(|\mathbf{E}_i| + |\mathbf{E}_r|) - \sqrt{\varepsilon_{j+1}/\mu}\,|\mathbf{E}_t|$. The continuity of E_x results in $\cos\theta_j\,(|\mathbf{E}_i| - |\mathbf{E}_r|) - \cos\theta_{j+1}\,|\mathbf{E}_t|$ under consideration of the geometrical conditions. Solving the equations gives the Fresnel equations for p-polarized light, here for the interface of the jth and $(j+1)^{\text{th}}$ layer:

$$E_{r,j} = r_j E_{i,j}, \tag{3.22}$$

$$E_{t,j+1} = t_j E_{i,j} \tag{3.23}$$

with the reflection and transmission factor for the electric field

$$r_j = \frac{n_{j+1}\cos(\theta_j) - n_j\cos(\theta_{j+1})}{n_{j+1}\cos(\theta_j) + n_j\cos(\theta_{j+1})} \tag{3.24}$$

$$t_j = \frac{2n_j\cos(\theta_j)}{n_{j+1}\cos(\theta_j) + n_j\cos(\theta_{j+1})} \tag{3.25}$$

The reflectance R and the transmittance T of light are given by $R = r^2$ and $T = t^2$. It follows $R + T = 1$ which is a consequence of energy conservation. Note that $\mu = 1$ is assumed for these equations, which is a good approximation for optical light [72, 74, 75].

3.1.4 Transfer-Matrix Formalism

With the calculated angles θ_j, the reflection and transmission amplitudes r_j and t_j at every interface, a transfer-matrix method [67–71, 76] enables the calculation of the electric field amplitude as well as the absorption profile in a sample containing multiple materials and taking interference effects into account. The matrix formalism considers the amplitudes of the forward and backward propagating electric fields:

$$\begin{pmatrix} E_{t,0} \\ E_{r,0} \end{pmatrix} = \mathbf{S} \cdot \begin{pmatrix} E_{t,\text{sub}} \\ E_{r,\text{sub}} \end{pmatrix} \tag{3.26}$$

where the propagation of the electromagnetic wave through the layer structure is represented by the propagation matrix $\mathbf{S}$. To derive the propagation matrix we have to consider the phase change during the propagation of the electromagnetic wave through the layer with thickness d_j which is changing by

$$\mathbf{L}_j = \begin{cases} \begin{pmatrix} 1 & 0 \\ 0 & 1 \end{pmatrix} & j = 0 \\[12pt] \begin{pmatrix} e^{-ik_{j,z}d_j} & 0 \\ 0 & e^{ik_{j,z}d_j} \end{pmatrix} & j > 0 \end{cases} \tag{3.27}$$

with

$$k_{j,z} = \frac{2\pi n_j}{\lambda}\cos(\theta_j). \tag{3.28}$$

At the vacuum – sample interface ($j = 0$) the phase of the electromagnetic wave is set to 0 for simplicity. At every interface j the amplitudes of the forward and backward propagating electromagnetic waves are

changed by

$$\mathbf{J}_j = \frac{1}{t_j} \begin{pmatrix} 1 & r_j \\ r_j & 1 \end{pmatrix}. \tag{3.29}$$

The resulting transfer matrix describing the complete multilayer structure is the matrix product of all propagation and phase change matrices:

$$\mathbf{S} = (\mathbf{L}_0 \cdot \mathbf{J}_0) \cdot (\mathbf{L}_1 \cdot \mathbf{J}_1) \cdots (\mathbf{L}_m \cdot \mathbf{J}_m)$$

$$= \prod_{k=0}^{m} \mathbf{L}_k \cdot \mathbf{J}_k. \tag{3.30}$$

With this transfer matrix, the reflection and transmission for the complete sample results in

$$R_{\text{sample}} = \left| \frac{\mathbf{S}_{(1,0)}}{\mathbf{S}_{(0,0)}} \right|^2,$$

$$T_{\text{sample}} = \Re \left(\frac{n_{\text{sub}}^* \cos(\theta_{\text{sub}})}{n_0 \cos(\theta_0)} \right) \left| \frac{1}{\mathbf{S}_{(0,0)}} \right|^2 \tag{3.31}$$

where the index $m + 1$ is labeled sub for substrate. To get the depth dependence of the absorbed light intensity, we have to calculate the matrix for the intermediate field for every layer

$$\mathbf{D}_{\text{sub}} = \frac{1}{\mathbf{S}_{(0,0)}} \begin{pmatrix} 1 & 0 \\ 0 & 1 \end{pmatrix}, \tag{3.32}$$

$$\mathbf{D}_j = \left(\prod_{k=j}^{m} \mathbf{L}_k \cdot \mathbf{J}_k \right) \cdot \mathbf{D}_{\text{sub}}. \tag{3.33}$$

The amplitude of the electric light field is given for the forward propagating beam and the backward propagating beam by

$$E_{\text{t},j}(z) = \mathbf{D}_{j,(0,0)} \, e^{ik_{j,z} z} \tag{3.34}$$

$$E_{\text{r},j}(z) = \mathbf{D}_{j,(1,0)} \, e^{-ik_{j,z} z} \tag{3.35}$$

with the out-of-plane wave vector $k_{j,z}$ given by equation (3.28) for every layer. Note that the parameter z is the depth of every individual layer j.

We can simplify the mathematical description by setting the amplitude of the electromagnetic field in x direction to 0, due to the rotation symmetry. The electric field then reads

$$\mathbf{E}_j(z) = \begin{pmatrix} 0 \\ E_{\text{t},j}(z) \cos(\theta_j) - E_{\text{r},j}(z) \cos(\theta_j) \\ -E_{\text{t},j}(z) \sin(\theta_j) - E_{\text{r},j}(z) \sin(\theta_j) \end{pmatrix} \tag{3.36}$$

With the electric field (3.36) the intensity is calculated as

$$I_j(z) = \Re \left(\mathbf{E}_j(z) \cdot \mathbf{E}_j^*(z) \right) \tag{3.37}$$

and the related absorption profile of the jth layer in the sample is given by

$$dA(z) = 2 \Re \left(\frac{n_j \cos(\theta_j)}{n_0 \cos(\theta_0)} \right) \Im (k_{j,z}) I_j(z) \tag{3.38}$$

for every layer. Merging of all m layers results in the full absorption profile.

The necessary optical constants for the calculation can be found in databases [77], publications or can be measured for example with ellipsometry [76, 78]. The thickness of the individual layers can also be

inferred from ellipsometry data or measured directly with x-ray reflectivity (XRR) [79, 80] as exemplified in articles I, II, IV, VI and IX.

3.2 Heat and Heat Transport

THE energy supplied by the laser excitation with a spatial profile (given by the rules of the electrodynamic Maxwell equations as discussed in the last section) is absorbed in the material. Depending on the excitation process, the energy is stored in electronic, lattice, or magnetic excitations of the material and results in an increased energy density of the typically coupled systems.

The heat capacity relates the energy density ρ^Q in a system to the temperature T:

$$\rho_e^Q = \int_0^{T_e} C_e(T)\mathrm{d}T = \int_0^{T_e} \gamma^S T \mathrm{d}T, \tag{3.39}$$

$$\rho_{ph}^Q = \int_0^{T_{ph}} C_{ph}(T)\mathrm{d}T, \tag{3.40}$$

$$\rho_{sp}^Q = \int_0^{T_{sp}} C_{sp}(T)\mathrm{d}T, \tag{3.41}$$

where $C_e(T)$, $C_{ph}(T)$, and $C_{sp}(T)$ are the electronic, lattice and magnetic heat capacity of the material per unit volume, respectively. In the Sommerfeld model the electronic heat capacity increases linearly with the temperature of the electronic system, T_e. The proportionality constant is the Sommerfeld constant γ^S [60, 81]. The phonon lattice heat capacity can be described by the Debye model [60]. Using models for the electronic and lattice heat capacity allows for separating the magnetic heat capacity from the measured total heat capacity, which was used in article V.

The redistribution of the light-induced energy in the material can occur by (thermal) transport within the electronic, lattice and magnetic subsystems and by energy exchange between these subsystems. For samples that consist of very thin layers where the mean free path of the energy transporting (quasi)-particles, e.g. electrons, phonons, and magnons is larger than the thickness of the system, the heat transport can be described by coupled heat baths for every subsystem, disregarding the spatial dependence. This kind of model is introduced in the next section and is used in article I to describe the thermal energy (heat) transfer from a combined system (electrons + nickel lattice) to the gold lattice on a 100 ps time scale.

For layers and layer structures larger than the mean free path the conduction of heat has to be accounted for. In article II the measurement and a modeling of the non-intuitive heat transport from an excited platinum layer to a nickel layer through 100 nm of copper are shown and discussed.

3.2.1 Exchange of Heat

The exchange of heat between N coupled subsystems is described by rate equations in form of differential equations [82, 83]:

$$\frac{\partial T_n}{\partial t} = \sum_{n'} \frac{g_{n,n'}}{C_n} \left(T_{n'} - T_n \right), \tag{3.42}$$
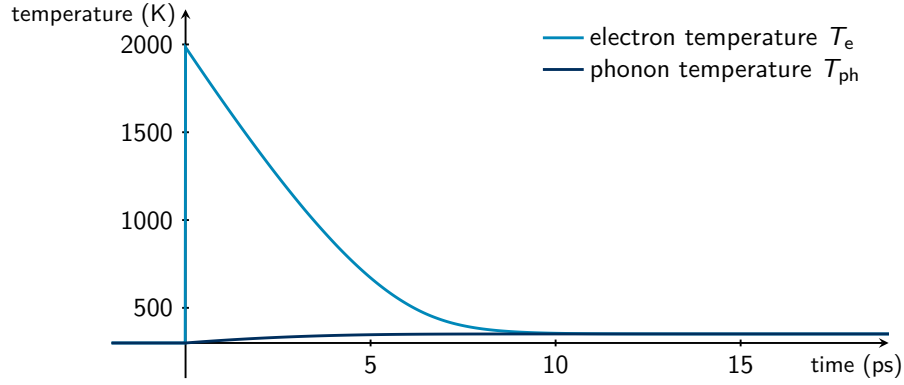
Figure 3.2

Solution of a two-temperature model for the excitation of a 10 nm gold film: The electron temperature T_e reaches $\approx 2000\,\text{K}$ after a 30 fs laser excitation with an absorbed fluence of $130\,\mu\text{J/cm}^2$. (Note this is equivalent to an incoming fluence of $3\,\text{mJ/cm}^2$. With the transfer-matrix formalism from section 3.1.4 an absorption of 4% is calculated: 28% are reflected and 68% transmitted). On a 3-ps time-scale the energy is transferred to the phonon system (lattice). After $\approx 10\,\text{ps}$ electrons and phonons are in equilibrium at 350 K.[1]

where $n, n' \in [1, \ldots, N]$ and $n \neq n'$. In this equation T_n is typically the electron or phonon temperature T_e, T_{ph} with the respective heat capacities $C_n = C_e$, C_{ph} and $g_{n,n'} = g_{e,ph}$ is the electron–phonon coupling constant, describing the rate at which heat is exchanged between electrons and phonons. The solution to this equation assuming temperature-independent heat capacities for a single unit cell or a single spatially equilibrated thin film is an exponential temperature decay of one system and a simultaneous rise of the other. The characteristic time scale of this process is the electron–phonon coupling time $\tau_{e,ph} = C_e C_{ph}/\left(g_{e,ph}\left(C_e + C_{ph}\right)\right)$. Note that $\tau_{e,ph}$ is only a constant, assuming temperature-independent heat capacities.

Considering the temperature dependence of the electronic heat capacity (cf. equation 3.39) results in an almost linear decay of the electron temperature in the first picoseconds. For a thin gold film this temporal evolution of the electron and phonon temperatures are shown in figure 3.2.

In article III we investigate the transient lattice strain of laser-excited gold nanotriangles. The observed transient strain is due to mechanical stress, which has two contributions: the electron and phonon subsystems produce a different stress for the same amount of deposited energy, which is commonly expressed by different Grüneisen parameters that are given by equation (3.51) and discussed in more detail in section 3.3.1. A model for the strain and stress in a gold nanotriangle after laser excitation depends on the ratio of the Grüneisen constants and an energy transfer time given by the electron–phonon coupling constant. Fitting the model to the ultrafast x-ray diffraction (UXRD) data determines the ratio of the Grüneisen constants and the electron–phonon coupling time of gold nanotriangles.

As already mentioned a model based on coupled subsystems is used in article I to describe the observed lattice strains of a 5 nm gold and a 10 nm nickel layer. The heat exchange between a gold and nickel layer is described by two coupled heat baths: (i) the gold lattice and (ii) the joint heat bath of directly excited electrons in gold and nickel as well as the strongly coupled nickel lattice. Here the heat baths scale with the phonon heat capacities times the layer thicknesses as the electron heat capacities are negligibly small compared to the phonon heat capacities. This model describes only the coupling in gold, because the nickel phonons are assumed to be already thermally equilibrated with the electrons. However the electron–phonon coupling constant $g_{e,ph}$ in our model is scaled with the gold layer thickness.

---

[1] Calculated with the UDKM1DSIM toolbox [84]. Relevant parameters are taken from article I.

3.2.2 Heat Conduction

If the layer thickness is larger than the mean free path of the heat conductors, the heat conduction can be described by thermal diffusion. The speed of the diffusion process is given by the thermal conductivity κ, which specifies the amount of energy transported per time and length. In metals the heat is transported mainly by electrons. In a microscopic picture the electrons carry the thermal energy given by the heat capacity C_e at Fermi velocity v_F through the unit volume of the material. These conduction electrons are scattered multiple times with other electrons or the lattice, i.e. phonons, thus they can be described by a diffusion process with a temperature gradient. The resulting thermal conductivity of the electrons for the isotropic case is

$$\kappa_e = \frac{1}{3}\frac{C_e v_F^2}{\nu} \tag{3.43}$$

where ν is the collision rate. In introductory textbooks the mean free path $\bar{l} = v_F/\nu$ is often used instead of the collision rate [60]. The collision rate consists of two contributions: (i) the electron–electron collision rate $\nu_{e,e} = AT_e^2$ and (ii) the electron–phonon collision rate $\nu_{e,ph} = BT_{ph}$ [85, 86]. With these equations and the temperature-dependent electron heat capacity given by the Sommerfeld model (cf. equation (3.39)) an electron and phonon temperature-dependent conductivity is given by

$$\kappa_e = \frac{1}{3}\gamma^S v_F^2 \frac{T_e}{AT_e^2 + BT_{ph}}. \tag{3.44}$$

Only for extreme electron temperatures the electron–electron collision term AT_e^2 becomes relevant. For typical temperatures after laser excitation T_e, $T_{ph} \ll 1\,\text{eV}/k_B$ and for the electron–electron collision rate follows $\nu_{e,e} \ll \nu_{e,ph}$ [85]. In this case, the simplified equation for the conductivity in non-equilibrium condition, i.e. $T_e \neq T_{ph}$, is

$$\kappa_e = \frac{1}{3}\gamma^S v_F^2 \frac{T_e}{BT_{ph}} = \kappa_0 \frac{T_e}{T_{ph}} \tag{3.45}$$

where κ_0 is the heat conductivity for electrons and phonons in equilibrium.

For example, the electron temperature after laser excitation rapidly increases to thousands of Kelvin (cf. figure 3.2), which leads to a higher thermal conductivity, i.e. the amount of energy transported by an electron is increased. When the phonon temperature increases on subsequent time scales (e.g. due to electron–phonon coupling) the heat conductivity is reduced by a shorter mean free path of the heat conducting electrons.

The heat diffusion is modeled by Fourier's law, which connects the heat transfer to a temperature gradient. In introductory textbooks the following equation is given [87]:

$$C\frac{\partial T}{\partial t} = -\kappa\frac{\partial^2 T}{\partial z^2}. \tag{3.46}$$

Considering the temperature dependence of the heat conductivity $\kappa(T)$, expanding this equation to N subsystems and connecting them with the subsystem coupling constant $g_{n,n'}$ gives a set of N equations (N-temperature model (NTM)) [84, 88–90]:

$$C_n(T_n,z)\frac{\partial T_n(z)}{\partial t} = \frac{\partial}{\partial z}\left(\kappa_n(T_n,T_{n'},...,z)\frac{\partial T_n(z)}{\partial z}\right) + \sum_{n'} g_{n,n'}(T_n,T_n',z) + S_n(z,t), \tag{3.47}$$

where the heat transfer is the temporal change of the individual heat of the nth system, given by the heat capacity $C_n(T_n)$ at a temperature T_n. A source term $S_n(z,t)$ describes the laser excitation of the material that typically occurs in the electronic subsystem. The heat capacity, the heat conductivity, the coupling term, and the source term are material-dependent. For a heterostructure these values depends on the

sample depth z in the model because of the different materials along the z coordinate.

We solved these equations for two coupled systems (electrons and phonons) with a numerical solver [84] to calculate the transport from a thin laser excited platinum layer to a nickel layer though a 100 nm copper in article II. For different copper thicknesses we found a linear increase of the arrival time, identified by the rise of the electron temperature in nickel to 1%, 10% or 33% of the maximum electron temperature in nickel. This linear increase could potentially be misinterpreted as ballistic electron transport that takes place at the constant Fermi velocity.

3.3 Stress and Strain

AFTER laser excitation or heating of a material, an expansion of the material is typically observed. This is related to an excitation of electrons or phonons by heating due to the deposited laser energy. This energy is stored in kinetic energy of electrons or vibrations of the lattice (phonons) and can produce an electronic or phononic pressure in the solid, the stress σ.

In figure 3.3 a typical anharmonic potential of an atomic bond is sketched: With increased temperature or energy density the amplitude of the vibrations is increased. For this reason the equilibrium position (lattice constant) is shifted to larger distances, which produces pressure (stress) in the system. In equilibrium, the stress σ results in an expansion, i.e. strain η. In this section I will introduce a thermodynamic model, which describes the generation of stress and strain by introducing the Grüneisen constant that relates energy to stress or equilibrium strain.

3.3.1 Thermodynamics of (Negative) Thermal Expansion

A macroscopic view to describe thermal expansion is given by thermodynamics [45, 91, 92]: The volumetric thermal expansion β is defined as the relative change of the volume V per temperature change $\mathrm{d}T$ at constant pressure p:

$$\beta = \frac{1}{V}\left(\frac{\partial V}{\partial T}\right)_p . \tag{3.48}$$
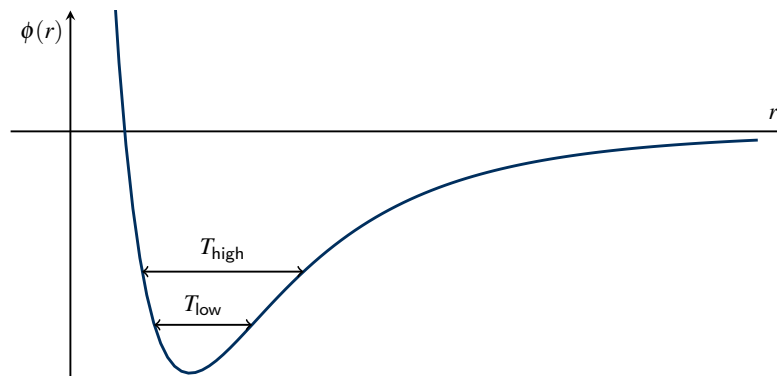
Figure 3.3

A anharmonic potential $\phi(r)$ is sketched, as could describe the binding forces in dependence of the atomic distance r of an atom: The minimum of the curve gives the lattice constant at 0 K. Increasing the temperature from low temperature T_{low} to high temperatures T_{high} results in a larger amplitude of the atomic vibrations, indicated by the arrows and in an increased mean position, representing a larger lattice constant. Thus, the anharmonic potential leads to a positive thermal expansion [91].

Using Maxwell's relations for thermodynamic potentials, β can be expressed as

$$\beta = \frac{1}{V}\left(\frac{\partial V}{\partial T}\right)_p = -\frac{1}{V}\left(\frac{\partial S}{\partial p}\right)_T = -\frac{1}{V}\left(\frac{\partial V}{\partial p}\right)_T\left(\frac{\partial S}{\partial V}\right)_T = \chi_T\left(\frac{\partial S}{\partial V}\right)_T, \tag{3.49}$$

where χ_T is the isothermal compressibility. Hence, β is related to the entropy change of the material.

For example the entropy change in water below 4°C causes a negative thermal expansion (NTE). There the break-up of the tetrahedral H-bonding causes an increase of entropy and a contraction of water, which compensates the expansion due to thermal heating [91].

Another transformation of the equation (3.49) relates β to thermally induced stress (pressure) at constant volume. This occurs directly after laser excitation of a solid due to the limitation of the expansion by the sound velocity:

$$\beta = \chi_T\left(\frac{\partial p}{\partial T}\right)_V = \left(\frac{\partial p}{\partial T}\right)_V\left(-\frac{\partial \ln V}{\partial p}\right)_T = \left(\frac{C_V}{V}\right)\Gamma\left(-\frac{\partial \ln V}{\partial p}\right)_T, \tag{3.50}$$

where C_V/V is the volumetric heat capacity and Γ is the Grüneisen parameter. The heat capacity determines how much energy the material gains during a given temperature increase and the thermodynamic Grüneisen parameter Γ determines how much stress is generated by this energy [91]:

$$\Gamma = \frac{1}{C_V/V}\left(\frac{\partial p}{\partial T}\right)_V = \left(\frac{\partial p}{\partial(U/V)}\right)_V, \tag{3.51}$$

where U is the internal energy of a system, the total energy contained within the system available for thermodynamic transformations. From equations (3.50) and (3.51) follows:

$$\Gamma = \frac{\beta V}{\chi_T C_V}. \tag{3.52}$$

For isotropic solids, the volumetric thermal expansion coefficient β is connected to the linear expansion coefficient by $\beta = 3\alpha$ [45].

The internal energy U, just as the entropy S, can have different contributions for example from a magnetic order and its change is related to NTE by a negative Grüneisen parameter. This is observed in rare earth metals, e.g. holmium [46], and used for modeling of the ultrafast stress σ and the resulting strain η in article VI:

$$\sigma = \Gamma\rho^Q \quad \rightarrow \quad \eta = \sigma\chi = \Gamma\chi\rho^Q. \tag{3.53}$$

More common than the compressibility χ is the inversely related bulk modulus given as $K = 1/\chi$. The bulk modulus describes volumetric elasticity and for isotropic materials it is connected to Young's modulus E, which describes the tensile elasticity by $K = E/(3-6\nu)$, where ν is Possion's ratio [87]. A more detailed view on the impact of Poisson's ratio on ultrafast experiments, where the in-plane dynamics is usually frozen on the characteristic time scales of the experiments, is given in section 3.4.2.

The advantage of the Grüneisen parameter is its small variations over a wide temperature range. Because of this, the Grüneisen parameter is also named Grüneisen constant [91–93]. Furthermore, the Grüneisen parameter can be used in situations where no temperature can be defined, for example for phonons and electrons. One Grüneisen parameter is not always sufficient to quantify the thermal expansion or stress for all excitations and materials due to the possibility of different Grüneisen parameters for different phonon modes introduced in the following section 3.3.2.

3.3.2 Microscopic View on Stress Generation

After the optical excitation the energy may be stored in different subsystems according to the excitation mechanism. A typical mechanism in semiconductors is the deformation potential, where the inter-atomic forces are modified due to the absorption of a photon, which changes the electronic configuration of the material. This relates to a change of the inter-atomic distances [81, 94, 95]. In metals the Sommerfeld model describes the behavior of free electrons. The electronic pressure is driven by the kinetic energy of the free electrons per volume and the variation of the energy δE per volume V can be described as the electronic heat capacity C_e times the electronic temperature T_e. This description already assumes that the electronic system is thermalized and can be described by a Fermi distribution with temperature T_e. The stress of the electronic system is then given by equation (3.53) and the differential of equation (3.39):

$$\sigma_e = \Gamma_e \frac{\delta E}{V} = \Gamma_e C_e \delta T_e, \tag{3.54}$$

where Γ_e is the electronic Grüneisen parameter, which ist equal to 2/3 for spherical parabolic bands within the Sommerfeld model [60, 94], but differs for real materials [45, 96].

A more general form considering different occupation density changes $\delta n_e(\mathbf{k})$ of the energy states $E_e(\mathbf{k})$ of the electrons and their specific Grüneisen constants $\Gamma_e(\mathbf{k})$ is

$$\sigma_e = \sum_{\mathbf{k}} \Gamma_e(\mathbf{k}) E_e(\mathbf{k}) \delta n_e(\mathbf{k}), \tag{3.55}$$

where $\mathbf{k}$ is the wave vector of the electrons [50, 94, 95, 97]. Note that under the assumption of equal Grüneisen constants for all excited modes, for a non-thermal energy distribution the stress is proportional to the variation of the energy δE. If this energy distribution is equilibrated, i.e. it is a Fermi-Dirac distribution, it can be described by a single temperature value.

Another excitation mechanism is the thermoelastic stress. This mechanism describes the volume change under temperature increase, i.e. thermal expansion [94]. Thermoelastic strain is caused by the thermal expansion, which is in isotropic materials $\eta = 3\alpha\delta T$, where α is the linear thermal expansion coefficient and δT_{ph} the lattice temperature change. With increased phonon population the average lattice constant is increased by the anharmonic lattice potential (see figure 3.3) [81]. A more general description comparable to equation (3.55) takes into account different phonon modes and their occupation

$$\sigma_{ph} = \sum_{\mathbf{k}} \Gamma_{ph}(\mathbf{k}) E_{ph}(\mathbf{k}) \delta n_{ph}(\mathbf{k}) \tag{3.56}$$

where $\Gamma_{ph}(\mathbf{k})$ are the lattice Grüneisen constants of the individual phonon modes, $\delta n_{ph}(\mathbf{k}))$ the phonon occupation density changes and $E_{ph}(\mathbf{k})$ the phonon energy states. Assuming a thermalized phonon system above the Debye temperature simplifies this equation to

$$\sigma_{ph} \approx \Gamma_{ph} C_{ph} \delta T_{ph}, \tag{3.57}$$

where the phonon system is determined by an averaged Grüneisen parameter Γ_{ph} [94], the lattice heat capacity C_{ph}, and lattice temperature change δT_{ph}.

Equation (3.54) and (3.57) have now the same appearance: The stress is given by a unitless proportionality constant, the Grüneisen coefficient and scales with the excitation energy.

3.4 Coherent Phonon Excitation and Propagation

THE thermoelastic stress due to electron or phonon heating of a material initiates a strain change, which results in expansion as explained in section 3.3. This ultrafast process creates a phonon wave packet consisting of phonons with large periods, which are coherently excited by the driving phonon or electron stress. This coherently excited wave packet is known as acoustic hypersound wave. Figure 3.4 depicts the different types of excited sound waves by a point source at the surface of a semi-infinite material: The longitudinal and transverse sound waves propagate inside the bulk material. The surface acoustic wave (SAW), i.e. the Rayleigh mode and the surface skimming longitudinal wave (SSLW) exist on the surface.

Focusing on longitudinal sound waves with wavelengths much larger than the atomic distances propagating along one symmetry direction of a crystal, the acoustic dynamics after laser excitation are described by a 1D wave equation, where the laser excitation is represented in the wave equation by the driving stress gradient $\partial \sigma / \partial z$ inside the sample [87]:

$$\frac{\partial^2 u}{\partial t^2} - v^2 \frac{\partial^2 u}{\partial z^2} = -\frac{1}{\rho} \frac{\partial \sigma}{\partial z}, \tag{3.58}$$

where u, v and ρ are the atomic displacement field, the sound velocity and mass density. Therefore, sound waves are generated only at positions of unbalanced stress as the surface, layer interfaces, or at stress gradients due to the excitation profile.

3.4.1 Discretized Lattice Dynamics

A discretized solution of this problem for a crystal on an atomic level is given by the linear chain model (LCM) based on Hooke's law. In the limit of large wavelengths compared to the discretization distance the solution is equivalent to the solution of the continuum model (equation (3.58)). For every
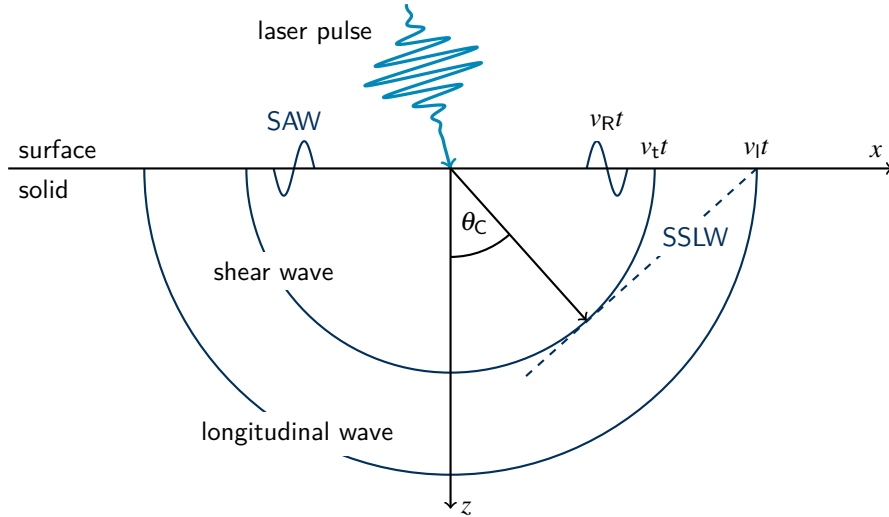
Figure 3.4

Generation of different types of sound waves by a point or line source in an isotropic solid. The longitudinal and transverse sound waves travel with their respective sound velocities v_l and v_t, indicated by two semicircles. The surface acoustic wave (SAW), i.e. the Rayleigh mode, is located at the surface and propagates with the speed v_R. The wavefront of the surface skimming longitudinal wave (SSLW) indicated by the dashed line exists under an angle smaller than the critical angle $\theta_c = \sin(v_t/v_l)$ because the solution of longitudinal wave does not satisfy the boundary condition of a surface [98–100].

atom or unit cell a differential equation

$$m_n \frac{\partial^2 u_n}{\partial t^2} = -k_n \big(u_n - u_{n-1}\big) - k_{n+1} \big(u_n - u_{n+1}\big) + S_n(t) \tag{3.59}$$

is given, where u_n is the displacement of the nth atom (unit cell) with a mass m_n and a spring constant k_n. The atomic mass m_n, the atomic distance (lattice constant) c_n and the sound velocity v_n determine the spring constant $k_n = m_n v_n^2 / c_n^2$. The thermal stress can be introduced in this model by the source term $S_n(t)$, which can be visualized as sticks tensioning the springs between the atoms. An instantaneous change of the stick length releases a sound wave propagating through the linear chain because of the abrupt change of length of the springs.

This system of equations can be solved with numerical methods, for example with the UDKM1DSIM toolbox [84]. The solutions are used in articles I, II, VI–IX, XIII and XIV to compare the result from heat exchange and heat transport models with UXRD data on time scales where the dynamics is dominated by acoustic sound waves and their reflections from interfaces. Furthermore, the cover of this thesis is an example of a spatiotemporal representation of the calculated strain in a thin film heterostructure calculated with the UDKM1DSIM toolbox [84].

Assuming an instantaneous formation of the expansive thermal stress, its shape is transferred to the excited sound wave as the leading compressive and following expansive part of the bi-polar sound wave. When this sound wave travels in or out of a layer, the measured time-dependent strain change is given by the integral over the shape of the sound wave, which gives full access to the excitation profile. Even if the driving stress is time-dependent due to electron–phonon coupling, magnetic coupling, or transport processes, the shape information can be extracted by simulations as shown in article VI and VII. The individual acoustic timings due to the passages of the excited sound wave and their reflections through interfaces allow for a precise layer thickness determination inside the sample. Article VIII shows that this method is also applicable for non-crystalline layers, which are not observable with UXRD, using the characteristic signal of the sound wave and its reflections observed in adjacent crystalline layers.

If the amplitude of the sound wave is sufficiently large, non-linear processes start to be relevant: extending the LCM to an Fermi-Pasta-Ulam chain with non-linear springs (second-order terms and damping) allows the description of the self-interaction of a sound wave [97, 101, 102]. In article XII we observe non-linear phonon propagation, in particular, the second harmonic generation of a synthesized monochromatic acoustic phonon wave packet. For long traveling distances these non-linear interactions become relevant and new high frequency components of the sound wave are generated: First the bipolar strain-wave changes in a self-steepening process to an N-wave and later the formation of a train of ultra-short compressive sound waves (solitons) follows if the damping is small [97, 103, 104].

3.4.2 Poisson Effect in Ultrafast Strain Experiments

If out-of-plane strain observed in an ultrafast experiment is compared quantitatively with strain measured due to a temperature change in an equilibrium experiment, for example to get the temperature of the lattice at a specific time after excitation, an in-plane clamping of the lattice on the ultrafast time scale has to be considered.

In an experiment where the sample is heated slowly, the heating creates a stress in all crystal directions, which results in a strain along all crystal directions. This strain is described by the linear expansion coefficient α or the volume change by the volumetric thermal expansion β (see section 3.3.1). In the ultrafast experiment, the introduced energy also leads to stress in all crystal directions, but the stress produces only strain if there is a stress gradient (see equation 3.58). For the out-of-plane axis the average

strain rises in $\approx 20\,\mathrm{ps}$ for a $100\,\mathrm{nm}$ thick layer (assuming a sound velocity of $5\,\mathrm{nm/ps}$). The in-plane expansion time is given by the size of the excitation spot: assuming a $1\,\mathrm{mm}$ spot size leads to a expansion time of $200\,\mathrm{ns}$.

Thus, in an ultrafast experiment this can be considered as in-plane clamping, which leads to an increased expansion. A thought experiment using the Poisson's ratio relates the lack of in-plane strain to an increased out-of-plane strain η_{uf} according to the elastic properties of the material:

$$\eta_{\mathrm{uf}} = \left(1 + \frac{C_{13}}{C_{33}} \frac{\alpha_1 + \alpha_2}{\alpha_3}\right) \eta_{\mathrm{th}}, \tag{3.60}$$

where C_{ij} are the elastic constants C_{ij} (in Voigt notation [60]), α_j the linear expansion coefficients, and η_{th} the strain measured in a static heating experiment [105, 106].

A more sophisticated way to describe the in- and out-of-plane dynamics of a thin film or small cubes is obtained from the continuum elasticity theory. This describes the spatiotemporal variations of the displacement u_i with

$$\frac{\partial^2 u_i}{\partial t^2} = \frac{1}{\rho} \sum_j \frac{\partial \sigma_{ij}}{\partial x_j}, \tag{3.61}$$

where ρ the mass density and

$$\sigma_{ij} = \sigma_{ij}^{\mathrm{ext}} + \sum_{kl} C_{ijkl} \eta_{kl} \tag{3.62}$$

the total stress consisting of the introduced stress $\sigma_{ij}^{\mathrm{ext}}$ and the dependence of the strain $\eta_{ij} = \mathrm{1/2}(\partial u_i/\partial x_j + \partial u_j/\partial x_i)$[87], scaled by the elastic constant tensor C_{ijkl} (here with all indices). As shown in article X a simplification of theses equations for a thin iron platinum (FePt) needle leads to the following equation for the out-of-plane motion, which is typically measured in our UXRD experiments

$$\rho \frac{\partial^2 u_\perp}{\partial t^2} = \frac{\partial}{\partial z} \left(C_{33}\eta_\perp + 2C_{31}\eta_\| - \sigma_\perp^{\mathrm{sp}} - \sigma_\perp^{\mathrm{e\text{-}ph}}\right) \tag{3.63}$$

$$= \frac{\partial}{\partial z} \left(\sigma_\perp + \sigma_\perp^{\mathrm{Poisson}} - \sigma_\perp^{\mathrm{sp}} - \sigma_\perp^{\mathrm{e\text{-}ph}}\right), \tag{3.64}$$

where $\|$ and $\perp$ represent the in- and out-of-plane components of the stress and strain. For FePt also a stress component $\sigma_\perp^{\mathrm{sp}}$ of the magnetic subsystem has to be considered that counteracts the phonon stress component $\sigma_\perp^{\mathrm{e\text{-}ph}}$ due to the negative Grüneisen parameter of the magnetic subsystem. In equilibrium, i.e. $\partial^2 u_\perp/\partial t^2 = 0$, the out-of-plane strain is given by

$$\eta_\perp = -2\frac{C_{31}}{C_{33}}\eta_\| + \frac{\sigma_\perp^{\mathrm{sp}}}{C_{33}} + \frac{\sigma_\perp^{\mathrm{e\text{-}ph}}}{C_{33}}. \tag{3.65}$$

In this case, a negative out-of-plane strain $\eta_\perp$ occurs if the negative spin-stress $\sigma_\perp^{\mathrm{sp}}$ and the elastic Poisson stress $-2C_{31}\eta_\|$, which only exist due to the in-plane strain, overcompensate the expansive electron–phonon stress $\sigma_\perp^{\mathrm{e\text{-}ph}}$. Transfering this result to a slowly heated continuous thin film (slow enough to circumvent the creation of sound waves), where an in-plane expansion is still absent on fast time scales, i.e. $\eta_\| = 0$, results in an increased out-of-plane strain under the assumption of a small or no spin stress contribution.

These considerations are highly relevant for the quantitative analysis of the observed lattice strain in an ultrafast experiment. The direct mapping of lattice strain in an ultrafast experiment to the deposited energy or a temperature change only results in the correct magnitude of the quantities if one considers the Poisson contribution.

3.4.3 Acoustic Waves on Surfaces

In addition to acoustic waves propagating in the bulk of a material, there are solutions of the wave equation that are localized at the material's surface, so called surface acoustic waves (SAWs). These SAWs are similar to water waves, but in contrast to water waves the potential energy depends on elastic resilience instead of gravity. SAWs are also named after their discoverer Lord Rayleigh [107]: Rayleigh mode or wave. The SAW has a longitudinal component and a vertical shear component, so that they can fulfill the boundary conditions at the surface. A fixed point on the surface follows an elliptical path during the passage of a SAW. In figure 3.4 the SAW is sketched at the surface traveling with its sound velocity v_R.

In addition to the SAW other modes such as the SSLW also modulate the surface. The SSLW exists due to the boundary conditions, which are not fulfilled by the bulk longitudinal sound waves at the surface [98–100]. In comparison to the SAW, the SSLW has a higher sound velocity: on the surface it propagates with the speed of the longitudinal sound wave [99]. Furthermore, the SSLW radiates energy into the depth of the sample and therefore its amplitude is highly damped. The SSLW occurs in the region below a critical angle ($\Theta > \Theta_C$) as sketched in figure 3.4 [99]. Its wavefront is parallel to the dashed line.

In the experiments related to articles XV–XVII two counter propagating SAWs and SSLWs are excited by a diffraction grating generated by two laser pulses tilted with respect to each other. The diffraction grating selects the spatial period of the SAW and SSLW. After the ultrafast excitation, multiple modes are excited (as sketched in figure 3.4). Measuring time-resolved x-ray reflectivity (TR-XRR) in a grazing incidence geometry allows to decompose the excited modes as shown in article XVI from the measured surface deformation.

This excitation method also allows us to implement a coherent control scheme for the spatiotemporal acoustic dynamics and also allows for the spatial deformations excited by heat. In article XVII we explain a method and a setup to perform coherent control of surface modes: This setup allows exciting the sample with two spatiotemporally shifted diffraction gratings. With a spatial phase shift of π of the two temporally delayed pulses the sample experiences no thermal transient grating, only an overall displacement of the sample surface. If the excitation is performed without a spatial phase shift, the thermal transient grating is enhanced. Changing the temporal delay of the two pulses cancels or amplifies the acoustic surface modes depending on their frequency.

Furthermore, the method can be used as a thermal and acoustic switch on ultrafast time scales. In article XV we show that the thermal and acoustic grating can be controlled on a time scale shorter than the period of the SAW. In this way we implemented an ultrafast shutter in a grazing incidence x-ray diffraction geometry. The limiting factor is the necessary high amplitude of the surface modulation to achieve a high efficiency of such a switch or shutter. If only a fast switch is needed, for example to select single x-ray bunches from a synchrotron pattern, the excitation can be changed from femtosecond to nanosecond pulses. This allows the heat to flow into the sample depth during the optical excitation and thus increase the damage fluence. This allows for building efficient x-ray switches as shown in article XVI.

Ultrafast X-Ray Diffraction (UXRD)

$\mathbf{X}$-RAYS are used in many different experimental techniques in order to measure stoichiometric, magnetic and structural properties of materials using the advantage of the wide energy range of the x-rays between 30 eV and 500 keV [16, 19]. For time resolved experiments, short x-ray pulses can be generated by synchrotron radiation facilities, such as the BESSY II operated by the Berliner Elektronenspeicherring-Gesellschaft für Synchrotronstrahlung (BESSY) or the European Synchrotron Radiation Facility (ESRF) or x-ray free-electron lasers (XFELs). Lab-based solutions are plasma x-ray sources (PXSs), which have a time resolution comparable to XFELs.

The experiments presented in this thesis are performed in two different synchrotron facilities: BESSY II operated by BESSY and ESRF, and also a lab based solution including a laser-driven table-top source was used. The x-rays are used for structural analysis by (i) x-ray reflectivity (XRR) to investigate layer thickness in a multilayer thin film sample and also surface deformations and (ii) x-ray diffraction (XRD), which allows us to access the lattice parameters of the sample. Furthermore, XRD can be used to study the strain inside a sample, which gives access to the temperature or energy density. In addition to a temperature increase, for example due continuous wave (CW) laser heating, energy deposited by a laser pulse is monitored by ultrafast x-ray diffraction (UXRD). The detected strain inside is a combination of the induced stress by the energy stored in lattice vibrations, electrons, and magnetic excitations.

In this chapter, a closer view of the laser-driven table-top PXS setup and the upgrades and modification, which I implemented during my PhD project are presented. Before the UXRD setup and its modifications are described in section 4.2, I will give an overview of the XRD method and the data evaluation in section 4.1. In section 4.3 the magneto-optic Kerr effect (MOKE) and optical reflectivity setup is presented, which I built to enable measurements of the magnetic sample response at the PXS setup simultaneously or under identical excitation conditions with the UXRD measurements.

4.1 X-Ray Diffraction (XRD)

$\mathbf{T}$HE samples studied in the context of this thesis consist of single crystalline layers. The periodic arrangement of the atoms of the samples results in a constructive and destructive interference of the diffracted x-rays. The samples used here are oriented with a high-symmetry axis perpendicular to the surface and repeat their atomic structure with the inter-atomic lattice distance d or in reciprocal space with $|\mathbf{q}| = 2\pi/d$. The interference condition is given by the Laue condition

$$\mathbf{k}_{\text{in}} - \mathbf{k}_{\text{out}} = \mathbf{q}, \tag{4.1}$$

where $\mathbf{k}_{\text{in}}$ is the wave vector of the incidence x-ray beam and $\mathbf{k}_{\text{out}}$ is the wave vector of the diffracted x-ray beam [60]. The length of the wave vector is related to the wavelength of the x-rays by $|\mathbf{k}| = 2\pi/\lambda$,
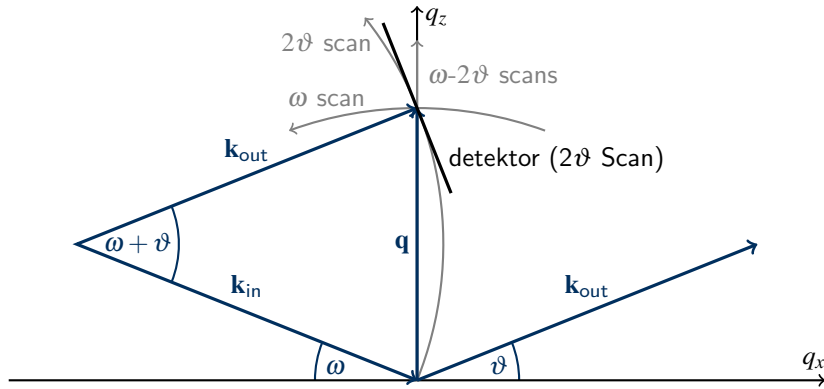
Figure 4.1
Incoming and outgoing x-ray radiation represented by their wave vectors $\mathbf{k}_{in}$ and $\mathbf{k}_{out}$ in coordinate system of the reciprocal space (q_x, q_z) including the real space angles between sample and x-ray radiation and an area detector. Different types of scans through the reciprocal space are indicated by gray arrows [108].

and the direction of the wave vector is given by the geometrical conditions imposed by the conservation of momentum. A special representation of the Laue condition is the Bragg condition

$$d = \frac{n\lambda}{2\sin\vartheta}, \tag{4.2}$$

which relates the distance of the lattice planes to the diffraction angle ϑ. If the diffraction occurs at a periodic structure along an axis perpendicular to the surface, the diffraction angle ϑ is defined as the angle between the surface of the sample and both the incident and diffracted x-ray beam. The maxima of the diffraction intensity, so called Bragg reflections are observed in scans where the angle of the incoming x-ray beam to sample ϑ is varied and the angle between the incident beam and the detector is set to 2ϑ. From the angular position of Bragg reflections the related lattice constants are calculated using equation (4.2).

Modern area detectors allow accessing not only specular but also non-specular reflections of x-ray photons without performing time-consuming mesh scans. In order to analyze the recorded images of the area detector, a transformation from real space to reciprocal space is used. The nonlinear transformation

$$\mathbf{q} = \begin{pmatrix} q_x \\ q_z \end{pmatrix} = |\mathbf{k}| \begin{pmatrix} -\cos\omega + \cos\vartheta \\ \sin\omega + \sin\vartheta \end{pmatrix} \tag{4.3}$$

relates the angle of incidence ω and the angle of the diffracted x-rays ϑ to the scattering vector $\mathbf{q}$ [17, 108]. The geometrical relations between the real and reciprocal space quantities are illustrated in figure 4.1.

A Bragg peak appears in reciprocal space at a specific position: The q_z component gives access to the distance of the lattice planes with $d = 2\pi/q_z$. For thin layers the peak width in q_z is inversely related to the layer thickness. However, structural imperfections of the samples and thermal effects may lead to peak broadening q_z and q_x. Reciprocal space maps containing various Bragg peaks of different materials, i.e. different layers, are shown in articles III, VI, VII and VIII. The results by means of integrating the intensity in reciprocal space map along the q_x direction yielding the material specfic Bragg peaks of a sample are shown in articles I, III, VI, VII, VIII and IX. More detailed descriptions of this method are given in [106, 108, 109]. For samples with broad peaks along the q_x direction, it is useful to measure the dynamics after excitation at a fixed detector angle. This method saves a lot of measurement time, resulting in a better signal to noise ratio in comparison to measurements using angle scans. Depending on the peak shape in reciprocal space and the measured angles it may be necessary to renormalize the measured peak shift in order to extract the correct lattice strain [108, 110].

4.2 Ultrafast X-Ray Diffraction Setup

THE laser-driven table-top UXRD setup is an optical pump and hard x-ray probe setup. The main experimental component is a laser-driven plasma x-ray source (PXS) driven by the same laser system providing the pump pulse. The hard x-ray generation is based on the excitation of a copper target, where electrons are accelerated in the electromagnetic field of the femtosecond laser pulse. The recombination of electrons with copper ions produces the characteristic x-ray emission lines, while the acceleration of electrons gives a bremsstrahlung background. The copper target only emits x-ray radiation in presence of electrons accelerated by the electric field of the laser pulse or scattering processes of hot electrons in the copper target. This means the x-ray pulse duration is in the same order as the duration of the exciting femtosecond laser pulse [24]. The x-ray radiation is subsequently monochromatized and focused onto the investigated sample.

In the following I describe the optimized setup and the modifications, which I built during my doctoral studies. In figure 4.2 an overview of the full setup is shown. A top view including the optical paths is sketched in figures 4.3 and 4.4. The setup is built on two laser tables, each of them having the dimensions of $1.5\,\text{m} \times 3\,\text{m}$. On the first table, the laser system is placed: A laser oscillator (Coherent Mantis) provides broadband femtosecond laser pulses, which are amplified in a Coherent Legend Elite regenerative amplifier with a second single path amplifier. The Ti:Sa amplifier laser system provides 35 fs short pulses at a central wavelength of 800 nm with an energy of 8 mJ at a 1 kHz repetition rate. I modified laser system with an active beam stabilization system and an additional pulse compressor in order to independently vary the pulse duration of the pump and probe pulses. For the x-ray generation about 70 to 90% of the pulse energy is used depending on the selected beamsplitter. A detailed description is given in sections 4.2.1 and 4.2.2.

The pump and probe pulses are guided to the second table on which the PXS source and the exper-
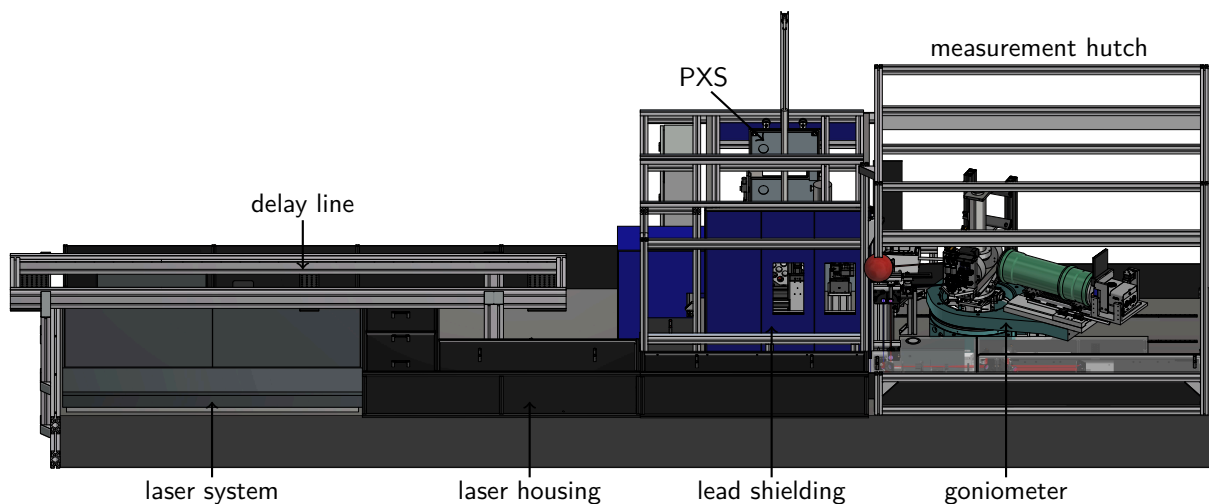
Figure 4.2

UXRD setup: Femtosecond pulses are generated by the amplifier laser system on the left side. The laser beam is transferred to the PXS setup that is inside a lead shielding (blue). X-rays produced by the PXS are focused onto the sample on the goniometer. The pump beam path of the experiments is located at the front in the laser housing to minimize the impact of air fluctuations. A closed-cycle cryostat and a MOKE and optical reflectivity setup is mounted onto the goniometer. The outer circle of the goniometer carries an x-ray area detector and a flight tube. Above the laser system a delay line is installed for measurements with long delays of up to tens of nanoseconds between the pump and probe pulse.
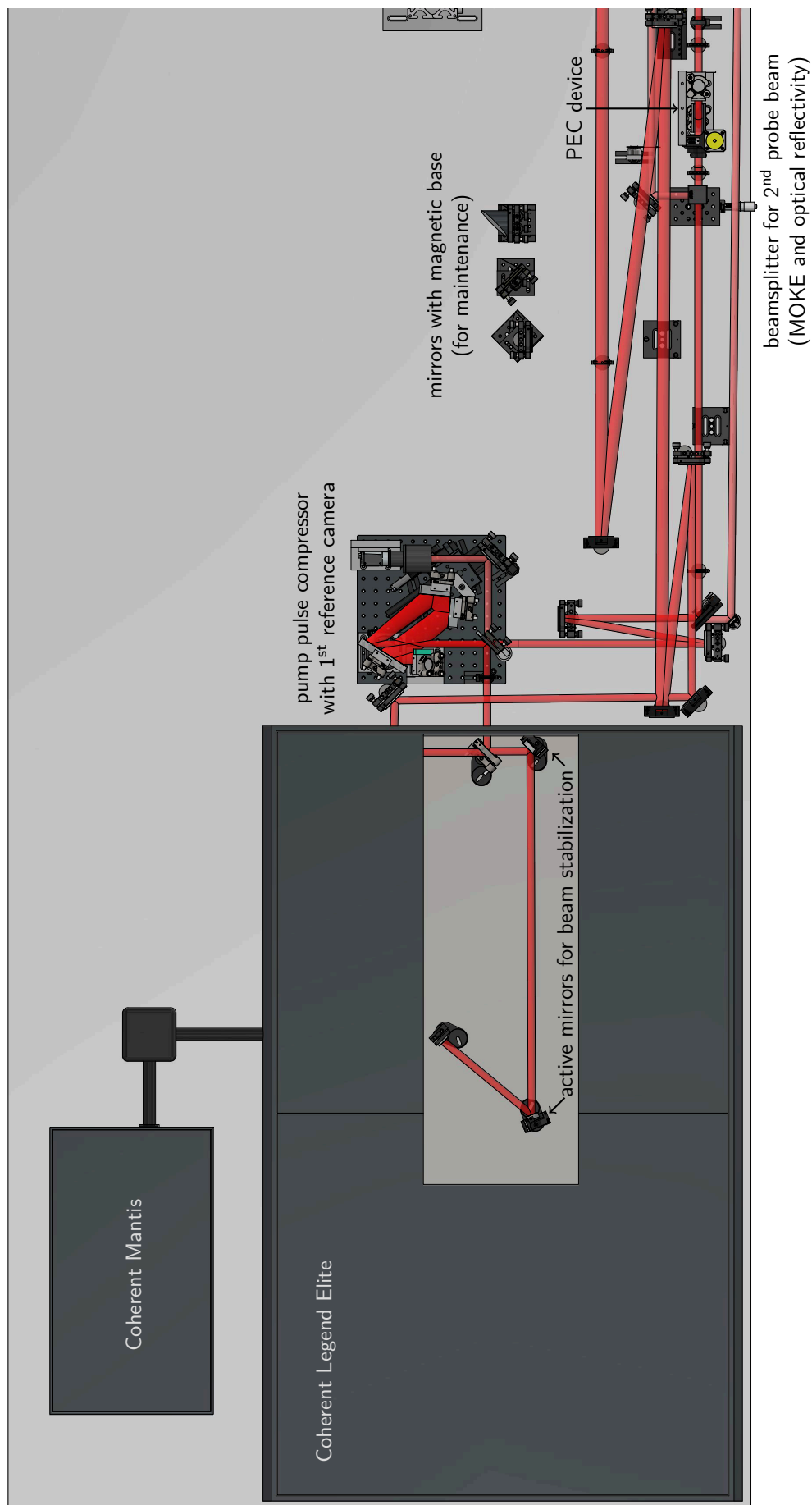
Figure 4.3
UXRD setup (top view of the setup): The sketch shows the first laser table and the beam paths including the laser system with active mirrors for the beam stabilization, the additional pulse compressor for the pump beam, the beamsplitter for the second probe beam and the pulse energy change (PEC) device to change the pump pulse energy. Two motorized mirrors inside the amplifier housing used for a beam stabilization readjusting the beam to two cameras. Four laser beams are guided to second laser table: the probe beam for x-ray generation, the probe beam for the MOKE and optical reflectivity setup, the pump beam and a reference beam for the beam stabilization.

reference camera

sample environment

goniometer

flight tube

x-ray area detector

x-ray reference detector

Montel optic

motorized mirror

probe beam periscope

in-vacuo 2ⁿᵈ harmonic generation

active mirror

chopper

telescope

2ⁿᵈ reference camera

delay stage and double-pulse generator

PXS
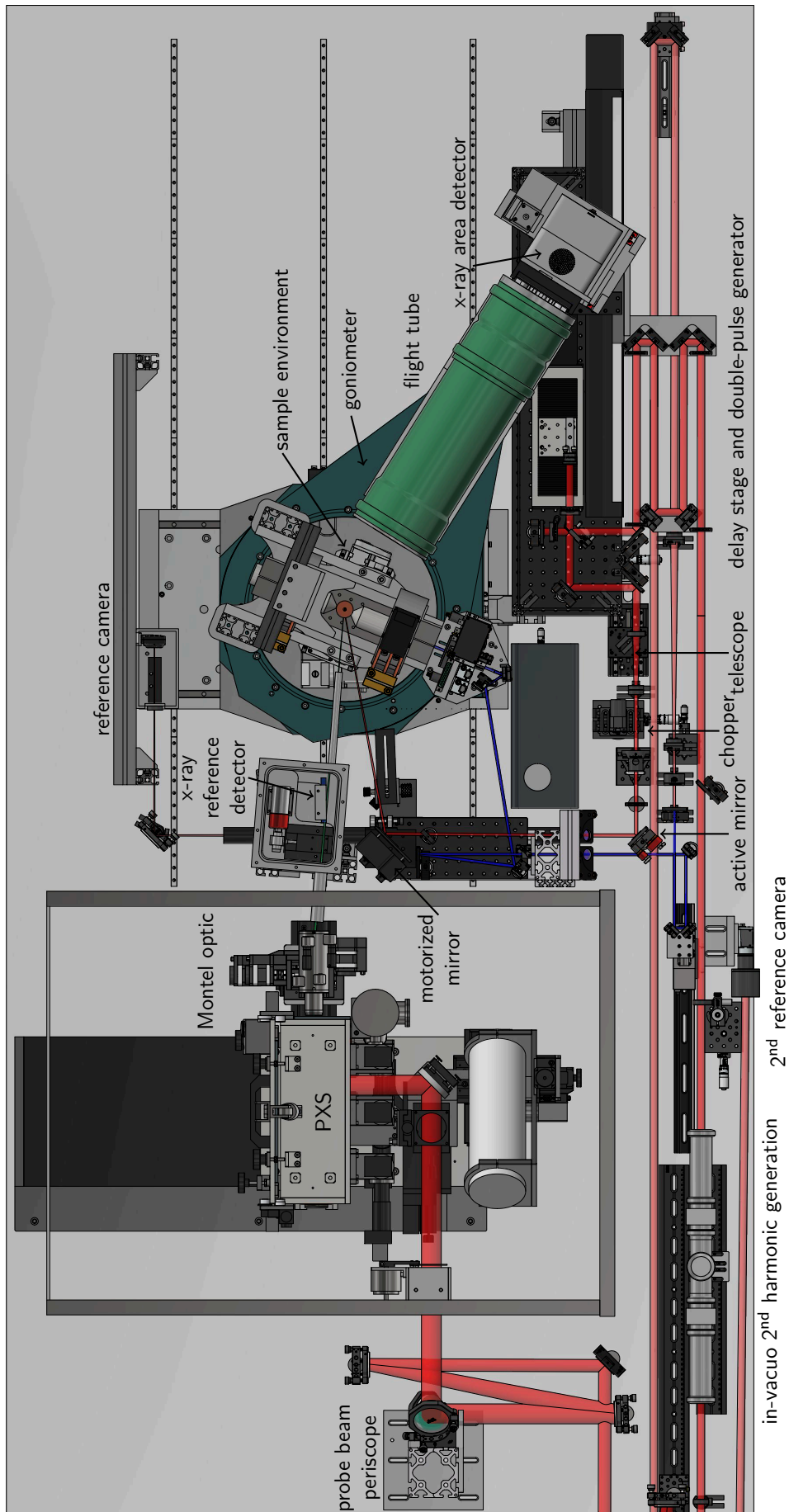
Figure 4.4

UXRD setup (top view of the setup): The sketch shows the second optical table and the pump and probe beam paths. The probe beam for x-ray generation is guided thorough a periscope to the PXS setup and the generated x-ray radiation is focused by a Montel optic to the center of the goniometer passing the x-ray reference detector. The inner circle of goniometer supports the sample environment which carries the MOKE and optical reflectivity setup. The outer circle carries an x-ray area detector and a flight tube. The probe beam path for the MOKE and optical reflectivity is located next to the pump beam path, which includes the 2ⁿᵈ harmonic generation, the delay stage and the double-pulse generator.

imental hutch are located. It contains the x-ray diffraction instrumentation, the sample environment including a cryostat, an electromagnet, and an optical setup to measure time-resolved MOKE and transient reflectivity. On the way to the PXS source, the probe beam is expanded twofold with two mirror telescopes. Inside the PXS source the laser beam is focused onto a typically 15 μm thick copper tape in order to produce the x-ray radiation [14, 23–27]. The x-ray spectrum is generated in the full solid angle and a fraction of about $2° \times 2°$ is collected with a Montel optic which consists of two perpendicular curved multilayer mirrors, optimized for Copper K_α radiation. The Montel optic monochromizes and focuses the x-ray pulse onto the sample [30]. In addition to the main focus point, the Montel optic has a secondary focus line irradiating a semiconductor x-ray detector behind the Montel optic to yield a single shot reference for the generated x-ray intensity [111]. To enable a higher x-ray flux on the sample, I had a motorized movable vacuum chamber with Kapton entrance and exit windows constructed and installed it around the semiconductor x-ray reference detector. This increases the usable x-ray flux of the setup by a factor of about 2.

To perform the angle scans (ϑ-2ϑ) a goniometer is used for the sample positioning as well as the sample and detector rotation. The goniometer also performs the 2ϑ rotation of the area detector (Dectris Pilatus 100k) and supports the sample environment, which allows cooling the sample down to 15 K with a closed-cycle cryostat. In section 4.3 more details of the sample environment are given and the setup for MOKE and optical reflectivity measurements is presented. As part of an upgrade, the area detector was mounted on a motorized platform for optimization of the vertical positioning, which is necessary if the sample is slightly tilted. This is mostly relevant to the measurements performed at a long distance between the sample and the detector. Evacuated flight tubes optimized for the default distances of 66.6 cm and for long distances of 145 cm are used to further reduce the x-ray absorption in the air. This is shown in green in figures 4.2 and 4.4.

As part of a major upgrade, I have renewed and expanded the optical pathways, as well as the devices that are presented in the following sections. To achieve a mechanically stable setup all optomechanical components are mounted on custom stainless-steel pedestal pillar posts. The complete laser beam path is covered in order to minimize air fluctuations and to improve the laser safety.

The amplified laser pulse is separated into pump and probe pulse by a beam splitter which I added inside the laser system in order to guide both pulses to individual grating compressors (see section 4.2.2). To adjust the pump pulse energy, a half-wave plate in combination with a polarizer is used (in the following called PEC device). A detailed description is given in section 4.2.3. This PEC device is placed at the end of the first laser table after a second beam splitter with a reflection to transmission ratio of 5:95 that provides the probe pulses for the MOKE and optical reflectivity setup. On the pump arm, an in-vacuo setup for the 2nd harmonic generation can be installed. It delivers a pump pulse with the central wavelength of 400 nm which performs the excitation for the experiments published in articles I, V, XI and XIII. The delay stage is installed in the pump arm and includes a secondary setup for the generation of a pulse pair with an adjustable pulse-to-pulse delay. The delay stage covers a temporal range of 8 ns and an optional 2nd pulse can be delayed up to 0.5 ns with respect to the first pulse. The optical path of the delay stage and setup for the generation of double pulses are described in more detail in section 4.2.5.

After the delay stage, the excitation beam is lifted by a periscope to the sample height and is directed onto the sample. Before a motorized lens telescope providing an adjustable beam diameter. The last mirror before the sample is motorized and used to optimize the spatial overlap with the x-ray beam on the sample. This is typically performed with a reference sample [106, 111–113].

A camera is located in the same distance as the sample with respect to the first mirror of the periscope which is back side polished. It monitors the beam position and shape using the transmission through the

back side polished mirror of the periscope and is used for stabilization of the beam with an active feedback loop steering a motorized mirror in front of the periscope. During an experiment, this stabilization compensates the spatial shift of the laser beam caused by mechanical inaccuracy of the delay stage and the other optical components.

4.2.1 Beam Stabilization

A self-build beam stabilization system is installed in the experimental setup in order to improve mid- and long-term stability of the laser. It compensates the drifts after turning on the laser system and the drifts occurring over weeks, which would otherwise require daily realignment of the laser beam through the apertures placed in the beam path after the amplifier is warmed up.

We use only one beam stabilization system for the pump and probe beams using two motorized mirrors which are located before the beamsplitter that splits the main beam into pump and probe arms. Note that due to the separate compressors, the splitting of the pump and probe beam takes place directly before the compressor inside the laser system. The two mirrors routing the beam from the last telescope, that increases the beam diameter after the single path amplifier to the final size are exchanged by motorized Newport agilis piezo optical mounts providing a sufficient resolution. The mirrors are shown in figure 4.3 in the cut-out of the laser system. The feedback loop is based on two Basler acA1280-60gm GigE cameras monitoring the beam. One is located inside the pulse compressor of the pump pulse (see figures 4.3 and 4.5) and monitors the transmission through the in-coupling mirror of the compressor. The second camera takes the transmitted laser beam of a 45° reflecting mirror behind the compressor of the pump arm (see figure 4.3) which is directed towards the measurement hutch and detected there by the 2nd camera (see figure 4.4).

The software was written in Python by Lisa Willig [114, 115] and the algorithm works by aligning a beam with the two mirrors onto two target position on the cameras. The distance of the detected beam position to the target position in each camera is calculated. If this value reaches a threshold the software starts the repositioning of the beam to the target positions on the cameras automatically. A benefit of the beam stabilization is higher repeatability, accuracy and the opportunity to realign the laser beam during measurements.

4.2.2 Separate Compressors for Pump and Probe Beams

The maximum x-ray flux per pulse [116–118] and the efficiency of the 2nd harmonic generation depend strongly on the pulse duration of the laser. Therefore two different compressors are used for pump and probe arms in order to adjust the optimal pulse duration for one arm independently from the other. Furthermore, the linear chirp of the optical components can be compensated separately. Using two compressors requires a compensation of the temporal shift between the pump and the probe arms every time the pulse duration is slightly changed.

Figure 4.5 shows a schematic drawing of the 2nd compressor installed on the pump arm that changes the pump pulse duration. The beam routing resembles a mirrored copy of the existing compressor inside the laser system, which now affects the probe pulse duration. While in the probe compressor, the beam enters on the lower level and leaves at the higher one, in the newly build compressor the beam enters the higher level and leaves at the lower level. This results in a lower beam height of the pump beam compared to the probe beam, which is required for the PEC device for the pump fluence adjustment described in the next section.

The uncompressed laser pulse enters on the right side and is reflected by an in-coupling mirror on
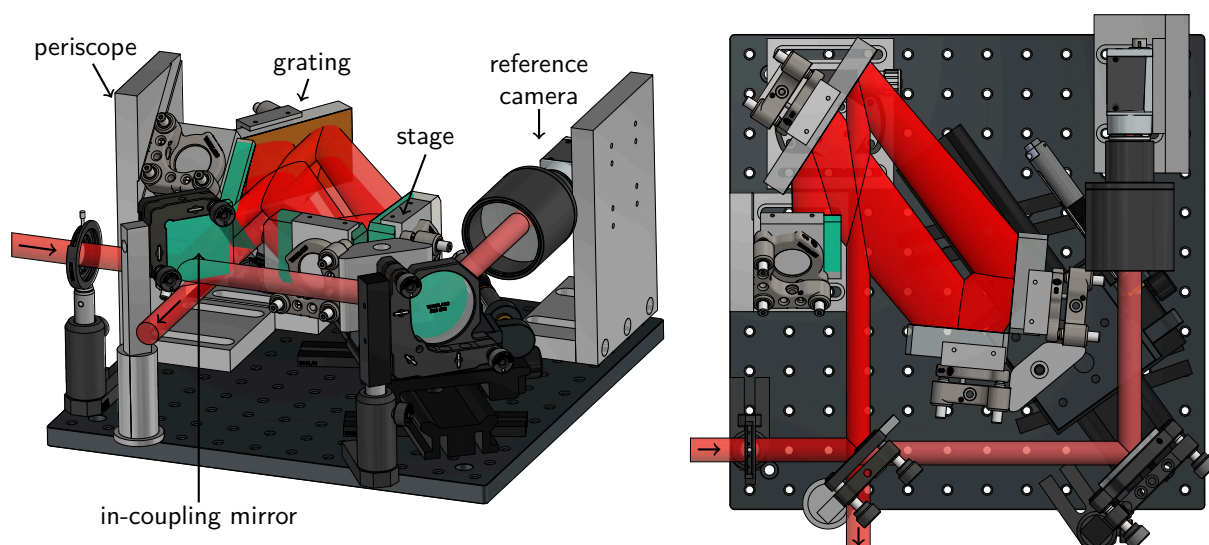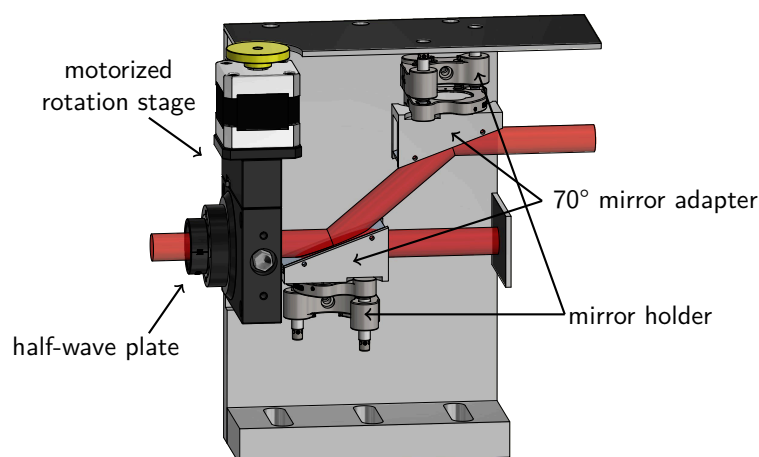
Figure 4.5
  3D and top view of the pump pulse compressor including the beam path in red and the first reference camera of
  the beam stabilization in the upper right corner. The laser pulse enters on the left side and is guided to the grating
  where it is diffracted into the first order. The delay between red and blue wavelength components is adjusted with
  the stage and the pulse is routed back to grating, where it diffracted onto the periscope. The periscope guides the
  pulse to a lower level, where it follows the same way back and leaves at the bottom side as an ultrashort pulse.

a grating. The grating is optimized to diffract nearly all energy in the 1st order. The pulse starts to be divergent because of the different wavelengths inside an ultrashort laser pulse. The next two mirrors are mounted on a motorized stage and reflect the pulse back to the grating from where it is again diffracted as an elliptically-shaped parallel pulse. A pair of mirrors act as a periscope and guide the pulse to the lower level, where the pulse follows the same way back. The pulse exits from the compressor as a compressed ultrashort pulse below the in-coupling mirror. The motorized stage adjusts the length of the divergent beam path. Due to the different path lengths for red and blue wavelength components, the pulse can be compressed or stretched by moving this stage.

The in-coupling mirror is back side polished to monitor the beam position with the reference camera of the beam stabilization system. The full setup is placed in a closed box next to the laser and is filled with nitrogen as the entire laser system in order to prevent drifts due to humidity changes inside the laboratory.

4.2.3 Pump Energy Change Device (PEC Device)

The pulse energy change (PEC) device consists of a zero-order half-wave plate in combination with polarizers and is used for adjusting the pump pulse energy. The polarizers are broadband thin film polarizers which separate the polarization by reflection. Two subsequent polarizers increase the contrast and lead to a parallel incoming and outgoing beam. This setup has the advantage that the beam size is not reduced and the linear and non-linear chirp is minimized. A solid aluminum stand was constructed to mount two thin-film laser polarizers with a 70° angle of incidence. A rendering of the setup is shown in figure 4.6. The zero-order half-wave plate for 780 nm is mounted in a rotation stage at the entrance of the device and rotates the incoming *p*-polarized light. Two *s*-polarized light-reflecting mirrors are positioned vertically to the laser table. This results in an outgoing upper *p*-polarized beam and a lower *s*-polarized beam. The *s*-polarized light transmitted through the first mirror can be blocked or used to align

Figure 4.6

3D view of the PEC device: This device consists of a zero-order half-wave plate mounted in a motorized rotation stage and two thin-film laser polarizers to allow changing the excitation energy of the pump pulse. The lower *s*-polarized beam is blocked and the upper *p*-polarized beam is guided to the experiment.

the incoming laser beam. The solid construction prevents any serious displacement of the optomechanical components, which is potentially dangerous especially due to the upward-directed laser beam.

Via calibration, the motorized wave plate position is directly related to the power at the sample position and to a reference power measured by a second power meter behind a back side polished mirror. In combination with the camera used for the stabilization of the spatial overlap of both pump and probe beams, the fluence can also be controlled during the experiment. Furthermore, it is possible to automatically correct the fluence changes occurring during a theta ϑ-2ϑ scan due to the different spot sizes on the sample as ϑ is varied.

4.2.4 Second Harmonic Generation

An in-vacuo second harmonic generation setup can be inserted between the PEC device and the delay stage if a 400 nm excitation is necessary. The setup is depicted in figure 4.4 at its position without the additional focusing and the color change of the pump beam. Two convex lenses with 500 mm focal length are installed as a Keplerian telescope in which a 100 μm beta-barium borate (BBO) crystal is placed slightly in front of the focus point to realize frequency doubling with high efficiency. To prevent plasma generation at the focus point due to the high intensity, the focus point and the BBO are located in a vacuum chamber. To separate the 400 nm from the fundamental beam two exchangeable long pass dichroic mirrors are used on the delay stage.

4.2.5 Delay Stage and Double-Pulse Generator

One of the main components of a pump-probe setup is a delay stage. The PXS setup uses a 600 mm stage to achieve delay times between pump and probe pulses of a few femtoseconds up to 8 ns of delay. The stage is mounted vertically on the table as shown in figure 4.7 to reduce mechanical instabilities during the movement. Behind the delay stage, a double-pulse generator based on a Michelson interferometer is located as seen in the lower part of figure 4.7.

The stage has four fixed apertures that allows checking the path of the in- and outgoing beams, respectively. The four mirror holders on the movable part of the stage are top-mount mirror holders to
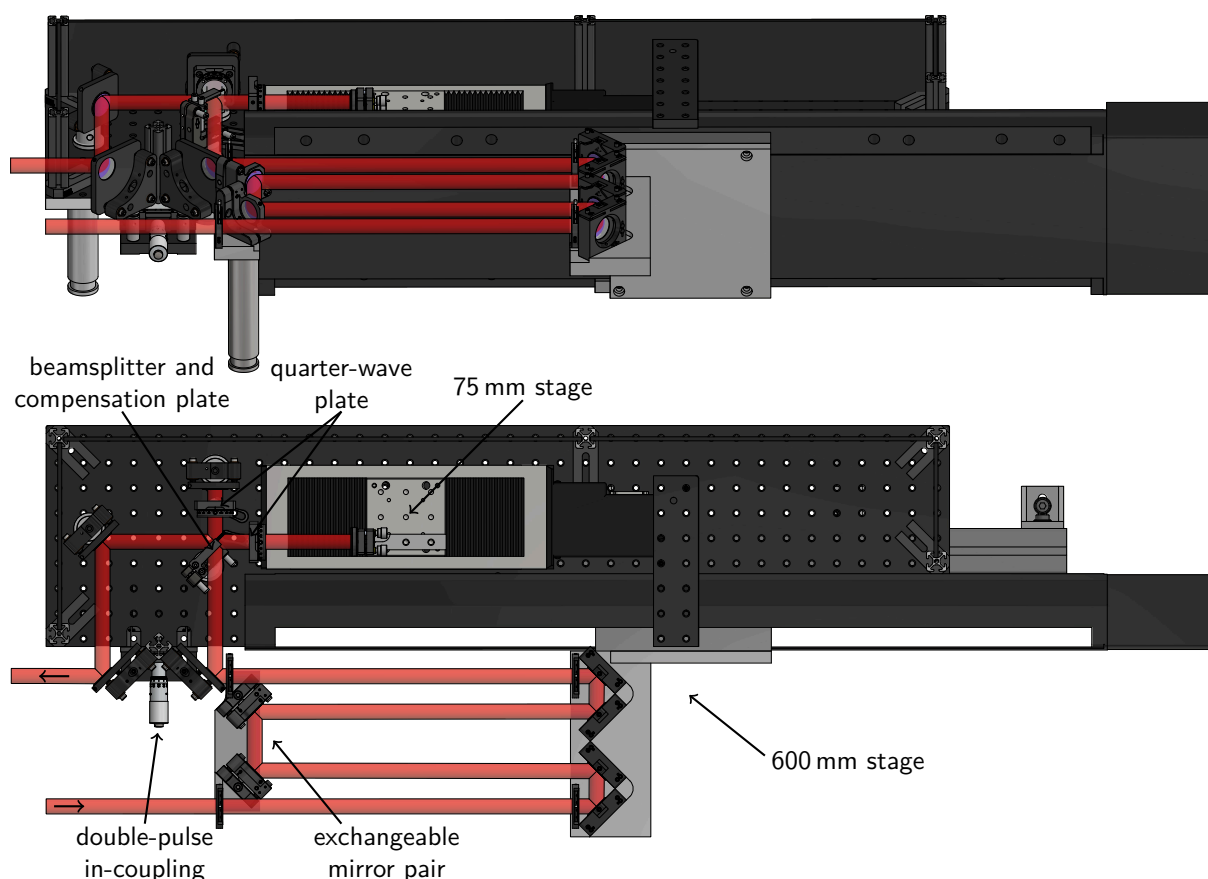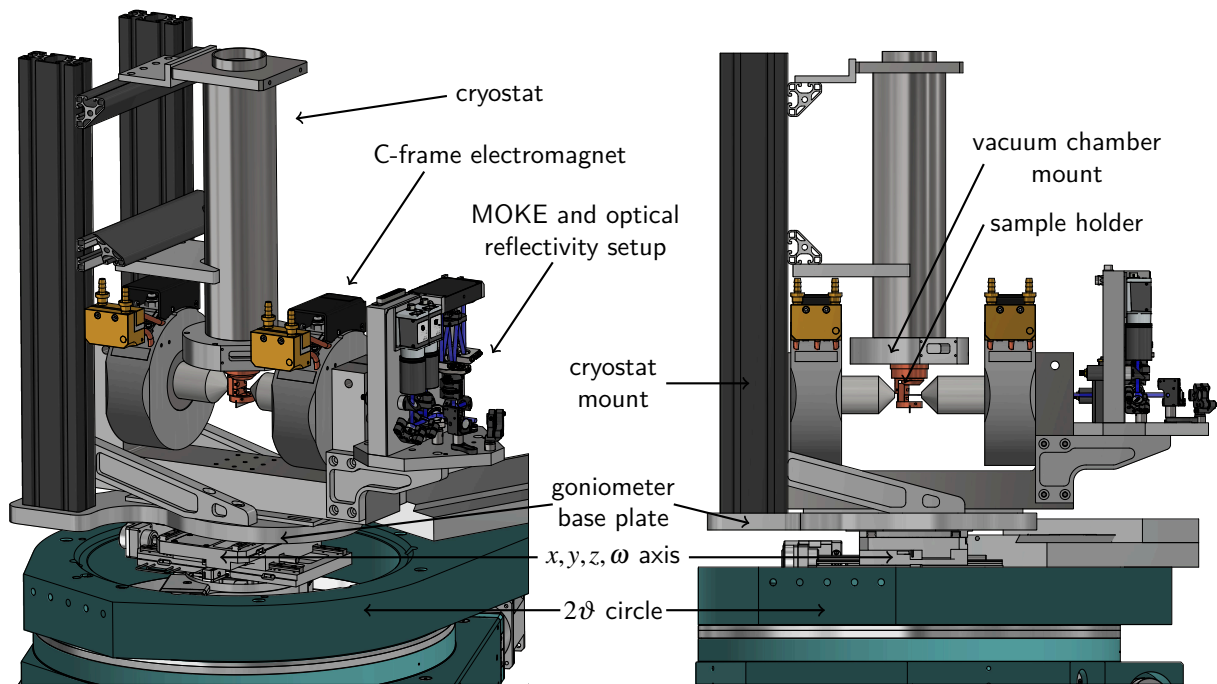
Figure 4.7

3D and top view of the delay stage and double-pulse generator: the laser pulse reaches the device from the lower-left corner and passes four times through the 600 mm delay stage, resulting in an 8 ns delay in total. Behind the stage, the pulse can enter a double-pulse generator (a Michelson interferometer), which generates a sequence of two pulses which have a delay of up to 0.5 ns. The interferometer is equipped with quarter-wave plates in each arm acting as effective half-wave plate to adjust the pulse energy individually of both pulse.

achieve a high mirror density and easy access for alignment. The two fixed mirrors of the stage assembly are mirror mounts with an exchangeable front plate. One pair contains 400 nm and 800 nm reflecting mirrors and another pair long pass dichroic mirrors that separate 400 nm and 800 nm light. They are exchanged if the excitation is performed with 400 nm instead of the fundamental 800 nm pulses.

Behind the 8 ns stage, two additional mirrors moved by a manual stage let the beam enter the double-pulse generator or directly pass through, depending on the manual stage position. If the laser pulses enter the interferometer two pulses with a variable temporal delay of up to 0.5 ns are generated. The temporal delay of the generated pulses is set by a second stage. To compensate for different self-focusing effects of the pulses in the beamsplitter, a beamsplitter compensation plate is used. The compensation plate allows each pulse to propagate four times through a glass substrate of the same thickness. Each interferometer arm also contains a zero-order quarter-wave plate, which effectively acts as a half-wave plate due to the double pass of the laser pulse. This can be used in combination with a Glan-Laser calcite polarizer to accurately adjust the fluence of each pulse individually. Due to the extended beam path of the double-pulse generation, an additional delay of approximately 1.3 ns for the first laser pulse has to be compensated using the main delay stage.

cryostat

C-frame electromagnet

MOKE and optical reflectivity setup

cryostat mount

goniometer base plate

x, y, z, ω axis

2ϑ circle

vacuum chamber mount

sample holder

Figure 4.8

3D and side view of the inner goniometer circle carrying the sample environment: A base plate holds the mount of the cryostat located at the left side, which places the cryostat in the center of rotation of the goniometer. At the bottom of the cryostat, the copper sample holder is located. In addition, the base plate carries the electromagnet, consisting of a C-frame with a coil and a pole on each side. On the right side of the C-frame the MOKE and optical reflectivity setup are mounted. The 400 nm probe beam of this setup is focused by a lens through the right pole onto the sample.

4.2.6 Sample Environment

The recently extended sample environment consists of a goniometer, an electromagnet, a cryostat and a heater with an extended temperature range. The sample environment allows the sample to be positioned in the x-ray beam, to be heated and cooled and to be exposed to magnetic fields. For positioning the sample the goniometer offers an x, y, z and ω axis. The vibration decoupled cold head of a closed cycle cryostat is located on top of the goniometer. The cryostat can reach temperatures down to 15 K (see figure 4.8). The copper sample holder provides two places for exchangeable blocks that simplifies changing the samples. The second block is usually used for the reference sample. To provide the necessary thermal insulation, a vacuum chamber with a small Kapton window for incoming x-rays, a wide Kapton window for the diffracted x-rays, and a quartz glass window for the pump pulse is available. The maximum temperature is limited to 350 K. To achieve higher temperatures a second heater is mounted inside the sample holder. The thermal isolation of this heater to the cryostat is realized via a sapphire and a Kapton plate.

A 3 kW electromagnet is used to apply an out-of-plane magnetic field to the sample. The magnet is based on a GMW 3480 dipole magnet with an extended C-frame. With a pole distance of 10 mm a field of 1.6 T is achievable at the sample position: To use these fields in combination with the cryostat a slim copper sample holder and a vacuum chamber with inlets for the poles has to be used. The electromagnet also provides the magnetic field for the MOKE measurements where the C-frame supports the MOKE setup.

4.3 Magneto-Optic Kerr Effect (MOKE) and Optical Reflectivity Setup

T
HE combination of different experimental techniques in one experimental setup allows tracking of energy inside different energy reservoirs, i.e. different subsystems of one sample and therefore enables the investigation of the coupling between these energy reservoirs. To perform such measurements a setup is needed which combines time-resolved measurements of the strain by UXRD, the magnetic state by magneto-optic Kerr effect (MOKE), and the electronic system by optical reflectivity measurements. The experimental setup for measuring the MOKE is a miniaturized version of the one presented by Lisa Willig [115, 119]. The setup was built in a polar MOKE geometry, with the external field and the probe pulse incidence aligned perpendicular to the sample surface. This geometry is sensitive to the out of plane component [120] and allows us to design an experimental setup preventing collisions between pump, x-ray probe, optical probe, and mechanical devices. The probe pulse for MOKE measurements has a center wavelength of 400 nm, which ensures a high magneto-optical contrast for many magnetic materials and simplifies the separation of pump and probe. After reflection of this probe pulse on the sample, it is detected by a balanced photodiode measuring the polarization change. To get access to the optical reflectivity of the sample, another photodiode measures the reflectivity in combination with a reference photodiode to normalize the signal to the probe beam intensity. The MOKE and optical reflectivity setup is doweled to the setup mounts on the C-frame to recover its position and beam paths after reattaching the setup (see figure 4.8).

The pump beam is the same pump beam used for the x-ray experiments (see figures 4.3 and 4.4). To reduce noise of the optical detection, an optical chopper with a frequency of 500 Hz is used.

The probe pulse for the MOKE and optical reflectivity setup is reflected out of the pump beam with a
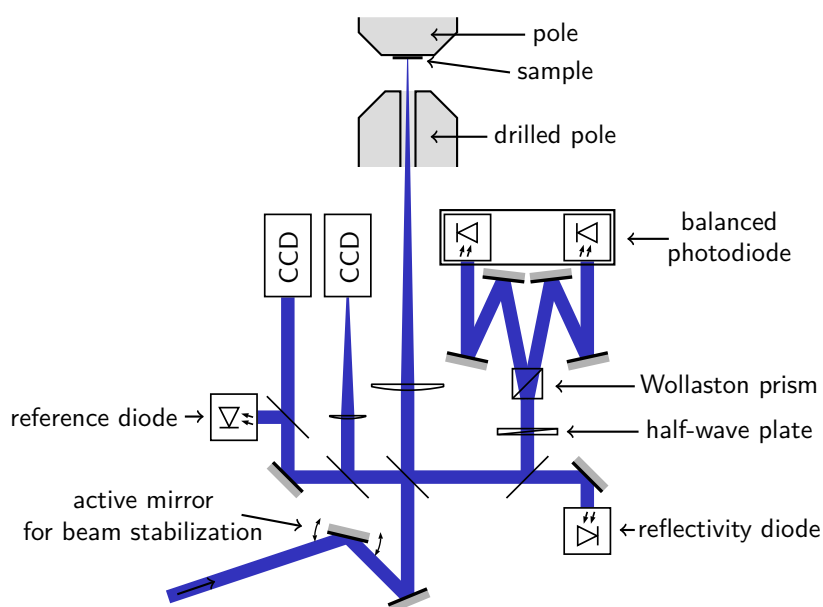
Figure 4.9

Sketched beam path of the MOKE and optical reflectivity setup. The 400 nm probe pulse enters through two active steering mirrors (the 2nd is sketched). A part of the beam is used to detected a reference intensity and the beam positions for the beam stabilization on the left side, while the other part is focused thorough a pole onto the sample. The amplitude and the Kerr rotation of the reflection is measured by a photodiode and a balanced photodiode on the right side.

Figure 4.10

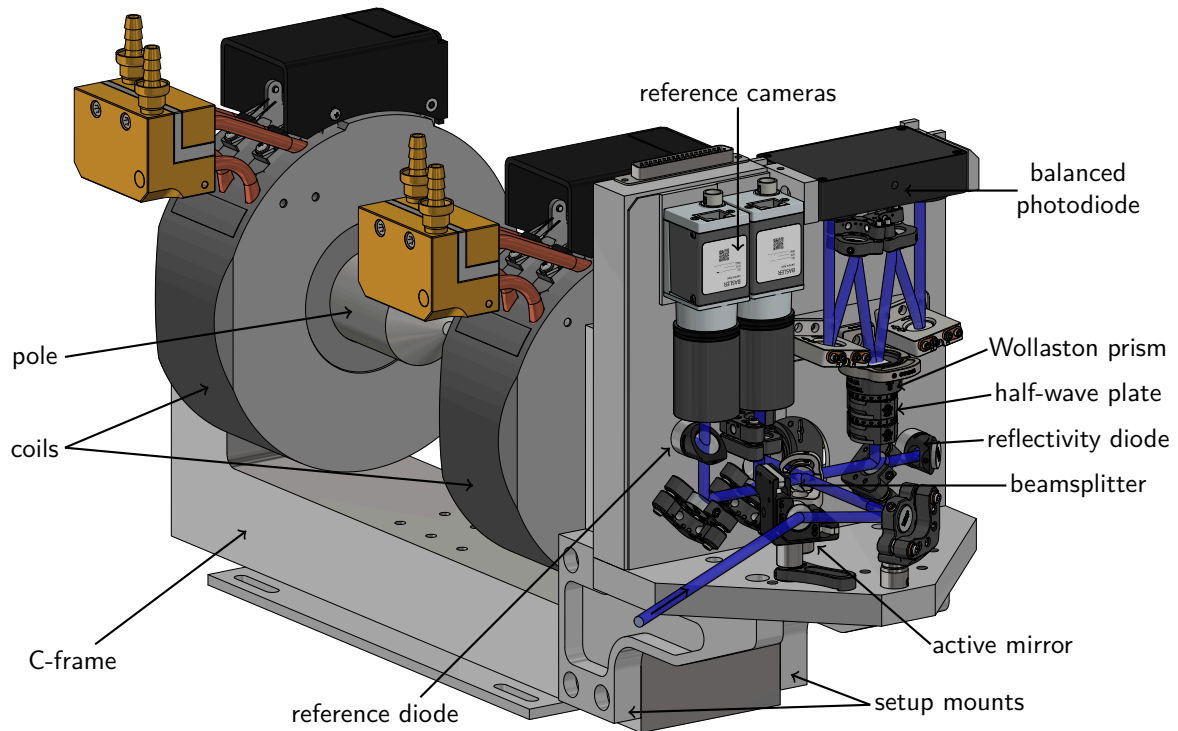3D view of the MOKE and optical reflectivity setup mounted on two setup mounts of the C-frame of the electromagnet. The schematic sketch shows the setup consisting of two perpendicular planes: The horizontal plane directs the probe beam to the sample and back, whereas the vertical plane contains the detection diodes and reference cameras.

beamsplitter, which is located in front of the PEC device as shown in figure 4.3. The probe pulse is guided below the pump pulse path, where it is converted to 400 nm with a second BBO crystal. A motorized 25 mm stage is used to align the timing with the x-ray probe pulse. Next to the periscope for the pump pulse, another periscope lifts the probe to the level of the x-ray beam, where it then enters the MOKE and optical reflectivity setup, shown in detail in figures 4.10 and 4.9. The setup is structured in two planes where the optical components needed for the detection are mounted on a plane perpendicular to the optical table. The setup is constructed on a $180\,\text{mm} \times 180\,\text{mm} \times 160\,\text{mm}$ CNC machined aluminum base, which is supported by two arms of the C-frame of the electromagnet as shown in figure 4.10.

The probe beam enters the setup via two motorized mirrors, which can actively realign the beam after a movement is detected by two cameras (the same principle as used for the beam stabilization shown in section 4.2.1). This is necessary when the inner goniometer circle is rotated during a ϑ-2ϑ scan. The next mirror directs the beam through a 50:50 beamsplitter onto the sample. The reflection of the beamsplitter is used on the left side of the vertical plane to observe the beam position by two cameras and for the reference photodiode measuring the incident pulse intensity. The transmission through the beamsplitter is focused onto the sample where the probe beam is reflected. The second reflection at the beamsplitter guides the probe beam to the right side of the vertical part of the setup. For detection in a photodiode the transmission of another beamsplitter is detected to measure the time-resolved reflectivity of the sample. The reflection on this beamsplitter is guided through a zero-order half-wave plate and a Wollaston prism to detect the Kerr rotation by a balanced photodiode. All signals are measured by boxcar integrators and recorded by a National Instruments measurement card (for more detail see [115]).
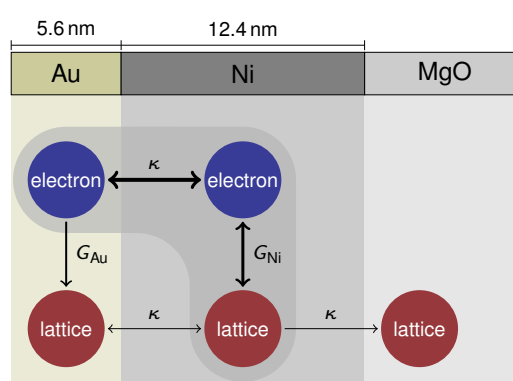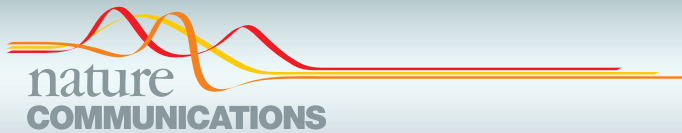
CHAPTER FIVE

Articles

Article I

Layer specific observation of slow thermal equilibration in ultrathin metallic nanostructures by femtosecond x-ray diffraction

Jan-Etienne Pudell, Alexei Maznev, Marc Herzog, Matthias Kronseder, Christian Back, Grégory Malinowski, Alexander von Reppert, and Matias Bargheer

Ultrafast heat transport in nanoscale metal multilayers is of great interest in the context of optically induced demagnetization, remagnetization and switching. If the penetration depth of light exceeds the bilayer thickness, layer-specific information is unavailable from optical probes. Femtosecond diffraction experiments provide unique experimental access to heat transport over single digit nanometer distances. Here, we investigate the structural response and the energy flow in the ultrathin double-layer system: gold on ferromagnetic nickel. Even

though the excitation pulse is incident from the Au side, we observe a very rapid heating of the Ni lattice, whereas the Au lattice initially remains cold. The subsequent heat transfer from Ni to the Au lattice is found to be two orders of magnitude slower than predicted by the conventional heat equation and much slower than electron-phonon coupling times in Au. We present a simplified model calculation highlighting the relevant thermophysical quantities.

ARTICLE

Layer specific observation of slow thermal equilibration in ultrathin metallic nanostructures by femtosecond X-ray diffraction

J. Pudell[1], A.A. Maznev[2], M. Herzog[1], M. Kronseder[3], C.H. Back[3,4], G. Malinowski[5], A. von Reppert[1] & M. Bargheer[1,6]

Ultrafast heat transport in nanoscale metal multilayers is of great interest in the context of optically induced demagnetization, remagnetization and switching. If the penetration depth of light exceeds the bilayer thickness, layer-specific information is unavailable from optical probes. Femtosecond diffraction experiments provide unique experimental access to heat transport over single digit nanometer distances. Here, we investigate the structural response and the energy flow in the ultrathin double-layer system: gold on ferromagnetic nickel. Even though the excitation pulse is incident from the Au side, we observe a very rapid heating of the Ni lattice, whereas the Au lattice initially remains cold. The subsequent heat transfer from Ni to the Au lattice is found to be two orders of magnitude slower than predicted by the conventional heat equation and much slower than electron–phonon coupling times in Au. We present a simplified model calculation highlighting the relevant thermophysical quantities.

[1] Institut für Physik & Astronomie, Universität Potsdam, Karl-Liebknecht-Str. 24-25, 14476 Potsdam, Germany. [2] Department of Chemistry, Massachusetts Institute of Technology, Cambridge, MA 02139, USA. [3] Physics Department, Technical University Munich, 85748 Garching, Germany. [4] Institut für Experimentelle und Angewandte Physik, Universität Regensburg, 93040 Regensburg, Germany. [5] Institut Jean Lamour (UMR CNRS 7198), Université Lorraine, Vandœuvre-lès-Nancy 54506, France. [6] Helmholtz-Zentrum Berlin for Materials and Energy GmbH, Wilhelm-Conrad-Röntgen Campus, BESSY II, Albert-Einstein-Str. 15, 12489 Berlin, Germany. Correspondence and requests for materials should be addressed to A.v.R. (email: reppert@uni-potsdam.de) or to M.B. (email: bargheer@uni-potsdam.de)

Ultrafast heating and cooling of thin metal films has been studied extensively to elucidate the fundamentals of electron–phonon interactions[1–7] and heat transport at the nanoscale[8–13]. The energy flow in metal multilayers following optical excitation attracted particular attention in the context of heat-assisted magnetic recording[14,15] and all-optical magnetic switching[16–18]. The role of temperature in optically induced femtosecond demagnetization is intensely discussed, particularly with regard to multipulse switching scenarios[19]. Two- or three-temperature models (TTMs) are often used to fit the experimental observations[20]. The microscopic three-temperature model (M3TM)[20], which uses Elliot–Yafet spin-flip scattering as the main mechanism for ultrafast demagnetization is often contrasted against superdiffusive spin transport[21]. Such electron transport is closely related to ultrafast spin-Seebeck effects[22,23], which require a description with independent majority and minority spin temperatures. The heat flow involving electrons, phonons, and spins has been found to play a profound role in ultrafast magnetization dynamics[24,25]. The description of the observed dynamics in TTMs or the M3TM are challenged by ab initio theory which explicitly holds the nonequilibrium distribution responsible for the very fast photoinduced demagnetization[26,27]. The presence of multiple subsystems (lattice, electrons, and spins), e.g., in ferromagnetic metals[5,28], poses a formidable challenge for experimental studies of their coupling and thermal transport on ultrafast time scales when these subsystems are generally not in equilibrium with each other[26,27,29]. Temperature dynamics in metal films are typically monitored using optical probe pulses via time-domain thermoreflectance (TDTR)[12]. This technique has been a workhorse of nanoscale thermal transport studies, but experiences significant limitations when applied to ultrathin multilayers with individual layer thicknesses falling below the optical skin depth, which are in the focus of ultrafast magnetism research[22–24,30–32]. Optical probes are generally sensitive to electronic and lattice temperatures, although in some cases the lattice temperature[13] or the spin temperature[24] may be deduced. In order to understand the thermal energy flow, it is highly desirable to directly access the temperature of the lattice, which provides the largest contribution to the specific heat. Ultrafast X-ray diffraction is selectively sensitive to the crystal lattice, and material-specific Bragg angles enable measurements of multiple layers even when they are thinner than the optical skin depth and/or buried below opaque capping layers[33–35]. The lattice constant variations of each layer can be measured with high absolute accuracy, making it possible to determine the amount of deposited heat in metal bilayers that was debated recently[30–32]. The great promise of ultrafast X-ray diffraction (UXRD) for nanoscale thermal transport measurements and ultrafast lattice dynamics has already been demonstrated in experiments with synchrotron-based sources[33–36]. However, limited temporal resolution of these experiments (~100 ps) only allowed to study heat transport on a relatively slow (nanosecond) time scale and over distances >100 nm. Ultrafast nanoscale thermal transport research will greatly benefit from femtosecond X-ray sources. While free electron laser facilities are in very high demand, an alternative is offered by laser-based plasma sources of femtosecond X-rays[37,38], which lack the coherence and high flux of a free electron laser but are fully adequate for UXRD measurements[6,39,40]. As an example, a recent experiment on 6 nm thick Au nanotriangles[39] confirmed the $\tau_{Au}^0 = 5$ ps electron–phonon equilibration time generally accepted for high fluence excitation of Au[3,6,41,42]. For similar fluences ultrafast electron diffraction reported $\tau_{Ni}^0 = 0.75$ to 1 ps for Ni thin films between room temperature and Curie temperature T_C[7,43].

In this report, we demonstrate that the use of a femtosecond X-ray probe enables thermal transport measurements over a distance as small as ~5 nm in a Au/Ni bilayer with thickness $d_{Au} = 5.6$ nm and $d_{Ni} = 12.4$ nm grown on MgO. By monitoring the dynamics of the lattice constants of Au and Ni, we find that the Ni lattice fully expands within about 2 ps, while the Au lattice initially remains cold even if a significant fraction of the excitation light is absorbed by the electronic subsystem in Au. The Au lattice then heats up slowly, reaching the maximum temperature about 80 ps after the optical excitation. The observed thermal relaxation of the bilayer structure is two orders of magnitude slower than 1 ps predicted by the heat equation and also much slower than the usual electron–phonon equilibration time $\tau_{Au}^0 = $ 1–5 ps (see Table 1)[3,41,42]. We explain this surprising result in a model (see Fig. 1) based on the keen insight into the physics of the thermal transport in Au–Pt bilayers offered in recent studies[11,13], which showed that nonequilibrium between electrons and lattice in Au persists for a much longer time in a bilayer than in a single Au film. We find, furthermore, that on the spatial scale of our experiment thermal transport by phonons in metals can no longer be neglected. Our results underscore challenges for thermal transport modeling on the nanometer scale. On the other hand, they demonstrate the great potential of the UXRD for monitoring thermal transport under experimental conditions typical for studies of ultrafast magnetism[20,44].

Results

Experiment. We use femtosecond laser pulses at 400 and 800 nm to excite the electron system of Au and Ni through the Au top layer. The sample structure and the calculated absorption profiles are shown in Fig. 1. We note that for 400 nm pulses the absorbed energy density $\rho_{Au,Ni}^Q$ in Au and Ni is similar, whereas for 800 nm almost no light is absorbed in Au. The much higher absorption of 400 nm light in Au is a result of the larger real part of the refractive index[31,32]. For our 5.6 nm thick Au film, the destructive interference of light reflected at the interfaces additionally contributes to the suppressed absorption at 800 nm.

The strains $\varepsilon_{Au,Ni}$ determined via Bragg's law from UXRD data (Fig. 2b, c) can be converted to lattice temperature changes $\Delta T_{Au,Ni}$ and energy density changes $\rho_{Au,Ni}^Q$ via

$$\varepsilon_{Au,Ni} = \alpha_{Au,Ni}^{uf} \Delta T_{Au,Ni} \tag{1}$$

$$\varepsilon_{Au,Ni} = \frac{\alpha_{Au,Ni}^{uf}}{C_{Au,Ni}} \rho_{Au,Ni}^Q \tag{2}$$

Table 1 Thermophysical parameters of Au and Ni

Parameter	Gold	Nickel
Lattice specific heat, C^{ph} (10^6 Jm^{-3} K^{-1})	2.5[54]	3.8[55]
Sommerfeld constant, γ^S (Jm^{-3} K^{-2})	67.5[2]	1074[2]
Electron–phonon coupling constant, g (10^{16} Wm^{-3} K^{-1})	1–4[2]	36–105[2]
e-ph coupling time isolated layers @1000 K, τ^0 (ps)	1.7–6.7	1–3
e-ph coupling time equilibrated electrons @1000 K, τ (ps)	26–107	1–3
Thermal conductivity, κ (Wm^{-1} K^{-1})	318[56]	90[56]
Thermal conductivity (lattice), κ^{ph} (Wm^{-1} K^{-1})	5[56]	9.6[56]
Expansion coefficient with Poisson correction, α^{uf} (10^{-5} K^{-1})	3.16[57]	2.8[57]

Literature values for material parameters relevant for modeling the heat transfer after laser excitation. For C^{ph} we use the parameters at room temperature. The e-ph coupling time ranges are calculated for 1000 K to show that for an equilibrated electron system, the e-ph coupling time in Ni is much shorter than in Au
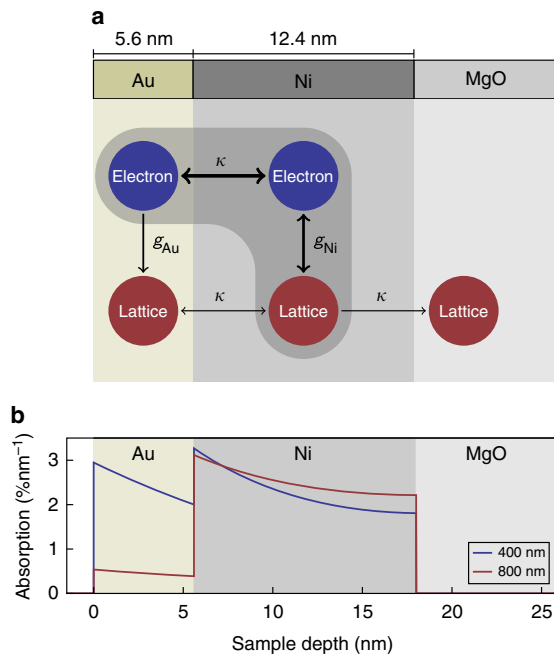
ARTICLE

Fig. 1 Schematic of heat reservoirs in the sample structure. **a** Layer stacking of the metallic heterostructure: Au on Ni deposited on an MgO substrate. Each layer has a phonon heat reservoir. The metal layers additionally have an electronic heat reservoir. The heat contained in the Ni spin system is included in the electron system. The electron–phonon coupling constants g_{Au} and g_{Ni} parametrize the local energy flow among electrons and phonons within each layer, whereas the thermal conductivity κ indicates spatial heat transport. **b** Calculated optical absorption profiles in the metallic bilayer
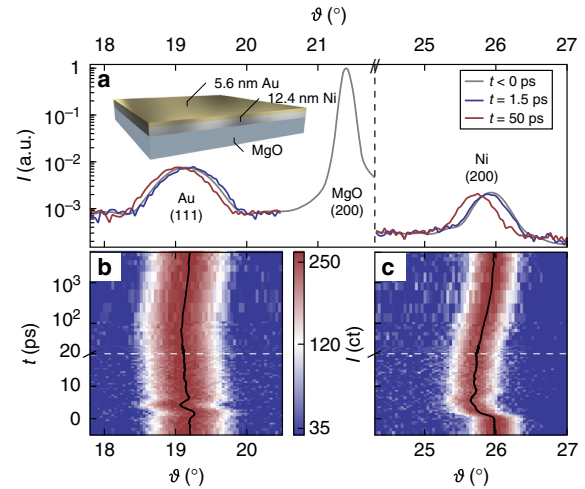

Fig. 2 Experimental data. **a** X-ray diffraction pattern of the sample (see inset) evidencing the crystalline orientation of the Au and Ni nanolayers. Colored lines visualize transient shifts of the Bragg peaks at selected times. Their full time evolution is shown in panels (**b**) for Au and **c** for Ni along with the respective peak center positions (black line). The white dashed line indicates the axis break from linear to logarithmic time scale

using effective out-of-plane expansion coefficients $\alpha_{Au,Ni}^{uf}$ and specific heats $C_{Au,Ni}$, which are generally temperature dependent. For our experimental conditions temperature-independent coefficients are good approximations. The effective expansion coefficients $\alpha_{Au,Ni}^{uf}$ take into account the crystalline orientation of the films and the fact that on ultrafast (uf) timescales the film can exclusively expand out-of plane, since the uniform heating of a large pump-spot region leads to a one-dimensional situation, as in-plane forces on the atoms by the thermal stresses vanish. For details about $\alpha_{Au,Ni}^{uf}$ and a description how heat in electrons and phonons drive the transient stress via macroscopic Grüneisen coefficients see the Methods section.

We now discuss the information that can be directly inferred from the measured transient strains (Fig. 3) in the laser-excited metallic bilayer without any advanced modeling. For convenience, we added two right vertical axes to Fig. 3a, b showing the layer-specific temperature and energy density according to Eqs. (1) and (2). Initially Ni expands, while the Au layer gets compressed by the expansion of the Ni film. Around 3 ps Au shows a pronounced expansion, when the compression wave turns into an expansion wave upon reflection at the surface. Less pronounced signatures of the strain wave are observed in Ni as well. A surprisingly long time of about 80 ps is required to reach the maximum expansion of Au by transport of heat from the adjacent Ni until $T_{Au} \approx T_{Ni}$. For times $t > 100$ ps, cooling by heat transfer to the substrate dominates the signal. In Fig. 3c we show the heat energy ΔQ_{MgO} flowing through a unit area A into the

Fig. 3 Transient energy densities and temperatures. Transient lattice strain ε in the Au film (**a**) and the Ni film (**b**) as measured by UXRD after excitation with 400 nm (blue) and 800 nm (red) light pulses. The right axis label the temperature change ΔT and the energy density ρ^Q calculated from ε. **c** Red and blue dots show the energy per unit area $\Delta Q/A$ obtained from (**a**, **b**) by multiplication with $d_{Au,Ni}$. The red and blue lines show thermal dynamics with acoustic oscillations removed, yielding the true energy per unit area $\Delta Q/A$. The black dashed line shows the sum of these energies. The gray line is the thermal energy that has been transported into the substrate

substrate, which we can directly calculate from the measured energy densities via

$$\Delta Q_{\mathrm{MgO}}(t)/A = -d_{\mathrm{Au}}\Delta\rho_{\mathrm{Au}}^{Q}(t) - d_{\mathrm{Ni}}\Delta\rho_{\mathrm{Ni}}^{Q}(t). \qquad (3)$$

$\Delta\rho_{\mathrm{Ni,Au}}^{Q}(t) = \rho_{\mathrm{Ni,Au}}^{Q}(t) - \rho_{\mathrm{Ni,Au}}^{Q}(0)$ are the changes of the energy densities ρ_{Ni}^{Q} and ρ_{Au}^{Q} with respect to the initially deposited energy densities. Even when the temperatures are equilibrated at $t > 100$ ps, ρ_{Ni}^{Q} and ρ_{Au}^{Q} differ strongly because of the different specific heat of Au and Ni. Figure 3c confirms that within the first 20 ps the heat energy $\Delta Q_{\mathrm{Au}} = d_{\mathrm{Au}}\Delta\rho_{\mathrm{Au}}^{Q}$ flowing from Ni into Au is similar to the amount ΔQ_{MgO} transported into the substrate. At about 150 ps half of the energy deposited in the film has been transported into the substrate. However, leaking a fraction of the thermal energy to the insulating substrate does not explain why the ultrathin Au layer is not much more rapidly heated via electronic heat transport typical of metals.

Modeling. Inspired by the recent studies using TDTR[11,13] we set up a modified two-temperature model graphically represented in Fig. 1b to rationalize the slow Au heating observed in Fig. 3a. We first justify this simplified modeling. The high electron conductivity—potentially including ballistic and superdiffusive electrons—rapidly equilibrates the electron systems of Ni and Au. The fact that the Au layer is equally compressed in the first 2 ps irrespective of the excitation wavelengths is an experimental proof of the rapid equilibration of electron temperatures. Otherwise the high electron pressure in Au after 400 nm excitation (cf. Fig. 1c) would counterbalance the compression caused by the Ni expansion[6]. As Ni has a much larger Sommerfeld constant (Table 1) the electronic specific heat $C^{\mathrm{e}} = \gamma^{S}T$ is dominated by Ni and the ratio of energy densities $\rho_{\mathrm{Ni}}^{Q}/\rho_{\mathrm{Au}}^{Q} \approx 10$ is large at 1 ps. A significant electronic interface resistance[45] that would prevent a rapid equilibration of electron temperatures in Au and Ni is clearly incompatible with our measurements at 400 nm. If the electrons did not equilibrate much faster than 1 ps and effectively remove the heat deposited in the electron system of Au, we would not observe the same strong compression of the Au lattice, since electronic pressure would instantaneously force the Au to expand[6,7,40,43]. In the diffuse-mismatch model, the electronic interface conductance of metals increases linearly with the temperature and can be calculated from the Sommerfeld constant and the Fermi velocity[45]. Immediately after excitation, the electron temperature reaches several thousand Kelvin, which leads to a subpicosecond thermalization of the electrons in simulations, including the interface resistance.

The electron–phonon coupling constant in Ni is much larger than in Au (Table 1). Consequently, nearly all photon energy initially absorbed in the electronic system is funneled into the Ni lattice, even when one third of the absorbed energy is initially deposited in the electronic system of Au with 400 nm excitation. In contrast, the electron–phonon coupling times $\tau_{\mathrm{Au,Ni}}^{0} = C_{\mathrm{Au,Ni}}^{\mathrm{e}}/g_{\mathrm{Au,Ni}}$ for Au and Ni are not very different if the films are not in contact, because the large electronic specific heat $C_{\mathrm{Ni}}^{\mathrm{e}}$ of Ni cancels its large electron–phonon coupling constant g_{Ni} (see Table 1). However, in the bilayer, the electrons in Au and Ni rapidly form an equilibrated heat bath with $C_{\mathrm{tot}}^{\mathrm{e}} \approx C_{\mathrm{Ni}}^{\mathrm{e}}$. Now only the electron–phonon coupling constant determines the coupling time: $\tau_{\mathrm{Ni}} = C_{\mathrm{tot}}^{\mathrm{e}}/g_{\mathrm{Ni}} \ll C_{\mathrm{tot}}^{\mathrm{e}}/g_{\mathrm{Au}} = \tau_{\mathrm{Au}}$.

We start the numerical modeling when a quasi-equilibrium temperature in the combined system $C_{\mathrm{com}} = C_{\mathrm{Au}}^{\mathrm{e}} + C_{\mathrm{Ni}}^{\mathrm{e}} + C_{\mathrm{Ni}}^{\mathrm{ph}} \approx C_{\mathrm{Ni}}^{\mathrm{e}} + C_{\mathrm{Ni}}^{\mathrm{ph}} \approx C_{\mathrm{Ni}}$ is established after electron–phonon equilibration in Ni around $\tau_{\mathrm{Ni}} = C_{\mathrm{tot}}^{\mathrm{e}}/g_{\mathrm{Ni}} \approx C_{\mathrm{Ni}}^{\mathrm{e}}/g_{\mathrm{Ni}} \approx 1$ ps. Since $C_{\mathrm{Ni}}^{\mathrm{ph}} \gg C_{\mathrm{Ni}}^{\mathrm{e}} \gg C_{\mathrm{Au}}^{\mathrm{e}}$ and $d_{\mathrm{Ni}} > d_{\mathrm{Au}}$, we refer to the combined system as C_{Ni}

in the equations. Since the energy stored in each layer is proportional to their thickness and the energy transfer rate from electrons to phonons in Au is proportional to the Au volume $V_{\mathrm{Au}} \propto d_{\mathrm{Au}}$, the differential equations describing this special TTM represented in Fig. 1b read

$$d_{\mathrm{Au}}C_{\mathrm{Au}}^{\mathrm{ph}}\frac{\partial T_{\mathrm{Au}}^{\mathrm{ph}}}{\partial t} = d_{\mathrm{Au}}g_{\mathrm{Au}}\left(T_{\mathrm{Ni}} - T_{\mathrm{Au}}^{\mathrm{ph}}\right) \qquad (4)$$

$$d_{\mathrm{Ni}}C_{\mathrm{Ni}}\frac{\partial T_{\mathrm{Ni}}}{\partial t} = d_{\mathrm{Au}}g_{\mathrm{Au}}\left(T_{\mathrm{Au}}^{\mathrm{ph}} - T_{\mathrm{Ni}}\right). \qquad (5)$$

Note that the two temperatures in this model are the temperature of the Au lattice, $T_{\mathrm{Au}}^{\mathrm{ph}}$ and the temperature of the combined system, which is denoted as T_{Ni}, keeping in mind that this Ni temperature equals the Au electron temperature. For small temperature changes over which the specific heats are approximately constant, the solution to this system of equations is an exponential decay of $T_{\mathrm{Ni}} \sim e^{-t/\tau}$ and a concomitant rise of the Au lattice temperature $T_{\mathrm{Au}} \sim (1 - e^{-t/\tau})$ on the characteristic timescale

$$\tau = \frac{1}{g_{\mathrm{Au}}\left(\frac{1}{C_{\mathrm{Au}}} + \frac{d_{\mathrm{Au}}}{d_{\mathrm{Ni}}}\frac{1}{C_{\mathrm{Ni}}}\right)}. \qquad (6)$$

Due to the small film thickness and the rapid electronic heat diffusion, we do not assume any gradient in the temperatures of each film. At about 1 ps after excitation we define the initial conditions as $T_{\mathrm{Ni}}(1\,\mathrm{ps}) = T_{\mathrm{Ni}}^{\mathrm{i}}$ and $T_{\mathrm{Au}}^{\mathrm{i}} \approx 0$. The final temperature after equilibrating the temperatures of the two thin films, neglecting heat transport to the substrate is

$$T^{\mathrm{f}} = T^{\mathrm{i}}\frac{d_{\mathrm{Ni}}C_{\mathrm{Ni}}}{d_{\mathrm{Au}}C_{\mathrm{Au}}^{\mathrm{ph}} + d_{\mathrm{Ni}}C_{\mathrm{Ni}}}. \qquad (7)$$

This very simple model (dashed lines of Fig. 4a) for the transient quasi-equilibrium temperatures agrees very well with the data. In particular, the exponential rise of T_{Au} and the exponential decay of T_{Ni} converge around 80 ps. Deviations at longer times originate mainly from heat transport into the MgO substrate, which is not included in the model (dashed lines).

The only fitting parameters of our model are the initial temperature T^{i} and the electron–phonon coupling constant of Au. With our simple model we get the best fit using $g_{\mathrm{Au}} = 6.5 \times 10^{16}\,\mathrm{W\,m^{-3}\,K^{-1}}$, which is somewhat larger than the range from 1 to $4 \times 10^{16}\,\mathrm{W\,m^{-3}\,K^{-1}}$ reported in the literature[2,3]. If—as an example—we reduce the electron–phonon coupling constant to the value of $4 \times 10^{16}\,\mathrm{W\,m^{-3}\,K^{-1}}$, the calculated equilibration of T_{Au} and T_{Ni} is much too slow. Including electronic interface resistance would make it even slower. The missing energy transfer rate, however, can be easily rationalized by phonon heat conductivity κ^{ph}. If we fully disregarded electronic heat conduction in Au, the literature value for $\kappa_{\mathrm{Au}}^{\mathrm{ph}}$ given in Table 1 would lead to an equilibration of Au and Ni temperature exclusively via phonons three times faster than we observe. The phonon heat transport is probably much less efficient than this prediction because of additional interface resistances for phonon heat transport and because the mean free path of phonons is on the order of the layer thickness[8,10]. However, we do not attempt to quantify κ^{ph} and g_{Au} here. We only note qualitatively that to conform to the expected values of electron–phonon coupling in Au, the phonon heat conduction must become important in nanoscale multilayers, even though
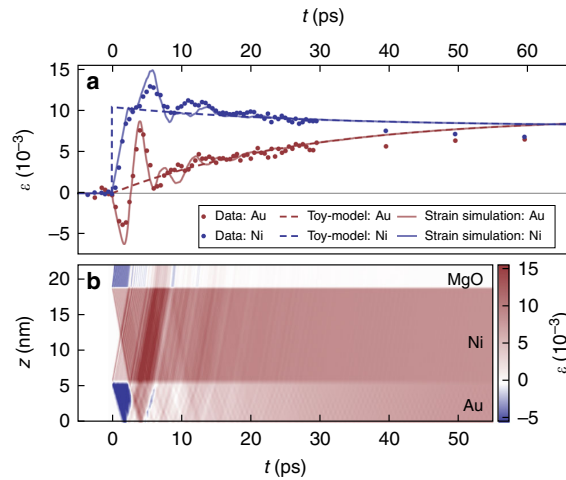
ARTICLE

Fig. 4 Comparison of models with the experimental data. **a** Dots indicate the measured strain ε. The dashed lines represent the strain calculated from the average heating of the layers according to the model visualized in Fig. 1b. Solid lines are simulations, which are based on this model and additionally include the strain waves triggered by the impulsive excitation (see Methods section). Heat transport to the substrate is not included. **b** Color-coded strain ε as a function of sample depth and time t, which is simulated assuming a spatially homogeneous transient thermal stress in each layer which is proportional to the dashed lines in (**a**). Spatial averaging of the strain $\varepsilon(t)$ in each layer yields the solid lines in panel (**a**)

normally the heat conduction in metals is dominated by electrons ($\kappa \gg \kappa^{ph}$ see Table 1). Phonon heat transport is not included in our numerical calculations, because in fact the heat diffusion equation is not valid at such small length scales below the phonon mean free path. Similarly, a complex theoretical modeling would be required to simulate the heat transport to the substrate, e.g., by heat transfer from Ni electrons to MgO phonons at the interface[46]. Figure 3c provides a benchmark of the experimentally determined phonon heat transport into the substrate.

Discussion

In summary, the modified TTM model (Eqs. (4) and (5)) captures the essence of heat transport between ultrathin metal films: the electrons in Au and Ni are rapidly equilibrated. This is evidenced by the fact that 400 and 800 nm excitation both initially only heat Ni, regardless of the energy absorbed in Au. For 400 nm excitation we showed an intricate process of shuttling heat energy back and forth between the layers: the electrons first rapidly transport energy from Au into Ni (e–e equilibration $\ll$ 1 ps) before they transport some of the heat back from the Ni phonons to the Au phonons. Finally, the heat flows back through Ni toward the substrate. Heat transport by phonons can account for a fraction of the Au heating. The energy transported from the Ni phonons via Ni and Au electrons into the Au lattice is throttled by the weak electron–phonon coupling in Au. We believe that our results will have an important impact on ultrafast studies of the spin-Seebeck effect, superdiffusive electron transport as well as optical demagnetization and remagnetization. Precise measurements of the total heat in the system after few picoseconds will help to determine the actually required laser fluence in ultrafast demagnetization studies, which currently diverge by an order of magnitude in the literature[44,47]. The lattice is not only discussed as the sink of angular momentum in the ultrafast demagnetization: with its dominant heat capacity the lattice constitutes the heat bath which controls the speed of reordering of the spin

systems at high fluence[20,44]. Our detailed account of heat flow in Ni after photo-excitation must influence the interpretation of MOKE data, which were fitted in previous studies[20,48] by using a value for the specific heat of the Ni phonon system which is a factor of two below the Dulong–Petit value.

We have demonstrated the power of UXRD in probing nanoscale heat transport in an ultrathin metallic bilayer system which is relevant to current magnetic recording developments such as heat-assisted magnetic recording. To understand the all-optical-[15] and helicity-dependent[49] switching in ferrimagnets and two different timescales observed in the demagnetization of transition metals[20,44] or rare earths[50,51], precise calibration of the lattice temperature is crucial. We are convinced that the direct access to the lattice, the layer-specific information for layers thinner than the optical skin depth, the conceptual simplicity of the arguments and the experimental geometry make the paper particularly useful for comparisons to previous[20,30–32,44] and future work on optical manipulation of spins.

Methods

Sample growth and UXRD. Ni/Au stacks with different Ni and Au thicknesses were grown by molecular beam epitaxy onto a MgO(001) substrate at 100 °C. The MgO(001) substrates were degassed at 350 °C for 10 min. The pressure during growth never exceeded 6^{-10} mbar. We measured the layer thicknesses $d_{Au} = 5.6$ nm and $d_{Ni} = 12.4$ nm of the investigated sample by X-ray reflectivity. The 24 lattice planes of Au yield a symmetric (111) Bragg reflection (Fig. 2a) at $\vartheta = 19.29°$, well separated from the symmetric (200) Ni peak at 25.92° originating from 70 lattice planes. The lattice strains $\varepsilon_{Ni,Au}(t) = -\cot(\vartheta(t))\Delta\vartheta(t)$ perpendicular to the sample surface are directly retrieved from the time-resolved Bragg-peak positions ϑ (t) (Fig. 2b, c)[58,39,40]. These UXRD data were recorded at our laser-driven plasma X-ray source at the University of Potsdam, that emits 200 fs X-ray pulses with a photon energy of 8 keV. The sample was excited by p-polarized 400 and 800 nm laser pulses of about 100 fs duration with a pulse energy of 0.3 mJ and a diameter of 1.5 mm (FWHM). Since the angle between the pump pulse and the Bragg-reflecting X-ray probe pulse is fixed in the setup, we take into account the modified angle of incidence of the optical pulse of 44° (51°) with respect to the surface normal for the Ni (Au) reflection to calculate the incident fluence of 9 (8) mJ/cm² and an absorbed fluence of 3 (2.9) mJ/cm² for our bilayer system using a matrix formalism, which also yields the absorption profiles at 400 and 800 nm excitation shown in Fig. 1c[52]. The above values are for 800 nm excitation, and the 400 nm data in Fig. 3 are scaled up for better comparison of the two different excitation conditions.

Correction of the thermal expansion coefficient. The effective expansion coefficient $\alpha_{Au,Ni}^{uf}$ valid for heating a thin epitaxial layer is based on the lattice constants and strains predicted from equilibrium thermal expansion coefficients, corrected according to the Poisson effect[53]. In cubic materials with (100) surface orientation the ratio of the observed ultrafast (uf) strain and the strain $\varepsilon^{eq} = \alpha^{eq}(T)\Delta T$ along the (100) direction calculated from equilibrium value (eq) is $\varepsilon/\varepsilon^{eq} = \alpha^{uf}(T)/\alpha^{eq}$ $(T) = 1 + 2C_{12}/C_{11} = 2.2$ for Ni and would be 2.6 for Au. For the Au (111) cubic crystal surface, the above equation is still valid if the elastic constants are calculated in the rotated coordinate system, in which the x-axis is [111]. We find that the newly obtained C_{11} and C_{12} coincidentally yield the same correction factor of 2.2 for Au (111) as for Ni (100).

Strain waves prove ultrafast electron-equilibration. The pronounced compression and expansion of the Au layer (see Fig. 4a) clearly originates from the laser-induced stress generated in Ni. In order to show that our modified TTM predicting negligible energy density in Au immediately after the excitation can quantitatively explain the signal oscillations, we have used the transient temperatures $T_{Ni,Au}(t)$ from our TTM as input parameters for a full thermo-elastic simulation using the udkm1Dsim toolbox, which are represented as solid lines in Fig. 4a[59]. For convenience, Fig. 4b shows the spatio-temporal strain map from which the solid lines in Fig. 4a are calculated by spatial averaging over the layer for each time delay. Multiple reflections of strain waves at the interfaces are strongly damped by transmission to the substrate.

Macroscopic Grüneisen coefficients. Several recent ultrafast X-ray diffraction and electron diffraction experiments on thin metal films have highlighted two contributions of electrons and phonons to the transient stress σ, which drives the observed strain waves. A very useful concept uses the macroscopic Grüneisen coefficient Γ^e and Γ^{ph}, which relate the energy densities ρ^Q to the stress $\sigma = \Gamma\rho$. While in Au the electronic Grüneisen constant $\Gamma_{Au}^e = 1.5$ is about half of its phonon counterpart $\Gamma_{Au}^{ph} = 3.0$, in Ni $\Gamma_{Ni}^e = 1.5$ is only slightly different from $\Gamma_{Ni}^{ph} = 1.7$[6,7]. For our analysis the distinction of the origin of pressure in Ni is not very relevant, since the redistribution of energy from electrons to phonons only increases the

ARTICLE

stress by 15%. In Au the electron pressure is negligible in our bilayer system, since due to the large electronic specific heat of Ni and the subpicosecond equilibration among the electrons, all the energy is accumulated in Ni. The ab initio modeling discussed in connection to the recent UXRD study on Fe points out that both electron–phonon coupling parameters and phonon Grüneisen coefficients depend on the phonon mode[5,29]. While in that study the scattering of X-rays from individual phonon modes selected by the scattering geometry may require a mode-specific analysis, we believe that measuring the lattice expansion via a Bragg-peak shift looks at an average response of the lattice to all phonon modes, and hence a mode-averaged analysis is reasonable if there is no selective excitation of modes with extraordinarily different Grüneisen coefficients.

Data availability. The data that support the findings of this study are available from the corresponding authors on reasonable request.

References

1. Waldecker, L., Bertoni, R., Ernstorfer, R. & Vorberger, J. Electron–phonon coupling and energy flow in a simple metal beyond the two-temperature approximation. *Phys. Rev. X* **6**, 021003 (2016).
2. Lin, Z., Zhigilei, L. V. & Celli, V. Electron–phonon coupling and electron heat capacity of metals under conditions of strong electron–phonon nonequilibrium. *Phys. Rev. B* **77**, 75133 (2008).
3. Hohlfeld, J. et al. Electron and lattice dynamics following optical excitation of metals. *Chem. Phys.* **251**, 237–258 (2000).
4. Sun, C.-K., Vallée, F., Acioli, L., Ippen, E. P. & Fujimoto, J. G. Femtosecond investigation of electron thermalization in gold. *Phys. Rev. B* **48**, 12365–12368 (1993).
5. Henighan, T. et al. Generation mechanism of terahertz coherent acoustic phonons in Fe. *Phys. Rev. B* **93**, 220301 (2016).
6. Nicoul, M., Shymanovich, U., Tarasevitch, A., von der Linde, D. & Sokolowski-Tinten, K. Picosecond acoustic response of a laser-heated gold-film studied with time resolved x-ray diffraction. *Appl. Phys. Lett.* **98**, 191902 (2011).
7. Wang, X. et al. Electronic Grüneisen parameter and thermal expansion in ferromagnetic transition metal. *Appl. Phys. Lett.* **92**, 121918 (2008).
8. Cahill, D. G. et al. Nanoscale thermal transport. *J. Appl. Phys.* **93**, 793 (2003).
9. Siemes, M. E. et al. Quasiballistic thermal transport from nanoscale interfaces observed using ultrafast coherent soft x-ray beams. *Nat. Mater.* **9**, 26–30 (2010).
10. Maznev, A. A. & Johnson, J. A. Onset of nondiffusive phonon transport in transient thermal grating decay. *Phys. Rev. B* **84**, 1–8 (2011).
11. Wang, W. & Cahill, D. G. Limits to thermal transport in nanoscale metal bilayers due to weak electron–phonon coupling in Au and Cu. *Phys. Rev. Lett.* **109**, 1–5 (2012).
12. Cahill, D. G. et al. Nanoscale thermal transport II. *Appl. Phys. Rev.* **1**, 011305 (2014).
13. Gyung-Min Choi, R. B., Wilson & Cahill, D. G. Indirect heating of Pt by short-pulse laser irradiation of Au in a nanoscale Pt/Au bilayer. *Phys. Rev. B* **89**, 064307 (2014).
14. Challener, W. A. et al. Heat-assisted magnetic recording by a near-field transducer with efficient optical energy transfer. *Nat. Photonics* **3**, 220–224 (2009).
15. Xu, Y. et al. Ultrafast magnetization manipulation using single femtosecond light and hot-electron pulses. *Adv. Mater.* **29**, 1703474 (2017).
16. Stanciu, C. D. et al. All-optical magnetic recording with circularly polarized light. *Phys. Rev. Lett.* **99**, 47601 (2007).
17. Kirilyuk, A., Kimel, A. V. & Rasing, Th Ultrafast optical manipulation of magnetic order. *Rev. Mod. Phys.* **82**, 2731–2784 (2010).
18. Mangin, S. et al. Engineered materials for all-optical helicity-dependent magnetic switching. *Nat. Mater.* **13**, 286–292 (2014).
19. El Hadri, M. S. et al. Two types of all-optical magnetization switching mechanisms using femtosecond laser pulses. *Phys. Rev. B* **94**, 064412 (2016).
20. Koopmans, B. et al. Explaining the paradoxical diversity of ultrafast laser-induced demagnetization. *Nat. Mater.* **9**, 259–265 (2010).
21. Battiato, M., Carva, K. & Oppeneer, P. M. Superdiffusive spin transport as a mechanism of ultrafast demagnetization. *Phys. Rev. Lett.* **105**, 027203 (2010).
22. Schellekens, A. J., Kuiper, K. C., De Wit, R. & Koopmans, B. Ultrafast spin-transfer torque driven by femtosecond pulsed-laser excitation. *Nat. Commun.* **5**, 4333 (2014).
23. Alekhin, A. et al. Femtosecond spin current pulses generated by the nonthermal spin-dependent seebeck effect and interacting with ferromagnets in spin valves. *Phys. Rev. Lett.* **119**, 017202 (2017).
24. Choi, G.-M., Moon, C.-H., Min, B.-C., Lee, K.-J. & Cahill, D. G. Thermal spin-transfer torque driven by the spin-dependent seebeck effect in metallic spin-valves. *Nat. Phys.* **11**, 576 (2015).
25. Kimling, J. & Cahill, D. G. Spin diffusion induced by pulsed-laser heating and the role of spin heat accumulation. *Phys. Rev. B* **95**, 014402 (2017).
26. Carva, K., Battiato, M. & Oppeneer, P. M. Ab initio investigation of the Elliott–Yafet electron–phonon mechanism in laser-induced ultrafast demagnetization. *Phys. Rev. Lett.* **107**, 207201 (2011).
27. Carva, K., Battiato, M., Legut, D. & Oppeneer, P. M. Ab initio theory of electron–phonon mediated ultrafast spin relaxation of laser-excited hot electrons in transition-metal ferromagnets. *Phys. Rev. B* **87**, 184425 (2013).
28. Reid, A. H. et al. Beyond a phenomenological description of magnetostriction. *Nat. Commun.* **9**, 388 (2018).
29. Maldonado, P., Carva, K., Flammer, M. & Oppeneer, P. M. Theory of out-of-equilibrium ultrafast relaxation dynamics in metals. *Phys. Rev. B* **96**, 174439 (2017).
30. Eschenlohr, A. et al. Ultrafast spin transport as key to femtosecond demagnetization. *Nat. Mater.* **12**, 332–336 (2013).
31. Khorsand, A. R., Savoini, M., Kirilyuk, A. & Rasing, Th Optical excitation of thin magnetic layers in multilayer structures. *Nat. Mater.* **13**, 101–102 (2014).
32. Eschenlohr, A. et al. Reply to "Optical excitation of thin magnetic layers in multilayer structures". *Nat. Mater.* **13**, 102–103 (2014).
33. Highland, M. et al. Ballistic-phonon heat conduction at the nanoscale as revealed by time-resolved X-ray diffraction and time-domain thermoreflectance. *Phys. Rev. B* **76**, 075337 (2007).
34. Shayduk, R. et al. Nanoscale heat transport studied by high-resolution time-resolved x-ray diffraction. *New J. Phys.* **13**, 093032 (2011).
35. Koc, A. et al. Ultrafast x-ray diffraction thermometry measures the influence of spin excitations on the heat transport through nanolayers. *Phys. Rev. B* **96**, 014306 (2017).
36. Sheu, Y. M. et al. Thermal transport in a semiconductor heterostructure measured by time-resolved X-ray diffraction. *Phys. Rev. B* **78**, 045317 (2008).
37. Schick, D. et al. Normalization schemes for ultrafast x-ray diffraction using a table-top laser-driven plasma source. *Rev. Sci. Instrum.* **83**, 025104 (2012).
38. Zamponi, F. et al. Femtosecond hard x-ray plasma sources with a kilohertz repetition rate. *Appl. Phys. A* **96**, 51–58 (2009).
39. von Reppert, A. et al. Watching the vibration and cooling of ultrathin gold nanotriangles by ultrafast x-ray diffraction. *J. Phys. Chem. C* **120**, 28894–28899 (2016).
40. von Reppert, A. et al. Persistent nonequilibrium dynamics of the thermal energies in the spin and phonon systems of an antiferromagnet. *Struct. Dyn.* **3**, 054302 (2016).
41. Hartland, G. V. Measurements of the material properties of metal nanoparticles by time-resolved spectroscopy. *Phys. Chem. Chem. Phys.* **6**, 5263–5274 (2004).
42. Del Fatti, N., Arbouet, A. & Vallée, F. Femtosecond optical investigation of electron–lattice interactions in an ensemble and a single metal nanoparticle. *Appl. Phys. B* **84**, 175–181 (2006).
43. Wang, X. et al. Temperature dependence of electron–phonon thermalization and its correlation to ultrafast magnetism. *Phys. Rev. B* **81**, 220301 (2010).
44. Roth, T. et al. Temperature dependence of laser-induced demagnetization in Ni: a key for identifying the underlying mechanism. *Phys. Rev. X* **2**, 021006 (2012).
45. Gundrum, B. C., Cahill, D. G. & Averback, R. S. Thermal conductance of metal–metal interfaces. *Phys. Rev. B* **72**, 245426 (2005).
46. Sokolowski-Tinten, K. et al. Electron–lattice energy relaxation in laser-excited thin-film Au-insulator heterostructures studied by ultrafast mev electron diffraction. *Struct. Dyn.* **4**, 054501 (2017).
47. Atxitia, U., Chubykalo-Fesenko, O., Walowski, J., Mann, A. & Münzenberg, M. Evidence for thermal mechanisms in laser-induced femtosecond spin dynamics. *Phys. Rev. B* **81**, 174401 (2010).
48. Kim, J.-W., Vomir, M. & Bigot, J.-Y. Ultrafast magnetoacoustics in nickel films. *Phys. Rev. Lett.* **109**, 166601 (2012).
49. Alebrand, S., Hassdenteufel, A., Steil, D., Cinchetti, M. & Aeschlimann, M. Interplay of heating and helicity in all-optical magnetization switching. *Phys. Rev. B Condens. Matter Mater. Phys.* **85**, 1–5 (2012).
50. Frietsch, B. et al. Disparate ultrafast dynamics of itinerant and localized magnetic moments in gadolinium metal. *Nat. Commun.* **6**, 8262 (2015).
51. Rettig, L. et al. Itinerant and localized magnetization dynamics in antiferromagnetic ho. *Phys. Rev. Lett.* **116**, 257202 (2016).
52. Yariv, A. & Yeh, P. *Optical waves in Layered Media*. (Wiley, New York, 1988).
53. Lee, H. J. et al. Optically induced lattice dynamics probed with ultrafast X-ray diffraction. *Phys. Rev. B* **77**, 132301 (2008).
54. Takahashi, Y. & Akiyama, H. Heat capacity of gold from 80 to 1000 k. *Thermochim. Acta* **109**, 105–109 (1986).
55. Meschter, P. J., Wright, J. W., Brooks, C. R. & Kollie, T. G. Physical contributions to the heat capacity of nickel. *J. Phys. Chem. Solids* **42**, 861–871 (1981).

ARTICLE

56. Stojanovic, N., Maithripala, D. H. S., Berg, J. M. & Holtz, M. Thermal conductivity in metallic nanostructures at high temperature: electrons, phonons, and the wiedemann-franz law. *Phys. Rev. B* **82**, 075418 (2010).
57. Nix, F. C. & MacNair, D. The thermal expansion of pure metals: copper, *gold*, aluminum, *nickel*, and iron. *Phys. Rev.* **60**, 597–605 (1941).
58. Schick, D. et al. Ultrafast reciprocal-space mapping with a convergent beam. *J. Appl. Crystallogr.* **46**, 1372-1377 (2013).
59. Schick, D. et al. udkm1Dsim—A simulation toolkit for 1D ultrafast dynamics in condensed matter. *Comput. Phys. Commun.* **185**, 651-660 (2014)

Author contributions
J.P. and A.v.R. conducted and analyzed the experiments. M.K. and. C.H.B. grew the nanostructures. A.A.M. and A.v.R contibuted key ideas to the interpretation, G.M. provided context to ultrafast magnetism. J.P., A.v.R and M.H. did the simulations and modeling. J.P. initiated and M.B. supervised and coordinated the project. All authors contributed to the writing of the manuscript.

Additional information
Competing interests: The authors declare no competing interests.

Reprints and permission information is available online at http://npg.nature.com/reprintsandpermissions/

Publisher's note: Springer Nature remains neutral with regard to jurisdictional claims in published maps and institutional affiliations.

Article II

Heat transport without heating?–An ultrafast x-ray perspective into a metal heterostructure

Jan-Etienne Pudell, Maximilian Mattern, Michel Hehn, Grégory Malinowski, Marc Herzog, and Matias Bargheer

When the spatial dimensions of metallic heterostructures shrink below the mean free path of its conduction electrons, the transport of electrons and hence the transport of thermal energy by electrons continuously changes from diffusive to ballistic. Electron-phonon coupling sets the mean free path to the nanoscale and the time for equilibration of electron and lattice temperatures to the picosecond range. A particularly intriguing situation occurs in trilayer heterostructures combining metals with very different electron-phonon coupling strength: Heat energy deposited in few atomic layers of Pt is transported into a nanometric Ni film, which is heated more than the Cu film through which the heat is released. Femtosecond pump-probe experiments with hard X-ray pulses provide a layer-specific probe of the heat energy. A purely diffusive two-temperature model with increased thermal conductivity of hot electrons excellently reproduces the observed signals from all three layers. At the time when the Ni lattice is maximally heated, no significant heat has entered the Cu lattice. This phenomenon would be enhanced in thinner layers where ballistic transport dominates. In this context it is shown that purely diffusive transport can lead to a linear time-to-length dependence that must not be misinterpreted as ballistic transport.

FULL PAPER
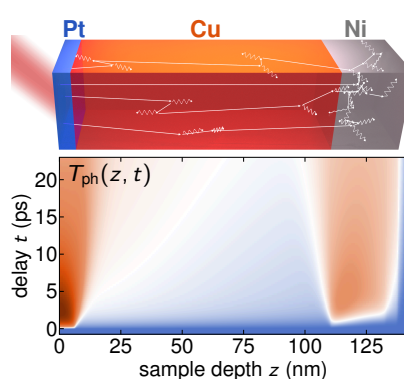
Heat Transport without Heating?—An Ultrafast X-Ray Perspective into a Metal Heterostructure

Jan-Etienne Pudell, Maximilian Mattern, Michel Hehn, Grégory Malinowski, Marc Herzog, and Matias Bargheer*

When the spatial dimensions of metallic heterostructures shrink below the mean free path of its conduction electrons, the transport of electrons and hence the transport of thermal energy by electrons continuously changes from diffusive to ballistic. Electron–phonon coupling sets the mean free path to the nanoscale and the time for equilibration of electron and lattice temperatures to the picosecond range. A particularly intriguing situation occurs in trilayer heterostructures combining metals with very different electron–phonon coupling strength: Heat energy deposited in few atomic layers of Pt is transported into a nanometric Ni film, which is heated more than the Cu film through which the heat is released. Femtosecond pump-probe experiments with hard X-ray pulses provide a layer-specific probe of the heat energy. A purely diffusive two-temperature model with increased thermal conductivity of hot electrons excellently reproduces the observed signals from all three layers. At the time when the Ni lattice is maximally heated, no significant heat has entered the Cu lattice. This phenomenon would be enhanced in thinner layers where ballistic transport dominates. In this context it is shown that purely diffusive transport can lead to a linear time-to-length dependence that must not be misinterpreted as ballistic transport.

1. Introduction

In macroscopic engineering contexts, heat transport in metals is well described by the heat equation using macroscopic thermophysical parameters of the constituent materials and additional interface thermal resistances.[1,2] This differential equation is analogous to the diffusion of quasiparticles carrying heat.[3] In metals both conduction electrons and phonons contribute,

J.-E. Pudell, M. Mattern, Dr. M. Herzog, Prof. M. Bargheer
Institut für Physik & Astronomie
Universität Potsdam
Karl-Liebknecht-Str. 24-25, 14476 Potsdam, Germany
E-mail: bargheer@uni-potsdam.de
J.-E. Pudell, Prof. M. Bargheer
Helmholtz-Zentrum Berlin für Materialien und Energie GmbH
Wilhelm-Conrad-Röntgen Campus, BESSY II, 12489 Berlin, Germany
Prof. M. Hehn, Dr. G. Malinowski
Institut Jean Lamour (UMR CNRS 7198)
Université Lorraine
2 allée André Guinier, Campus Artem, Nancy 54000, France

The ORCID identification number(s) for the author(s) of this article can be found under https://doi.org/10.1002/adfm.202004555.

and the non-equilibrium between these two subsystems has to be taken into account at short time and length scales. Ab-initio modeling of this complex problem is an active field of theoretical physics.[4–7] While the electrons rapidly acquire a Fermi-distribution, the temperature of the lattice may not be a well defined quantity for hundreds of picoseconds.[8] The non-thermal occupation of phonon modes can be described by mode-specific temperatures.[5] When the length scale of the system falls below the mean free path of the heat carrying quasiparticles, a superdiffusive and finally ballistic regime of energy transport is reached as the number of scattering events per quasiparticle approaches zero (cf. **Figure 1**a).[9–11] For timescales beyond the thermalization of the electron system, which is typically much faster than electron-phonon (e-ph) coupling, thermal transport within each subsystem can be approximated within a diffusive two-temperature model (TTM).

Remarkably, if electrons injected into a metal layer from one side traverse it ballistically at the Fermi velocity, the electronic energy is transported through the layer without heating it. In a superdiffusive regime only a small part of the electron energy dissipated by few scattering events remains in the layer. In magnetic metals, the spin degree of freedom not just complicates the problem by offering additional scattering channels.[9] The controlled manipulation of spins by hot electrons or lattice strain is a growing field of active research as it may revolutionize data processing and storage.[12–16] Superdiffusive electrons excited by femtosecond light pulses have been shown to lead to demagnetization, spin precession, and magnetization switching both in experiment and theory.[9,17–19] Electronically controlled heat pulses highlighted the potential for embedding these phenomena in modern CMOS technology.[20,21] Time-domain thermoreflectance is becoming an increasingly useful tool in material science for determining thermal conductivities of the constituents and interfaces in heterostructures.[2] However, for metal layers thinner than their skin depth the analysis is complicated. The optical response mixes contributions of adjacent layers. Thus, layers sandwiched between two metals cannot be independently analyzed. Femtosecond pump-probe experiments using X-rays can yield important additional insights, particularly when probing specific subsystems containing the heat energy.[22–27] Recently, ultrafast X-ray diffraction (UXRD) experiments revealed the unconventional heat transport in a bilayer of 5 nm Au and 10 nm Ni. It does not matter
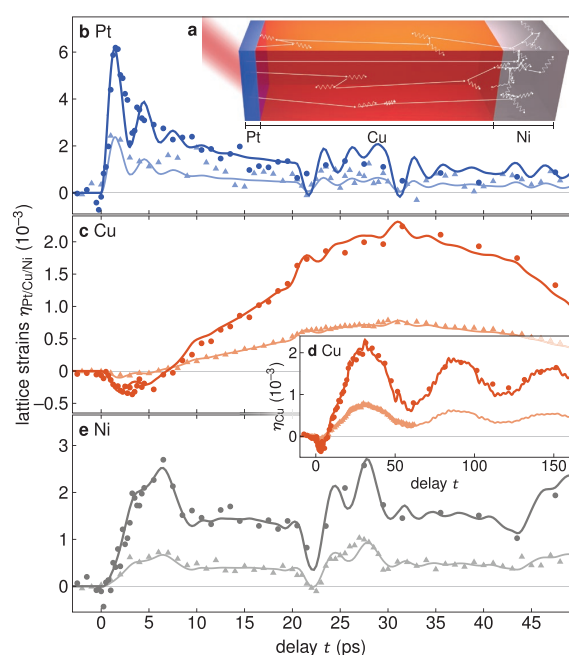
Figure 1. Layer specific UXRD data. a) Sketch of the heat transport from the exited Pt layer (blue) by electrons through a Cu layer (orange) to a Ni layer (gray). b–e) Transient lattice strains $\eta_{Pt/Cu/Ni}$ for two different excitation fluences (6.5 mJ cm^{-2} [faint colors] and 20 mJ cm^{-2} [bright colors]) of Pt, Cu, and Ni, respectively. The continuous lines originate from a simulation considering diffusion according to a TTM with the temperature-dependent electron heat conductivity according to Equation (2).

if the optical absorption occurs in Au or Ni—the electronic heat energy is very rapidly ($\lesssim 1$ ps) captured by the electrons and phonons in Ni, whereas the Au lattice heats up surprisingly slowly on a 100 ps timescale. This observation can be rationalized by a modified TTM.[25]

Here we show that electronic heat energy deposited in a 6 nm Pt film is very rapidly transported by hot electrons through a 100 nm thick Cu layer without significantly heating it. The electronic heat energy is rapidly extracted by a 20 nm thick Ni layer at the backside of the Cu layer, because Ni offers a large electronic heat capacity, which is proportional to the electronic density of states at the Fermi level.[28] Rapid e-ph coupling in Ni cools down the Ni electrons, preserving a large temperature gradient between the electron systems in Cu and Ni. We experimentally confirm this model by measuring the lattice expansion of Pt, Cu, and Ni by UXRD with sub-picosecond time resolution in a laser-based laboratory setup. Directly after laser pulse excitation of the Pt layer, the buried Ni layer shows a very rapid expansion, whereas the Cu layer is initially compressed before it slowly expands. A fully diffusive TTM of the coupled phonon and electron heat transport excellently reproduces the data simultaneously for all three layers and for several excitation conditions with one set of parameters. The model shows that the Ni lattice is heated by hot electrons much faster and to higher temperatures than the Cu lattice. Although our modeling clearly simplifies the analysis by neglecting ballistic

or superdiffusive transport and non-thermal distributions in the phonon system,[5,6] the observed phenomenon of counter-intuitive heating of the back-end of the heterostructure is described correctly. In fact, it is underestimated, since ballistic or superdiffusive motion of electrons would even increase the heating of the distant Ni layer.

Moreover, the conceptually simple diffusive modeling made us aware of a potential pitfall in deducing the transport mechanism in photoexcited metal layers from pump-probe experiments: Our model surprisingly predicts that the rise time $\tau_{10\%}$ of the Ni electron temperature to the 10% level of its maximum temperature change depends linearly on the Cu layer thickness d. Given the exclusively diffusive character of our model, our finding implies that an interpretation of similar experimental signatures as a manifestation of ballistic transport may be illegitimate. In contrast, the rise time by an absolute temperature change ΔT of the Ni layer shows the dependence $\tau_{\Delta T} \propto d^2$, which is characteristic of diffusion.

2. UXRD Experiment

We excite a metal heterostructure with a femtosecond laser pulse which is essentially absorbed in the 6 nm thick Pt cap layer (see experimental section). Figure 1 shows the transient average lattice strain of Pt (Figure 1b), Cu (Figure 1c,d) and Ni (Figure 1e) measured by UXRD for two different excitation fluences. The Pt layer expands immediately after the optical excitation. The maximum expansion is observed at $t = 1.5$ ps, as expected from the propagation of the expansion wave through the Pt layer at the sound velocity v_{Pt}.[29] The pronounced minimum at $t = 3$ ps indicates the back-reflection of the expansion wave at the sample surface leading to a strongly damped oscillation of the Pt layer thickness with period $T_{Pt} = 3$ ps. Within 25 ps the Pt strain decreases to a nearly constant level of $\eta_{Pt} = 1 \cdot 10^{-3}$ by thermal transport to the Ni and Cu layer. Surprisingly, it is the buried Ni layer that expands right after the Pt, reaching a maximum expansion around 6 ps. The asymmetry of the maximum is due to the reflection of the Ni expansion wave at the interfaces of the Ta buffer layer and the glass substrate (see Section 3 for a thorough modeling). The Ni signal modulation in the 20–30 ps range is caused by the pronounced acoustic strain pulse launched by the Pt layer and its reflections. Thermal expansion of the Cu layer, through which the heat was conducted to the Ni layer, occurs later and triggers a Cu thickness oscillation with 60 ps period, which results from acoustic reflections at the sample surface and the glass interface.

The delayed slow heating of the Cu layer is directly evidenced by the initial compression of Cu prevailing for more than 5 ps (Figure 1c). Only the first $t = 3$ ps can be explained by the compressive leading part of the bipolar strain wave launched by the Pt expansion. After this time, even the expansive part of this bipolar strain pulse has completely entered the Cu layer.[26,27] The additional prolonged compression of Cu must originate from the leading part of a bipolar strain wave generated in the buried Ni layer that is almost four times thicker than the Pt. The combined experimental data of Figure 1 directly show that the Ni layer expands much faster and stronger than the Cu layer, through which the heat is conducted toward the Ni layer in the first place.

3. Modeling

In the previous section we have implicitly used the lattice expansion as a layer-specific thermometer. Indeed, the thermal strain $\eta \propto \sigma$ is proportional to the driving stress $\sigma = \Gamma \rho^Q$, which is in turn proportional to the energy density ρ^Q. Here, Γ is the macroscopic Grüneisen constant. In metals, at least two contributions to the stress must be distinguished, namely, electrons and phonons. At room temperature the specific heat of the phonons C_{ph} is nearly constant in the Dulong-Petit limit. Therefore, the change of the phonon energy density $\Delta \rho_{ph}^Q = C_{ph} \Delta T_{ph}$ due to the laser excitation is proportional to the phonon temperature rise ΔT_{ph}. This makes our X-ray thermometer simple to read at timescales beyond 1 ps, when the energy in the electron system can be neglected. In this limit, the measured strain is directly proportional to the phonon temperature rise, $\eta \propto \Delta T_{ph}$. In contrast, the energy density change in the electron system $\Delta \rho_e^Q = C_e(T_e) \Delta T_e$ has a quadratic contribution in ΔT_e due to the Sommerfeld model of the electronic heat capacity $C_e(T_e) = \gamma^S (T_e^0 + \Delta T_e)$ where γ^S is the Sommerfeld constant and T_e^0 is the starting temperature. The electronic stress contribution $\sigma_e = \Gamma_e \rho_e^Q$ is only present in the first picosecond, but it strongly influences the shape and size of the strain waves.

The timings of the three measured strain transients in Figure 1 already indicate that Ni heats up strongly before Cu even gets warm. In the following we lay out a more quantitative analysis using a diffusive 1D TTM.[30] The model describes the evolution of the electron and lattice temperatures due to diffusion and mutual coupling using the classical TTM:

$$C_e(T_e)\frac{\partial T_e}{\partial t} = \frac{\partial}{\partial z}\left(\kappa_e(T_e, T_{ph})\frac{\partial T_e}{\partial z}\right) + g(T_{ph} - T_e) + S_e(z,t)$$
$$C_{ph}\frac{\partial T_{ph}}{\partial t} = \frac{\partial}{\partial z}\left(\kappa_{ph}\frac{\partial T_{ph}}{\partial z}\right) + g(T_e - T_{ph}) \qquad (1)$$

The laser pulse heats the electrons via the source term $S_e(z, t)$, $\kappa_{e/ph}$ are the electron and phonon thermal conductivities, respectively, and g is the e-ph coupling parameter. The spatial coordinate z is directed perpendicular to the sample surface.

The phonons contribute to heat transport; however, already in thermal equilibrium the electron heat conductivity dominates by far.[28] For a correct description of the non-equilibrium transport, it is vital to include the dependence of the electron heat conductivity κ_e on the phonon and electron temperatures.[31–34] In the relevant temperature range the electronic specific heat can be approximated by $C_e = \gamma^S T_e$ and the mean scattering time of the electrons $\tau_e \propto 1/T_{ph}$ is dominated by e-ph scattering.[31–34] For the conduction band electrons of Cu, kinetic gas theory yields

$$\kappa_e(T_e, T_{ph}) = \frac{1}{3}C_e v_F \bar{l} = \frac{1}{3}C_e v_F^2 \tau_e = \kappa_e^0 \frac{T_e}{T_{ph}} \qquad (2)$$

The empirical equilibrium conductivity κ_e^0 encodes γ^S, the Fermi velocity v_F and the proportionality constant in $\tau_e \propto 1/T_{ph}$. The mean free path $\bar{l} = v_F \tau_e$ is independent of T_e and only depends on T_{ph}. This text-book model was recently applied to model the in-plane heat transport in a nanometric metal film.[35]

Table 1. Thermophysical parameters of Pt, Cu, Ni, Ta, and the glass substrate taken from the indicated literature. Values in brackets are optimized values for the simulation.

	Pt	Cu	Ni	Ta	Glass
γ^S (mJ cm^{-3} K^{-2})	0.74[33]	0.10[33]	1.06[33]	0.38[51]	–
C_{ph} (J cm^{-3} K^{-1})	2.85[52]	3.44	3.94	2.33[51]	1.80[53]
κ_e^0 (W m^{-1} K^{-1})	66[54]	396[33]	81[33,55]	52	–
κ_{ph} (W m^{-1} K^{-1})	5[54]	5	9.6[55]	5	1[53]
g (PW m^{-3} K^{-1})	400[56]	63[56]	360[56]	100	–
ρ (g cm^{-3})	21.45	8.96	8.91	16.68	2.54[53]
v_s (nm^{-1} ps)	4.2[57,58]	5.2[56,90]	6.3[61]	4.2	5.7[53]
Γ_e	2.4[62] (0.9)	0.9[62] (1.1)	2.0[62]	1.3[62]	–
Γ_{ph}	3.0[62] (2.5)	1.7[62] (2.1)	1.65[62]	1.5[62]	0.3[53]

The thermophysical parameters used in our modeling are listed in **Table 1**. For an incident excitation fluence of 20 mJ cm^{-2} we obtain the spatio-temporal temperature maps $T_{e/ph}(z, t)$ of the electron and phonon systems shown in **Figure 2**. For convenience, the heterostructure is shown at the top of Figure 2. We find that the hot electrons (Figure 2a) very rapidly (few 100 fs) diffuse from the Pt through the Cu into the Ni layer. Due to the strong e-ph coupling in Ni, the electron energy is rapidly dissipated to the Ni lattice, thus preserving a large temperature gradient between the electron systems in Cu and Ni. The electron temperature equilibrates throughout the heterostructure within 1.4 ps. Figure 2c emphasizes the decisive role of the large electronic heat capacity of Pt and Ni, which originates from the large electronic density of states at the Fermi level. The Ni layer is buried far beyond the skin depth of the metal heterostructure and can only be heated by transport through Cu. Figure 2b reveals that the lattice temperature of the Ni layer rises within 1–2 ps. The Pt lattice gets heated on a similar timescale to even higher temperatures, because the Pt layer directly absorbs the photon energy. The rapid diffusion of hot electrons competes with the strong e-ph coupling in Pt. The energy density of the phonons in Figure 2d is nearly identical to the temperature map in Figure 2b since the lattice heat capacity is constant close to the Dulong-Petit limit. Note that the existence of interfaces between different metals may give rise to thermal interface resistance. The fact that we do not need to take interface resistances into account in order to obtain agreement between experiment and calculations suggests that such interface effects are negligible here.

After e-ph equilibration the phonons carry the vast majority of energy density. Thus they dominate the reading of our thermometer. In order to compare the calculated lattice temperature to the measured strain at short timescales, we must include a modeling of the strain waves launched in the heterostructure, which are considerably driven by the electronic stress. Therefore, the spatio-temporal electron and phonon temperature maps in Figure 2 are used as input to calculate the transient strain by integrating a one dimensional masses-and-springs model.[36] It takes into account the absence of in-plane strains and the concomitant out-of-plane contraction.[37] The spatio-temporal strain $\eta(z, t)$ (**Figure 3**) is used to calculate the X-ray diffraction pattern by dynamical X-ray diffraction theory.[26,30,38]
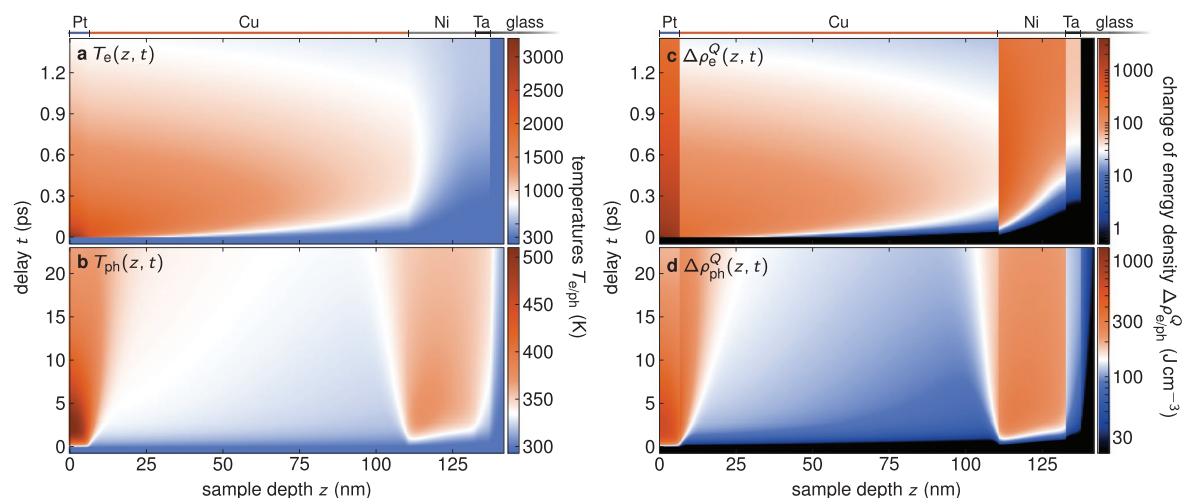
Figure 2. Result of the diffusive TTM of heat transport with temperature-dependent electron heat conductivity: a) Electron temperature, b) phonon temperature, c) change of electron energy density, and d) change of phonon energy density of the hetero-structure after excitation with an incident fluence of 20 mJ cm^{-2}. In the buried Ni film the energy density of the electron system and the lattice temperature rise faster than in the heat-conducting Cu layer.

The evaluation of the simulated Bragg peak shifts is plotted as continuous lines in **Figures** 1 and **4**.

Figure 4 compares two limiting cases calculated in the TTM to the continuous lines reproduced from Figure 1. The calculations leading to the dotted lines depict the dynamics that follow an instantaneously thermalized electron system that adopts a spatially homogeneous electron temperature throughout the heterostructure. This mimics the fastest possible electron transport that one would expect for approximate ballistic motion. We note, however, that homogeneous heating of the electron system necessarily would require also efficient scattering events within the Cu film. It strongly overestimates the expansion of the Ni layer and the relative amplitude of the Cu compression. As an opposite limit of slow transport, the modeling that yields the dashed lines assumes a temperature-independent electron heat conductivity. This leads to slower heat transport exaggerating the expansion of the Pt layer and underrating the Ni expansion, since the e-ph coupling dumps the energy to the Pt and Cu lattice before propagation to Ni. In this case also the initial compression of Cu is too short-lived because it now exclusively results from the Pt expansion.

We emphasize that only the TTM with temperature-dependent electron heat conductivity (continuous lines) can model the fluence dependence shown in Figure 1 with a fixed set of parameters. Figure 4d–f shows the simulated fluence dependence for the strain in all three layers normalized by the excitation fluence. The increased relative energy transport can be identified by the disproportionally increasing strain of the
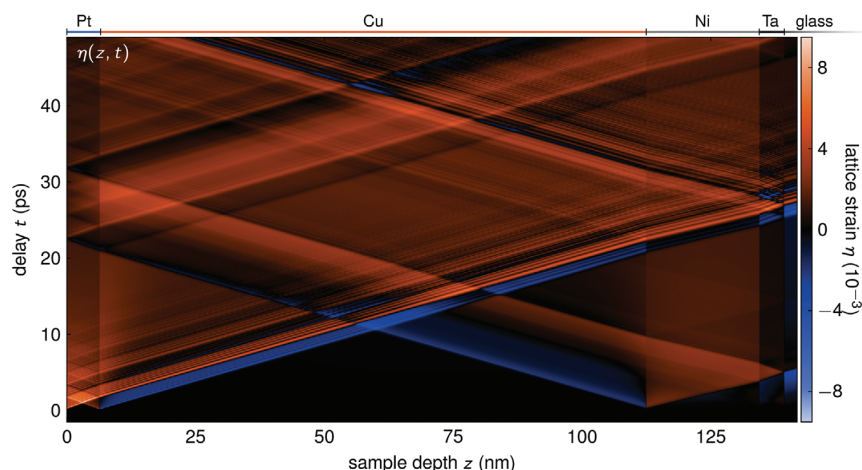

Figure 3. Calculated spatio-temporal strain $\eta(z, t)$ for an incidence fluence of 20 mJ cm^{-2}. After the excitation, the lattice starts to expand at the interfaces sending strain waves through the heterostructure. As indicated by the blue color, the Pt and Ni layers compress the Cu layer directly after excitation.
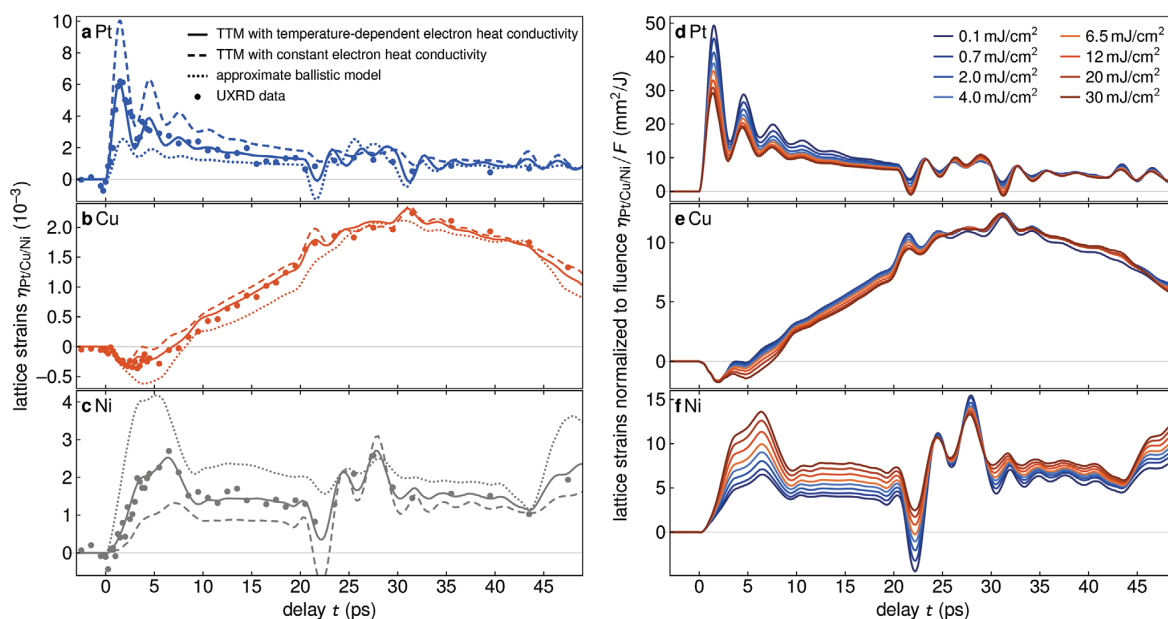
2004555 (4 of 8)

Figure 4. Limiting cases of electron transport and fluence dependence: Simulations of the UXRD data in comparison with the 20 mJ cm^{-2} UXRD data for a) Pt, b) Cu and c) Ni. The continuous lines originate from a simulation considering the temperature-dependent electron heat conductivity according to Equation (2). The dashed lines assume a constant electron heat conductivity with $T_e = T_{ph}$ in Equation (2) and the dotted lines result from an approximate ballistic model, which assumes a homogeneous initial electron temperature throughout the metal layers. The simulated fluence dependence with temperature-dependent electron heat conductivity reveals characteristic features: The strain of d) Pt and e) Cu normalized to the excitation fluence decreases with increasing fluence, whereas it increases for f) Ni. This is a manifestation of the enhanced thermal conductivities at elevated electron temperatures.

Ni layer with increased excitation fluence. The heat capacity of conduction electrons increases with temperature. Hence, for a temperature-independent e-ph coupling constant, the relaxation time in Pt is shorter at low fluence. This drives the high-frequency coherent oscillations originating in Pt more efficiently. Accordingly, at 22 ps the leading compression of the bipolar strain pulse originating from Pt strongly compresses the Ni layer. Normalized to the deposited energy, this compression is larger at low fluence. At high fluence, the increased electron heat conductivity in Cu (Equation (2)) and in parts also the longer e-ph coupling time in Pt facilitate a more efficient energy transport toward Ni. This causes the enhanced initial expansion of the Ni layer.

4. Discussion

Our diffusive model predicts that on a time scale of several tens of picoseconds heat is transported from Ni into the Cu lattice, that is, in the opposite direction of the initial heat flow in the electron system. This can be clearly seen in the temperature map at the Cu/Ni interface in Figure 2c. The inclusion of ballistic and superdiffusive aspects would even increase the electronic transport out of Pt through Cu into Ni and therefore enhance this backward heat transport.

In this article we do not take the challenge to fully model superdiffusive transport in this heterostructure, which would

require a precise description of the band structures and all possible scattering processes of electrons and phonons of each material. Modeling the role of the interfaces would add yet another level of complexity. The mean free path $\xi \approx 25$ nm of electrons excited in Cu by 800 nm photons is considerably shorter than in noble metals,[39,40] making diffusive transport a reasonable approximation for 100 nm films. Therefore, we compare the diffusive to the ballistic limit in a simple manner. **Figure 5**a shows the normalized electron and lattice temperature evolution in Ni for different Cu layer thicknesses according to our fully diffusive model with temperature-dependent electron heat conductivity.

In order to illustrate that certain evaluations of experimental signatures may lead to erroneous conclusions regarding the mechanism of heat transport, we show different evaluations of the rise time of the Ni electron temperature in the first 6 ps in Figure 5b. The blue lines indicate the time at which the electronic temperature rises by selected absolute values ΔT_e^{Ni}. They show the expected depth dependence $z \propto \sqrt{t}$ for diffusive transport. Note that, for example, for $d \gtrsim 400$ nm the 10 K threshold in Ni is not overcome on the time scale of non-equilibrium electron conduction according to Equation (2). Instead, Ni is heated up by 10 K much later at about 1.5 ns (c.f. Figure 5a) via transport of locally equilibrated electrons and phonons. In contrast, the orange lines in Figure 5b report the time it takes the electron temperature in Nickel to rise to $f = 1\%$, $f = 10\%$ and $f = 33\%$ of the maximum electronic temperature in Ni
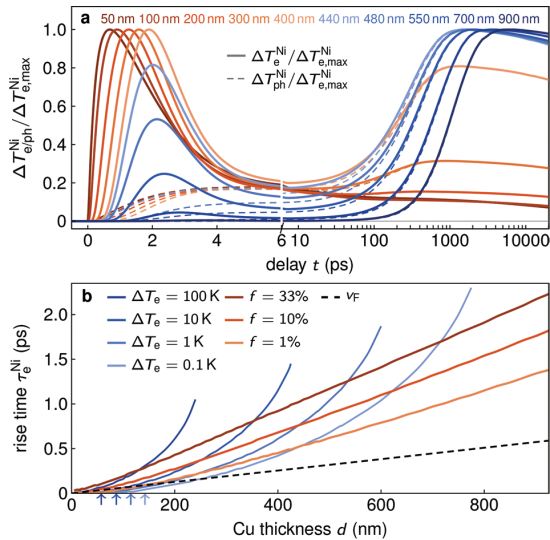
Figure 5. Dependence of the temperature evolutions in Ni on the thicknesses of the Cu transport layer. a) Transient layer-averaged electron and phonon temperature in Ni normalized to the respective maximum electron temperature for various thicknesses of the Cu layer. Up to approx. 400 nm the maximum temperature is reached within 2 ps by non-equilibrium heat transport according to Equation (5). Beyond this thickness near-equilibrium transport yields the maximum in the ns range. b) Rise time of the electron temperature in Ni to various absolute temperature thresholds ΔT_e^{Ni} in blue color code, together with arrows indicating up to which depth T_e^{Cu} has reached this threshold immediately by direct absorption of photons. Red color code for the rise time to various fractions f of maximum electron temperature, f. The time-length relation is linear for the relative threshold, whereas the absolute threshold yields the expected quadratic behavior.

within the first 6 ps for the respective Cu thickness. This rise to a certain percentage of the maximum is analogous to normalizing transients to their respective maximum and inferring the time-thickness relation by reading the crossing time for a given threshold f as reported in many studies.[12,41–43] This approach was first presented in the seminal paper by Brorson et al. on Au films[44] which are much thicker than the Cu films in similar early experiments.[45] The linear time-thickness relations found in those studies were interpreted as a manifestation of ballistic electron transport. Despite the purely diffusive character of our model, the analysis considering the rise time to a relative threshold f (orange lines in Figure 5b) also yields a linear dependence $z \propto t$ which is therefore obviously not a sufficient observation to conclude ballistic electron transport.[46] For comparison, the black dashed line in Figure 5b depicts the arrival time of ballistic electrons with Fermi velocity $v_F = 1.57 \times 10^6$ m s^{-1}[28] at the backside of a Cu layer of thickness d. For very thin Cu films and small relative temperature thresholds the diffusion appears to be faster than the ballistic motion. This is partially caused by the slight direct optical excitation of the Cu layer (see experimental section and arrows in Figure 5b). However, generally the diffusion approximation may yield heat transport that is faster than the group velocity of the heat carrying particles, that is, inconsistent with underlying concepts of the specific heat and heat transport by quasiparticles.

Several approaches can be taken to cure this property of the heat equation,[3,10,47] which occurs when the length scale of the system is below the mean free path of the heat-carrying particles. The blue arrows in Figure 5b indicate, however, that the direct heating of Cu in a depth of 100 nm by the absorption of photons cannot be neglected when discussing tiny temperature changes (see figure caption for further details).

In the following, we investigate the origin of the surprising linear time-thickness relation from a fully diffusive model in more detail. For that purpose, we derive an analytic expression for electronic heat diffusion in the presence of e-ph coupling by solving the diffusive TTM (Equation (1)) for an isolated semi-infinite surface-heated Cu layer. For simplicity, we assume a constant phonon temperature $T_{ph} = T_e^0$, approximating $C_{ph} \gg C_e$, and a temperature-independent electron heat conductivity κ_e. This results in an uncoupled heat equation with a term accounting for the loss of heat from electrons to phonons:

$$\frac{\partial \Delta T_e}{\partial t} = \frac{\kappa_e}{C_e}\frac{\partial^2 \Delta T_e}{\partial z^2} - \frac{g}{C_e}\Delta T_e \tag{3}$$

with $\Delta T_e = T_e - T_{ph}$. The solution is given by

$$\Delta T_e(z,t) \propto \sqrt{\frac{C_e}{4\pi\kappa_e t}}\exp\left(-\frac{C_e z^2}{4\kappa_e t}\right)\exp\left(-\frac{g}{C_e}t\right) \tag{4}$$

which is a product of the Gaussian textbook solution of the heat equation and an exponential damping term due to e-ph coupling. At a distance $z = d$ from the heated surface, the electron temperature attains its maximum at time

$$t_{max} = \frac{C_e}{4g}\left(\sqrt{1 + \frac{4g}{\kappa_e}d^2} - 1\right) \tag{5}$$

This expression is asymptotically linear for thick Cu layers with thickness $d \gg \sqrt{\kappa_e/4g} \approx 40$ nm which is consistent with our numerical solutions presented in Figure 5. The e-ph coupling strength g is crucial for the existence and timing t_{max} of the maximum electron temperature, and hence for the linear asymptotic dependence of Equation (5). We note that the numerical modeling including a temperature-dependent electron heat conductivity according to Equation (2) yields the same asymptotically linear behavior.

In summary, we emphasize the relevance of the non-equilibrium heat transport at small lengths scales as illustrated in Figure 5a: The normalized transient electron temperature rise in Ni is the decisive parameter, since it is the large electron heat capacity of Ni together with the large e-ph coupling in Ni which dominates the counter-intuitive phenomena. For thin Cu transport layers the maximum electron temperature in Ni is reached within the first 2 ps. For $d \gtrsim 400$ nm, the electron temperature has its maximum three orders of magnitude later, as the transport now occurs dominantly close to thermal equilibrium (cf. Figure 5a).

5. Conclusion

In conclusion, we presented ultrafast X-ray diffraction experiments that unveil unconventional heat transport by hot

electrons in a metallic heterostructure. After laser-heating the front end of the structure, the lattice of the back end is heated much more rapidly and efficiently than the part through which the heat is transported via conduction electrons. We highlight the crucial role of the high density of states at the Fermi level of the Ni layer at the back end of the structure. It attracts the heat energy ultrarapidly into its large heat reservoir and dumps the energy into lattice vibrations of Ni owing to its strong e-ph interaction. Subsequently, the lattice of the intermediate Cu layer is even heated from the backside. Our modeling approach considering purely diffusive transport reproduces our data very consistently, although partially ballistic or superdiffusive heat transport definitely occurs in Cu. The conceptual simplicity of our approach, however, also brings to light that the mere existence of a linear space-time relationship in the experimental data is not sufficient to identify a ballistic transport mechanism.

6. Experimental Section

Sample Growth: The metal heterostructure (Figure 1a) was sputtered onto a glass substrate (Corning 1737 AMLCD) in the following layering sequence: 6.6 nm Pt on 104 nm Cu on a 22 nm Ni on a 5 nm amorphous Ta adhesion layer. As described below, static X-ray diffraction reveals a (1 1 1)-orientation of the relaxed Pt, Cu and Ni layers.

UXRD Measurement: A reciprocal space map of the multilayer sample is obtained by detecting the symmetrically and asymmetrically diffracted X-rays on an area detector (Dectris PILATUS 100K) while sample and detector are rotated in a classical $\theta - 2\theta$ scheme. The reciprocal space map shows three material specific (1 1 1)-oriented Bragg peaks, which are located at $\theta_{Pt} = 19.75°$, $\theta_{Cu} = 21.65°$, and $\theta_{Ni} = 22.25°$. The sample was excited with *p*-polarized 100 fs laser pulses at 800 nm having an incident laser power of 330 mW or 110 mW at 1 kHz repetition rate. The footprint of laser beam was approximately 1.1 × 0.9 mm² (major and minor FWHM-diameter). For the 330 mW measurement the incidence angle of the laser was 50° (47.5°) with respect to the surface normal for the measurements on the Pt (Cu and Ni) Bragg reflection(s), which results in an incident fluence of 19 (20) mJ cm⁻². For the 110 mW measurement the incidence angle was 47.5° resulting in an incident fluence of 6.5 mJ cm⁻². The optical absorption profile calculated from the respective dielectric functions by a matrix formalism[25,48] reveals that over 86% of the absorbed energy of the near-infrared pump (800 nm) deposited inside the Pt layer and 14% are deposited in the first 12 nm (1/e) of the Cu layer. The sample was probed under a fixed angle with 200 fs X-ray probe pulses at a wavelength of 1.54 Å (Cu K$_\alpha$) derived from the laser-driven plasma X-ray source (PXS)[49] and detected by an area detector at a fixed position. For each layer, the strain derived from the transient shift $\Delta\theta$ of the Bragg peak (center of mass) was used as a proportional measure of the average energy density in each layer.[25,26,50]

Simulation Methods: The TTM, strain, and X-ray diffraction simulations are carried out using the UDKM1DSIM MATLAB toolbox.[30] For each material, values for the heat conductivities $\kappa_{e,ph}$, the specific heats $C_{e,ph}$, the Sommerfeld constants γ^S, and the electron-phonon coupling constants g are taken from the literature as given in Table 1. Constant values were applied for the specific heat and heat conductivity of the phonon system. Also the e-ph coupling parameter g was assumed to be temperature-independent, which is a reasonable approximation in the temperature range of the study. The electronic specific heat $C_e(T_e) = \gamma^S T_e$ depends on temperature according to the Sommerfeld model, and the temperature dependence of the non-equilibrium electron heat conductivity is given in Equation (2). The laser excitation is accounted for by the source term $S_e(z, t)$ whose spatial profile is dictated by the optical absorption calculated by a matrix formalism.[25,48] The calculated spatio-temporal electron and phonon temperature maps (Figure 2) were used as input to calculate the transient strain by integrating a linear masses-and-springs model[36] considering the geometrical limitation of thin films on ultrafast timescales.[27,37] The modeled strain was leveled to the 330 mW UXRD data by scaling the source term accordingly. The Grüneisen coefficient of Pt and Cu had to be adjusted by approximately ±20% to match the observed expansion between 300 ps to 1 ns, where the temperatures of all metal layers are in equilibrium. This is reasonable given that properties in thin films often slighly differ from to bulk properties. All values are kept fixed for both fluences, that is, for the simulation matching the 110 mW UXRD data only the source term is divided by the factor 3. From the resulting strain map $\eta(z,t)$ (Figure 3), the X-ray diffraction pattern was calculated by dynamical X-ray diffraction theory. The calculated time-dependent Bragg peaks were evaluated in the same way as the experimental UXRD data to obtain the simulated transient layer-averaged strains shown in Figures 1 and 4.

Conflict of Interest

The authors declare no conflict of interest.

[1] D. G. Cahill, W. K. Ford, K. E. Goodson, G. D. Mahan, A. Majumdar, H. J. Maris, R. Merlin, S. R. Phillpot, *J. Appl. Phys.* **2003**, *93*, 793.

[2] D. G. Cahill, P. V. Braun, G. Chen, D. R. Clarke, S. Fan, K. E. Goodson, P. Keblinski, W. P. King, G. D. Mahan, A. Majumdar, H. J. Maris, S. R. Phillpot, E. Pop, L. Shi, *Appl. Phys. Rev.* **2014**, *1*, 011305.

[3] W. Dreyer, H. Struchtrup, *Continuum Mech. Thermodyn.* **1993**, *5*, 3.

[4] S. Weber, B. Rethfeld, *Appl. Surf. Sci.* **2017**, *417*, 64, 10th International Conference on Photoexcited Processes and Applications.

[5] P. Maldonado, K. Carva, M. Flammer, P. M. Oppeneer, *Phys. Rev. B* **2017**, *96*, 173.

[6] U. Ritzmann, P. M. Oppeneer, P. Maldonado, Theory of out-of-equilibrium electron and phonon dynamics in metals after ultrafast laser excitation, **2019**, URL http://arxiv.org/pdf/1911.12414v1.

[7] P. Maldonado, T. Chase, A. H. Reid, X. Shen, R. K. Li, K. Carva, T. Payer, M. Horn von Hoegen, K. Sokolowski-Tinten, X. J. Wang, P. M. Oppeneer, H. A. Dürr, *Phys. Rev. B* **2020**, *101*, 10.

[8] L. Waldecker, R. Bertoni, R. Ernstorfer, J. Vorberger, *Phys. Rev. X* **2016**, *6*, 945.

[9] M. Battiato, K. Carva, P. M. Oppeneer, *Phys. Rev. Lett.* **2010**, *105*, 027203.

[10] G. Chen, *Phys. Rev. Lett.* **2001**, *86*, 2297.

[11] M. Battiato, K. Carva, P. M. Oppeneer, *Phys. Rev. B* **2012**, *86*, 2.

[12] Y. Xu, M. Deb, G. Malinowski, M. Hehn, W. Zhao, S. Mangin, *Adv. Mater.* **2017**, *29*, 42.

[13] M. Deb, E. Popova, M. Hehn, N. Keller, S. Mangin, G. Malinowski, *Phys. Rev. B* **2018**, *98*, 444.

[14] A. V. Scherbakov, A. S. Salasyuk, A. V. Akimov, X. Liu, M. Bombeck, C. Brüggemann, D. R. Yakovlev, V. F. Sapega, J. K. Furdyna, M. Bayer, *Phys. Rev. Lett.* **2010**, *105*, 117204.

[15] J.-W. Kim, M. Vomir, J.-Y. Bigot, *Phys. Rev. Lett.* **2012**, *109*, 166601.

[16] O. Kovalenko, T. Pezeril, V. V. Temnov, *Phys. Rev. Lett.* **2013**, *110*, 266602.

[17] G. Malinowski, F. Dalla Longa, J. H. H. Rietjens, P. V. Paluskar, R. Huijink, H. J. M. Swagten, B. Koopmans, *Nat. Phys.* **2008**, *4*, 855.

[18] A. J. Schellekens, K. C. Kuiper, R. R. J. C. de Wit, B. Koopmans, *Nat. Commun.* **2014**, *5*, 4333.

[19] A. Melnikov, I. Razdolski, T. O. Wehling, E. T. Papaioannou, V. Roddatis, P. Fumagalli, O. Aktsipetrov, A. I. Lichtenstein, U. Bovensiepen, *Phys. Rev. Lett.* **2011**, *107*, 076601.

[20] Y. Yang, R. B. Wilson, J. Gorchon, C.-H. Lambert, S. Salahuddin, J. Bokor, *Sci. Adv.* **2017**, *3*, e1603117.

[21] R. B. Wilson, J. Gorchon, Y. Yang, C.-H. Lambert, S. Salahuddin, J. Bokor, *Phys. Rev. B* **2017**, *95*, 18.

[22] A. von Reppert, J. Pudell, A. Koc, M. Reinhardt, W. Leitenberger, K. Dumesnil, F. Zamponi, M. Bargheer, *Struct. Dyn.* **2016**, *3*, 054302.

[23] A. von Reppert, R. M. Sarhan, F. Stete, J. Pudell, N. Del Fatti, A. Crut, J. Koetz, F. Liebig, C. Prietzel, M. Bargheer, *J. Phys. Chem. C* **2016**, *120*, 28894.

[24] A. Koc, M. Reinhardt, A. von Reppert, M. Rössle, W. Leitenberger, K. Dumesnil, P. Gaal, F. Zamponi, M. Bargheer, *Phys. Rev. B* **2017**, *96*, 429.

[25] J. Pudell, A. A. Maznev, M. Herzog, M. Kronseder, C. H. Back, G. Malinowski, A. von Reppert, M. Bargheer, *Nat. Commun.* **2018**, *9*, 3335.

[26] J. Pudell, A. von Reppert, D. Schick, F. Zamponi, M. Rössle, M. Herzog, H. Zabel, M. Bargheer, *Phys. Rev. B* **2019**, *99*, 094304.

[27] A. von Reppert, M. Mattern, J.-E. Pudell, S. P. Zeuschner, K. Dumesnil, M. Bargheer, *Struct. Dyn.* **2020**, *7*, 024303.

[28] N. W. Ashcroft, N. D. Mermin, *Solid State Physics*, repr edition, Brooks/Cole Thomson Learning, South Melbourne **2012**.

[29] D. Schick, M. Herzog, A. Bojahr, W. Leitenberger, A. Hertwig, R. Shayduk, M. Bargheer, *Struct. Dyn.* **2014**, *1*, 064501.

[30] D. Schick, A. Bojahr, M. Herzog, R. Shayduk, C. von Korff Schmising, M. Bargheer, *Comput. Phys. Commun.* **2014**, *185*, 651.

[31] S.-S. Wellershoff, J. Hohlfeld, J. Güdde, E. Matthias, *Appl. Phys. A: Mater. Sci. Process.* **1999**, *69*, S99.

[32] A. P. Kanavin, I. V. Smetanin, V. A. Isakov, Y. V. Afanasiev, B. N. Chichkov, B. Wellegehausen, S. Nolte, C. Momma, A. Tünnermann, *Phys. Rev. B: Condens. Matter Mater. Phys.* **1998**, *57*, 14698.

[33] J. Hohlfeld, S.-S. Wellershoff, J. Güdde, U. Conrad, V. Jähnke, E. Matthias, *Chem. Phys.* **2000**, *251*, 237.

[34] P. B. Corkum, F. Brunel, N. K. Sherman, T. Srinivasan-Rao, *Phys. Rev. Lett.* **1988**, *61*, 2886.

[35] A. Block, M. Liebel, R. Yu, M. Spector, Y. Sivan, F. J. García de Abajo, N. F. van Hulst, *Sci. Adv.* **2019**, *5*, eaav8965.

[36] M. Herzog, D. Schick, P. Gaal, R. Shayduk, C. Korff Schmising, M. Bargheer, *Appl. Phys. A* **2012**, *106*, 489.

[37] A. von Reppert, L. Willig, J.-E. Pudell, S. P. Zeuschner, G. Sellge, F. Ganss, O. Hellwig, J. A. Arregi, V. Uhlíř, A. Crut, M. Bargheer, *Sci. Adv.* **2020**, *6*, eaba1142.

[38] S. P. Zeuschner, T. Parpiiev, T. Pezeril, A. Hillion, K. Dumesnil, A. Anane, J. Pudell, L. Willig, M. Rössle, M. Herzog, A. von Reppert, M. Bargheer, *Struct. Dyn.* **2019**, *6*, 024302.

[39] C. A. Schmuttenmaer, M. Aeschlimann, H. E. Elsayed-Ali, R. J. D. Miller, D. A. Mantell, J. Cao, Y. Gao, *Phys. Rev. B* **1994**, *50*, 8957.

[40] J. Cao, Y. Gao, H. E. Elsayed-Ali, R. J. D. Miller, D. A. Mantell, *Phys. Rev. B: Condens. Matter Mater. Phys.* **1998**, *58*, 10948.

[41] N. Bergeard, M. Hehn, S. Mangin, G. Lengaigne, F. Montaigne, M. L. M. Lalieu, B. Koopmans, G. Malinowski, *Phys. Rev. Lett.* **2016**, *117*, 147203.

[42] G. Malinowski, N. Bergeard, M. Hehn, S. Mangin, *Z. Phys. B: Condens. Matter Quanta* **2018**, *91*, 3251.

[43] T. Juhasz, H. E. Elsayed-Ali, G. O. Smith, C. Suárez, W. E. Bron, *Phys. Rev. B: Condens. Matter Mater. Phys.* **1993**, *48*, 15488.

[44] S. D. Brorson, J. G. Fujimoto, E. P. Ippen, *Phys. Rev. Lett.* **1987**, *59*, 1962.

[45] H. E. Elsayed-Ali, T. B. Norris, M. A. Pessot, G. A. Mourou, *Phys. Rev. Lett.* **1987**, *58*, 1212.

[46] H. Jang, J. Kimling, D. G. Cahill, *Phys. Rev. B* **2020**, *101*, 6.

[47] C. Cattaneo, J. K. de Fériet, Académie des sciences, *Sur une forme de l'équation de la chaleur éliminant le paradoxe d'une propagation instantanée*, Comptes rendus hebdomadaires des séances de l'Académie des sciences. Gauthier-Villars, **1958**.

[48] A. Eschenlohr, M. Battiato, P. Maldonado, N. Pontius, T. Kachel, K. Holldack, R. Mitzner, A. Föhlisch, P. M. Oppeneer, C. Stamm, *Nat. Mater.* **2014**, *13*, 102.

[49] D. Schick, A. Bojahr, M. Herzog, C. von Korff Schmising, R. Shayduk, W. Leitenberger, P. Gaal, M. Bargheer, *Rev. Sci. Instrum.* **2012**, *83*, 025104.

[50] D. Schick, R. Shayduk, A. Bojahr, M. Herzog, C. von Korff Schmising, P. Gaal, M. Bargheer, *J. Appl. Crystallogr.* **2013**, *46*, 1372.

[51] V. Y. Bodryakov, A. N. Bashkatov, *Russ. Metall (Metally)* **2013**, *2013*, 671.

[52] R. Shayduk, V. Vonk, B. Arndt, D. Franz, J. Strempfer, S. Francoual, T. F. Keller, T. Spitzbart, A. Stierle, *Appl. Phys. Lett.* **2016**, *109*, 043107.

[53] Corning Incorporated, *Corning 1737 AMLCD Glass*, **2002**.

[54] M. J. Duggin, *J. Phys. D: Appl. Phys.* **1970**, *3*, L21.

[55] X. Zheng, D. Cahill, P. Krasnochtchekov, R. Averback, J. Zhao, *Acta Mater.* **2007**, *55*, 5177.

[56] Z. Lin, L. V. Zhigilei, V. Celli, *Phys. Rev. B* **2008**, *77*, 075133.

[57] R. E. Macfarlane, J. A. Rayne, C. K. Jones, *Phys. Lett.* **1965**, *18*, 91.

[58] S. M. Collard, R. B. McLellan, *Acta Metall. Mater.* **1992**, *40*, 699.

[59] F. A. A. Radwan, *World Congress on Engineering 2012. July 4–6, 2012. London, UK.* **2010**, 2189 1221.

[60] H. M. Ledbetter, E. R. Naimon, *J. Phys. Chem. Ref. Data* **1974**, *3*, 897.

[61] J. R. Neighbours, F. W. Bratten, C. S. Smith, *J. Appl. Phys.* **1952**, *23*, 389.

[62] R. S. Krishnan, R. Srinivasan, S. Devanarayanan, B. R. Pamplin, *Thermal Expansion of Crystals: International Series in The Science of The Solid State*, Elsevier Science, Burlington **1979**.

Article III

Watching the vibration and cooling of ultrathin gold nanotriangles by ultrafast x-ray diffraction

Alexander von Reppert, Radwan Mohamed Sarhan, Felix Stete, **Jan-Etienne Pudell**, Natalia Del Fatti, Aurélien Crut, Joachim Koetz, Ferenz Liebig, Claudia Prietzel, and Matias Bargheer

We study the vibrations of ultrathin gold nanotriangles upon optical excitation of the electron gas by ultrafast X-ray diffraction. We quantitatively measure the strain evolution in these highly asymmetric nano-objects, providing a direct estimation of the amplitude and phase of the excited vibrational motion. The maximal strain value is well reproduced by calculations addressing pump absorption by the nanotriangles and their resulting thermal expansion. The amplitude and phase of the out-of-plane vibration mode with 3.6 ps period dominating the observed oscillations are related to two distinct excitation mechanisms. Electronic and phonon pressures impose stresses with different time dependences. The nanosecond relaxation of the expansion yields a direct temperature sensing of the nano-object. The presence of a thin organic molecular layer at the nanotriangle/substrate interfaces drastically reduces the thermal conductance to the substrate.
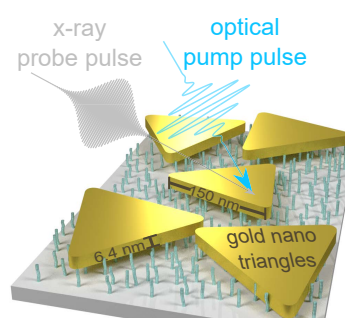
Watching the Vibration and Cooling of Ultrathin Gold Nanotriangles by Ultrafast X-ray Diffraction

A. von Reppert,[†] R. M. Sarhan,[†,∥] F. Stete,[†,∥] J. Pudell,[†] N. Del Fatti,[‡] A. Crut,[‡] J. Koetz,[§] F. Liebig,[§] C. Prietzel,[§] and M. Bargheer*[,†,⊥]

[†]Institut für Physik & Astronomie, Universität Potsdam, Karl-Liebknecht-Str. 24-25, 14476 Potsdam, Germany
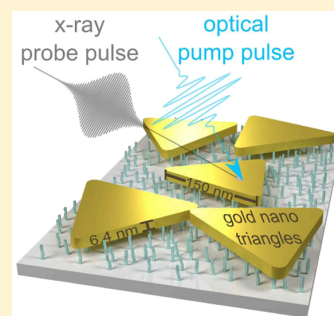
[‡]FemtoNanoOptics Group, Institut Lumière Matière, Université de Lyon, CNRS-Université Lyon 1, 69622 Villeurbanne, France

[§]Institut für Chemie, Universität Potsdam, Karl-Liebknecht-Str. 24-25, 14476 Potsdam, Germany

[∥]Humboldt-Universität zu Berlin, School of Analytical Sciences Adlershof (SALSA), Albert-Einstein-Str. 5-9, 10099 Berlin, Germany

[⊥]Helmholtz Zentrum Berlin, Albert-Einstein-Str. 15, 12489 Berlin, Germany

ABSTRACT: We study the vibrations of ultrathin gold nanotriangles upon optical excitation of the electron gas by ultrafast X-ray diffraction. We quantitatively measure the strain evolution in these highly asymmetric nano-objects, providing a direct estimation of the amplitude and phase of the excited vibrational motion. The maximal strain value is well reproduced by calculations addressing pump absorption by the nanotriangles and their resulting thermal expansion. The amplitude and phase of the out-of-plane vibration mode with 3.6 ps period dominating the observed oscillations are related to two distinct excitation mechanisms. Electronic and phonon pressures impose stresses with different time dependences. The nanosecond relaxation of the expansion yields a direct temperature sensing of the nano-object. The presence of a thin organic molecular layer at the nanotriangle/substrate interfaces drastically reduces the thermal conductance to the substrate.

INTRODUCTION

Metallic nanoparticles have been in the focus of intensive research over decades,[1] in part because they may potentially help to realize large bandwidth optical nanoelectromechanical systems or similar small and fast devices.[2] From the perspective of physical chemistry, colloidal particles present versatile and accessible nano-objects, which can be grown as spheres, rods, cubes, pyramids, platelets, or prisms, just to name a few examples. Special shapes are useful for tailoring the plasmon-resonance and catalytic activity of the particles or to optimize them for surface-enhanced Raman scattering. Investigations of the ultrafast thermal and vibrational dynamics of such nanostructures[3−6] are often justified by applications like photothermal therapy or catalysis.[7] The strong interest in these phenomena also lies in the fundamental questions of how heat transport and vibrational response are altered on the nanoscale, when surface effects may start to play a role, making the validity of continuum descriptions questionable.[8−12] Recently the focus of ultrafast studies has shifted from spherical particles over nanorods toward truly asymmetric structures such as prisms.[4,13−15] These particles often exhibit special crystalline structures with well-defined orientation,[16] which influence not only the growth and stability but also the optical and acoustic properties.[17]

The vibrational dynamics of nano-objects have been studied by a myriad of ultrafast optical pump–probe experiments looking at absorption, reflection, or scattering of ensembles.[3,4,6] Because the polydispersity of the samples leads to a dephasing of the observed vibrations, more recently such experiments were carried out on individual nano-objects.[18,19] Although much has been learned by optical techniques and the simulations using continuum mechanics or molecular dynamics, a thorough discussion of purely optical measurements is required to obtain information about the amplitude and phase with which individual vibrational modes are excited.[4,5,20,21] Ultrafast structural tools such as ultrafast X-ray or electron diffraction are the most direct ways to study changes of the crystal lattice induced by laser excitation. Although diffraction on the femtosecond time scale started to become available 20 years ago, only very few studies of nanoparticle dynamics with dynamics faster than 100 ps have been reported.[22−24] An experiment at the free-electron laser has monitored the breathing[25] and melting[26] of a single few hundred nanometers large ellipsoidal nanocrystal. Studying asymmetric and much thinner objects has, however, remained a challenge, and, in general, ultrafast single-particle studies using X-rays can exclusively be performed at free-electron laser facilities.[10] Demonstrating the possibility to use a laser-based femtosecond X-ray source for ultrafast structural measurements on ensembles of nanoparticles is therefore a major breakthrough.

We present such ultrafast X-ray diffraction (UXRD) experiments that precisely determine the average out-of-plane

strain $\varepsilon(t)$ of an ensemble of <111> oriented gold nanotriangles (NTs) as a function of the time delay t after the excitation. On the basis of the sound velocity v_{111} = 3.528 nm/ps along the [111] direction,[27] the oscillation period of T = 3.6 ps corresponding to the fastest out-of-plane vibration mode yields a particle thickness $d_0 = v_{111} \cdot T/2$ = 6.4 nm, consistent with particle shape characterized by thorough TEM measurements. The amplitude of the first oscillation and the maximal expansion ε_{max} = 3 × 10^{-3} of the particle after ~20 ps are consistent with a 1D acoustic model, where the expansion mode of the film is excited by a time-dependent pressure $\sigma(t)$ imposed by hot electrons and phonons. The pump−pulse absorption is calculated by a complete 3D numerical optical model.[19,28,29] A careful analysis by electron microscopy is used to prove that the NTs shape is robust under the experimental conditions. From the measured lattice strain, ε, one can directly read the temperature change ΔT_0 via

$$\epsilon = \int_{T_0}^{T_0 + \Delta T_0} \alpha_{Au}(T) \, dT \tag{1}$$

using the expansion coefficient $\alpha_{Au}(T)$ measured in thermal equilibrium. The cooling on the nanosecond time scale evidences the rather good thermal insulation given by the ~1 nm thick organic layer that was used for functionalizing the surface of the silicon substrate.

■ EXPERIMENTAL SECTION

Very thin gold NTs were prepared in a one-step synthesis in the presence of mixed AOT/phospholipid vesicles via a process that can be described by an Ostwald ripening growth mechanism.[31] To reduce the polydispersity of the product, the anisotropic nanoparticles were separated by using a combined polyelectrolyte/AOT micelle depletion flocculation.[31] The NTs were deposited on a silicon wafer functionalized by 3-mercaptopropyltrimethoxysilane (3-MPTMS).[32] The NTs were attached to the thiol group at a distance of ~1 nm above the Si surface. AFM investigations of >40 nanoplatelets reveal an average thickness of 8.5 ± 1.5 nm. Subtracting 1 nm of the 3-MPTMS layer, this is in full agreement with the 6.4 nm platelet thickness derived from the UXRD data. Figure 1 shows a thorough characterization of the sample by electron microscopy. The sideview (Figure 1a) of two individual NTs with 6.7 and 8.2 nm thickness illustrates the thickness of ~7.5 ± 1.5 nm. While the base length of the NTs is ~150 nm with a large size distribution (Figure 1d), the distribution of the platelet-thickness is rather sharp. The zoom into the NTs (Figure 1b)) can be Fourier-transformed to determine the periodicity of the lattice structure. Figure 1c proves the <111> orientation of the entire triangle.[30] Figure 1e confirms that the NTs are intact after UXRD experiments performed at a base temperature T_0 = 24 K with a pump wavelength of 400 nm and a fluence of F = 2.9 mJ/cm^2. Figure 1f,g shows the permanent deformation of the NTs under similar fluence conditions at room temperature. The UXRD experiments[33−35] subsequently discussed in this paper were conducted under the nondestructive conditions T_0 = 24 K and F = 2.9 mJ/cm^2. The pump pulses had a duration of ~80 fs, and the pulse length of the hard X-ray probe pulses at 8 keV derived from a laser-driven plasma source reduced the time resolution of the setup to ~200 fs.[34,35] Figure 2 illustrates the static XRD characterization of the sample in the geometry of the UXRD setup.[34] Figure 2b shows the reciprocal space map of the
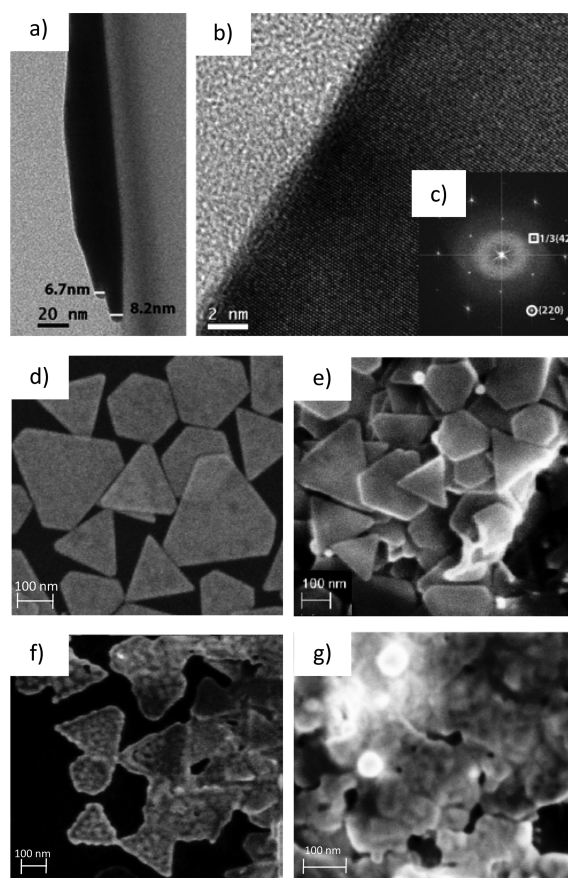
Figure 1. TEM and SEM pictures of the gold nanotriangle sample. (a) TEM sideview of gold-NTs. (b) High-resolution TEM and (c) its Fourier transform show 1/3{422} and {220} reflections characteristic of NTs with <111> orientation.[30] (d) SEM micrograph showing the polydisperse nature of the nanoplatelets. (e) SEM micrograph of the sample after the pump−probe experiment at T_0 = 24 K with F = 2.9 mJ/cm^2. (f) SEM micrograph of the sample after treatment with F = 3 mJ/cm^2 at room temperature. (g) Same for F = 5 mJ/cm^2. Triangles deform or melt together and reshape to spheres.

pristine sample, whereas the integrated X-ray diffraction intensity as a function of the Bragg angle θ in Figure 2a also reports a comparison to the diffraction from a sample after excessive irradiation with optical pump-pulses at 300 K. The reshaping of the Bragg peak indicating the permanent deformation of the gold particles at high fluence excitation at room temperature is clearly visible also in the reciprocal space map (not shown). The very weak and broad reflection from the gold (1 1 1) lattice planes (Figure 2b) renders the UXRD data acquisition extremely difficult, especially because the fluence must be reduced such that no sample damage occurs during several hours of optical pumping. Figure 2c compares the shifted Bragg peaks after 2.1 and 19 ps in the UXRD experiment with the Bragg peak at negative pump−probe delay. At low temperature and with the applied fluence the shape of these peaks is unchanged during the acquisition of the UXRD data.

Article

Figure 2. (a) Integrated X-ray intensity as a function of the Bragg angle θ for the pristine sample (black) and for a sample spot that was excessively irradiated at room temperature (red). Inset: Schematic of the ideal situation where all gold-NTs are attached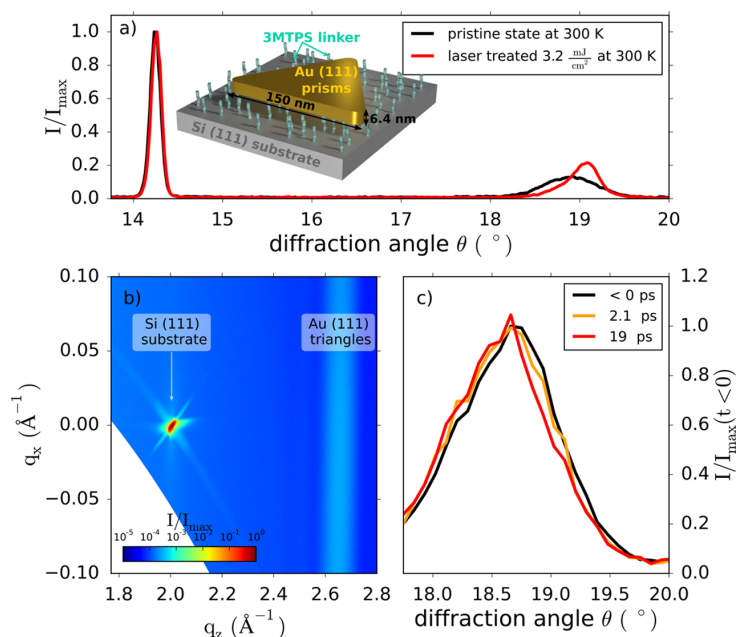 to the surface with equally long organic spacer molecules. (b) Reciprocal space map showing the sharp Si substrate peak and the very weak and broad reflection of the gold NTs. The diffraction does not correspond to a Debye−Scherrer ring but to a single-crystal diffraction with a large mosaic spread of about $\pm 5°$ originating from the nonperfect sample that also contains stacked NTs. (c) Integrated X-ray diffraction intensity for three different time delays at a fluence of 2.9 mJ/cm^2 that does not permanently modify the sample. We essentially observe a peak shift to smaller angles, indicating the ultrafast out-of-plane expansion.

■ RESULTS AND DISCUSSION

Figure 3 shows the lattice strain $\varepsilon(t)$ as a function of the time delay t after excitation of the gold NTs at $T_0 = 24$ K with 400 nm pulses. The fluence $F = 2.9$ mJ/cm^2 is given by the light intensity on the sample surface at the incidence angle of 40°. The femtosecond pulse excitation leads to an oscillation of the measured out-of-plane strain with a period of $T = 3.6$ ps, which is consistent with the fundamental breathing mode of a film with thickness 6.4 nm. The strain reaches a first maximum of $\varepsilon = 2.3 \pm 0.3 \times 10^{-3}$ after ∼2 ps. The signal oscillates and reaches a maximum of $\varepsilon_{max} = 3 \pm 0.3 \times 10^{-3}$ after ∼20 ps. The lattice slowly contracts on a nanosecond time scale as the heat flows out of the nanoparticle.

To interpret the observed maximum expansion ε_{max}, we calculated the temperature rise of a gold NT originating from the absorption of 400 nm pulses under 40° incidence. We computed the absorption cross-section using a finite-element approach accounting for the inhomogeneous nano-object environment induced by its deposition on a silicon substrate,[19,28,29] yielding $\sigma_{abs} = 1200$ nm^2 for NTs with 6.4 nm thickness and 150 nm side length. Neglecting heat transfer to the environment on short time scale, the temperature rise of a thermalized gold NT $\Delta T_0 = 285$ K at $T_0 = 24$ K is calculated by numerical integration of

$$\sigma_{abs}F/(\rho_{Au}V) = \int_{T_0}^{T_0 + \Delta T_0} c_{Au}(T) \, \mathrm{d}T \qquad (2)$$

where $\rho_{Au} = 19.3$ g/cm^3 is the density, $c_{Au}(T)$ is the strongly temperature-dependent heat capacity of gold, and V is the volume of the particle. From eq 1 we calculate an expansion of

$\varepsilon^{calc} = 3 \times 10^{-3}$, in excellent agreement with the data. For room temperature, the calculation yields the same result. This can be understood by invoking the Grüneisen parameter of gold, γ, which is a temperature-independent[36,37] measure of the thermal stress $\sigma = \gamma \cdot Q$ upon deposition of an energy density Q.[37] The heat expansion coefficient $\alpha(T)$ and heat capacity $c(T)$ share the same temperature dependence, both for the electronic contribution and for the phonon contribution, which are given by their quantum nature. Therefore, the electronic and phononic Grüneisen parameters of gold $\gamma_e \sim \alpha_e(T)/c_e(T)$ and $\gamma_p \sim \alpha_p(T)/c_p(T)$ are independent of temperature.

To quantitatively describe the oscillation of the signal at short times, we have to account for the fact that the optical excitation first heats up the electron gas, yielding a corresponding electron stress σ_e driving the out-of-plane expansion of the NT. We estimate an electronic temperature rise of $T_e(100 \text{ fs}) = 4000$ K from the electronic specific heat of $c_e(T) = \gamma_s T$, where $\gamma_s = 3.7 \times 10^{-6}$J/(gK) is the Sommerfeld-coefficient of gold.[38] The electron pressure $\sigma_e(t) = \gamma_e Q_e(t) = \gamma_e Q_{max}^e e^{-t/\tau_e}$ relaxes with the characteristic electron−phonon coupling time τ_e. With the same time constant, the phonon pressure $\sigma_p(t) = \gamma_p Q_{eq}^p (1 - e^{-t/\tau_e})$ rises until the electron and phonon temperatures have equilibrated. The electron−phonon coupling time in gold in the low perturbation limit is 1 ps at room temperature and 0.6 ps at 24 K.[39,40] However, under strong excitation conditions, the electronic heat capacity c_e rises with temperature, and equilibration times can exceed 5 ps under our conditions.[38,41,42] At $t = 20$ ps, we can safely assume that the electron and phonon system have reached a mutual
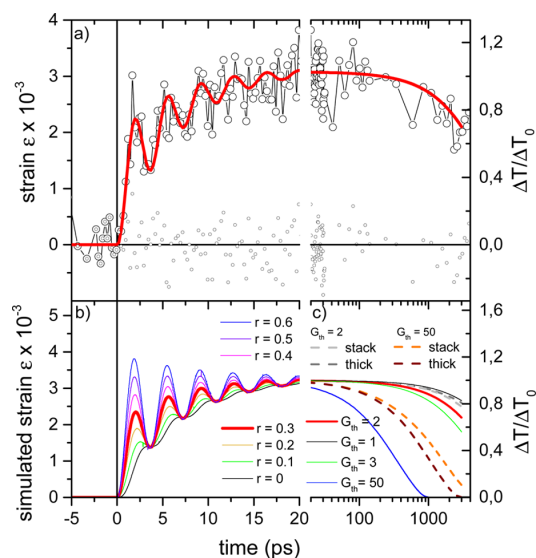
67

Figure 3. (a) Time-dependent strain measured by UXRD (open circles) together with the best fits from the models (red lines). The time axis is split according to the two models. The small dots represent the difference of the data and the simulation indicating only little contributions from additional vibrational modes. The relative error 3×10^{-4} of the strain measurement is estimated from the variation of data for $t < 0$ and around the maximum. (b) Model simulation according to eq 4 with a single oscillator driven by the phononic and electronic stresses according to eq 3. $r = \gamma_e/\gamma_p$ is ratio of the electronic and phononic Grüneisen parameters. (c) Results from the 3D heat-transport simulations. The thin lines are obtained for a single Au triangle separated from Si by a layer with a thermal interface conductance G_{th} in MW/(m^2 K). The fat red line indicates the best fit that is reproduced in panel a. The dashed lines are cross-checks for heat transport out of three stacked NTs (see the text).

thermal equilibrium so that a single temperature suffices to describe both systems.

The UXRD data provide a unique access to the phase and amplitude of the oscillations, which are both sensitive to the exact form of the total driving stress, which is given by the following functional form[42−44]

$$\sigma(t) = \sigma_e(t) + \sigma_p(t) = \sigma_\infty H(t)\left(1 + \left(\frac{\gamma_e}{\gamma_p} - 1\right)e^{-t/\tau_e}\right)$$

(3)

where $H(t)$ denotes the Heaviside function. The maximum stress $\sigma_\infty = C_{eff}\varepsilon(20 \text{ ps})$ can be deduced from the measured strain and the effective elastic modulus C_{eff} along the [111] direction. To model the early time vibrations (Figure 3a), we consider the homogeneous increase of the particle thickness $d(t)$ as the only relevant vibrational mode with frequency ω_0 and damping rate η. It is excited by the time-dependent stress $\sigma(t)$ stated in eq 3. The explicit differential equation used to describe the time-dependent out-of-plane strain $\varepsilon(t) = \frac{d(t) - d_0}{d_0}$ of the particles is then

$$\frac{d^2\varepsilon}{dt^2} + 2\eta\frac{d\varepsilon}{dt} + \omega_0^2\varepsilon = P\sigma(t)$$

(4)

The constant prefactor P on the right-hand side is due to dimensional reasons as it relates the driving stress $\sigma(t)$ to an acceleration of the strain. The equation of motion can be solved using the Green's function of the damped harmonic oscillator $G(t, t') = H(t - t')\frac{i}{\omega_- - \omega_+}(e^{i\omega_+(t-t')} - e^{i\omega_-(t-t')})$, where $\omega_\pm = i\eta \pm \sqrt{\omega_0^2 - \eta^2}$. The time-dependent strain can then simply be found via integration

$$\varepsilon(t) = P\int_{-\infty}^{t'} G(t, t')\sigma(t')\, dt' \propto \int_{-\infty}^{t'} G(t, t')\sigma(t')\, dt'$$

(5)

The magnitude of the prefactor P is dictated by the strain that is attained after the oscillations are damped out. We vary $P \cdot \sigma_\infty$ to match the signal at $t = 20$ ps and adjust the ratio r of the Grüneisen parameters to $r = \gamma_e/\gamma_p = 0.3$ and the damping constant $\eta = 0.15$ ps^{-1} to match the amplitude of the first oscillations. The time constant $\tau_e = 6.5$ ps is found to be close to those previously measured in similar strong perturbation conditions.[38] Figure 3a shows the measured data (open circles) together with the fit according to this model (red line) up to 20 ps. The black dots in Figure 3 represent the difference $\varepsilon_{exp}(t) - \varepsilon_{sim}(t)$ of the data and the simulation. They give an estimate of how much vibrational modes with lower frequency contribute to the out-of-plane expansion of the NTs. Because of the lateral size distribution, we expect that contributions by low-frequency modes rapidly dephase and thus are below the noise level. The left panel of Figure 3b shows simulations with a ratio $r = \gamma_e/\gamma_p$ varied from 0 to 0.6. The best fit is obtained for $r = 0.3$, a value that is smaller than the theoretical ratio expected for bulk gold $r = 0.5$[42] but consistent with other experiments performed on acoustic vibrations of small noble-metal nanoparticles.[43] We note that for $0 < r < 1$ the phase of the oscillation is delayed more and more as r approaches zero. For $r > 1$ the oscillations would start somewhat earlier. Therefore, both the amplitude and the phase of the observed UXRD signal allow us to assess the temporal form of the driving stress $\sigma(t)$.

For larger time delays (right panel), we plot the data on a logarithmic time axis and the red line represents the results of a 3D finite-element model of NT cooling, accounting for both 3D heat diffusion and thermal resistance at the triangle/substrate interface. We simulated a 6.4 nm thick gold triangle with initial temperature $T_i = T_0 + \Delta T$, which is attached to a Si substrate with a fixed temperature of $T_0 = 24$ K at the backside. Initial heating of the absorbing substrate was neglected as it weakly affects the cooling dynamics of the triangle due to the high thermal conductivity of silicon. We take the temperature-dependent bulk values[45−47] of the heat capacity $c_{Au/Si}$ and thermal conductivity $\kappa_{Au/Si}$ for Si and Au and account for the 1 nm thick organic layer by imposing a thermal interface conductance of $G_{th} = 2$ MW/(m^2 K) between Au and Si. This numerical value yields the best fit to the data in the model where a single gold particle is separated from the Si surface by an organic layer. For an epitaxial Au film on Si, one would expect an interface conductance of 50 to 150 MW/(m^2 K), which would lead to a much faster cooling.[48] For convenience, heat diffusion simulations with varying interface conductance are shown in Figure 3c for $t > 20$ ps as thin solid lines. The best fit $G_{th} = 2$ MW/(m^2 K) is shown as a thick line. To estimate the systematic error originating from the model, we also simulated the heat flow out of a "stack" of three gold NTs, which, in addition to the finite Au/Si thermal interface conductance G_{th}, have the same interface conductance between each gold

　Article

particle. As a further crosscheck, we have plotted results for "thick" NTs with a triple thickness and with only one interface with G_{th} from the gold to Si. All three models require the heat flow out of the particles to be strongly reduced by the 1 nm organic layer in comparison with a direct contact of Au on Si to achieve a good fit. The interface conductance is considerably lower than the values above 50 MW/(m^2 K) derived for Au−water interfaces with various surface functionalizations[49] and for the interface conductance of Au to Quartz across a self-assembled monolayer.[50,51] The attempt to rationalize the reduced heat flow by a low thermal conductivity of the 1 nm thick 3-MPTMS layer would require a value of 2×10^{-3} W/mK typical of dilute gases. We can therefore conclude that the slow cooling dynamics observed experimentally mostly originates from a low thermal conductance at the Au−Si interface.

■ CONCLUSIONS

Ultrafast X-ray diffraction measurements on an ensemble of 6.4 nm thick gold NTs directly and quantitatively measure the out-of plane expansion dynamics after optical excitation at 400 nm. The primary oscillatory motion can be explained by a single damped out-of-plane breathing mode with a period of $T = 3.6$ ps. The phase and amplitude of the UXRD signal are sensitive measures of the functional form $\sigma(t)$ of the time-dependent stress from hot electrons and phonons. The cooling time of several nanoseconds is dictated by the 1 nm thin organic layer that connects the gold-NTs to the silicon substrate. We can rationalize the observations by numerical models. In comparison with the situation expected for a thin gold layer on Si, our experiments demonstrate a slight modification of the relative ratio of the electronic and phononic Grüneisen parameters and a surprisingly strong reduction of heat conduction by a thin organic functional layer. Future UXRD studies on monodisperse asymmetric Au nanoparticles might also be able to quantify the contributions of other vibrational modes and can finally lead to a microscopic understanding of their reshaping under laser excitation. We believe that this pioneering experiment studying the dynamics of nanoparticles with a laser-based femtosecond X-ray source may trigger a broad range of novel experiments, for example, studying the nanoparticle temperature in photocatalytic experiments or during the magnetic heating of nanoparticles for catalysis. We emphasize that the heat-transport characteristics can be obtained by our method via synchrotron-based time-resolved X-ray diffraction, which is accessible for users from any field of natural sciences.

■ AUTHOR INFORMATION

Corresponding Author

*E-mail: bargheer@uni-potsdam.de. Tel: +49 (0)331 977 4272. Fax: +49 (0)331 977 5493.

ORCID ●

M. Bargheer: 0000-0002-0952-6602

Notes

The authors declare no competing financial interest.

■ REFERENCES

(1) Tchebotareva, A.; Ruijgrok, P.; Zijlstra, P.; Orrit, M. Probing the Acoustic Vibrations of Single Metal Nanoparticles by Ultrashort Laser Pulses. *Laser Photonics Reviews* **2010**, *4*, 581−597.

(2) Chen, K.; Razinskas, G.; Feichtner, T.; Grossmann, S.; Christiansen, S.; Hecht, B. Electromechanically Tunable Suspended Optical Nanoantenna. *Nano Lett.* **2016**, *16*, 2680−2685.

(3) Crut, A.; Maioli, P.; Del Fatti, N.; Vallée, F. Time-Domain Investigation of the Acoustic Vibrations of Metal Nanoparticles: Size and Encapsulation Effects. *Ultrasonics* **2015**, *56*, 98−108.

(4) Crut, A.; Maioli, P.; Del Fatti, N.; Vallée, F. Acoustic Vibrations of Metal Nano-Objects: Time-Domain Investigations. *Phys. Rep.* **2015**, *549*, 1−43.

(5) Huang, W.; Qian, W.; El-Sayed, M. A. Coherent Vibrational Oscillation in Gold Prismatic Monolayer Periodic Nanoparticle Arrays. *Nano Lett.* **2004**, *4*, 1741−1747.

(6) Hartland, G. V. Coherent Excitation of Vibrational Modes in Metallic Nanoparticles. *Annu. Rev. Phys. Chem.* **2006**, *57*, 403−430.

(7) Blum, O.; Shaked, N. Prediction of Photothermal Phase Signatures from Arbitrary Plasmonic Nanoparticles and Experimental Verification. *Light: Sci. Appl.* **2015**, *4*, e322.

(8) Cahill, D. G.; Ford, W. K.; Goodson, K. E.; Mahan, G. D.; Majumdar, A.; Maris, H. J.; Merlin, R.; Phillpot, S. R. Nanoscale Thermal Transport. *J. Appl. Phys.* **2003**, *93*, 793−818.

(9) Cahill, D. G.; Braun, P. V.; Chen, G.; Clarke, D. R.; Fan, S.; Goodson, K. E.; Keblinski, P.; King, W. P.; Mahan, G. D.; Majumdar, A.; et al. Nanoscale Thermal Transport. II. 2003−2012. *Appl. Phys. Rev.* **2014**, *1*, 011305.

(10) Hartland, G. V.; Shang Lo, S. Spectroscopy Beyond the Single-Particle Limit. *Science* **2013**, *341*, 36−37.

(11) Sauceda, H. E.; Mongin, D.; Maioli, P.; Crut, A.; Pellarin, M.; Del Fatti, N.; Vallée, F.; Garzón, I. L. Vibrational Properties of Metal Nanoparticles: Atomistic Simulation and Comparison with Time-Resolved Investigation. *J. Phys. Chem. C* **2012**, *116*, 25147−25156.

(12) Juvé, V.; Crut, A.; Maioli, P.; Pellarin, M.; Broyer, M.; Del Fatti, N.; Vallée, F. Probing Elasticity at the Nanoscale: Terahertz Acoustic Vibration of Small Metal Nanoparticles. *Nano Lett.* **2010**, *10*, 1853−1858.

(13) Major, T. A.; Lo, S. S.; Yu, K.; Hartland, G. V. Time-Resolved Studies of the Acoustic Vibrational Modes of Metal and Semi-conductor Nano-objects. *J. Phys. Chem. Lett.* **2014**, *5*, 866−874.

(14) Mahmoud, M. A.; O'Neil, D.; El-Sayed, M. A. Shape- and Symmetry-Dependent Mechanical Properties of Metallic Gold and Silver on the Nanoscale. *Nano Lett.* **2014**, *14*, 743−748.

(15) Fedou, J.; Viarbitskaya, S.; Marty, R.; Sharma, J.; Paillard, V.; Dujardin, E.; Arbouet, A. From Patterned Optical Near-Fields to High Symmetry Acoustic Vibrations in Gold Crystalline Platelets. *Phys. Chem. Chem. Phys.* **2013**, *15*, 4205−4213.

(16) Köth, A.; Appelhans, D.; Prietzel, C.; Koetz, J. Asymmetric Gold Nanoparticles Synthesized in the Presence of Maltose-Modified Poly(ethyleneimine). *Colloids Surf., A* **2012**, *414*, 50−56.

(17) Goubet, N.; Yan, C.; Polli, D.; Portalès, H.; Arfaoui, I.; Cerullo, G.; Pileni, M.-P. Modulating Physical Properties of Isolated and Self-Assembled Nanocrystals through Change in Nanocrystallinity. *Nano Lett.* **2013**, *13*, 504−508.

(18) Zijlstra, P.; Orrit, M. Single Metal Nanoparticles: Optical Detection, Spectroscopy and Applications. *Rep. Prog. Phys.* **2011**, *74*, 106401.

(19) Crut, A.; Maioli, P.; Del Fatti, N.; Vallée, F. Optical Absorption and Scattering Spectroscopies of Single Nano-Objects. *Chem. Soc. Rev.* **2014**, *43*, 3921−3956.

(20) Del Fatti, N.; Voisin, C.; Chevy, F.; Vallée, F.; Flytzanis, C. Coherent Acoustic Mode Oscillation and Damping in Silver Nanoparticles. *J. Chem. Phys.* **1999**, *110*, 11484−11487.

(21) Bonacina, L.; Callegari, A.; Bonati, C.; van Mourik, F.; Chergui, M. Time-Resolved Photodynamics of Triangular-Shaped Silver Nanoplates. *Nano Lett.* **2006**, *6*, 7−10.

Article

(22) Ruan, C.-Y.; Murooka, Y.; Raman, R. K.; Murdick, R. A. Dynamics of Size-Selected Gold Nanoparticles Studied by Ultrafast Electron Nanocrystallography. *Nano Lett.* **2007**, *7*, 1290−1296.

(23) Plech, A.; Kürbitz, S.; Berg, K.-J.; Graener, H.; Berg, G.; Grésillon, S.; Kaempfe, M.; Feldmann, J.; Wulff, M.; von Plessen, G. Time-Resolved X-Ray Diffraction on Laser-Excited Metal Nanoparticles. *Europhys. Lett.* **2003**, *61*, 762−768.

(24) Plech, A.; Kotaidis, V.; Grésillon, S.; Dahmen, C.; von Plessen, G. Laser-Induced Heating and Melting of Gold Nanoparticles Studied by Time-Resolved X-Ray Scattering. *Phys. Rev. B: Condens. Matter Mater. Phys.* **2004**, *70*, 195423.

(25) Clark, J. N.; Beitra, L.; Xiong, G.; Higginbotham, A.; Fritz, D. M.; Lemke, H. T.; Zhu, D.; Chollet, M.; Williams, G. J.; Messerschmidt, M.; et al. Ultrafast Three-Dimensional Imaging of Lattice Dynamics in Individual Gold Nanocrystals. *Science* **2013**, *341*, 56−59.

(26) Clark, J. N.; Beitra, L.; Xiong, G.; Fritz, D. M.; Lemke, H. T.; Zhu, D.; Chollet, M.; Williams, G. J.; Messerschmidt, M. M.; Abbey, B.; et al. Imaging Transient Melting of a Nanocrystal using an X-Ray Laser. *Proc. Natl. Acad. Sci. U. S. A.* **2015**, *112*, 7444−7448.

(27) Neighbours, J. R.; Alers, G. A. Elastic Constants of Silver and Gold. *Phys. Rev.* **1958**, *111*, 707−712.

(28) Davletshin, Y. R.; Lombardi, A.; Cardinal, M. F.; Juvé, V.; Crut, A.; Maioli, P.; Liz-Marzán, L. M.; Vallée, F.; Del Fatti, N.; Kumaradas, J. C. A Quantitative Study of the Environmental Effects on the Optical Response of Gold Nanorods. *ACS Nano* **2012**, *6*, 8183−8193.

(29) Pertreux, E.; Lombardi, A.; Florea, I.; Spuch-Calvar, M.; Gómez-Graña, S.; Ihiawakrim, D.; Hirlimann, C.; Ersen, O.; Majimel, J.; Tréguer-Delapierre, M.; et al. Surface Plasmon Resonance of an Individual Nano-Object on an Absorbing Substrate: Quantitative Effects of Distance and 3D Orientation. *Adv. Opt. Mater.* **2016**, *4*, 567−577.

(30) Germain, V.; Li, J.; Ingert, D.; Wang, Z. L.; Pileni, M. P. Stacking Faults in Formation of Silver Nanodisks. *J. Phys. Chem. B* **2003**, *107*, 8717−8720.

(31) Liebig, F.; Thünemann, A.; Koetz, J. Ostwald Ripening Growth Mechanism of Gold Nanotriangles in Vesicular Template Phases. *Langmuir* **2016**, *32*, 10928−10935.

(32) Xie, W.; Walkenfort, B.; Schlücker, S. Label-Free SERS Monitoring of Chemical Reactions Catalyzed by Small Gold Nanoparticles Using 3D Plasmonic Superstructures. *J. Am. Chem. Soc.* **2013**, *135*, 1657−1660.

(33) Schick, D.; Shayduk, R.; Bojahr, A.; Herzog, M.; von Korff Schmising, C.; Gaal, P.; Bargheer, M. Ultrafast Reciprocal-Space Mapping with a Convergent Beam. *J. Appl. Crystallogr.* **2013**, *46*, 1372−1377.

(34) Schick, D.; Bojahr, A.; Herzog, M.; von Korff Schmising, C.; Shayduk, R.; Leitenberger, W.; Gaal, P.; Bargheer, M. Normalization Schemes for Ultrafast X-Ray Diffraction Using a Table-Top Laser-Driven Plasma Source. *Rev. Sci. Instrum.* **2012**, *83*, 025104.

(35) Schick, D.; Bojahr, A.; Herzog, M.; Gaal, P.; Vrejoiu, I.; Bargheer, M. Following Strain-Induced Mosaicity Changes of Ferroelectric Thin Films by Ultrafast Reciprocal Space Mapping. *Phys. Rev. Lett.* **2013**, *110*, 095502.

(36) Nix, F. C.; MacNair, D. The Thermal Expansion of Pure Metals: Copper, Gold, Aluminum, Nickel, and Iron. *Phys. Rev.* **1941**, *60*, 597−605.

(37) McLean, K. O.; Swenson, C. A.; Case, C. R. Thermal Expansion of Copper, Silver, and Gold Below 30 K. *J. Low Temp. Phys.* **1972**, *7*, 77−98.

(38) Del Fatti, N.; Arbouet, A.; Vallée, F. Femtosecond Optical Investigation of Electron-Lattice Interactions in an Ensemble and a Single Metal Nanoparticle. *Appl. Phys. B: Lasers Opt.* **2006**, *84*, 175−181.

(39) Groeneveld, R. H. M.; Sprik, R.; Lagendijk, A. Femtosecond Spectroscopy of Electron-Electron and Electron-Phonon Energy Relaxation in Ag and Au. *Phys. Rev. B: Condens. Matter Mater. Phys.* **1995**, *51*, 11433−11445.

(40) Arbouet, A.; Voisin, C.; Christofilos, D.; Langot, P.; Del Fatti, N.; Vallée, F.; Lermé, J.; Celep, G.; Cottancin, E.; Gaudry, M.; et al. Electron-Phonon Scattering in Metal Clusters. *Phys. Rev. Lett.* **2003**, *90*, 177401.

(41) Kiel, M.; Möhwald, H.; Bargheer, M. Broadband Measurements of the Transient Optical Complex Dielectric Function of a Nanoparticle/Polymer Composite upon Ultrafast Excitation. *Phys. Rev. B: Condens. Matter Mater. Phys.* **2011**, *84*, 165121.

(42) Nicoul, M.; Shymanovich, U.; Tarasevitch, A.; von der Linde, D.; Sokolowski-Tinten, K. Picosecond Acoustic Response of a Laser-Heated Gold-Film Studied with Time-Resolved X-Ray Diffraction. *Appl. Phys. Lett.* **2011**, *98*, 191902.

(43) Voisin, C.; Del Fatti, N.; Christofilos, D.; Vallée, F. Time-Resolved Investigation of the Vibrational Dynamics of Metal Nanoparticles. *Appl. Surf. Sci.* **2000**, *164*, 131−139.

(44) Wright, O. B. Ultrafast Nonequilibrium Stress Generation in Gold and Silver. *Phys. Rev. B: Condens. Matter Mater. Phys.* **1994**, *49*, 9985−9988.

(45) Ho, C. Y.; Powell, R. W.; Liley, P. E. Thermal Conductivity of the Elements. *J. Phys. Chem. Ref. Data* **1972**, *1*, 279−421.

(46) Flubacher, P.; Leadbetter, A.; Morrison, J. The Heat Capacity of Pure Silicon and Germanium and Properties of their Vibrational Frequency Spectra. *Philos. Mag.* **1959**, *4*, 273−294.

(47) Geballe, T. H.; Giauque, W. F. The Heat Capacity and Entropy of Gold from 15 to 300K. *J. Am. Chem. Soc.* **1952**, *74*, 2368−2369.

(48) Duda, J. C.; Yang, C.-Y. P.; Foley, B. M.; Cheaito, R.; Medlin, D. L.; Jones, R. E.; Hopkins, P. E. Influence of Interfacial Properties on Thermal Transport at Gold:Silicon Contacts. *Appl. Phys. Lett.* **2013**, *102*, 081902.

(49) Ge, Z.; Cahill, D. G.; Braun, P. V. Thermal Conductance of Hydrophilic and Hydrophobic Interfaces. *Phys. Rev. Lett.* **2006**, *96*, 186101.

(50) Losego, M.; Grady, M.; Sottos, N.; Cahill, D.; Braun, P. Effects of Chemical Bonding on Heat Transport Across Interfaces. *Nat. Mater.* **2012**, *11*, 502−506.

(51) O'Brien, P.; Shenogin, S.; Liu, J.; Chow, P.; Laurencin, D.; Mutin, P.; Yamaguchi, M.; Keblinski, P.; Ramanath, G. Bonding-Induced Thermal Conductance Enhancement at Inorganic Hetero-interfaces Using Nanomolecular Monolayers. *Nat. Mater.* **2012**, *12*, 118−122.

Article IV

Scaling-up nano-plasmon catalysis: the role of heat dissipation

Radwan Mohamed Sarhan, Wouter Koopman, **Jan-Etienne Pudell**, Felix Stete, Matthias Rössle, Marc Herzog, Clemens Nikolaus Zeno Schmitt, Ferenc Liebig, Joachim Koetz, and Matias Bargheer

Nanoscale heating by optical excitation of plasmonic nanoparticles offers a new perspective of controlling chemical reactions, where heat is not spatially uniform as for conventional macroscopic heating, but strong temperature gradients exist around microscopic hot spots. In nanoplasmonics, metal particles act as a nanosource of light, heat, and energetic electrons driven by resonant excitation of their localized surface plasmon resonance. For the example of the coupling reaction of 4-nitrothiophenol (4-NTP) into 4,4'-dimercaptoazobenzene (DMAB), we show that besides the nanoscopic heat distribution at hot spots, also the microscopic distribution of heat dictated by the spot size of the light focus plays a crucial role in the design of plasmonic nano-reactors. Small laser spot sizes enable high intensities to drive plasmon-assisted catalysis. This facilitates the observation of such reactions by surface enhanced Raman scattering, but it challenges attempts to scale nanoplasmonic chemistry up to large areas, where the excess heat must be dissipated by one-dimensional heat transport.
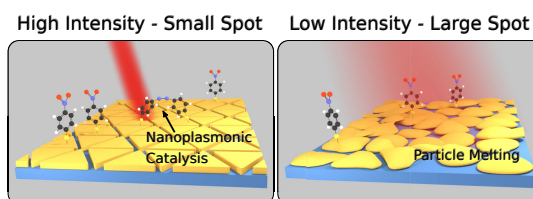
Scaling Up Nanoplasmon Catalysis: The Role of Heat Dissipation

Radwan M. Sarhan,[†,§] Wouter Koopman,*,[†] Jan Pudell,[†] Felix Stete,[†,§] Matthias Rössle,[∥]
Marc Herzog,[†] Clemens N. Z. Schmitt,[⊥] Ferenc Liebig,[‡] Joachim Koetz,[‡] and Matias Bargheer[†,∥]

[†]Institute of Physics and Astronomy and [‡]Institute of Chemistry, University of Potsdam, 14476 Potsdam, Germany
[§]School of Analytical Sciences Adlershof (SALSA), Humboldt-Universität zu Berlin, Albert-Einstein-Str. 5-9, 10099 Berlin, Germany
[∥]Helmholtz Zentrum Berlin, Albert-Einstein-Straße 15, 12489 Berlin, Germany
[⊥]Max Planck Institute of Colloids and Interfaces, 14476 Potsdam, Germany

Ⓢ *Supporting Information*

ABSTRACT: Nanoscale heating by optical excitation of plasmonic nanoparticles offers a new perspective of controlling chemical reactions, where heat is not spatially uniform as in conventional macroscopic heating but strong temperature gradients exist around microscopic hot spots. In nanoplasmonics, metal particles act as a nanosource of light, heat, and energetic electrons driven by resonant excitation of their localized surface plasmon resonance. As an example of the coupling reaction of 4-nitrothiophenol into 4,4′-dimercaptoazobenzene, we show that besides the nanoscopic heat distribution at hot spots, the microscopic distribution of heat dictated by the spot size of the light focus also plays a crucial role in the design of plasmonic nanoreactors. Small sizes of laser spots enable high intensities to drive plasmon-assisted catalysis. This facilitates the observation of such reactions by surface-enhanced Raman scattering, but it challenges attempts to scale nanoplasmonic chemistry up to large areas, where the excess heat must be dissipated by one-dimensional heat transport.
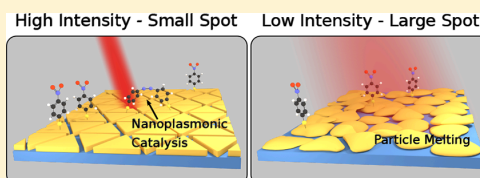
■ INTRODUCTION

Thermoplasmonics is a recently developed field of research, which started in 2002 for medical purposes.[1] Metal nanoparticles (NPs) have been used as a nanosource of heat for several applications such as photothermal cancer therapy,[2−5] bioimaging,[6] and nanosurgery.[7] Likewise, chemistry can benefit from nanoplasmonics, since many chemical reactions are heavily influenced by heat.[8−11]

Plasmonic metal nanostructures can be tuned to efficiently interact with light, converting the photons' energy into energetic charge carriers and heat. This allows noble metal nanoparticles to act as nanoreactors.[12] Chemical transformations of molecules attached to the particles' surfaces are fostered by the enhanced electromagnetic field at the particle surface along with generated energetic charge carriers and heat. As a result, plasmonic NPs present a unique playground for steering chemical transformation by light at the nanoscale.[13]

The first indications of nanoplasmonic chemistry were discovered in investigations using a micro-Raman apparatus to study surface enhanced Raman scattering (SERS) activity on nanoparticle templates.[14−16] In several microscope-based SERS experiments, the photons used for the Raman spectroscopy happen to also drive a catalytic reaction.[17−19] Recently, several important reaction types have been reported to be driven or catalyzed by plasmonic NPs such as the decomposition of organic molecules,[20,21] dissociation of hydrogen,[22,23] and oxidation−reduction reactions.[24,25]

In the current understanding, these chemical transformations are initialized by photogenerated energetic electrons. In addition, several studies have shown that the heat deposited in the particles by optical excitation enhances the reactions.[26−29] Heating by optical excitation of NPs is different from the conventional macroscopic heating because the heated volume is confined to certain hot spots or to the nanoparticle size. This may be exploited for controlling reactions at the nanometer scale and at specific locations. Around hot spots the cooling is generally three-dimensional (3D) and hence for low NP concentrations the heat can be quickly dissipated. Studying this nanoparticle heating is however rather difficult, as nanoscale thermometers are required.

In this article, we provide experimental evidence that removal of excess heat from the nanoscopic reaction site is a crucial factor for successful plasmonic chemistry, more importantly, for scaling up the plasmonic catalysis. In particular, the cooling geometry and the heat conductivity of the structure limits the maximum area of the plasmon-driven reaction, given by the spot size of the optical excitation. On the one hand, the light intensity (power per unit area) must have a minimum value to trigger plasmon-assisted catalytic reaction, but at the same time, the maximum power (not intensity) is limited by NP melting and/or destruction of the reactant or product molecules by excessive laser-driven static heating.

We investigated the static heating imposed on gold nanotriangles (NTs) by optical excitation by monitoring the shift of the nanoparticles' Bragg reflection via synchrotron-based X-ray diffraction (XRD). Subsequently, we verified, by SERS microscopy at very low light intensity, whether the plasmon-assisted reaction took place. Our measurements show that for small laser excitation spot sizes, the product formation could proceed, whereas for large spot sizes for the same light intensities, the SERS spectrum completely vanished. We reason that for microscopic excitation spot sizes, the deposited heat can be dissipated into a half sphere of the substrate in all three dimensions. In contrast, for very large excitation areas, the heat transport into the substrate is only in one dimension and therefore less effective. Therefore, the heat is trapped in the substrate for a much longer time, which enables melting of the plasmonic particles (the reaction platform). XRD measurements of the nanotriangles' lattice constant confirm that small laser excitation spot sizes lead to a lower temperature increase compared to the large spots for the same incident intensity. The faster rate of the 3D heat dissipation in a small excitation spot allows the excitation of the system with high light intensities necessary for the formation of the reaction product. In contrast, slower one-dimensional (1D) heat dissipation perpendicular to the substrate plane occurs for large spots sizes. The less efficient heat removal leads to higher temperatures and melting of the nanotriangles, as confirmed by scanning electron microscopy (SEM).

This phenomenon does not only explain the great success of observing plasmon-driven chemical reaction in SERS microscopes but also simultaneous absence of experiments evidencing plasmon-driven reactions over large surface areas. It also hints at the main advantage of nanoplasmonics for controlling chemical reactions, since unprecedented large heat dissipation rates can be found in a narrow spatial region of the hot spots.

■ MATERIALS AND EXPERIMENTAL METHODS

We used the plasmon-driven dimerization of 4-nitrothiophenol (4-NTP) into 4,4′-dimercaptoazobenzene (DMAB) as a model reaction.[30−32] This reaction is known to occur only in the presence of a plasmonic platform such as gold, silver, and copper nanoparticles.[33,34] The reaction is reasoned to occur as a result of the hot electrons generated upon the plasmon excitation,[35−37] whereas the influence of the plasmon-generated heat is a point of debate.[29,38] Here, we used a homogeneous large-scale monolayer of approximately 7 nm thick gold nanotriangles (NTs) deposited on substrates as the plasmonic platform.[39] The gold NTs were prepared using a one-step method in a mixed dioctyl sodium sulfo-succinate (AOT)/phospholipon vesicle phase in the presence of poly(N,N'-diallyl-N,N'-dimethylammonium-alt-3,5-bis-carboxyphenylmaleamic carboxylate (PalPhBisCarb) as a structure-directing agent and separated from spherical gold nanoparticles by depletion flocculation in the presence of AOT micelles.[40] The monolayer was formed at the liquid/air interface using a mixture of ethanol and toluene,[39] and it was then deposited on glass and silicon substrates after controlled evaporation of the solvents (compare Figure 1a). The extinction spectrum of the monolayer displayed a broad plasmon band located in the range of 500−2000 nm (inset in Figure 1), where it is in a good resonance with the excitation wavelengths. 4-NTP molecules were self-assembled on the gold NTs monolayer.
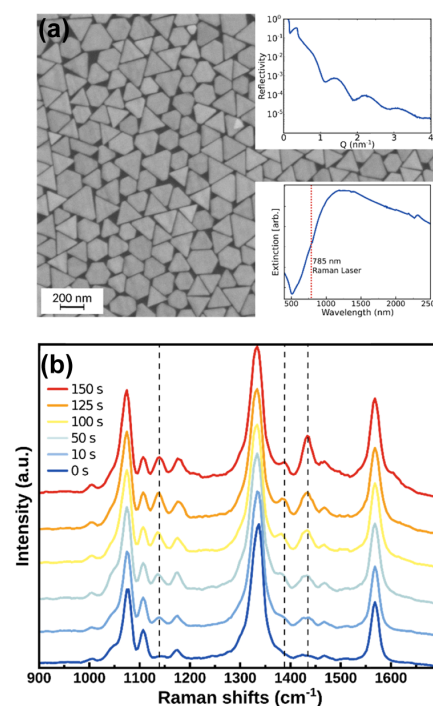

Figure 1. (a) SEM images of the gold NTs monolayer. The upper inset shows the X-ray reflectometry (XRR) data confirming a large-scale monolayer of approximately 7 nm thickness. The lower inset shows the optical extinction of a NT monolayer. (b) Time-dependent SERS spectra of 4-NTP assembled on the monolayer. Dashed lines indicate the three main product vibrational bands of DMAB.

The reaction was studied by SERS microscopy. Pronounced differences in the Raman spectra of the reactant (NTP) and product (DMAB) allowed us to assess the formation of DMAB. The heat expansion of the nanotriangles induced by continuous laser irradiation was measured by static X-ray diffraction at the KMC3-XPP end station of the Berlin synchrotron radiation facility BESSY II. A flat monolayer ordering of the nanotriangle SERS platform guaranteed that the lattice constant perpendicular to the triangles was oriented out of the substrate plane for all particles, which allows for low-intensity X-ray diffraction measurements in the symmetric Bragg configuration in any conventional XRD device.[39,41] The out-of-plane lattice expansion of the gold nanotriangles was calibrated by a careful measurement of the particles' lattice temperature. We conducted all experiments on different irradiated spots with varying sizes using different focusing conditions.

■ RESULTS AND DISCUSSION

We start our explanation by showing spectra of the 4-NTP molecules chemisorbed on our gold nanotriangle template in a typical SERS microscope with a 5 μm spot size (full width at half maximum, FWHM) using a continuous wave laser of 785 nm wavelength with a power of 30 mW. Figure 1a shows the transmission electron microscopy images of the well-ordered template and the X-ray reflectometry (XRR) results (inset) confirming that the platform indeed consists of a large area monolayer of gold nanotriangles with a thickness of 7 ± 2 nm on silicon. In this experiment, the laser light is simultaneously
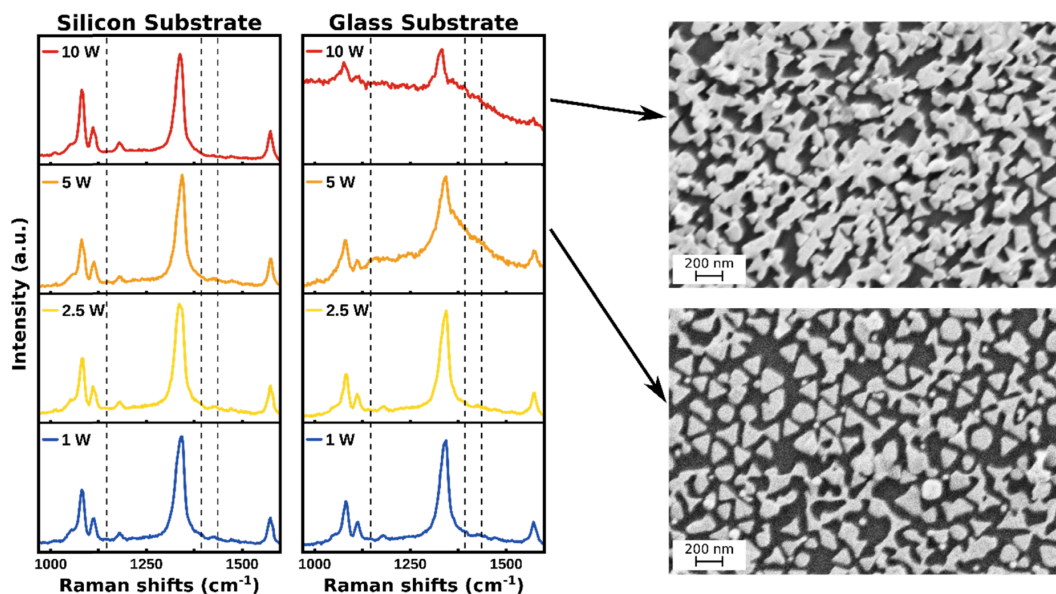
Figure 2. Low-intensity SERS spectra of 4-NTP assembled on gold NTs deposited on silicon and glass substrate probed after the sample was irradiated with different laser powers with 5 mm spot size for 5 min. Dashed lines show the frequencies, where the DMAB product would be expected. SEM images show the melting of the gold NTs on glass substrate for 5 W (lower image) and for 10 W (upper image).

responsible for SERS detection and for triggering the plasmon-assisted reaction. The time-dependent SERS spectra in Figure 1b confirm the transformation of 4-NTP to DMAB. The 4-NTP spectrum at 0 s displays main vibrational modes at 1082, 1332, and 1575 cm^{-1}, assigned to the C−H bending, NO$_2$ symmetric stretching, and C=C stretching modes of the 4-NTP,[42,43] respectively. After few seconds, new Raman peaks appear at 1134, 1387, and 1434 cm^{-1}, which are assigned to the C−N symmetric stretching and the N=N stretching vibrational modes of the DMAB confirming the coexistence of both molecules.[44,45] The light intensity in these experiments attains a very high value of 10 kW/cm^2. In the rest of the paper, we use far less intensity for SERS sensing to avoid driving the chemical reaction with the SERS laser.

In a first naïve attempt to drive the same reaction across an area that was larger than typically investigated in a microscope, we used a high-power diode laser module operating at 920 nm with a power up to 25 W. We increased the irradiated area by a factor of 10^6 to 5 mm spot diameter (FWHM), varying the irradiation power from 1 to 10 W, i.e., a 30- to 300-fold increase of the laser power. After irradiation for 5 min, the irradiated spots were investigated using the Raman microscope with very low laser power and short integration time (0.5 mW and 1 s). The SERS spectra of such spots are displayed in Figure 2 for the NTs deposited on silicon and glass substrates. The reaction clearly did not occur (no bands at the dashed lines, which indicate where product bands are expected). No signature of DMAB molecules was observed because we in fact decreased the intensity $I = P/A$ by a factor of 3000 to 30 000 compared to the microscopic irradiation. The Raman spectrum of the sample on glass changes at 5 W, acquiring a large background contribution, and the Raman peaks become hardly visible for 10 W irradiation. Melting of the NTs was found to be the reason as confirmed by SEM images (Figure 2), despite the very low laser intensity. Similar damage and no DMAB was observed for the silicon substrate after irradiating the sample

with 15 W. The melting at higher laser power is related to the thermal conductivity of the glass, which is 2 orders of magnitude smaller than that for the silicon substrate. Therefore, the heating of the gold induced by light is dissipated more quickly by the substrate to avoid melting of the NPs.

The fact that the particles already melt at the intensity of 400 mW/cm^2 under the large spot really makes it surprising that in a microscope focus the intensity can be easily increased by 3 orders of magnitude above this intensity without any signs of melting. It illustrates at the same time the great opportunities of nanoscale heating.

To check the role of the focusing conditions, the laser driving the reaction was focused through different plano-convex lenses onto the sample irradiating spots of different sizes. The laser power was tuned to obtain approximately the same final laser intensity.

Figure 3 shows the Raman spectra taken from spots irradiated with an intensity of about 50 kW/cm^2. The SERS spectra recorded on the spots with 70 and 115 μm diameter generated by 30 and 50 mm focusing lenses show the characteristic DMAB Raman peaks, which indicate the plasmon-driven coupling reaction. The intensity of the DMAB peak decreases relative to the 4-NTP peak with increasing spot size. For the 175 μm spots (75 mm lens), the peaks are hardly discernible and for the 230 μm spots (100 mm lens), the Raman spectrum only consists of a noisy electronic background from the hot and molten NPs, which is confirmed by SEM images similar to the ones shown in Figure 2. The hot spots of the plasmonic platform, which provide the largest SERS enhancement and the largest reaction yield, melts first and therefore the excessive heating deteriorates the reaction rate.

The heat dissipation, excluding light absorption, was numerically calculated solving the 3D heat equation by means of a numerical finite elements (FEM) solver (COMSOL
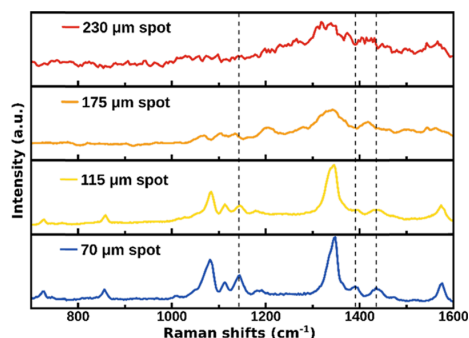
75

Figure 3. SERS spectra of 4-NTP assembled on gold NTs and probed with different laser spot sizes of 70, 115, 175, and 230 μm diameter. The intensity of the exciting laser beam in all four measurements is identical.

Multiphysics) using the temperature-dependent heat capacity and heat conductivity for gold,[46,47] silicon,[46−48] and glass.[49,50] In our model, the laser heating was simulated using a homogeneous heating of an area of the size of the laser spot (von Neumann boundary condition), whereas the lower substrate interface was kept at a constant temperature of $T = 288.15$ K. Indeed, the irradiated spot size strongly in fluences the rate of heat dissipation. Small spots demonstrate a three-dimensional temperature gradient (Figure 4a), indicative of a three-dimensional heat flow. On the other hand, in the center portions of the larger spots with the same excitation intensity, the heat mainly dissipates along the temperature gradient perpendicular to the substrate (Figure 4b), resulting in less efficient one-dimensional heat transport for a large fraction of the spot. Therefore, small spots cool faster and can absorb and dissipate much larger intensities without NP melting. Such high level of absorbed and dissipated energy enables the formation of DMAB molecules. Attempts to flow the same amount of energy per unit area through a large spot inevitably leads to melting of the NPs.

Irradiating the NP continuously with different laser intensities on different spot sizes (100, 250, and 500 μm), we measured their temperatures by XRD via lattice heat expansion. The analysis is based on the detection of the shifts

in the (222) Bragg reflection of the gold NTs in $\Theta-2\Theta$ scans. This shift was then transformed to the temperature change of the NTs based on Bragg's law and the linear thermal expansion

$$\cot\theta\Delta\theta = \frac{\Delta c}{c} = -\alpha\Delta T$$

Here, $\Delta\theta$ is the shift of the Bragg peak, $\Delta c/c$ is the relative change of the out-of-plane lattice constant, and $\alpha = 1.49 \times 10^{-5}$ $1/K$ is the thermal expansion coefficient of the gold nanotriangles previously measured by X-ray diffraction using conventional heating, which is slightly increased compared to bulk gold.[51] To perform the Bragg-angle-based temperature measurement during laser irradiation, the sample was glued with silver paste onto a Peltier cooled sample holder with an active feedback loop stabilized to 288.15 K.

Figure 4c shows the temperature of the gold NTs measured for different spot sizes on a 0.5 mm thick Si substrate, which increases linearly with the laser intensity. For a large spot of 500 μm, a laser intensity of approximately 10 kW/cm^2 is sufficient to increase the particle temperature to 96 K. For a small spot of 100 μm, a 10 times larger intensity leads to less heating of only 70 K. For glass substrates, the heating is even more dominant, and Figure 4c compares the 500 μm spot on Si to a glass substrate. The silicon substrate has considerably higher thermal conductivity. For high laser intensities, a Bragg peak sharpening is observed that is related to an increase of the gold NTs thickness due a particle coalescence (for more information, see the Supporting Information).

FEM simulations of the temperature increases using the model described earlier con firm that the temperature changes can be fully explained by the different spot sizes (solid lines in Figure 4c,d). The simulated temperature increases indeed match the measured temperature increases very well. It should be noted that a phenomenological absorption factor was used to adapt the simulation to the measurements. It reduced the total power entering the simulation to take into account both the optical absorption coefficient of the sample and the possible heat resistances at the gold−substrate interface. The same absorption factor was used for each substrate material.
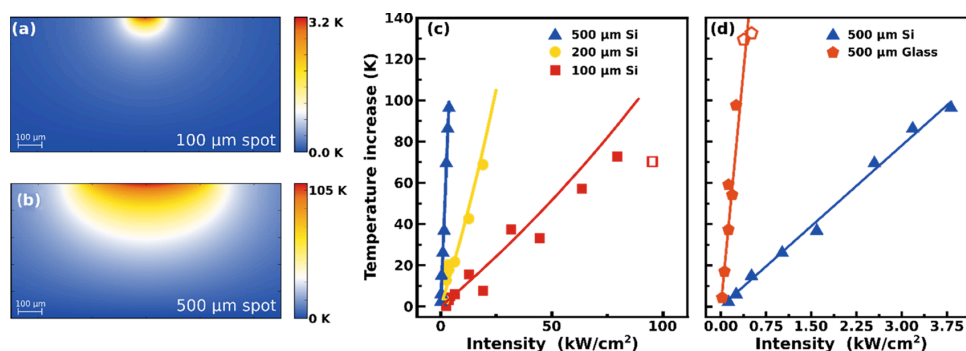
Figure 4. (a, b) FEM simulation of the temperature gradient in the substrate for an excitation intensity of 100 kW/cm^2 with two different spot sizes. The temperature change of the gold NTs as determined from the Bragg-re flection shift (c) as a function of the laser intensity due to irradiation with different laser spot sizes on silicon and (d) on di fferent substrates for the same spot size of 500 μm. The solid lines represent the result of a FEM simulation of the temperature increase. The un filled symbols in (c) and (d) represent intensities at which a Bragg peak sharpening was observed. The model does not consider the light absorption.

CONCLUSIONS

In conclusion, we have shown that driving a plasmonic chemical reaction on a SERS template structure with a fixed light intensity is only possible up to a certain maximum area of the laser focus because the heat transport turns from 3D to 1D and the excessive heating destroys the sample structure. The silicon substrate turns out to be more suited for plasmonic chemistry than conventional glass substrates, since its high thermal conductivity improves the dissipation of heat and therefore a higher light intensity can be used with more photons triggering the reaction and without melting the plasmonic template structure. This is true, although additional photons are absorbed in the substrate. With laser wavelength above the silicon band gap and by appropriate thermal engineering, the substrate heating could be further reduced.

These microscopic findings underline the importance of heat transport at the nanoscale for a profound understanding of nanoplasmonic chemistry. Although time-resolved measurements of the gold NT's lattice temperature rise with sub-picosecond time resolution has been recently reported, there is so far no report on driving plasmon-assisted chemistry with femtosecond laser pulses.

ASSOCIATED CONTENT

Ⓢ Supporting Information

The Supporting Information is available free of charge on the ACS Publications website at DOI: 10.1021/acs.jpcc.8b12574.

> Damage caused by irradiation; X-ray reflectivity of gold nanotriangles; X-ray diffraction (XRD); determination of the linear expansion coefficient; temperature-dependent lattice constant (PDF)

AUTHOR INFORMATION

Corresponding Author
*E-mail: koopman@uni-potsdam.de.

ORCID Ⓞ
Wouter Koopman: 0000-0001-5402-345X
Joachim Koetz: 0000-0001-9113-1337
Matias Bargheer: 0000-0002-0952-6602

Notes
The authors declare no competing financial interest.

REFERENCES

(1) Boyer, D.; Tamarat, P.; Maali, A.; Lounis, B.; Orrit, M. Photothermal imaging of nanometer-sized metal particles among scatterers. *Science* **2002**, *297*, 1160−1163.

(2) Cognet, L.; Berciaud, S.; Lasne, D.; Lounis, B. Photothermal methods for single nonluminescent nano-objects. *Anal. Chem.* **2008**, *80*, 2288−2294.

(3) Huang, X.; Jain, P. K.; El-Sayed, I. H.; El-Sayed, M. A. Plasmonic photothermal therapy (PPTT) using old nanoparticles. *Lasers Med. Sci.* **2008**, *23*, 217−228.

(4) Hirsch, L. R.; Stafford, R. J.; Bankson, J. A.; Sershen, S. R.; Rivera, B.; Price, R. E.; Hazle, J. D.; Halas, N. J.; West, J. L. Nanoshell-mediated near-infrared thermal therapy of tumors under magnetic resonance guidance. *Proc. Natl. Acad. Sci. U.S.A.* **2003**, *100*, 13549−13554.

(5) Govorov, A. O.; Richardson, H. H. Generating heat with metal nanoparticles. *Nano Today* **2007**, *2*, 30−38.

(6) Timko, B. P.; Dvir, T.; Kohane, D. S. Remotely triggerable drug delivery systems. *Adv. Mater.* **2010**, *22*, 4925−4943.

(7) Pelton, M.; Aizpurua, J.; Bryant, G. Metal-nanoparticle plasmonics. *Laser Photonics Rev.* **2008**, *2*, 136−159.

(8) Baffou, G.; Quidant, R. Thermo-plasmonics: using metallic nanostructures as nano-sources of heat. *Laser Photonics Rev.* **2013**, *7*, 171−187.

(9) Zhang, Y.; Nelson, T.; Tretiak, S.; Guo, H.; Schatz, G. C. Plasmonic hot-carrier-mediated tunable photochemical reactions. *ACS Nano* **2018**, *12*, 8415−8422.

(10) Hattori, Y.; Abdellah, M.; Rocha, I.; Pavliuk, M. V.; Fernandes, D. L. A.; Sá, J. Light-induced ultrafast proton-coupled electron transfer responsible for H2 evolution on silver plasmonics. *Mater. Today* **2018**, *21*, 590−593.

(11) Cao, L.; Barsic, D. N.; Guichard, A. R.; Brongersma, M. L. Plasmon-assisted local temperature control to pattern individual semiconductor nanowires and carbon nanotubes. *Nano Lett.* **2007**, *7*, 3523−3527.

(12) Long, R.; Li, Y.; Song, L.; Xiong, Y. Coupling solar energy into reactions: Materials design for surface plasmon-mediated catalysis. *Small* **2015**, *11*, 3873−3889.

(13) Link, S.; Masiello, D. J. Introduction: Plasmonics in chemistry. *Chem. Rev.* **2018**, *118*, 2863−2864.

(14) Cui, L.; Wang, P.; Fang, Y.; Li, Y.; Sun, M. A plasmon-driven selective surface catalytic reaction revealed by surface-enhanced Raman scattering in an electrochemical environment. *Sci. Rep.* **2015**, *5*, No. 11920.

(15) Fang, Y.; Li, Y.; Xu, H.; Sun, M. Ascertaining p,p'-dimercaptoazobenzene produced from p-aminothiophenol by selective catalytic coupling reaction on silver nanoparticles. *Langmuir* **2010**, *26*, 7737−7746.

(16) Huang, Y.-F.; Zhu, H.-P.; Liu, G.-K.; Wu, D.-Y.; Ren, B.; Tian, Z.-Q. When the signal is not from the original molecule to be detected: chemical transformation of para-aminothiophenol on Ag during the SERS measurement. *J. Am. Chem. Soc.* **2010**, *132*, 9244−9246.

(17) van Schrojenstein Lantman, E. M.; Deckert-Gaudig, T.; Mank, A. J. G.; Deckert, V.; Weckhuysen, B. M. Catalytic processes monitored at the nanoscale with tip-enhanced Raman spectroscopy. *Nat. Nanotechnol.* **2012**, *7*, 583−586.

(18) Sun, M.; Xu, H. A novel application of plasmonics: plasmon-driven surface-catalyzed reactions. *Small* **2012**, *8*, 2777−2786.

(19) Chen, X.-J.; Cabello, G.; Wu, D.-Y.; Tian, Z.-Q. Surface-enhanced Raman spectroscopy toward application in plasmonic photocatalysis on metal nanostructures. *J. Photochem. Photobiol., C* **2014**, *21*, 54−80.

(20) Chen, H. L.; Li, C.-J.; Peng, C.-J.; Leu, H.-J.; Hung, W.-H. Plasmon-induced hot electrons on mesoporous carbon for decomposition of organic pollutants under outdoor sunlight irradiation. *ACS Appl. Mater. Interfaces* **2017**, *9*, 327−334.

(21) Kowalska, E.; Yoshiiri, K.; Wei, Z.; Zheng, S.; Kastl, E.; Remita, H.; Ohtani, B.; Rau, S. Hybrid photocatalysts composed of titania modified with plasmonic nanoparticles and ruthenium complexes for decomposition of organic compounds. *Appl. Catal., B* **2015**, *178*, 133−143.

(22) Mukherjee, S.; Libisch, F.; Large, N.; Neumann, O.; Brown, L. V.; Cheng, J.; Lassiter, J. B.; Carter, E. A.; Nordlander, P.; Halas, N. J. Hot electrons do the impossible: Plasmon-induced dissociation of H2 on Au. *Nano Lett.* **2013**, *13*, 240−247.

(23) Zhou, L.; Zhang, C.; McClain, M. J.; Manjavacas, A.; Krauter, C. M.; Tian, S.; Berg, F.; Everitt, H. O.; Carter, E. A.; Nordlander, P.; et al. Aluminum nanocrystals as a plasmonic photocatalyst for hydrogen dissociation. *Nano Lett.* **2016**, *16*, 1478−1484.

(24) Yasuda, S.; Yoshii, T.; Chiashi, S.; Maruyama, S.; Murakoshi, K. Plasmon-induced selective oxidation reaction at single-walled carbon nanotubes. *ACS Appl. Mater. Interfaces* **2017**, *9*, 38992−38998.

`Article`

(25) de Nijs, B.; Benz, F.; Barrow, S. J.; Sigle, D. O.; Chikkaraddy, R.; Palma, A.; Carnegie, C.; Kamp, M.; Sundararaman, R.; Narang, P.; et al. Plasmonic tunnel junctions for single-molecule redox chemistry. *Nat. Commun.* **2017**, *8*, No. 994.

(26) Adleman, J. R.; Boyd, D. A.; Goodwin, D. G.; Psaltis, D. Heterogenous catalysis mediated by plasmon heating. *Nano Lett.* **2009**, *9*, 4417−4423.

(27) Xu, P.; Kang, L.; Mack, N. H.; Schanze, K. S.; Han, X.; Wang, H.-L. Mechanistic understanding of surface plasmon assisted catalysis on a single particle: cyclic redox of 4-aminothiophenol. *Sci. Rep.* **2013**, *3*, No. 2997.

(28) Bora, T.; Zoepfl, D.; Dutta, J. Importance of plasmonic heating on visible light driven photocatalysis of gold nanoparticle decorated Zinc oxide nanorods. *Sci. Rep.* **2016**, *6*, No. 26913.

(29) Golubev, A. A.; Khlebtsov, B. N.; Rodriguez, R. D.; Chen, Y.; Zahn, D. R. T. Plasmonic heating plays a dominant role in the plasmon-induced photocatalytic reduction of 4-nitrobenzenethiol. *J. Phys. Chem. C* **2018**, *122*, 5657−5663.

(30) Kang, L.; Han, X.; Chu, J.; Xiong, J.; He, X.; Wang, H.-L.; Xu, P. In situ surface-enhanced Raman spectroscopy study of plasmon-driven catalytic reactions of 4-nitrothiophenol under a controlled atmosphere. *ChemCatChem* **2015**, *7*, 1004−1010.

(31) Xie, W.; Walkenfort, B.; Schlücker, S. Label-free SERS monitoring of chemical reactions catalyzed by small gold nanoparticles using 3D plasmonic superstructures. *J. Am. Chem. Soc.* **2013**, *135*, 1657−1660.

(32) Yan, X.; Wang, L.; Tan, X.; Tian, B.; Zhang, J. Surface-enhanced Raman spectroscopy assisted by radical capturer for tracking of plasmon-driven redox reaction. *Sci. Rep.* **2016**, *6*, No. 30193.

(33) Dong, B.; Fang, Y.; Chen, X.; Xu, H.; Sun, M. Substrate-, wavelength-, and time-dependent plasmon-assisted surface catalysis reaction of 4-nitrobenzenethiol dimerizing to p,p'-dimercaptoazobenzene on Au, Ag, and Cu films. *Langmuir* **2011**, *27*, 10677−10682.

(34) Cho, F.-H.; Kuo, S.-C.; Lai, Y.-H. Surface-plasmon-induced azo coupling reaction between nitro compounds on dendritic silver monitored by surface-enhanced Raman spectroscopy. *RSC Adv.* **2017**, *7*, 10259−10265.

(35) Ding, Q.; Chen, M.; Fang, Y.; Zhang, Z.; Sun, M. Plasmon-driven diazo coupling reactions of p -nitroaniline via −NH 2 or −NO 2 in atmosphere environment. *J. Phys. Chem. C* **2017**, *121*, 5225−5231.

(36) Zhang, Z.; Chen, L.; Sun, M.; Ruan, P.; Zheng, H.; Xu, H. Insights into the nature of plasmon-driven catalytic reactions revealed by HV-TERS. *Nanoscale* **2013**, *5*, 3249−3252.

(37) Zhang, Z.; Kinzel, D.; Deckert, V. Photo-Induced or plasmon-induced reaction: Investigation of the light-induced azo-coupling of amino groups. *J. Phys. Chem. C* **2016**, *120*, 20978−20983.

(38) Kim, K.; Choi, J.-Y.; Shin, K. S. Surface-enhanced Raman scattering of 4-nitrobenzenethiol and 4-aminobenzenethiol on silver in icy environments at liquid nitrogen temperature. *J. Phys. Chem. C* **2014**, *118*, 11397−11403.

(39) Liebig, F.; Sarhan, R. M.; Sander, M.; Koopman, W.; Schuetz, R.; Bargheer, M.; Koetz, J. Deposition of gold nanotriangles in large scale close-packed monolayers for X-ray-based temperature calibration and SERS monitoring of plasmon-driven catalytic reactions. *ACS Appl. Mater. Interfaces* **2017**, *9*, 20247−20253.

(40) Liebig, F.; Sarhan, R. M.; Prietzel, C.; Reinecke, A.; Koetz, J. "Green" gold nanotriangles: synthesis, purification by polyelectrolyte/micelle depletion flocculation and performance in surface-enhanced Raman scattering. *RSC Adv.* **2016**, *6*, 33561−33568.

(41) von Reppert, A.; Sarhan, R. M.; Stete, F.; Pudell, J.; Del Fatti, N.; Crut, A.; Koetz, J.; Liebig, F.; Prietzel, C.; Bargheer, M. Watching the vibration and cooling of ultrathin gold nanotriangles by ultrafast X-ray diffraction. *J. Phys. Chem. C* **2016**, *120*, 28894−28899.

(42) Ling, Y.; Xie, W. C.; Liu, G. K.; Yan, R. W.; Wu, D. Y.; Tang, J. The discovery of the hydrogen bond from p-nitrothiophenol by Raman spectroscopy: guideline for the thioalcohol molecule recognition tool. *Sci. Rep.* **2016**, *6*, No. 31981.

(43) Kuo, S.-C.; Tasi, J.-J.; Li, J.-S.; Hou, Z.-H.; Li, C.-H.; Jeng, U.-S.; Lai, Y.-H. Enhancement of surface enhanced Raman scattering activity of Au nanoparticles through the mesostructured metallic nanoparticle arrays. *APL Mater.* **2014**, *2*, No. 113310.

(44) Shin, D. Two different behaviors in 4-ABT and 4,4 '-DMAB surface enhanced Raman spectroscopy. *J. Raman Spectrosc.* **2017**, *48*, 343−347.

(45) Kim, K.; Shin, D.; Kim, K. L.; Shin, K. S. Surface-enhanced Raman scattering of 4,4 '-dimercaptoazobenzene trapped in Au nanogaps. *Phys. Chem. Chem. Phys.* **2012**, *14*, 4095−4100.

(46) Ho, C. Y.; Powell, R. W.; Liley, P. E. Thermal conductivity of the elements. *J. Phys. Chem. Ref. Data* **1972**, *1*, 279−421.

(47) Pankratz, L. B.; Mrazek, R. V. *Thermodynamic Properties of Elements and Oxides*; U.S. Department of the Interior, Bureau of Mines, 1982.

(48) Desai, P. D. Thermodynamic properties of iron and silicon. *J. Phys. Chem. Ref. Data* **1986**, *15*, 967−983.

(49) Kingery, W. D. Heat-conductivity processes in glass. *J. Am. Ceram. Soc.* **1961**, *44*, 302−304.

(50) Lucks, C. F.; Deem, H. W.; Wood, W. D. *Thermal Properties of Six Glasses and Two Graphites*; Battelle Memorial Institute: Columbus, OH, 1960; Vol. 39.

(51) Nix, F. C.; MacNair, D. The thermal expansion of pure metals: copper, gold, aluminum, nickel, and iron. *Phys. Rev.* **1941**, *60*, 597−605.

Article IV – Supplemental Material

Scaling-Up Nano-Plasmon Catalysis: The Role of Heat Dissipation

Radwan M. Sarhan,[1, 2] Wouter Koopman,[1] Jan Pudell,[1] Felix Stete,[1, 2] Matthias Rössle,[3] Marc Herzog,[1] Clemens N. Z. Schmitt,[4] Ferenc Liebig,[5] Joachim Koetz,[5] and Matias Bargheer[1, 3]

[1]*Institute of Physics and Astronomy, University of Potsdam, 14476 Potsdam, Germany*
[2]*School of Analytical Sciences Adlershof (SALSA),*
Humboldt-Universität zu Berlin, Albert-Einstein-Str. 5-9, 10099 Berlin, Germany
[3]*Helmholtz-Zentrum Berlin, Albert-Einstein-Str. 15, 12489 Berlin, Germany*
[4]*Max Planck Institute of Colloids and Interfaces, 14476 Potsdam, Germany*
[5]*Institute of Chemistry, University of Potsdam, 14476 Potsdam, Germany*

DAMAGE CAUSED BY IRRADIATION

We confirmed by SEM (Figure S1) that the degradation of the Raman spectra presented in Figure 3 of the manuscript were caused by damages to the nanoparticle substrate. As the high total power of the excitation laser beam could not dissipate quickly enough, a partial melting of the particles occurred.
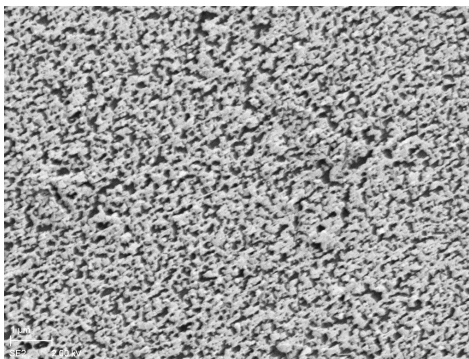
FIG. S1. **SEM 175 µm spot:** $8\,\mu m \times 5.5\,\mu m$ SEM image of from the center of the irradiated spot with a diameter of 175 µm. The damage due to the melting of the nanotriangles is clearly visible.

X-RAY REFLECTIVITY OF GOLD NANO TRIANGLES

X-ray reflectivity (XRR) is a technique that allows the surface-sensitive characterization of thin layers by interference of specular reflections of the bottom and top interfaces of the layer that give rise to characteristic minima and maxima as function of the energy transfer, $Q = 4/\lambda \; \sin\vartheta$, with ϑ being the incidence angle of the X-rays with wavelength λ onto the sample. We measured a monolayer of gold nano triangles (NTs) on a Silicon substrate at the XPP-KMC-3 endstation at the synchrotron BESSY II. The incidence angle of the X-rays on the sample was scanned between 0 and 3° incidence angle, which corresponds to $Q = 0$ to $4\,nm^{-1}$ in reciprocal space. The corresponding dataset shown in the inset of Fig. 1a) contains a dominant oscillation frequency that corresponds to a wavelength of $\lambda = 0.9\,nm^{-1}$ determined by a Fourier-transformation. This wavelength corresponds to a layer-thickness of $7 \pm 2\,nm$. The absence of higher frequencies in the signal proofs that our sample contains a negligible part of stacked gold-nano-triangles over the X-ray spot size of approximately $0.5 \times 10\,mm^2$.

X-RAY DIFFRACTION (XRD)

We measured at the XPP-KMC-3 endstation at the synchrotron source BESSY II the 222 Bragg reflection of the [111] oriented gold NTs at the X-ray energy of 8 keV. We selected the 2nd order Bragg reflection to minimize the X-ray footprint. The sample was mounted on Peltier-cooled sample mount, which results in a stable substrate

temperature of 15°C that was attached with silver paint to the Peltier cooler. In Figure S2a) and b) we show the Bragg peaks of the gold NTs on Si and glass substrates for different Laser intensities, respectively. For every measured laser intensity, a new spot on the sample was selected and measured before illumination (black thick curves) and during illumination. For every measurement we waited 60 s for thermal equilibration between gold NTs.
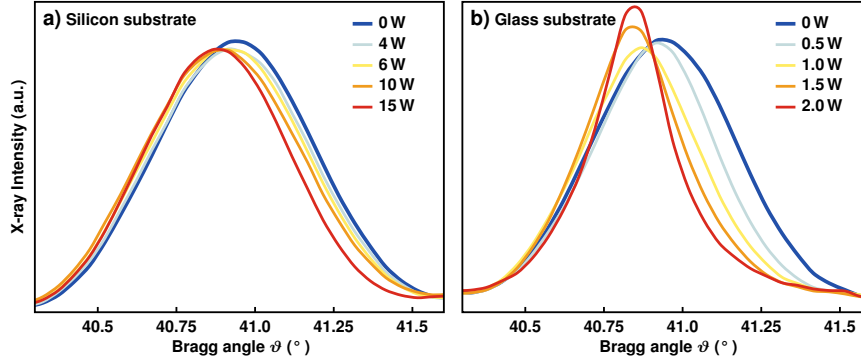
FIG. S2. **XRD results:** Bragg peak shift of gold NTs on a) a silicon substrate and b) glass substrate for different intensities. The Bragg peak shift to smaller angles due to heating of the gold NTs. On the glass substrate a sharpened peak is observed for high intensities.

We note a peak sharpening at high intensities. For very thin layer we can neglect typical Bragg broadening effects and the width of the Bragg peak is approximately given by the thickness. In our case the peak width is slightly smaller as theoretical values for 7 nm layers, which indicates a small amount of stacked gold NTs (5-10%). After illumination of the sample with glass substrate with high intensities we observe a sharpened Bragg peak that is related to thicker nano particles. This indicates a particle coalescence of the gold NTs.

DETERMINATION OF THE LINEAR EXPANSION COEFFICIENT

The temperature-dependent shift of the Bragg peak allows us to calculate the linear expansion coefficient for gold NTs along the [111] direction. It is measured with a closed-cycle cryostat setup available at the XPP-KMC-3 endstation at the synchrotron source BESSY II that allows the variation of the sample temperature from 20 to 350 K. From the Bragg Peak position the out-of-plane lattice constant in [111] direction is extracted and shown in Figure S3. A linear fit yields the linear expansion coefficient of $\alpha = 1.49 \cdot 10^{-5}\,1/K$.
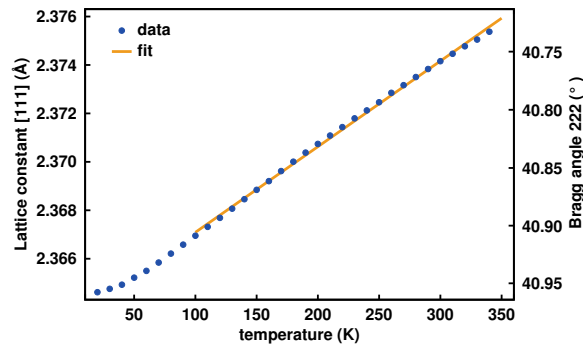
FIG. S3. **The Temperature-dependent lattice constant** is measured from 20 to 350 K and fitted to extract the linear expansion coefficient α.

Article V

Persistent nonequilibrium dynamics of the thermal energies in the spin and phonon systems of an antiferromagnet

Alexander von Reppert, **Jan-Etienne Pudell**, Azize Koç, Matthias Reinhardt, Wolfram Leitenberger, Karine Dumesnil, Flavio Zamponi, and Matias Bargheer

We present a temperature and fluence dependent Ultrafast X-Ray Diffraction study of a laser-heated antiferromagnetic dysprosium thin film. The loss of antiferromagnetic order is evidenced by a pronounced lattice contraction. We devise a method to determine the energy flow between the phonon and spin system from calibrated Bragg peak positions in thermal equilibrium. Reestablishing the magnetic order is much slower than the cooling of the lattice, especially around the Néel temperature. Despite the pronounced magnetostriction, the transfer of energy from the spin system to the phonons in Dy is slow after the spin-order is lost.

Persistent nonequilibrium dynamics of the thermal energies in the spin and phonon systems of an antiferromagnet

A. von Reppert,[1] J. Pudell,[1] A. Koc,[2] M. Reinhardt,[2] W. Leitenberger,[1]
K. Dumesnil,[3] F. Zamponi,[1] and M. Bargheer[1,2,a]

[1]*Institut für Physik and Astronomie, Universität Potsdam, Karl-Liebknecht-Str. 24-25, 14476 Potsdam, Germany*
[2]*Helmholtz Zentrum Berlin, Albert-Einstein-Str. 15, 12489 Berlin, Germany*
[3]*Institut Jean Lamour (UMR CNRS 7198), Université Lorraine, Boulevard des Aiguillettes B.P. 239, F-54500 Vandoeuvre les Nancy Cédex, France*

We present a temperature and fluence dependent Ultrafast X-Ray Diffraction study of a laser-heated antiferromagnetic dysprosium thin film. The loss of antiferromagnetic order is evidenced by a pronounced lattice contraction. We devise a method to determine the energy flow between the phonon and spin system from calibrated Bragg peak positions in thermal equilibrium. Reestablishing the magnetic order is much slower than the cooling of the lattice, especially around the Néel temperature. Despite the pronounced magnetostriction, the transfer of energy from the spin system to the phonons in Dy is slow after the spin-order is lost. © *2016 Author(s). All article content, except where otherwise noted, is licensed under a Creative Commons Attribution (CC BY) license (http://creativecommons.org/licenses/by/4.0/).*
[http://dx.doi.org/10.1063/1.4961253]

INTRODUCTION

The unexpectedly fast magnetization loss in magnetic thin films upon photoexcitation observed two decades ago[1] stimulated extensive research aiming at ultrafast data storage and related applications. Experiments using different schemes for probing the changes induced in magnetic systems by optical light pulses have been employed. They range from visible magneto-optical Kerr effect (MOKE),[2,3] extreme ultraviolet MOKE,[4] x-ray magnetic circular dichroism[5–8] over photoelectron spectroscopy[9–11] to ultrafast x-ray diffraction (UXRD)[12] and resonant x-ray scattering.[13] The discussions are mainly focused on the transfer of angular momentum or the loss of spin-order in the framework of two- or three-temperature models. Antiferromagnets are believed to support even faster local angular momentum changes, since the average spin remains zero.[7,14] The multifarious behavior of transition metals and 4f magnetic materials, however, have eluded so far the effort to be described by a unique physical picture.[3,15,16] The demagnetization aspects at ultrashort timescales are an exciting first step of the full magnetization dynamics. The remagnetization is another fundamental issue, especially in the perspective of possible technological applications, which has received less attention. Few authors have approached the problem of how fast and through which intermediate steps the remagnetization occurs.[13,17–20] Different models have been developed to simulate the dynamics on longer timescales.[21–24] Some of them point out the important role of fluctuations and domain formation close to the phase transition. In particular, resonant x-ray diffraction experiments from the dysprosium spin-spiral have shown that some disorder of the spin system persists more than 10 ns, especially for high fluence excitation.[13]

However, a characterization of the influence of the temperature and excitation density on the remagnetization dynamics is still missing. In fact, a detailed account of the energy in the phonon and spin systems at the different stages of the remagnetization has not been reported.

---

[a]bargheer@uni-potsdam.de. URL: http://www.udkm.physik.uni-potsdam.de

Dysprosium (Dy) is a thoroughly characterized material[25–28] with a pronounced magnetostrictive expansion of the lattice constant c. The 4f electrons, coupled via the 5d electrons (i.e., RKKY coupling), are responsible for its magnetic properties.[27,28] All magnetic materials show magnetostriction, i.e., a change of the lattice constant that depends on the magnetization $M(T)$. Only a single UXRD study has so far explored the magnetostrictive strain on ultrafast timescales,[12] although the existing UXRD setups have been constantly improved and allow for measuring minute lattice strains on ultrafast timescales.[29] In general, the lattice strain occurs as a response to stress imposed by a modified energy density. This is particularly evident, when the Grüneisen concept is used, e.g., for separating the electron and phonon contribution to photoinduced stress.[30,31] Although the extension to magnetic systems was suggested,[30] this powerful approach has not been realized.

Here, we analyze temperature- and excitation-fluence-dependent UXRD data from an 80 nm Dy thin film to characterize the nonequilibrium spin and lattice dynamics triggered by ultrafast heating of the electron system by a near-infrared laser pulse. The central and surprising result of our analysis can be directly read from the experimental data: The lattice contraction originating from the spin-disorder persists on the nanosecond timescale when the lattice heat is already dissipated to the substrate. The Bragg peak shift is a direct measure of the time-dependent strain $\varepsilon(t) = \Delta c(t)/c$ in the out-of-plane lattice constant c which is linearly related to the deposited heat Q_{tot} in the film. From these two measured variables $\epsilon(t)$ and Q_{tot}, we determine the transient energy densities $Q_{\text{P}}(t)$ and $Q_{\text{S}}(t)$ in the phonon and spin excitations, respectively, from a numerically robust analysis. Our model adopts the linear relation of these energy densities to the experimentally observed lattice strain via separate nearly temperature independent constants for the phonon and spin systems (see Eq. (1)). Therefore, our analysis in a "two-thermal-energies-model" (TTEM) is independent of modifications of the spatial excitation profile. In comparison with a "two-temperatures-model" (TTM),[1,32] our TTEM has the advantage that the energy contained in random motion of the phonon and spin excitations is a well-defined quantity even in strong nonequilibrium-situations, where the temperature is not.

The electron system of the Y cap layer and the dysprosium layer are photoexcited, and the multilayer system is cooled through the substrate. Here, we examine how the thermal energy in the dysprosium layer is distributed between the phonon and the spin system.

RESULTS

Linear relation of strain to lattice- and spin-energy

The sample is an 80 nm thick (0 0 0 1) oriented Dy film grown on a sapphire substrate with a 100 nm Niobium and 10 nm Yttrium (Y) buffer layer. The structure is capped with another 18 nm thin Y layer (see Fig. 3(e)) in order to support the helical spin ordering in the thin Dy film[34] and to prevent oxidation.

We have carefully measured the lattice constant $c(T)$ of the Dy thin film as a function of temperature. The lattice strain derived from the Bragg peak position (black dots in Fig. 1(a)) shows a pronounced expansion below the Néel temperature $T_{\text{N}} = 180$ K, which results from the antiferromagnetic spin-ordering. Fig. 1(b) shows the linear expansion coefficient $\alpha(T)$ derived from this measurement, with a pronounced negative thermal expansion below 180 K. The constant-pressure specific heat C in Fig. 1(c) is taken from the literature (black line).[33] We separated the strain $\varepsilon(T) = \varepsilon_{\text{P}}(T) + \varepsilon_{\text{S}}(T)$, its derivative $\alpha(T)$, and the heat capacity $C(T) = C_{\text{P}}(T) + C_{\text{S}}(T)$ into phonon and spin contributions (cf. Fig. 1). We determined the combined electron and phonon contribution from the specific heat of the non-magnetic rare earth lutetium,[35] which is in agreement with a simple Debye approximation. Near its maximum at T_N the spins carry more than half of the specific heat, whereas the specific heat of the electrons is negligible in the relevant temperature range. Fig. 1(a) exemplifies the separation of the strain $\varepsilon(T) = \varepsilon_{\text{P}}(T) + \varepsilon_{\text{S}}(T)$ for the initial temperature $T_{\text{i}} = 120$ K. This is the equilibrium temperature given by the thermostate before deposition of the heat Q by the laser pulse.

In thermal equilibrium, more and more modes with frequency ω fulfill the relation $k_B T > \hbar\omega$ with rising temperature, which therefore contribute a thermally accessible degree of
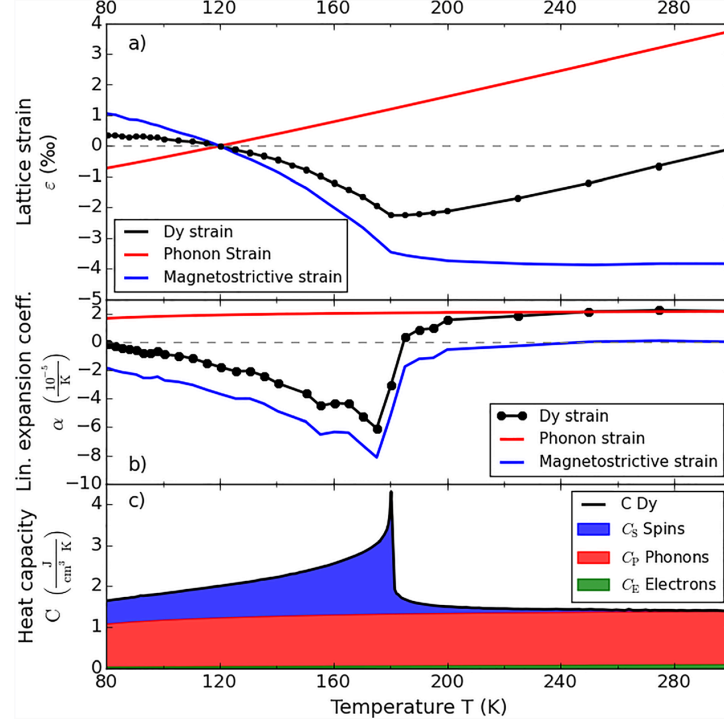
FIG. 1. Temperature dependence of the equilibrium properties of Dy. (a) Black: strain along the c-axis in the Dy film obtained by static X-Ray diffraction measurements on the hcp (0 0 0 2) reflection. The red and blue curves represent the lattice strain contributions for heating the phonons and the magnetic system. (b) Thermal expansion coefficients of Dy derived from the data in panel (a). (c) Heat capacity reported for bulk Dy[33] decomposed into C_P, C_S, and C_E.

freedom.[36] As a consequence, both the thermal expansion coefficient α and the specific heat strongly vary with the temperature T. However, if we numerically calculate the lattice strains $\varepsilon_{P,S}$ as a function of the energy densities $Q_{P,S}$, a linear relation is obtained (see solid lines in Fig. 2). While the phonon contribution simply extrapolates to high Q until the melting of the lattice is observed, the spin contribution to the energy density is limited (blue area in Fig. 1(c)). The linear relation of strain and energy suggests the definition of parameters $\beta_{P,S} = C_{P,S}(T)/\alpha_{P,S}(T)$ which measure the infinitesimal energy density required to yield an additional strain at the temperature T. These parameters are essentially inverse macroscopic Grüneisen constants $\Gamma_{P,S} = K/\beta_{P,S}$, where K is the bulk modulus of Dy.[37]

Microscopic theories define mode-specific Grüneisen constants, which may vary both in magnitude and sign.[38] However, if we assume a non-equilibrium situation which has no selective population of special modes, we can assume the lattice strain

$$\varepsilon_{P,S} = \int_T^{T+\Delta T} \alpha_{P,S}(T)dT = \frac{Q_{P,S}}{\beta_{P,S}} = \frac{\Gamma_{P,S}Q_{P,S}}{K} \tag{1}$$

to be proportional to the average increase of the energy density Q_P and Q_S of the phonon and spin systems, respectively. The parameters β or Γ are independent of T to a first approximation, making our non-equilibrium data analysis very robust. While $\Gamma_P \approx 0.6$ and $\Gamma_S \approx -1.8$ are dimensionless quantities, $\beta_P = 63\,\text{kJ/cm}^3$ and $\beta_S = -20\,\text{kJ/cm}^3$ can be interpreted as a characteristic energy densities required to expand or contract a solid. For example, the energy density $Q = 0.01 \cdot \beta$ expands or contracts the solid by 1%, depending on the sign of β. The weak temperature dependence of the bulk modulus $K \approx 41\,\text{GPa} = 41\,\text{kJ/cm}^3$ adds some subtle difference near the phase transition. We note that
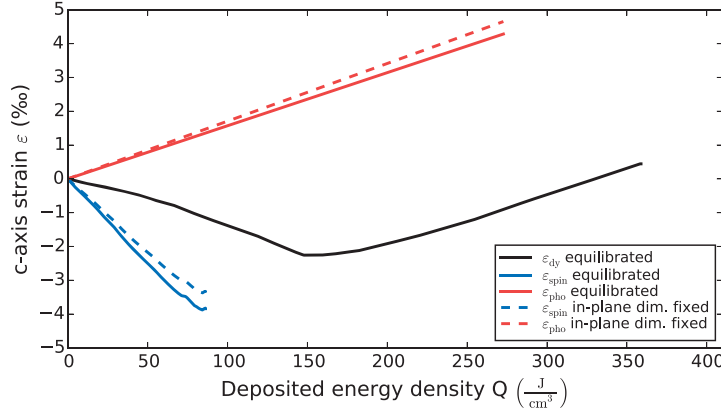
FIG. 2. Lattice strain as a function of the total heat Q_{tot} (black), for $T_{Start} = 120$ K. The red and blue curves show the separation into strain driven by heat in the phonons Q_P and in spin excitations Q_S. Although the black line is strongly curved, the separation into spin and phonon contributions yields a linear dependence. Note that the maximum heat in the spin system is given by the blue area in Fig. 1(c), i.e., the spin contribution to the specific heat C_S. The dashed lines show the result after taking into account that, on ultrafast timescales, the lattice cannot expand in plane.

for the same amount of energy the lattice contraction resulting from the spin excitation is three times larger than the expansion due to phonon heating, also above T_N. Even above T_N, where the spin-contribution to the specific heat is strongly reduced (Fig. 1(c)), the negative thermal expansion driven by spin excitations persists (Fig. 1(b)).

Ultrafast x-ray diffraction data

We now describe the UXRD data of Dy after ultrafast heating of the electrons in Y and Dy by a 100 fs, 800 nm laser pulse. The optical penetration depth of 24 nm was determined by ellipsometry. The lattice response is probed by diffraction of 250 fs Cu-K$_\alpha$ pulses originating from a tabletop Plasma-X-Ray source.[29,39] Fig. 3(a) shows the transient strain $\varepsilon(t)$ for different pump fluences F of the excitation pulse at the initial temperature $T_i = 160$ K $< T_N$. The incident fluence F is determined as the average intensity divided by the pumped area on the sample in the top-hat approximation, and the pump pulse is about four times larger than the probe pulse. For small fluences, the Dy lattice contracts within less than 30 ps given by the timescale of sound propagation through 18 nm Y and 80 nm Dy. In contrast, for high fluences, we first see a rapid Dy lattice expansion that relaxes on a few-nanosecond timescale. To visualize this threshold behavior, Fig. 3(b) shows the lattice strain $\varepsilon(t = 45$ ps) as a function of the fluence. Below $F_{th} = 2$ mJ/cm^2, a higher fluence leads to a more thorough disordering of the spin system and a concomittant lattice contraction. Above this threshold, additional energy leads to a linear expansion indicative of preferential excitation of phonons. For lower starting temperatures, a higher threshold fluence is required. The excitation of the spin system saturates due to the abrupt decrease of the specific heat of the spin system at T_N.

Fig. 3(c) shows the temperature dependence of the photoinduced Dy strain for a fixed fluence of 6.8 mJ/cm^2. For $T_i > T_N$, we observe the expected rapid phonon heat driven expansion superimposed with oscillations originating from coherent acoustic phonons (reflection of the strain waves at the interfaces of the multilayer) followed by a slow recovery of the lattice constant as heat flows towards the substrate. The red dashed line indicates the excellent agreement of a heat transport simulation according to the Fourier heat law through the layered system which we map on the strain axis by reading the experimentally determined strain in Fig. 1(a) at the calculated average temperature. For the heat diffusion we used the specific heat[40] $C_p = 162.3$ J/kg K and the heat conductivity[41] $\kappa = 11.7$ W/mK reported in the literature (for details see Ref. 42). We note that the negative slope of the data from 0.1 to 1 ns (Fig. 3(c)) is exactly the same for all initial temperatures (gray dashed lines). Since for $T_i = 200$ K this slope is dictated only by the phonon
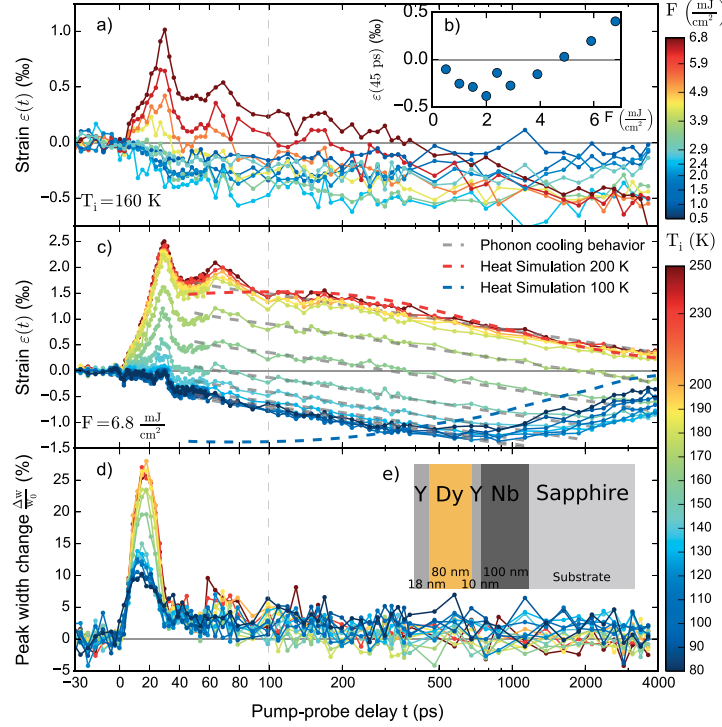
FIG. 3. UXRD data. (a) Time resolved lattice strain $\varepsilon(t)$ for $T_i = 160\,\mathrm{K}$ for different excitation fluences. (b) $\varepsilon(45\,\mathrm{ps})$ as a function of fluence. The initial strain rises linearly above the threshold fluence $F_{th} = 2\,\mathrm{mJ/cm^2}$. (c) Lattice strain $\varepsilon(t)$ and (d) the relative peak width change for different initial temperatures at fixed excitation fluence $F = 6.8\,\mathrm{mJ/cm^2}$. Dashed lines in (c) indicate the expected lattice strain according to simulations of the heat conduction. (e) Layering sequence of the sample.

heat transport, we conclude that this is the case for all temperatures. The blue dashed line shows the strain resulting from a heat transport simulation for $T_i = 100\,\mathrm{K}$. The lattice contraction resulting from the increased spin excitation is captured by the simulations, since it is encoded in the negative thermal expansion coefficient. However, in contrast to the observed minimum around 500 ps, the simulation predicts a contracted lattice right after the excitation, because solving the Fourier-law for heat diffusion assumes the material parameters for thermal equilibrium, i.e., where the phonons and the magnetic system have the same temperature.

The Bragg peak width change (Fig. 3(d)) shows that in both the paramagnetic and the antiferromagnetic phases the width starts rising about 1 ps after the excitation. A simple masses and springs model[43] confirms that the quasi-instantaneous stress originating from phonon heating yields a strong expansion wave with an exponential spatial profile starting at the surface. This wave travels into the Dy layer, and the maximum peak width is reached after about 18 ps when half the Dy layer is expanded. The width returns to near the initial value after 35 ps, when this strain front traverses the Dy-Y interface. This is consistent with the observation that at this time the average lattice constant determined from the peak shift (Fig. 3(c)) of Dy experiences a rapid contraction, as the expansion wave is transmitted towards the substrate. It is relevant to argue why the average lattice constant does not change in the first 35 ps for start temperatures between 80 and 130 K, although the peak width very strikingly shows an immediate inhomogeneous lattice deformation. The strong average expansion of Dy triggered by phonon heating must be cancelled by substantial contractive wavefronts starting at the Dy-Y interfaces due to the quasi-instantaneous loss of the magnetic order and the strong magnetostrictive coupling. The average cancellation suggests that at $t = 35\,\mathrm{ps}$ about 25% of the energy heat up

the magnetic system, while less than 75% heat up the phonon system according to the two Grüneisen constants.

The data in Fig. 3(c) confirm the threshold behavior: The laser induced average lattice strain remains unchanged from $T_i = 80$ to 130 K in agreement with the nearly temperature-independent Grüneisen constants. Then, the observed initial strain gradually increases up to $T_i = 180$ K, where it saturates.

Data analysis in a two-thermal-energy-model

The description of the UXRD data clearly showed that assuming a thermal equilibrium between the spin and phonon system on the nanosecond timescale is incompatible with the observations. Therefore, we analyze the flow of thermal energy among the spin and phonon systems within a model, where Q_S and Q_P are a function of time and space. We explicitly avoid a microscopic simulation in order to emphasize which conclusion can be drawn from the data under the assumption that the lattice strain is proportional to the energies in the two subsystems according to Eq. (1). To simplify the analysis, we start at times $t = 45$ ps where we may safely neglect a separate contribution of electrons, assuming them to be in thermal equilibrium with the phonons since electron-phonon coupling times in metals are expected on the order of few picoseconds at maximum.[7,10]

As a first step in our analysis, we calibrate the total energy densities $Q_{tot,i}$ deposited by the laser excitation. At $T_i = 250$ K, all available energy Q_{tot}^{250K} heats up the lattice, leading to a temperature increase of about 90 K corresponding to $\varepsilon = 0.2\%$. According to ellipsometric measurements of the sample, the optical absorption varies by less than 5%, so the total amount of energy deposited is $Q_{tot}^T = Q_{tot}^{250K}$ for all temperatures.

In the following, we discuss the measured data in terms of a nonequilibrium "two-thermal-energies-model" (TTEM) that satisfies energy conservation (Eq. (2)) and the linear superposition of magnetostrictive and thermoelastic strains (Eq. (3))

$$Q_{tot}(t) = Q_S(t) + Q_P(t), \tag{2}$$

$$\varepsilon_{tot}(t) = \varepsilon_S(Q_S(t)) + \varepsilon_P(Q_P(t)). \tag{3}$$

This approach circumvents problems with the definition of temperature in nonequilibrium situations, the lack of literature data for the spin-phonon coupling constant and the separated contributions of the spin and phonon system to the heat conductivities, which would be necessary to obtain predictions from the differential equations of a standard TTM.[1,32] We assume that the excitation pulse instantaneously deposits the previously calibrated initial energy density $Q_{tot,i}$ in the Y cap layer and the top of the Dy layer via the very fast coupling of hot electrons to phonons and spins.[7] The deposited energy is rapidly divided into the initial phonon energy density $Q_{P,i}$ and the initial energy $Q_{S,i}$ in magnetic excitations. Each energy density (stress) manifests itself as a lattice strain $\varepsilon_{P,S}(Q_{P,S})$, which superimpose to yield the measured strain. For analyzing the time resolved data, we take into account the effect of in-plane clamping of the lattice expansion according to Poisson's ratio (dashed lines in Fig. 2) as detailed in Ref. 42. Since both Grüneisen parameters are approximately constant as a function of temperature (see Fig. 1(c)), a linear relation between imparted energy and lattice strain emerges. This makes the analysis applicable even though the spin- and the phonon system may not be internally thermalized to one temperature $T_{S,P}$ over the film depth.

First, we solve the system of equations, Eqs. (2) and (3), for the initial time $t_i = 45$ ps, where the electron and phonon system are equilibrated but no energy has flown to the substrate. From the two measured variables $Q_{tot}(t_i)$ and $\varepsilon_{tot}(t_i)$, we calculate the energy in the spin $Q_S(t_i)$ and the phonon system $Q_P(t_i)$. This procedure is visualized in Figs. 4(a) and 4(d). The total energy density $Q_{tot}(t_i)$ (red + blue area in Fig. 4(d)) in the sample is calibrated from the measurements in the paramagnetic phase, i.e., at $T_i = 250$ K where the energy exclusively excites phonons, so that the deposited energy can therefore directly be found via Eq. (1) from the measured lattice strain ($\varepsilon_{tot}(t_i) = \varepsilon_P(t_i)$).
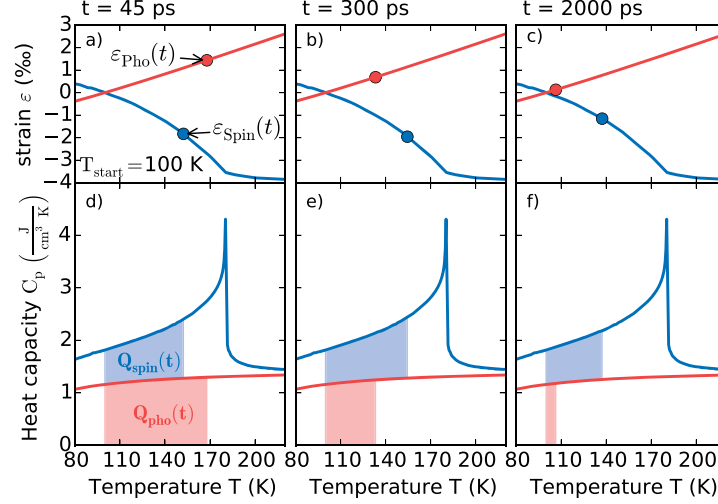
FIG. 4. Visualization of the TTEM at $T_i = 100$ K for three different time delays. The measured total strain $\varepsilon_{tot}(t)$ and the total heat energy Q_{tot} allow deriving the individual phonon and spin contributions to the strain and the heat. The upper panels (a)–(c) show the separation of strain contributions according to Fig. 1(a) and the lower panels (d)–(f) show the transient heat as an area under the specific heat curve according to Fig. 1(c). Note that for the analysis only the energy densities are required. From the figures one can read that, e.g., after 2 ns, the Q_S would correspond to an equilibrium spin temperature of 140 K whereas Q_P corresponds to an equilibrium phonon temperature of 108 K. Although the temperature definitely has a strong gradient across the film, the analysis of the average heat $Q_{P;S}$ is robust, because of the linear relation $\varepsilon_{P;S} \sim Q_{P;S}$.

For excitation with $F = 6.8$ mJ/cm^2, this TTEM yields $Q_{S,i}$ and $Q_{P,i}$ and their fraction of the total energy is depicted in Fig. 5(b). It shows that essentially 35% of the energy is initially deposited in the spin system for $T_i \ll T_N$. Here, we assume that only the deposition of energy in each subsystem immediately leads to the stress according to the higher energy density, which causes the corresponding strain at delays larger than the time needed to the sound wave to propagate through Dy. We can safely assume that no energy has left the Dy layer by thermal transport shortly after excitation.

To obtain a solution of the system of equations for arbitrary times t as visualized in Fig. 4, we make two alternative approximations for the evolution of $Q_{tot}(t)$ in the dysprosium layer. $Q_{tot}(t)$ is reduced by phononic and electronic heat conduction to the substrate. As a lower boundary, we assume that the total heat flows out of the film as fast as if all energy would be stored in the phonons, i.e., $Q_{tot}^T(t) = Q_{tot}^{250K}(t)$. The direct flow of excitations from the magnetic system in the Dy layer to the adjacent nonmagnetic materials is not possible so that coupling energy in the spin system to phonons is the only channel of magnetic energy dissipation. Therefore, this assumption overestimates the heat flow to the substrate when a substantial fraction of $Q_{tot}^T(t)$ is in spin excitations and we obtain the lower curves in Fig. 5(a). The data analysis within the first approximation indicates that close to T_N the energy in the spin system dissipates very slowly. To estimate an upper bound (Fig. 5(a)) we use the second approximation $Q_{tot}^T(t) = Q_{S,i}^T + Q_{P,i}^T(Q_{tot}^{250K}(t)/Q_{tot,i}^{250K})$. It assumes that only the fraction of energy initially deposited in the phonon system can flow out of the film. This clearly overestimates the total energy in the Dy layer for long times t after the excitation, because the energy initially deposited in the magnetic system cannot leave the Dy layer and Q_{tot} can never drop below $Q_{S,i}$. This approximation is especially suitable for initial conditions where $Q_{S,i} \ll Q_{P,i}$, i.e., at high temperatures. Fig. 5(a) shows the result of the TTEM data analysis for five representative temperatures using both approximations for $Q_{tot}(t)$. The heat dissipation from the phonon system is much faster than for the spin system. At very early times some transfer of thermal energy from the phonons into the spin system is observed. Referring to Fig. 4, we can observe that the main findings in Fig. 5 are already seen in the raw data. The upper panel of Fig. 4 illustrates that
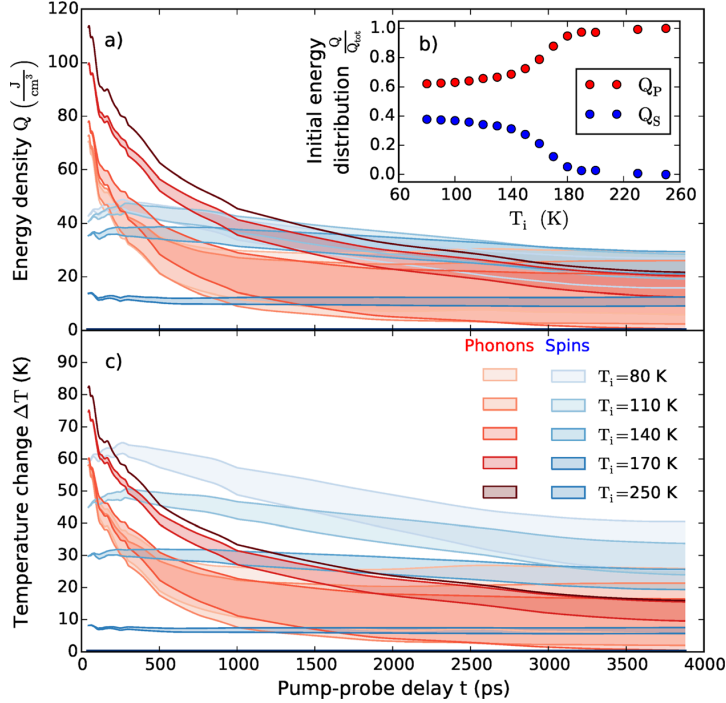
FIG. 5. TTEM results extracted from the experimental data at a fluence of $F = 6.8\,\text{mJ/cm}^2$. (a) Energy in the phonon- and spin excitations derived from the data as described in the text. Q_P^{80K} and Q_P^{110K} are hard to distinguish. (b) Initial energy distribution between phonons and spins at 45 ps. (c) Temperature changes obtained from (a) via the corresponding heat-capacities $C_{S,P}(T)$ (Fig. 1(b)). The resulting temperatures indicate a long-lasting non-equilibrium between phonons and spins. In panel (c), no temperature change of the spin system is plotted for $T_i = 250\,\text{K}$ because its heat capacity is zero $C_S(250\,\text{K}) = 0$.

transient heat in the spin system leads to a contraction and transient heat in the phonon system leads to an expansion. The Grüneisen coefficients tell us that the energy in the spin system is three times more effective in straining the lattice than the energy contained in phonons. For the illustrated initial temperature of $T_i = 100\,\text{K}$, we observe at 45 ps that about three times more energy is required in the phonon system to nearly balance the contraction resulting from energy in the spin excitations. $\epsilon_p(45\,\text{ps})$ is slightly smaller than $\epsilon_s(45\,\text{ps})$, consistent with the slight contraction seen in Fig. 3(c). Around 300 ps, the phonon energy Q_p has greatly decreased (Fig. 4(e)) by conduction of heat to the substrate, while $Q_s(300\,\text{ps}) \sim Q_s(45\,\text{ps})$. Therefore, the contractive strain ϵ_s prevails and leads to the pronounced contraction seen in Fig. 3(c) around 300 ps. At 2 ns, there is almost no positive transient strain ϵ_p due to phonons left (Fig. 4(c)) because $Q_p \sim 0$, and also Q_s is greatly reduced (see Fig. 4(f)). In the raw data, this is seen as the recovery of the negative strain, which slowly approaches zero on this nanosecond timescale.

DISCUSSION

Our analysis derives the flow of heat among the spin and lattice system directly from experimental data. In order to make it comparable to a conventional TTM, we present time-resolved temperature changes derived from the above TTEM using the static temperature-dependent heat capacity in Fig. 1(c). Initially, the temperature in the phonon system is higher than the temperature of the spin system, especially when T_i approaches T_N. While the phonons in Dy cool rapidly to the substrate, T_S rises slightly within the first 200 ps even when the average temperature of the spin system is already higher than the average phonon temperature.

Such behavior may be rationalized by a spatial nonequilibrium or—equivalently—by a nonequilibrium population of modes in microscopic theories. The subsequent cooling of the spin-system is found to be much slower. When the initial temperature T_i approaches T_N from below, the timescale for reordering (i.e., cooling) of the magnetic system dramatically increases: essentially, a decoupling of the two heat reservoirs from each other is observed. For example, for a starting temperature $T_i = 170$ K, $\Delta T_S \simeq 8$ K remains constant for 4 ns although initially $\Delta T_P \simeq 70$ K. From the experimental findings, we can give at least three indications that not only the two "temperatures" T_S and T_P are different, but that each of the subsystems is in a non-equilibrium situation. (i) As discussed above, the heat flow between spins and phonons is not controlled by the temperature difference. (ii) The heat simulation for $T_i = 250$ K which matches the experimental data predicts a strong temperature gradient in the Dy layer. Definitely, the phonons are spatially not in equilibrium over the sample thickness of 80 nm for more than 1 ns. (iii) The detected increase in the peak width in the first 35 ps while no peak shift is observed in the anti-ferromagnetic phase, which clearly calls for different spatial profiles of the excitations in the phonon and spin system. Probably, in the laser-heated region of the Dy layer $T_P > T_S$ while at the back interface to Y $T_P < T_S$. Potentially, the local excited mode spectrum cannot be approximated by a Bose-distribution with two temperatures at all.

CONCLUSION

In conclusion, we have discussed UXRD data in the rare earth Dy to obtain clear evidence that the phonon and spin systems are mutually not in thermal equilibrium for several nanoseconds after optical excitation. We demonstrate a method to extract the transient energy densities $Q_S(t)$ and $Q_P(t)$ deposited in the spins and the phonons from the UXRD data. In the antiferromagnetic phase, approximately 35% of the energy heats up and disorders the spin system, leading to a rapid contraction of the lattice. Although the spins can exclusively dissipate their heat to phonons and electrons in Dy, the cooling rate of the magnetic system that finally leads to a reordering of the spin-system depends only weakly on the transient phonon temperature.

We hope that our experimental analysis will inspire theoreticians to model the spatiotemporal coupled excitations in rare earth metals and we believe that it is an important contribution in the context of the debate about ultrafast angular-momentum transfer to the lattice. Our observations are indicative for a rapid disorder in the spin system—inducing a contractive force, indicating a very strong spin-lattice interaction in the ordered phase. On the other hand the transfer of energy from the magnetic system to the phonons is very slow (on the nanosecond timescale), in particular, close to the phase-transition, giving strong evidence for a critical behavior. This suggests a rather weak spin-phonon coupling for (partially) disordered spins.

ACKNOWLEDGMENTS

[1]E. Beaurepaire, J.-C. Merle, A. Daunois, and J.-Y. Bigot, "Ultrafast spin dynamics in ferromagnetic nickel," Phys. Rev. Lett. **76**, 4250 (1996).

[2]A. Kirilyuk, A. V. Kimel, and Th. Rasing, "Ultrafast optical manipulation of magnetic order," Rev. Mod. Phys. **82**, 2731–2784 (2010).

[3]B. Koopmans, G. Malinowski, F. Dalla Longa, D. Steiauf, M. Fahnle, T. Roth, M. Cinchetti, and M. Aeschlimann, "Explaining the paradoxical diversity of ultrafast laser-induced demagnetization," Nat. Mater. **9**, 259–265 (2010).

[4]S. Mathias, C. La-O-Vorakiat, P. Grychtol, P. Granitzka, E. Turgut, J. M. Shaw, R. Adam, H. T. Nembach, M. E. Siemens, S. Eich *et al.*, "Probing the timescale of the exchange interaction in a ferromagnetic alloy," Proc. Natl. Acad. Sci. U.S.A. 109, 4792–4797 (2012).

[5]A. Eschenlohr, M. Battiato, P. Maldonado, N. Pontius, T. Kachel, K. Holldack, R. Mitzner, A. Föhlisch, P. M. Oppeneer, and C. Stamm, "Ultrafast spin transport as key to femtosecond demagnetization," Nat. Mater. **12**, 332–336 (2013).

[6]M. Wietstruk, A. Melnikov, C. Stamm, T. Kachel, N. Pontius, M. Sultan, C. Gahl, M. Weinelt, H. A. Dürr, and U. Bovensiepen, "Hot-electron-driven enhancement of spin-lattice coupling in Gd and Tb 4*f* ferromagnets observed by femtosecond x-ray magnetic circular dichroism," Phys. Rev. Lett. **106**, 127401 (2011).

[7]C. Trabant, "Ultrafast photoinduced phase transitions in complex materials probed by time-resolved resonant soft x-ray diffraction," Ph.D. thesis, Universität Potsdam, 2014.

[8]C. von Korff Schmising, B. Pfau, M. Schneider, C. M. Günther, M. Giovannella, J. Perron, B. Vodungbo, L. Müller, F. Capotondi, E. Pedersoli, N. Mahne, J. Lüning, and S. Eisebitt, "Imaging ultrafast demagnetization dynamics after a spatially localized optical excitation," Phys. Rev. Lett. **112**, 217203 (2014).

[9]R. Carley, K. Dobrich, B. Frietsch, C. Gahl, M. Teichmann, O. Schwarzkopf, P. Wernet, and M. Weinelt, "Femtosecond laser excitation drives ferromagnetic gadolinium out of magnetic equilibrium," Phys. Rev. Lett. **109**, 057401 (2012).

[10]U. Bovensiepen, "Coherent and incoherent excitations of the Gd(0001) surface on ultrafast timescales," J. Phys.: Condens. Matter **19**, 083201 (2007).

[11]B. Frietsch, J. Bowlan, R. Carley, M. Teichmann, S. Wienholdt, D. Hinzke, U. Nowak, K. Carva, P. M. Oppeneer, and M. Weinelt, "Disparate ultrafast dynamics of itinerant and localized magnetic moments in gadolinium metal," Nat. Commun. **6**, 8262 (2015).

[12]C. von Korff Schmising, M. Bargheer, M. Kiel, N. Zhavoronkov, M. Woerner, T. Elsaesser, I. Vrejoiu, D. Hesse, and M. Alexe, "Accurate time delay determination for femtosecond X-ray diffraction experiments," Appl. Phys. B **88**, 1–4 (2007).

[13]M. C. Langner, S. Roy, A. F. Kemper, Y.-D. Chuang, S. K. Mishra, R. B. Versteeg, Y. Zhu, M. P. Hertlein, T. E. Glover, K. Dumesnil, and R. W. Schoenlein, "Scattering bottleneck for spin dynamics in metallic helical antiferromagnetic dysprosium," Phys. Rev. B **92**, 184423 (2015).

[14]A. V. Kimel, A. Kirilyuk, A. Tsvetkov, R. V. Pisarev, and Th. Rasing, "Laser-induced ultrafast spin reorientation in the antiferromagnet TmFeO$_3$," Nature **429**, 850–853 (2004).

[15]M. Battiato, K. Carva, and P. M. Oppeneer, "Superdiffusive spin transport as a mechanism of ultrafast demagnetization," Phys. Rev. Lett. **105**, 027203 (2010).

[16]G. P. Zhang, W. Hubner, G. Lefkidis, Y. Bai, and T. F. George, "Paradigm of the time-resolved magneto-optical Kerr effect for femtosecond magnetism," Nat. Phys. **5**, 499–502 (2009).

[17]T. Kise, T. Ogasawara, M. Ashida, Y. Tomioka, Y. Tokura, and M. Kuwata-Gonokami, "Ultrafast spin dynamics and critical behavior in half-metallic ferromagnet: Sr$_2$FeMoO$_6$," Phys. Rev. Lett. **85**, 1986–1989 (2000).

[18]X. J. Liu, Y. Moritomo, A. Nakamura, H. Tanaka, and T. Kawai, "Critical behavior of a photodisordered spin system in doped manganite," Phys. Rev. B **64**, 100401 (2001).

[19]T. Ogasawara, K. Ohgushi, Y. Tomioka, K. S. Takahashi, H. Okamoto, M. Kawasaki, and Y. Tokura, "General features of photoinduced spin dynamics in ferromagnetic and ferrimagnetic compounds," Phys. Rev. Lett. **94**, 087202 (2005).

[20]S. Muhammad, "Ultrafast magnetization dynamics of lanthanide metals and alloys," Ph.D. thesis, Freie Universität Berlin, 2012.

[21]A. Manchon, Q. Li, L. Xu, and S. Zhang, "Theory of laser-induced demagnetization at high temperatures," Phys. Rev. B **85**, 064408 (2012).

[22]J. Kimling, J. Kimling, R. B. Wilson, B. Hebler, M. Albrecht, and D. G. Cahill, "Ultrafast demagnetization of FePt: Cu thin films and the role of magnetic heat capacity," Phys. Rev. B **90**, 224408 (2014).

[23]U. Atxitia and O. Chubykalo-Fesenko, "Ultrafast magnetization dynamics rates within the Landau-Lifshitz-Bloch model," Phys. Rev. B **84**, 144414 (2011).

[24]N. Kazantseva, U. Nowak, R. W. Chantrell, J. Hohlfeld, and A. Rebei, "Slow recovery of the magnetisation after a sub-picosecond heat pulse," Europhys. Lett. **81**, 27004 (2008).

[25]F. J. Darnell and E. P. Moore, "Crystal structure of dysprosium at low temperatures," J. Appl. Phys. **34**, 1337–1338 (1963).

[26]W. C. Koehler, "Magnetic properties of rare-earth metals and alloys," J. Appl. Phys. **36**, 1078–1087 (1965).

[27]B. Coqblin, *The Electronic Structure of Rare-Earth Metals and Alloys: The Magnetic Heavy Rare-Earths* (Academic Press, 1977), p. xvi.

[28]J. Jensen and A. R. Mackintosh, *Rare Earth Magnetism - Structures and Excitations* (Clarendon Press, 1991).

[29]D. Schick, A. Bojahr, M. Herzog, C. von Korff Schmising, R. Shayduk, W. Leitenberger, P. Gaal, and M. Bargheer, "Normalization schemes for ultrafast x-ray diffraction using a table-top laser-driven plasma source," Rev. Sci. Instrum. **83**, 025104 (2012).

[30]S. Nie, X. Wang, H. Park, R. Clinite, and J. Cao, "Measurement of the electronic Grüneisen constant using femtosecond electron diffraction," Phys. Rev. Lett. **96**, 025901 (2006).

[31]M. Nicoul, U. Shymanovich, A. Tarasevitch, D. von der Linde, and K. Sokolowski-Tinten, "Picosecond acoustic response of a laser-heated gold-film studied with time-resolved x-ray diffraction," Appl. Phys. Lett. **98**, 191902 (2011).

[32]S. I. Anisimov, B. L. Kapeliovitch, and T. L. Perel'man, "Electron emission from metal surfaces exposed to ultrashort laser pulses," Sov. Phys. - JETP **2**, 375–377 (1974).

[33]V. K. Pecharsky, K. A. Gschneidner, Jr., and D. Fort, "Superheating and other unusual observations regarding the first order phase transition in Dy," Scr. Mater. **35**, 843–848 (1996).

[34]K. Dumesnil, C. Dufour, Ph. Mangin, G. Marchal, and M. Hennion, "Magnetoelastic and exchange contributions to the helical-ferromagnetic transition in dysprosium epitaxial films," Europhys. Lett. **31**, 43 (1995).

[35]L. D. Jennings, R. E. Miller, and F. H. Spedding, "Lattice heat capacity of the rare earths. Heat capacities of yttrium and lutetium from 15–350 °k," J. Chem. Phys. **33**, 1849–1852 (1960).

[36]N. W. Ashcroft and N. D. Mermin, *Solid State Physics* (Cengage Learning, 2011).

[37]S. B. Palmer and E. W. Lee, "The elastic constants of dysprosium and holmium," Proc. R. Soc. Lond., Ser. A **327**, 519–543 (1972).

[38]O. B. Wright, "Ultrafast nonequilibrium stress generation in gold and silver," Phys. Rev. B **49**, 9985–9988 (1994).

[39]F. Zamponi, Z. Ansari, C. von Korff Schmising, P. Rothhardt, N. Zhavoronkov, M. Woerner, T. Elsaesser, M. Bargheer, T. Trobitzsch-Ryll, and M. Haschke, "Femtosecond hard x-ray plasma sources with a kilohertz repetition rate," Appl. Phys. A **96**, 51–58 (2009).

[40]B. Y. Mueller and B. Rethfeld, "Thermodynamic model of ultrafast magnetization dynamics," Phys. Rev. B **90**, 144420 (2014).

[41]C. Y. Ho, R. W. Powell, and P. E. Liley, "Thermal conductivity of the elements," J. Phys. Chem. Ref. Data **1**, 279–421 (1972).

[42]A. von Reppert, "Ultrafast magnetostriction in dysprosium studied by femtosecond X-Ray diffraction," M.S. thesis, Universität Potsdam, 2015.

[43]D. Schick, A. Bojahr, M. Herzog, R. Shayduk, C. von Korff Schmising, and M. Bargheer, "UDKM1DSIM—A simulation toolkit for 1D ultrafast dynamics in condensed matter," Comput. Phys. Commun. **185**, 651–660 (2014).

Article VI

Ultrafast negative thermal expansion driven by spin disorder

Jan-Etienne Pudell, Alexander von Reppert, Daniel Schick, Flavio Zamponi, Matthias Rössle, Marc Herzog, Hartmut Zabel, and M. Bargheer

We measure the transient strain profile in a nanoscale multilayer system composed of yttrium, holmium, and niobium after laser excitation using ultrafast x-ray diffraction. The strain propagation through each layer is determined by transient changes in the material-specific Bragg angles. We experimentally derive the exponentially decreasing stress profile driving the strain wave and show that it closely matches the optical penetration depth. Below the Néel temperature of Ho, the optical excitation triggers negative thermal expansion, which is induced by a quasi-instantaneous contractive stress and a second contractive stress contribution increasing on a 12-ps timescale. These two timescales were recently measured for the spin disordering in Ho [Rettig et al., Phys. Rev. Lett. 116, 257202 (2016)]. As a consequence, we observe an unconventional bipolar strain pulse with an inverted sign traveling through the heterostructure.

Ultrafast negative thermal expansion driven by spin disorder

J. Pudell,[1] A. von Reppert,[1] D. Schick,[2,3] F. Zamponi,[1] M. Rössle,[1,3] M. Herzog,[1] H. Zabel,[4] and M. Bargheer[1,3,*]

[1]*Institut für Physik und Astronomie, Universität Potsdam, Karl-Liebknecht-Strasse 24-25, 14476 Potsdam, Germany*
[2]*Max-Born-Institut Berlin, Max-Born-Straße 2a, 12489 Berlin, Germany*
[3]*Helmholtz Zentrum Berlin, Albert-Einstein-Strasse 15, 12489 Berlin, Germany*
[4]*Fakultät für Physik und Astronomie, Ruhr-Universität Bochum, 44780 Bochum, Germany*

We measure the transient strain profile in a nanoscale multilayer system composed of yttrium, holmium, and niobium after laser excitation using ultrafast x-ray diffraction. The strain propagation through each layer is determined by transient changes in the material-specific Bragg angles. We experimentally derive the exponentially decreasing stress profile driving the strain wave and show that it closely matches the optical penetration depth. Below the Néel temperature of Ho, the optical excitation triggers negative thermal expansion, which is induced by a quasi-instantaneous contractive stress and a second contractive stress contribution increasing on a 12-ps timescale. These two timescales were recently measured for the spin disordering in Ho [Rettig *et al.*, Phys. Rev. Lett. **116**, 257202 (2016)]. As a consequence, we observe an unconventional bipolar strain pulse with an inverted sign traveling through the heterostructure.

I. INTRODUCTION

In most of the research on ultrafast magnetism the lattice was considered only as an angular momentum sink [1–3]. Ultrafast effects on the lattice induced by demagnetization have been discussed surprisingly rarely [4–7]. Time-resolved magneto-optical Kerr measurements and optical picosecond ultrasonics are the workhorse for many researchers [1,2,8–12]. Ultrafast electron diffraction (UED) or ultrafast x-ray diffraction (UXRD) experiments that directly observe the transient lattice strain induced by ultrafast demagnetization have been discussed only sporadically [4,5,13–15]. Several ultrafast diffraction studies on the transition metals Ni and Fe [16–18] discuss the strain waves excited by electron and phonon stresses σ_e and σ_{ph}, and theory predicts relevant electron-phonon (*e*-ph) coupling constants [19] even with mode specificity [20]. Very recently, granular FePt films were studied by UXRD [21] and UED [5]. The rapid out-of-plane lattice contraction could be convincingly ascribed to changes in the tetragonality of the lattice by *ab initio* calculations of the total ground-state energy for the spin system in the paramagnetic and ferromagnetic phases [5]. To simulate the dynamic changes in a system with several degrees of freedom it is common to apply multiple-temperature models [5,9] which assume that each subsystem can be described by an individual temperature T_i, although it has been shown that different phonon modes may be out of thermal equilibrium for 100 ps [20]. Specialized techniques allow for assigning timescales to specific electronic processes and orbitals or bands [3,22–25]. This is particularly relevant in the magnetic rare earths, where the exchange interaction between the localized $4f$ spin and orbital magnetic moments

is mediated by the itinerant $5d6s$ conduction electrons via the Ruderman–Kittel–Kasuya–Yosida (RKKY) interaction [26,27]. In antiferromagnetically ordered phases the question of angular momentum transfer is less relevant since the net magnetization is zero. Rare-earth elements prove to be a versatile testing ground for understanding how rapidly ultrafast demagnetization leads to stress in the crystal lattice. We selected Ho since a recent resonant hard x-ray scattering experiment measured that the demagnetization of both the localized $4f$ moments and the itinerant conduction electrons proceed on a fast 200-fs timescale attributed to electron-spin interaction and a slow 9-ps timescale for coupling phonons to the spins [22].

In this paper we use UXRD at a laser-based femtosecond plasma x-ray source (PXS) to show that the ultrafast laser excitation of Ho below its Néel temperature $T_N = 132$ K generates negative stress that rises on the two timescales for disordering the spin system [22] and drives bipolar strain wave packets with an inverted sign compared to common materials without negative thermal expansion (NTE) [8,28]. We use the material specificity of UXRD to cross-check the individual lattice constant changes in this metallic multilayer system, which is opaque to optical probes.

In the paramagnetic (PM) phase of Ho, the analysis is simplified by the complete spin disorder, and we show that the spatial excitation profile of the driving stress can be derived by probing the bipolar strain pulse in the adjacent Y and Nb buffer layers. The spatial stress profile is approximately given by the penetration depth of the pump pulses. The UXRD experiment in the antiferromagnetic (AFM) phase reveals an instantaneous compensation of the expansive electron and phonon stress in Ho by the negative instantaneous stress component $\sigma_{sp,0}$ due to spin disorder. In addition to this subpicosecond negative-stress component, the negative stress $\sigma_{sp}(t)$ keeps rising on a 12-ps timescale. These negative-stress

*bargheer@uni-potsdam.de; http://www.udkm.physik.uni-potsdam.de

components in Ho are evidenced in the adjacent Y and Nb by the extended leading expansive edge of the propagating bipolar strain pulse, which has an opposite sign compared to excitation of Ho in the PM phase. Thus, we observe dynamic stress rising on the two timescales on which disordering of the spin helix was observed by resonant x-ray scattering [22]. However, we emphasize that the observed lattice contraction in Ho is about 20 times larger than the peak shift of the magnetic Bragg peak that was observed for very similar fluence [22] because it, in fact, measures the period of spin helix which is incommensurate with the lattice.

In a broader context, our observation of ultrafast lattice contraction in Ho is discussed as an example of a rapid entropy-driven manifestation of the NTE phenomenon, which may occur on different timescales in various materials ranging from nonmagnetic molecular nanocrystals [29] and oxides with open oxygen frameworks [30] to ferroelectrics [31] and magnetically ordered systems like Heusler alloys [32].

II. SPIN-GRÜNEISEN CONSTANT AND NTE

In laser-excited magnetic systems, the role of a nonequilibrium within and/or among the different subsystems is heavily debated. The prevalent basis of the discussions is multiple-temperature models. In thermal equilibrium, standard thermodynamic approaches emphasize the role of the entropy S by calculating the equilibrium lattice constants from the minimum of the Gibbs free energy $G = U + pV - TS$ [33,34]. For a discussion of lattice dynamics, where the change in volume V is driven by a pressure p or, for an anisotropic case, the strain ε is driven by a stress σ, we can circumvent the discussion of a (non)equilibrium temperature by considering the energy density ρ^Q.

It is common to evoke the macroscopic Grüneisen coefficients (GCs) $\Gamma_{e,ph}$ for phonons and electrons, which describe the efficiency of generating stress $\sigma_{e,ph} = \Gamma_{e,ph} \rho^Q_{e,ph}$ by a heat energy density $\rho^Q_{e,ph}$ [34]. If $\Gamma_e \neq \Gamma_{ph}$, ultrafast diffraction allows inferring the time-dependent $\sigma(t)$ from the observed transient strain $\varepsilon(t)$ [16,17,35]. Hooke's law relates ε linearly to σ and hence to the energy densities $\rho^Q_{e,ph}$ deposited in each subsystem. The Grüneisen concept was extended to stress resulting from spin excitations in Ni and Fe [33,36], but the experimental verification remained ambiguous [16–18]. Thermodynamic analysis affirms that the GCs generally measure how entropy S depends on strain ε [37]. While for a gas of phonons or electrons the entropy usually increases with the volume, the phenomenon of NTE generally occurs when the entropy S decreases upon expansion, i.e., $\partial S/\partial \varepsilon < 0$. There are various origins of NTE [33,34]; however, for spin-ordered phases of rare earths, the NTE along the c axis of the hexagonal lattice is very large and clearly associated with the energy density ρ^Q_{sp} of the spin system. Figure 1(a) shows the three contributions $C_{e,ph,sp}(T)$ to the specific heat [38,39]. The negligible contribution of the electron system is barely visible as a gray area below the red shaded phonon contribution. The blue shaded spin contribution is very large for all temperatures below T_N, and close to the second-order phase transition to the PM phase it is even larger than the phonon contribution. Figure 1(b) indicates the change in the c-axis lattice constant, which is negative, when the spin contribution
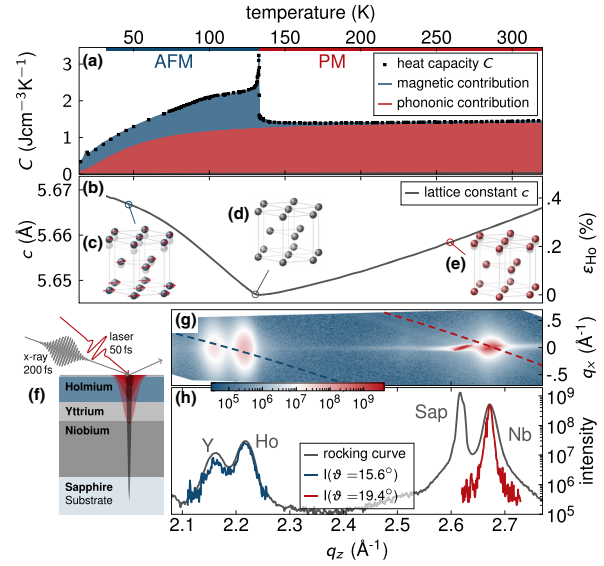

FIG. 1. (a) Specific heat of Ho [38,39] separated into the three contributions $C_{e,ph,sp}(T)$, where the electron contribution $C_e(T)$ is hardly visible and the spin contribution C_{sp} even exceeds the phonon contribution C_{ph} at some temperatures. (b) c axis of the Ho thin film as a function of temperature, showing large NTE below $T_N = 132$ K. (c)–(e) Schematics of the hexagonal lattice illustrating the c-axis lattice change and the helical spin order below T_N. (f) Schematic of the layer stacking and the pump-probe geometry. (g) The RSM including separated Bragg peaks of Y, Ho, sapphire, and Nb. The slices of the RSM used for (h) and the time-resolved measurements are shown in red (Nb) and blue (Ho+Y). (h) The projection of the full RSM (gray) and measurements along the slices with a fixed angle ω (red and blue).

to the specific heat is large. Surprisingly, also in these systems exhibiting a divergent specific heat at the phase transition, the spin GC Γ_{sp} is essentially independent of T [13,14], even though the total GC [37] varies strongly with T. Separating phonon and spin contributions to the thermal expansion and the heat capacity of Ho yields $\Gamma_{ph}/\Gamma_{sp} \approx -0.2$ [33,37]. This implies that equal energy densities in the spin and phonon system lead to a five times larger contractive stress, which overwhelms the expansive phonon stress. The separate GC $\Gamma_{e,ph,sp}$ are independent of T because the T dependences of the specific heat $C_{e,ph,sp}(T)$ and the thermal expansion coefficient $\alpha_{e,ph,sp}(T)$, which originate from the quantum nature of the excitations, cancel out [33,34]. This linear dependence of energy density and stress in each subsystem makes the Grüneisen concept useful and causes temperature and thermal equilibrium within each subsystem to be properties of secondary relevance to the dynamics. Nonetheless, the temperature-dependent specific heats $C_{e,ph,sp}(T)$ map the multiple-thermal energy model onto classical multiple-temperature models.

III. EXPERIMENTAL DETAILS

The multilayer stack was grown by molecular beam epitaxy on sapphire in the sequence 128 nm Nb, 34 nm Y,

46 nm Ho with a thin capping layer of 4 nm Y and 3 nm Nb [see Fig. 1(f)]. X-ray reflectivity measurements confirm the total thickness of the metallic multilayer on the sapphire substrate; 200-fs hard x-ray probe pulses with a photon energy of 8 keV are derived from the PXS at the University of Potsdam [40]. The *p*-polarized 50-fs laser pulses with a diameter of 1500 μm (FWHM) excite the sample at an incidence angle of about 52°. The incident fluence of the 800-nm pump pulses is 3 mJ/cm^2; an absorbed fluence of 1.7 mJ/cm^2 is calculated according to the refractive index obtained by spectroscopic ellipsometry. The penetration depth is 21 nm at 800 nm for all temperatures. A schematic of the sample and the pump-probe geometry is given in Fig. 1(f).

The reciprocal space map (RSM) of the multilayer system including separated Bragg peaks of Y, Ho, sapphire, and Nb at room temperature is shown in Fig. 1(g). The map is obtained by recording the symmetrically and asymmetrically diffracted x rays on the area pixel detector (Dectris PILATUS 100K) as a function of the "rocking" angle ω between the sample surface and the center of the convergent femtosecond x-ray beam [40]. The gray line in Fig. 1(h) shows a projection of the full RSM onto the out-of-plane component q_z. The red and blue lines indicate typical x-ray diffraction curves derived from the dashed cuts through reciprocal space indicated by the red and blue lines in Fig. 1(g). These cuts are given by the x rays' angle of incidence ω chosen for the UXRD experiments. The center position of the Bragg reflection is obtained by fitting a Gaussian function to each layer peak.

IV. RESULTS

Figure 2 summarizes the strain in all three layers for the PM phase of Ho (red) and in the helical AFM phase of Ho around 40 K (blue). The individual data points were obtained by fitting a Gaussian function to each layer peak. In the PM phase two characteristic times are identified from the UXRD data: At $t = 17$ ps, Ho has reached the maximum expansion. This indicates the time it takes the expansive sound to travel from the surface to the Y interface. At this time the leading compressive part of the bipolar strain wave packet [8,28] has fully propagated from the Ho into the Y layer, as evidenced by the pronounced minimum in the Y strain (see Fig. 3 for an illustration of the strain wave). At $t = 26$ ps the zero crossing of the bipolar strain wave packet traverses the Y/Nb interface, which yields the pronounced minimum in the Nb strain. These characteristic time points yield the layer thicknesses given above.

The UXRD data recorded in the AFM phase of Ho directly show a delay of the contractive strain in Ho [Fig. 2(a), blue line]. The minimum of the Ho strain at about 23 ps is delayed by about 6 ps compared to the maximum in the PM phase. The signal in Y [Fig. 2(b)] confirms that also the propagating bipolar strain wave packet has a reversed sign of the strain amplitude at low temperature and a delay of about 6 ps. In the PM phase, the leading compressive part of the strain launched in Ho by thermal expansion reduces the out-of-plane lattice spacing in Y, although the Y layer is also excited by the pump pulse [28]. In the AFM phase the contractive stress in Ho dominates and reverses the sign of the bipolar
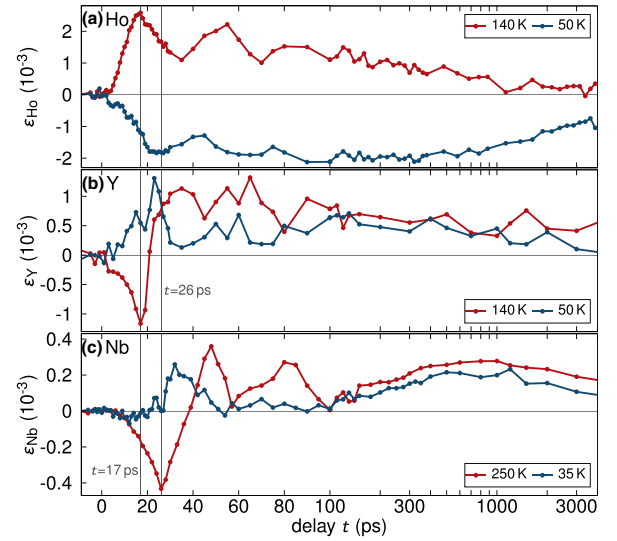

FIG. 2. Transient lattice strain ε for (a) Ho, (b) Y, and (c) Nb after laser excitation in the PM (red) and AFM (blue) phases as determined from UXRD. The thin solid line at 17 ps indicates the time it takes the maximum expansion starting at the surface to propagate to the Ho/Y interface. At this time Ho is maximally expanded, and Y is fully compressed since the expansive part of the bipolar strain is fully in the Ho layer, whereas the leading compressive part is only in the Y layer. The thin line at 26 ps indicates the same fully compressed situation for the Nb layer. In the AFM phase Ho [in (a)] has a 6-ps delay of the maximal contraction compared to the maximal PM expansion.

strain. Hence, the Ho contraction expands the adjacent Y, assisted by the small expansive stress from direct optical excitation of Y. The UXRD signal from the Nb layer is even cleaner, as a negligible amount of light is absorbed in this layer. Therefore, we repeated the experiments on Nb. The obtained signal [Fig. 2(c)] had to be scaled appropriately due to the slightly different base temperature and fluence. The tiny negative lattice constant change in Nb [Fig. 2(c)] in the first 15 ps is due to the stress generated in Y, and the crossover to the strong expansion starts around 10 ps, when the leading expansive part of the bipolar strain wave packet generated by the exponentially decaying compressive stress in Ho reaches the Nb layer. The very short wiggle of the average Nb layer strain at 26 ps heralds the rather strong but spatially narrow bipolar strain wave packet launched by the 7-nm-thick Nb/Y capping layer. The time perfectly coincides with the arrival of the wave created by surface expansion that was already observed in the PM phase. The same feature from the capping layer is also clearly observed in the Y data at 19 ps. In the PM data set, this feature is absent since the cap layer and the Ho layer both expand with similar amplitude.

For $t > 200$ ps the sound wave reflections have ceased, and we can safely interpret the expansion and contraction of each layer by the average energy densities $\rho_{e,ph,s}$. For earlier time delays, the spatially averaged thermal stress in each layer can be obtained from the data by averaging out the oscillations. For timescales shorter than the characteristic
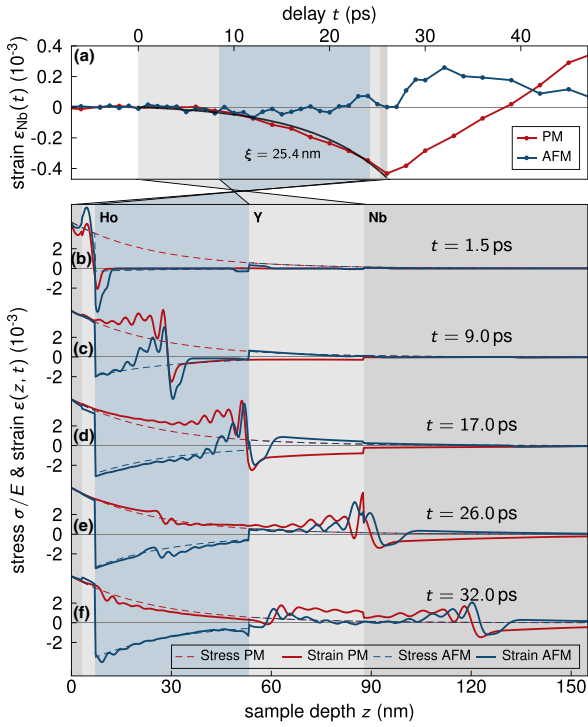
FIG. 3. (a) Zoom of the first 45 ps of the Nb data from Fig. 2(c). The black line shows an exponential fit to the strain in the PM phase, which is used to extract the driving stress via Hooke's law. (b)–(f) Stress (dashed) and strain profiles for selected delays in the heterostructure from a simulation. To avoid unimportant rapid oscillations in this graph, the temporal stress profile was smoothed by a 0.5-ps Gaussian function. The NTE stress in Ho rises with $\tau = 12$ ps. The inverted strain profile is most prominently seen in (c) and (d) in the Y and Nb layers, respectively. As an illustration, a video sequence of this temporal evolution of the stress profile and the strain wave is given in the Supplemental Material [41].

FIG. 4. The simulated spatiotemporal strain profiles show the traveling sound waves in the heterostructure in the (a) PM and (b) AFM phases. (c)–(e) Simulated strain for the PM phase in the three layers (red) is compared to the data. (f)–(h) Simulations for the AFM phase with varying time constant $\tau = 0, 6, 12,$ and 18 ps. The best match to the data is obtained for $\tau = 12$ ps.

oscillation period of the layer, however, the transient stress must be obtained from modeling the elastic response of the system. The measured transient (negative) thermal expansion $\varepsilon(t) = \varepsilon_{\text{th}}(t) + \varepsilon_{\text{sw}}(t)$ is a linear superposition of the averaged thermal strain $\varepsilon_{\text{th}}(t)$ and the layer-averaged amplitude of the hypersound waves $\varepsilon_{\text{sw}}(t)$ triggered by the rapid expansion following the ultrashort pulse excitation, which reflect from the interfaces.

V. ANALYSIS

In this section we highlight the potential of UXRD for deriving the spatial form of the stress driving the observed strain [42,43]. In Fig. 3(a) we analyze the UXRD data recorded for the Nb layer in the PM state of Ho, zooming in on the pronounced compression signal of the Nb layer. The average strain ε_{Nb} shows an increasing compression slowly starting at $t = 0$ when the bipolar strain wave packet starts entering the Nb layer. Neglecting sound velocity differences in the heterostructure, an exponential spatial stress profile generates

a bipolar strain pulse with a compressive leading edge that has an exponential spatial dependence as well [28].

Thus, from the measured strain in a dedicated detection layer, we can show that the spatial stress profile in fact decays exponentially with the characteristic length scale $\xi = 25$ nm which matches the value calculated from the optical constants measured by ellipsometry. For direct comparison with the data we plotted in Fig. 3(a) the stress $\sigma_{\text{PM}} = \sigma_0 e^{-z/\xi}$ onto the measured strain data using an appropriate scaling by Hooke's law. In the AFM phase (blue) the spin and phonon stress contributions approximately cancel out immediately after excitation. In Figs. 3(b)–3(f) we show the spatial stress profiles used in the further analysis of the data via simulations as dashed lines.

VI. MODELING AND DISCUSSION

Now we discuss the numerical modeling of the observed strain that is necessary to derive the transient stress changing faster than the characteristic thickness modulation time of the layers. In the PM phase of Ho we calculate the transient strain [Fig. 4(a)] by integrating the equation of motion for a linear masses-and-springs model using the UDKM1DSIM toolbox [44]. The experimentally derived exponential spatial form of the stress σ_{PM} serves as an input. Figures 4(c)–4(e) show the excellent agreement of the simulations with the measured data for all three layers in the PM phase when

using the exponentially decaying stress profile $\xi = 25$ nm derived above. For simplicity, we assume an instantaneous rise of the combined e-ph stress. Separate electron and phonon GCs do not improve the fit in Figs. 4(c)–4(e). We note that the energy density in each subsystem is linearly proportional to the stress and strain in each layer. The spatiotemporal strain shown in Fig. 4(a) is used as input parameter for the calculation of the x-ray diffraction pattern by dynamical x-ray diffraction theory. The positions of the simulated Bragg peaks are obtained by fitting a Gaussian function as done in the experimental data analysis. For illustration, Figs. 3(b)–3(f) depict the spatial strain profiles for selected time delays, which are cross sections of the spatiotemporal strain profiles in Figs. 4(a) and 4(b), leading to the fits in Fig. 4(c)–4(h). Figures 3(b)–3(f) contain the transient spatial stress profiles (dashed lines) used as input for the simulation. After about 30 ps [Figs. 3(e) and 3(f)] the simulated strain profile is very close to the simple stress-strain relation, with only a slight deviation due to residual hypersound waves. The observed signal oscillations (Fig. 4) due to hypersound waves reflected at the interfaces of all three layers are reproduced by the model.

To simulate the corresponding spatiotemporal strain [Fig. 4(b)] when Ho is excited in the AFM phase, we have to take into account the negative stress induced by spin disorder, which adds to the positive e-ph stress; the dynamics become richer and challenge the modeling. We model the transient stress $\sigma = \Gamma_{\text{e-ph}}\rho_{\text{e-ph}}^{Q} + \Gamma_{\text{sp}}\rho_{\text{sp}}^{Q}$ [Figs. 3(b)–3(f)] from the balance of thermal energy densities in the combined e-ph system $\rho_{\text{e-ph}}^{Q}$ and in the spin system ρ_{s}^{Q}:

$$\rho_{\text{e-ph}}^{Q}(t) = \rho_{\text{e-ph},\infty}^{Q} + \rho_{\text{dyn}}^{Q} e^{-t/\tau}, \tag{1}$$

$$\rho_{\text{sp}}^{Q}(t) = \rho_{\text{sp},0}^{Q} + \rho_{\text{dyn}}^{Q}(1 - e^{-t/\tau}), \tag{2}$$

$$\rho_{\text{laser}}^{Q} = \rho_{\text{e-ph},\infty}^{Q} + \rho_{\text{sp},0}^{Q} + \rho_{\text{dyn}}^{Q}. \tag{3}$$

In the first 70 ps in Figs. 4(f)–4(h), we may disregard heat transport and assume local conversion of energy $\rho_{\text{e-ph}}^{Q}(t)$ to $\rho_{\text{sp}}^{Q}(t)$ with a coupling time τ. In this model the energy density ρ_{laser}^{Q} imparted by the laser is partially converted to the spin system quasi-instantaneously as $\rho_{\text{sp},0}^{Q}$. ρ_{dyn}^{Q} is transferred from the e-ph system to the spins on the timescale τ. $\rho_{\text{e-ph},\infty}^{Q}$ is the heat remaining in the e-ph system until heat transport starts to become relevant. The variables $Q_{\text{e-ph}}$, Q_{sp}, and Q_{dyn} have to fulfill energy conservation and approach thermal equilibrium for $t \gg \tau$. The remaining parameter is used to match the amplitude of the signal. The partitioning into only two simulated heat reservoirs is chosen because $\rho_{\text{e-ph}}^{Q}$ and ρ_{sp}^{Q} trigger competing expansive and contractive stresses, respectively. We do not attempt to separate the electron and phonon contributions because this seperation did not improve the fit with the data in the PM phase either. The essential fitting parameter is τ, which we initially assumed coincided with the slow timescale for demagnetization of $\tau_2 = 9$ ps observed by resonant x-ray scattering (RXS) [22]. The fast timescale $\tau_1 = 0.6$ ps is beyond the time resolution we can extract from the lattice dynamics of layers with a thickness on the order of 50 nm. For the modeling we assume an instantaneous

coupling of heat energy into the spin system described by $\rho_{\text{sp},0}^{Q}$ in Eq. (2), which mimics τ_1 for the spin disordering observed via RXS, which is attributed to a rapid spin-flip scattering of the optically excited conduction band electrons, enabled by the strong spin-orbit interaction in Ho [22]. Figures 4(f)–4(h) show the excellent agreement achieved simultaneously in the signals from all three layers for $\tau = 12$ ps. Especially, the initial contraction of Ho and the delayed expansion of Nb are very sensitive to variations of τ, as can be seen in the thin lines depicting the simulated signal in Figs. 4(f) and 4(h)

We would like to point out that the intense bipolar strain wave packet launched by the expansion of the capping layer at low temperatures evident from Fig. 4(b) enhances our confidence in the model since it is directly observed in the signal: The short dips in the Y strain [Fig. 4(g)] at 18 ps and in the Nb strain [Fig. 4(h)] at 26 ps indicate the arrival of the narrow compressive part of the bipolar strain pulse, independent of τ. For $\tau = 0$ ps, the maximum in the Nb strain coincides with the minimum observed in the PM phase of Ho. Thus, when all the energy transferred to the spin system arrives there instantaneously, Fig. 4(h) is a nearly perfect mirror image of Fig. 4(e). The increasing delay of the maximum in Nb for increasing τ can be assigned to the delayed NTE stress induced by spin disordering. The blue line in Fig. 3(f) shows once more that the total strain essentially follows the NTE stress profile in Ho (dashed line). Variation of the spatial stress profile of the spin excitation, e.g., to a homogeneous demagnetization profile throughout the layer, has a negligible effect on the Ho signal and does not improve the agreement with the Y and Nb signals.

Finally, we would like to discuss the observation of ultrafast negative stress on the subpicosecond timescale in the context of NTE in general.

NTE requires a specific interaction, where the energy decreases with changes in the volume [33,36]. For Ho the dominant interaction is the exchange interaction J_{exc}, and it was shown earlier that the expansion coefficient $\alpha \sim \partial J_{\text{exc}}/\partial c$ scales with the strain-induced change in the exchange interaction J_{exc} [27,45]. From a statistical physics perspective, the spin entropy $S = R\ln(2J + 1)$ must be dominated by the large angular momentum J of the localized $4f$ moments. Hence, the heat energy density ρ_{sp}^{Q} associated with the spin disordering and the concomitant stress $\sigma(t) = \Gamma_{\text{sp}}\rho_{\text{sp}}^{Q}(t)$ is also mainly connected to the localized spins. On the other hand, the RKKY interaction requires the itinerant electrons to mediate the coupling. It is not self-evident if a disordering of the optically excited itinerant electrons alone would be able to explain the full magnitude of the negative stress. In the Ho system, the recent work by Rettig $et~al.$ [22] confirmed that both types of electrons disorder on the same timescale; however, it will be interesting to test the situation in other systems, such as Gd, where disparate timescales have been observed [46].

VII. CONCLUSION

In conclusion, we have reported that ultrafast laser-induced disordering of the spin system of Ho proceeds on two timescales and triggers NTE via ultrafast stress mediated by

the exchange interaction. On the subpicosecond timescale already nearly half of the negative stress is present, and it fully balances the expansive stress from electrons and phonons. According to the ratio of GCs $\Gamma_{\text{e-ph}}/\Gamma_{\text{sp}} = -0.2$ this balance implies that 20% of the energy absorbed in the Ho layer has excited the spin system. Within $\tau = 12\,\text{ps}$, the fraction of energy in the spin system rises to 40%. If we consider the fact that for the ferromagnetic rare earth Gd, different timescales for disordering the localized and itinerant orbitals have been observed, it is not clear on which timescale the stress should occur. We believe that this study may trigger similar investigations in other systems with NTE since it is

not obvious that the thermodynamic relation predicting stress $\sigma = \Gamma \rho^Q$ proportional to the energy density in a subsystem will hold in time-dependent nonequilibrium situations and for any origin of the negative entropy-volume relation required for NTE.

[1] E. Beaurepaire, J.-C. Merle, A. Daunois, and J.-Y. Bigot, Ultrafast Spin Dynamics in Ferromagnetic Nickel, Phys. Rev. Lett. **76**, 4250 (1996).

[2] J.-Y. Bigot, M. Vomir, and E. Beaurepaire, Coherent ultrafast magnetism induced by femtosecond laser pulses, Nat. Phys. **5**, 515 (2009).

[3] C. Stamm, T. Kachel, N. Pontius, R. Mitzner, T. Quast, K. Holldack, S. Khan, C. Lupulescu, E. F. Aziz, M. Wietstruk, H. A. Dürr, and W. Eberhardt, Femtosecond modification of electron localization and transfer of angular momentum in nickel, Nat. Mater. **6**, 740 (2007).

[4] C. V. Korff Schmising, A. Harpoeth, N. Zhavoronkov, Z. Ansari, C. Aku-Leh, M. Woerner, T. Elsaesser, M. Bargheer, M. Schmidbauer, I. Vrejoiu, D. Hesse, and M. Alexe, Ultrafast magnetostriction and phonon-mediated stress in a photoexcited ferromagnet, Phys. Rev. B **78**, 060404 (2008).

[5] A. H. Reid, X. Shen, P. Maldonado, T. Chase, E. Jal, P. W. Granitzka, K. Carva, R. K. Li, J. Li, L. Wu, T. Vecchione, T. Liu, Z. Chen, D. J. Higley, N. Hartmann, R. Coffee, J. Wu, G. L. Dakovski, W. F. Schlotter, H. Ohldag, Y. K. Takahashi, V. Mehta, O. Hellwig, A. Fry, Y. Zhu, J. Cao, E. E. Fullerton, J. Stöhr, P. M. Oppeneer, X. J. Wang, and H. A. Dürr, Beyond a phenomenological description of magnetostriction, Nat. Commun. **9**, 388 (2018).

[6] G. Malinowski, F. Dalla Longa, J. H. H. Rietjens, P. V. Paluskar, R. Huijink, H. J. M. Swagten, and B. Koopmans, Control of speed and efficiency of ultrafast demagnetization by direct transfer of spin angular momentum, Nat. Phys. **4**, 855 (2008).

[7] D. Rudolf, C. La-O-Vorakiat, M. Battiato, R. Adam, J. M. Shaw, E. Turgut, P. Maldonado, S. Mathias, P. Grychtol, H. T. Nembach, T. J. Silva, M. Aeschlimann, H. C. Kapteyn, M. M. Murnane, C. M. Schneider, and P. M. Oppeneer, Ultrafast magnetization enhancement in metallic multilayers driven by superdiffusive spin current, Nat. Commun. **3**, 1037 (2012).

[8] C. Thomsen, H. T. Grahn, H. J. Maris, and J. Tauc, Surface generation and detection of phonons by picosecond light pulses, Phys. Rev. B **34**, 4129 (1986).

[9] B. Koopmans, G. Malinowski, F. Dalla Longa, D. Steiauf, M. Fähnle, T. Roth, M. Cinchetti, and M. Aeschlimann, Explaining the paradoxical diversity of ultrafast laser-induced demagnetization, Nat. Mater. **9**, 259 (2010).

[10] M. Hofherr, P. Maldonado, O. Schmitt, M. Berritta, U. Bierbrauer, S. Sadashivaiah, A. J. Schellekens, B. Koopmans, D. Steil, M. Cinchetti, B. Stadtmüller, P. M. Oppeneer,

S. Mathias, and M. Aeschlimann, Speed and efficiency of femtosecond spin current injection into a nonmagnetic material, Phys. Rev. B **96**, 100403 (2017).

[11] A. V. Kimel, A. Kirilyuk, P. A. Usachev, R. V. Pisarev, A. M. Balbashov, and T. Rasing, Ultrafast non-thermal control of magnetization by instantaneous photomagnetic pulses, Nature (London) **435**, 655 (2005).

[12] J.-W. Kim, M. Vomir, and J.-Y. Bigot, Ultrafast Magnetoacoustics in Nickel Films, Phys. Rev. Lett. **109**, 166601 (2012).

[13] A. Koc, M. Reinhardt, A. von Reppert, M. Rössle, W. Leitenberger, M. Gleich, M. Weinelt, F. Zamponi, and M. Bargheer, Grueneisen-approach for the experimental determination of transient spin and phonon energies from ultrafast x-ray diffraction data: Gadolinium, J. Phys.: Condens. Matter **29**, 264001 (2017).

[14] A. von Reppert, J. Pudell, A. Koc, M. Reinhardt, W. Leitenberger, K. Dumesnil, F. Zamponi, and M. Bargheer, Persistent nonequilibrium dynamics of the thermal energies in the spin and phonon systems of an antiferromagnet, Struct. Dyn. **3**, 054302 (2016).

[15] F. Quirin, M. Vattilana, U. Shymanovich, A.-E. El-Kamhawy, A. Tarasevitch, J. Hohlfeld, D. von der Linde, and K. Sokolowski-Tinten, Structural dynamics in FeRh during a laser-induced metamagnetic phase transition, Phys. Rev. B **85**, 020103 (2012).

[16] X. Wang, S. Nie, J. Li, R. Clinite, M. Wartenbe, M. Martin, W. Liang, and J. Cao, Electronic Grüneisen parameter and thermal expansion in ferromagnetic transition metal, Appl. Phys. Lett. **92**, 121918 (2008).

[17] X. Wang, S. Nie, J. Li, R. Clinite, J. E. Clark, and J. Cao, Temperature dependence of electron-phonon thermalization and its correlation to ultrafast magnetism, Phys. Rev. B **81**, 220301 (2010).

[18] T. Henighan, M. Trigo, S. Bonetti, P. Granitzka, D. Higley, Z. Chen, M. P. Jiang, R. Kukreja, A. Gray, A. H. Reid, E. Jal, M. C. Hoffmann, M. Kozina, S. Song, M. Chollet, D. Zhu, P. F. Xu, J. Jeong, K. Carva, P. Maldonado, P. M. Oppeneer, M. G. Samant, S. S. P. Parkin, D. A. Reis, and H. A. Dürr, Generation mechanism of terahertz coherent acoustic phonons in Fe, Phys. Rev. B **93**, 220301 (2016).

[19] Z. Lin, L. V. Zhigilei, and V. Celli, Electron-phonon coupling and electron heat capacity of metals under conditions of strong electron-phonon nonequilibrium, Phys. Rev. B **77**, 075133 (2008).

[20] P. Maldonado, K. Carva, M. Flammer, and P. M. Oppeneer, Theory of out-of-equilibrium ultrafast relaxation dynamics in metals, Phys. Rev. B **96**, 174439 (2017).

[21] A. von Reppert, L. Willig, J.-E. Pudell, M. Rössle, W. Leitenberger, M. Herzog, F. Ganss, O. Hellwig, and M. Bargheer, Ultrafast laser generated strain in granular and continuous FePt thin films, Appl. Phys. Lett. **113**, 123101 (2018).

[22] L. Rettig, C. Dornes, N. Thielemann-Kühn, N. Pontius, H. Zabel, D. L. Schlagel, T. A. Lograsso, M. Chollet, A. Robert, M. Sikorski, S. Song, J. M. Glownia, C. Schüßler-Langeheine, S. L. Johnson, and U. Staub, Itinerant and Localized Magnetization Dynamics in Antiferromagnetic Ho, Phys. Rev. Lett. **116**, 257202 (2016).

[23] N. Thielemann-Kühn, D. Schick, N. Pontius, C. Trabant, R. Mitzner, K. Holldack, H. Zabel, A. Föhlisch, and C. Schüßler-Langeheine, Ultrafast and Energy-Efficient Quenching of Spin Order: Antiferromagnetism Beats Ferromagnetism, Phys. Rev. Lett. **119**, 197202 (2017).

[24] B. Pfau, S. Schaffert, L. Müller, C. Gutt, A. Al-Shemmary, F. Büttner, R. Delaunay, S. Düsterer, S. Flewett, R. Frömter, J. Geilhufe, E. Guehrs, C. M. Günther, R. Hawaldar, M. Hille, N. Jaouen, A. Kobs, K. Li, J. Mohanty, H. Redlin, W. F. Schlotter, D. Stickler, R. Treusch, B. Vodungbo, M. Kläui, H. P. Oepen, J. Lüning, G. Grübel, and S. Eisebitt, Ultrafast optical demagnetization manipulates nanoscale spin structure in domain walls, Nat. Commun. **3**, 1100 (2012).

[25] M. Doerr, M. Rotter, and A. Lindbaum, Magnetostriction in rare-earth based antiferromagnets, Adv. Phys. **54**, 1 (2005).

[26] M. A. Ruderman and C. Kittel, Indirect exchange coupling of nuclear magnetic moments by conduction electrons, Phys. Rev. **96**, 99 (1954).

[27] F. J. Darnell, Magnetostriction in dysprosium and terbium, Phys. Rev. **132**, 128 (1963).

[28] D. Schick, M. Herzog, A. Bojahr, W. Leitenberger, A. Hertwig, R. Shayduk, and M. Bargheer, Ultrafast lattice response of photoexcited thin films studied by x-ray diffraction, Struct. Dyn. **1**, 064501 (2014).

[29] R. M. van der Veen, O.-H. Kwon, A. Tissot, A. Hauser, and A. H. Zewail, Single-nanoparticle phase transitions visualized by four-dimensional electron microscopy, Nat. Chem. **5**, 395 (2013).

[30] G. Ernst, C. Broholm, G. R. Kowach, and A. P. Ramirez, Phonon density of states and negative thermal expansion in ZrW$_2$O$_8$, Nature (London) **396**, 147 (1998).

[31] J. Chen, L. Fan, Y. Ren, Z. Pan, J. Deng, R. Yu, and X. Xing, Unusual Transformation from Strong Negative to Positive Thermal Expansion in PbTiO$_3$-BiFeO$_3$ Perovskite, Phys. Rev. Lett. **110**, 115901 (2013).

[32] S. Khmelevskyi, I. Turek, and P. Mohn, Large Negative Magnetic Contribution to the Thermal Expansion in Iron-Platinum Alloys: Quantitative Theory of the Invar Effect, Phys. Rev. Lett. **91**, 037201 (2003).

[33] T. H. K. Barron, J. G. Collins, and G. K. White, Thermal expansion of solids at low temperatures, Adv. Phys. **29**, 609 (1980).

[34] G. D. Barrera, J. A. O. Bruno, T. H. K. Barron, and N. L. Allan, Negative thermal expansion, J. Phys.: Condens. Matter **17**, R217 (2005).

[35] M. Nicoul, U. Shymanovich, A. Tarasevitch, D. von der Linde, and K. Sokolowski-Tinten, Picosecond acoustic response of a laser-heated gold-film studied with time-resolved x-ray diffraction, Appl. Phys. Lett. **98**, 191902 (2011).

[36] G. K. White, Thermal expansion at low temperatures - V. Dilute alloys of manganese in copper, J. Phys. Chem. Solids **23**, 169 (1962).

[37] G. K. White, Phase transitions and the thermal expansion of holmium, J. Phys.: Condens. Matter **1**, 6987 (1989).

[38] B. C. Gerstein, M. Griffel, L. D. Jennings, R. E. Miller, R. E. Skochdopole, and F. H. Spedding, Heat capacity of holmium from 15 to 300°K, J. Chem. Phys. **27**, 394 (1957).

[39] K. D. Jayasuriya, S. J. Campbell, and A. M. Stewart, Specific heat study of a holmium single crystal, J. Phys. F **15**, 225 (1985).

[40] D. Schick, A. Bojahr, M. Herzog, C. von Korff Schmising, R. Shayduk, W. Leitenberger, P. Gaal, and M. Bargheer, Normalization schemes for ultrafast x-ray diffraction using a table-top laser-driven plasma source, Rev. Sci. Instrum. **83**, 025104 (2012).

[41] See Supplemental Material at http://link.aps.org/supplemental/10.1103/PhysRevB.99.094304 for a video sequence of the temporal evolution of the stress profile and the strain wave in the paramagnetic and antiferromagnetic phases of holmium.

[42] P. Ruello and V. E. Gusev, Physical mechanisms of coherent acoustic phonons generation by ultrafast laser action, Ultrasonics **56**, 21 (2015).

[43] A. I. H. Persson, A. Jarnac, X. Wang, H. Enquist, A. Jurgilaitis, and J. Larsson, Studies of electron diffusion in photo-excited Ni using time-resolved x-ray diffraction, Appl. Phys. Lett. **109**, 203115 (2016).

[44] D. Schick, A. Bojahr, M. Herzog, R. Shayduk, C. von Korff Schmising, and M. Bargheer, UDKM1DSIM - A simulation toolkit for 1D ultrafast dynamics in condensed matter, Comput. Phys. Commun. **185**, 651 (2014).

[45] E. Pytte, Spin-phonon interactions in a Heisenberg ferromagnet, Ann. Phys. (NY) **32**, 377 (1965).

[46] B. Frietsch, J. Bowlan, R. Carley, M. Teichmann, S. Wienholdt, D. Hinzke, U. Nowak, K. Carva, P. M. Oppeneer, and M. Weinelt, Disparate ultrafast dynamics of itinerant and localized magnetic moments in gadolinium metal, Nat. Commun. **6**, 8262 (2015).

Article VI – Supplemental Material
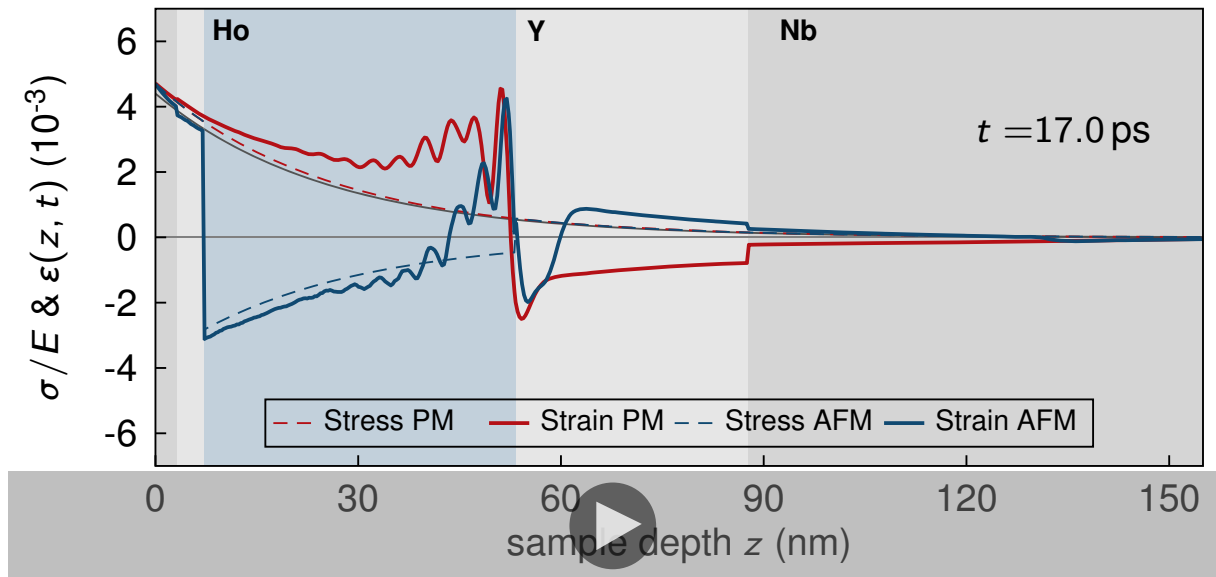
Article VI – Supplementary Video

Associated to the FIG. 3(b)–(f) in article VI a full video sequence of the simulation is given in the supplementary material: The sequence shows the temporal evolution of stress (dashed line) and strain (solid line) in the hetrostructure Nb / Y / Ho / Y / Nb on a sapphire substrate after photoexcitation in the PM phase (blue) and AFM phase (red). The transient strain profile was simulated with a linear-chain-model [84] based on the spatio-temporal stress $\sigma(z,t) = \Gamma_{\text{e-ph}}\rho_{\text{e-ph}}^{Q}(z,t) + \Gamma_{\text{sp}}\rho_{\text{sp}}^{Q}(z,t)$, as described in article VI. The temporal stress profile was smoothed by a 0.5 ps Gaussian function to avoid high frequency oscillations in the graph.[1]

---

[1]The video sequence can be played by several pdf-viewers including *Adobe Acrobat* and *XODO*. Depending on the pdf-viewer it is necessary to click multiple times on the figure to start the video sequence.

Article VII

Unconventional picosecond strain pulses resulting from the saturation of magnetic stress within a photoexcited rare earth layer

Alexander von Reppert, Maximilian Mattern, **Jan-Etienne Pudell**, Steffen Peer Zeuschner, Karine Dumesnil, and M. Bargheer

Optical excitation of spin-ordered rare earth metals triggers a complex response of the crystal lattice since expansive stresses from electron and phonon excitations compete with a contractive stress induced by spin disorder. Using ultrafast x-ray diffraction experiments, we study the layer specific strain response of a dysprosium film within a metallic heterostructure upon femtosecond laser-excitation. The elastic and diffusive transport of energy to an adjacent, non-excited detection layer clearly separates the contributions of strain pulses and thermal excitations in the time domain. We find that energy transfer processes to magnetic excitations significantly modify the observed conventional bipolar strain wave into a unipolar pulse. By modeling the spin system as a saturable energy reservoir that generates substantial contractive stress on ultrafast timescales, we can reproduce the observed strain response and estimate the time- and space dependent magnetic stress. The saturation of the magnetic stress contribution yields a non-monotonous total stress within the nanolayer, which leads to unconventional picosecond strain pulses.
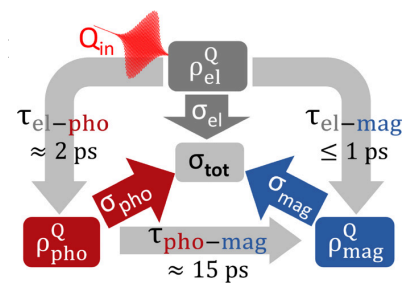
Unconventional picosecond strain pulses resulting from the saturation of magnetic stress within a photoexcited rare earth layer (F) This paper was selected as Featured

A. von Reppert,[1] (iD) M. Mattern,[1] J.-E. Pudell,[1,2] S. P. Zeuschner,[1,2] (iD) K. Dumesnil,[3] and M. Bargheer[1,2,a] (iD)

AFFILIATIONS

[1]Institut für Physik & Astronomie, Universität Potsdam, Karl-Liebknecht-Str. 24-25, 14476 Potsdam, Germany
[2]Helmholtz Zentrum Berlin, Albert-Einstein-Str. 15, 12489 Berlin, Germany
[3]Institut Jean Lamour (UMR CNRS 7198), Université Lorraine, 54000 Nancy, France

[a]Author to whom correspondence should be addressed: bargheer@uni-potsdam.de

ABSTRACT

Optical excitation of spin-ordered rare earth metals triggers a complex response of the crystal lattice since expansive stresses from electron and phonon excitations compete with a contractive stress induced by spin disorder. Using ultrafast x-ray diffraction experiments, we study the layer specific strain response of a dysprosium film within a metallic heterostructure upon femtosecond laser-excitation. The elastic and diffusive transport of energy to an adjacent, non-excited detection layer clearly separates the contributions of strain pulses and thermal excitations in the time domain. We find that energy transfer processes to magnetic excitations significantly modify the observed conventional bipolar strain wave into a unipolar pulse. By modeling the spin system as a saturable energy reservoir that generates substantial contractive stress on ultrafast timescales, we can reproduce the observed strain response and estimate the time- and space dependent magnetic stress. The saturation of the magnetic stress contribution yields a non-monotonous total stress within the nanolayer, which leads to unconventional picosecond strain pulses.

I. INTRODUCTION

Experiments that probe the strain response of the atomic lattice that results from the light-matter interaction of a femtosecond optical pulse with an opto-acoustic transducer material can be subsumed as picosecond ultrasonics.[1,2] They yield fundamental insights into physical processes within the laser-excited thin film, such as electron–phonon coupling,[3–5] hot electron propagation,[6,7] and electron–hole pair generation.[8,9] This is possible because the lattice strain is the deterministic, elastic response to a physical stress that itself contains the time- and length-scales of the energy transfer processes within the transducer region. Research in this field has developed from studying the elementary processes in metals[3,4] and semiconductors[8,10] to the point that various thermal and non-thermal mechanisms for the stress generation have been distinguished.[11]

Picosecond ultrasonics within magnetic materials offers a route to study spin-lattice interactions in the time domain. An additional motivation comes from the prospect that strain assisted magnetization manipulation could lead to faster, potentially field-free data storage

techniques, with increased storage densities.[12,13] Recent experiments have shown that electronically generated surface-acoustic-waves are able to switch the magnetization by nanosecond strain pulses.[14,15] Precession of the magnetization due to traversing picosecond strain pulses that transiently modify the crystal field anisotropy has been observed in many common and technologically relevant magnets such as nickel,[16,17] GaMnAs,[18,19] galfenol,[20] and doped yttrium–iron–garnet.[21,22] The inverse effect, i.e., lattice stress that originates from the change of the magnetic state, is less explored by time-resolved investigations although examples, such as the metamagnetic phase-transition in FeRh[23,24] and the change in the tetragonality of FePt[25,26] and SrRuO$_3$,[27] exist. For static and low frequency applications, it is known that metallic, magnetostrictive transducers complement the frequently used piezoelectric ceramics with the advantage of increased conductivity and ductility.[28] The class of heavy rare earth elements exhibits an exceptionally large magnetostriction[29] where the stress that can be generated by spin disorder is not only contractive but also dominates over the expansive phonon contribution as we have confirmed by

probing the structural response of laser-excited gadolinium,[30] holmium,[31] and dysprosium (Dy).[32,33] Ultrafast x-ray diffraction (UXRD) is a suitable tool for quantitatively probing the strain generation and propagation as well as the accompanying heat flow in crystalline heterostructures that are either inseparable or potentially opaque to all-optical probing schemes.[34–36]

Here, we present the ultrafast lattice response of a laser-excited Dy thin film within a metallic heterostructure, where we use a buried niobium (Nb) layer for separating strain pulses from the lattice expansion that results from heat diffusion. We systematically analyze the lattice dynamics as a function of the temperature-dependent magnetic order and the laser excitation energy density. The strain-pulse observed in the Nb detection layer changes upon cooling well below $T_{\text{Néel}}$ from a bipolar compression-expansion feature that is characteristic of a fast expansive stress to an almost unipolar expansion that results from a slowly rising contractive stress within the transducer. By modeling the strain response of the heterostructure, we obtain separated spatio-temporal stress-profiles for both the expansive phonon stress and the contractive magnetic stress. The stress within the Dy layer changes from expansive to contractive because the energy conversion to the spin system is saturated only in the strongly excited near surface region. To reproduce the observed low-temperature strain-response within a one dimensional elastic model, we have to assume a contractive stress contribution that rises nearly instantaneously and counteracts the quasi-instantaneous expansive, thermoelastic stress from hot phonons and electrons. In addition, a second contractive contribution is needed that rises with an $\approx$15 ps time constant. These timescales match the sub-picosecond electron-spin coupling and the subsequent phonon-spin coupling that were reported by previous demagnetization experiments in heavy rare earth elements.[37–39] For high excitation densities, we observe an additional increase in the spin-stress on a longer timescale. We attribute this to phonon mediated energy transport processes from surface-near regions of complete demagnetization to regions with partial magnetic order deeper in the sample, which have been photoexcited less. The energy transfer to the magnetic system removes energy from the phonon system. The storage of heat in spin disorder in Dy is documented by a reduced thermal expansion of the buried Nb detection layer, which only accepts heat from electrons and phonons.

The presented experiments extend our previous works[32,33] that mainly discuss the evolution of the average Dy layer strain on timescales $t > 45$ ps, by an analysis of the initial picosecond strain response for $t < 180$ ps. The main experimental novelty is the use of a dedicated non-magnetic and non-excited detection layer that allows for a clear separation of elastic waves and thermal expansion following the diffusion of heat. In addition, we now discuss a spatially resolved model for the magnetic stress evolution and its saturation within the Dy layer, which is at the origin of the unconventional picosecond strain response.

This paper consists of three main parts: in Sec. II, we present the sample characterization and the temperature dependent lattice expansion of the transducer and detection layer and introduce the concept of Grüneisen constants that are central to the following analysis. Section III contains the main experimental findings on the temperature and excitation energy dependent strain within the transducer and detection layer studied by UXRD. Section IV is devoted to the modeling of the spatiotemporal stress profile and corroborates the experimental findings.

II. STATIC PROPERTIES

In the following, we provide a brief overview over the relevant properties that are later probed by time-resolved experiments. We depict a representative x-ray diffraction pattern and discuss the material specific thermal expansion response that shows fingerprints of the magnetic phase-transition within the Dy layer. We introduce the thermodynamic concept of a Grüneisen constant that relates the energy density for phonons and magnetic excitations to their stress on the crystal lattice.

A. Sample characterization by x-ray diffraction

The static and temperature dependent characterization of the Dy sample by x-ray diffraction is provided in Fig. 1. In the inset of Fig. 1(b), we display a schematic of the investigated metallic heterostructure. It consists of a 80 nm (0001)-oriented Dy transducer layer grown in between two yttrium (Y) hcp-(0001) layers (22 nm on top of and 5 nm below Dy) on-top of a 102 nm niobium (Nb) body centered cubic (110)-oriented film that enables the crystalline growth on a sapphire (Al_2O_3) hcp-(11–20) substrate[40] and serves as an additional strain detection layer. X-ray diffraction, using a microfocus $Cu - K_\alpha$ radiation source, yields a reciprocal space projection that is depicted in Fig. 1(c), where the four different diffraction maxima that correspond to the material specific lattice constants are clearly separated along the out-of-plane reciprocal-space coordinate q_z. These Bragg-peaks are seen as diffraction intensity maxima in Fig. 1(a), where we show the
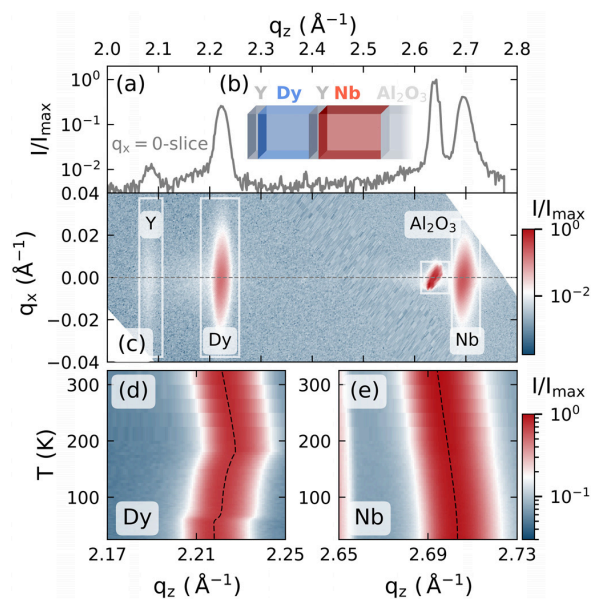
FIG. 1. Static x-ray diffraction results: (a) x-ray diffraction intensity of the sample structure that is schematically depicted in the inset (b). The material specific Bragg peaks are labeled in the reciprocal space map shown in (c). The temperature dependent peak-shifts that contrast the negative thermal expansion in the FM and AFM phase of dysprosium to the monotonous peak shift of the PM niobium are depicted in (d) and (e), respectively.

slice of the reciprocal space at $q_x = 0$. In the main experiments, we observe the time-dependent shift of the Dy and Nb diffraction peaks after laser-excitation and extract the resulting average lattice strain η of these materials in a laser-pump, x-ray diffraction-probe scheme, with a time-resolution of approximately 200 fs as described previously.[35,41,42]

An important reference for our interpretation of the lattice response upon laser-excitation is the equilibrium thermal expansion and contraction during heating of the sample structure. The temperature dependent peak-shift that we extract by heating from 25 K to 350 K is depicted in Figs. 1(d) and 1(e) for Dy and Nb, respectively, where the dashed lines indicate the peak center positions as obtained by Gaussian fits. The monotonous shift of the niobium peak to smaller q_z represents the common positive thermal expansion behavior. This contrasts with the thermal expansion seen in the dysprosium peak that exhibits a pronounced negative thermal expansion (NTE) between 40 K and 180 K as well as a change between expansion and contraction at 180 K.

B. Temperature-dependent material properties

The temperature dependent lattice strain $\eta = (c(T) - c_0)/c_0$ of the c-axis with $c_0 = c(T = 250 \, \text{K})$ in the hcp unit cell of the investigated thin Dy film is depicted in Fig. 2. For comparison, we relate it to the lattice constant change[43] [Fig. 2(a)] and to the heat capacity[44] of bulk Dy [Fig. 2(b)]. Changes in the thermal expansion are known to coincide with changes within the magnetic order and magnetic
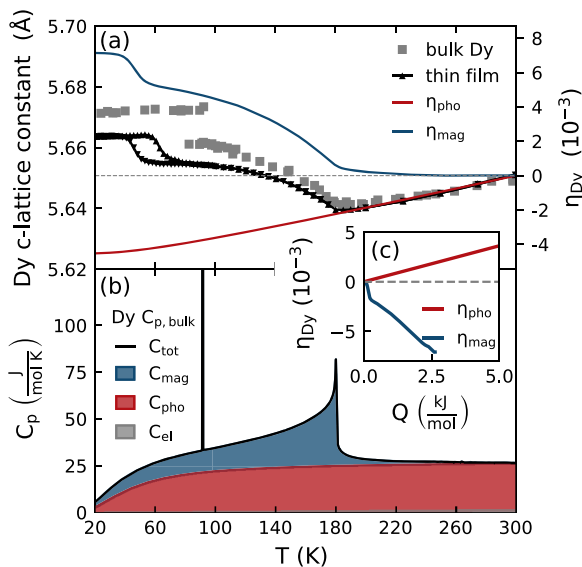

FIG. 2. Subsystem separation of (a) the static strain and (b) heat capacity contributions in Dy: The temperature-dependent c-axis of Dy and the heat capacity show a pronounced change at the AFM-PM phase transition at $T_{\text{Néel}} \approx 180 \, \text{K}$. The FM-AFM phase transition that occurs at $T_{\text{Curie}} \approx 90 \, \text{K}$ for bulk Dy is shifted to lower temperatures in the used thin film sample. The inset in (c) shows the strain per deposited energy, which results from the separation of the strain and heat capacity into the contributions of phonon and spin excitations, which are indicated in red and blue, respectively.

contributions to the strain can exceed 10^{-3}.[29,45] Elemental Dy has one of the highest magnetic moments of 10.64 μ_B per atom, which order ferromagnetically (FM) below $T_{\text{Curie,bulk}} \approx 90 \, \text{K}$ and antiferromagnetically (AFM) between T_{Curie} and $T_{\text{Néel}} \approx 180 \, \text{K}$ above which Dy becomes paramagnetic (PM).[46–48] The large magnetic moment originates mainly from the localized magnetic moments of the partially filled $4f$-electron orbitals that interact via the delocalized 5d6s-conduction band electrons by the Ruderman-Kittel-Kasuya-Yosida (RKKY)-mechanism.[47,48] The magnetic easy axis in the FM phase lies along the a-axis in the basal plane of the hexagonal unit cell and the AFM phase exhibits a helical spin ordering that is characterized by a finite turn angle between the magnetic moments for neighboring unit cells along the c-axis direction.[46]

Magnetostriction in rare earth elements is often discussed within the so-called standard model of magnetostriction pioneered by Callen and Callen.[49,50] This formalism takes both single-ion and two-ion interactions into account.[50,51] Single-ion contributions originate from the interaction of the crystal field with the anisotropic $4f$-orbitals, which leads to a lattice deformation upon magnetization change due to the intrinsic spin–orbit coupling.[51,52] The case of vanishing orbital momentum, that is realized in Gadolinium, demonstrates the importance of the exchange-striction mechanism that explains the occurrence of magnetostriction even for spherically symmetric charge distributions.[51] Exchange-striction is a two-ion contribution that originates from a distance-dependent magnetic interaction energy (here provided by the oscillatory RKKY-interaction[53]) that in turn affects the equilibrium position of the magnetic ions based on their alignment.[51,52] A unified, potentially even microscopic model that explains the temperature and field dependent magnetostriction for the entire class of heavy rare earth elements does not exist.[51,52]

C. Grüneisen concept

In the discussion of the time-resolved strain, we employ a macroscopic, thermodynamic approach that approximates the laser-generated stresses to be directly proportional to the energy densities deposited in the corresponding subsystems. We introduce the main idea at first for the static thermal expansion of Dy. The origin of our approach dates back to 1912 when Grüneisen recognized that the contributions of the lattice vibrations to the volumetric thermal expansion coefficient $\beta(T)$ of elemental solids and their heat capacity $C_V(T)$ at constant volume V share the same temperature dependence, so that their ratio can be simplified to a dimensionless, nearly temperature-independent parameter.[54] The concept of this Grüneisen constant Γ has been employed continuously and was further generalized for the discussion of the thermal expansion in solids.[55–57] The thermodynamic derivation yields the macroscopic Γ as[55]

$$\Gamma = KV \frac{\beta(T)}{C_V(T)}, \tag{1}$$

wherein K represents the bulk modulus. This approach can be extended to account for different excitations that contribute energy reservoirs r in a solid by introducing dedicated Γ_r.[55] The generalization to the case of anisotropic expansion requires the use of anisotropic linear thermal expansion coefficients $\alpha_i(T)$ and anisotropic Grüneisen constants Γ_i as well as the proper directional elastic constants c_{ij} (Ref. 55) as exemplified for the rare earth Holmium.[58] For simplicity,

we consider the elastic strain response to be purely one-dimensional. This is justified if the probed region is homogeneously excited along the lateral dimension, so that its picosecond response shows no in-plane strain. We thus limit the discussion to the out-of-plane response of the materials so that we will drop the directional indices for the out-of-plane stress $\sigma_3 = c_{33}\eta_3$ in the following. For sufficiently small ΔT, Eq. (1) can be transformed to the linear relation

$$\sigma_r = \Gamma_r \rho_r^Q \qquad (2)$$

between the stress σ_r and the laser-induced energy density $\rho_r^Q(\Delta T) = \int_T^{T+\Delta T} C_r(T')dT'$, wherein the subscript, r, denotes one of the energy reservoirs. For the case of Dy, we separate the total strain response to stress contributions from electronic excitations (r = el), phonons (r = pho), and magnetic excitations (r = mag).

In Fig. 2, we demonstrate the separation of the subsystem contributions to the equilibrium lattice strain and heat capacity in Dy from which we subsequently extract the ratio of the Grüneisen parameters for the combined electron-phonon and magnetic excitations. Using the heat capacity of the chemically equivalent non-magnetic heavy rare earth Lutetium, scaled according to the Debye temperature of Dy, provides an estimate for the combined electron and phonon contribution to the specific heat.[59] This is indicated by the red shading in Fig. 2(b). The estimated electronic contribution to the heat capacity C corresponds to the very small gray shaded area in Fig. 2(b), which we obtain from a Sommerfeld model [$C_{el} = \gamma_{Dy}T$ with $\gamma_{Dy} = 4.9$ mJ/(mol K)].[60] Electronic excitations thus only store a sizeable energy fraction at high electron temperatures that are attained only directly after laser-excitation. For that reason, we label the combined electron-phonon subsystem in the following as phonon contribution (r = pho) unless stated otherwise.

Assuming a constant Grüneisen parameter for the phonon contribution, we obtain an estimate for the thermal expansion of non-magnetic Dy (η_{pho}) that we represent by the red line in Fig. 2(a). By subtracting η_{pho} and C_{pho} from the measured lattice strain and the combined heat capacity, we obtain the contribution of magnetic excitations to the strain and heat capacity, which is indicated by the blue line in Fig. 2(a) and blue shaded area in Fig. 2(b), respectively. From this separation, we can directly extract the strain per deposited energy for the phonon and magnetic subsystem, which is displayed in the inset in Fig. 2(c). Indeed, the linear slope of the magnetic strain in Fig. 2(c) reconfirms the linear relation of stress and energy density of Eq. (2) for the spin system. The linear strain-energy-density relation for the phonon strain is in agreement with previous analysis of the thermal expansion of solids[55,61] and in particular, the non-magnetic rare earth Lutetium[62] where Grüneisen parameters Γ are found that are nearly constant over an extended range of temperatures even when $C(T)$ and $\beta(T)$ are T-dependent. Recently, this was extended to the separated magnetic and nonmagnetic contributions of the thermal expansion of Dy.[32,33] The slope of the resulting curves is proportional to the Grüneisen parameter since the relevant elastic constant c_{33} changes by less than 10% across the displayed temperature region.[63] The ratio of the Grüneisen constants $\Gamma_{mag}/\Gamma_{pho} \approx -3$ indicates that magnetic excitations in Dy are three times more efficient in the stress generation per deposited energy as compared to phonons.

As opposed to the AFM-PM transition that is of second order, the FM-AFM transition is a first order phase transition with a latent heat of 50.7 J/mol.[44] In our thin film sample, we see that this phase transition occurs between 60 K and 75 K upon heating. We attribute the shift and broadening of the phase transition to epitaxial strains. The FM-AFM phase transition leads to orthorhombic in-plane distortions that are clamped near the interfaces. Since a measurement of the temperature-dependent heat capacity of the Dy transducer within our heterostructure is not possible, we can only specify that the observed negative strain per deposited energy of the spin system is potentially even larger in the region of the FM-AFM transition. Note, however, that this contraction results mainly from the FM-AFM phase transition, since within the FM phase the lattice expands for rising temperatures.

The presented subsystem separation can be applied to gadolinium[30] and holmium,[31] which exhibit similarly large negative Grüneisen parameters for magnetic excitations. Heavy rare earth metals are an interesting class of materials for lattice dynamics since their magnetic heat capacity C_{mag} and the associated entropy of magnetic excitations $\delta S_{mag} = \Delta Q_{mag}/T$ are comparable to the phonon contribution over a large temperature region.[31,55,58] This renders Dy a suitable candidate for experiments that investigate the magnetic contributions, that lead to the NTE response, within a time-resolved experiment.

III. TIME-RESOLVED EXPERIMENTS

The main experimental results of our study are summarized in Figs. 3 and 4, which display representative picosecond strain responses for both the Dy transducer and the buried Nb detection layer at different starting temperatures T and excitation energy densities F. In our UXRD experiments, the sample is subjected to 110 fs-long, p-polarized laser pulses with a central wavelength of 800 nm at a repetition rate of 1 kHz. The laser excitation profile corresponds to a 2D-Gaussian contour with approximately 1.6×1.2 mm^2 full width at half maximum along its principal axis. The optical pump-pulses are incident under $36°$ for measuring the Dy response and $40°$ for the Nb measurements where the angle is given relative to the surface plane of the sample. The x-ray probe-pulses are generated using a laser-based plasma x-ray source,[64] monochromatized to Cu-K$_\alpha$-radiation, and focused onto the sample using a Montel optic[65] with a diamond shaped 300×300 μm^2 beam focus on the sample. The sample temperature is monitored via a thermocouple adjacent to the sample and all reported fluence values are provided as incident energy density that is calculated from the incident laser power and the beam footprint.

A. Temperature dependent UXRD experiments

First, we discuss the results displayed in Fig. 3, where a fixed energy density of 7.2 mJ/cm^2 is used to excite the sample for different initial temperatures, sampling the different magnetic orders. The results obtained in the PM phase at $T = 250$ K are displayed by red open symbols and represent the non-magnetic response of the investigated metallic heterostructure. We find an expansion of the Dy layer that reaches its maximum within 30 ps, which corresponds to the time it takes to propagate strain from the air/Y interface through the Dy layer to the Dy/Y interface. After traversing the 5 nm Y interlayer, this expansion enters the Nb layer at approximately 31.5 ps. This expansion pulse is preceded by a compression that results from the fast rise of the spatially inhomogeneous expansive stress. The resulting bipolar shape of the propagating strain pulse is well known in picosecond
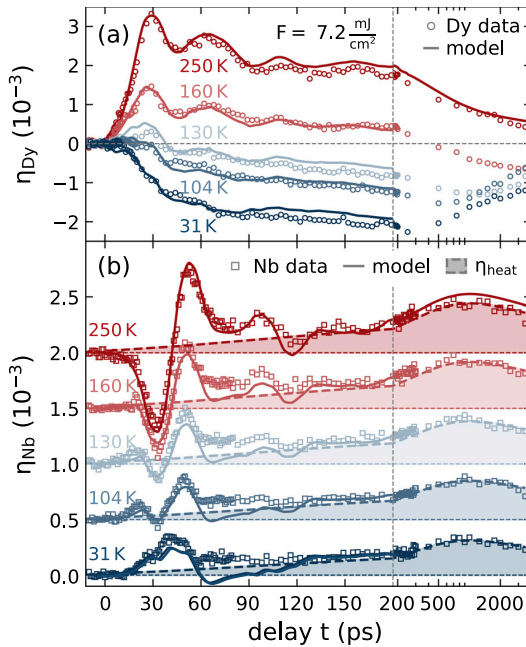
FIG. 3. Temperature-dependent strain response of (a) the Dy transducer and (b) the Nb detection layer for a fixed excitation energy density of $F = 7.2$ mJ/cm^2. Open symbols represent the average strain of the layers extracted from the Bragg peak shift observed by UXRD. Solid lines represent the simulated UXRD response obtained from a one-dimensional elastic model subjected to time-dependent phonon and magnetic stresses that are detailed in the modeling Sec. IV. The shaded region in (b) indicates the estimated thermal contribution to the Nb strain. The linear to logarithmic axis break (vertical, dashed line) allows the simultaneous comparison of the picosecond strain pulse and the subsequent thermal expansion. Nb curves are offset for clarity.

FIG. 4. Same depiction as in Fig. 3 used for the excitation energy density dependent strain response of (a) the Dy transducer and (b) the Nb detection layer for the fixed $T = 130$ K. All curves are offset for clarity. The initial transducer response changes from contraction to expansion as the excitation energy is increased, which coincides with the appearance of the delayed bipolar strain feature in the coherent phonon response of the buried detection layer.

acoustics; however, optical detection schemes often probe the wave returning back to the surface after a reflection.[1,2,5]

UXRD experiments can monitor the bipolar strain pulse traversing a buried detection layer: The classical bipolar wave first leads to a negative average strain in this layer and before it turns positive, a zero average strain indicates equal expansive and contractive parts in this layer.[35,66] The nearly bipolar shape of the Nb strain in Fig. 3(b) within the first 75 ps is characteristic of a symmetric strain pulse that is generated by a total stress that rises fast compared to the strain-propagation time through the laser-excited transducer. Echos of the laser-generated picosecond strain pulses that occur due to the partial reflection at the layer interfaces lead to a damped oscillation of the average strain in the Dy transducer and a second bipolar feature in the Nb detection layer between 80 ps and 125 ps.

In addition to these signatures of the coherent phonon wave packets, we observe a slowly increasing strain that originates from the excitation of incoherent phonons in the materials. This thermal expansion contribution of the excited Dy transducer is observed to decay on a nanosecond timescale by heat diffusion toward the substrate. This diffusion leads to a transient thermal expansion in the Nb detection layer that exhibits its maximum at approximately 1 ns after the
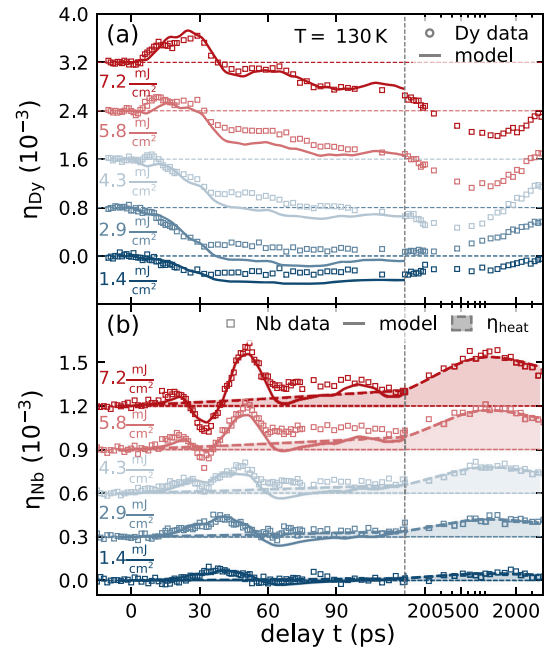
excitation. To highlight the contribution of heat transport to the Nb expansion, we added dashed lines and shaded areas to Fig. 3(b). These lines are all scaled copies $A(T)\bar{\eta}_{heat}(t)$ of the transient average strain $\bar{\eta}_{heat}(t)$ in the Nb layer, which fit the 250 K data. This line could be drawn through the data by averaging out any coherent oscillations, but here we used the simulated expansion according to a Fourier heat law model discussed below. The temperature dependent factor $A(T)$ is determined by scaling the temperature-independent $\bar{\eta}_{heat}(t)$ to the Nb data between 200 ps and 3 ns. $A(T)$ decreases significantly with temperature T, indicating that part of the energy density is stored in magnetic excitations that become accessible below $T_{Néel}$ within the Dy transducer. The details of the modeling including a plot of $A(T)$ are discussed in Sec. IV.

Looking at the short timescale, we find that the magnetic excitations accessible upon lowering the temperature transform the transducer response continuously from a rapid expansion to a relatively slow contraction [Fig. 3(a)]. The coherent phonon oscillations in Dy become significantly weaker. In the Nb-detection layer [Fig. 3(b)], this coherent picosecond strain wave is observed to change from a large bipolar shape with a leading compression to a weaker unipolar expansion. At intermediate temperatures, a bipolar strain wave with reduced amplitude compared to the PM phase is preceded by an expansion, which we attribute to contractive stress at the back side of the Dy layer, which absorbs the smallest energy density.

B. Excitation density dependent strain-response

This hypothesis was checked by the excitation-density dependent measurements that we depict in Fig. 4. We repeated the UXRD experiment for a systematic variation of excitation fluences at a fixed initial sample temperature of $T = 130$ K in the AFM phase of Dy. The increase in the deposited energy in the heterostructure can be seen directly as an increase in the transient thermal expansion of the Nb detection layer beyond 100 ps. The shaded area in Fig. 4(b) again indicates our estimate of the incoherent strain contribution that we obtain by scaling the strain $\bar{\eta}_{heat}(t)$ from the PM phase to approximate the data between 0.2 and 3 ns. The resulting amplitude $A(130\,K, F)$ scales super-linearly with F, indicating a saturation of the energy transfer to magnetic excitations (cf. Sec. IV E). Note that the magnetic contribution to the specific heat C_{mag} above $T_{Néel}$ is small but finite [Fig. 2(b)]. According to the equilibrium analysis, the Grüneisen constant Γ_{mag} has the same value above $T_{Néel}$, as the slope in Fig. 2(c) remains constant toward the end. Similar to the temperature dependent experiments, we find a strong qualitative change of the picosecond strain response in our heterostructure. For low excitation energies $F < 4.3$ mJ/cm^2, we observe an average contraction of the Dy transducer that goes along with the unipolar expansion of the Nb layer. For $F > 4.3$ mJ/cm^2, we observe an initial expansion of the Dy transducer that changes to an average contraction at delays much larger than the 30 ps that it takes for strain propagation through the layer.

The strain pulse measured in the Nb detection layer [Fig. 4(b)] exhibits a unipolar expansion feature for low excitation energy densities. For higher fluences, this expansion is superimposed by a bipolar strain response expected for the excitation of phonons, i.e., the dominant signal in the PM phase. However, here we confirm that the bipolar strain pulse is preceded by an expansion. Since this leading expansion is rationalized by a contractive stress at the backside of the Dy transducer, the high fluence data directly show that the magnetic excitations at the back side of the Dy transducer are not saturated. The simultaneous expansion at the Dy front side, however, triggers the bipolar waveform which is observed in the detection layer with a delay given by the sound propagation. This waveform confirms a saturation of the magnetic excitation in the Dy front part, because it is the trailing part of the strain pulse, which is considerably changed by the increasing fluence. The fraction of the transducer, where expansive stress from the combined electron-phonon system dominates over the contractive stress, extends over a thicker part of the layer for higher excitation energy densities.

Before discussing the resulting quantitative findings and the modeling approach, we briefly summarize the experimental conclusions that can be drawn directly from the presented UXRD data. For low excitation energies and temperatures, we observe that the magnetic rare earth transducer contracts on average as opposed to the expansion that is observed in the PM phase. For intermediate temperatures, we can infer that the front of the transducer expands while its backside contracts. This behavior can be rationalized by a spatially dependent saturation of the magnetic stress that originates from the inhomogeneous energy deposition profile. We find that the strain propagation maps the stress profile onto a nearly background-free, time-dependent signal of the average strain in the buried Nb detection layer. Since heat diffusion takes longer than strain waves, detecting the propagated strain wave in the detection layer separates the strain contribution of coherent and incoherent phonons, which are

superimposed within the photoexcited Y and Dy layer. The additional layer thus provides a nanometric depth-resolution of the UXRD experiments using hard x-rays, which otherwise exhibit an extinction length on the order of few μm. The heat transport observed via the thermal expansion of the adjacent Nb layer is found to be reduced below the magnetic ordering temperatures. This can be directly seen in the area under the curve for the average strain in Nb [Fig. 4(b)], which is smaller at low temperatures. This is quantitatively depicted in Fig. S1(c) of the supplementary material.

IV. MODELING SPATIO-TEMPORAL STRESS

Our modeling approach is designed to identify the ingredients that are necessary to rationalize the observed temperature- and excitation fluence-dependent strain-response of the magnetic rare earth transducer. To that end, we model a time- and space dependent driving stress $\sigma_{tot}(z, t) = \sigma_{pho}(z, t) + \sigma_{mag}(z, t)$ generated by energy transfer to magnetic excitations that acts in addition to the electron-phonon stress calibrated by the response in the PM phase. The measured average strain $\bar{\eta}$ for $t > 100$ ps only encodes the average stress in the Nb layer originating from the heat diffusion. The qualitative analysis of the strain wave detected in Nb for $t < 100$ ps already indicated that we are able to extract temporal variations $\sigma(z, t)$ of the spatial stress profile in the Dy by modeling the strain wave launched into the Nb detection layer. As shown in Figs. 3 and 4, we find qualitative and quantitative agreement between our model and data.

In the following, we first discuss the general assumptions of our modeling approach before we specify the simulation steps and assumptions for the modeled electron-phonon stress and the magnetic stress contributions.

A. General model assumptions

We assume the energy transfer processes between the stress-contributing subsystems schematically shown in Fig. 5(a), with coupling-times that correspond to the stress rise-times depicted in Fig. 5(b). The spatial stress profiles in the Dy layer are exemplified in Fig. 5(c) for the parameters $T = 130$ K and $F = 7.2$ mJ/cm^2 that are representative of the AFM sample response. The total energy provided by the laser pulse is distributed between electron-phonon excitations that exert an expansive stress and magnetic-excitations that exert a contractive stress within the Dy layer. The energy is assumed to be deposited with the same inhomogeneous spatial profile to phonon- and magnetic excitations. The magnetic excitations however induce a contractive stress whose amplitude is three times larger than the expansive stress that is generated by electron-phonon excitations with the same energy density, according to the static Grüneisen analysis [Fig. 2(c)]. We keep as many simulation parameters as possible constant throughout the modeling. This includes the three coupling times illustrated in Fig. 5, the ratio of the initial energy redistribution from electrons to spins and phonons, and the maximum value for the spin energy density given by the saturation value ρ_{mag}^{sat}. We assume that the spatial energy distribution in the magnetic subsystem follows the profile of the phonon energy-density obtained by modeling the PM phase. This profile changes in time according to the heat diffusion, and we implicitly assume that the coupling of energy from phonons to spins is effective enough to prevent different spatial profiles of the contributing excitations. However, when the magnetic energy density exceeds the saturation value ρ_{mag}^{sat}, we truncate it. This truncation yields the
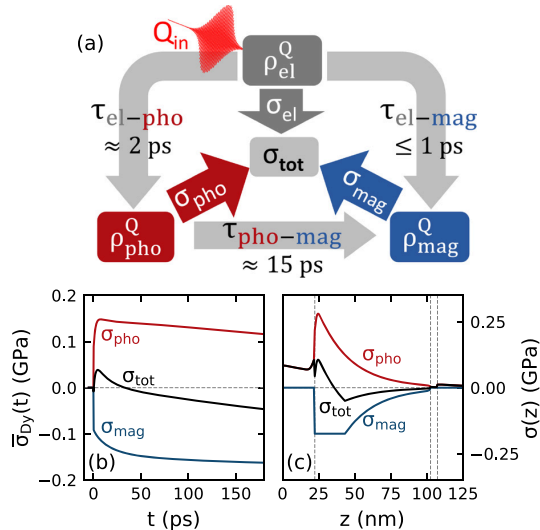
FIG. 5. (a) Schematic stress contributions used in the modeling approach. Arrows and labels indicate the modeled energy transfer processes between the subsystems and the assumed coupling-timescales τ. The resulting time-dependence of the spatially averaged stress contributions in Dy (b) and the used stress profile 100 fs after excitation (c) are shown exemplarily for $T = 130$ K and $F = 7.2$ mJ/cm^2. Vertical dashed lines in (c) indicate interfaces of the Y/Dy/Y/Nb heterostructure. This illustrates that the total stress evolution is a superposition of the expansive electron-phonon stress and the contractive magnetic stress both in the space- and time-domain.

non-monotonous spatial variation of the total driving stress as a function of temperature and excitation fluence. The temporal variation owes to the fact that the fraction of energy coupled rapidly to the phonon system is larger than into the magnetic system. Therefore, the additional 15 ps spin-phonon coupling time leads to a slow rise of the spin excitation and a decay of the phonon excitation.

We limit the modeling time to 180 ps since we expect remagnetization effects to significantly contribute to the strain at later times via magnetostriction. A full description would require a detailed model for the recovery of the magnetic order including both thermal transport and nucleation, growth, and coalescence of magnetic domains. This is beyond the scope of our one-dimensional thermodynamical approach. We furthermore refrain from a time- and space-dependent three-temperature model that has been previously used to rationalize the demagnetization of the magnetic specimen,[67,68] because it would require many, potentially temperature dependent, material constants for all layers in our heterostructure that are not known with the required accuracy. To what extend a three temperature model would capture the demagnetization and remagnetization of both the itinerant ($5d6s$) conduction band electrons and the localized $4f$ electrons in heavy rare earth metals is a matter of current research debate.[39,69,70]

B. Simulated spatio-temporal stress contributions

The modeled time-dependent stress profiles, separated into the expansive, contractive and the total stress contributions are displayed

in Figs. 6(a)–6(o). The first row [Figs. 6(a)–6(e)] shows the expansive electron-phonon stress (σ_{pho}). In the PM-phase (250 K), σ_{pho} is identical to the total stress (σ_{tot}), shown in the third row. For the low temperature magnetic phases, the energy transfer to magnetic excitations reduces the amplitude of σ_{pho} [Figs. 6(b)–6(e)] without changing the relative spatio-temporal form, and at the same time, it creates the magnetic-stress contribution (σ_{mag}) shown in the second row [Figs. 6(f)–6(j)]. The resulting total stress σ_{tot} [Figs. 6(k)–6(o)] strongly depends on the initial temperature and excitation energy. This is supported by the modeled spatiotemporal stress profile and strain response for the excitation energy density dependent experiments at $T = 130$ K that we display in Sec. S5 of the supplementary material. The modeled strain response [Figs. 6(p)–6(t)] contains the propagating strain pulses that are launched at gradients of the driving stress in addition to the strain contribution of the local driving stress.

While the saturation level of the magnetic stress changes for the T-dependent measurements, F-dependent measurements vary the deposited energy density for a fixed maximum magnetic stress. In both cases, we observe that the absolute value of the total stress that acts on the lattice is reduced in comparison to the competing contributions from magnetic- and phonon excitations. Even though the total stress is contractive at the end of most simulation scenarios, the maximum contraction is attained slower than the magnetic stress rise time due to the time-dependent balance of phonon and magnetic stresses. The reappearance of the bipolar strain pulse in the detection layer response for high excitation energies thus occurs since the total stress at the top Y/Dy interface is dominated by an unbalanced electron-phonon stress.

C. Simulation steps

We use the modular UDKM1DSIM[71] MATLAB library to model the time-dependent energy density, strain, and x-ray reflectivity of the non-magnetic heterostructure response. The solid, dark-red line in Figs. 3(a) and 3(b) corresponds to the strain that we obtain from the simulated transient x-ray diffraction peak shift. In the first step, we calculate the time-dependent temperature changes upon laser excitation using a one-dimensional Fourier heat diffusion model from the thermophysical properties of the materials in the PM phase that we list in Sec. S3 of the supplementary material. The resulting spatiotemporal energy density is subsequently translated to a stress that acts as the driving force on a linear chain of masses and springs, which calculates the time-resolved layer strain with unit-cell resolution. The final simulation step employs a transfer matrix algorithm that yields the Bragg-peak evolution of the strained sample according to dynamical x-ray diffraction theory. Section S3 of the supplementary material shows a flow chart of the simulation steps including the relevant equations. The good quantitative agreement between UXRD data and simulation indicates that our model is a suitable representation of the sample properties and non-magnetic processes (i.e., layer thicknesses, optical excitation parameters, stress profiles, and rise-times) in the PM phase of Dy. We keep all the parameters given in Table I of the supplementary material fixed throughout the modeling, even in the FM and AFM phase, since these parameters describe the electron-phonon system. Section IV E describes how we added the contractive negative stress according to Eq. (2) for excitation in the AFM and FM phase.
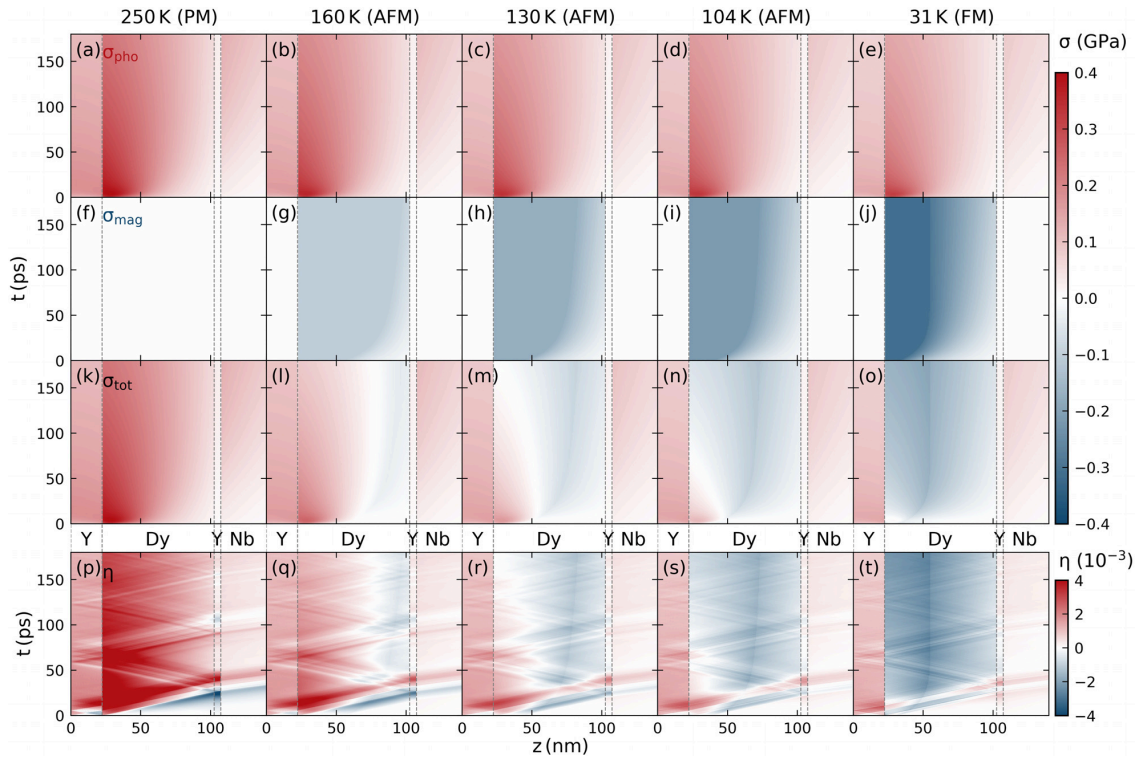
FIG. 6. Modeled spatiotemporal stress and strain response in our heterostructure for a fixed excitation with $F = 7.2$ mJ/cm^2 at different starting temperatures. The phonon-stress contributions (a)–(e) and the magnetic-stress contributions (f)–(j) in the first and second row add to the total stress provided in the third row (k)–(o). This illustrates the temperature and time-dependent energy transfer and the saturation effects due to the finite amount of energy that can be transferred to magnetic excitations. The resulting strain response of a linear chain of masses and springs model that contains contributions from both coherent and incoherent phonons is shown at the bottom (p)–(t). These strain maps are used to simulate the time-dependent Bragg peak shift that yields the modeled Dy and Nb strain response in Fig. 3. Vertical dashed lines indicate the interfaces within the Y/Dy/Y/Nb heterostructure.

D. Electron-phonon stress contribution

Both the Dy and the Nb strain responses in the PM-phase are used to calibrate the electron-phonon stress contribution. The electron-phonon coupling is included by a 2 ps time-constant of the expansive stress and a ratio between the Grüneisen constants $\Gamma_{el}/\Gamma_{pho} = 0.5$ for both the Y and Dy layers. These parameters are chosen to fit the observed expansion of the Dy layer and the coherent phonon oscillation amplitude of the PM response and are fixed for the subsequent modeling. To illustrate the effect of the stress rise time on the shape of the strain pulse seen by UXRD in the detection layer, we present the elastic-response-simulations of the average strain within a simplified structure that contains only a transducer and a detection layer in Sec. S2 of the supplementary material. To recover the observed direct rise of the Dy strain after laser excitation, we have to assume a reduced absorption and thermal expansion in the 21 nm thick Y capping layer, which would otherwise compress the adjacent Dy. Although the estimated expansion of the Y layer is reduced by 40% compared to the literature value, we stress that this parameter is kept fixed for all subsequent simulations that focus on the T-dependent

magnetic response. One possible explanation for this deviation could be a partial oxidation of the capping layer since the metallic sample was kept at ambient conditions prior to the measurements.

To match the slow nanosecond decay of the Dy strain as well as the delayed rise of the expansion in the Nb layer, we use an effective thermal conductivity value for the Dy layer that is reduced by approximately 40% compared to the bulk literature value to account for thermal interface resistance effects. Using the material-specific elastic constants, we can then transform the energy densities ρ_r into an estimated spatiotemporal profile of the driving stress $\sigma_r = \Gamma_r \rho_r$ according to the Grüneisen concept [Figs. 6(a) and 6(k)]. This stress drives the elastic response shown in Fig. 6(p). The modeled strain matches both the Dy transducer and Nb detection layer response qualitatively and quantitatively over the entire 3.5 ns simulation time as shown in Fig. 3.

E. Magnetic stress contribution

To minimize the number of parameters for the simulations in the AFM and FM phase, we not only keep all thermophysical parameters describing the e-ph system fixed. We also use the shape of the

116

spatiotemporal phonon stress-profile $\eta_{\text{heat}}(z,t)$ extracted in the PM phase. We reduce its amplitude in all layers (Y, Dy and Nb) according to the fraction of the energy that is transferred to magnetic excitations that is shown in Fig. 7 as red squares. The blue squares represent $1-\eta_{\text{heat}}$, which is proportional to the fraction of energy that is stored in the magnetic system of Dy on the few ns timescale. The lines in Fig. 7 show the relative weight of the energy densities in the phonon (red) and magnetic system (blue) in our model. We find a qualitative agreement with the data if locally a fraction of 25% of the excitation energy is deposited instantaneously into the magnetic system to account for subpicosecond electron-spin couplings and additionally a second energy fraction of 25% of the excitation energy is subsequently transferred from phonon to magnetic excitations by the phonon-spin coupling. Only when this energy transfer locally exceeds the maximum energy density $\rho_{\text{mag}}^{\text{sat}}$ in the spin system, we truncate the energy transfer from phonons to spins. Thus, to account for the experimentally observed reduced energy transport to the adjacent layer in the magnetic phase of Dy, we reduce the energy density in the Nb and Y layers and add the removed fraction to the Dy layer where the energy is distributed between magnetic and phonon excitation. We use $\rho_{\text{mag}}^{\text{sat}}$ as a free parameter in the modeling and find the best agreement with our data with $\rho_{\text{mag}}^{\text{sat}}(T_{\text{start}}) = 0.81 \int_{T_{\text{start}}}^{\infty} C_{\text{mag}}(T')dT'$, using the literature bulk values for $C_{\text{mag}}(T')$. We believe that either the thin film value for $C_{\text{mag}}(T')$ is smaller compared to the bulk value, or only a reduced fraction of the magnetic heat capacity of the thin film is accessible upon ultrafast laser excitation. Our model reproduces the trends of the experimentally observed reduced energy flow in Fig. 7 as a function of the starting temperature and the fluence correctly. The energy fraction that is not detected in Nb persists in the magnetic excitations of Dy that act as a saturable heat sink. The saturation can be seen by the reduced energy fraction in the magnetic excitations closer to $T_{\text{Néel}}$ and the decrease in the magnetic energy fraction for higher excitation densities. The blue lines representing the fraction of heat in the magnetic system around 180 ps in our model report a systematically larger value than the blue squares derived from the experiment of the Nb strain

between 0.2 and 3 ns. This is in line with the previous analysis of persistent magnetic excitations in Dy decaying within a few ns.[32]

We use energy transfer times that are in agreement with recent ultrafast demagnetization studies in AFM-dysprosium[38] and holmium.[39] The resonant diffraction studies independently report both a subpicosecond demagnetization, which is attributed to electron-spin coupling and a second demagnetization timescale on the order of 15 ps, which is attributed to phonon-spin coupling. Systematic modeling of our data yields that both timescales are necessary to capture the early time strain response of the transducer. A substantial fraction of the magnetic stress needs to be present within the first ps to balance the otherwise expansive electron-phonon response. However, our modeling shows that not all energy is instantaneously transferred to magnetic excitations since the resulting stress would drive a contraction that is significantly faster than the observed response.

In addition to these two intrinsic demagnetization timescales, we observe a contraction of the Dy transducer for larger pump-probe delays. This effect is most pronounced at high excitation densities and T close to and above $T_{\text{Néel}}$. Our simulations show that this can be rationalized by two energy transport effects within the inhomogeneously excited heterostructure. First there is thermal diffusion of phonon excitations within the inhomogeneously heated Dy. This transports energy from the near surface region where spin-excitations are saturated into the depth of the transducer, where the spin energy density is below the saturation threshold. The coupling of energy from phonons to the spins decreases the expansive phonon stress and increases the contractive magnetic stress contribution. The transport of phonon heat out of the Dy layer into the Nb reduces the expansion further. This allows us to model the spatial spin-stress profile. Although the quantitative link between the magnetic stress and the sublattice magnetization in the time-domain is largely unexplored, we can argue qualitatively that the saturation of the spin-stress will be linked to regions of complete demagnetization. For static thermal expansion experiments, it has been reported that the magnetostrictive stress is proportional to the square of the sublattice-magnetization.[43,72] Thus, we can speculate that the modeled magnetic stress profile is qualitatively similar to the demagnetization profile. More precisely, we assume that the observed magnetic stress profile reflects the demagnetization of the 4f-electrons of the heavy rare earth. These anisotropic orbitals carry large, localized magnetic moments that distinguish rare earth materials from 3d-transition metals that exhibit by far smaller magnetostriction.

The color code of Fig. 6 provides a qualitative overview over the temperature dependent stress contributions that we focus on in the current report. For a more quantitative comparison, we refer the reader to Sec. S5 of the supplementary material. There we show outlines of the modeled spatial stress profiles at 6 ps, 45 ps, and 180 ps alongside the time dependence of the modeled stress contributions for both the T- and F-dependent experiments.

Our current modeling provides a plausible scenario for the driving stress. A satisfactory agreement between the data and modeling definitively requires three energy transfer timescales to the spin system. The first energy transfer to the magnetic excitations has to rise equally fast or faster than the electron-phonon stress to cancel the expansive electron-phonon stress in the first few ps. The second timescale has to be in the range of 10–20 ps to model the contraction of the Dy layer and the unipolar expansion wave observed in the Nb layer.
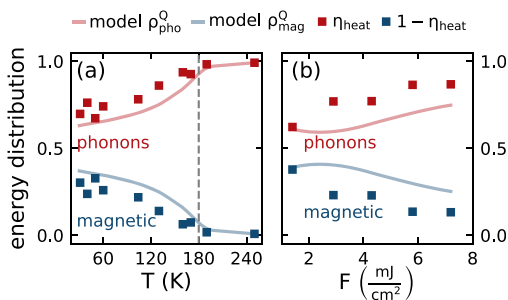
FIG. 7. Estimated energy distribution between magnetic- and phonon excitations within the rare earth transducer for the presented temperature- (a) and excitation energy dependent (b) measurements at fixed $F = 7.2$ mJ/cm² and $T = 130$ K, respectively. Data points correspond to the fitted amplitude $A(T, F)$ of the thermal expansion $A(T,F)\eta_{\text{heat}}(t)$ of the Nb detection layer (shaded areas in Figs. 3 and 4), normalized to the PM phase value $A(250 \text{ K})$. Solid lines represent the energy distribution at the last time step $t = 180$ ps of the spatiotemporal stress–strain simulation. The fraction of deposited energy in the spin system decreases when approaching $T_{\text{Néel}}$ from low temperatures as well as for higher fluences.

The third process on a timescale larger than 40 ps is given by thermal transport within the Dy layer. This is the simplest possible temporal behavior of the stress that is consistent with our data.

So far, we have also treated the FM and AFM response equally although there exists an additional first order phase-transition in the low temperature phase and the demagnetization of the ferromagnetic phase was reported to occur slower than in the antiferromagnetic Dy.[38] We attribute the reasonable agreement for the FM phase at $T = 31$ K to the use of a large excitation energy density that drives mainly spin excitations with the calibrated Grüneisen constant of the AFM phase. These magnetic-excitations seem to dominate the magnetostrictive response at high excitation energy densities compared to the potential contribution of the latent heat that is necessary to undergo the metamagnetic FM-AFM transition. A detailed study of the magnetostriction at the FM-AFM transition is deferred to future investigations.

V. CONCLUSION

The presented picosecond strain dynamics in a laser-excited heterostructure containing a rare-earth transducer shows strong magnetic contributions to the lattice response. Both the picosecond strain pulse and the thermal transport are affected by energy transfer processes to magnetic excitations. The transient strain observed in a buried detection layer directly shows the saturation of the contractive magnetic stress component, which occurs when an increasing fraction of the Dy layer is excited across its magnetic phase transition. The spatially varying sign of the stress within the Dy layer triggers unconventional strain pulses, which exhibit a leading expansive part in front of the conventional bipolar strain pulse. Our modeling yields an estimate for the time- and space-dependent profile of the additional magnetic stress contribution to the lattice dynamics. The magnetic excitations act as a saturable heat reservoir, which stores a significant fraction of the excitation energy and exerts a contractive stress that dominates over the phonon contribution. We expect this finding to be generic for the magnetic phase in the class of heavy rare earth materials in the periodic table of elements $_{64}$Gd–$_{69}$Tm. The observed energy transfer timescales are in agreement with recent demagnetization experiments. This indicates that the magnetostrictive response can be used to probe the time-dependent evolution of the sublattice magnetization.

Our investigation demonstrates the capabilities of UXRD experiments in a transducer-detector geometry to observe non-trivial spatial stress profiles. We emphasize that extracting the stress profile in the transducer by UXRD from an adjacent crystalline detection layer can be applied to investigate non-crystalline transducer films. The combination of picosecond acoustics experiment, UXRD detection, and elastic modeling can be used to study the strain generation by energy transfer to other degrees of freedom. This comprises, in particular, phase-transition effects such as studies of ferroelectric and charge order transition as well as investigations of other magnetostrictive materials, which may hold hitherto unknown functionalities.

SUPPLEMENTARY MATERIAL

See the supplementary material for a complete overview of the UXRD results (Sec. S1) and simulations (Sec. S2) that illustrate the effect of the stress rise time, stress profile length, and the detection layer thickness for the strain response in a simplified transducer-detector heterostructure. Section S3 provides an overview of the mathematical relations relevant for the strain simulation and a list of the relevant thermophysical material properties, including a description of the Poisson correction factor for the Grüneisen constant. Section S4 shows a detailed plot of the spatiotemporal stress contributions for the T- and F-dependent modeling that comprises stress-profiles at selected times and the time dependent average stress within the Dy layer.

REFERENCES

[1]C. Thomsen, H. T. Grahn, H. J. Maris, and J. Tauc, "Surface generation and detection of phonons by picosecond light pulses," Phys. Rev. B **34**, 4129–4138 (1986).

[2]O. Matsuda, M. C. Larciprete, R. Li Voti, and O. B. Wright, "Fundamentals of picosecond laser ultrasonics," Ultrasonics **56**, 3–20 (2015).

[3]M. Nicoul, U. Shymanovich, A. Tarasevitch, D. von der Linde, and K. Sokolowski-Tinten, "Picosecond acoustic response of a laser-heated gold-film studied with time-resolved x-ray diffraction," Appl. Phys. Lett. **98**, 191902 (2011).

[4]O. B. Wright, "Ultrafast nonequilibrium stress generation in gold and silver," Phys. Rev. B **49**, 9985–9988 (1994).

[5]T. Saito, O. Matsuda, and O. B. Wright, "Picosecond acoustic phonon pulse generation in nickel and chromium," Phys. Rev. B **67**, 205421 (2003).

[6]G. Tas and H. J. Maris, "Electron diffusion in metals studied by picosecond ultrasonics," Phys. Rev. B **49**, 15046–15054 (1994).

[7]M. Lejman, V. Shalagatskyi, O. Kovalenko, T. Pezeril, V. V. Temnov, and P. Ruello, "Ultrafast optical detection of coherent acoustic phonons emission driven by superdiffusive hot electrons," J. Opt. Soc. Am. B **31**, 282 (2014).

[8]O. B. Wright, O. Matsuda, B. Perrin, and V. E. Gusev, "Ultrafast carrier diffusion in gallium arsenide probed with picosecond acoustic pulses," Phys. Rev. B **64**, 3–6 (2001).

[9]E. S. Young, A. V. Akimov, R. P. Campion, A. J. Kent, and V. Gusev, "Picosecond strain pulses generated by a supersonically expanding electron-hole plasma in GaAs," Phys. Rev. B **86**, 1–13 (2012).

[10]O. B. Wright and V. E. Gusev, "Acoustic generation in crystalline silicon with femtosecond optical pulses," Appl. Phys. Lett. **66**, 1190–1192 (1995).

[11]P. Ruello and V. E. Gusev, "Physical mechanisms of coherent acoustic phonons generation by ultrafast laser action," Ultrasonics **56**, 21–35 (2015).

[12]O. Kovalenko, T. Pezeril, and V. V. Temnov, "New concept for magnetization switching by ultrafast acoustic pulses," Phys. Rev. Lett. **110**, 266602 (2013).

[13]W. Li, B. Buford, A. Jander, and P. Dhagat, "Acoustically assisted magnetic recording: A new paradigm in magnetic data storage," IEEE Trans. Magn. **50**, 37–40 (2014).

[14]L. Thevenard, I. S. Camara, S. Majrab, M. Bernard, P. Rovillain, A. Lemaître, C. Gourdon, and J.-Y. Duquesne, "Precessional magnetization switching by a surface acoustic wave," Phys. Rev. B **93**, 134430 (2016).

[15]I. S. Camara, J. Y. Duquesne, A. Lemaître, C. Gourdon, and L. Thevenard, "Field-free magnetization switching by an acoustic wave," Phys. Rev. Appl. **11**, 1 (2019).

[16]J.-W. Kim, M. Vomir, and J.-Y. Bigot, "Ultrafast magnetoacoustics in nickel films," Phys. Rev. Lett. **109**, 166601 (2012).

[17]J. W. Kim, M. Vomir, and J. Y. Bigot, "Controlling the spins angular momentum in ferromagnets with sequences of picosecond acoustic pulses," Sci. Rep. **5**, 1–7 (2014).

[18] A. V. Scherbakov, A. S. Salasyuk, A. V. Akimov, X. Liu, M. Bombeck, C. Brüggemann, D. R. Yakovlev, V. F. Sapega, J. K. Furdyna, and M. Bayer, "Coherent magnetization precession in ferromagnetic (Ga,Mn)As induced by picosecond acoustic pulses," Phys. Rev. Lett. **105**, 1–4 (2010).

[19] M. Bombeck, J. V. Jäger, A. V. Scherbakov, T. Linnik, D. R. Yakovlev, X. Liu, J. K. Furdyna, A. V. Akimov, and M. Bayer, "Magnetization precession induced by quasitransverse picosecond strain pulses in (311) ferromagnetic (Ga,Mn)As," Phys. Rev. B **87**, 1–5 (2013).

[20] J. V. Jäger, A. V. Scherbakov, T. L. Linnik, D. R. Yakovlev, M. Wang, P. Wadley, V. Holy, S. A. Cavill, A. V. Akimov, A. W. Rushforth, and M. Bayer, "Picosecond inverse magnetostriction in galfenol thin films," Appl. Phys. Lett. **103**, 032409 (2013).

[21] Y. Hashimoto, D. Bossini, T. H. Johansen, E. Saitoh, A. Kirilyuk, and T. Rasing, "Frequency and wavenumber selective excitation of spin waves through coherent energy transfer from elastic waves," Phys. Rev. B **97**, 1–5 (2018); arXiv:1710.08087.

[22] M. Deb, E. Popova, M. Hehn, N. Keller, S. Mangin, and G. Malinowski, "Picosecond acoustic-excitation-driven ultrafast magnetization dynamics in dielectric Bi-substituted yttrium iron garnet," Phys. Rev. B **98**, 174407 (2018); arXiv:1807.00610.

[23] S. O. Mariager, F. Pressacco, G. Ingold, A. Caviezel, E. Möhr-Vorobeva, P. Beaud, S. L. Johnson, C. J. Milne, E. Mancini, S. Moyerman, E. E. Fullerton, R. Feidenhans'l, C. H. Back, and C. Quitmann, "Structural and magnetic dynamics of a laser induced phase transition in FeRh," Phys. Rev. Lett. **108**, 87201 (2012).

[24] F. Quirin, M. Vattilana, U. Shymanovich, A.-E. El-Kamhawy, A. Tarasevitch, J. Hohlfeld, D. von der Linde, and K. Sokolowski-Tinten, "Structural dynamics in FeRh during a laser-induced metamagnetic phase transition," Phys. Rev. B **85**, 20103 (2012).

[25] A. H. Reid, X. Shen, P. Maldonado, T. Chase, E. Jal, P. W. Granitzka, K. Carva, R. K. Li, J. Li, L. Wu, T. Vecchione, T. Liu, Z. Chen, D. J. Higley, N. Hartmann, R. Coffee, J. Wu, G. L. Dakovski, W. F. Schlotter, H. Ohldag, Y. K. Takahashi, V. Mehta, O. Hellwig, A. Fry, Y. Zhu, J. Cao, E. E. Fullerton, J. Stöhr, P. M. Oppeneer, X. J. Wang, and H. A. Dürr, "Beyond a phenomenological description of magnetostriction," Nat. Commun. **9**, 388 (2018).

[26] A. von Reppert, L. Willig, J.-E. Pudell, M. Rössle, W. Leitenberger, M. Herzog, F. Ganss, O. Hellwig, and M. Bargheer, "Ultrafast laser generated strain in granular and continuous FePt thin films," Appl. Phys. Lett. **113**, 123101 (2018).

[27] C. von Korff Schmising, A. Harpoeth, N. Zhavoronkov, Z. Ansari, C. Aku-Leh, M. Woerner, T. Elsaesser, M. Bargheer, M. Schmidbauer, I. Vrejoiu, D. Hesse, and M. Alexe, "Ultrafast magnetostriction and phonon-mediated stress in a photoexcited ferromagnet," Phys. Rev. B **78**, 60404 (2008).

[28] E. D. T. De Lacheisserie, *Magnetostriction: Theory and Applications of Magnetoelasticity* (CRC, 1993).

[29] F. Darnell, "Temperature dependence of lattice parameters for Gd, Dy, and Ho," Phys. Rev. **130**, 1825–1828 (1963).

[30] A. Koc, M. Reinhardt, A. von Reppert, M. Rössle, W. Leitenberger, M. Gleich, M. Weinelt, F. Zamponi, and M. Bargheer, "Grueneisen-approach for the experimental determination of transient spin and phonon energies from ultrafast x-ray diffraction data: Gadolinium," J. Phys.: Condens. Matter **29**, 264001 (2017).

[31] J. Pudell, A. von Reppert, D. Schick, F. Zamponi, M. Rössle, M. Herzog, H. Zabel, and M. Bargheer, "Ultrafast negative thermal expansion driven by spin disorder," Phys. Rev. B **99**, 094304 (2019); arXiv:pudell2019a.

[32] A. von Reppert, J. Pudell, A. Koc, M. Reinhardt, W. Leitenberger, K. Dumesnil, F. Zamponi, and M. Bargheer, "Persistent nonequilibrium dynamics of the thermal energies in the spin and phonon systems of an antiferromagnet," Struct. Dyn. **3**, 054302 (2016).

[33] A. Koc, M. Reinhardt, A. von Reppert, M. Rössle, W. Leitenberger, K. Dumesnil, P. Gaal, F. Zamponi, and M. Bargheer, "Ultrafast x-ray diffraction thermometry measures the influence of spin excitations on the heat transport through nanolayers," Phys. Rev. B **96**, 014306 (2017); arXiv:1701.05918.

[34] J. Pudell, A. Maznev, M. Herzog, M. Kronseder, C. Back, G. Malinowski, A. von Reppert, and M. Bargheer, "Layer specific observation of slow thermal equilibration in ultrathin metallic nanostructures by femtosecond x-ray diffraction," Nat. Commun. **9**, 3335 (2018); arXiv:1803.04034.

[35] S. P. Zeuschner, T. Parpiiev, T. Pezeril, A. Hillion, K. Dumesnil, A. Anane, J. Pudell, L. Willig, M. Rössle, M. Herzog, A. von Reppert, and M. Bargheer, "Tracking picosecond strain pulses in heterostructures that exhibit giant magnetostriction," Struct. Dyn. **6**, 024302 (2019).

[36] Y. Gao, Z. Chen, Z. Bond, A. Loether, L. E. Howard, S. LeMar, S. White, A. Watts, B. C. Walker, and M. F. DeCamp, "Reconstructing longitudinal strain pulses using time-resolved x-ray diffraction," Phys. Rev. B **88**, 525A (2013).

[37] A. Eschenlohr, M. Sultan, A. Melnikov, N. Bergeard, J. Wieczorek, T. Kachel, C. Stamm, and U. Bovensiepen, "Role of spin-lattice coupling in the ultrafast demagnetization of gd 1- x tb x alloys," Phys. Rev. B **89**, 214423 (2014).

[38] N. Thielemann-Kühn, D. Schick, N. Pontius, C. Trabant, R. Mitzner, K. Holldack, H. Zabel, A. Föhlisch, and C. Schüßler-Langeheine, "Ultrafast and energy-efficient quenching of spin order: antiferromagnetism beats ferromagnetism," Phys. Rev. Lett. **119**, 197202 (2017); arXiv:1703.03689.

[39] L. Rettig, C. Dornes, N. Thielemann-Kühn, N. Pontius, H. Zabel, D. L. Schlagel, T. A. Lograsso, M. Chollet, A. Robert, M. Sikorski, S. Song, J. M. Glownia, C. Schüßler-Langeheine, S. L. Johnson, and U. Staub, "Itinerant and localized magnetization dynamics in antiferromagnetic Ho," Phys. Rev. Lett. **116**, 257202 (2016).

[40] K. Dumesnil, C. Dufour, P. Mangin, G. Marchal, and M. Hennion, "Magnetic structure of dysprosium in epitaxial Dy films and in Dy/Er superlattices," Phys. Rev. B **54**, 6407–6420 (1996).

[41] D. Schick, M. Herzog, A. Bojahr, W. Leitenberger, A. Hertwig, R. Shayduk, and M. Bargheer, "Ultrafast lattice response of photoexcited thin films studied by x-ray diffraction," Struct. Dyn. **1**, 064501 (2014).

[42] D. Schick, R. Shayduk, A. Bojahr, M. Herzog, C. von Korff Schmising, P. Gaal, and M. Bargheer, "Ultrafast reciprocal-space mapping with a convergent beam," J. Appl. Crystallogr. **46**, 1372–1377 (2013).

[43] F. J. Darnell and E. P. Moore, "Crystal structure of dysprosium at low temperatures," J. Appl. Phys. **34**, 1337–1338 (1963).

[44] V. Pecharsky, K. Gschneidner, and D. Fort, "Superheating and other unusual observations regarding the first order phase transition in Dy," Scr. Mater. **35**, 843–848 (1996).

[45] S. Legvold, J. Alstad, and J. Rhyne, "Giant magnetostriction in dysprosium and holmium single crystals," Phys. Rev. Lett. **10**, 509–511 (1963).

[46] W. C. Koehler, "Magnetic properties of rare earth metals and alloys," J. Appl. Phys. **36**, 1078–1087 (1965).

[47] R. Elliott, *Magnetic Properties of Rare Earth Metals* (Springer Science & Business Media, 1972).

[48] J. Jensen and A. R. Mackintosh, *Rare Earth Magnetism* (Clarendon, Oxford, 1991).

[49] E. R. Callen and H. B. Callen, "Static magnetoelastic coupling in cubic crystals," Phys. Rev. **129**, 578–593 (1963).

[50] E. Callen and H. B. Callen, "Magnetostriction, forced magnetostriction, and anomalous thermal expansion in ferromagnets," Phys. Rev. **139**, A455–A471 (1965).

[51] M. Doerr, M. Rotter, and A. Lindbaum, "Magnetostriction in rare-earth based antiferromagnets," Adv. Phys. **54**, 1–66 (2005).

[52] L. Benito, J. Arnaudas, M. Ciria, C. de La Fuente, and A. del Moral, "The magnetostriction of Tb, Dy and Ho revisited," J. Phys.: Condens. Matter **16**, 7151 (2004).

[53] W. Nolting and A. Ramakanth, *Quantum Theory of Magnetism* (Springer Science & Business Media, 2009).

[54] E. Grüneisen, "Theorie des festen zustandes einatomiger elemente," Ann. Phys. **344**, 257–306 (1912).

[55] T. Barron, J. Collins, and G. K. White, "Thermal expansion of solids at low temperatures," Adv. Phys. **29**, 609–730 (1980).

[56] J. Chen, L. Hu, J. Deng, and X. Xing, "Negative thermal expansion in functional materials: Controllable thermal expansion by chemical modifications," Chem. Soc. Rev. **44**, 3522–3567 (2015); arXiv:1612.08814.

[57] M. T. Dove and H. Fang, "Negative thermal expansion and associated anomalous physical properties: Review of the lattice dynamics theoretical foundation," Rep. Prog. Phys. **79**, 066503 (2016).

[58] G. K. White, "Phase transitions and the thermal expansion of holmium," J. Phys.: Condens. Matter **1**, 6987–6992 (1989).

[59] L. D. Jennings, R. E. Miller, and F. H. Spedding, "Lattice heat capacity of the rare earths. Heat capacities of yttrium and lutetium from 15–350K," J. Chem. Phys. **33**, 1849–1852 (1960).

[60] W. M. Haynes, *CRC Handbook of Chemistry and Physics*, CRC Handbook of Chemistry and Physics, 93rd ed. (Taylor & Francis, 2012).

[61] T. Barron, "Grüneisen parameters for the equation of state of solids," Ann. Phys. **1**, 77–90 (1957).

[62] J. J. Tonnies, K. A. Gschneidner, and F. H. Spedding, "Elastic moduli and thermal expansion of lutetium single crystals from 4.2 to 300k," J. Appl. Phys. **42**, 3275–3283 (1971).

[63] S. B. Palmer and E. W. Lee, "The elastic constants of dysprosium and holmium," Proc. R. Soc. A **327**, 519–543 (1972).

[64] D. Schick, A. Bojahr, M. Herzog, C. v K. Schmising, R. Shayduk, W. Leitenberger, P. Gaal, and M. Bargheer, "Normalization schemes for ultrafast x-ray diffraction using a table-top laser-driven plasma source," Rev. Sci. Instrum. **83**, 025104 (2012).

[65] M. Bargheer, N. Zhavoronkov, R. Bruch, H. Legall, H. Stiel, M. Woerner, and T. Elsaesser, "Comparison of focusing optics for femtosecond x-ray diffraction," Appl. Phys. B: Lasers Opt. **80**, 715–719 (2005).

[66] C. Rose-Petruck, R. Jimenez, T. Guo, A. Cavalleri, C. W. Siders, F. Rksi, *et al.*, "Picosecond -milliångström lattice dynamics measured by ultrafast X-ray diffraction," Nature **398**(6725), 310–312 (1999).

[67] E. Beaurepaire, J.-C. Merle, A. Daunois, and J.-Y. Bigot, "Ultrafast spin dynamics in ferromagnetic nickel," Phys. Rev. Lett. **76**, 4250–4253 (1996).

[68] B. Koopmans, G. Malinowski, F. Dalla Longa, D. Steiauf, M. Fähnle, T. Roth, M. Cinchetti, and M. Aeschlimann, "Explaining the paradoxical diversity of ultrafast laser-induced demagnetization," Nat. Mater. **9**, 259–265 (2010).

[69] B. Frietsch, J. Bowlan, R. Carley, M. Teichmann, S. Wienholdt, D. Hinzke, U. Nowak, K. Carva, P. M. Oppeneer, and M. Weinelt, "Disparate ultrafast dynamics of itinerant and localized magnetic moments in gadolinium metal," Nat. Commun. **6**, 8262 (2015).

[70] K. Bobowski, M. Gleich, N. Pontius, C. Schüßler-Langeheine, C. Trabant, M. Wietstruk, B. Frietsch, and M. Weinelt, "Influence of the pump pulse wavelength on the ultrafast demagnetization of Gd(0 0 0 1) thin films," J. Phys. Condens. Matter **29**, 234003 (2017).

[71] D. Schick, A. Bojahr, M. Herzog, R. Shayduk, K. C. von Schmising, and M. Bargheer, "udkm1Dsim—A simulation toolkit for 1D ultrafast dynamics in condensed matter," Comput. Phys. Commun. **185**, 651 (2014).

[72] C. Kittel, "Model of exchange-inversion magnetization," Phys. Rev. **120**, 335–342 (1960).

120

Article VII – Supplemental Material

Supplementary material to: Unconventional picosecond strain pulses resulting from the saturation of magnetic stress within a photoexcited rare earth layer

A. von Reppert,[1] M. Mattern,[1] J.-E. Pudell,[1,2] S. P. Zeuschner,[1,2] K. Dumesnil,[3] and M. Bargheer[1,2,*]

[1]*Institut für Physik & Astronomie, Universität Potsdam,*
Karl-Liebknecht-Str. 24-25, 14476 Potsdam, Germany
[2]*Helmholtz Zentrum Berlin, Albert-Einstein-Str. 15, 12489 Berlin, Germany*
[3]*Institut Jean Lamour (UMR CNRS 7198), Université Lorraine, 54000 Nancy, France*
(Dated: February 24, 2020)

S1. OVERVIEW OF EXPERIMENTAL RESULTS

In Fig. S1 we present a complete overview of the temperature and excitation energy dependent UXRD measurements from which a selection is shown in Fig. 3 and Fig. 4 of the main manuscript. The data are presented without offset to allow for direct comparison. The insets (Fig. S1(c) and Fig. S1(f)) show the Nb detection layer strain averaged for over $t > 200\,\mathrm{ps}$. This model-independent measure for the thermal expansion indicates the reduced energy transport from the Dy film to the Nb detection layer at $T < T_{\mathrm{Néel}} = 180\,\mathrm{K}$ (see S1(c)). The saturation of the energy transfer to the finite energy reservoir of magnetic excitations is heralded by the non-linear fluence dependence that is pointed out by the grey dashed line in Fig. S1(f) and further discussed in the main text.
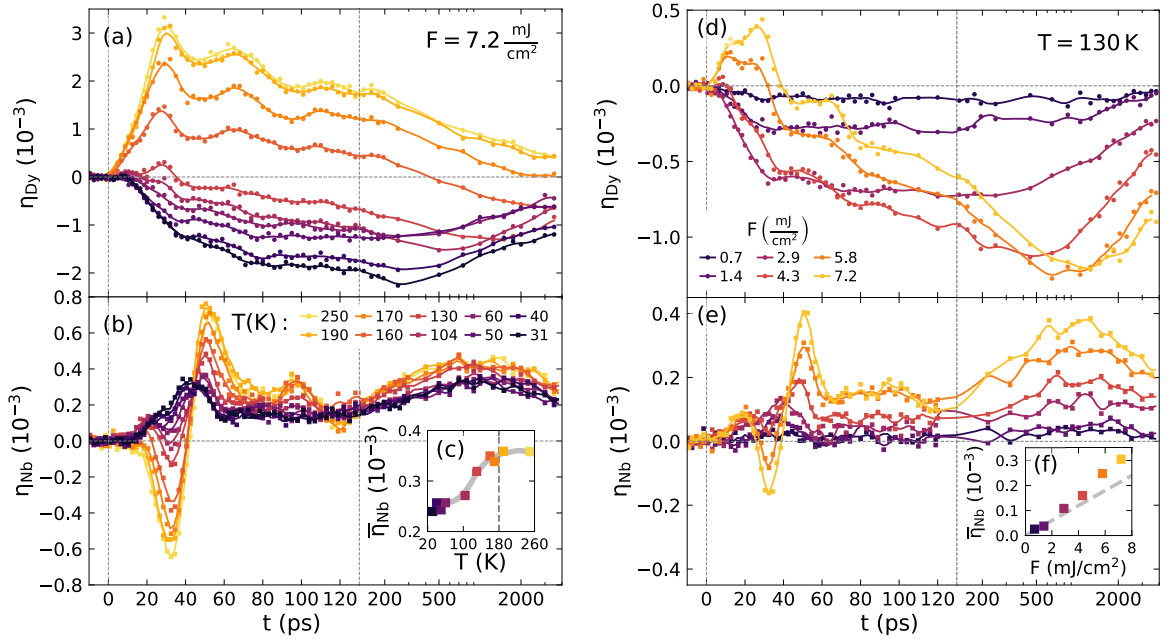
FIG. S1. **Overview of experimental results:** Temperature-dependent strain response η of the Dy transducer (a) and the Nb detection layer (b) for a fixed excitation fluence of $F = 7.2\,\mathrm{mJ/cm^2}$. The linear to logarithmic axis break at 130 ps (vertical, grey, dashed line) allows the simultaneous depiction of the changes in the picosecond strain pulse and the nanosecond thermal expansion response. Inset (c) shows the average thermal expansion of the Nb detection layer from 200 ps to 4000 ps. Solid lines serve as guide to the eye. The experimental results for varying the excitation fluence at a fixed start temperature $T = 130\,\mathrm{K}$ are depicted in the same way in (d)–(f). The dashed line in (f) highlights the small non-linear increase of the thermal expansion of the Nb detection layer.

* bargheer@uni-potsdam.de; http://www.udkm.physik.uni-potsdam.de

S2. SIMPLIFIED MODEL SIMULATIONS

In this section we discuss the modeled strain response for an idealized transducer-detection layer sample that is depicted in Fig. S2(a). We present the characteristics of the picosecond strain response that relate to the rise time τ and the profile length ξ of the driving stress as well as the layer thicknesses d_1 and d_2. We compare the simulations to selected experimental data to illustrate the influence of these parameters on the expected picosecond strain response, as it is briefly discussed in the main text.
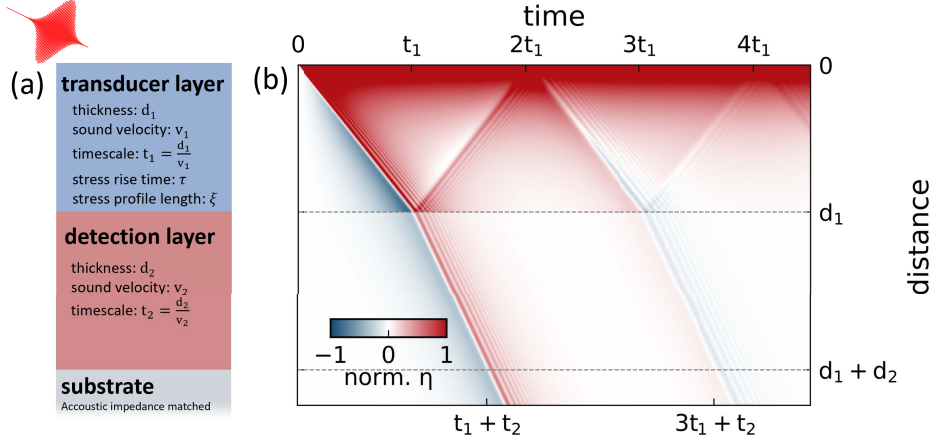

FIG. S2. **Strain response of a simplified transducer-detection layer system:** (a) Schematic visualization of the structure, which consists of an absorbing transducer ($d_1 \approx 95$ nm, $v_1 \approx 3$ nm/ps) adjacent to a non-absorbing layer ($d_2 \approx 103$ nm, $v_2 \approx 5$ nm/ps on top of a semi-infinite substrate with good acoustic impedance matching to the film. (b) A typical spatio-temporal strain $\eta(z,t)$ profile that results from an instantaneous ($\tau = 0$, expansive stress ($\sigma > 0$) with an exponentially decaying profile ($\xi = 25$ nm) within the transducer layer. Tick marks indicate significant points in time that result from the characteristic timescales $t_1 = d_1/v_1$ and $t_2 = d_2/v_2$. In the following we discuss the strain response averaged over the transducer- (η_1) and detection-layer (η_2).

The presented model simulations illustrate the influence of the driving stress characteristics τ, ξ on the strain response. We deliberately omit the complications that arise from the multiple reflections at additional interfaces, thermal transport and the sensitivity function for hard x-ray diffraction experiments. The presented simulations are obtained using the phonon class of the modular UDKM1DSIM[1] MATLAB library that simulates the strain response of a linear chain of masses and springs for different idealized scenarios for the driving stress sigma $\sigma(z,t)$ with unit cell resolution. The mechanical properties of the transducer and detection layer system have been chosen to match our sample structure where the Y interlayers are replaced by Dy. We emphasize that the observed response can be generalized to any two-layer system by introducing the natural timescales $t_1 = d_1/v_1 \approx 30.6$ ps and $t_2 = d_2/v_2 \approx 20.2$ ps that it takes to propagate strain through the layers at the speed of sound.

A. Signatures of the stress rise time

Fig. S3 shows the effect of different rise times τ for the driving stress $\sigma(t) = \sigma_\infty(1 - \exp(-t/\tau))$ on the average strain response of the transducer layer $\eta_1(t)$ and detection layer $\eta_2(t)$. The spatial profile is fixed throughout this simulation series to be an exponential stress profile $\sigma(z) = \sigma_{max}\exp(-z/\xi)$ with a decay-length $\xi = 25\,\mathrm{nm}$. The direct comparison between the expansive stress (Fig. S3(a)–(d)) and contractive stress (Fig. S3(e)–(h)) shows that the simulated strain results for both the transducer and detection layer are identical except for a change of sign. We relate the simulation of η_1 and η_2 to the two representative data sets at 250 K and 31 K for η_{Dy} and η_{Nb} that are shown in Fig. 3 of the main manuscript.
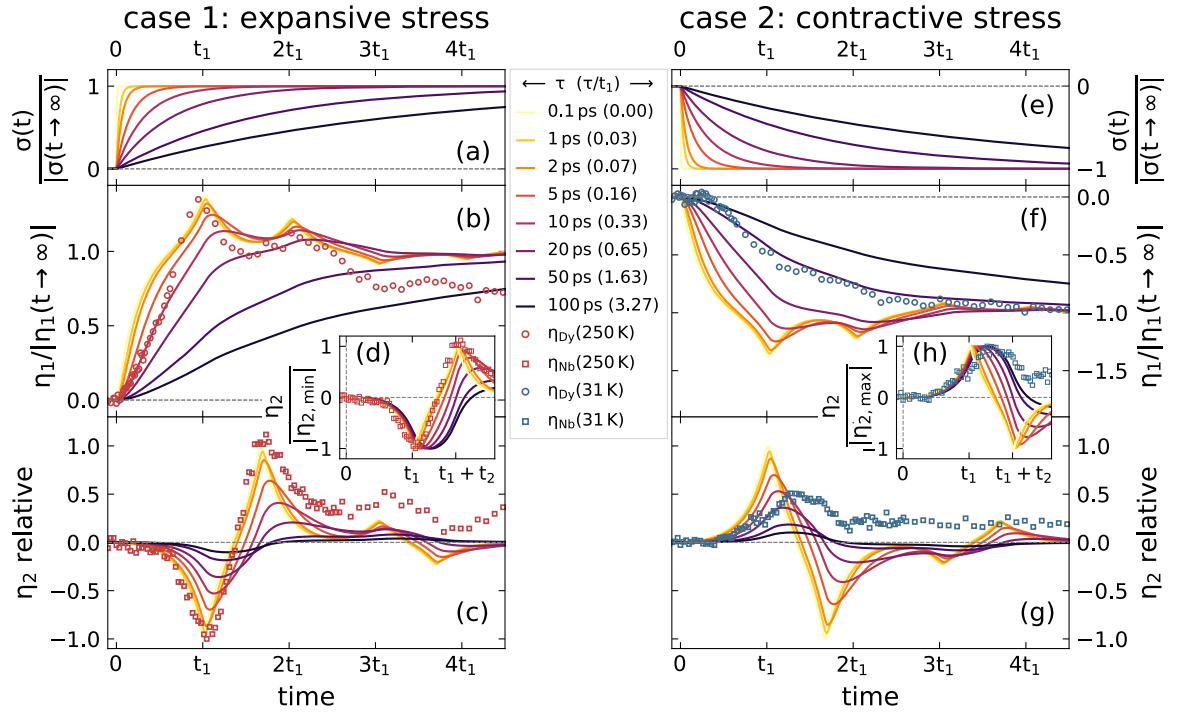

FIG. S3. **Effects of the stress rise time τ on the picosecond strain response:** We compare the cases of an expansive stress (a)–(d) and a contractive stress (e)–(g) within the transducer. The top panels (a) and (e) depict the time-dependence of the stress. The middle panels (b) and (f) show the simulated average strain in the transducer layer normalized to the value attained for large delays. The bottom panels (c) and (g) display the corresponding average strain in the buried detection layer relative to the maximum strain amplitude for the fast rising stress. The insets (d) and (h) compare the shape of the simulated curves by normalizing to the maximum contraction and expansion respectively. The experimentally observed strain responses for $T = 250\,\mathrm{K}$ is best described by a fast rising expansive stress whereas the sample response at 31 K resembles that of a slowly contracting transducer.

A qualitative comparison with the shape of the experimental results shows that the response within the paramagnetic phase of Dy ($T = 250\,\mathrm{K}$, $F = 7.2\,\mathrm{mJ/cm^2}$) can be rationalized by fast rising expansive stress $\tau < 5\,\mathrm{ps}$ that launches a pronounced bipolar strain pulse into the adjacent detection layer. Deviations of the simulated η_1 and $\eta_{Dy}(250\,\mathrm{K})$ for small delays $t < t_1$ can be rationalized by the neglected Y capping layer of the real sample structure. For $t > t_1$ η_{Dy} exhibits a decay that is not reproduced in the simulations since we neglect thermal transport to adjacent layers.

The experimentally observed contraction for the magnetically ordered phase of Dy ($T = 31\,\mathrm{K}$ $F = 7.2\,\mathrm{mJ/cm^2}$) shows the best agreement with a slowly rising total stress that increases with $\tau > 40\,\mathrm{ps}$. The reduced amplitude and the nearly uni-polar shape of the strain pulse launched into the detection layer is incompatible with a fast rising total stress. The absence of pronounced peaks in the slowly rising contraction of the Dy transducer at t_1 and t_2 corroborates this finding.

This brief, qualitative analysis of the stress rise times provides a first rough overview over the signal interpretation. To quantitatively capture the measurement results we require a more complex model that is outlined in the main manuscript.

B.   Signatures of the stress profile length and layer thicknesses

To calibrate the expansive electron-phonon stress and the layer thicknesses we employ the results of the strain response of non-magnetic heterostructure in the PM phase of Dy at 250 K. Fig. S4 illustrates the influence of the spatial shape of the stress profile $\sigma(z)$ that is parametrized as $\sigma(z) = \sigma_{max} \exp(-z/\xi)$ and the thickness of the detection layer d_2. Compared to the simplified simulation series one finds that the measured response in the PM phase of Dy is best described by $\xi \approx 25$ nm and $d_2 \approx 100$ nm. The full simulation of the PM phase presented in Fig. 3 of the main manuscript includes the additional Y-layers, heat diffusion and a simulation of the X-ray diffraction signal that are omitted here for clarity.
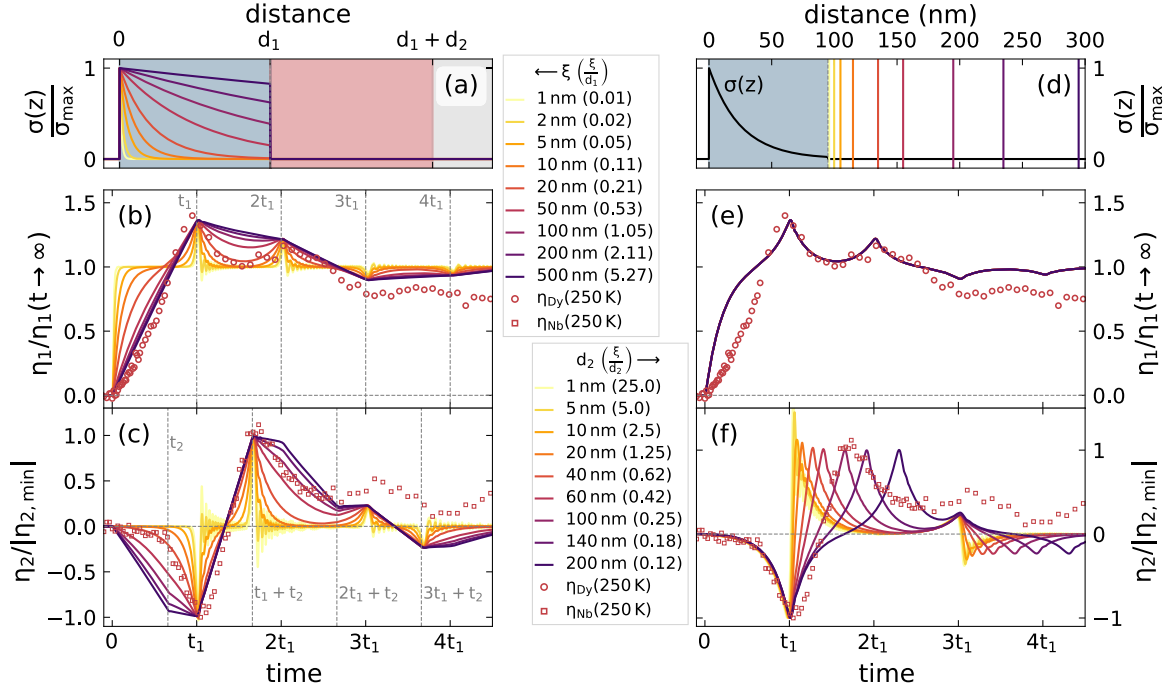
FIG. S4. **Influence of the stress profile $\sigma(z)$ and detection layer thickness d_2 on the observed strain response η:** (a)–(c) Simulated dependence of strain in the bilayer on the exponential stress profile length ξ for an instantaneous stress $\tau \rightarrow 0$. Panel (a) depicts the different stress profiles within the transducer layer. Panels (b) and (c) show the temporal shape of the average transducer and detection layer strain respectively. Dashed lines and tick marks relate characteristic strain signatures to the natural timescales t_1 and t_2 of the sample. Panels (d)–(f) show the influence of the detection layer thickness d_2 on the strain signal. Colored lines in (d) indicated the different detection layer thicknesses in relation to the stress-profile within the transducer. While the transducer strain response shown in (e) is not affected by d_2, the timing of the second part of the bipolar strain pulse shifts.

S3. MODELING DETAILS

In subsection S3 A we provide an overview over the implementation and mathematical relations of the simulation that are described textually in the main manuscript. In subsection S3 B we provide the relevant thermophysical parameters for the materials within the heterostructure. In subsection S3 C we discuss a Gedankenexperiment that illustrates the effect of different boundary conditions on the observed strain for equilibrium heating and ultrafast laser heating of thin film samples.

A. Sequence of the simulation steps

For the modeling we use the modular UDKM1DSIM toolbox package that developed by Schick et al.[1]. We only introduce an additional magnetic stress contribution (a force term in the linear chain model for the strain evolution) according to the linear dependence of stress and energy density in the magnetic subsystem. In Fig S5 a schematic block diagram that summarizes the simulation steps for the PM and AFM simulations together with the mathematical relations for the strain calculation provided in the following paragraphs.

The complexity of the required model leads to the fact that there is no single analytical equation but rather a set of thermophysical - relations that we evaluate numerically on a unit-cell grid. We discuss first the central equations for the modeling of the PM phase response and subsequently for the AFM phase.

Paramagnetic phase   Antiferro- / Ferromagnetic phase
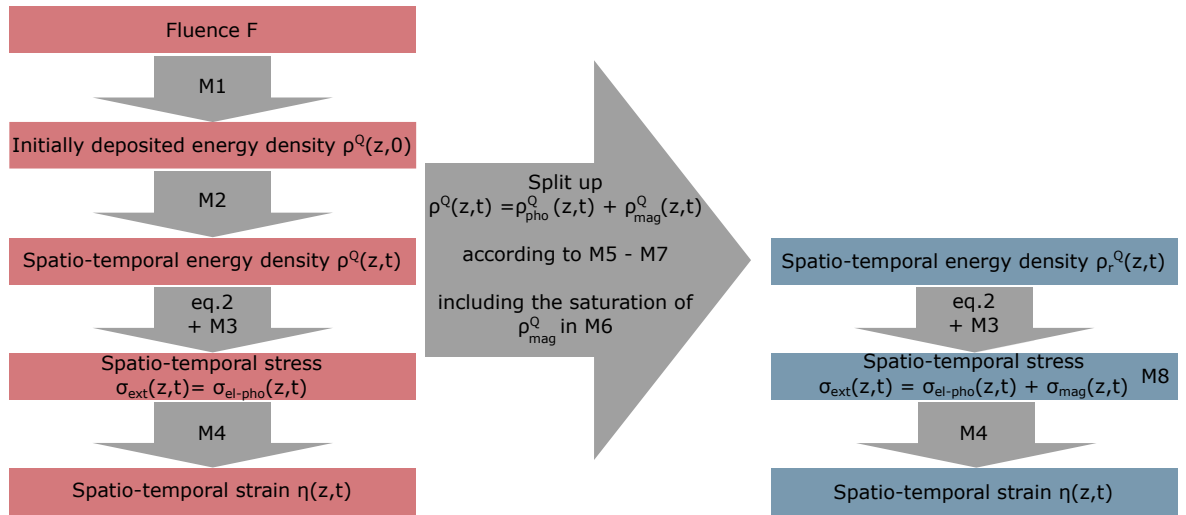
FIG. S5. **Schematic block diagram for the simulation steps:** The left side shows the simulation of the PM-phase strain response using the UDKM1DSIM toolbox. The right side shows the modification to model the AFM phase response by the additional stress that arises from the energy transfer to magnetic excitations.

1. Paramagnetic-phase simulation

First we provide the relations for simulating the electron-phonon stress at 250 K (following the left side of the block diagram in Fig. S5).

Step 1: The initial temperature jump to $T_{\text{start}} + \Delta T(z)$ after laser-excitation is calculated from:

$$\rho_{\text{tot}}^{Q} = \int_{T_{\text{start}}}^{T_{\text{start}}+\Delta T(z)} C(T')\mathrm{d}T' = \frac{F}{\xi}e^{-\frac{z}{\xi}} \tag{M1}$$

with the heat capacity $C(T)$, optical penetration depth ξ, and absorbed fluence F.

Step 2: The subsequent spatio-temporal-energy flow is approximated using a 1D heat diffusion equation. The heat transport in Dy, Y and Nb proceeds via electrons and phonons. The electronic conductivity contributes a larger fraction, but the fast

electron-phonon coupling allows us to approximate the transport by a one-temperature-model. For the combined electron-phonon temperature $T(z,t)$ we use:

$$C\rho\frac{\partial T}{\partial t} = \frac{\partial}{\partial z}\left(\kappa\frac{\partial T}{\partial z}\right),$$ (M2)

with the heat capacity C, density ρ and heat conductivity κ.

Step 3: The conversion between the local energy density and strain is done using the Grüneisen relation between stress and energy density given in the main manuscript (eq. 2 of the main text), and the electron-phonon coupling is implemented as a change in the stress by an empirical electron-phonon time-constant τ_{el-pho}:

$$\sigma_{el-pho}(t,z) = \Gamma_{pho}\rho_{pho}^{Q}(t,z) + \Gamma_{el}\rho_{el}^{Q}(t,z) = \Gamma_{pho}\rho_{tot}^{Q}(t,z)(1-e^{-\frac{t}{\tau_{el-pho}}}) + \Gamma_{el}\rho_{tot}^{Q}(t,z)(e^{-\frac{t}{\tau_{el-pho}}}).$$ (eq. 2)

Thus the stress only depends on the ratio of their different Grüneisen constants $\frac{\Gamma_{el}}{\Gamma_{pho}}$:

$$\sigma_{el-pho}(t,z) = \sigma_{pho}(t,z)H(t)\left(1+\left(\frac{\Gamma_{el}}{\Gamma_{pho}}-1\right)e^{-\frac{t}{\tau_{el-pho}}}\right).$$ (M3)

where $H(t)$ is a Heaviside function and $\sigma_{pho}(t,z) = \Gamma_{ph}\rho_{tot}^{Q}(t,z)$ is the value attained after electron-phonon equilibration. The ratio $\frac{\Gamma_{el}}{\Gamma_{pho}} \approx 0.5$ and $\tau_{el-pho} = 2\,\text{ps}$ are used in all simulations.

Step 4: The resulting stress $\sigma_{ext} = \sigma_{el-pho}$ enters as an external forcing into the 1D - elastic wave equation of the atomic displacement u.:

$$\rho\frac{\partial^2 u_i}{\partial t^2} = \frac{\partial}{\partial z}(c_{33}\frac{\partial u}{\partial z}+\sigma_{ext})$$ (M4)

This continuum elasticity relation is solved numerically using a linear chain of masses and springs model as provided by the modular UDKM1DSIM toolbox. Due to the homogeneous laser excitation we neglect any shear forces so that the local out-of-plane strain $\eta(z,t)$ follows then directly from the local displacement $u(z,t)$ according to $\eta = \frac{\partial u}{\partial z}$.

2. AFM-phase simulation

The simulation of the strain response in the magnetic phase is similar to the non-magnetic sample. The main difference is that an additional stress term (σ_{mag}) appears in equation M4.

The magnetic stress generation is subject to the following constraints: Energy conservation requires $\int \rho_{tot}^{Q}(t,z)\mathrm{d}z$ to be the same for all simulated experiments with the same excitation fluence. This yields the relation:

$$\int \rho_{tot}^{Q}(t,z)\mathrm{d}z = \int \left(\rho_{pho}^{Q}(t,z)+\rho_{mag}^{Q}(t,z)\right)\mathrm{d}z,$$ (M5)

with

$$\rho_{pho}^{Q}(t,z) = f_{pho}(t)\rho_{pho,PM}^{Q}(t,z)$$

$$\rho_{mag}^{Q}(t,z) = \begin{cases} f_{mag}(t)\rho_{pho,PM}^{Q}(t,z) & \text{if } f_{mag}(t)\rho_{pho,PM}^{Q}(t,z) \leq \rho_{mag,max}^{Q}(T_{start}) \\ \rho_{mag,max}^{Q}(T_{start}) & \text{if } f_{mag}(t)\rho_{pho,PM}^{Q}(t,z) > \rho_{mag,max}^{Q}(T_{start}) \\ 0 & \text{if } z \text{ is in } Y, Nb, Al_2O_3 \end{cases}$$ (M6)

where the time-dependent energy transfer to magnetic excitations is modeled with two time-scales according to:

$$f_{mag}(t) = \left(A_1 H(t)+A_2\left(1-e^{-\frac{t}{\tau_2}}\right)\right).$$ (M7)

The parameters $A_1 = A_2 = 0.255$ and $\tau_2 = 15\,\text{ps}$ are used in all AFM and FM simulations. The total external stress thus has two contributions in the magnetic phase:

$$\sigma_{ext}(t,z) = \sigma_{el-pho}(t,z)+\sigma_{mag}(t,z) = \Gamma_{pho}\rho_{pho}^{Q}(t,z)+\Gamma_{el}\rho_{el}^{Q}(t,z)+\Gamma_{mag}\rho_{mag}^{Q}(t,z),$$ (M8)

B. List of Thermo-physical simulation parameters

Carrying out strain simulations using the UDKM1DSIM toolbox [1] requires the thermophysical and elastic properties of the materials within the sample as input. An overview of the simulation parameters at $T = 250\,\mathrm{K}$ is provided in Tab. I. References are given and where not otherwise specified the values are taken from the CRC Handbook of Chemistry and Physics, 93rd Edition, by Haynes Haynes [2]. Values that are marked by an asterisk (*) are adjusted for the simulation to match the observed result. In that case the corresponding literature value is provided in parentheses. Especially the properties of the Y cap layer needed to be altered to find a satisfactory fit with the measured data. The reduction of the absorption and thermal expansion of this cap layer is attributed to a (partial) oxidation of this layer since the sample was kept at ambient conditions prior to the measurements.

TABLE I. **Material properties used for the strain simulation.**

property / material	Y	Dy	Nb	Al_2O_3
number of simulated unit cells	37 (22 nm) 8 (5 nm)	142 (80 nm)	220 (103 nm)	1890 (900 nm)
unit cell orientation	(0001)	(0001)	(110)	(11−20)
crystal structure	hcp	hcp	bcc	hcp
lattice constant (Å)				
c-axis out-of-plane	6.03 (5.73*)	5.65	4.67	4.76
a-axis in-plane	3.65	3.59	4.67	12.80
b-axis in-plane	3.65	3.59	3.30	8.24
order of reflex	2	2	1	2
q_z-position in simulation ($\mathrm{\AA}^{-1}$)	2.083	2.225	2.694	2.643
elastic constants (GPa)	from [3]	from [4]	from [5]	from [6]
c_{33}	77.8	78.3	246.7	498.1
c_{13}	20.0	22.5	133.7	110.9
c_{11}	79.0	74.2	246.7	496.8
c_{12}	28.7	25.5	133.7	163.6
density ρ (g/cm^{-3})	4.47	8.6	8.57	4.05
out-of-plane sound velocity v (nm/ps)	4.15	3.10	5.08	11.14
acoustic impedance (g/cm^{-3} nm/ps)	18.54	26.50	43.56	44.853
molar mass (g/mol)	88.91	162.5	92.91	101.96
lin. therm. expansion ($10^{-6}\,\mathrm{K}^{-1}$)				
thin film: out-of-plane $\alpha_\perp$	7.14* (11.9)	18.27	7.6	–
bulk: out-of-plane $\alpha_\perp$	19.7 [7]	20.3 [7]	7.6 [8]	6.6 [9]
bulk: in-plane $\alpha_\parallel$	6.2 [7]	4.7 [7]	7.6 [8]	–
Poisson correction factor for Γ_{pho}: $1 + \frac{c_{13}}{c_{33}}\frac{2\alpha_\parallel}{\alpha_\perp}$	1.1	1.1	2.4	–
Poisson correction factor for Γ_{mag}: $1 - \frac{c_{13}^2}{(c_{11}+c_{12})c_{33}}$	-	0.87	-	-
specific heat C_p (J kg^{-1}K^{-1})	291.49 [10]	167.3 [11]	270.88 [2]	657.22 [12]
thermal conductivity κ (W m^{-1}K^{-1})	24.8 [13]	6.7* (11.1 [13])	53.0 [13]	58.33 [14]
optical penetration depth (nm)	72* (24)	22* (24)	25	∞

C. Effect of boundary conditions in equlibrium- and laser-heating experiments

Within the analysis of our experiment we use the Grüneisen coefficients that were extracted from equilibrium heating conditions where the sample is in equilibrium with the adjacent cryostat. In these equilibrium heating experiments the sample temperature is equilibrated over minutes so that the materials are given enough time to expand both in-plane and out-of-plane. On the contrary in the laser-excitation experiments the probed sample area is excited homogeneously by the laser-pulse and we probe the strain on a sub-nanosecond to nanosecond timescale that is too short for the in-plane strains to develop due to the strain propagation at the speed of sound. The following section provides the equations that we use to approximate the effect of the boundary conditions for ultrafast and equilibrium heating in our sample. Fig S6 displays a schematic Gedankenexperiment

that illustrates that the absence of in-plane motion on ultrafast timescales increases the out-of-plane expansion of electron-phonon stresses. The same effect decreases the out-of-plane contraction by magnetic stresses on ultrafast timescales. The following formulas are designed to provide a quantitative estimate of the resulting difference between the Grüneisen constant extracted from equilibrium measurements and the Grüneisen constant that is applicable in the time-resolved experiments under in-plane fixation conditions.

(a) Electron-phonon stresses

0. unexcited material
1. Unconstrained response to phonon stress
2. in - plane compression to original dimension

(b) Magnetic stresses

0. unexcited material
1. Unconstrained response to magnetic stress
2. in - plane compression to original dimension

out-of-plane

in-plane

In-plane clamping increases the out-of-plane expansion

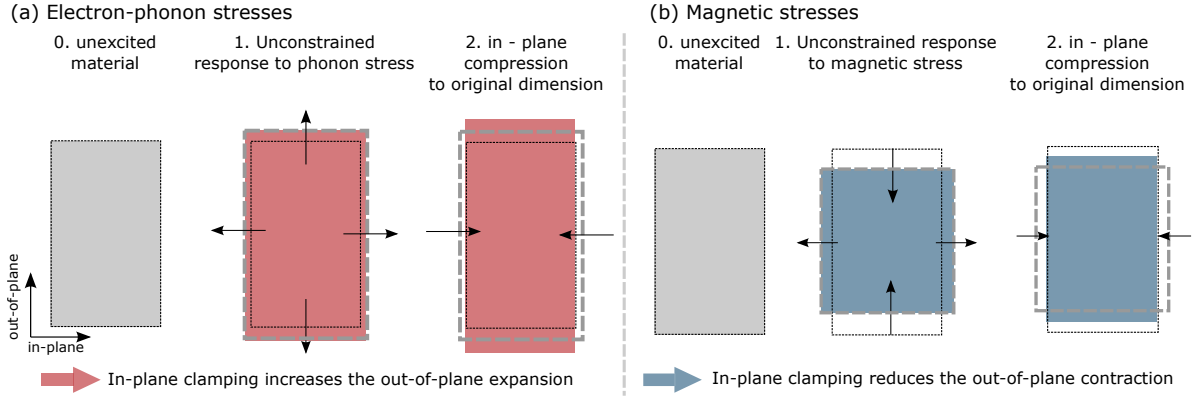In-plane clamping reduces the out-of-plane contraction

FIG. S6. **Gedankenexperiment on the effect of in-plane fixation on the out-of-plane strain:** The first step shows the equilibrium response of the thin film without in-plane constraints and the second step illustrates the result of the in-plane fixation. (a) Effect for the expansive stress of electrons and phonons, where the out-plane strain increases. (b) Effect on the magnetic stress that is dominated by a uniaxial contraction along the out-of-plane c-axis and a small in-plane expansion. Here the in-plane fixation leads to a smaller contraction compared to the equilibrium response.

The general linear relation between stress σ and strain η from linear elastic theory is tensor like and is stated in equation P1 with the help of the stiffness tensor c_{ijkl}.

$$\sigma_{ij} = \sum_{kl} c_{ijkl} \eta_{kl} \tag{P1}$$

Using the symmetry properties of a hexagonal system and applying the compressed Voigt notation (1 = 11, 2 = 22, 3 = 33, 4 = 23, 5 = 31, 6 = 12) equation (P1) can be simplified to the six relations (P2) with the five independent material parameters $c_{11}, c_{33}, c_{12}, c_{13}$ and c_{44} ($c_{66} = 0.5(c_{11} - c_{12})$).[15]

$$\underbrace{\begin{pmatrix} \sigma_1 \\ \sigma_2 \\ \sigma_3 \\ \sigma_4 \\ \sigma_5 \\ \sigma_6 \end{pmatrix}}_{\text{stress}} = \underbrace{\begin{pmatrix} c_{11} & c_{12} & c_{13} & 0 & 0 & 0 \\ c_{12} & c_{11} & c_{13} & 0 & 0 & 0 \\ C_{13} & C_{13} & C_{33} & 0 & 0 & 0 \\ 0 & 0 & 0 & c_{44} & 0 & 0 \\ 0 & 0 & 0 & 0 & c_{44} & 0 \\ 0 & 0 & 0 & 0 & 0 & c_{66} \end{pmatrix}}_{\text{elastic constants } c_{ij}} \underbrace{\begin{pmatrix} \eta_1 \\ \eta_2 \\ \eta_3 \\ \eta_4 \\ \eta_5 \\ \eta_6 \end{pmatrix}}_{\text{strain}} \tag{P2}$$

In the experiments presented here I neglect any shear strain effects. This reduces the system to the three coupled equations stated in (P3). The off-diagonal elements c_{13} couple the in-plane strains η_1 and η_2 to the out-of-plane strain η_3. This manifests itself by an in-plane strain response to a uniaxial out-of-plane stress σ_3, which is quantified by Poisson's number $\nu = -\frac{\eta_1}{\eta_3} = \frac{c_{13}}{c_{11}+c_{12}}$.

$$\begin{pmatrix} \sigma_1 \\ \sigma_2 \\ \sigma_3 \end{pmatrix} = \begin{pmatrix} c_{11} & c_{12} & c_{13} \\ c_{12} & c_{11} & c_{13} \\ c_{13} & c_{13} & c_{33} \end{pmatrix} \begin{pmatrix} \eta_1 \\ \eta_2 \\ \eta_3 \end{pmatrix} \tag{P3}$$

This transverse strain (i. e. Poisson effect) is at the origin of the necessary modification of the Grüneisen constant that has been extracted from equilibrium measurements for the simulation of ultrafast strain responses. For a given temperature change ΔT the unconstrained equilibrium heating the strains will be $\eta_1^{\text{eq}} = \eta_2^{\text{eq}} = \alpha_\parallel \Delta T$ and $\eta_3^{\text{free}} = \alpha_\perp \Delta T$ (Step 1 in Fig. S6(a)).

Under laser-excitation the in-plane expansion is constrained due to the homogeneous excitation of the sample where the in-plane strain relaxation is limited to the timescales of hundreds of nanoseconds by the speed of sound and the excitation spotsize. To account for this we can calculate the additional out-of-plane strain η_3' that results from the in-plane stress $\sigma_1' = \sigma_2'$ that is necessary to compress the material to its initial dimensions (Step 2 in Fig. S6(a)). The corresponding system of equation is:

$$
\begin{pmatrix} \sigma_1' \\ \sigma_2' \\ 0 \end{pmatrix} = \begin{pmatrix} c_{11} & c_{12} & c_{13} \\ c_{12} & c_{11} & c_{13} \\ c_{13} & c_{13} & c_{33} \end{pmatrix} \begin{pmatrix} \eta_1' \\ \eta_2' \\ \eta_3' \end{pmatrix}
\tag{P4}
$$

Solving relation (P4) for η_3' leads to :

$$
\eta_3' = -\frac{C_{13}}{C_{33}}(\eta_1' + \eta_2') = \frac{C_{13}}{C_{33}}(2\alpha_\parallel \Delta T)
\tag{P5}
$$

The corresponding correction factor for unconstrained equilibrium heating and constrained ultrafast-heating is the ratio of the clamped (η_3^{clamped}) and free expansion (η_3^{free}):

$$
\frac{\eta_3^{\text{clamped}}}{\eta_3^{\text{free}}} = \frac{\eta_3^{\text{free}} + \eta_3'}{\eta_3^{\text{free}}} = 1 + \frac{C_{13}}{C_{33}}\frac{2\alpha_\parallel}{\alpha_\perp}.
\tag{P6}
$$

The resulting, so-called Poisson correction factor for the thermoelastic expansion due to electron and phonon excitations $1 + \frac{C_{13}}{C_{33}}\frac{2\alpha_\parallel}{\alpha_\perp}$ is provided in table I for all materials.

1. Special case for the (110)-oriented - Niobium layer

For the Nb (110)-oriented cubic crystal surface, the above discussion remains valid but the elastic constants need to be calculated in the rotated coordinate system, where the new z-axis coincides with the [110]-direction. For the in-plane directions we choose the cartesian coordinate system with the x-axis pointing along the [1-10]- and the y axis along the [001]-direction.

The different representations of the stiffness tensor c in two different coordinate systems are related via:

$$
\widetilde{c}_{ijkl} = c_{pqrs}(\vec{e}_p \cdot \widetilde{\vec{e}}_i)(\vec{e}_q \cdot \widetilde{\vec{e}}_j)(\vec{e}_r \cdot \widetilde{\vec{e}}_k)(\vec{e}_s \cdot \widetilde{\vec{e}}_l)
\tag{P7}
$$

The new relations in the contracted Voigt notation are:

$$
\begin{pmatrix} \sigma_1 \\ \sigma_2 \\ \sigma_3 \\ \sigma_4 \\ \sigma_5 \\ \sigma_6 \end{pmatrix} = \begin{pmatrix} \widetilde{c}_{33} & \widetilde{c}_{12} & \widetilde{c}_{13} & 0 & 0 & 0 \\ \widetilde{c}_{12} & \widetilde{c}_{22} & \widetilde{c}_{13} & 0 & 0 & 0 \\ \widetilde{c}_{13} & \widetilde{c}_{13} & \widetilde{c}_{33} & 0 & 0 & 0 \\ 0 & 0 & 0 & \widetilde{c}_{44} & 0 & 0 \\ 0 & 0 & 0 & 0 & \widetilde{c}_{55} & 0 \\ 0 & 0 & 0 & 0 & 0 & \widetilde{c}_{44} \end{pmatrix} \begin{pmatrix} \eta_1 \\ \eta_2 \\ \eta_3 \\ \eta_4 \\ \eta_5 \\ \eta_6 \end{pmatrix}
\tag{P8}
$$

It contains the 7 different material constants given in table II.

$\widetilde{c}_{33}$ (GPa)	$\widetilde{c}_{12}$ (GPa)	$\widetilde{c}_{13}$ (GPa)	$\widetilde{c}_{22}$ (GPa)	$\widetilde{c}_{44}$ (GPa)	$\widetilde{c}_{55}$ (GPa)
221.45	138.7	162.85	245.6	29.3	53.4

TABLE II. Elements of the transformed stiffness tensor

The resulting Poisson correction factor for the thermoelastic expansion of (110)-oriented Nb is thus turns out to be $1 + \frac{\widetilde{c}_{13}}{\widetilde{c}_{33}}\frac{2\alpha_\parallel}{\alpha_\perp} \approx 2.4$

2. *Special case for magnetic stress in the Dy layer*

The effect of the in-plane fixation on the contractive magnetic strain has to be estimated using a different formula since it is to a first approximation driven by a uniaxial stress along the c-axis [16]. Due to the Poisson effect, such a uniaxial out-of-plane stress leads not only to an out-of-plane contraction but also to an in-plane expansion. This requires a similar scaling factor between the magnetic Grüneisen coefficient that is determined from unconstrained equilibrium measurements when it is used to simulate time-resolved experiments under in-plane fixation conditions. The corresponding two step scheme for the calculation of the correction factor is displayed in Fig. S6(b). Explicitly we substitute $\eta_1' = \eta_2' = -\nu \eta_{3,\text{mag}}$ into equation (P4) where $\nu = \frac{c_{13}}{c_{11}+c_{12}}$ and again solve the system of equations for η_3', which yields.

$$\eta_{3,\text{mag}}' = -2\nu \frac{c_{13}}{c_{33}} \eta_{3,\text{mag}}^{\text{free}} \tag{P9}$$

$$\Rightarrow \frac{\eta_{3,\text{mag}}^{\text{clamped}}}{\eta_{3,\text{mag}}^{\text{free}}} = \frac{\eta_{3,\text{mag}}^{\text{free}} + \eta_{3,\text{mag}}'}{\eta_{3,\text{mag}}^{\text{free}}} = 1 - 2\nu \frac{c_{13}}{c_{33}} = 1 - \frac{c_{13}^2}{(c_{11}+c_{12})c_{33}} \tag{P10}$$

Inserting the elastic constants known for Dysprosium[4] into relation (P10) leads to the estimate that approximately 13% less contraction is observed under laser excitation as compared to unconstrained equilibrium heating. This correction factor for the magnetic Grüneisen factor in Dysprosium is added to table I.

S4. SPATIO-TEMPORAL STRESS MAPS

Here we provide a complete overview of the modeled stress maps that are driving the linear chain of masses and springs model to obtain the simulated UXRD strain response via the UDKM1DSIM toolbox [1]. The resulting strain simulations for the Dy transducer and the Nb detection layer are shown as solid lines in Fig. 3 and 4 of the main text for the temperature and excitation energy dependent experiments respectively. For completeness we also reproduce Fig. 6 of the main text since it allows for the direct comparison of the similarities and differences in the modeled stress response between temperature- and excitation energy density dependent measurements.
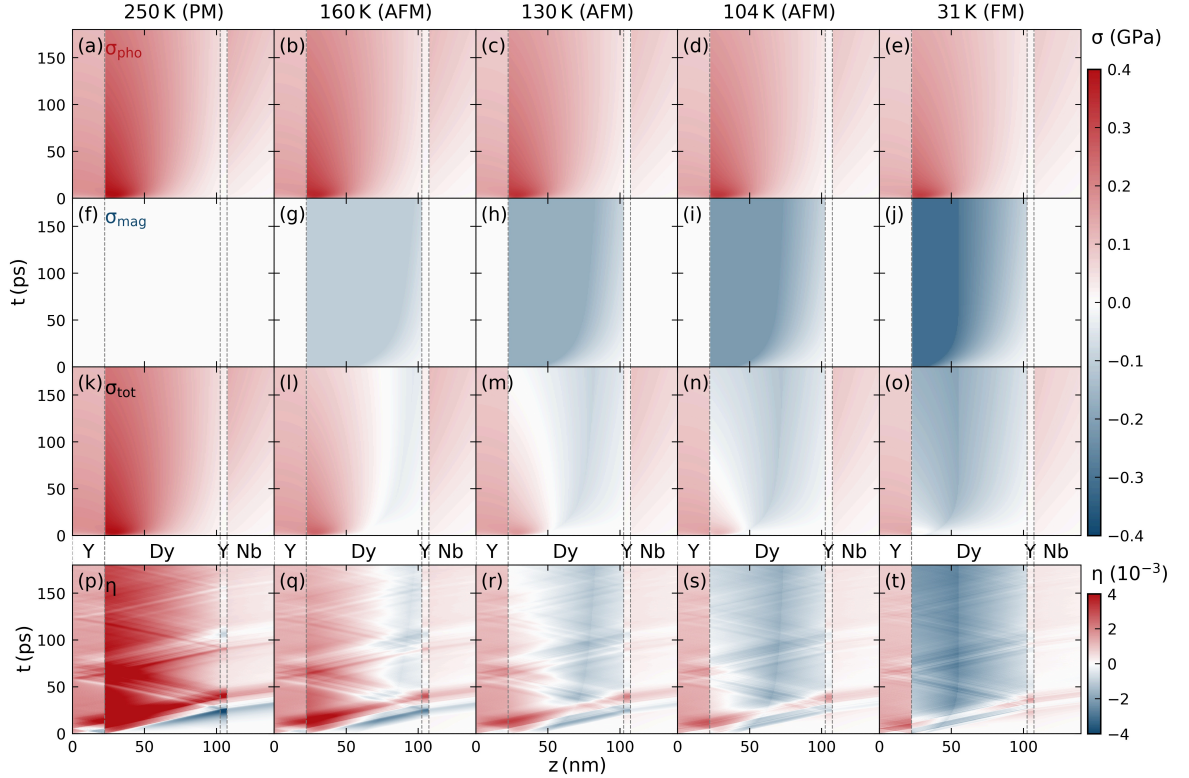

FIG. S7. **Separated stress contributions σ for the temperature dependent simulations.** Top row shows the electron-phonon stress σ_{pho}, second row the stress contributions σ_{mag} by magnetic excitations and the third row shows the total stress σ_{tot} as the sum of both contributions. Note that the compensation point that separates areas of dominantly expansive and dominantly compressive stress in the transducer shifts more and more towards the top of the Dy layer. The simulated strain dynamics that include both the coherent and incoherent strain response is depicted in the bottom row ((p)–(t)). Strain pulses that propagate at the speed of sound and get reflected at the material interfaces (indicated by dashed lines), superimposing the slowly varying strain proportional to the thermal stress.

Fig. S7 visualizes the trend in the picosecond stress for different starting temperatures but fixed pulse energy for the excitation. The observed changes in the total stress originate from the temperature dependent maximal energy density that can be deposited in the spin system. The top row of Fig. S7((a)–(e)) displays the electron-phonon stress (σ_{pho}) that varies slightly in amplitude due to the energy transfer to magnetic excitations. The second row ((f)–(j)) shows the temperature dependent contribution of the magnetic excitations (σ_{mag}) where the homogeneous color at the top of the Dy transducer indicates the saturated spin-stress. The closer the starting temperature is to $T_{Néel}$, the smaller is the maximal magnetic stress amplitude and the larger is the fraction of the transducer with fully saturated spin stress. The resulting total stress is depicted in the third row ((k)–(o)). It shows that the Dy transducer has an expansive stress at the top and a contractive stress at its bottom interface. The strain response (last row (p)–(t)), simulated using the UDKM1DSIM[1] toolbox, is driven by the presented total stress. The homogeneous strain contribution that can be attributed to the thermal expansion i.e. incoherent phonons is superimposed by picosecond strain pulses i.e. coherent phonon wavepackets that are reflected at the interfaces.

Although the color code of Fig. S7 provides a qualitative overview over the temperature dependent stress contributions, a more quantitative comparison is possible when the spatial stress profiles are compared for selected simulation times. To

that end we provide the time dependent average stress in the Dy transducer as well as the spatial energy distribution profiles depicted in Fig. S8(a)–(e) and (f)–(j) respectively. The modeled spatial stress profiles are shown at 6, 45, and 180 ps alongside the time dependence of the contractive and expansive stress contributions. The selected times for the spatial profiles are chosen such that the contributions from the 2 ps – electron-phonon and instantaneous el-spin coupling, the 15 ps – spin-phonon coupling and the heat diffusion process can be judged separately.
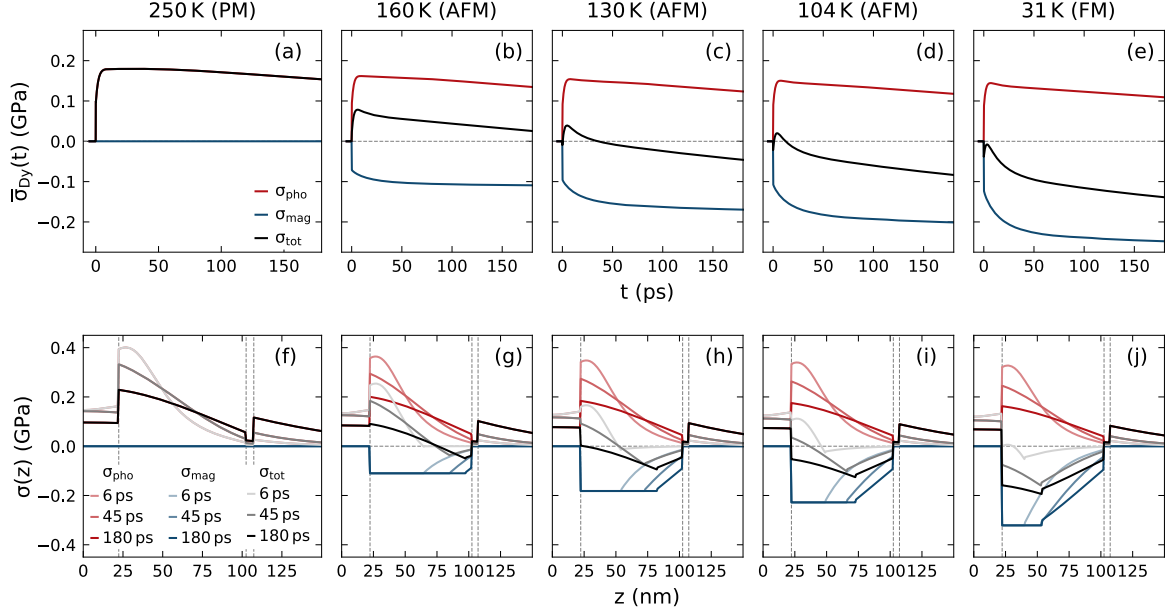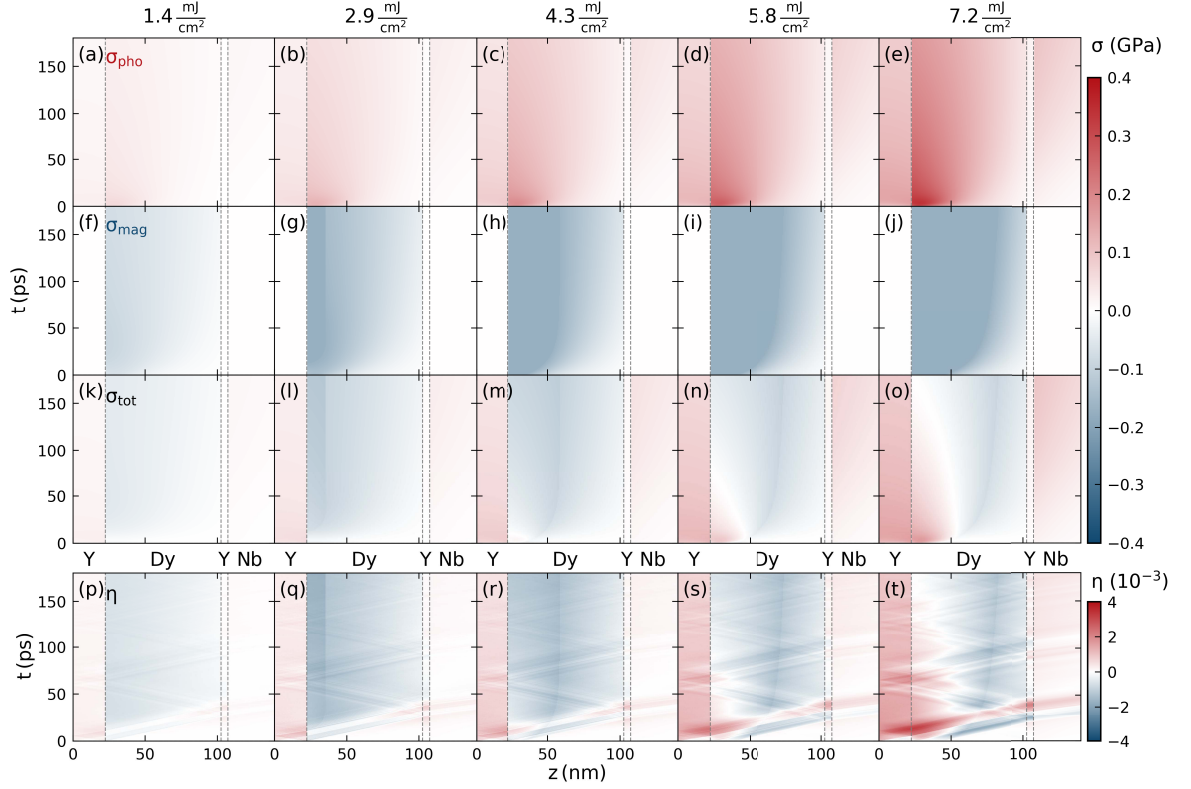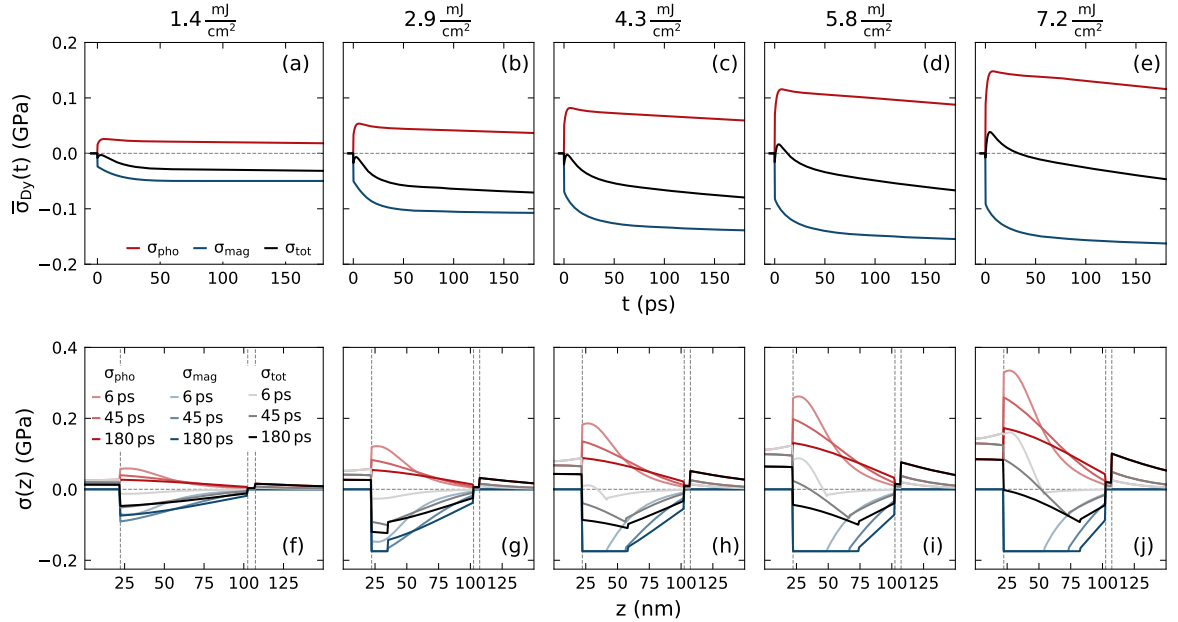

FIG. S8. **Stress contributions for the T-dependent modeling.** The top row ((a)–(e)) shows the time-dependence of the average stress in the sample for the electron-phonon, magnetic and total stress. The phonon response consists of an instantaneous step followed by a 2 ps rise time that is designed to mimic the electron-phonon coupling. The subsequent slow decay originates from thermal transport of energy to adjacent layers. The stress by magnetic excitations exhibits an instantaneous rise, an approx. 15 ps rise and an additional slow rise as deeper and deeper parts of the dysprosium layer experience spin excitation by thermal transport. The lower panel ((f)–(j)) shows the spatial form of the driving stress with discontinuous slopes arising from the initial spin-saturation.

The stress maps that correspond to the modeled excitation-energy dependent experiments at a fixed starting temperature of $T = 130$ K are presented in Fig. S9. In this series of experiments the maximal energy that can be deposited into magnetic excitations is constant while the energy deposited by the excitation pulses is increased, which is complementary to the previously discussed temperature dependent experiments. For low excitation energy densities we find that the total stress within the transducer is contractive throughout the entire layer since the larger Grüneisen constant of the spin excitations dominates the stress response. The saturation of σ_{mag} for high excitation densities leads to an expansive stress at the top of the transducer. This results in the recovery of the bipolar strain pulse feature observed in the strain response via UXRD for higher excitation energy densities. The bipolar strain response is however preceded by an expansion that is triggered by the contraction at the backside of the Dy transducer.

FIG. S9. **Separated stress contributions for the excitation fluence dependent simulations at** $T = 130\,\mathrm{K}$**.** Same plot layout as Fig. S7.

FIG. S10. **Separated stress contributions for the excitation fluence dependent simulations at** $T = 130\,\mathrm{K}$**.** Same plot layout as Fig. S8

[1] D. Schick, A. Bojahr, M. Herzog, R. Shayduk, K. C. von Schmising, and M. Bargheer, udkm1DsimA simulation toolkit for 1D ultrafast dynamics in condensed matter, Computer Physics Communications **185**, 10.1016/j.cpc.2013.10.009 (2014).

[2] W. M. Haynes, *CRC Handbook of Chemistry and Physics, 93rd Edition*, CRC Handbook of Chemistry and Physics (Taylor & Francis, 2012).

[3] J. F. Smith and J. A. Gjevre, Elastic constants of yttrium single crystals in the temperature range 4.2–400k, Journal of Applied Physics **31**, 645 (1960).

[4] S. B. Palmer and E. W. Lee, The elastic constants of dysprosium and holmium, Proceedings of the Royal Society of London. Series A. Mathematical and Physical Sciences **327**, 519 (1972).

[5] K. J. Carroll, Elastic constants of niobium from 4.2 to 300k, Journal of Applied Physics **36**, 3689 (1965).

[6] W. E. Tefft, Elastic constants of synthetic single crystal corundum, Journal of research of the National Bureau of Standards. Section A, Physics and chemistry **70A**, 277 (1966).

[7] F. H. Spedding, J. J. Hanak, and A. H. Daane, High temperature allotropy and thermal expansion of the rare-earth metals, Journal of the Less Common Metals **3**, 110 (1961).

[8] R. Roberge, Lattice parameter of niobium between 4.2 and 300 K, Journal of the Less Common Metals **40**, 161 (1975).

[9] M. Lucht, M. Lerche, H.-C. Wille, Y. V. Shvyd'ko, H. D. Rüter, E. Gerdau, and P. Becker, Precise measurement of the lattice parameters of a-al2o3 in the temperature range 4.5–250 k using the mössbauer wavelength standard, Journal of Applied Crystallography **36**, 1075 (2003).

[10] L. D. Jennings, R. E. Miller, and F. H. Spedding, Lattice heat capacity of the rare earths. heat capacities of yttrium and lutetium from 15–350k, The Journal of Chemical Physics **33**, 1849 (1960).

[11] V. K. Pecharsky, K. a. Gschneidner Jr., and D. Fort, Superheating and other unusual observations regarding the first order phase transition in Dy, Scripta Materialia **35**, 843 (1996).

[12] D. C. Ginnings and G. T. Furukawa, Heat capacity standards for the range 14 to 1200k, Journal of the American Chemical Society **75**, 522 (1953).

[13] C. Y. Ho, R. W. Powell, and P. E. Liley, Thermal Conductivity of the Elements, Journal of Physical and Chemical Reference Data **1**, 279 (1972).

[14] E. R. Dobrovinskaya, L. A. Lytvynov, and V. Pishchik, *Sapphire. Material, Manufacturing, Applications* (Springer, 2009).

[15] D. Royer and E. Dieulesaint, *Elastic waves in solids: Including nonlinear dynamics*, 3rd ed., Advanced texts in physics (Springer, Berlin, 2000).

[16] P. C. Landry, Variation of the helicomagnetic turn angle in dysprosium, Physical Review **156**, 578 (1967).

Article VIII

Tracking picosecond strain pulses in heterostructures that exhibit giant magnetostriction

Steffen Peer Zeuschner, Tymur Parpiiev, Thomas Pezeril, Arnaud Hillion, Karine Dumesnil, Abdelmadjid Anane, **Jan-Etienne Pudell**, Lisa Willig, Matthias Rössle, Marc Herzog, Alexander von Reppert, and Matias Bargheer

We combine ultrafast X-ray diffraction (UXRD) and time-resolved Magneto-Optical Kerr Effect (MOKE) measurements to monitor the strain pulses in laser-excited $TbFe_2$/Nb heterostructures. Spatial separation of the Nb detection layer from the laser excitation region allows for a background free characterization of the laser-generated strain pulses. We clearly observe symmetric bipolar strain pulses when the excited TbFe2 surface terminates the sample and a decomposition of the strain wavepacket into an asymmetric bipolar and a unipolar pulse, when a SiO_2 glass capping layer covers the excited $TbFe_2$ layer. The inverse magnetostriction of the temporally separated unipolar strain pulses in this sample leads to a MOKE signal that linearly depends on the strain pulse amplitude measured through UXRD. Linear chain model simulations accurately predict the timing and shape of UXRD and MOKE signals that are caused by the strain reflections from multiple interfaces in the heterostructure.

Tracking picosecond strain pulses in heterostructures that exhibit giant magnetostriction

S. P. Zeuschner,[1,2] T. Parpiiev,[3] T. Pezeril,[3] A. Hillion,[4] K. Dumesnil,[4] A. Anane,[5] (iD) J. Pudell,[2] L. Willig,[2] M. Rössle,[1] (iD) M. Herzog,[2] (iD) A. von Reppert,[2,a)] (iD) and M. Bargheer[1,2] (iD)

AFFILIATIONS

[1]Helmholtz-Zentrum Berlin, Wilhelm-Conrad-Röntgen-Campus, BESSY II, Albert-Einstein-Straße 15, 12489 Berlin, Germany
[2]Institute of Physics and Astronomy, University of Potsdam, Karl-Liebknecht-Straße 24-25, 14476 Potsdam, Germany
[3]Institut des Molécules et Matériaux du Mans (UMR CNRS 6283), Université du Maine, 72085 Le Mans Cedex, France
[4]Institut Jean Lamour (UMR CNRS 7198), Université de Lorraine, 54000 Nancy, France
[5]Unité Mixte de Physique, CNRS, Thales, Univ. Paris-Sud, Université Paris-Saclay, 91767, Palaiseau, France

[a)]reppert@uni-potsdam.de

ABSTRACT

We combine ultrafast X-ray diffraction (UXRD) and time-resolved Magneto-Optical Kerr Effect (MOKE) measurements to monitor the strain pulses in laser-excited $TbFe_2$/Nb heterostructures. Spatial separation of the Nb detection layer from the laser excitation region allows for a background-free characterization of the laser-generated strain pulses. We clearly observe symmetric bipolar strain pulses if the excited $TbFe_2$ surface terminates the sample and a decomposition of the strain wavepacket into an asymmetric bipolar and a unipolar pulse, if a SiO_2 glass capping layer covers the excited $TbFe_2$ layer. The inverse magnetostriction of the temporally separated unipolar strain pulses in this sample leads to a MOKE signal that linearly depends on the strain pulse amplitude measured through UXRD. Linear chain model simulations accurately predict the timing and shape of UXRD and MOKE signals that are caused by the strain reflections from multiple interfaces in the heterostructure.

I. INTRODUCTION

The generation, propagation, and detection of laser-induced strain waves contain rich physics that has been studied extensively since the seminal work of Thomsen *et al.*, which exploited photoelasticity for detection.[1,2] Ingenious all-optical probing schemes for GHz to THz phonons have since then been used to investigate strain waves in multiple materials,[3–6] vibrational modes of nanoparticles,[7] shear waves,[8] nonlinear propagation effects,[9,10] and acoustic solitons.[11,12] Strain waves that originate from coherent phonon excitation can attain transient stresses on the order of GPa, which have been shown to interact with other phenomena such as phase transitions,[13,14] quantum well bandgaps,[15] piezo-[16]/ferroelectricity,[17] and magnetism.[18–22] Such interactions are not only of fundamental interest but may also become relevant for applications as soon as the understanding allows for controllability.[23,24]

In order to study the response to pure strain pulses, it is beneficial to spatially separate the laser excited transducer from the probed layer. The inherent limitation given by the finite optical penetration of the visible light in the transducer is often circumvented by backside probing schemes.[10,21] The development of (sub)-picosecond hard X-ray diffraction has opened the possibility to directly obtain the time-resolved strain amplitude[25–28] with penetration depths in the few μm regime. The separation of the layer peaks in reciprocal space allows for material specific probing of the energy flow[29,30] and strain evolution[31,32] in nanoscopic, crystalline heterostructures.

The envisioned manipulation of the polarization and magnetization states in ferroic materials via strain relies on a strong coupling between spin or electronic degrees of freedom and the atomic lattice.[23,33] In this regard, rare-earth-based alloys such as Terfenol ($TbFe_2$) have attracted attention due to the discovery of "giant magnetostriction,"[34,35]

i.e., lattice strains in excess of 10^{-3} caused by magnetization change. Among the binary rare-earth alloys, TbFe$_2$ exhibits the largest magnetostriction.[36] It combines the large exchange interaction of the 3d orbital in Iron (Fe) with the large magnetic moment of 9μ_B per Tb atom and the large spin-orbit coupling associated with 4f orbitals. The exchange coupling results in a ferrimagnetic alignment of the Fe and Tb moments with the Curie point ($T_C \approx 700$ K) considerably above room temperature.[37] TbFe$_2$ crystallizes in a cubic C$_{15}$ Laves phase structure, where the $\langle 111 \rangle$-direction is the magnetic easy axis, which can be modeled by the cubic crystalline anisotropy constants $K_1 = -1.2 \times 10^8$ erg/cm^3 and $K_2 = 2.08 \times 10^7$ erg/cm^3.[38] The resulting high coercivity is often reduced for application purposes by introducing Dy ($\langle 001 \rangle$ easy axis) to obtain the ternary alloy Terfenol-D (Tb$_x$Dy$_{1-x}$Fe$_2$). The desired low coercivity with large magnetostriction that is favorable for magneto-acoustic transduction applications can be tailored by different ratios x, where $x = 0.27$ is found to be optimal at room temperature.[39] Despite the potentially rich, coupled magnetization, and lattice dynamics in this magnetostrictive ferrimagnet, there have been only a few reports[8,23] that aim at quantifying and correlating the strain evolution and its coupling to the magnetization by time-resolved measurements in binary rare-earth alloys.

Here, we display the different capabilities of table-top ultrafast X-ray diffraction (UXRD) and all-optical methods to probe the strain propagation and evolution in a layered magnetostrictive heterostructure. Femtosecond laser pulses are used to excite the rare-earth alloy TbFe$_2$, which serves as a transducer for strain waves into adjacent layers. UXRD measurements observe the arrival and shape of the strain waves in a thin, buried detection layer. From this, we extract the stress profile that generates the strain wave in the inhomogeneously excited TbFe$_2$ layer. The timings of the observed experimental features are rationalized by modeling the strain propagation in this multilayer sample using a 1-dimensional linear chain model of masses and springs. The modeling is shown to be particularly useful when the transducer is capped by a transparent layer so that the conventional symmetric bipolar strain pulse is split into an asymmetric bipolar pulse travelling into the transducer and a unipolar strain pulse that is reflected at the sample-surface after a time determined by the transparent layer thickness. Complementary to the UXRD data, we employ an all-optical polarization sensitive measurement that probes the strain propagation in a transparent silica (SiO$_2$) acoustic delay line. Time-resolved magneto-optical-Kerr-effect (MOKE) measurements are shown to be a very sensitive probe for the arrival of the multiple strain echoes at the top of the laser-excited TbFe$_2$ layer, which can be used to complement the bulk sensitive UXRD.

II. EXPERIMENTAL DETAILS

We investigate laser-excited samples that consist of (110) oriented Terfenol (TbFe$_2$) layers grown by MBE on (11$\bar{2}$1) oriented Sapphire (Al$_2$O$_3$) with a buried Niobium (Nb) (110) buffer layer as previously described.[38,40] The basic sample structure is only capped by a 2 nm thin protective Titanium (Ti) layer, which does not significantly contribute to the experimental transients. We therefore refer to sample 1 as uncapped. The second sample was instead capped with an 885 nm thick amorphous silica (SiO$_2$) layer. The UXRD measurements are carried out at a laser-driven, plasma-based diffraction setup (PXS) that supplies 200 fs X-ray pulses at Cu K_α-energy.[41] The table-top laser-pump X-ray-probe setup uses p-polarized excitation pulses at

a central wavelength of 800 nm, with a 1 kHz repetition rate and a full width at half maximum spot size of a 2-dimensional Gaussian function of 1.4 mm × 1.5 mm for the laser pulses and 0.3 mm × 0.3 mm spot size of the X-ray pulses. Using the top-hat approximation with the 1/e width for the laser excitation profile and the pulse energy, we calculate the fluence for the TbFe$_2$ and Nb experiments, respectively. The pump-fluence at the Nb angle is approximately 4% larger compared to the TbFe$_2$ experiments since the 1.6° larger diffraction angle leads to a smaller laser footprint, whereas the Fresnel reflection coefficient for the p-polarized laser light decreases by approximately 1.4%.

A representative reciprocal-space map (RSM) of the uncapped sample structure obtained at the PXS alongside the static X-ray diffraction curve and the temporal evolution of the material specific Bragg peaks are displayed in Fig. 1. In the probed RSM volume, we find three separated peaks with their maximum intensity at the out-of-plane reciprocal space coordinate $q_z = 2.42$ Å^{-1}, 2.64 Å^{-1}, and 2.69 Å^{-1}, which are attributed to TbFe$_2$ (220), Al$_2$O$_3$ (11$\bar{2}$1), and Nb (110), respectively, according to their bulk lattice plane spacings. The layer thicknesses set by the sample growth are 500 nm TbFe$_2$ on top of 50 nm Nb and 330 μm Al$_2$O$_3$ as schematically depicted in Fig. 1(e).

The TbFe$_2$ diffraction peak is significantly broadened along the in-plane reciprocal space coordinate q_x compared to the instrument function limited Al$_2$O$_3$ substrate peak. This is a hallmark for microcrystalline domains that in this case exhibit a large mosaic spread of 1.5° around the bulk diffraction angle,[40] very similar to previously reported UXRD experiments on ferroelectric samples.[42,43] The presence of such structural imperfections in the TbFe$_2$ becomes evident by comparison to the diffraction peak of the Nb layer, which exhibits a much smaller width in q_x. The blue and orange lines in Fig. 1(b) represent the reciprocal space slices that are probed in our setup for two fixed angles of incidence (AOI) ω that are chosen to be selectively sensitive to the TbFe$_2$ and Nb lattice strains, respectively.

The combination of an optic that focuses X-rays onto the sample with a convergence of $\Delta\omega \approx 0.3°$ (Montel optic from Layertec) and an X-ray area pixel detector (Dectris PILATUS-100k) allows for swift data acquisition that avoids time-consuming mesh scans of the AOI (ω) and the diffraction angle (θ). Each pixel of the X-ray area detector is mapped to reciprocal space coordinates q_x and q_z using the mapping routine described in a previous publication,[42] which is applicable in the thin film regime. Using this fixed angle detection scheme, the flux of 10^6 photons/s incident on the sample is sufficient to probe the evolution of the material specific diffraction peaks and the laser excited heterostructure with subpicosecond time resolution within few hours. The X-ray diffraction curves of the unexcited sample at the Nb and TbFe$_2$ AOI are indicated by orange and blue solid lines in Fig. 1(a) and their time evolution is represented by Figs. 1(c) and 1(d) for Nb and TbFe$_2$, respectively. The dashed lines in Figs. 1(c) and 1(d) indicate the temporal evolution of the peak center that is extracted by fitting the diffraction signal with a Gaussian line profile at each delay. This extracted Bragg peak position in reciprocal space is inversely proportional to the lattice constant d of the material via $q_{z,\text{Fit}}(t) = \frac{2\pi}{d_{\text{Fit}}(t)}$. UXRD thus probes the time-resolved strain $\varepsilon(t)$, defined as the change of the average lattice constant d relative to the unexcited sample $\varepsilon = \frac{d(t) - d(t<0)}{d(t<0)}$. The presented UXRD measurements were carried out without the external magnetic field. The application of static magnetic fields on the order of $\mu_0 H = 500$ mT in- and out-of-plane only leads
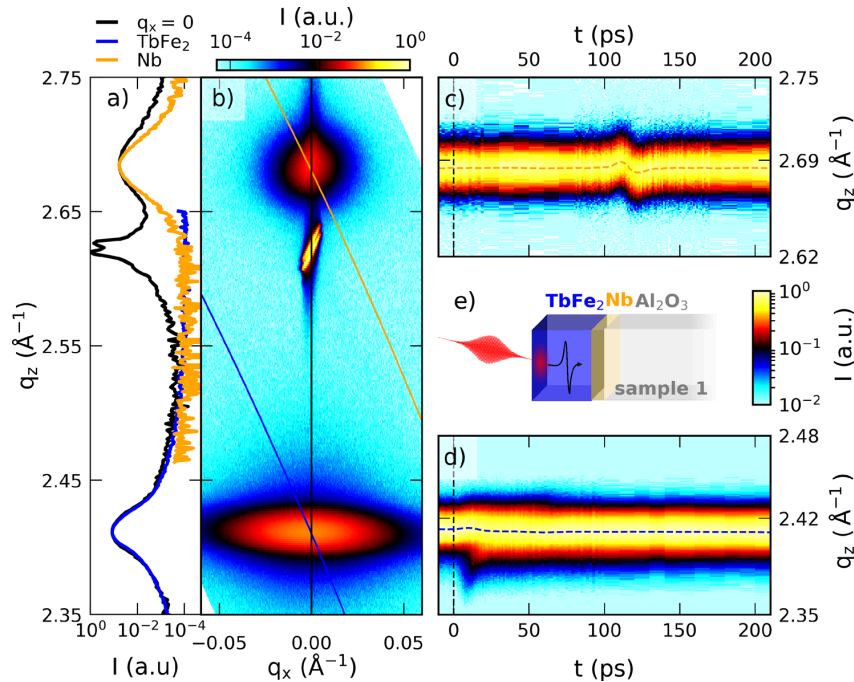
FIG. 1. Characterization of sample 1 via X-ray diffraction: (a) slice of the reciprocal space map shown in (b) at $q_x = 0$ (black line). The blue and orange lines in (a) correspond to the probed reciprocal slice when using the convergent beam of the X-ray focusing optic and area detector at the lab-based diffraction setup at a fixed angle of incidence. (c) and (d) depict the temporal evolution of the Nb and TbFe$_2$ peak at 13.3 mJ/cm^2, respectively, with the fitted peak position indicated by dashed lines. (e) Schematic depiction of the uncapped sample structure.

to minor modification of the UXRD signals consistent with a slightly increased sound velocity.

III. ANALYSIS AND DISCUSSION OF THE RESULTS
A. Signatures from the sample without SiO$_2$ capping

Before discussing the transient strain of the SiO$_2$ capped Terfenol (TbFe$_2$) structures, it is instructive to rationalize the signals seen in the UXRD experiment on the uncapped sample 1 that is schematically depicted in Fig. 1(e) for a fluence of 12.7 mJ/cm^2 and 13.3 mJ/cm^2 for the TbFe$_2$ and Nb, respectively. At first we discuss the strain evolution in the directly excited, approximately 500 nm thick TbFe$_2$ layer shown in Fig. 2(a). The blue data points show the experimentally obtained strain from Gaussian fits to the diffraction curves. The representative fits and raw time-resolved data from Figs. 1(c) and 1(d) are shown in Fig. S1 of the supplementary material. Beyond 20 ps, we observe an expansion that manifests in a shift of the diffraction peaks to smaller q_z. Within the first 20 ps, one observes a transient shift of the majority of the Bragg peak to larger q_z, which coincides with the appearance of a shoulder at smaller q_z. Between 40 and 80 ps, we detect a pronounced, triangular shaped strain increase and subsequent decrease in addition to an overall rising background.

No background is observed in the strain response of the 50 nm thin, buried Nb layer displayed in Fig. 2(b). The strain in the Nb layer is close to zero up to 4 ns (not shown), except for the very pronounced, nearly symmetric bipolar strain pulse that starts with a contraction at approximately 90 ps, reverses sign at 117 ps, and ceases at approximately 150 ps. The diffraction peak evolution of the thin Nb layer displayed in Fig. 1(c) exhibits a large peak shift that corresponds to a
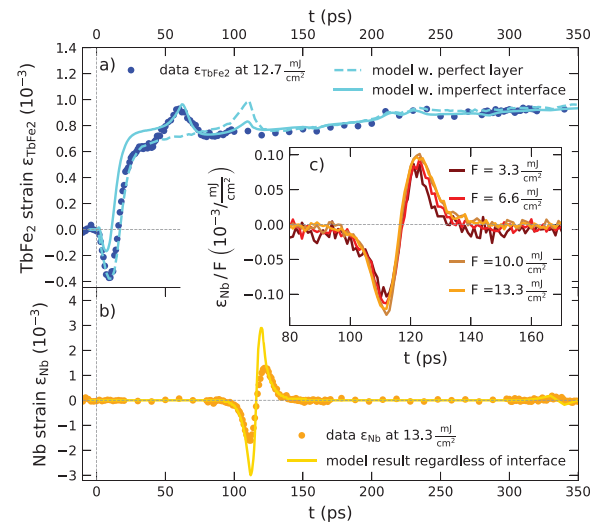
FIG. 2. Transient strain signatures of sample 1 without SiO$_2$ capping: (a) and (b) display transient strains extracted from the average peak shift via Gaussian lineshape fits and the simulated strain response using the udkm1Dsim toolbox as lines. The dashed line in (a) corresponds to a model with a full single-crystalline TbFe$_2$ layer whereas the solid line takes a disordered TbFe$_2$ layer at the TbFe$_2$/Nb interface into account. Inset (c) depicts the transient strain pulse in the Nb layer normalized to the different excitation fluences.

strain amplitude of 1.5‰, which is only present during a short time window. The inset (c) in Fig. 2 shows the strain oscillation in Nb for different pump fluences, normalized to the fluence of the laser pulses. Since the transient strain curves nearly coincide, our data evidence a linear fluence dependence for this strain oscillation feature in Nb up to 13.3 mJ/cm².

The interpretation of the UXRD data from the thick TbFe₂ layer is based on the insights into ultrafast lattice response of photoexcited thin films studied by UXRD, which were previously discussed by Schick et al.[44] The laser illumination leads to the excitation of coherent and incoherent phonons, which superimpose in the strain response of the absorbing layer.[2] The strain pulse composed of the coherent excitation of phonons subsequently propagates at the longitudinal acoustic phonon velocity whereas the thermal energy leaves the excited layer by a slower diffusion process.

Our experiment represents the limiting case of an inhomogeneously excited transducer since the TbFe₂ layer thickness is approximately 25 times larger than the 19.9 nm light intensity penetration depth at 800 nm, which we obtain from ellipsometry measurements using a commercial setup and analyzing software (SENTECH), as discussed in Sec. III of the supplementary material. The appearance of a marked shoulder in the TbFe₂ diffraction signal on the lower q_z side for the main diffraction in Fig. 1(d) signals the existence of a highly strained surface layer on top of the nearly unperturbed TbFe₂. Schick et al.[44] have analyzed in detail that the exponential stress profile originating from inhomogeneous laser heating leads to an initial compression of the majority of the layer. Since the Gaussian fit is most sensitive to the central region of the diffraction peak, we observe the leading compressive strain front as a shift of the Bragg peak maximum to larger angles in the first 15 ps. When the free surface expansion propagates into the material at the speed of sound, the strong expansive component finally shifts the Bragg peak maximum to smaller angles. We attribute the remaining slope to the heat transport that equilibrates the inhomogeneous temperature profile within the TbFe₂ layer on a timescale of hundreds of picoseconds to several nanoseconds.

The strain response of the Nb layer seen in Fig. 2(b) confirms that the thermal transport occurs mainly within the TbFe₂ layer since we observe no thermal expansion that would appear as a background within our 4 ns measurement window. The bipolar strain pulse marks the delayed passage of the coherently excited phonon wave packet, which is launched at the sample-air interface, through the buried Nb layer. The detected diffraction peak shift of the 50 nm thick detection layer thus shows a background-free signal of the strain pulse, consisting of a compressive leading edge, which is followed by an expansive trailing edge as it is known from previous picosecond acoustic investigations.[2,45] The smaller layer thickness leads to higher average strain signals and sharper features as compared to the strain detected in the thick transducer layer.

The signature of the exit of the bipolar strain pulse from the probed TbFe₂ layer is an increase in the average layer strain followed by a decrease back to the thermal expansion background since the leading compressive edge exits while the trailing expansive part is still in the layer. In our experiment, we observe a pronounced delay between the exit of the strain wave from the TbFe₂ layer, at approximately 40 ps and its arrival in the adjacent Nb at 90 ps. This 50 ps delay of the signatures can only be rationalized if the strain pulse traverses a TbFe₂ layer that does not contribute significantly to the X-ray

diffraction signal. Using v_{sound} = 3.94 nm/ps, known for polycrystalline TbFe₂,[46] this corresponds to a layer with a thickness of approximately 187 nm TbFe₂ that has a considerably different texture. Structural inhomogeneities are in-line with the mosaic peak broadening and the comparably small X-ray diffraction intensity of the TbFe₂ peak. The existence of a structurally imperfect interface layer at the TbFe₂-Nb interface is further supported by Atomic Force microscopy measurements that observed that the rare-earth alloy layer growth proceeds first as separated 3-dimensional islands that only coalesce to form a continuous film for thicknesses on the order of 100 nm and above.[38] The large in-plane lattice-constant mismatch of 11.6% between the underlying Nb template and the TbFe₂ is reduced by a thin FeNb layer but is probably the origin for the large mosaicity and for the limited coherence length along the growth direction,[47] which amounts to 50 nm in the present TbFe₂ film.

Modeling the excitation and propagation of picosecond acoustic strain pulses is achieved by solving the partial differential equation for the time-dependent local strain in which the given spatio-temporal stress profile acts as source term.[2,44,48] The thin film geometry reduces this to a 1-dimensional problem as the laser excitation spot is much larger than the film thickness of the nanostructure and the probed X-ray spot. Numerical solutions for the strain evolution in nanoscopic layers are frequently applied in nanoscopic heterostructure geometries where multiple interface reflections complicate analytical solutions.[32,48,49] In Figs. 2(a) and 2(b), we compare the UXRD data to simulation results obtained with the udkm1Dsim toolbox package that we used to calculate the time-resolved strain response based on a linear chain model of masses and springs. Although details of the software are given in the reference publication,[50] we briefly outline the workflow of the modeling. Upon input of the thermophysical material properties and the known sample geometry that are listed in Table I of the supplementary material, we first calculate the absorbed optical energy density and temperature profiles according to the heat diffusion equation[51] with unit cell resolution. The resulting spatio-temporal temperature profile represents the thermoelastic stress that drives a linear chain of masses and springs, where the masses represent individual unit cells. In the last simulation step, the obtained time-resolved strains are used as an input for the computation of the time-dependent dynamical X-ray diffraction signal.[52] The resulting diffraction peaks are fitted with a Gaussian line profile to yield the strain signal displayed as lines in Figs. 2(a) and 2(b).

The dashed line in Fig. 2(a) shows the modeled strain of a structurally perfect 436 nm thick TbFe₂ layer on top of a 50 nm Nb layer attached to an Al₂O₃ substrate. The simulation data represented by the solid line assume only 249 nm structurally perfect TbFe₂ on top of a 187 nm TbFe₂ layer with substantial disorder. The improved fit of the model regarding the triangular feature beginning at 40 ps substantiates the evidence for a structurally different TbFe₂ layer at the Nb interface. The total TbFe₂ layer thickness is determined by the arrival time of the bipolar strain pulse in Nb using the directionally averaged speed of sound of v_{sound} = 3.94 nm/ps for polycrystalline TbFe₂,[46] due to the lack of exact elastic constants for single-crystalline TbFe₂. Despite the agreement between the simulated and experimental strains in the TbFe₂ layer, the simulation substantially overestimates the bipolar strain pulse amplitude in the Nb layer. This may be accounted for by taking into account a slowly rising stress profile in TbFe₂ and acoustic damping as well as scattering of the coherent phonons at the interface.[53–55]

B. Signals in the SiO₂ capped sample

The central experimental result of this work is summarized in Fig. 3. Here, we combine the experimental results from a sample capped by an amorphous SiO_2 layer as sketched in the inset of Fig. 3(e). Figure 3(a) shows the spatio-temporal strain profile that is obtained within the linear chain model for the second sample structure with the stacking sequence 882 nm SiO_2 / 342 nm $TbFe_2$ / 50 nm Nb / Al_2O_3 substrate, which is solved by the udkm1Dsim toolbox.[50] Red and blue colors correspond to regions of expansive and compressive strain, respectively. One observes that the expansion of the laser-heated region slowly spreads as the heat diffuses within the $TbFe_2$ layer. Now, the bipolar strain pulse that is launched towards the substrate is clearly asymmetric, where a large-amplitude leading compressive part is followed by a smaller expansive tail. In addition, a unipolar compression pulse propagates in the SiO_2 capping layer towards the surface where it is converted into an expansion. The simulated strain in Fig. 3(a) clarifies that for a very thin capping layer, the expansive unipolar wave reflected
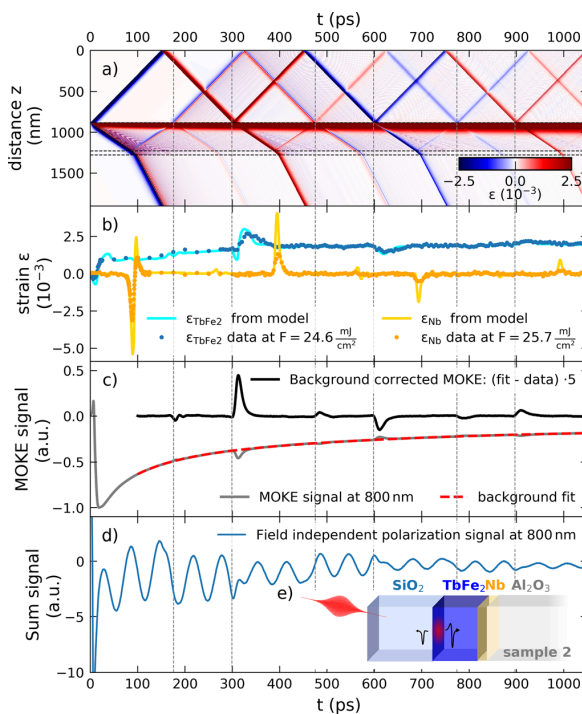
at the surface would superimpose with the small expansive tail of the asymmetric bipolar wave to form the symmetric bipolar wave observed in sample 1, see Fig. 2. Multiple reflections of the strain pulses occur at the material interfaces indicated by horizontal dashed lines where the reflection and transmission arise due to the acoustic impedance mismatch.[2,56,57] A direct comparison of the simulation results is presented in Sec. IV of the supplementary material.

The occurrence of multiple unipolar strain pulse echoes that traverse the $TbFe_2$ and Nb layers at different timings is readily seen in the UXRD data presented in Fig. 3(b). The modeled average strain shown as solid lines accurately predicts the timing and shape of the observed features but the amplitude of the Nb strain is substantially overestimated. This may indicate a finite electron-phonon-coupling time and scattering of the coherent phonons in $TbFe_2$ from structural imperfections, which are both not captured in the current modeling. The presented UXRD data were obtained under identical excitation conditions as the experiments on the uncapped sample except for the larger pump-fluence 24.6 mJ/cm², which leads to an increase in the detected strain amplitudes.

In the following, we discuss the results of time-resolved MOKE measurements, which probe the change of the polarization state of the probe light upon reflection due to the permanent magnetization of the sample. The measurement displayed in Fig. 3(c) was carried out close to the polar MOKE geometry with an external out-of-plane magnetic field of $\mu_0 H = 800$ mT using 200 fs laser pulses at a central wavelength of approximately 800 nm, a repetition rate of 250 kHz, and a pump fluence of approximately 2.7 mJ/cm². In these measurements, the difference of the polarization changes for opposite external field orientations $[S(H_{up}) - S(H_{down})]$ is probed using the reflection of 800 nm probe-light-pulses analyzed by a half-wave plate in combination with a Wollaston-prism and a balanced photo-diode. Lock-in detection using an acousto-optical modulation of the pump beam intensity at 50 kHz was employed. The resulting polar MOKE signal displayed as a solid grey line essentially probes the out-of-plane magnetization component of the $TbFe_2$ layer within the 19.9 nm optical penetration depth and is probably sensitive to the Fe sub-lattice.[58] Subtraction of the slowly varying thermal background approximated by a double-exponential decay (red line) from the MOKE signal (grey line) reveals multiple sharp peaks in the residual black curve. By comparison with the linear chain model results in Fig. 3(a), it becomes obvious that the observed features occur at the time when the longitudinal strain pulse echoes traverse the top few nanometers of the $TbFe_2$ layer given by the penetration depth of the probe pulse. Note that the sign of the peaks correlates with the sign of the (unipolar) strain-pulse echoes and that even the small reflections from the $TbFe_2$/Nb interface produce observable MOKE signatures at around 180, 485, and 790 ps.

Figure 3(d) displays the time-resolved polarization analysis signal of the reflected 800 nm probe beam independent of the magnetization state, which is obtained from the sum signal $[S(H_{up}) + S(H_{down})]$ of the balanced detection. Similar time-resolved Brillouin scattering experiments have shown that the observed oscillations originate from the interference of the reflected light from the traveling strain pulse in the transparent SiO_2 medium and the static interfaces.[59,60] Pronounced phase jumps in this Brillouin signal occur when the strain pulses invert their sign due to the reflection at the SiO_2/air interface.[56,61]

Consequently, the strain propagation as modeled by the 1-dimensional-linear chain model accurately predicts the timings of all

FIG. 3. Time-resolved signals from the SiO_2 capped sample structure: (a) spatio-temporal strain simulation result that highlights the occurrence of multiple echoes from bipolar and unipolar strain pulses. Horizontal dashed lines indicate the layer interfaces of the schematic sample geometry displayed in (e). (b) Comparison of the strain signal from UXRD measurements and udkm1Dsim toolbox simulations. (c) Time-resolved all-optical MOKE signal S: $[S(H_{up}) - S(H_{down})]$. The background subtracted signal shows pronounced peaks when strain pulses traverse the SiO_2/$TbFe_2$ interface, which are marked by vertical dashed lines. The field-independent polarization change $[S(H_{up}) + S(H_{down})]$ shown in (d) is dominated by oscillations of the time-resolved Brillouin scattering signal of the strain pulses within the SiO_2 capping.

the experimental signals we observed in this heterostructure. We have employed a single temperature model for the driving stress on the lattice. This certainly oversimplifies the equilibration process of the electron-, lattice-, and spin-subsystems to occur instantaneously. A detailed analysis of the dynamics prior to the equilibration is beyond the scope of the current investigation as it requires the knowledge of the thermophysical properties for each sub-system as well as the coupling constants of this largely unexplored material.

C. Experimental results from the buried detection layer

In the henceforth presented data analysis, we put the focus on the qualitative and quantitative information that can be directly extracted from the UXRD signal in the buried Nb detection layer. In Fig. 4(a), we see that the normalized, background-subtracted MOKE signal originating from TbFe$_2$ matches the normalized Nb strain when shifted by 84 ps, which is the longitudinal acoustic propagation time through the TbFe$_2$ layer. This agreement proves a linear relation between the lattice strain and the observed MOKE signal. The slight discrepancies at 485 and 790 ps probably originate from the fact that the MOKE signal results from a superposition of the strain pulses reflected at the surface and at the TbFe$_2$/Nb interface, which traverse the top TbFe$_2$ layer simultaneously [see Fig. 3(a)]. Since only part of the reflection at the TbFe$_2$/Nb interface is again reflected at the TbFe$_2$/SiO$_2$ interface, the Nb layer senses a different strain wave composition. It will be important for future experiments investigating the interaction of shear waves with the magnetization to accurately identify also the small longitudinal acoustic pulse echoes in such multilayered structures. Previous picosecond acoustic investigations in magnetic samples have observed that strain pulses can exert a torque on the sample magnetization $\vec{M}$ via a transient modification of the crystalline anisotropy, often resulting in a damped precessional motion of $\vec{M}$.[18,62,63] Although a torque on the magnetization by the strain pulse is expected, the absence of precessional oscillations challenges the theoretical interpretation of the

observed MOKE signal based on the Landau-Lifshitz-Gilbert model. Crystalline defects in the TbFe$_2$, resulting in small magnetic domains,[63] in combination with a magneto-crystalline anisotropy and damping could drastically suppress the coherent precessional signal. The signal might have contributions from a modulation of the reflectivity driven by the photoelastic effect;[21] however, the reflectivity signal does not exhibit significant spikes at the echo positions. In any case, the striking resemblance of the detected strain pulses in the Nb layer to extracted features in the MOKE measurements demonstrates a high sensitivity of MOKE for probing strain pulses arriving at the TbFe$_2$ surface.

In Fig. 4(b), we compare the initial bipolar strain pulses from the capped and uncapped samples, normalized to their compressive part. We observe that the leading, compressive parts coincide, whereas the expansive parts in the SiO$_2$ capped sample 2 are strongly reduced. The black dashed line indicates a single exponential fit to the falling edge of the compressive strain with a time constant of 4.6 ps, which translates to a spatial extension of approximately 18 nm using $v_{sound} = 3.94$ nm/ps. This value provides an estimation of the spatial extension of the driving stress profile.[3,64] This matches the optical penetration depth obtained from ellipsometry, which shows that potential hot-electron diffusion does not substantially increase the excitation profile length.

The evolution of the unipolar strain pulse within the SiO$_2$ capping is shown in Fig. 4(c), where we compare the first and second unipolar strain echoes that traverse the Nb layer at 396 ps and 695 ps to the initial pulse launched into the SiO$_2$ capping. The latter is extracted from the difference between the bipolar strain pulses observed on the capped and uncapped samples. In this analysis, we assume that the laser generated stress profile is identical in the capped and uncapped TbFe$_2$ samples and that the difference of the initially detected bipolar strain pulse seen in Fig. 4(b) originates solely from partial reflection of the expansion at the top TbFe$_2$ interface. The FWHM of the detected strain signals increases from 9 to 16 and 21 ps. The modeling does not include any broadening mechanisms and reports echoes with a constant width of 8 ps FWHM. Anharmonic interactions in the lattice potential have been shown to change the shape and broaden high amplitude coherent phonon wavepackets.[65] Contributions from the SiO$_2$ surface roughness should also be taken into account.

IV. CONCLUSION

In this work, we have combined multiple techniques to follow the trajectory of strain pulses that are generated by femtosecond laser pulses exploiting the giant magnetostriction material Terfenol (TbFe$_2$) as a transducer. MOKE measurements in TbFe$_2$ are shown to provide a surface sensitive method to probe strain pulses at the top of the metallic TbFe$_2$ that is complementary to bulk sensitive X-ray diffraction.

Probing the strain pulse in a thin, buried detection layer adjacent to an optically opaque transducer via UXRD allows for a characterization of the coherent strain pulse separately from heat expansion without frontside-pump backside-probe schemes. By detecting the strain pulse in the buried and perfect Nb layer, we demonstrate how UXRD can clearly locate the structurally imperfect fraction of the TbFe$_2$ layer in this opaque heterostructure. Contrary to all-optical methods, UXRD provides a quantitative measure of the average lattice strain that does not require detailed knowledge of photo elastic coefficients and optical properties. In combination with 1-dimensional-linear chain models, UXRD can provide quantitative information on realistic strains with unit cell resolution, which can be
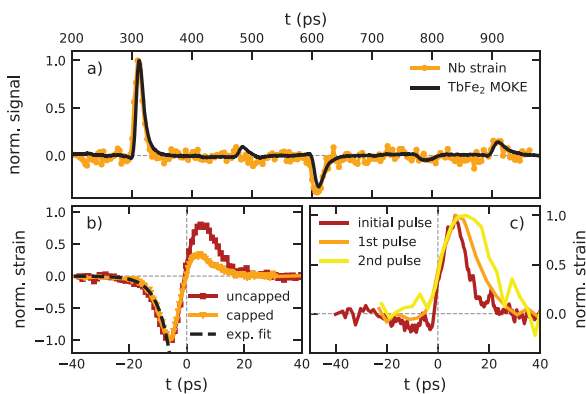
FIG. 4. Analysis of the strain pulse signatures: (a) comparison of the coherent phonon strain contribution seen in the MOKE and UXRD signal, scaled to the maximum amplitude and shifted to overlap in time. (b) Comparison of the initial asymmetric bipolar strain pulse in the capped sample 2 and the symmetric bipolar strain in the uncapped sample 1, to an exponential fit with a time-constant of 4.56 ps. (c) Evolution of the strain pulse after passing the SiO$_2$ layer multiple times.

used as input for modeling strain-assisted magnetization switching approaches.[23] The obtained maximum strain amplitude in $TbFe_2$ of 2‰ is well below the deterministic switching limit of a few percent strain, but the local heating substantially lowers the anisotropy[66] as it is known from heat-assisted magnetic recording schemes.

The combination of MOKE and UXRD outlines a potential path towards an experimental calibration of the magneto-elastic coefficient, i.e., the magnetization change per strain amplitude for picosecond acoustic pulses. Such a quantity is not only relevant for testing fundamental research that models magneto-elastic couplings but also represents a valuable input for application-oriented research.

We believe that probing the strain-pulse in a buried detection layer is a versatile method for studying the stress generation profile as it separates coherent from incoherent phonon excitations. It will be especially useful in situations where multiple mechanisms with different spatial or temporal characteristics superimpose in the strain generation process as it is the case in (anti-)ferromagnetic[67,68] materials. The use of an acoustic delay line further introduces the possibility to study the evolution of the strain pulse shape and to calibrate the magnetization response to unipolar compression and expansion pulses. This will support important future steps towards a full understanding of the demagnetization process especially in high-anisotropy, giant magnetostriction materials. A combination of time-resolved probes that monitor different degrees of freedom within the same experiment will foster the understanding of the intricate couplings between electron-, spin-, and lattice systems in solids, which forms the basis for many useful devices.

SUPPLEMENTARY MATERIAL

See supplementary material for the details of the time evolution of the $TbFe_2$ and Nb Bragg peaks (S1) and the material parameters used in the modeling (S2). Furthermore, we provide the complex index of refraction and the resulting optical properties that were extracted from spectroscopic ellipsometry on the uncapped $TbFe_2$ sample (S3) as well as a section that compares the modeling results for the strain propagation in the capped and uncapped samples (S4).

ACKNOWLEDGMENTS

REFERENCES

[1] C. Thomsen et al., "Coherent phonon generation and detection by picosecond light pulses," Phys. Rev. Lett. **53**, 989–992 (1984).

[2] C. Thomsen, H. T. Grahn, H. J. Maris, and J. Tauc, "Surface generation and detection of phonons by picosecond light pulses," Phys. Rev. B **34**, 4129–4138 (1986).

[3] O. B. Wright and K. Kawashima, "Coherent phonon detection from ultrafast surface vibrations," Phys. Rev. Lett. **69**, 1668–1671 (1992).

[4] T. Saito, O. Matsuda, and O. B. Wright, "Picosecond acoustic phonon pulse generation in nickel and chromium," Phys. Rev. B **67**(20), 205421 (2003).

[5] Y. Sugawara et al., "Watching ripples on crystals," Phys. Rev. Lett. **88**, 185504 (2002).

[6] O. B. Wright, "Ultrafast nonequilibrium stress generation in gold and silver," Phys. Rev. B **49**, 9985–9988 (1994).

[7] G. V. Hartland, "Coherent vibrational motion in metal particles: Determination of the vibrational amplitude and excitation mechanism," J. Chem. Phys. **116**, 8048–8055 (2002).

[8] T. Pezeril, "Laser generation and detection of ultrafast shear acoustic waves in solids and liquids," Opt. Laser Technol. **83**, 177–188 (2016).

[9] A. Bojahr et al., "Second harmonic generation of nanoscale phonon wave packets," Phys. Rev. Lett. **115**, 195502 (2015).

[10] C. Klieber, V. E. Gusev, T. Pezeril, and K. A. Nelson, "Nonlinear acoustics at GHz frequencies in a viscoelastic fragile glass former," Phys. Rev. Lett. **114**, 065701 (2015).

[11] H.-Y. Hao and H. J. Maris, "Experiments with acoustic solitons in crystalline solids," Phys. Rev. B **64**, 64302 (2001).

[12] P. J. S. van Capel and J. I. Dijkhuis, "Time-resolved interferometric detection of ultrashort strain solitons in sapphire," Phys. Rev. B **81**, 144106 (2010).

[13] P. Ruello, S. Zhang, P. Laffez, B. Perrin, and V. Gusev, "Laser-induced coherent acoustical phonons mechanisms in the metal-insulator transition compound $NdNiO_3$: Thermal and nonthermal processes," Phys. Rev. B **79**, 94303 (2009).

[14] S. H. Kim, B. J. Kim, T. Y. Jeong, Y. S. Lee, and K. J. Yee, "Coherent phonon spectroscopy of the phase transition in VO_2 single crystals and thin films," J. Appl. Phys. **117**, 163107 (2015).

[15] A. V. Akimov, A. V. Scherbakov, D. R. Yakovlev, C. T. Foxon, and M. Bayer, "Ultrafast band-gap shift induced by a strain pulse in semiconductor heterostructures," Phys. Rev. Lett. **97**(3), 037401 (2006).

[16] M. R. Armstrong et al., "Observation of terahertz radiation coherently generated by acoustic waves," Nat. Phys. **5**, 285–288 (2009).

[17] C. K. Schmising et al., "Coupled ultrafast lattice and polarization dynamics in ferroelectric nanolayers," Phys. Rev. Lett. **98**, 257601 (2007).

[18] J.-W. Kim, M. Vomir, and J.-Y. Bigot, "Ultrafast magnetoacoustics in nickel films," Phys. Rev. Lett. **109**, 166601 (2012).

[19] J. V. Jäger et al., "Picosecond inverse magnetostriction in galfenol thin films," Appl. Phys. Lett. **103**, 032409 (2013).

[20] V. N. Kats et al., "Ultrafast changes of magnetic anisotropy driven by laser-generated coherent and noncoherent phonons in metallic films," Phys. Rev. B **93**, 214422 (2016).

[21] L. Thevenard et al., "Effect of picosecond strain pulses on thin layers of the ferromagnetic semiconductor (Ga,Mn)(As,P)," Phys. Rev. B **82**, 104422 (2010).

[22] M. Deb et al., "Picosecond acoustic-excitation-driven ultrafast magnetization dynamics in dielectric Bi-substituted yttrium iron garnet," Phys. Rev. B **98**, 174407 (2018).

[23] O. Kovalenko, T. Pezeril, and V. V. Temnov, "New concept for magnetization switching by ultrafast acoustic pulses," Phys. Rev. Lett. **110**, 266602 (2013).

[24] A. V. Scherbakov et al., "Ultrafast control of light emission from a quantum-well semiconductor microcavity using picosecond strain pulses," Phys. Rev. B **78**, 241302(R) (2008).

[25] C. Rose-Petruck et al., "Picosecond-milliangstrom lattice dynamics measured by ultrafast X-ray diffraction," Nature **398**, 310–312 (1999).

[26] A. M. Lindenberg et al., "Time-resolved x-ray diffraction from coherent phonons during a laser-induced phase transition," Phys. Rev. Lett. **84**, 111–114 (2000).

[27] D. A. Reis et al., "Probing impulsive strain propagation with x-ray pulses," Phys. Rev. Lett. **86**, 3072–3075 (2001).

[28] T. Henighan et al., "Generation mechanism of terahertz coherent acoustic phonons in Fe," Phys. Rev. B **93**, 220301(R) (2016).

[29] M. Highland et al., "Ballistic-phonon heat conduction at the nanoscale as revealed by time-resolved x-ray diffraction and time-domain thermoreflectance," Phys. Rev. B **76**, 075337 (2007).

[30] A. Koc et al., "Ultrafast x-ray diffraction thermometry measures the influence of spin excitations on the heat transport through nanolayers," Phys. Rev. B **96**, 014306 (2017).

[31] M. Bargheer et al., "Coherent atomic motions in a nanostructure studied by femtosecond X-ray diffraction," Science **306**, 1771–1773 (2004).

[32] J. Pudell et al., "Layer specific observation of slow thermal equilibration in ultrathin metallic nanostructures by femtosecond X-ray diffraction," Nat. Commun. **9**, 3335 (2018).

[33] W. Eerenstein, N. D. Mathur, and J. F. Scott, "Multiferroic and magnetoelectric materials," Nature **442**, 759–765 (2006).

[34] A. E. Clark and H. S. Belson, "Giant room-temperature magnetostrictions in TbFe₂ and DyFe₂," Phys. Rev. B **5**, 3642–3644 (1972).

[35] N. C. Koon, A. I. Schimdler, and F. L. Carter, "Giant magnetostriction in cubic rare earth-iron compounds of the type RFe₂," Phys. Lett. A **37**, 413–414 (1971).

[36] A. Clark and D. Crowder, "High temperature magnetostriction of TbFe₂ and Tb.₂₇Dy.₇₃Fe₂," IEEE Trans. Magn. **21**, 1945–1947 (1985).

[37] K. H. J. Buschow and R. P. van Stapele, "Magnetic properties of some cubic rare-earth-iron compounds of the type RFe₂ and RₓY₁₋ₓFe₂," J. Appl. Phys. **41**, 4066–4069 (1970).

[38] A. Mougin, C. Dufour, K. Dumesnil, and P. Mangin, "Strain-induced magnetic anisotropy in single-crystal RFe₂ (110) thin films (R = Dy, Er, Tb, Dy₀.₇ Tb₀.₃, Sm, Y)," Phys. Rev. B **62**, 9517–9531 (2000).

[39] R. Bergstrom et al., "Morphotropic phase boundaries in ferromagnets: Tb₁₋ₓDyₓFe₂ alloys," Phys. Rev. Lett. **111**, 017203 (2013).

[40] V. Oderno, C. Dufour, K. Dumesnil, P. Mangin, and G. Marchal, "Epitaxial growth of (110) DyFe₂, TbFe₂, and Dy₀.₇Tb₀.₃Fe₂ thin films by molecular beam epitaxy," J. Cryst. Growth **165**, 175–178 (1996).

[41] D. Schick et al., "Normalization schemes for ultrafast x-ray diffraction using a table-top laser-driven plasma source," Rev. Sci. Instrum. **83**, 025104 (2012).

[42] D. Schick et al., "Ultrafast reciprocal-space mapping with a convergent beam," J. Appl. Crystallogr. **46**, 1372–1377 (2013).

[43] D. Schick et al., "Following strain-induced mosaicity changes of ferroelectric thin films by ultrafast reciprocal space mapping," Phys. Rev. Lett. **110**, 095502 (2013).

[44] D. Schick et al., "Ultrafast lattice response of photoexcited thin films studied by X-ray diffraction," Struct. Dyn. **1**, 064501 (2014).

[45] P. Ruello and V. E. Gusev, "Physical mechanisms of coherent acoustic phonons generation by ultrafast laser action," Ultrasonics **56**, 21–35 (2015).

[46] A. E. Clark, H. S. Belson, and R. E. Strakna, "Elastic properties of rare-earth-iron compounds," J. Appl. Phys. **44**, 2913–2914 (1973).

[47] A. Mougin et al., "Strain in single-crystal RFe₂ (110) thin films (R = Y, Sm, Gd, Tb, Dy₀.₇Tb₀.₃, Dy, Er, Lu)," Phys. Rev. B **59**, 5950–5959 (1999).

[48] M. Nicoul, U. Shymanovich, A. Tarasevitch, D. von der Linde, and K. Sokolowski-Tinten, "Picosecond acoustic response of a laser-heated gold-film studied with time-resolved x-ray diffraction," Appl. Phys. Lett. **98**, 191902 (2011).

[49] M. Herzog et al., "Analysis of ultrafast X-ray diffraction data in a linear-chain model of the lattice dynamics," Appl. Phys. A **106**, 489–499 (2012).

[50] D. Schick et al., "udkm1Dsim—A simulation toolkit for 1D ultrafast dynamics in condensed matter," Comput. Phys. Commun. **185**, 651–660 (2014).

[51] I. A. Veres, T. Berer, and P. Burgholzer, "Numerical modeling of thermoelastic generation of ultrasound by laser irradiation in the coupled thermoelasticity," Ultrasonics **53**, 141–149 (2013).

[52] S. A. Stepanov et al., "Dynamical x-ray diffraction of multilayers and superlattices: Recursion matrix extension to grazing angles," Phys. Rev. B **57**, 4829–4841 (1998).

[53] M. Hase, Y. Miyamoto, and J. Tominaga, "Ultrafast dephasing of coherent optical phonons in atomically controlled GeTe/Sb₂Te₃ superlattices," Phys. Rev. B **79**, 174112 (2009).

[54] M. Hase and M. Kitajima, "Interaction of coherent phonons with defects and elementary excitations," J. Phys. Condens. Matter **22**, 073201 (2010).

[55] G. Chen et al., "Increased phonon scattering by nanograins and point defects in nanostructured silicon with a low concentration of germanium," Phys. Rev. Lett. **102**(19), 196803 (2009).

[56] D. Royer and E. Dieulesaint, Elastic Waves in Solids I (Springer, 1996), Chap. I.

[57] A. I. H. Persson, H. Enquist, A. Jurgilaitis, B. P. Andreasson, and J. Larsson, "Real-time observation of coherent acoustic phonons generated by an acoustically mismatched optoacoustic transducer using x-ray diffraction," J. Appl. Phys. **118**, 185308 (2015).

[58] A. R. Khorsand et al., "Element-specific probing of ultrafast spin dynamics in multisublattice magnets with visible light," Phys. Rev. Lett. **110**, 107205 (2013).

[59] M. Lejman et al., "Ultrafast acousto-optic mode conversion in optically birefringent ferroelectrics," Nat. Commun. **7**, 12345 (2016).

[60] A. Bojahr et al., "Brillouin scattering of visible and hard X-ray photons from optically synthesized phonon wavepackets," Opt. Express **21**, 21188 (2013).

[61] E. Pavlenko et al., "Azobenzene-functionalized polyelectrolyte nanolayers as ultrafast optoacoustic transducers," Nanoscale **8**, 13297 (2016).

[62] A. V. Scherbakov et al., "Coherent magnetization precession in ferromagnetic (Ga,Mn)As induced by picosecond acoustic pulses," Phys. Rev. Lett. **105**, 117204 (2010).

[63] T. L. Linnik et al., "Theory of magnetization precession induced by a picosecond strain pulse in ferromagnetic semiconductor (Ga,Mn)As," Phys. Rev. B **84**, 214432 (2011).

[64] J. Pudell et al., "Ultrafast negative thermal expansion driven by spin-disorder," Phys. Rev. B (to be published).

[65] A. Bojahr, M. Herzog, D. Schick, I. Vrejoiu, and M. Bargheer, "Calibrated real-time detection of nonlinearly propagating strain waves," Phys. Rev. B **86**, 144306 (2012).

[66] A. Clark, R. Abbundi, and W. Gillmor, "Magnetization and magnetic anisotropy of TbFe₂, DyFe₂, Tb₀.₂₇Dy₀.₇₃Fe₂ and TmFe₂," IEEE Trans. Magn. **14**, 542–544 (1978).

[67] A. von Reppert et al., "Persistent nonequilibrium dynamics of the thermal energies in the spin and phonon systems of an antiferromagnet," Struct. Dyn. **3**, 054302 (2016).

[68] A. von Reppert et al., "Ultrafast laser generated strain in granular and continuous FePt thin films," Appl. Phys. Lett. **113**, 123101 (2018).

Article IX

Ultrafast laser generated strain in granular and continuous FePt thin films

Alexander von Reppert, Lisa Willig, **Jan-Etienne Pudell**, Matthias Rössle, Wolfram Leitenberger, Marc Herzog, Fabian Ganss, Olav Hellwig, and Matias Bargheer

We employ ultrafast X-ray diffraction to compare the lattice dynamics of laser-excited continuous and granular FePt films on MgO (100) substrates. Contrary to recent results on free-standing granular films, we observe in both cases a pronounced and long-lasting out-of-plane expansion. We attribute this discrepancy to the in-plane expansion, which is suppressed by symmetry in continuous films. Granular films on substrates are less constrained and already show a reduced out-of-plane contraction. Via the Poisson effect, out-of-plane contractions drive in-plane expansion and vice versa. Consistently, the granular film exhibits a short-lived out-of-plane contraction driven by ultrafast demagnetization which is followed by a reduced and delayed expansion. From the acoustic reflections of the observed strain waves at the film-substrate interface, we extract a 13% reduction of the elastic constants in thin 10 nm FePt films compared to bulk-like samples.

Ultrafast laser generated strain in granular and continuous FePt thin films

A. von Reppert,[1] L. Willig,[1] J.-E. Pudell,[1] M. Rössle,[2] W. Leitenberger,[1] M. Herzog,[1]
F. Ganss,[3] O. Hellwig,[3,4] and M. Bargheer[1,2,a)]

[1]*Institut für Physik und Astronomie, Universität Potsdam, Karl-Liebknecht-Str. 24-25, 14476 Potsdam,
Germany*
[2]*Helmholtz-Zentrum Berlin für Materialien und Energie GmbH, Wilhelm-Conrad-Röntgen Campus, BESSY II,
Albert-Einstein-Str. 15, 12489 Berlin, Germany*
[3]*Institut für Physik, Technische Universität Chemnitz, Reichenhainer Str. 70, 09126 Chemnitz, Germany*
[4]*Institut für Ionenstrahlphysik und Materialforschung, Helmholtz-Zentrum Dresden-Rossendorf,
Bautzner Landstrasse 400, 01328 Dresden, Germany*

We employ ultrafast X-ray diffraction to compare the lattice dynamics of laser-excited continuous and granular FePt films on MgO (100) substrates. Contrary to recent results on free-standing granular films, we observe in both cases a pronounced and long-lasting out-of-plane expansion. We attribute this discrepancy to the in-plane expansion, which is suppressed by symmetry in continuous films. Granular films on substrates are less constrained and already show a reduced out-of-plane contraction. Via the Poisson effect, out-of-plane contractions drive in-plane expansion and vice versa. Consistently, the granular film exhibits a short-lived out-of-plane contraction driven by ultrafast demagnetization which is followed by a reduced and delayed expansion. From the acoustic reflections of the observed strain waves at the film-substrate interface, we extract a 13% reduction of the elastic constants in thin 10 nm FePt films compared to bulk-like samples. © 2018 Author(s). All article content, except where otherwise noted, is licensed under a Creative Commons Attribution (CC BY) license (http://creativecommons.org/licenses/by/4.0/). https://doi.org/10.1063/1.5050234

The L1$_0$ ordered phase of FePt is a prominent example of a highly anisotropic material with a simple unit cell, which can be easily stabilized in nanoscale thin films.[1,2] Its technological relevance originates from the large uniaxial magnetic anisotropy (K_u),[2,3] which makes FePt the material of choice for heat-assisted magnetic recording (HAMR) schemes.[4,5] Established bulk characterization methods for thermophysical properties, i.e., elastic constants (C_{ij}), heat capacity (C_p), thermal conductivity (κ), and thermal expansion coefficients (α), are mostly inapplicable in such nanoscale thin film materials. The envisioned applications nevertheless substantiate the need for a thorough characterization of all involved properties.

Ideally, the inaccessible properties of the material could be calculated on an *ab-initio* basis. The so far simulated properties relevant to the HAMR process range from the Curie temperature variation in granular films[6,7] over *ab-initio* models for mode specific electron phonon coupling constants[8] up to full multiscale models for the magnetization dynamics.[9] Apart from recent mode specific calculations of the phonon Grüneisen constants[10] (Γ) and extensive work on the elastic constants,[11–13] predictions for C_p, κ, and α are lacking, which hints at the complexity of full *ab-initio* theoretical approaches.

Experimental methods tailored to be applicable in the thin-film regime have been developed alongside the improved thin film growth techniques. Specifically, for FePt, time-domain thermoreflectance in combination with 1D thermal transport models has been used to extract the heat conductivity and thermal boundary resistances.[14,15] Even an estimate for the diverging magnetic specific heat

has been obtained.[16] The out-of-plane elastic constant C_{33} has been determined by picosecond ultrasonics from the coherent phonon propagation monitored by an all-optical pump-probe method[17] and electromagnetic-acoustic resonance.[18] Diffraction studies on L1$_0$ FePt compounds report a strong anisotropy in the thermal expansion upon equilibrium heating where the dominant in-plane expansion heralds anisotropic stresses.[19,20]

A recent time-resolved investigation has combined the direct access to the structural dynamics of FePt nanograins via ultrafast electron diffraction (UED) with direct measurements of the Fe magnetization by resonant soft X-ray diffraction.[10] This study connected the obtained experimental interpretation with the insight of *ab-initio* theory to study the complex coupled dynamics initiated by the simultaneous action of electronic, magnetic, and phononic stress contributions.[10] The ultrafast demagnetization and potentially anisotropic electron and phonon stresses were found to drive a pronounced out-of-plane contraction that decays to zero within 20 ps. For this experiment, the FePt nanograins embedded in a carbon matrix were transferred from the substrate to an ultrathin metal grid suitable for UED and the out-of-plane lattice motion was derived from asymmetric diffraction peaks. Ultrafast X-ray diffraction (UXRD) in the symmetric Bragg reflection geometry is an established method for measurements of the lattice expansion of thin films and heterostructures that are supported by a substrate.[21,22] A synchrotron-based UXRD study[23] on continuous FePt films has reported an out-of-plane expansion upon photo-excitation; however, the time resolution was insufficient to observe the acoustic vibrations.[10]

Here, we present laser-based UXRD experiments on FePt in the L1$_0$ phase on MgO substrates with a time resolution of approximately 200 fs. We compare the lattice

---

a)bargheer@uni-potsdam.de

response of a continuous crystalline FePt thin film to the nano-granular FePt samples in a carbon matrix relevant for magnetic recording. Both samples are investigated as-grown onto the MgO (100) substrates. In contrast to the out-of-plane contraction in free-standing granular FePt films, observed by UED in the transmission geometry on a transmission electron microscopy (TEM) grid,[10] we observe an ultrafast out-of-plane expansion within 2.5 ps limited by the sound velocity. From the observed coherent phonon oscillations period of 4.6 ps and a precise measurement of the film thickness $d = 9.7$ nm by X-ray reflectivity (XRR), we derive an out-of-plane longitudinal acoustic sound velocity of 4.2 nm/ps which is in line with the previously reported elastic constants[17] and with the periods observed by UED.[10] We discuss that the out-of-plane structural dynamics strongly varies for different film morphologies because out-of-plane contractions are coupled to in-plane expansion by the Poisson effect. Our study thus illustrates the capabilities of laboratory-based UXRD for determining the elastic constants in ultrathin samples. From a conceptually simple one-dimensional linear chain (LC) model, we furthermore obtain the different stresses that drive the out-of-plane response in granular and thin-film media.

We compare granular and continuous FePt films that are both in the $L1_0$ phase and grown onto MgO (100) oriented substrates. The continuous film was prepared by magnetron-sputtering Fe and Pt from a composite FePt target onto a substrate preheated to 500 °C. The granular film was sputtered from a FePt-carbon composite target with approximately 30 vol. % C onto a substrate preheated to 650 °C. The c-axis and magnetization are oriented out-of-plane. XRR was carried out to characterize the film thicknesses at the KMC3-XPP endstation[24] at the BESSY II synchrotron radiation facility. Using programs from the reflpak suite,[25] the XRR data in Figs. 1(a) and 1(c) were analyzed and fitted by the resulting electron density depicted in Figs. 1(e) and 1(f). The insets (b) and (d) depict the inferred sample structures. The Kiessig fringes of the granular film decay quickly, confirming the increased surface roughness known from cross sectional TEM images of comparable samples.[2,26]

Scanning electron microscopy (SEM) images of similarly prepared samples (not shown) display that the granular film consists of segregated FePt-nanograins with a size distribution centered at approximately 10 nm embedded in amorphous carbon that magnetically decouples the grains. This is confirmed by the magnetic hysteresis measurements shown in Fig. 1(g) carried out using a commercial SQUID-vibrating sample magnetometer (Quantum Design). The granular sample exhibits a large coercive field of approximately $\mu_0 H = 5$ T, which is desirable for HAMR, whereas the thin film switches at a considerably reduced field of $\mu_0 H = 0.4$ T via domain wall motion, which is inhibited in granular samples.[27] The saturation magnetization for the granular film is reduced by a factor of 0.7 as compared to the continuous film, which agrees with the volume filling factor of FePt in the non-magnetic carbon estimated from SEM images.

Using UXRD, we monitor the Bragg peak shift in the symmetric Bragg diffraction geometry and thus the out-of-plane lattice expansion of the two different crystalline
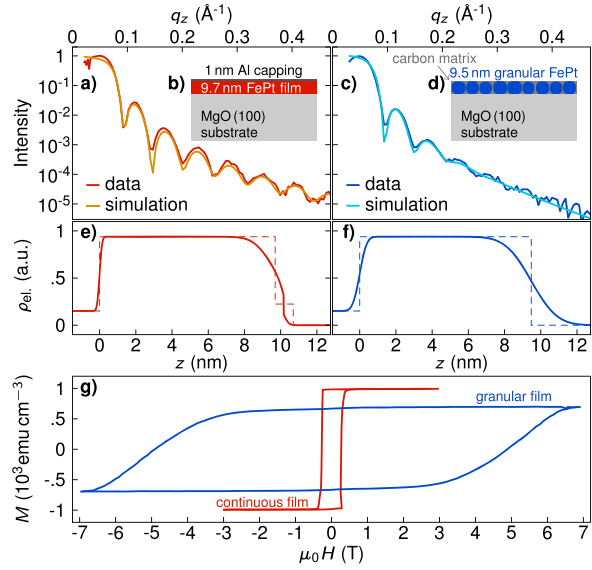

FIG. 1. Sample characterization: X-ray reflectivity data of the continuous (a) and granular (c) film. Orange and cyan colored lines indicate the fit result obtained by assuming the electron densities shown in (e) and (f). Sample structures derived from the electron density without roughness [dashed lines in (e) and (f)] are schematically shown in the insets (b) and (d). The magnetization hysteresis in (g) shows a strongly enhanced coercivity and a reduced saturation magnetization of the granular film compared to the continuous film.

specimens with sub-picosecond time resolution at a laboratory-based diffraction setup.[28] Figure 2(a) displays the Bragg diffraction curve of the unexcited granular and continuous film samples and the inset (b) schematically shows the diffraction and pump-probe geometry. The MgO (002) substrate peak is located at $\theta = 21.45°$, and the (002) FePt-peaks appear approximately at $\theta = 24.6°$. We optically excite the samples with p-polarized pump pulses with a central wavelength of 800 nm and a pulse duration of 100 fs. From the 0.2 mJ pulse energy at a 1 kHz repetition rate with a 1.4 mm × 1.5 mm (FWHM) beam profile incident under $\beta = 45°$ relative to the surface normal, we calculate an incident fluence of 6 mJ cm^{-2}. Using a transfer matrix algorithm for the optical absorption calculation[29] and literature values for the optical properties,[30] we find that a fraction of 25% of the incident energy is absorbed in the continuous FePt material. The hard X-ray probe-pulses with a duration of 200 fs are generated by a laser driven X-ray source, monochromatized, and focused onto the sample using a Montel optic[31] with a convergence of approximately 0.3°. This produces a flux of approximately 10^6 photons/s at the sample in the energy range of Cu-K α_1/α_2 X-ray characteristic line emission. To obtain the time-resolved strain from the diffracted intensity I, the detector images are mapped to the out-of-plane reciprocal space coordinate q_z as described previously.[32] $I(q_z)$ is then fitted by a Gaussian line profile, in order to extract the position of the (002) Bragg peaks $q_{z,\text{fit}}(t)$ for each delay t between pump and probe pulses. Using $q_z(t) = 4\pi/c(t)$, we obtain the evolution of the average FePt lattice plane spacing $c(t)$ in real space. The resulting strain $\varepsilon(t) = (c(t) - c_0)/c_0$, using $c_0 = c(t < 0)$, is depicted in Figs. 2(c) and 2(d).
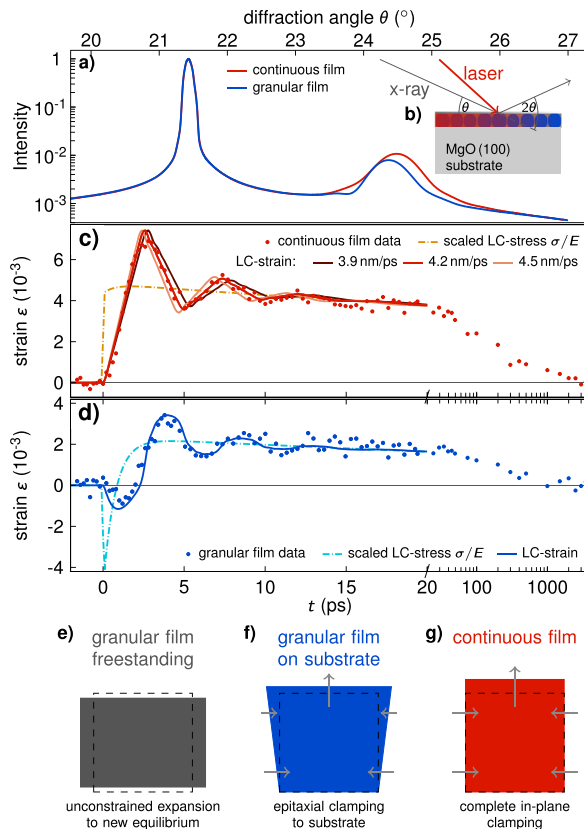
FIG. 2. X-ray diffraction and simulations: (a) Characterization of the samples using X-ray diffraction in the reflection geometry shown in the inset (b). Data points in (c) and (d) show the strain extracted from the shift of the FePt (002) Bragg peaks of the continuous and granular film in reciprocal space. Solid lines in (c) and (d) represent the transient strains that result from the applied time dependent stresses (dashed lines), in a linear chain (LC) model. The lattice dynamics in the first 10 ps of the granular film differ significantly from the strain observed in a continuous film. An initially contractive stress is required to obtain a qualitative agreement between simulation and measurement. (e)–(g) Schematic of clamping mechanisms that we believe to affect the out-of-plane expansion for the three different growth cases: (e) free-standing (f) granular film on a substrate and (g) continuous film on a substrate.

We first discuss the transient strain of the continuous FePt film [Fig. 2(c)]. An out-of-plane lattice expansion of up to 0.7% rises to its maximum within 2.8 ± 0.2 ps. Subsequently, an oscillation with a period of $T = 4.6 \pm 0.2$ ps superimposes the strain relaxation that originates from the flow of thermal energy to the substrate. From the measured T and d, we obtain the longitudinal acoustic sound velocity $v_s = 2d/T = 4.2 \pm 0.2$ nm/ps.[33,34]

We observe a considerable out-of-plane expansion of approximately 0.4% at $t = 20$ ps for the continuous thin film after the coherent strain wave oscillations end due to repeated partial transmission into the substrate. At such large delays, the observed strain ε scales linearly with the quasi-thermal stress σ according to Hooke's law $\sigma = E\varepsilon$. In metal films, the observed strain originates from a stress that is a superposition of the contributions from energy deposition into the electron and lattice system.[33,35–37] In the particular case of magnetically ordered materials, additional stress

originating from the excitation of the spin system has been reported.[10,21] Assuming thermal equilibration of these contributing subsystems, the observed strain ε directly indicates the transient temperature rise ΔT via $\varepsilon = \alpha \Delta T$. For such a simplified analysis, we can extract an effective linear thermal expansion coefficient α, which incorporates all contributing stresses, e.g., electron and phonon pressure, magnetostriction, and the coupling of in- and out-of-plane strain by the Poisson effect by a very coarse estimation of the temperature rise. Considering the dominant contribution of the phonons to the specific heat of approximately[16] $C_p = 3.5 \times 10^6$ $J\,m^{-3}\,K^{-1}$, we estimate from the absorbed laser fluence F_a and the film thickness d: $\Delta T = F_a/(dC) \approx 147$ K. This yields an estimate for the effective linear thermal expansion coefficient,[38] which is applicable only on timescales where the electron-spin-phonon system is in a quasi-equilibrium while in-plane strain propagation is still negligible: $\alpha = \varepsilon/\Delta T \approx 2.7 \times 10^{-5}$ K^{-1}. The observed decaying strain for times $t > 20$ ps is attributed to a cooling of the FePt film by phonon heat transport to the insulating substrate, in agreement with previous synchrotron studies.[23] In our coarse approximation, we refer to a quasi-equilibrium, since recent theoretical developments in the modeling of time-resolved experiments that go beyond two or three temperature models indicate that such an equilibration process may take many tens of picoseconds due to mode dependent electron phonon couplings[8,10,37] or potentially weak spin-lattice coupling.[21]

In order to further interpret the measurement on the epitaxial thin film, we simulate the results in a 1-dimensional LC model of coupled masses and springs. The simulations are carried out using the strain calculation module from the udkm1Dsim toolbox simulation package.[39] We calculate the response to a time-dependent expansive stress that is assumed to be homogenous across the FePt thin films motivated by the optical penetration depth[30] for 800 nm light in FePt of approximately 24.2 nm, which is large compared to the 9.7 nm film thickness. The dashed-dotted line in Fig. 2(c) shows the total time-dependent stress that leads to the observed transient strain, with multiple acoustic reflections shown as solid lines. It is rather close to a step function with a rising edge given by the laser pulse duration. A slight additional rise and decay can be attributed to a conversion of electronic to phonic stress and the onset of heat transport to the substrate, respectively. For convenience, we have added the simulated strain as solid lines to Fig. 2(c) assuming different longitudinal acoustic sound velocities v_s from which we can obtain the elastic constant $C_{33} = \rho v_s^2 \approx 267$ GPa using $v_s = 4.2$ nm/ps. We use the density $\rho = 15\,113$ kg/m^3 of FePt calculated from atomic weights and the known unit cell dimensions of the conventional tetragonal unit cell of parameters $c = 3.72$ Å and $a = 3.85$ Å of FePt.[20] The derived C_{33} value lies just at the lower bound of the range of 242 – 371 GPa from theoretical considerations.[11–13] It agrees well with the observed reduction of the elastic constant of FePt specimen from 309 to about 250 GPa, when the thickness is less than 40 nm.[17] The temperature dependence of the elastic constants observed under equilibrium heating[18] supports an even further decrease in the transient bulk modulus resulting from a laser-induced temperature increase. The surprisingly small $v_s = 2.2$ nm/ps reported for the free standing

grains[10] might be due to a missing factor of 2 since for spheres, the expected period $T = d/v_s$ must be calculated using the diameter d of the laser excited particles instead of their radius.

Now, we discuss the dynamics in our nano-granular film. The oscillation period is nearly identical to the continuous film, as expected for the same layer thickness. The in-plane dynamics of the granular film occur with a similar period because the average grain size equals the thickness. Its out-of-plane contraction within the first 2.5 ps [Fig. 2(d)] confirms the ultrafast contractive stress contribution that was reported for the free-standing granular film.[10] The contractive stress component was shown to originate from the release of magnetostriction due to the transient demagnetization of the FePt.[10] The timescale of the demagnetization varies depending on the experimental conditions but is usually fitted by an exponential decay with time constants smaller than 0.5 ps.[10,26,27] The magnetization recovers within several tens of picoseconds, depending on the excitation fluence.[10,26] For larger time delays ($t > 2.5$ ps), we definitely observe a long-lasting lattice expansion, which has only about half the amplitude of the continuous film. The contractive stress driven by spin-excitations is still operative due to the slow remagnetization, but the phonon-driven heat expansion prevails. As we argue below, the crossover from compressive to tensile strain is due to partial constraints to the in-plane motion of the nanograins. The contraction observed in the free standing film is thus probably stopped as soon as the in-plane grain expansion is inhibited by the epitaxial pinning to the MgO substrate and the surrounding carbon matrix, which is also pinned to the substrate. In the case of the continuous epitaxial film, such in-plane constraints completely inhibit the compressive strain at early delays.

For the epitaxial continuous film, the 1D LC model is an excellent approximation for the first 20 ps, since in-plane motion is prohibited by symmetry. In the nano-granular sample, this symmetry is broken and various anisotropic driving stresses can occur so that a modeling of the three-dimensional response of particles with anisotropic elastic properties embedded in a carbon matrix would be required. The inhomogeneous size distribution with unknown coupling strength to the substrate further challenges *ab-initio* treatment. Here, we analyze the strain response of the FePt granular sample grown on a substrate, because it connects the previous research on free-standing nanograins[10] and epitaxial thin films[23] and since it is the relevant geometry used in HAMR media. For a simplified simulation of the observed out-of-plane strain, we assume the effective out-of-plane stress shown in Fig. 2(d) as a dashed-dotted line, which includes contributions from an in-plane expansion that leads to an out-of-plane contractive stress via Poisson's ratio. We speculate that the crossover from a contractive to an expansive out-of-plane stress within about 1 ps is due to the fact that the in-plane expansion concomitant with the out-of-plane contraction is hindered by epitaxial clamping to the substrate and the carbon matrix. This contribution of the Poisson effect adds to the out-of-plane contraction driven by ultrafast spin disordering.[10]

Figures 2(e)–2(g) schematically show our current understanding of the pronounced differences for free-standing grains vs. continuous epitaxial films of FePt, with nano-granular films on a substrate as an intermediate case. While the nearly free-standing grains, which are more loosely embedded in a carbon matrix on a TEM grid, can contract out-of-plane because they can expand in-plane, the continuous film cannot expand in-plane. This suppresses the contraction out-of-plane and an expansion due to electron and phonon stresses prevails. For the nano-granular film on the substrate, the in-plane expansion is still somewhat suppressed due to the carbon matrix and due to epitaxial strain resulting from the pinning to the substrate.

In conclusion, we have shown that laser-excited FePt in the L1$_0$ phase essentially expands out-of-plane, if the continuous film or the nano-grains are epitaxially attached to a substrate. From the observed strain-wave oscillations, we obtain the out-of-plane sound velocity and thus the elastic constant C_{33}, well in line with the reported decrease for films of few nm thickness.[17] Our experiments showcase the capabilities of table-top UXRD to monitor transient stresses via the resulting coherent strain waves. The subpicosecond time-resolution of the experiments reveal a markedly different response of the granular sample compared to the continuous film. This proves the relevance of different balances of the in-plane stresses for the out-of-plane lattice dynamics. Few previous experimental studies assume that the related Poisson effect enhances the amplitude of ultrafast generated strain in continuous films;[21,38,40] however, an unambiguous general proof for this enhancement is so far missing.

The complexity of the anisotropic nanogranular samples calls for modeling approaches that go beyond harmonic oscillator models[8,16] or the 1D approximation that is frequently applied in laser-excited bulk materials or continuous thin films since the seminal work of Thomson *et al.*[41] We envision that time-resolved studies of various properties of nanoparticles could be cross-fertilized by the development of three-dimensional model calculations since they are often intricately linked to the lattice via changes in their band structure.

[1] S. Wicht, S. Wee, O. Hellwig, V. Mehta, S. Jain, D. Weller, and B. Rellinghaus, J. Appl. Phys. **119**, 115301 (2016).

[2] O. Mosendz, S. Pisana, J. Reiner, B. Stipe, and D. Weller, J. Appl. Phys. **111**, 07B729 (2012).

[3] D. Weller, A. Moser, L. Folks, M. Best, W. Lee, M. Toney, M. Schwickert, J.-U. Thiele, and M. Doerner, IEEE Trans. Magn. **36**, 10 (2000).

[4] D. Weller, O. Mosendz, G. Parker, S. Pisana, and T. S. Santos, Phys. Status Solidi A **210**, 1245 (2013).

[5] D. Weller, G. Parker, O. Mosendz, A. Lyberatos, D. Mitin, N. Y. Safonova, and M. Albrecht, J. Vac. Sci. Technol., B **34**, 060801 (2016).

[6] O. Hovorka, S. Devos, Q. Coopman, W. J. Fan, C. J. Aas, R. F. L. Evans, X. Chen, G. Ju, and R. W. Chantrell, Appl. Phys. Lett. **101**, 052406 (2012).

[7] S. Pisana, S. Jain, J. Reiner, G. Parker, C. Poon, O. Hellwig, and B. Stipe, Appl. Phys. Lett. **104**, 162407 (2014).

[8] P. Maldonado, K. Carva, M. Flammer, and P. M. Oppeneer, Phys. Rev. B **96**, 174439 (2017).

[9] N. Kazantseva, D. Hinzke, U. Nowak, R. W. Chantrell, U. Atxitia, and O. Chubykalo-Fesenko, Phys. Rev. B **77**, 184428 (2008).

[10] A. H. Reid, X. Shen, P. Maldonado, T. Chase, E. Jal, P. W. Granitzka, K. Carva, R. K. Li, J. Li, L. Wu, T. Vecchione, T. Liu, Z. Chen, D. J. Higley,

N. Hartmann, R. Coffee, J. Wu, G. L. Dakovski, W. F. Schlotter, H. Ohldag, Y. K. Takahashi, V. Mehta, O. Hellwig, A. Fry, Y. Zhu, J. Cao, E. E. Fullerton, J. Stöhr, P. M. Oppeneer, X. J. Wang, and H. A. Dürr, Nat. Commun. **9**, 388 (2018).

[11]J. Kim, Y. Koo, and B.-J. Lee, J. Mater. Res. **21**, 199 (2006).

[12]M. Müller, P. Erhart, and K. Albe, J. Phys.: Condens. Matter **19**, 326220 (2007).

[13]N. Zotov and A. Ludwig, Intermetallics **16**, 113 (2008).

[14]A. Chernyshov, D. Treves, T. Le, F. Zong, A. Ajan, and R. Acharya, J. Appl. Phys. **115**, 17B735 (2014).

[15]A. Giri, S. H. Wee, S. Jain, O. Hellwig, and P. E. Hopkins, Sci. Rep. **6**, 32077 (2016).

[16]J. Kimling, J. Kimling, R. Wilson, B. Hebler, M. Albrecht, and D. G. Cahill, Phys. Rev. B **90**, 224408 (2014).

[17]N. Nakamura, A. Uranishi, M. Wakita, H. Ogi, M. Hirao, and M. Nishiyama, Appl. Phys. Lett. **98**, 101911 (2011).

[18]N. Nakamura, N. Yoshimura, H. Ogi, and M. Hirao, J. Appl. Phys. **114**, 093506 (2013).

[19]R. Nicula, O. Crisan, A. Crisan, I. Mercioniu, M. Stir, and F. Vasiliu, J. Alloys Compd. **622**, 865 (2015).

[20]Y. Tsunoda and H. Kobayashi, J. Magn. Magn. Mater. **272**, 776 (2004).

[21]A. von Reppert, J. Pudell, A. Koc, M. Reinhardt, W. Leitenberger, K. Dumesnil, F. Zamponi, and M. Bargheer, Struct. Dyn. **3**, 054302 (2016).

[22]A. Von Reppert, R. Sarhan, F. Stete, J. Pudell, N. Del Fatti, A. Crut, J. Koetz, F. Liebig, C. Prietzel, and M. Bargheer, J. Phys. Chem. C **120**, 28894 (2016).

[23]D. Xu, C. Sun, D. Brewe, S.-W. Han, P. Ho, J. Chen, S. Heald, X. Zhang, and G. Chow, J. Appl. Phys. **115**, 243907 (2014).

[24]M. Reinhardt and W. Leitenberger, J. Large-Scale Res. Facil. **2**, 89 (2016).

[25]P. A. Kienzle, K. V. O'Donovan, J. F. Ankner, N. Berk, and C. Majkrzak, "NCNR Reflectometry Software," (2006).

[26]J. Mendil, P. Nieves, O. Chubykalo-Fesenko, J. Walowski, T. Santos, S. Pisana, and M. Münzenberg, Sci. Rep. **4**, 3980 (2014).

[27]T. Shima, K. Takanashi, Y. K. Takahashi, and K. Hono, Appl. Phys. Lett. **81**, 1050 (2002).

[28]D. Schick, A. Bojahr, M. Herzog, C. V. K. Schmising, R. Shayduk, W. Leitenberger, P. Gaal, and M. Bargheer, Rev. Sci. Instrum. **83**, 025104 (2012).

[29]L. Le Guyader, A. Kleibert, F. Nolting, L. Joly, P. Derlet, R. Pisarev, A. Kirilyuk, T. Rasing, and A. Kimel, Phys. Rev. B **87**, 054437 (2013).

[30]Z. H. Cen, B. X. Xu, J. F. Hu, J. M. Li, K. M. Cher, Y. T. Toh, K. D. Ye, and J. Zhang, Opt. Express **21**, 9906 (2013).

[31]M. Bargheer, N. Zhavoronkov, R. Bruch, H. Legall, H. Stiel, M. Woerner, and T. Elsaesser, Appl. Phys. B **80**, 715 (2005).

[32]D. Schick, R. Shayduk, A. Bojahr, M. Herzog, C. von Korff Schmising, P. Gaal, and M. Bargheer, J. Appl. Crystallogr. **46**, 1372 (2013).

[33]M. Nicoul, U. Shymanovich, A. Tarasevitch, D. von der Linde, and K. Sokolowski-Tinten, Appl. Phys. Lett. **98**, 191902 (2011).

[34]D. Schick, M. Herzog, A. Bojahr, W. Leitenberger, A. Hertwig, R. Shayduk, and M. Bargheer, Struct. Dyn. **1**, 064501 (2014).

[35]S. Nie, X. Wang, H. Park, R. Clinite, and J. Cao, Phys. Rev. Lett. **96**, 25901 (2006).

[36]K. Sokolowski-Tinten, X. Shen, Q. Zheng, T. Chase, R. Coffee, M. Jerman, R. K. Li, M. Ligges, I. Makasyuk, M. Mo, A. H. Reid, B. Rethfeld, T. Vecchione, S. P. Weathersby, H. A. Dürr, and X. J. Wang, Struct. Dyn. **4**, 054501 (2017).

[37]T. Henighan, M. Trigo, S. Bonetti, P. Granitzka, D. Higley, Z. Chen, M. P. Jiang, R. Kukreja, A. Gray, A. H. Reid, E. Jal, M. C. Hoffmann, M. Kozina, S. Song, M. Chollet, D. Zhu, P. F. Xu, J. Jeong, K. Carva, P. Maldonado, P. M. Oppeneer, M. G. Samant, S. S. P. Parkin, D. A. Reis, and H. A. Dürr, Phys. Rev. B **93**, 220301 (2016).

[38]J. Pudell, A. A. Maznev, M. Herzog, M. Kronseder, C. H. Back, G. Malinowski, A. von Reppert, and M. Bargheer, Nat. Commun. **9**, 3335 (2016).

[39]D. Schick, A. Bojahr, M. Herzog, C. von Korff Schmising, R. Shayduk, and M. Bargheer, Comput. Phys. Commun. **185**, 651 (2014).

[40]H. J. Lee, J. Workman, J. S. Wark, R. D. Averitt, A. J. Taylor, J. Roberts, Q. McCulloch, D. E. Hof, N. Hur, S.-W. Cheong, and D. J. Funk, Phys. Rev. B **77**, 132301 (2008).

[41]C. Thomsen, H. T. Grahn, H. J. Maris, and J. Tauc, Phys. Rev. B **34**, 4129 (1986).

Article X

Spin stress contribution to the lattice dynamics of FePt

Alexander von Reppert, Lisa Willig, **Jan-Etienne Pudell**, Steffen Peer Zeuschner, Gabriel Sellge, Fabian Ganss, Olav Hellwig, Jon Ander Arregi, Vojtěch Uhlíř, Aurélien Crut and Matias Bargheer

Invar-behavior occurring in many magnetic materials has long been of interest to materials science. Here, we show not only invar behavior of a continuous film of FePt but also even negative thermal expansion of FePt nanograins upon equilibrium heating. Yet, both samples exhibit pronounced transient expansion upon laser heating in femtosecond x-ray diffraction experiments. We show that the granular microstructure is essential to support the contractive out-of-plane stresses originating from in-plane expansion via the Poisson effect that add to the uniaxial contractive stress driven by spin disorder. We prove the spin contribution by saturating the magnetic excitations with a first laser pulse and then detecting the purely expansive response to a second pulse. The contractive spin stress is reestablished on the same 100-ps time scale that we observe for the recovery of the ferromagnetic order. Finite-element modeling of the mechanical response of FePt nanosystems confirms the morphology dependence of the dynamics.

PHYSICS

Spin stress contribution to the lattice dynamics of FePt

A. von Reppert[1,2], L. Willig[1,2], J.-E. Pudell[1,2], S. P. Zeuschner[1,2], G. Sellge[3,4], F. Ganss[3], O. Hellwig[3,4], J. A. Arregi[5], V. Uhlíř[5,6], A. Crut[7], M. Bargheer[1,2]*

Invar-behavior occurring in many magnetic materials has long been of interest to materials science. Here, we show not only invar behavior of a continuous film of FePt but also even negative thermal expansion of FePt nanograins upon equilibrium heating. Yet, both samples exhibit pronounced transient expansion upon laser heating in femtosecond x-ray diffraction experiments. We show that the granular microstructure is essential to support the contractive out-of-plane stresses originating from in-plane expansion via the Poisson effect that add to the uniaxial contractive stress driven by spin disorder. We prove the spin contribution by saturating the magnetic excitations with a first laser pulse and then detecting the purely expansive response to a second pulse. The contractive spin stress is reestablished on the same 100-ps time scale that we observe for the recovery of the ferromagnetic order. Finite-element modeling of the mechanical response of FePt nanosystems confirms the morphology dependence of the dynamics.

INTRODUCTION

Invar materials exhibit almost zero thermal expansion over a wide temperature range (*1*). Although the discovery of a 10-fold reduction of the thermal expansion of the $Fe_{0.65}Ni_{0.35}$ alloy compared to its pure elements (*2*) dates back to 1897, its origin remained an active area of solid-state research over the next century (*3–5*). Invar behavior requires a mechanism that counteracts the thermal expansion resulting from anharmonic phonon-phonon interactions. For magnetic invar materials, it is found that the required contractive stress originates from an increased volume for the spin-ordered state compared to the disordered state that can now be predicted in different ab initio approaches (*4*, *5*). Quantitative, time-resolved studies of the structural dynamics have recently started to explore the response of the lattice to magnetic stresses (*6–12*), which are attributed to the transfer of angular momentum (*6*, *7*), energy (*8*, *12*), and entropy (*9*) from and to the spin system. In this context, it is interesting to ask how invar materials respond to laser-induced heating on the picosecond time scale and to determine the lattice dynamics induced by counteracting contributions of phonon and spin stresses.

One approach for the separation of the magnetic response from the ever-present phonon contribution to the lattice dynamics in laser-excited metals is to compare the structural response above and below the magnetic ordering temperature (*8–10*). This is sometimes prohibited by irreversible modifications of the material under heating. A demagnetized state can also be created transiently by femtosecond laser excitation (*13*, *14*) and characterized by applying a pump-probe sequence, where a second pump pulse excites the nonequilibrium state generated by the first pump pulse. Double-pulse excitation

experiments not only have been used to demonstrate intriguing coherent control of the magnetization (*15–17*) and lattice dynamics (*18*, *19*) but they also revealed that the induced magnetization dynamics, (*20*) total transient demagnetization (*21*), and magnetic anisotropy (*22*) critically depend on the pulse-to-pulse separation.

Invar behavior is found in many Fe-containing alloys (*1*, *23*). The magnetic recording medium FePt in the fully ordered $L1_0$ phase is receiving particular attention due to its large uniaxial magnetic anisotropy energy ($K_u > 4.5$ J/cm^3) (*24*), which sustains nanoscopic magnetically stable bits with perpendicular magnetization. The envisioned heat-assisted magnetic recording scheme (*25*) aims at improving the magnetic information densities to exceed 2 Tb/in^2 in commercial products of the near future (*26*). The possibility to grow magnetic, oriented nanograins with a high degree of structural order makes this material an ideal candidate for studying the lattice using time-resolved diffraction techniques. In a recent ultrafast x-ray diffraction (UXRD) study, we have found a short-lived lattice contraction along the short out-of-plane *c* axis of the tetragonal unit cell of a nanogranular FePt film on a substrate, whereas continuous epitaxial thin films merely expanded under otherwise identical excitation conditions (*27*). Previously, ultrafast electron diffraction experiments had reported a transient *c*-axis contraction and in-plane expansion for freestanding FePt nanograins (*11*). Spin-polarized density functional theory consistently predicts this tetragonal distortion when comparing the spin-ordered ferromagnetic ground state to the paramagnetic phase with full spin disorder (*11*). In the same paper, a strongly anisotropic phonon stress was predicted, seven times larger in-plane than out-of-plane (*11*). In all three cases the material is the $L1_0$ phase of FePt. Therefore, the variability of the measured ultrafast dynamics suggests that the morphology and substrate-induced strain must have an important influence on the lattice dynamics at ultrafast time scales.

Here, we use fluence-dependent UXRD experiments on granular FePt thin films to show experimentally that the initial contraction originates from spin entropy, as it saturates for high fluence when the spin system is disordered. Weak excitation pulses trigger an initial contraction driven by spin stress, but expansive lattice stresses prevail after about 3 ps. The direct connection of spin disorder with the contractive stress is revealed by double-pulse excitation scenarios. When a strong first excitation pulse has essentially disordered the

[1]Institute of Physics and Astronomy, University of Potsdam, Karl-Liebknecht-Str. 24-25, 14476 Potsdam, Germany. [2]Helmholtz-Zentrum Berlin für Materialien und Energie GmbH, Wilhelm-Conrad-12 Röntgen Campus, BESSY II, Albert-Einstein-Str. 15, 12489 Berlin, Germany. [3]Institut für Physik, Technische Universität Chemnitz, Reichenhainer Str. 70, 09126 Chemnitz, Germany. [4]Institut für Ionenstrahlphysik und Materialforschung, Helmholtz-Zentrum Dresden-Rossendorf, Bautzner Landstrasse 400, 01328 Dresden, Germany. [5]CEITEC BUT, Brno University of Technology, Purkyňova 123, 612 00 Brno, Czechia. [6]Institute of Physical Engineering, Brno University of Technology, Technická 2, 616 69 Brno, Czechia. [7]FemtoNanoOptics Group, Institut Lumière Matière, Université de Lyon, CNRS-Université Lyon 1, 69622 Villeurbanne, France.
*Corresponding author. Email: bargheer@uni-potsdam.de

spin system, a second excitation pulse applied after a short delay only triggers expansion.

However, if the second pulse arrives about 100 ps later, the spin order has partially recovered, and the second pulse yields a contraction. This time scale for the recovery of the contractive stress is dictated by thermal transport and identical to the time scale of remagnetization observed in time-resolved magneto-optical Kerr effect (tr-MOKE) measurements. We model the coupled out-of-plane and in-plane lattice response of the nanograins using finite-element modeling (FEM) by varying the amplitude of the uniaxial contractive stress component $\sigma_\perp^{sp}$ associated with the spin disorder, which is the essential parameter for describing the two-pulse experiments. To provide a solid experimental basis for our interpretation, we compare granular films composed of FePt grains in a carbon matrix to continuous films, where the in-plane expansion on the picosecond time scale is forbidden by symmetry.

RESULTS

Time-resolved and static expansion

We first discuss the lattice response of FePt to laser excitation and equilibrium heating. Figure 1 (A and B) compares the lattice response of a granular and a continuous film of similar thickness to 100-fs pump laser pulses for incident laser fluences ranging from $F_{in} = 1.4$ to 11 mJ/cm^2 (see Materials and Methods for details). To show that lattice expansion beyond 3 ps is approximately proportional to F_{in} and thus to the energy density, we have normalized the observed out-of-plane strain $\eta_\perp$ to the incident laser fluence. Because the phonon system hosts most of the energy density at this time, the strain per fluence is approximately the same, and variations are due to energy absorbed in the spin system. The central finding for the granular film (Fig. 1A) is the pronounced contraction in the first 2 ps. Its absolute value is maximized for medium laser fluences, and the contraction disappears upon increasing the laser fluence further (see Supplementary Materials for the unscaled data). This already hints at the spin disorder as the driving mechanism of the contraction. The UXRD results in Fig. 1B show that the contraction is essentially absent for the continuous FePt film at all fluences. The small delay of the expansion observed in Fig. 1B for low laser fluences suggests that expansive and contractive out-of-plane stresses have different time dependences. Although the thermal expansion of bulk FePt solid solutions of different composition has been studied (28–31), static characterization of the out-of-plane expansion for continuous and granular L1$_0$-ordered thin films approaching the Curie temperature $T_C \approx 700$ K was, so far, not available. Our results in Fig 1C show that the out-of-plane dimension of L1$_0$-FePt behaves invar-like for the continuous film and even exhibits negative thermal expansion (NTE) for the granular FePt sample. The in-plane thermal expansion coefficient of FePt matches the value 1×10^{-5} K^{-1} of the MgO substrate (see Supplementary Materials), so that epitaxial stresses on the thin film upon equilibrium heating are expected to be small (11, 29, 31). Figure 1 thus directly contrasts that the FePt out-of-plane strain $\eta_\perp$ exhibits a pronounced difference between equilibrium heating, which shows NTE and invar behavior for granular and continuous FePt films, respectively, and ultrafast laser heating, where FePt mainly expands out-of-plane showing a positive strain $\eta_\perp = \Delta c/c$. We attribute the differences in $\eta_\perp(t)$ for the nanogranular and continuous FePt to the different magnitudes of in-plane strain $\eta_\parallel(t)$. The probed region is almost homogeneously heated as the excitation spot is three times
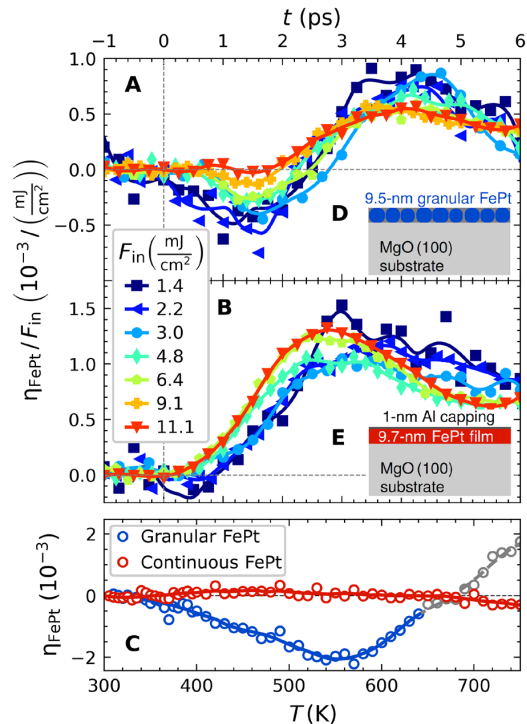

Fig. 1. Comparison of granular and continuous FePt film responses to laser excitation and equilibrium heating. (**A**) Normalized transient out-of-plane strain $\eta_\perp$ in FePt derived from the Bragg peak shift in UXRD experiments involving excitation of the granular FePt film with various incident fluences F_{in}. The observed strain is normalized to F_{in}. (**B**) Same for the continuous film. (**C**) Out-of-plane strain $\eta_\perp$ upon equilibrium heating for both samples. Points above 650 K are grayed out, because the Bragg peak intensity decrease by 20% of the granular sample may indicate a slight sample degradation. Solid lines serve as guide to the eye. The insets (**D**) and (**E**) schematically depict the sample structures.

larger than the probe pulses. Any in-plane stresses are therefore balanced by the adjacent unit cells for the continuous FePt film. The in-plane strain propagation from the edge of the excitation region to the probed region at the sound velocity sets the 100-ns time scale (much longer than those investigated in the time-resolved experiments) on which this in-plane fixation is relieved. For the granular FePt film, the inhomogeneity at the carbon-FePt interface enables transverse stresses and strains even on picosecond time scales, whereas they are forbidden by symmetry in the continuous film case. Under static heating conditions, both the substrate and the thin film can relax in-plane, which creates additional contractive elastic stresses out-of-plane via the Poisson effect. Thus, the static out-of-plane NTE of the granular film is reduced to an invar behavior in the continuous film, for which the in-plane expansion of FePt and hence the Poisson effect are limited by the epitaxial clamping to the substrate.

Double-pulse excitation: Spin stress tuning

The results of a double-pulse excitation scheme displayed in Fig. 2A confirm that the spin excitations drive the contraction in the granular FePt film. In these experiments, we use a first strong laser pulse (p$_1$) to saturate the spin excitations and a second, weaker laser pulse (p$_2$) for triggering subsequent dynamics with a delay Δt. The ultrashort
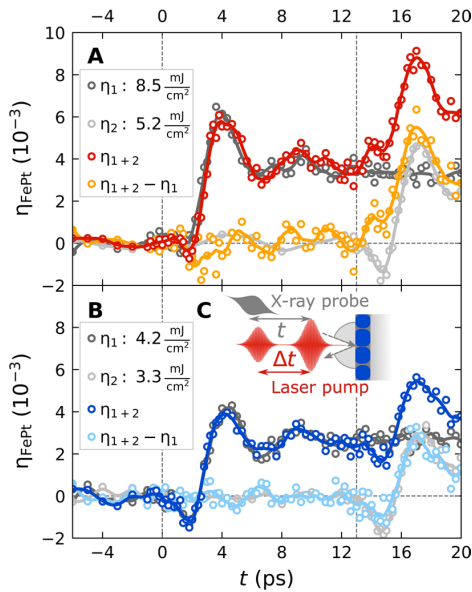
Fig. 2. UXRD with double-pulse excitation. (**A**) Transient strain $\eta(t)$ of the granular FePt film from UXRD with single- and double-pulse excitation. The first pulse at $t = 0$ has a fluence of $F_{in,1} = 8.5\,\mathrm{mJ/cm^2}$, and the second pulse at 13 ps is weaker ($F_{in,2} = 5.2\,\mathrm{mJ/cm^2}$). The nonequilibrium strains $\eta_{ne}(t) = \eta_{1+2}(t) - \eta_1(t)$ (orange) are derived by subtracting the dark gray curve from the red curve. This strain is induced by the photoexcitation in the nonequilibrium conditions set by the first pulse. (**B**) Same for weaker pump pulses $F_{in,1} = 4.2\,\mathrm{mJ/cm^2}$ and $F_{in,2} = 3.3\,\mathrm{mJ/cm^2}$, which only partially demagnetize the film. (**C**) Relative timing of the double-pulse excitation experiments.
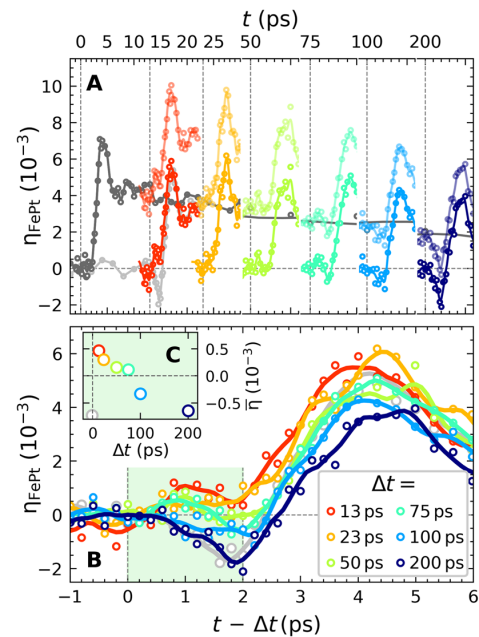
Fig. 3. Recovery of the spin entropy–driven lattice contraction. (**A**) Dark gray: transient strain $\eta_1(t)$ from UXRD with single-pulse excitation at $t = 0$ ($F_{in,1} = 8.5\,\mathrm{mJ/cm^2}$) for the granular film. Light-colored data: strain $\eta_{1+2}(t)$ observed for double-pulse excitation with the same first pulse and a second pulse with fluence ($F_{in,2} = 5.2\,\mathrm{mJ/cm^2}$) after $\Delta t = 13, 23, 50, 75, 100$, and 200 ps. The bright-colored data represent $\eta_{ne}(t) = \eta_{1+2}(t) - \eta_1(t)$. (**B**) Comparison of $\eta_{ne}(t - \Delta t)$ from (A) to the strain $\eta_2(t)$ obtained for excitation only with the second pulse (gray). (**C**) Average strain $\eta_{ne}(t - \Delta t)$ within the first 2 ps.

x-ray probe pulse detects the lattice dynamics $\eta_\perp(t)$ that is induced by this double-pulse excitation, as schematically depicted in Fig 2C. The dark gray data from Fig. 2A show the UXRD signal that characterizes the strain $\eta_1(t)$ due to a single strong pulse with $F_{in,1} = 8.5\,\mathrm{mJ/cm^2}$ at $t = 0$, which almost exclusively leads to expansion of the FePt film. In contrast, the light gray data representing the strain $\eta_2(t)$ generated by a weaker single pulse with $F_{in,2} = 5.2\,\mathrm{mJ/cm^2}$ arriving at $\Delta t = 13$ ps show a pronounced contraction at the onset of the second pulse, consistent with the fluence series in Fig. 1A. When both pulses excite the sample with the delay set to $\Delta t = 13$ ps, we observe the strain $\eta_{1+2}(t)$ (red data points). The orange points represent the additional strain $\eta_{ne}(t) = \eta_{1+2}(t) - \eta_1(t)$, which is induced by the photoexcitation of the sample in the nonequilibrium conditions previously set by the first pulse. It mainly differs from $\eta_2(t)$ (light gray curve in Fig. 2A) in the first 2 ps after the second laser pulse arrives. Clearly, there is no contraction at $t = 15$ ps just after the second pulse, if the sample was pre-excited with the first pulse. We conclude that the first pulse has essentially saturated the spin excitations. Figure 2B confirms this interpretation by reducing the fluences to $F_{in,1} = 4.2\,\mathrm{mJ/cm^2}$ and $F_{in,2} = 3.3\,\mathrm{mJ/cm^2}$ with the same timing. Now, $\eta_{ne}(t)$ shows approximately half of the contraction at $t = 15$ ps compared to $\eta_2(t)$ (light gray data) because the first pulse does not fully saturate the spin excitations.

Our double-pulse scheme also allows monitoring the recovery of the contractive stress by adjusting the timing between the excitation pulses for constant $F_{in,1}$ and $F_{in,2}$. Figure 3A depicts the results from Fig. 2A for tuning the double-pulse time delay Δt. Again, the gray

line shows the strain induced only by the first pump pulse with $F_{in,1} = 8.5\,\mathrm{mJ/cm^2}$. Within 200 ps, the cooling of the FePt lattice reduces the transient strain from $\eta_\perp = 4 \times 10^{-3}$ to the half value. The light-colored lines show the strain $\eta_{1+2}(t)$ observed for double-pulse excitation, and the bright colors show the nonequilibrium strain $\eta_{ne}(t) = \eta_{1+2}(t) - \eta_1(t)$. Figure 3B reproduces these data on a time axis where $t = 0$ indicates the arrival of the second pulse and compares $\eta_{ne}(t - \Delta t)$ to $\eta_2(t)$ (light gray), i.e., the response to the second pulse with and without pre-excitation. For a pulse delay of $\Delta t = 200$ ps, $\eta_{ne}(t - \Delta t)$ and $\eta_2(t)$ nearly coincide in the first 3 ps, indicating a reordering of the spin system within this time scale. For time delays shorter than $\Delta t = 75$ ps, the lattice expansion prevails. The red line ($\Delta t = 13$ ps) transforms continuously into the dark blue line ($\Delta t = 200$ ps) with increasing time delay, indicating the emergence of the contractive stress as the spin system can be disordered again by the second pulse.

Magnetization dynamics and energy density

To corroborate our findings about the spin stress contribution to the lattice dynamics, we analyze the magnetic system. The spin stress contribution to the strain response must vanish if the magnetic system is in a state close to its maximal entropy that can be reached either thermally or via laser-induced demagnetization. According to recent FEM simulations of the field enhancement effects in the optical absorption of a similar nanogranular sample (*32*), the temperature change due to the inhomogeneous optical absorption of the irregularly shaped FePt nano-islands varies between 10 and

30%. For $F_{\mathrm{in},1} = 8.5$ mJ/cm^2, we therefore estimate the temperature rise to be in the range $\Delta T = 300$ to 700 K. The majority of the nanogranular FePt will be transiently heated above the Curie temperature, which is about $T_{\mathrm{C}} \approx 650$ to 700 K for the current particle size (*33*).

Figure 4A contains tr-MOKE data for three selected fluences. We assume nearly full demagnetization for the incident fluence of 11 mJ/cm^2, as the signal does not increase beyond this fluence. Consistent with literature, this sets the initial demagnetization for the pulses (8.5 mJ/cm^2) used in the UXRD experiment from Figs. 3A and 2A at 85%. Because of the large out-of-plane anisotropy and the single-domain character of the grains (no domain wall propagation), we can use the tr-MOKE signal recorded with an external field of ±0.7 T as an estimation of the time-dependent average magnetization $M(t)$ of the sample (*34*). The static magnetization curve $M(T)$ of the granular FePt sample is depicted in Fig 4B. To relate the UXRD and tr-MOKE signal, we calculate an estimate for the spin contribution to the heat capacity (Fig. 4C) according to the mean field theory relation (*35*) $C_{\mathrm{sp}} \propto \frac{\partial M^2}{\partial T} = M \frac{\partial M}{\partial T}$, which agrees reasonably well with recent theoretical predictions represented by the dashed line (*36*).

The colored dashed lines in Fig. 4 (A to C) indicate how the MOKE signal, which is proportional to $M(t)$, is related to the auxiliary temperature $T(t)$ of the spin system for the specific time $t = \Delta t$ of the
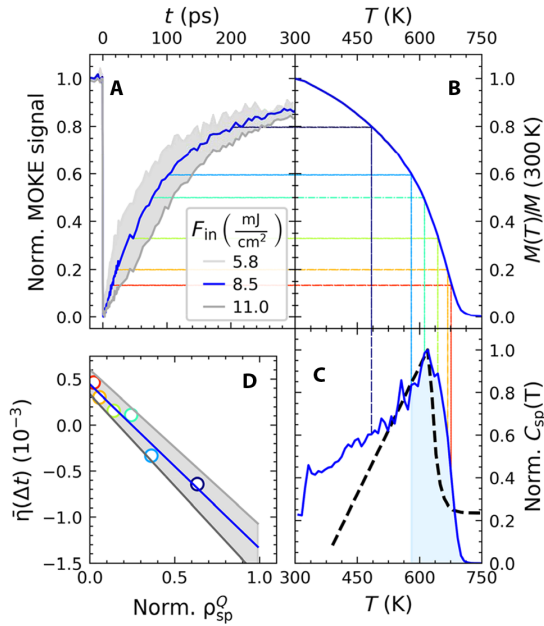
UXRD experiment. This temperature is used to estimate the energy density $\Delta\rho_{\mathrm{sp}}^{Q} = \int_{T} C_{\mathrm{sp}}(T')\,dT'$, which would be required to fully saturate the heat capacity $C_{\mathrm{sp}}(T)$ of the spin system. In a first-order analysis, the individual stresses from electrons, phonons, and spins $\sigma_{e,\mathrm{ph,sp}} = \Gamma_{e,\mathrm{ph,sp}}\rho_{e,\mathrm{ph,sp}}^{Q}$ are directly proportional to the heat energy densities $\rho_{e,\mathrm{ph,sp}}^{Q}$, and the dimensionless macroscopic Grueneisen coefficients $\Gamma_{e,\mathrm{ph,sp}}$ describe the efficiency for generating stress from energy in each of the three systems (*8*).

To combine UXRD and tr-MOKE, we reproduce on the vertical axis of Fig. 4D the average lattice strain $\overline{\eta}$ from Fig. 3C, while the horizontal axis quantifies the fraction of the energy density $\Delta\rho_{\mathrm{sp}}^{Q}(\Delta t)$ that the second pulse can still introduce into the spin system according to (Fig. 4C). For simplicity, we assume that after a short time delay $\Delta t = 15$ ps, the FePt is still nearly fully demagnetized (Fig. 4A), and almost no energy density $\Delta\rho_{\mathrm{sp}}^{Q}$ can be deposited into the spin system. Hence, the second pulse only induces expansion, i.e., positive $\overline{\eta}(\Delta t)$ in Fig. 4D by exciting electrons and phonons. With increasing Δt, the contractive stress $\sigma_{\mathrm{sp}} = \Gamma_{\mathrm{sp}}\Delta\rho_{\mathrm{sp}}^{Q}$ increases. The slope of Fig. 4D is proportional to the macroscopic Grueneisen constant Γ_{sp} of the spin system, which must, in fact, be negative to support the observed NTE or invar behavior (*3*, *37*).

Modeling

We experimentally find that the spin stress contribution recovers on a 100-ps time scale, consistent with the remagnetization of the grains. As domain wall propagation is not relevant within the nanoscopic grains on this time scale, the dynamics are governed by thermal transport to the carbon matrix and the substrate. Figure 4C illustrates that the energy density ρ_{sp}^{Q} and the associated spin entropy density $S_{\mathrm{sp}} \propto \rho_{\mathrm{sp}}^{Q}/T$ that can be induced by a second excitation after a given time delay Δt are finite. Statistical mechanics limits the maximum spin entropy to $S_{\mathrm{sp}} = Nk_{\mathrm{B}}\ln(2J+1)$, where J is the angular momentum per magnetic atom. This saturation provides the necessary mechanism for the reduced contractive stress contribution at high fluences in the otherwise linear stress-strain relations. NTE generally requires an increasing entropy with decreasing volume (*23*).

The main features of the fluence-dependent responses observed for the continuous and granular films (Fig. 1) and of the two-pulse excitation experiments (Figs. 2 and 3) can be qualitatively understood in the light of a simplified equation of motion [see Materials and Methods for the full three-dimensional (3D) equation]

Fig. 4. Semiquantitative approximation of the remaining spin energy from tr-MOKE measurements. (**A**) Transient MOKE data for the granular FePt film for various fluences, normalized (Norm.) to their maximum demagnetization. (**B**) Equilibrium magnetization $M(T)$ measurement for a similarly prepared granular FePt film obtained by vibrating sample magnetometry (VSM). (**C**) Spin-specific heat as derived via $C_{\mathrm{sp}} \approx M\frac{\partial M}{\partial T}$ (blue line) from $M(T)$ and calculations (*36*) (thick black dashed line). The colored dashed lines connect the graphs at selected times for which partial recovery of the spin entropy–driven contraction is observed (compare Fig 3). (**D**) Average strain $\overline{\eta}(\Delta t)$ in the first 2 ps after the second pulse (green area in Fig. 3B) as a function of the energy density $\Delta\rho_{\mathrm{sp}}^{Q}(\Delta t)$ that this second pulse can still introduce into the spin system. The light blue shaded area in (C) visualizes $\Delta\rho_{\mathrm{sp}}^{Q}$ for the case of $T(100\,\mathrm{ps}) = 580$ K, which gives rise to the light blue circle in (D).

$$\rho\frac{\partial^2 u_{\perp}}{\partial t^2} = \frac{\partial}{\partial z}\left(\underbrace{C_{33}\frac{\partial u_{\perp}}{\partial z}}_{\text{elast.}\sigma_{\perp}} + \underbrace{2\,C_{31}\eta_{\parallel}}_{\text{elast.}\sigma_{\perp}^{\text{Poi}}} - \underbrace{\sigma_{\perp}^{\text{sp}}}_{<0} - \underbrace{\sigma_{\perp}^{e-\text{ph}}}_{>0}\right) \quad (1)$$

At equilibrium, negative strain $\eta_{\perp} = \frac{\partial u_{\perp}}{\partial z} < 0$ occurs only if a contractive spin stress $\sigma_{\perp}^{\text{sp}}$ and the elastic Poisson stress contribution $\sigma_{\perp}^{\text{Poi}}(t) \sim \eta_{\parallel}(t)$ induced by in-plane strain $\eta_{\parallel}$ add constructively to overcome the expansive out-of-plane stress $\sigma_{\perp}^{e-\text{ph}}$ imposed by hot electrons and phonons. Equation 1 is valid in the case of a thin FePt needle, i.e., a cylinder with radius much smaller than height ($r \ll d$), because this allows us to assume that in-plane strains $\eta_{\parallel}$ are relaxed and equal in x and y directions. The main reason for writing Eq. 1 is to see that it can be further simplified for the continuous film because $\sigma_{\perp}^{\text{Poi}}$ is absent at ultrafast time scales for which $\eta_{\parallel} = 0$ for symmetry reasons. Thus, on ultrafast time scales, Eq. 1 with $\sigma_{\perp}^{\text{Poi}} = 0$ is exact, and the Poisson stress makes the out-of-plane response of the granular film response substantially different.

We complement this simple analysis of the FePt deformation dynamics by FEM simulations using the actual FePt nanostructure dimensions and considering 3D, nonsimplified equations of motion (see Materials and Methods and Supplementary Materials for technical details). The results for the granular FePt film are shown in Fig. 5, while those obtained for continuous films and free grains can be found in the Supplementary Materials. In each case, various values of the relative amplitude A^{sp} of the spin stress contribution were used to mimic its variation in the context of fluence dependence (Fig. 1—saturation of the contraction) and two-pulse excitation (Figs. 2 and 3—time-dependent recovery of the spin stress). A complete reproduction of the measured time-resolved signals is challenging, as it would require to precisely take into account the morphological dispersion of the FePt grains and the heat transfer to the carbon. Nevertheless, enable a good qualitative reproduction of the strain dynamics measured for granular FePt films, as can be seen by comparing the measured strain (Figs. 1A and 3B) with the simulated strain in Fig. 5B.

Figure 5A illustrates the electron-phonon, spin, and Poisson stress contributions, which drive the out-of-plane strain dynamics of granular films (Eq. 1). As expected, in the absence of the contractive spin stress ($A^{sp} = 0$), the total stress almost always remains positive. The computed out-of-plane strain dynamics correspond to oscillations of the FePt nanostructure configuration around an expanded equilibrium, with a total absence of out-of-plane compression throughout the motion (Fig. 5B). These computed strain dynamics agree well with experimental strain data where the spin contribution is strongly reduced via the use of high-fluence light pulses (Figs. 1 to 3). Conversely, a sufficient amplitude of A^{sp} (e.g., $A^{sp} = 0.2$, as in Fig. 5A) creates a negative average value of the computed total stress enabling out-of-plane FePt contractions (Fig. 5B), in agreement with the experimental observation of a contraction at the beginning of the dynamics. Moreover, the computed strains shown in Fig. 5B qualitatively reproduce both the maximal contraction at 1.7 ps and maximal expansion at 4.5 ps, observed in the context of both low-fluence single-pump experiments (Fig. 1A) and double-pulse excitation with large delay between pump pulses, i.e., recovered spin order (Fig. 3B). The FePt deformation computed at these two instants is illustrated for $A^{sp} = 0.2$ in Fig. 5. For the same range of A^{sp}, our FEM modeling of a continuous film (see Supplementary Materials) reproduces the absence of a contraction and the 0.5-ps phase shift observed in Fig. 1B for increasing fluence. Conversely, the Poisson effect is enhanced for free FePt grains (see Supplementary Materials) because the in-plane displacement is unconstrained. Our simulations qualitatively reproduce the large out-of-plane contractions observed previously (11).

A systematic variation of the simulation parameters shows that a reasonable agreement with the experimental data can be obtained only by assuming an anisotropic electron-phonon stress, with nonequal out-of-plane and in-plane amplitudes $\sigma_\perp^{e-ph,0} = A^{ani} \sigma_\parallel^{e-ph,0}$. However, the optimal value of the anisotropy parameter $A^{ani} \approx 3$ used for the simulations shown in Fig. 5 is more than twice smaller than predicted (11). Including an in-plane expansion resulting from spin stress (11) would even reduce A^{ani} further. Although the overall agreement between simulations and experiments is good, the simulations systematically underestimate the expansion beyond 3 ps observed experimentally. This may be compensated for by adding expansive stress in the carbon shell resulting from heat transfer from the FePt, which would decrease the Poisson stress $\sigma_\perp^{Poi}$ acting on FePt on long time scales.

Our modeling shows that the difference in the response of free grains, a granular film, and the continuous film mainly originates from the different in-plane boundary conditions, which suppress or partially allow the Poisson effect. We can reproduce the essential conclusion drawn from the double-pulse experiment (Fig. 3) that the initial out-of-plane contraction is driven by spin stress.
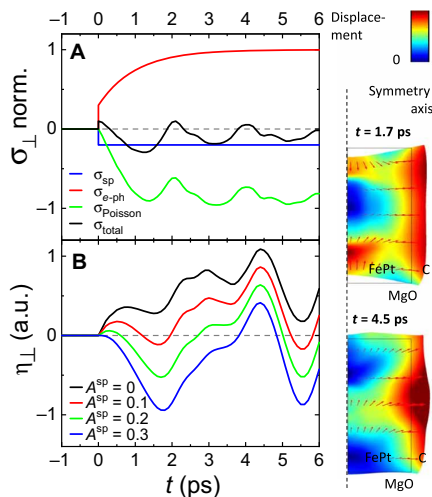
CONCLUSION

In conclusion, we have shown that laser-generated spin entropy drives a pronounced but short-lived lattice contraction of nanogranular FePt films in the L1$_0$ phase. In a double-pulse excitation scenario, the absence of a contraction after the second laser pulse quantifies the contractive stress contribution of the spin excitations, as they saturate when the FePt temperature approaches T_C. Fluence-dependent transient MOKE data confirm that the relaxation of the magnetization occurs on the same time scale as the spin entropy–driven contraction reappears.

Our elastic continuum modeling clarifies the important role of the Poisson effect in establishing the transient contraction of the granular film, which is not observed for the continuous film. We are confident that this double-pulse excitation scenario can be developed into a versatile tool for investigating coupled systems with many degrees of freedom, when a phase transition leads to the saturation for one of the driving stresses of the lattice response.

Fig. 5. FEM modeling of the mechanical response of a granular FePt film. (**A**) Time-dependent out-of-plane stresses $\sigma_\perp(t)$ acting on FePt for $A^{sp} = 0$ (no spin stress, solid lines) and $A^{sp} = 0.2$ (dashed lines). The Poisson stress component was deduced from the computed in-plane strains. (**B**) Average out-of-plane strain $\eta_\perp(t)$ in arbitrary units (a.u.) computed for various ratios A^{sp} of the spin and electron-phonon stress amplitudes. The computed FePt deformation at instants corresponding to maximal initial contraction and expansion for $A^{sp} = 0.2$ are illustrated at the right.

MATERIALS AND METHODS
X-ray and MOKE experiments
We performed laser-based UXRD pump-probe experiments with an x-ray pulse duration (38) of approximately 200 fs on two FePt thin films in the ordered L1$_0$ phase grown on MgO (001) oriented substrates. We observe the time-dependent evolution of the (002)

FePt diffraction peak, from which we deduce the time-resolved out-of-plane lattice strain of the FePt layer $\eta_\perp(t)$. The samples are excited by p-polarized pump pulses with a duration of 100 fs at a central wavelength of 800 nm, which are incident under 45° relative to the surface normal. The laser spot size of approximately 1.6 mm by 1.3 mm (full width at half maximum) ensures that a homogeneously excited sample area is probed by the x-rays that have rhombical 0.3 mm–by–0.3 mm profile (*39*). The tr-MOKE setup (*34*) uses comparable excitation parameters. For experimental details, see Supplementary Materials. Static x-ray diffraction measurements at different sample temperatures were recorded using a commercial diffraction setup (Rigaku SmartLab 9 kW system).

Sample preparation

A continuous FePt thin film was prepared by magnetron-sputtering Fe and Pt from a composite FePt target onto a substrate preheated to 500°C. Similarly, a granular FePt film was prepared at a slightly higher substrate temperature of 650°C by adding approximately 30 volume % of carbon to the sputtering target. X-ray reflectivity measured the sample thicknesses to be about d = 9.5 nm, where the continuous film is covered with an additional 1-nm layer of oxidized Al (*27*). According to scanning electron microscopy images of similarly prepared samples (see Supplementary Materials), the size distribution of the FePt nanograins segregated in a carbon matrix within the granular film is centered at approximately 8 nm. This nano-morphology yields a very large coercive field of approximately $\mu_0 H$ = 5 T, whereas the coercive field of the continuous film $\mu_0 H$ = 0.4 T is substantially smaller because of the possibility of domain wall motion that cannot occur in the nanogranular samples (*40*). The sample structures are schematically depicted as insets (C) and (D) in Fig. 1, and their properties and the measurement technique have been described in a previous publication (*27*).

FEM modeling

Finite-element simulations were performed using the Structural Mechanics Module of the COMSOL commercial software. It determines the spatiotemporal variations of displacement $u_i(x_1, x_2, x_3, t)$ by the numerical, approximation-free resolution of the continuum mechanics equation of motion in all Cartesian directions x_i

$$\rho \frac{\partial^2 u_i}{\partial t^2} = \sum_{j=1}^{3} \frac{\partial}{\partial x_j} \left(\sum_{k,l=1}^{3} C_{ijkl} \eta_{kl} - \sigma_{ij}^{ext} \right) \text{ with the strain } \eta_{kl} = \frac{1}{2} \left(\frac{\partial u_k}{\partial x_l} + \frac{\partial u_l}{\partial x_k} \right)$$

The simulation system was composed of a FePt cylinder with the radius r = 4 nm and d=10 nm height encapsulated by a cylindrical carbon shell of 2-nm thickness and same height supported on a MgO substrate. Note that the choice of such an axially symmetric geometry allowed us to perform 2D simulations, which are computationally much less expensive than 3D ones. Perfect mechanical contact was assumed at all internal interfaces of the system. Vanishing in-plane displacement was imposed on the lateral surface of the simulation domain, 6 nm away from its symmetry axis, to describe the absence of lateral contraction in films. Stress-free and low-reflecting boundary conditions were, respectively, used at the top of the FePt–carbon film and at the bottom of the MgO substrate.

FePt elastic anisotropy was neglected, and all materials were described by their density ρ, Young modulus Y, and Poisson ratio ν as listed in Table 1.

The time-dependent displacement fields $u_i(t)$ induced in this system by its sudden excitation were computed in the time domain, and the average out-of-plane strain in FePt $\eta_\perp(t) = \frac{\partial u_z(t)}{\partial z}$ was deduced by spatial integration.

The laser-induced excitation was described by a time-dependent diagonal matrix obtained by summing the contributions of an expansive, anisotropic electron-phonon stress with components $\sigma_{xx}^{e-ph}(t) = \sigma_{yy}^{e-ph}(t) = A^{ani} \sigma_{zz}^{e-ph}(t) = A^{ani} \sigma^{e-pho,0} \left(1 + \left(\frac{\gamma_e}{\gamma_{ph}} - 1 \right) e^{-\frac{t}{\tau}} \right) \Theta(t)$ accounting for energy dissipation from electrons to phonons after selective excitation of the former by light (*41*) and an instantaneously rising contractive uniaxial spin stress $\sigma_{zz}^{sp}(t) = \sigma_\perp^{sp,0} \Theta(t)$, where Θ is the Heaviside function. A τ = 1 ps electron-phonon coupling time and a $\frac{\gamma_e}{\gamma_{ph}}$ = 0.3 ratio of electron and phonon Grüneisen constants were used in the modeling. We approximate both the contractive spin stress and the expansive electron stress as instantaneous, i.e., much shorter than the 200 fs time resolution of our UXRD experiment. This is consistent with recent ultrafast electron calorimetry, which has shown that the energy transfer to the spin system in nickel is effective within the first 20 fs (*42*).

SUPPLEMENTARY MATERIALS

REFERENCES AND NOTES

1. E. F. Wasserman, Invar: Moment-volume instabilities in transition metals and alloys. *Handbook Ferromagn. Mater.* **5**, 237–322 (1990).
2. C. E. Guillaume, Recherches sur les aciers au nickel. Dilatations aux températures élevées; résistance électrique. *C. R. Acad. Sci.* **125**, 18 (1897).
3. R. J. Weiss, The origin of the `Invar'effect. *Proc. Phys. Soc.* **82**, 281 (1963).
4. M. Van Schilfgaarde, I. A. Abrikosov, B. Johansson, Origin of the invar effect in iron-nickel alloys. *Nature* **400**, 46–49 (1999).
5. S. Khmelevskyi, I. Turek, P. Mohn, Large negative magnetic contribution to the thermal expansion in iron-platinum alloys: Quantitative theory of the invar effect. *Phys. Rev. Lett.* **91**, 037201 (2003).
6. C. Dornes, Y. Acremann, M. Savoini, M. Kubli, M. J. Neugebauer, E. Abreu, L. Huber, G. Lantz, C. A. F. Vaz, H. Lemke, E. M. Bothschafter, M. Porer, V. Esposito, L. Rettig, M. Buzzi, A. Alberca, Y. W. Windsor, P. Beaud, U. Staub, D. Zhu, S. Song, J. M. Glownia, S. L. Johnson, The ultrafast Einstein–de Haas effect. *Nature* **565**, 209–212 (2019).
7. E. Jal, V. López-Flores, N. Pontius, T. Ferté, N. Bergeard, C. Boeglin, B. Vodungbo, J. Lüning, N. Jaouen, Structural dynamics during laser-induced ultrafast demagnetization. *Phys. Rev. B.* **95**, 184422 (2017).
8. A. von Reppert, J. Pudell, A. Koc, M. Reinhardt, W. Leitenberger, K. Dumesnil, F. Zamponi, M. Bargheer, Persistent nonequilibrium dynamics of the thermal energies in the spin and phonon systems of an antiferromagnet. *Struct. Dyn.* **3**, 054302 (2016).
9. J. Pudell, A. von Reppert, D. Schick, F. Zamponi, M. Rössle, M. Herzog, H. Zabel, M. Bargheer, Ultrafast negative thermal expansion driven by spin disorder. *Phys. Rev. B.* **99**, 094304 (2019).
10. C. von Korff Schmising, A. Harpoeth, N. Zhavoronkov, Z. Ansari, C. Aku-Leh, M. Woerner, T. Elsaesser, M. Bargheer, M. Schmidbauer, I. Vrejoiu, D. Hesse, M. Alexe, Ultrafast magnetostriction and phonon-mediated stress in a photoexcited ferromagnet. *Phys. Rev. B.* **78**, 060404 (2008).
11. A. H. Reid, X. Shen, P. Maldonado, T. Chase, E. Jal, P. W. Granitzka, K. Carva, R. K. Li, J. Li, L. Wu, T. Vecchione, T. Liu, Z. Chen, D. J. Higley, N. Hartmann, R. Coffee, J. Wu, G. L. Dakovski, W. F. Schlotter, H. Ohldag, Y. K. Takahashi, V. Mehta, O. Hellwig, A. Fry, Y. Zhu, J. Cao, E. E. Fullerton, J. Stöhr, P. M. Oppeneer, X. J. Wang, H. A. Dürr, Beyond a phenomenological description of magnetostriction. *Nat. Commun.* **9**, 388 (2018).

Table 1. Elastic parameters used in the modeling.

	FePt	C	MgO
ρ (kg/m^3)	14,700	2000	3580
Y (GPa)	237	200	249
ν	0.31	0.2	0.18

SCIENCE ADVANCES | RESEARCH ARTICLE

12. A. Koc, M. Reinhardt, A. von Reppert, M. Rössle, W. Leitenberger, M. Gleich, M. Weinelt, F. Zamponi, M. Bargheer, Grueneisen-approach for the experimental determination of transient spin and phonon energies from ultrafast x-ray diffraction data: Gadolinium. *J. Phys. Condens. Matter* **29**, 264001 (2017).

13. E. Beaurepaire, J.-C. Merle, A. Daunois, J.-Y. Bigot, Ultrafast spin dynamics in ferromagnetic nickel. *Phys. Rev. Lett.* **76**, 4250–4253 (1996).

14. J. Kimling, J. Kimling, R. B. Wilson, B. Hebler, M. Albrecht, D. G. Cahill, Ultrafast demagnetization of FePt:Cu thin films and the role of magnetic heat capacity. *Phys. Rev. B* **90**, 224408 (2014).

15. T. Kampfrath, A. Sell, G. Klatt, A. Pashkin, S. Mährlein, T. Dekorsy, M. Wolf, M. Fiebig, A. Leitenstorfer, R. Huber, Coherent terahertz control of antiferromagnetic spin waves. *Nat. Photonics* **5**, 31–34 (2011).

16. F. Hansteen, A. Kimel, A. Kirilyuk, T. Rasing, Nonthermal ultrafast optical control of the magnetization in garnet films. *Phys. Rev. B* **73**, 014421 (2006).

17. J. W. Kim, M. Vomir, J. Y. Bigot, Controlling the spins angular momentum in ferromagnets with sequences of picosecond acoustic pulses. *Sci. Rep.* **5**, 8511 (2014).

18. M. Sander, J. E. Pudell, M. Herzog, M. Bargheer, R. Bauer, V. Besse, V. Temnov, P. Gaal, Quantitative disentanglement of coherent and incoherent laser-induced surface deformations by time-resolved x-ray reflectivity. *Appl. Phys. Lett.* **111**, 261903 (2017).

19. D. C. Heinecke, O. Kliebisch, J. Flock, A. Bruchhausen, K. Köhler, T. Dekorsy, Selective excitation of zone-folded phonon modes within one triplet in a semiconductor superlattice. *Phys. Rev. B* **87**, 075307 (2013).

20. T. Cheng, J. Wu, T. Liu, X. Zou, J. Cai, R. W. Chantrell, Y. Xu, Dual-pump manipulation of ultrafast demagnetization in TbFeCo. *Phys. Rev. B* **93**, 064401 (2016).

21. K. Bühlmann, R. Gort, G. Salvatella, S. Däster, A. Fognini, T. Bähler, C. Dornes, C. A. F. Vaz, A. Vaterlaus, Y. Acremann, Ultrafast demagnetization in iron: Separating effects by their nonlinearity. *Struct. Dyn.* **5**, 044502 (2018).

22. J. Y. Shi, M. Tang, Z. Zhang, L. Ma, L. Sun, C. Zhou, X. F. Hu, Z. Zheng, L. Q. Shen, S. M. Zhou, Y. Z. Wu, L. Y. Chen, H. B. Zhao, Impact of ultrafast demagnetization process on magnetization reversal in $L1_0$ FePt revealed using double laser pulse excitation. *Appl. Phys. Lett.* **112**, 082403 (2018).

23. G. D. Barrera, J. A. O. Bruno, T. H. K. Barron, N. L. Allan, Negative thermal expansion. *J. Phys. Condens. Matter* **17**, R217–R252 (2005).

24. O. Mosendz, S. Pisana, J. W. Reiner, B. Stipe, D. Weller, Ultra-high coercivity small-grain FePt media for thermally assisted recording (invited). *J. Appl. Phys.* **111**, 07B729 (2012).

25. D. Weller, G. Parker, O. Mosendz, A. Lyberatos, D. Mitin, N. Y. Safonova, M. Albrecht, Review article: FePt heat assisted magnetic recording media. *J. Vac. Sci. Technol.* **34**, 060801 (2016).

26. K. Hono, Y. K. Takahashi, G. Ju, J.-U. Thiele, A. Ajan, X. Yang, R. Ruiz, L. Wan, Heat-assisted magnetic recording media materials. *MRS Bull.* **43**, 93–99 (2018).

27. A. von Reppert, L. Willig, J.-E. Pudell, M. Rössle, W. Leitenberger, M. Herzog, F. Ganss, O. Hellwig, M. Bargheer, Ultrafast laser generated strain in granular and continuous FePt thin films. *Appl. Phys. Lett.* **113**, 123101 (2018).

28. K. Sumiyama, M. Shiga, M. Morioka, Y. Nakamura, Characteristic magnetovolume effects in Invar type Fe-Pt alloys. *J. Phys. F Met. Phys.* **9**, 1665–1677 (1979).

29. Y. Tsunoda, H. Kobayashi, Temperature variation of the tetragonality in ordered PtFe alloy. *J. Magn. Magn. Mater.* **272–276**, 776–777 (2004).

30. R. Nicula, O. Crisan, A. D. Crisan, I. Mercioniu, M. Stir, F. Vasiliu, Thermal stability, thermal expansion and grain-growth in exchange-coupled Fe–Pt–Ag–B bulk nanocomposite magnets. *J. Alloys Compd.* **622**, 865–870 (2015).

31. P. Rasmussen, X. Rui, J. E. Shield, Texture formation in FePt thin films via thermal stress management. *Appl. Phys. Lett.* **86**, 191915 (2005).

32. P. W. Granitzka, E. Jal, L. Le Guyader, M. Savoini, D. J. Higley, T. Liu, Z. Chen, T. Chase, H. Ohldag, G. L. Dakovski, W. F. Schlotter, S. Carron, M. C. Hoffman, A. X. Gray, P. Shafer, E. Arenholz, O. Hellwig, V. Mehta, Y. K. Takahashi, J. Wang, E. E. Fullerton, J. Stöhr, A. H. Reid, H. A. Dürr, Magnetic switching in granular FePt layers promoted by near-field laser enhancement. *Nano Lett.* **17**, 2426–2432 (2017).

33. O. Hovorka, S. Devos, Q. Coopman, W. J. Fan, C. J. Aas, R. F. L. Evans, X. Chen, G. Ju, R. W. Chantrell, The Curie temperature distribution of FePt granular magnetic recording media. *Appl. Phys. Lett.* **101**, 052406 (2012).

34. L. Willig, A. Von Reppert, M. Deb, F. Ganss, O. Hellwig, M. Bargheer, Finite-size effects in ultrafast remagnetization dynamics of FePt. *Phys. Rev. B* **100**, 224408 (2019).

35. J. M. D. Coey, *Magnetism and Magnetic Materials* (Cambridge Univ. Press, 2012).

36. A. Lyberatos, G. J. Parker, Model of ballistic-diffusive thermal transport in HAMR media. *Jpn. J. Appl. Phys.* **58**, 045002 (2019).

37. T. H. K. Barron, J. G. Collins, G. K. White, Thermal expansion of solids at low temperatures. *Adv. Phys.* **29**, 609–730 (1980).

38. D. Schick, A. Bojahr, M. Herzog, C. von Korff Schmising, R. Shayduk, W. Leitenberger, P. Gaal, M. Bargheer, Normalization schemes for ultrafast x-ray diffraction using a table-top laser-driven plasma source. *Rev. Sci. Instrum.* **83**, 025104 (2012).

39. M. Bargheer, N. Zhavoronkov, R. Bruch, H. Legall, H. Stiel, M. Woerner, T. Elsaesser, Comparison of focusing optics for femtosecond x-ray diffraction. *Appl. Phys. B* **80**, 715–719 (2005).

40. T. Shima, K. Takanashi, Y. K. Takahashi, K. Hono, Preparation and magnetic properties of highly coercive FePt films. *Appl. Phys. Lett.* **81**, 1050–1052 (2002).

41. A. von Reppert, R. M. Sarhan, F. Stete, J. Pudell, N. Del Fatti, A. Crut, J. Koetz, F. Liebig, C. Prietzel, M. Bargheer, Watching the vibration and cooling of ultrathin gold nanotriangles by ultrafast x-ray diffraction. *J. Phys. Chem. C* **120**, 28894–28899 (2016).

42. P. Tengdin, W. You, C. Chen, X. Shi, D. Zusin, Y. Zhang, C. Gentry, A. Blonsky, M. Keller, P. M. Oppeneer, H. Kapteyn, Z. Tao, M. Murnane, Critical behavior within 20 fs drives the out-of-equilibrium laser-induced magnetic phase transition in nickel. *Sci. Adv.* **4**, eaap9744 (2018).

43. D. Schick, R. Shayduk, A. Bojahr, M. Herzog, C. von Korff Schmising, P. Gaal, M. Bargheer, Ultrafast reciprocal-space mapping with a convergent beam. *J. Appl. Cryst.* **46**, 1372–1377 (2013).

Science Advances
MAAAS

Supplementary Materials for

Spin stress contribution to the lattice dynamics of FePt

A. von Reppert, L. Willig, J.-E. Pudell, S. P. Zeuschner, G. Sellge, F. Ganss, O. Hellwig, J. A. Arregi, V. Uhlíř, A. Crut, M. Bargheer*

*Corresponding author. Email: bargheer@uni-potsdam.de

This PDF file includes:

1) Excitation fluence dependent strain of granular and continuous FePt

The fluence series of the time-resolved X-ray diffraction using single pulse excitation for both the granular and the continuous FePt film is displayed in figure S1: Figure S1 a) and b) show that the expansion maximum increases with increasing fluence. The contractive strain that occurs within the first 2ps that is observed in the granular film saturates at a contraction of approximately $2 \cdot 10^{-3}$. This threshold behavior already indicates a magnetic origin of the driving stress, as saturation of the spin contribution to the stress is predicted for a full demagnetization. The bottom panels c) and d) display the data normalized to the incident fluence as presented in the main text.
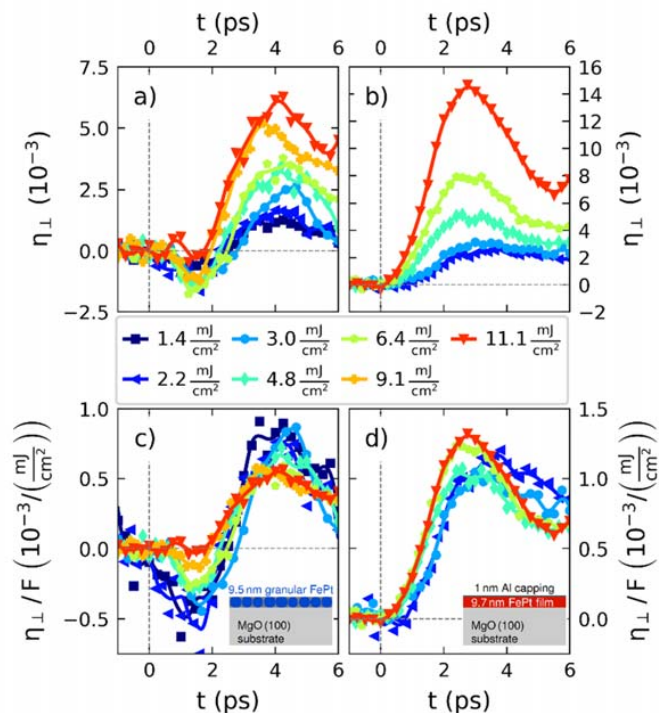

Figure S1: Comparison of the fluence dependent lattice dynamics of the two FePt thin films after laser excitation. a) and b) display the time dependent strain for the granular and continuous FePt film respectively. The data normalized to fluence are displayed in the low panel c) and d) below, where the insets display the schematic sample structure.

2) Temperature dependent thermal expansion of the granular and continuous FePt thin film

The static diffraction curve as well as the temperature dependent experiments on the FePt thin films that have been conducted on the samples after the time-resolved experiments were finished are depicted in figure S2. The static diffraction experiments were carried out at a Rigaku 9kW SmartLab system using a 4-circle goniometer that uses the characteristic Cu-$K_{\alpha 1}$ radiation ($\lambda (K_{\alpha 1}) = 1.54$ Å) of a rotating anode X-ray tube for diffraction. The sample was kept in an inert gas atmosphere inside a carbon dome chamber, while it was heated up to 800K. The diffraction curve in Fig S2a) exhibits sharp and intense MgO substrate peaks and smaller diffraction peaks, which can be attributed to

the FePt thin films. In order to extract the thermal expansion strain $\eta_{\perp,eq}$ of the FePt thin films and the MgO substrate, we observed the FePt (002) and the MgO (004) shift as a function of the sample temperature. From similar experiments we extract the in-plane strain upon equilibrium heating $\eta_{||,eq}$ by monitoring the peak shift of the FePt (220) and the MgO (440) diffraction peak.
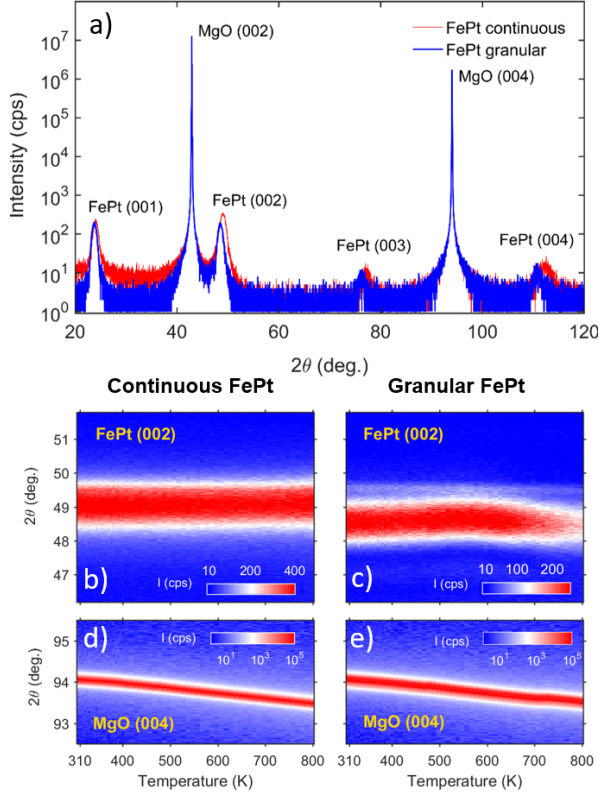

Figure S2 Static X-ray diffraction results: a) Rocking curves of the granular and continuous FePt thin films. The temperature dependence for the FePt (002) reflection for the continuous (b)) and the granular(c)) FePt exhibit only a very small shift, whereas the MgO substrates in c) and d) shift considerably to lower diffraction angles. The intensity decrease for the granular FePt above 650K indicates a modification of the structure, which prohibits reliable time-resolved experiments at temperatures above T_c

The out-of-plane ($\eta_{\perp,eq}$) and in-plane strains ($\eta_{||,eq}$) that we obtain from the peak shifts by peak fits to the temperature dependent diffraction data under equilibrium heating are displayed in figure S3. Figure S3a) quantifies that the continuous film exhibits invar behavior ($\alpha_{\perp,FePt,cont} \approx 0$) along the out-of-plane direction from 300K – 700K whereas the granular FePt exhibits a negative thermal expansion with an expansion coefficient of $\alpha_{\perp,FePt,gran,1} \approx -9 \cdot 10^{-6} \frac{1}{K}$ between 300K and 550K, which switches to a large positive thermal expansion of $\alpha_{\perp,FePt,gran,2} \approx 23 \cdot 10^{-6} \frac{1}{K}$ between 580 and 650K. Qualitatively similar observations have been made in the magnetovolume effect of FePt alloys with different composition by Sumiyama et al.[28]. Above 650 K we observe a decrease of the X-ray diffraction peak intensity of the granular FePt film that can be seen in Fig S2c). This

could be due to an irreversible carbon interdiffusion into the sample structure as the peak intensity remains reduced by 15% even after the sample has cooled to room temperature. This illustrates that experiments at elevated temperatures above $T > T_c \approx 700$ K modify the sample whereas transient heating above T_c on a picosecond timescale is reversible since no change of the Bragg peak intensity was observed after laser pulse excitation. The thermal expansion coefficient extracted from the MgO (004) peak shift is approximately $\alpha_{\perp,MgO} \approx 9.3 \cdot 10^{-6} \frac{1}{K}$ in reasonable agreement with literature.[31] The in-plane thermal expansion coefficient of both FePt morphologies that can be extracted from Figure S3 b) approximately matches the thermal expansion of the MgO substrate $\alpha_{\parallel,FePt} \approx 9 \cdot 10^{-6} \frac{1}{K}$.
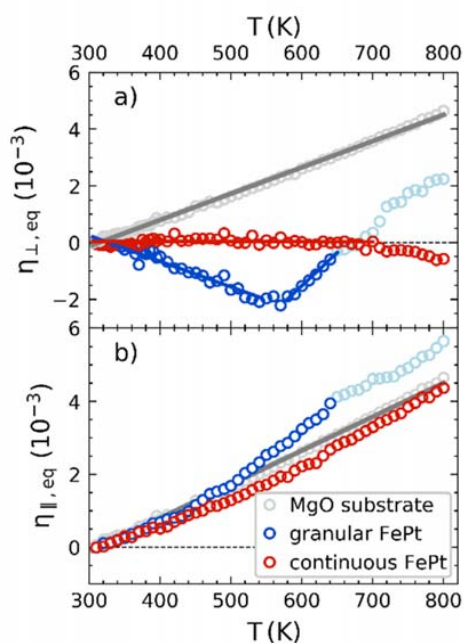
Figure S3 Static thermal expansion of the granular and continuous FePt thin film: a) Out-of-plane and b) in-plane strain extracted from the T-dependent peak shifts under equilibrium heating, where the solid lines indicate linear fits for the thermal expansion coefficients. The peak center position for a) the FePt (002) / MgO (004) and b) the FePt (220) Bragg peak were obtained by a Gaussian fits to the data from Figure S2.

3) SEM images of similarly prepared FePt samples

Figure S4 shows a scanning electron micrograph (SEM) image of a similarly prepared granular FePt sample as the one employed in our study. The bright parts are the FePt grains whereas the black parts correspond to the amorphous carbon. The images illustrate the approximate size distribution, which is centered around 8nm islands with an approximate 2nm carbon separation.

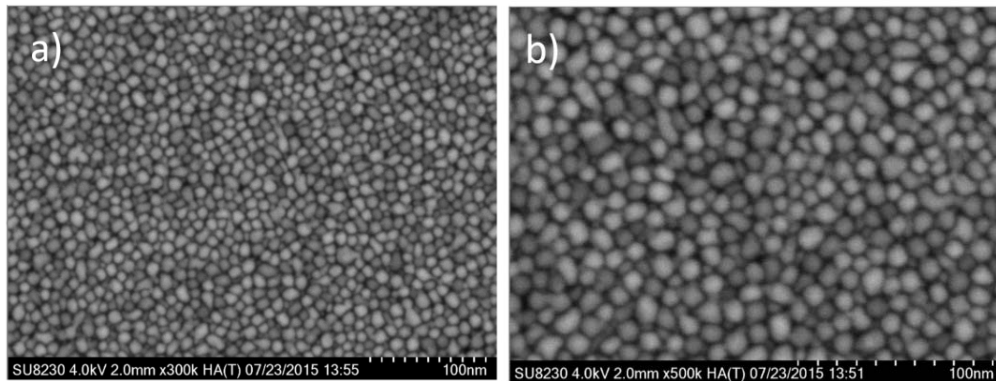**Figure S4: Scanning Electron Microscope images** of similarly prepared FePt samples, that illustrate the approximate size distribution for the granular specimen studied in the main text. Bright areas correspond to the FePt islands with an average diameter of approximately 8nm. The dark spacing in between the grains is due to the carbon nanolayer, which has an average thickness on the order of 2nm.

4) FEM modeling

FEM simulations were performed for both granular and continuous FePt films. To facilitate the comparison with the literature results reported for granular, matrix-free FePt films deposited on a TEM grid, the ideal case of a free FePt grain was also considered. Figure S5 shows the geometry of the FEM simulations, indicating the boundary conditions used in each case. Vanishing in-plane displacement at the cylinder lateral surface was assumed for continuous films bound to a substrate, while in-plane motion of the FePt surface was allowed in the granular film (at the FePt/C interface) and free nanoparticle cases.
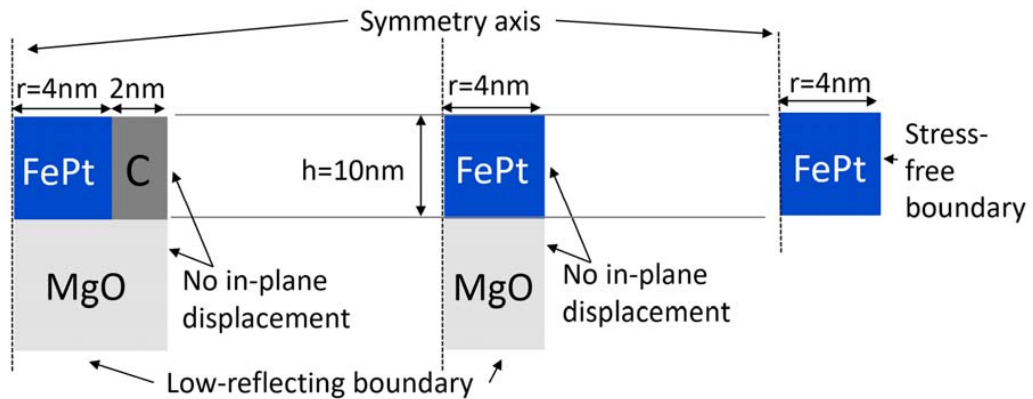

Figure S5: Geometry of the FEM simulations performed for three different FePt nanosystems: granular film (left), continuous film (middle) and free grain (right).

Fig. S6 shows the results of the FEM simulations for the continuous film (Fig. S6 a+b) and for a free FePt grain (Fig. S6 c+d), which complement those obtained for the granular film presented in Fig. 5 of the main text of the paper.

The simulations performed for the continuous film noticeably show a variation (by about 0.5 ps) with the amplitude of the spin stress contribution of the time at which the strain is maximal (Fig. S6 b), which is in agreement with experimental observations (Fig. 1b and S1b). The FEM results obtained for free grains (Fig. S6 d) are in qualitative agreement with the observations reported in the context of ultrafast electron-diffraction experiments[11].
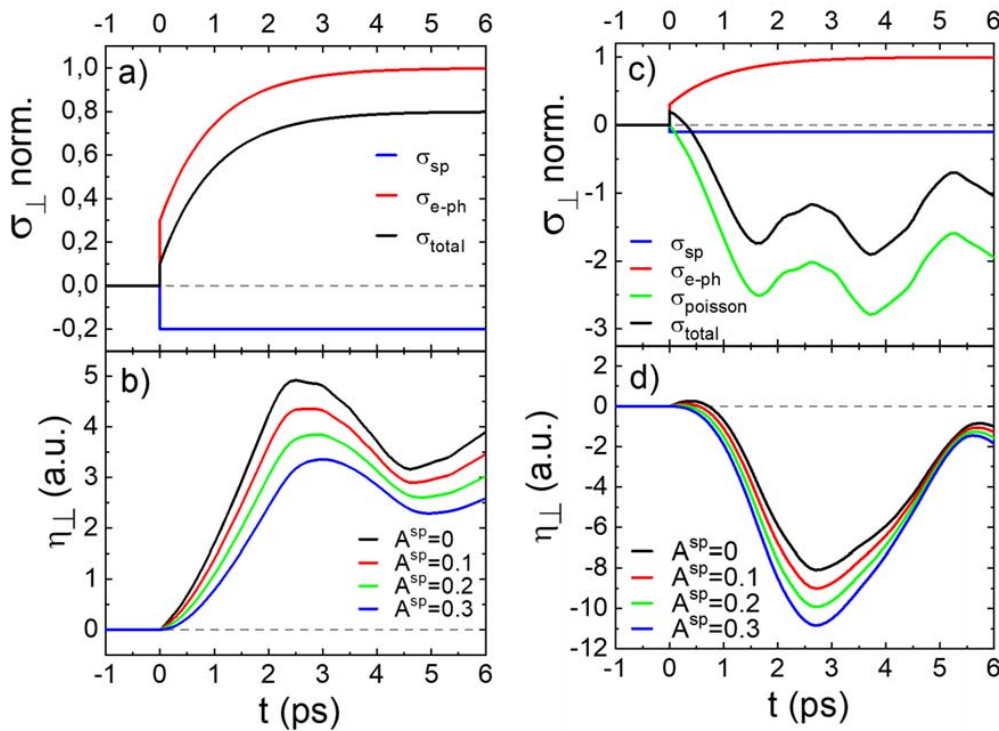
Figure S6: FEM modeling of the mechanical response of a continuous FePt film and a free FePt grain: a) time-dependent out of plane stresses $\sigma_\perp(t)$ acting on the FePt film for $A^{sp} = 0.2$ (solid lines). The dashed line shows the zero line corresponding to $\sigma_{sp} = 0$ for $A^{sp} = 0$ b) Average out of plane strain $\eta_\perp(t)$ in arbitrary units (a.u.) computed for various ratios A^{sp} of the spin and electron-phonon stress amplitudes. c-d) same a- b) for a free grain.

5) Laser based plasma x-ray source and femtosecond x-ray diffractometer

The principal components of the laser-based femtosecond plasma x-ray source (PXS) have remained unchanged since their installation nine years ago.[38] The input to the PXS are 50 fs laser pulses at a center wavelength of 800 nm with a pulse energy of 5 mJ at 1kHz

repetition rate that are focused by a 2 inch 90° off-axis parabolic mirror with a focal length of f = 10 cm into a vacuum chamber. At the focus, a 15 μm thick Cu band is transported fast enough to offer a fresh spot to each laser pulse impinging at a repetition rate of 1 kHz. The entrance and exit windows of the chamber are protected from the Cu plasma debris by moving plastic bands. The emitted x-rays are focused and monochromatized to the K_α doublet by a Montel multilayer optic with a convergence of 0.3° and a focal spot size of 200–300 μm FWHM at a distance d = 1000 mm from the PXS point source. The x-ray pulses contain only about 500-1000 photons per pulse on the sample. Key to the good signal to noise ratio are the gated CMOS 2D pixel detector and a careful optimization of the stability of the entire setup including the pump-laser. The x-rays are guided through evacuated tubes in order to avoid absorption and scattering by air molecules. The detector rests on the 2Θ arm of the 2-circle goniometer and detects scattered x-rays in the vicinity of the selected Bragg reflections, that are evaluated as reciprocal space mapping with a convergent beam[43].

Each data point in Figs. 1a,b), 2 and 3 took an acquisition time of about 120 s for the granular film and 70 s for the continuous film.

REFERENCES AND NOTES

1. E. F. Wasserman, Invar: Moment-volume instabilities in transition metals and alloys. *Handbook Ferromagn. Mater.* **5**, 237–322 (1990).

2. C. E. Guillaume, Recherches sur les aciers au nickel. Dilatations aux températures élevées; résistance électrique. *C. R. Acad. Sci.* **125**, 18 (1897).

3. R. J. Weiss, The origin of the 'Invar' effect. *Proc. Phys. Soc.* **82**, 281 (1963).

4. M. Van Schilfgaarde, I. A. Abrikosov, B. Johansson, Origin of the invar effect in iron-nickel alloys. *Nature* **400**, 46–49 (1999).

5. S. Khmelevskyi, I. Turek, P. Mohn, Large negative magnetic contribution to the thermal expansion in iron-platinum albys: Quantitative theory of the invar effect. *Phys. Rev. Lett.* **91**, 037201 (2003).

6. C. Dornes, Y. Acremann, M. Savoini, M. Kubli, M. J. Neugebauer, E. Abreu, L. Huber, G. Lantz, C. A. F. Vaz, H. Lemke, E. M. Bothschafter, M. Porer, V. Esposito, L. Rettig, M. Buzzi, A. Alberca, Y. W. Windsor, P. Beaud, U. Staub, D. Zhu, S. Song, J. M. Glownia, S. L. Johnson, The ultrafast Einstein–de Haas effect. *Nature* **565**, 209–212 (2019).

7. E. Jal, V. López-Flores, N. Pontius, T. Ferté, N. Bergeard, C. Boeglin, B. Vodungbo, J. Lüning, N. Jaouen, Structural dynamics during laser-induced ultrafast demagnetization. *Phys. Rev. B* **95**, 184422 (2017).

8. A. von Reppert, J. Pudell, A. Koc, M. Reinhardt, W. Leitenberger, K. Dumesnil, F. Zamponi, M. Bargheer, Persistent nonequilibrium dynamics of the thermal energies in the spin and phonon systems of an antiferromagnet. *Struct. Dyn.* **3**, 054302 (2016).

9. J. Pudell, A. von Reppert, D. Schick, F. Zamponi, M. Rössle, M. Herzog, H. Zabel, M. Bargheer, Ultrafast negative thermal expansion driven by spin disorder. *Phys. Rev. B* **99**, 094304 (2019).

10. C. von Korff Schmising, A. Harpoeth, N. Zhavoronkov, Z. Ansari, C. Aku-Leh, M. Woerner, T. Elsaesser, M. Bargheer, M. Schmidbauer, I. Vrejoiu, D. Hesse, M. Alexe, Ultrafast magnetostriction and phonon-mediated stress in a photoexcited ferromagnet. *Phys. Rev. B* **78**, 060404 (2008).

11. A. H. Reid, X. Shen, P. Maldonado, T. Chase, E. Jal, P. W. Granitzka, K. Carva, R. K. Li, J. Li, L. Wu, T. Vecchione, T. Liu, Z. Chen, D. J. Higley, N. Hartmann, R. Coffee, J. Wu, G. L. Dakovski, W. F. Schlotter, H. Ohldag, Y. K. Takahashi, V. Mehta, O. Hellwig, A. Fry, Y. Zhu, J. Cao, E. E. Fullerton, J. Stöhr, P. M. Oppeneer, X. J. Wang, H. A. Dürr, Beyond a phenomenological description of magnetostriction. *Nat. Commun.* **9**, 388 (2018).

12. A. Koc, M. Reinhardt, A. von Reppert, M. Rössle, W. Leitenberger, M. Gleich, M. Weinelt, F. Zamponi, M. Bargheer, Grueneisen-approach for the experimental determination of transient spin and phonon energies from ultrafast x-ray diffraction data Gadolinium. *J. Phys. Condens. Matter* **29**, 264001 (2017).

13. E. Beaurepaire, J.-C. Merle, A. Daunois, J.-Y. Bigot, Ultrafast spin dynamics in ferromagnetic nickel. *Phys. Rev. Lett.* **76**, 4250–4253 (1996).

14. J. Kimling, J. Kimling, R. B. Wilson, B. Hebler, M. Albrecht, D. G. Cahill, Ultrafast demagnetization of FePt:Cu thin films and the role of magnetic heat capacity. *Phys. Rev. B* **90**, 224408 (2014).

15. T. Kampfrath, A. Sell, G. Klatt, A. Pashkin, S. Mährlein, T. Dekorsy, M. Wolf, M. Fiebig, A. Leitenstorfer, R. Huber, Coherent terahertz control of antiferromagnetic spin waves. *Nat. Photonics* **5**, 31–34 (2011).

16. F. Hansteen, A. Kimel, A. Kirilyuk, T. Rasing, Nonthermal ultrafast optical control of the magnetization in garnet films. *Phys. Rev. B* **73**, 014421 (2006).

17. J. W. Kim, M. Vomir, J. Y. Bigot, Controlling the spins angular momentum in ferromagnets with sequences of picosecond acoustic pulses. *Sci. Rep.* **5**, 8511 (2014).

18. M. Sander, J. E. Pudell, M. Herzog, M. Bargheer, R. Bauer, V. Besse, V. Temnov, P. Gaal, Quantitative disentanglement of coherent and incoherent laser-induced surface deformations by time-resolved x-ray reflectivity. *Appl. Phys. Lett.* **111**, 261903 (2017).

19. D. C. Heinecke, O. Kliebisch, J. Flock, A. Bruchhausen, K. Köhler, T. Dekorsy, Selective excitation of zone-folded phonon modes within one triplet in a semiconductor superlattice. *Phys. Rev. B* **87**, 075307 (2013).

20. T. Cheng, J. Wu, T. Liu, X. Zou, J. Cai, R. W. Chantrell, Y. Xu, Dual-pump manipulation of ultrafast demagnetization in TbFeCo. *Phys. Rev. B* **93**, 064401 (2016).

21. K. Bühlmann, R. Gort, G. Salvatella, S. Däster, A. Fognini, T. Bähler, C. Dornes, C. A. F. Vaz, A. Vaterlaus, Y. Acremann, Ultrafast demagnetization in iron: Separating effects by their nonlinearity. *Struct. Dyn.* **5**, 044502 (2018).

22. J. Y. Shi, M. Tang, Z. Zhang, L. Ma, L. Sun, C. Zhou, X. F. Hu, Z. Zheng, L. Q. Shen, S. M. Zhou, Y. Z. Wu, L. Y. Chen, H. B. Zhao, Impact of ultrafast demagnetization process on magnetization reversal in $L1_0$ FePt revealed using double laser pulse excitation. *Appl. Phys. Lett.* **112**, 082403 (2018).

23. G. D. Barrera, J. A. O. Bruno, T. H. K. Barron, N. L. Allan, Negative thermal expansion. *J. Phys. Condens. Matter* **17**, R217–R252 (2005).

24. O. Mosendz, S. Pisana, J. W. Reiner, B. Stipe, D. Weller, Ultra-high coercivity small-grain FePt media for thermally assisted recording (invited). *J. Appl. Phys.* **111**, 07B729 (2012).

25. D. Weller, G. Parker, O. Mosendz, A. Lyberatos, D. Mitin, N. Y. Safonova, M. Albrecht, Review article: FePt heat assisted magnetic recording media. *J. Vac. Sci. Technol.* **34**, 060801 (2016).

26. K. Hono, Y. K. Takahashi, G. Ju, J.-U. Thiele, A. Ajan, X. Yang, R. Ruiz, L. Wan, Heat-assisted magnetic recording media materials. *MRS Bull.* **43**, 93–99 (2018).

27. A. von Reppert, L. Willig, J.-E. Pudell, M. Rössle, W. Leitenberger, M. Herzog, F. Ganss, O. Hellwig, M. Bargheer, Ultrafast laser generated strain in granular and continuous FePt thin films. *Appl. Phys. Lett.* **113**, 123101 (2018).

28. K. Sumiyama, M. Shiga, M. Morioka, Y. Nakamura, Characteristic magnetovolume effects in Invar type FePt alloys. *J. Phys. F Met. Phys.* **9**, 1665–1677 (1979).

29. Y. Tsunoda, H. Kobayashi, Temperature variation of the tetragonality in ordered PtFe alloy. *J. Magn. Magn. Mater.* **272–276**, 776–777 (2004).

30. R. Nicula, O. Crisan, A. D. Crisan, I. Mercioniu, M. Stir, F. Vasiliu, Thermal stability, thermal expansion and grain-growth in exchange-coupled FePt–Ag–B bulk nanocomposite magnets. *J. Alloys Compd.* **622**, 865–870 (2015).

31. P. Rasmussen, X. Rui, J. E. Shield, Texture formation in FePt thin films via thermal stress management. *Appl. Phys. Lett.* **86**, 191915 (2005).

32. P. W. Granitzka, E. Jal, L. Le Guyader, M. Savoini, D. J. Higley, T. Liu, Z. Chen, T. Chase, H. Ohldag, G. L. Dakovski, W. F. Schlotter, S. Carron, M. C. Hoffman, A. X. Gray, P. Shafer, E. Arenholz, O. Hellwig, V. Mehta, Y. K. Takahashi, J. Wang, E. E. Fullerton, J. Stöhr, A. H. Reid, H. A. Dürr, Magnetic switching in granular FePt layers promoted by near-field laser enhancement. *Nano Lett.* **17**, 2426–2432 (2017).

33. O. Hovorka, S. Devos, Q. Coopman, W. J. Fan, C. J. Aas, R. F. L. Evans, X. Chen, G. Ju, R. W. Chantrell, The Curie temperature distribution of FePt granular magnetic recording media. *Appl. Phys. Lett.* **101**, 052406 (2012).

34. L. Willig, A. Von Reppert, M. Deb, F. Ganss, O. Hellwig, M. Bargheer, Finite-size effects in ultrafast remagnetization dynamics of FePt. *Phys. Rev. B* **100**, 224408 (2019).

35. J. M. D. Coey, *Magnetism and Magnetic Materials* (Cambridge Univ. Press, 2012).

36. A. Lyberatos, G. J. Parker, Model of ballistic-diffusive thermal transport in HAMR media. *Jpn. J. Appl. Phys.* **58**, 045002 (2019).

37. T. H. K. Barron, J. G. Collins, G. K. White, Thermal expansion of solids at low temperatures. *Adv. Phys.* **29**, 609–730 (1980).

38. D. Schick, A. Bojahr, M. Herzog, C. von Korff Schmising, R. Shayduk, W. Leitenberger, P. Gaal, M. Bargheer, Normalization schemes for ultrafast x-ray diffraction using a table-top laser-driven plasma source. *Rev. Sci. Instrum.* **83**, 025104 (2012).

39. M. Bargheer, N. Zhavoronkov, R. Bruch, H. Legall, H. Stiel, M. Woerner, T. Elsaesser, Comparison of focusing optics for femtosecond x-ray diffraction. *Appl. Phys. B* **80**, 715–719 (2005).

40. T. Shima, K. Takanashi, Y. K. Takahashi, K. Hono, Preparation and magnetic properties of highly coercive FePt films. *Appl. Phys. Lett.* **81**, 1050–1052 (2002).

41. A. von Reppert, R. M. Sarhan, F. Stete, J. Pudell, N. Del Fatti, A. Crut, J. Koetz, F. Liebig, C. Prietzel, M. Bargheer, Watching the vibration and cooling of ultrathin gold nanotriangles by ultrafast x-ray diffraction. *J. Phys. Chem. C* **120**, 28894–28899 (2016).

42. P. Tengdin, W. You, C. Chen, X. Shi, D. Zusin, Y. Zhang, C. Gentry, A. Blonsky, M. Keller, P. M. Oppeneer, H. Kapteyn, Z. Tao, M. Murnane, Critical behavior within 20 fs drives the out-of-equilibrium laser-induced magnetic phase transition in nickel. *Sci. Adv.* **4,** eaap9744 (2018).

43. D. Schick, R. Shayduk, A. Bojahr, M. Herzog, C. von Korff Schmising, P. Gaal, M. Bargheer, Ultrafast reciprocal-space mapping with a convergent beam. *J. Appl. Cryst.* **46**, 1372–1377 (2013).
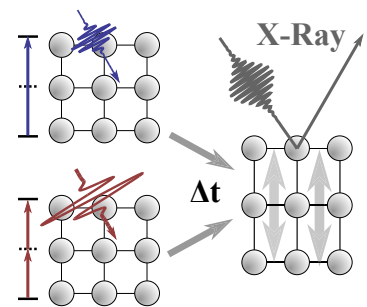
Article XI

Measurement of transient strain induced by two-photon excitation

Steffen Peer Zeuschner, **Jan-Etienne Pudell**, Alexander von Reppert, Marwan Deb, Elena Popova, Niels Keller, Matthias Rössle, Marc Herzog, and Matias Bargheer

By ultrafast x-ray diffraction we quantify the strain from coherent and incoherent phonons generated by one- and two-photon absorption. We investigated the ferrimagnetic insulator bismuth-doped yttrium iron garnet, which is a workhorse for laser-induced spin dynamics that may be excited indirectly via phonons. We identify the two-photon absorption by the quadratic intensity dependence of the transient strain and confirm a short lifetime of the intermediate state via the inverse proportional dependence on the pump-pulse duration. We determine the two-photon absorption coefficient using the linear relation between strain and absorbed energy density. For large intensities of about $1\,\text{TW/cm}^2$ considerable strain amplitudes of 0.1% are driven exclusively by two-photon absorption.

Measurement of transient strain induced by two-photon excitation

S. P. Zeuschner [1,2] J.-E. Pudell, [1,2] A. von Reppert, [1] M. Deb, [1] E. Popova, [3] N. Keller, [3] M. Rössle, [2]
M. Herzog, [1] and M. Bargheer [1,2,*]

[1]*Institute of Physics and Astronomy, University of Potsdam, Karl-Liebknecht-Str. 24-25, 14476 Potsdam, Germany*
[2]*Helmholtz-Zentrum Berlin für Materialien und Energie GmbH, Wilhelm-Conrad-Röntgen Campus, BESSY II, 12489 Berlin, Germany*
[3]*Groupe d'Etude de la Matiére Condensée (GEMaC), CNRS UMR 8635, Université Paris-Saclay, 78035 Versailles, France*

By ultrafast x-ray diffraction we quantify the strain from coherent and incoherent phonons generated by one- and two-photon absorption. We investigated the ferrimagnetic insulator bismuth-doped yttrium iron garnet, which is a workhorse for laser-induced spin dynamics that may be excited indirectly via phonons. We identify the two-photon absorption by the quadratic intensity dependence of the transient strain and confirm a short lifetime of the intermediate state via the inverse proportional dependence on the pump-pulse duration. We determine the two-photon absorption coefficient using the linear relation between strain and absorbed energy density. For large intensities of about 1 TW/cm^2 considerable strain amplitudes of 0.1% are driven exclusively by two-photon absorption.

Lattice dynamics is a unifying theme common to all laser-excited condensed matter systems, since their phonon subsystem provides a large bath for energy, entropy, and angular momentum transfer [1–4]. The ultrafast increase of the energy density in materials drives coherent atomic motion, i.e., sizable picosecond strain pulses [5–7], that add to the incoherent thermal expansion. Ultrafast x-ray diffraction (UXRD) has quantified these strain amplitudes generated in various materials, with a dependence on the incident fluence that is usually linear [5–8] or sublinear if saturation effects play a role [9]. In semiconductors and insulators the excitation of electrons across the band gap drives lattice strain [10–12]. However, the stresses by hot phonons often prevail [13]. In GaAs a nonlinear contribution to the fluence dependence of the strain adds to the saturating one-photon absorption [14]. Various time-resolved magneto-optical experiments in metallic magnets demonstrate the possibility to trigger and control magnetization precession [15–18], using laser-induced strain pulses. In contrast, most research on magnetic insulators, mainly oxides, emphasizes energy-efficient magnetization switching schemes [19,20] and nonthermal spin manipulation by the inverse Faraday effect [21], the inverse Cotton-Mouton effect [22], and photoinduced magnetic anisotropy [23]. Since these oxides have large band gaps, the processes are thought to proceed without absorption, and the generation of phonons is not always mentioned as a mechanism to drive spins. In some materials hybrid magnetoelastic modes are identified as the relevant excitations [24,25]. Among the magnetic oxides, yttrium iron garnet (YIG) provides the lowest magnon

damping. Below the charge-transfer transitions identified with the band gap of YIG, there are weaker crystal-field *d-d* transitions down to about 800 nm [26,27]. A large magneto-optical contrast is achieved by bismuth substitution [28], which connects this workhorse of magnon spintronics [29,30] and spin caloritronics [31] to optomagnetism. Recent publications on ferrimagnetic garnets reported magnetization dynamics via thermally induced crystalline anisotropy modification [23,32,33], similar to previous work in antiferromagnets [34–36]. More specifically, optically excited coherent and incoherent phonons are reported to generate spin waves (SWs) [27,37,38]. A quadratic fluence dependence of the spin-wave amplitude was discovered in several garnets already with moderate fluences below 15 mJ/cm^2 [25,38].

Here, we present nondestructive UXRD measurements on the very same Bi:YIG film [38], to quantify the lattice dynamics upon below-band-gap femtosecond laser excitation with fluences up to 100 mJ/cm^2. This corresponds to intensities, which are typical of experiments that manipulate magnetization in insulators by femtosecond light pulses [19,33,37,38], and we find a pronounced quadratic fluence dependence of the strain amplitude that quantifies coherent and incoherent phonons as propagating strain pulses and localized thermal expansion, respectively. The strain amplitude is inversely proportional to the pump pulse duration, which indicates a short lifetime of the intermediate state during the two-photon excitation. This is a quantitative and direct structural measurement of transient strain generated dominantly by two-photon absorption. We contrast this two-photon absorption process with direct above-band-gap excitation using near-ultraviolet (NUV) pulses. In this case, the lattice strain η depends linearly on the excitation fluence.

We investigate two similar (100)-oriented thin films of 150 and 135 nm $Bi_xY_{3-x}Fe_5O_{12}$ (Bi:YIG) with $x = 1$ and 2, respectively, grown on a (100)-oriented $Gd_3Ga_5O_{12}$ (GGG) substrate, schematically pictured in Fig. 1(b). The single-crystalline films were grown by pulsed laser deposition.
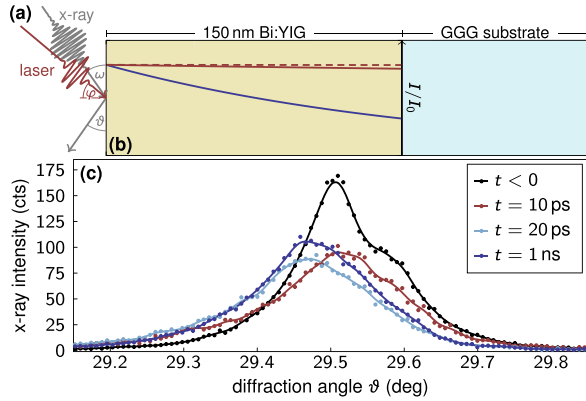
*bargheer@uni-potsdam.de

FIG. 1. (a) Sketched pump-probe geometry. (b) Sample structure and spatial intensity profiles in Bi:YIG for NUV (blue) and NIR illumination (red). For NIR light the linear absorption is negligible (dashed line) and it remains small (solid line) when including two-photon absorption, assuming an intensity of 1 TW/cm^2. (c) Scattered x-ray intensity is plotted as a function of ϑ, showing the (800) Bragg reflection of $Bi_2Y_1Fe_5O_{12}$ before 8 mJ/cm^2 NUV excitation and for a selection of pump-probe delays.

X-ray diffraction and spectroscopic ellipsometry reveal similar structural and optical properties of both Bi:YIG samples. Although the bismuth substitution enhances the electronic d-d transition probabilities for photon energies just below the band-gap energy [39], the optical properties are essentially identical for both samples at the excitation wavelengths $\lambda_{NUV} = 400$ nm and $\lambda_{NIR} = 800$ nm of our experiments. This is verified by ellipsometry, which yields an optical penetration depth of 170 nm at λ_{NUV}. For λ_{NIR} ellipsometry only yields a lower bound for the penetration depth which is consistent with the literature value of 65 μm [26–28]. The intensity profiles for both excitation wavelengths are depicted true to scale in Fig. 1(b). For our experiments the relevant difference of the samples is the higher elastic constant for the lower bismuth concentration. The larger speed of sound is partially compensated by the increased layer thicknesses such that we qualitatively find the same transient response to laser excitation. The increased lattice constant upon doping [40] does not affect our results as we examine solely the relative changes of the lattice. Thus the two samples allow us to crosscheck the amplitudes and timings of the photoinduced strain transients.

The UXRD data, exemplarily depicted in Fig. 1(c), are measured at the laser-driven table-top plasma x-ray source (PXS) [41] at the University of Potsdam with a 200-fs x-ray pulse duration at a wavelength of 154 pm (Cu $K\alpha$). The samples are excited at a 1 kHz repetition rate by p-polarized NUV pulses at 400 nm or NIR pulses at 800 nm under an angle of $\varphi = 40°$ [see Fig. 1(a)]. The incident fluence F_i is changed by a combination of a wave plate and polarizer. Changes in the spot size resulting from self-focusing at higher intensities, however, led us to adjust the full width at half maximum (FWHM) of the Gaussian-shaped pump pulses between 1.5 and 0.7 mm diameter, as controlled by a beam profiler. F_i is calculated by the top-hat approximation with the $1/e$ width for the laser excitation profile. The laser pulse
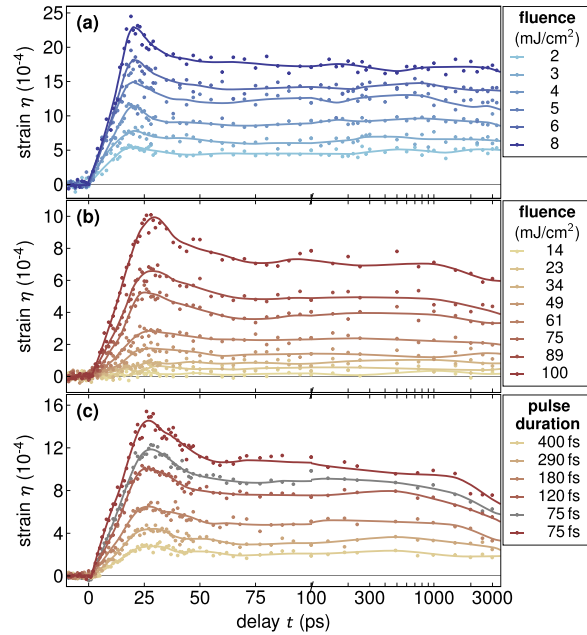

FIG. 2. Transient lattice strain η for different excitation parameters, measured with UXRD. Solid lines act as a guide to the eye. (a) Fluence series for $Bi_2Y_1Fe_5O_{12}$ with femtosecond NUV excitation. For $Bi_1Y_2Fe_5O_{12}$ we show (b) the fluence series with 120 fs NIR excitation and (c) the pulse duration series with 100 mJ/cm^2 NIR excitation. The gray data set has a similar pulse duration but opposite linear chirp.

duration is determined by a single-shot autocorrelator. X-ray pulses with a 0.3-mm-diam spot size probe the samples at delays up to $t = 3$ ns at a Bragg angle of $\omega = 29.5°$ [see Fig. 1(a)], associated with the symmetric (800) reflection for both samples. In Fig. 1(c), the scattered x-ray intensity of Bi:YIG around $\omega = \vartheta$, detected with a Pilatus 100k area detector from Dectris, is exemplarily displayed for four different pump-probe delays after an 8 mJ/cm^2, NUV femtosecond excitation. The transient angular shift $\Delta\vartheta(t)$ of the Bragg reflection is calculated by the center-of-mass change of the scattered intensity before and after excitation [42]. From this, we calculate the mean transient out-of-plane strain (i.e., the relative change of the layer thickness) in the Bi:YIG layer, $\eta(t)$, via Bragg's law modified by a geometric scaling factor f. According to our diffraction geometry, with the sample and area detector at fixed diffraction angles, and for a convergent x-ray beam we use $f \approx 2$ [43,44],

$$\eta(t) = -f\Delta\vartheta(t)\cot(\omega). \qquad (1)$$

First, we investigated the transient strain of Bi:YIG as a function of the excitation fluence for NUV illumination to determine the response to an above-band-gap excitation. The results for $Bi_2Y_1Fe_5O_{12}$ are shown in Fig. 2(a) and yield the typical linear scaling of the strain amplitude with the fluence in accordance with other studies on semiconductors and insulators [12,45]. This dependence is analyzed by the blue linear fit in Fig. 3(a), where the average strain $\bar{\eta}$ in
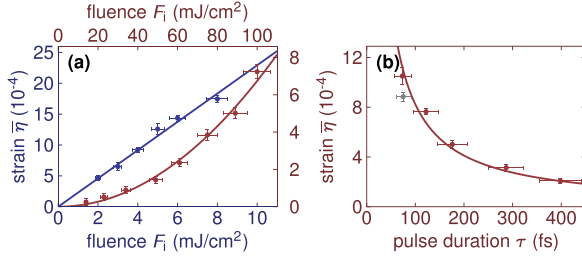
FIG. 3. Averaged lattice strain $\overline{\eta}$ in Bi:YIG between 75 ps and 1 ns evaluated from the data set in Fig. 2. (a) $\overline{\eta}$ as a function of the fluence at NUV excitation of $Bi_2Y_1Fe_5O_{12}$ (blue) and NIR excitation of $Bi_1Y_2Fe_5O_{12}$ (red). The NUV data are fitted with a linear function and a quadratic fluence dependence is observed for the NIR excitation as predicted by the presented modeling [see Eq. (7)]. (b) Pulse duration dependence of $\overline{\eta}$ upon NIR excitation of $Bi_1Y_2Fe_5O_{12}$. The gray data point was obtained under different chirp conditions. The solid line results from Eq. (7) with the same parameters as in (a). The vertical error bars are the standard deviation of η and the horizontal error bars are estimated from the pump spot size fluctuation and the GDD of the mirrors.

Bi:YIG from 75 ps to 1 ns is displayed as a function of the NUV fluence. The transient strain data in Fig. 2 exhibit multiple features characteristic of coherent and incoherent phonons. During the first 50 ps, the rising edge, the local maximum at 25 ps, and the falling edge are associated with a coherent and bipolar phonon wave packet launched by the absorption of an ultrashort laser pulse [12]. The time to reach the maximum expansion/strain is governed by the sound velocity in Bi:YIG and the film thickness. The falling edge relates to the movement of the expansive part of the bipolar wave packet out of the Bi:YIG layer [12]. The exact temporal behavior of the measured average strain depends on the spatial form of the wave packet [12]. The strain beyond 50 ps arises from heating, which is proportional to the absorbed energy [1,46,47]. Within our measurement window of 3 ns the thermal expansion shows almost no relaxation because of the slow heat transport out of Bi:YIG, as expected from the low thermal conductivity of garnet [48,49]. The dynamics of the film with $x = 1$ is identical when we scale the timing according to the different sound velocity and thickness.

Following the experiments for the excitation of spin waves [24,25,38,50], we excited Bi:YIG with NIR light with a short pulse duration (150 fs) and incident fluences up to 100 mJ/cm². We used the very same $x = 1$ sample as Deb *et al.* [38]. At fluences comparable to the NUV excitation no significant strain was detected. The results for fluences larger than 10 mJ/cm² are displayed in Fig. 2(b) and show a quadratic dependence of $\eta(t)$ on the fluence. Substantiated by the red line in Fig. 3(a), this quadratic fluence dependence indicates a two-photon strain generation process. Although the transient strain response for NIR excitation shown in Figs. 2(b) and 2(c) is very similar to the above-band-gap excitation shown in Fig. 2(a), three small differences in the observed strain signatures require discussion. The maximum at 25 ps in Fig. 2(b) is slightly delayed, because the higher sound velocity $v_1 = 6.3$ nm/ps for $x = 1$ as compared to

$v_2 = 5.4$ nm/ps for $x = 2$ [40,51] is overcompensated by the layer thickness d. Second, the subsequent falling edge shows an almost linear strain decrease from 25 to 50 ps for NIR excitation, whereas for NUV excitation the slope shows an exponential-like decrease. This is observed for both samples and is due to the nearly homogeneous nonlinear absorption in contrast to the steeper intensity profile for linear absorption, displayed in Fig. 1(b). The absorption profiles lead to different stress profiles inside the layer. Consequently, a rectangular-shaped bipolar strain wave is launched upon NIR excitation and a semiexponential-shaped bipolar strain wave is launched upon NUV excitation [8]. The average strain in the Bi:YIG layer is shaped accordingly [52], which we monitor directly with UXRD [3,8,53]. The different intensity profiles also determine the deposition of heat. This explains the third difference observed at timescales beyond 1 ns when $\eta(t)$ retains a constant value for NUV excitation and decreases at NIR excitation. We attribute this to a stronger heat gradient at the Bi:YIG/GGG interface and faster cooling to the substrate for NIR excitation.

We conclude our measurements with a variation of the NIR pulse duration to examine the lifetime of the transient state of the two-photon process. At a fluence of 100 mJ/cm² we tuned the pump pulse duration from $\tau = 75$ to 400 fs. The transient strain response, depicted in Fig. 2(c), is qualitatively very similar to the data in Fig. 2(b). The dependence of the average strain $\overline{\eta}(\tau)$ on the pulse duration τ is analyzed in Fig. 3(b). The fit shows an inverse proportionality between $\overline{\eta}$ and τ. The two-photon absorption for the shortest pulse durations of 75 fs with opposite linear chirp show deviations which we attribute to a higher-order chirp. The fit in Fig. 3(b) only includes the red data points which have the same sign of the linear chirp which was controlled by the grating compressor of the laser system. We corrected the pulse durations measured at the autocorrelator according to the group delay dispersion GDD $\approx -500 \pm 200$ fs² of the mirrors between the autocorrelator and the sample.

Both the fluence and pulse duration dependence of the strain are consistent with a model which is based on one- and two-photon absorption processes. In the following we present the modeling to fit the strain data in Fig. 3 and to determine the two-photon absorption coefficient β of Bi:YIG for NIR light. Lambert-Beer's law can be modified by a second-order term to account for two-photon absorption [see Eq. (2)] [54,55]. Starting from the attenuation of light in matter at the depth z due to one- and two-photon absorption, we solve the following equation for the intensity I,

$$\frac{\partial I}{\partial z} = -\alpha I - \beta I^2, \qquad (2)$$

where α is the one- and β the two-photon absorption coefficient. In the case of linear one-photon absorption, i.e., for NUV light, we set $\beta = 0$, which results in Lambert-Beer's law [see Eq. (3)]. In the case of NIR light, we set $\alpha = 0$ to model the strain generated solely by two-photon absorption as suggested by the data in Fig. 3(a). If I_0 is the incident intensity on the Bi:YIG layer, the solutions of Eq. (2) are

$$I(z) = \begin{cases} I_0 e^{-\alpha z} & \text{for NUV,} \\ \frac{I_0}{1+\beta I_0 z} & \text{for NIR.} \end{cases} \qquad (3)$$

Since the layer thickness is much smaller than the penetration depth of the NIR light, we may Taylor-expand Eq. (3) at $z = 0$, i.e., $I(z) = I_0 - \beta I_0^2 z + O(z^2)$. The linear spatial intensity dependence is a good approximation for NIR light [see Fig. 1(b)]. For time-resolved measurements, the incident intensity I_0 is time dependent. In this experiment, the excitation pulse can be well approximated by a Gaussian envelope $I_0(t) = 2\sqrt{\ln 2/\pi}\, F_i/\tau \exp(-4\ln 2\, t^2/\tau^2)$, where F_i is the incident fluence, and τ is the pulse duration at FWHM. The absorbed fluence inside the Bi:YIG layer $F_a(F_i, \tau)$ is calculated via temporal integration of the intensity difference from the sample surface ($z = 0$) to the layer-substrate interface ($z = d$)

$$F_a(F_i, \tau) = \int_{-\infty}^{\infty} I_0(t) - I(z = d, t)dt \qquad (4)$$

$$= \begin{cases} (1 - e^{-\alpha d})F_i & \text{for NUV,} \\ \sqrt{\dfrac{\ln 4}{\pi}}\beta d \dfrac{F_i^2}{\tau} - O\!\left(\dfrac{F_i^3}{\tau^2}\right) & \text{for NIR.} \end{cases} \qquad (5)$$

The stress σ on the lattice resulting from the energy density deposited by the pump pulse $\rho^Q = F_a/d$ is given by the macroscopic Grüneisen parameter Γ via $\sigma = \Gamma \rho^Q$ [3,46,47,56]. In the one-dimensional (1D) geometry of a homogeneously excited thin film with a cubic symmetry aligned to the sample surface, the strain response perpendicular to the surface is given by $\eta = \sigma/C_{11}$, where C_{11} is the cubic elastic constant. We estimate the mean strain in the Bi:YIG layer via the linear NUV absorption ($\beta = 0$),

$$\overline{\eta}_{\text{NUV}} = \frac{\Gamma}{C_{11}d}(1 - e^{-\alpha d})F_i. \qquad (6)$$

The 2.1×10^{-4} per mJ/cm^2 calculated from Eq. (6) is in reasonable agreement with the strain $\overline{\eta}_{\text{NUV}} = 2.3 \times 10^{-4}$ per mJ/cm^2 extracted from the blue line in Fig. 3(a). Here, we used a film thickness of $d = 135$ nm, the linear absorption coefficient for NUV light $\alpha = 6 \times 10^4$ cm^{-1}, the elastic constant $C_{11} = 190$ GPa for Bi$_2$Y$_1$Fe$_5$O$_{12}$, and the Grüneisen parameter of YIG, $\Gamma \approx 1$, reported in the literature [26,40,51,57]. The lattice strain $\overline{\eta}$ generated via nonlinear NIR absorption can also be calculated in the same manner with a different value of $C_{11} = 230$ GPa for Bi$_1$Y$_2$Fe$_5$O$_{12}$,

$$\overline{\eta}_{\text{NIR}} = \frac{\Gamma}{C_{11}}\sqrt{\frac{\ln 4}{\pi}}\beta\frac{F_i^2}{\tau}. \qquad (7)$$

This equation describes the functional dependence of the strain on the fluence F_i and the pulse duration τ which we discovered experimentally upon NIR excitation. The red curves in Fig. 3 are calculated with Eq. (7), fitting the data precisely if we use $\beta = 2.4$ cm/GW as the two-photon absorption coefficient. We visualized the spatial intensity profile according to two-photon absorption in Fig. 1(b) by the red solid line. As a crosscheck we note that $\alpha I < \beta I^2$, already

for comparably low intensities of $I = 0.1$ TW/cm^2 if we use the literature value $\alpha = 150$ cm^{-1} for NIR light [26]. This justifies neglecting the linear absorption term during the evaluation of the NIR data, since βI^2 is orders of magnitude larger than αI at intensities higher than $I = 1$ TW/cm^2.

A two-photon absorption coefficient of $\beta_{\text{YIG}} = 130$ cm/GW was reported for undoped YIG at photon energies of $(1.17 + 1.93)$ eV $= 3.1$ eV [58]. Mainly, a two-step process via the ${}^6A_{1g}({}^6S) \rightarrow {}^4T_{1g}({}^4G)$ and subsequent ${}^4T_{1g}({}^4G) \rightarrow {}^4T_{1g}({}^4P)$ Fe^{3+}-ion transitions in YIG and Bi:YIG accounts for the two-photon absorption in both materials [27,59,60], i.e., the two-photon transition proceeds via real and short-lived levels. The bismuth substitution affects the electronic and optical properties of YIG, e.g., increasing spin-orbit coupling, absorption, and even second-harmonic generation (SHG) efficiency [39,61,62]. In particular, the very weak ${}^6A_{1g}({}^6S) \rightarrow {}^4T_{1g}({}^4G)$ transition energy shifts with doping and therefore modulates the one- and two-photon absorption coefficients. According to our modeling the previously reported β_{YIG} would yield a strain of 4% and an absorption of 60% at large peak intensities of 1 TW/cm^2, which contradicts the measured values of 0.1% strain and less than 5% absorption.

To summarize, we used UXRD to directly measure the strain in nanolayered Bi:YIG excited via one- and two-photon absorption. We identify the two-photon process by the quadratic fluence dependence and the inversely proportional pulse duration dependence of the photoexcited strain. The latter also proves that the intermediate state is short lived. We substantiate our findings by a quantitative fit with Lambert-Beer's law with a two-photon absorption extension in combination with the Grüneisen approach, where the absorbed energy is proportional to the lattice strain, independent of how the photon energy is absorbed. From this, we determine the two-photon absorption coefficient $\beta \approx 2$ cm/GW for exciting Bi$_1$Y$_2$Fe$_5$O$_{12}$ at 800 nm. We believe that our quantitative evaluation of the strain generated by two-photon absorption is particularly important for a full understanding of light-driven spin manipulation in magnetic insulators [23,27,32–38], but it has more general relevance for ultrafast science on supposedly nonabsorbing or transparent matter. The large peak intensities around 1 TW/cm^2 necessary to drive 0.1% strain can be achieved both by high pump fluences and short pulse durations.

[1] J. Pudell, A. A. Maznev, M. Herzog, M. Kronseder, C. H. Back, G. Malinowski, A. von Reppert, and M. Bargheer, Layer specific observation of slow thermal equilibration in ultrathin metallic nanostructures by femtosecond X-ray diffraction, Nat. Commun. **9**, 3335 (2018).

[2] M. Highland, B. C. Gundrum, Y. K. Koh, R. S. Averback, D. G. Cahill, V. C. Elarde, J. J. Coleman, D. A. Walko, and E. C. Landahl, Ballistic-phonon heat conduction at the nanoscale as revealed by time-resolved x-ray diffraction and time-domain thermoreflectance, Phys. Rev. B **76**, 075337 (2007).

[3] J. Pudell, A. von Reppert, D. Schick, F. Zamponi, M. Rössle, M. Herzog, H. Zabel, and M. Bargheer, Ultrafast negative thermal expansion driven by spin disorder, Phys. Rev. B **99**, 094304 (2019).

[4] C. Dornes, Y. Acremann, M. Savoini, M. Kubli, M. J. Neugebauer, E. Abreu, L. Huber, G. Lantz, C. A. F. Vaz, H. Lemke, E. M. Bothschafter, M. Porer, V. Esposito, L. Rettig, M. Buzzi, A. Alberca, Y. W. Windsor, P. Beaud, U. Staub, D. Zhu *et al.*, The ultrafast Einstein–de Haas effect, Nature (London) **565**, 209 (2019).

[5] C. Thomsen, H. T. Grahn, H. J. Maris, and J. Tauc, Surface generation and detection of phonons by picosecond light pulses, Phys. Rev. B **34**, 4129 (1986).

[6] P. Ruello and V. E. Gusev, Physical mechanisms of coherent acoustic phonons generation by ultrafast laser action, Ultrasonics **56**, 21 (2015).

[7] O. Matsuda, M. C. Larciprete, R. Li Voti, and O. B. Wright, Fundamentals of picosecond laser ultrasonics, Ultrasonics **56**, 3 (2015).

[8] D. Schick, M. Herzog, A. Bojahr, W. Leitenberger, A. Hertwig, R. Shayduk, and M. Bargheer, Ultrafast lattice response of photoexcited thin films studied by X-ray diffraction, Struct. Dyn. **1**, 064501 (2014).

[9] D. Daranciang, M. J. Highland, H. Wen, S. M. Young, N. C. Brandt, H. Y. Hwang, M. Vattilana, M. Nicoul, F. Quirin, J. Goodfellow, T. Qi, I. Grinberg, D. M. Fritz, M. Cammarata, D. Zhu, H. T. Lemke, D. A. Walko, E. M. Dufresne, Y. Li, J. Larsson *et al.*, Ultrafast Photovoltaic Response in Ferroelectric Nanolayers, Phys. Rev. Lett. **108**, 087601 (2012).

[10] C. Rose-Petruck, R. Jimenez, T. Guo, A. Cavalieri, C. W. Siders, F. Rksi, J. A. Squier, B. C. Walker, K. R. Wilson, and C. P. J. Barty, Picosecond-milliangstrom lattice dynamics measured by ultrafast X-ray diffraction, Nature (London) **398**, 310 (1999).

[11] K. Sokolowski-Tinten, C. Blome, C. Dietrich, A. Tarasevitch, M. Horn von Hoegen, D. von der Linde, A. Cavalleri, J. Squier, and M. Kammler, Femtosecond X-Ray Measurement of Ultrafast Melting and Large Acoustic Transients, Phys. Rev. Lett. **87**, 225701 (2001).

[12] D. Schick, M. Herzog, H. Wen, P. Chen, C. Adamo, P. Gaal, D. G. Schlom, P. G. Evans, Y. Li, and M. Bargheer, Localized Excited Charge Carriers Generate Ultrafast Inhomogeneous Strain in the Multiferroic $BiFeO_3$, Phys. Rev. Lett. **112**, 097602 (2014).

[13] M. Bargheer, N. Zhavoronkov, J. C. Woo, D. S. Kim, M. Woerner, and T. Elsaesser, Excitation mechanisms of coherent phonons unravelled by femtosecond X-ray diffraction, Phys. Status Solidi A **243**, 2389 (2006).

[14] G. J. Williams, S. Lee, D. A. Walko, M. A. Watson, W. Jo, D. R. Lee, and E. C. Landahl, Direct measurements of multi-photon induced nonlinear lattice dynamics in semiconductors via time-resolved x-ray scattering, Sci. Rep. **6**, 39506 (2016).

[15] J. V. Jäger, A. V. Scherbakov, T. L. Linnik, D. R. Yakovlev, M. Wang, P. Wadley, V. Holy, S. A. Cavill, A. V. Akimov, A. W. Rushforth, and M. Bayer, Picosecond inverse magnetostriction in galfenol thin films, Appl. Phys. Lett. **103**, 032409 (2013).

[16] J.-W. Kim, M. Vomir, and J.-Y. Bigot, Ultrafast Magnetoacoustics in Nickel Films, Phys. Rev. Lett. **109**, 166601 (2012).

[17] J.-W. Kim, M. Vomir, and J.-Y. Bigot, Controlling the spins angular momentum in ferromagnets with sequences of picosecond acoustic pulses, Sci. Rep. **5**, 8511 (2015).

[18] D. Afanasiev, I. Razdolski, K. M. Skibinsky, D. Bolotin, S. V. Yagupov, M. B. Strugatsky, A. Kirilyuk, T. Rasing, and A. V. Kimel, Laser Excitation of Lattice-Driven Anharmonic Magnetization Dynamics in Dielectric $FeBO_3$, Phys. Rev. Lett. **112**, 147403 (2014).

[19] A. Stupakiewicz, K. Szerenos, D. Afanasiev, A. Kirilyuk, and A. V. Kimel, Ultrafast nonthermal photo-magnetic recording in a transparent medium, Nature (London) **542**, 71 (2017).

[20] F. Hansteen, A. Kimel, A. Kirilyuk, and T. Rasing, Femtosecond Photomagnetic Switching of Spins in Ferrimagnetic Garnet Films, Phys. Rev. Lett. **95**, 047402 (2005).

[21] A. V. Kimel, A. Kirilyuk, P. A. Usachev, R. V. Pisarev, A. M. Balbashov, and T. Rasing, Ultrafast non-thermal control of magnetization by instantaneous photomagnetic pulses, Nature (London) **435**, 655 (2005).

[22] C. Tzschaschel, K. Otani, R. Iida, T. Shimura, H. Ueda, S. Günther, M. Fiebig, and T. Satoh, Ultrafast optical excitation of coherent magnons in antiferromagnetic NiO, Phys. Rev. B **95**, 174407 (2017).

[23] A. Stupakiewicz, A. Maziewski, I. Davidenko, and V. Zablotskii, Light-induced magnetic anisotropy in Co-doped garnet films, Phys. Rev. B **64**, 064405 (2001).

[24] Y. Hashimoto, S. Daimon, R. Iguchi, Y. Oikawa, K. Shen, K. Sato, D. Bossini, Y. Tabuchi, T. Satoh, B. Hillebrands, G. E. W. Bauer, T. H. Johansen, A. Kirilyuk, T. Rasing, and E. Saitoh, All-optical observation and reconstruction of spin wave dispersion, Nat. Commun. **8**, 15859 (2017).

[25] Y. Hashimoto, D. Bossini, T. H. Johansen, E. Saitoh, A. Kirilyuk, and T. Rasing, Frequency and wavenumber selective excitation of spin waves through coherent energy transfer from elastic waves, Phys. Rev. B **97**, 140404(R) (2018).

[26] G. B. Scott, D. E. Lacklison, and J. L. Page, Absorption spectra of $Y_3Fe_5O_{12}$ (YIG) and $Y_3Ga_5O_{12}$:Fe^{3+}, Phys. Rev. B **10**, 971 (1974).

[27] M. Deb, P. Molho, B. Barbara, and J.-Y. Bigot, Controlling laser-induced magnetization reversal dynamics in a rare-earth iron garnet across the magnetization compensation point, Phys. Rev. B **97**, 134419 (2018).

[28] J. M. Robertson, S. Wittekoek, T. J. A. Popma, and P. F. Bongers, Preparation and optical properties of single crystal thin films of bismuth substituted iron garnets for magneto-optic applications, Appl. Phys. **2**, 219 (1973).

[29] A. V. Chumak, V. Vasyuchka, A. Serga, and B. Hillebrands, Magnon spintronics, Nat. Phys. **11**, 453 (2015).

[30] A. A. Serga, A. V. Chumak, B. Hillebrands, A. A. Serga, B. Hillebrands, A. V. Chumak, and T. Neumann, YIG magnonics, J. Phys. D **43**, 264002 (2010).

[31] G. E. W. Bauer, E. Saitoh, and B. J. van Wees, Spin caloritronics, Nat. Mater. **11**, 391 (2012).

[32] L. A. Shelukhin, V. V. Pavlov, P. A. Usachev, P. Y. Shamray, R. V. Pisarev, and A. M. Kalashnikova, Ultrafast laser-induced changes of the magnetic anisotropy in a low-symmetry iron garnet film, Phys. Rev. B **97**, 014422 (2018).

[33] C. S. Davies, K. H. Prabhakara, M. D. Davydova, K. A. Zvezdin, T. B. Shapaeva, S. Wang, A. K. Zvezdin, A. Kirilyuk, T. Rasing, and A. V. Kimel, Anomalously Damped

Heat-Assisted Route for Precessional Magnetization Reversal in an Iron Garnet, Phys. Rev. Lett. **122**, 027202 (2019).

[34] A. V. Kimel, A. Kirilyuk, A. Tsvetkov, R. V. Pisarev, and T. Rasing, Laser-induced ultrafast spin reorientation in the antiferromagnet TmFeO$_3$, Nature (London) **429**, 850 (2004).

[35] A. M. Kalashnikova, A. V. Kimel, R. V. Pisarev, V. N. Gridnev, A. Kirilyuk, and T. Rasing, Impulsive Generation of Coherent Magnons by Linearly Polarized Light in the Easy-Plane Antiferromagnet FeBO$_3$, Phys. Rev. Lett. **99**, 167205 (2007).

[36] A. M. Kalashnikova, A. V. Kimel, R. V. Pisarev, V. N. Gridnev, P. A. Usachev, A. Kirilyuk, and T. Rasing, Impulsive excitation of coherent magnons and phonons by subpicosecond laser pulses in the weak ferromagnet FeBO$_3$, Phys. Rev. B **78**, 104301 (2008).

[37] B. Koene, M. Deb, E. Popova, N. Keller, T. Rasing, and A. Kirilyuk, Spectrally resolved optical probing of laser induced magnetization dynamics in bismuth iron garnet, J. Phys.: Condens. Matter **28**, 276002 (2016).

[38] M. Deb, E. Popova, M. Hehn, N. Keller, S. Petit-Watelot, M. Bargheer, S. Mangin, and G. Malinowski, Femtosecond Laser-Excitation-Driven High Frequency Standing Spin Waves in Nanoscale Dielectric Thin Films of Iron Garnets, Phys. Rev. Lett. **123**, 027202 (2019).

[39] M. Deb, E. Popova, A. Fouchet, and N. Keller, Magneto-optical Faraday spectroscopy of completely bismuth-substituted Bi$_3$Fe$_5$O$_{12}$ garnet thin films, J. Phys. D **45**, 455001 (2012).

[40] G. G. Siu, C. M. Lee, and Y. Liu, Magnons and acoustic phonons in Y$_{3-x}$Bi$_x$Fe$_5$O$_{12}$, Phys. Rev. B **64**, 094421 (2001).

[41] D. Schick, A. Bojahr, M. Herzog, C. Von Korff Schmising, R. Shayduk, W. Leitenberger, P. Gaal, and M. Bargheer, Normalization schemes for ultrafast x-ray diffraction using a tabletop laser-driven plasma source, Rev. Sci. Instrum. **83**, 025104 (2012).

[42] The double-peak structure of the unexcited sample results from the $K\alpha_1$ and $K\alpha_2$ photons emitted by the source. The inhomogeneous excitation results in a broadening of the maxima.

[43] D. Schick, R. Shayduk, A. Bojahr, M. Herzog, C. von Korff Schmising, P. Gaal, and M. Bargheer, Ultrafast reciprocal-space mapping with a convergent beam, J. Appl. Crystallogr. **46**, 1372 (2013).

[44] M. Kozina, T. Hu, J. S. Wittenberg, E. Szilagyi, M. Trigo, T. A. Miller, C. Uher, A. Damodaran, L. Martin, A. Mehta, J. Corbett, J. Safranek, D. A. Reis, and A. M. Lindenberg, Measurement of transient atomic displacements in thin films with picosecond and femtometer resolution, Struct. Dyn. **1**, 034301 (2014).

[45] H. Wen, P. Chen, M. P. Cosgriff, D. A. Walko, J. H. Lee, C. Adamo, R. D. Schaller, J. F. Ihlefeld, E. M. Dufresne, D. G. Schlom, P. G. Evans, J. W. Freeland, and Y. Li, Electronic Origin of Ultrafast Photoinduced Strain in BiFeO$_3$, Phys. Rev. Lett. **110**, 037601 (2013).

[46] A. von Reppert, J. Pudell, A. Koc, M. Reinhardt, W. Leitenberger, K. Dumesnil, F. Zamponi, and M. Bargheer, Persistent nonequilibrium dynamics of the thermal energies in the spin and phonon systems of an antiferromagnet, Struct. Dyn. **3**, 054302 (2016).

[47] T. Henighan, M. Trigo, S. Bonetti, P. Granitzka, D. Higley, Z. Chen, M. P. Jiang, R. Kukreja, A. Gray, A. H. Reid, E. Jal, M. C.

Hoffmann, M. Kozina, S. Song, M. Chollet, D. Zhu, P. F. Xu, J. Jeong, K. Carva, P. Maldonado *et al.*, Generation mechanism of terahertz coherent acoustic phonons in Fe, Phys. Rev. B **93**, 220301(R) (2016).

[48] N. P. Padture and P. G. Klemens, Low thermal conductivity in garnets, J. Am. Ceram. Soc. **80**, 1018 (2005).

[49] G. A. Slack and D. W. Oliver, Thermal conductivity of garnets and phonon scattering by rare-earth ions, Phys. Rev. B **4**, 592 (1971).

[50] I. Razdolski, A. Alekhin, N. Ilin, J. P. Meyburg, V. Roddatis, D. Diesing, U. Bovensiepen, and A. Melnikov, Nanoscale interface confinement of ultrafast spin transfer torque driving non-uniform spin dynamics, Nat. Commun. **8**, 15007 (2017).

[51] M. Deb, E. Popova, M. Hehn, N. Keller, S. Mangin, and G. Malinowski, Picosecond acoustic-excitation-driven ultrafast magnetization dynamics in dielectric Bi-substituted yttrium iron garnet, Phys. Rev. B **98**, 174407 (2018).

[52] D. Schick, P. Gaal, A. Bojahr, W. Leitenberger, R. Shayduk, A. Hertwig, I. Vrejoiu, M. Herzog, and M. Bargheer, Ultrafast x-ray diffraction studies of photoexcited coherent phonons in SrRuO$_3$ thin films, arXiv:1301.3324.

[53] S. P. Zeuschner, T. Parpiiev, T. Pezeril, A. Hillion, K. Dumesnil, A. Anane, J. Pudell, L. Willig, M. Rössle, M. Herzog, A. von Reppert, and M. Bargheer, Tracking picosecond strain pulses in heterostructures that exhibit giant magnetostriction, Struct. Dyn. **6**, 24302 (2019).

[54] M. Bass, E. W. van Stryland, D. R. Williams, and W. L. Wolfe, *Handbook of Optics Volume I*, 2nd ed. (McGraw-Hill, New York, 1995).

[55] J.-C. Diels and W. Rudolph, *Ultrashort Laser Pulse Phenomena: Fundamentals, Techniques, and Applications on a Femtosecond Time Scale*, 2nd ed. (Elsevier/Academic, Amsterdam, 2006), p. 652.

[56] A. Koc, M. Reinhardt, A. von Reppert, M. Rössle, W. Leitenberger, M. Gleich, M. Weinelt, F. Zamponi, and M. Bargheer, Grueneisen-approach for the experimental determination of transient spin and phonon energies from ultrafast x-ray diffraction data: Gadolinium, J. Phys.: Condens. Matter **29**, 264001 (2017).

[57] G. A. Saunders, S. C. Parker, N. Benbattouche, and H. L. Alberts, Elastic and nonlinear acoustic properties of the terbium iron garnet Tb$_3$Fe$_5$O$_{12}$ in relation to those of other garnets, Phys. Rev. B **46**, 8756 (1992).

[58] S. I. Shablaev and R. V. Pisarev, Two-photon absorption spectroscopy of electronic states in yttrium iron garnet Y$_3$Fe$_5$O$_{12}$, J. Magn. Soc. Jpn. **11**, 19 (1987).

[59] J. F. Dillon, Optical absorptions and rotations in the ferrimagnetic garnets, J. Phys. Radium **20**, 374 (1959).

[60] K. A. Wickersheim and R. A. Lefever, Absorption spectra of ferric iron-containing oxides, J. Chem. Phys. **36**, 844 (1962).

[61] T. Oikawa, S. Suzuki, and K. Nakao, First-principles study of spin-orbit interactions in bismuth iron garnet, J. Phys. Soc. Jpn. **74**, 401 (2005).

[62] G. Petrocelli, S. Martellucci, and M. Richetta, Bismuth induced enhancement of the second-harmonic generation efficiency in bismuth-substituted yttrium iron garnet films, Appl. Phys. Lett. **63**, 3402 (1993).

Article XII

Second harmonic generation of nanoscale phonon wave packets

André Bojahr, Matthias Gohlke, Wolfram Leitenberger, **Jan-Etienne Pudell**, Matthias Reinhardt, Alexander von Reppert, Matthias Rössle, Mathias Sander, Peter Gaal and Matias Bargheer

Phonons are often regarded as delocalized quasiparticles with certain energy and momentum. The anharmonic interaction of phonons determines macroscopic properties of the solid, such as thermal expansion or thermal conductivity, and a detailed understanding becomes increasingly important for functional nanostructures. Although phonon-phonon scattering processes depicted in simple wave-vector diagrams are the basis of theories describing these macroscopic phenomena, experiments directly accessing these coupling channels are scarce. We synthesize monochromatic acoustic phonon wave packets with only a few cycles to introduce nonlinear phononics as the acoustic counterpart to nonlinear optics. Control of the wave vector, bandwidth, and consequently spatial extent of the phonon wave packets allows us to observe nonlinear phonon interaction, in particular, second harmonic generation, in real time by wave-vector-sensitive Brillouin scattering with x-rays and optical photons.

PHYSICAL REVIEW LETTERS

Second Harmonic Generation of Nanoscale Phonon Wave Packets

A. Bojahr,[1] M. Gohlke,[1] W. Leitenberger,[1] J. Pudell,[1] M. Reinhardt,[2] A. von Reppert,[1] M. Roessle,[1]
M. Sander,[1] P. Gaal,[2] and M. Bargheer[1,2,*]

[1]*Institut für Physik and Astronomie, Universität Potsdam, Karl-Liebknecht-Strasse 24-25, 14476 Potsdam, Germany*
[2]*Helmholtz Zentrum Berlin, Albert-Einstein-Strasse 15, 12489 Berlin, Germany*
(Received 1 June 2015; published 5 November 2015)

Phonons are often regarded as delocalized quasiparticles with certain energy and momentum. The anharmonic interaction of phonons determines macroscopic properties of the solid, such as thermal expansion or thermal conductivity, and a detailed understanding becomes increasingly important for functional nanostructures. Although phonon-phonon scattering processes depicted in simple wave-vector diagrams are the basis of theories describing these macroscopic phenomena, experiments directly accessing these coupling channels are scarce. We synthesize monochromatic acoustic phonon wave packets with only a few cycles to introduce nonlinear phononics as the acoustic counterpart to nonlinear optics. Control of the wave vector, bandwidth, and consequently spatial extent of the phonon wave packets allows us to observe nonlinear phonon interaction, in particular, second harmonic generation, in real time by wave-vector-sensitive Brillouin scattering with x-rays and optical photons.

Basic physics lectures introduce phonons as uncoupled quanta of the lattice excitation, i.e., delocalized quasiparticles with certain energy and momentum. The low-temperature heat capacity of insulators and blackbody radiation are fundamental macroscopic consequences of quantum mechanics. Anharmonic effects are introduced to discuss heat expansion and thermal transport, where only thermally activated phonons contribute to these phenomena. Typically, theory averages over thermally excited quantum states before properties of the "mean heat carrying phonon" are compared to macroscopic measurements like the temperature of a solid. Our Letter shows a route towards detailed experimental information on mode-specific nonlinear interactions. This will facilitate fundamental tests of the theory avoiding the calculation of thermal averages, which inevitably obscure the full information.

Such progress is of high relevance for the "hot topic" of heat transport manipulation in nanostructures which is driven by the enormous size reduction of integrated circuits [1–6] and the field of thermoelectrics. Recent work aims at improving the conversion of waste heat into usable energy by tailored phonon-phonon interaction processes [7–9]. Nonlinear effects have been predicted to yield efficient thermal diodes [10]. Only in a few cases has the full phonon dispersion relation including the linewidth (inverse lifetime) been measured by inelastic scattering [11–13], and at low wave vectors the instrumental resolution currently sets limits. Linewidth measurements yield mode-averaged dissipation, but experimental knowledge about the dominant coupled modes is unavailable. The free-electron lasers hold great promise to access the coupling in the femtosecond time domain using diffuse scattering and inelastic x-ray scattering [14,15]. Recently, the coupling of terahertz excited optical phonons with other optical phonons was

observed and presented as one example of nonlinear phonon interactions [16].

Nonlinear phononics as discussed here shows many analogies to nonlinear photonics in transparent media where high electromagnetic wave fields yield nonlinear polarizations. These processes are described by interacting photons that fulfill momentum and energy conservation. The description of these optical phenomena is robust and extremely well tested by an enormous number of experiments such as sum- and difference-frequency generation or four-wave mixing. The first analogous experiments on nonlinear phononics date back to the 1960s, when collisions of two ultrasound beams were studied in real time and space [17]. These experiments somewhat resembled nonlinear optics before the utilization of the laser. The required interaction volume was in the centimeter range, and the time resolution was limited by the 10 MHz ultrasound frequency. The phonon analogue of optical supercontinuum generation by femtosecond lasers was studied in seminal picosecond-ultrasonics experiments on the self-steepening of the strain-pulse fronts [18,19] which finally lead to acoustic solitons [20–22]. In these experiments, the excitation of nanometric strain waves was not wave-vector specific. Recent progress in the creation and detection of gigahertz and terahertz phonon wave packets also known as hypersonic strain waves makes them a perfect test ground to investigate phonon-phonon interaction processes on the nanoscale [23].

In this work, we combine the selective excitation of longitudinal acoustic phonon wave packets with time-resolved variants of x-ray and broadband Brillouin scattering [23] to investigate the nonlinear interaction of phonons with a specific wave vector. The experiments provide a high temporal and spatial resolution for observing phonon dynamics in real time over a broad range of wave vectors which

195502-1

PHYSICAL REVIEW LETTERS

correspond to the nanometer length scale. As the basic example of nonlinear phononics, we shaped giant and ultrashort phonon wave packets with well-defined momenta and observed the generation of their second harmonic (SH).

To create such giant amplitude strain waves, ultrashort laser pulses excite a metallic strontium ruthenate (SRO) film deposited on a bulk strontium titanate (STO) substrate, a system where we know the first-order lattice anharmonicity [19] and where the acoustic impedances of the thin film and substrate are nearly matched [24]. The metal film expansion induced by each laser pulse launches a bipolar strain pulse into STO [24]. A train of several laser pulses [Fig. 1(b)] with a defined temporal delay τ creates a phonon wave packet with a fundamental frequency of $\Omega = 2\pi/\tau$ [23,25,26]. If the laser-pulse train is composed of femtosecond pulses (blue lines in Fig. 1), the phonon wave packet exhibits
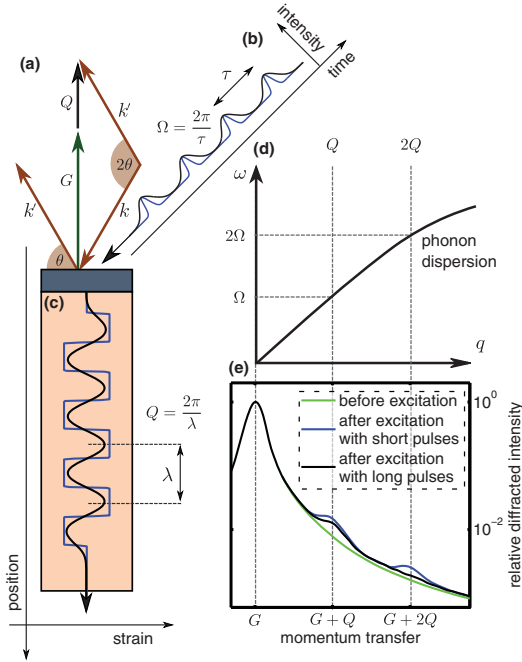

FIG. 1 (color). Preparation and observation of phonon wave packets. (a) X-rays with wave vector k are scattered (k') by the reciprocal lattice vector G plus a phonon with wave vector Q. (b) A metal film is excited by a laser-pulse train with short (blue) and long (black) pulses. (c) Short pulses excite phonon wave packets at the fundamental and higher harmonics [rectangular wave packet (blue)]. Excitation with long pulses suppresses higher harmonics and generates a sinusoidal wave (black). (d) The phonon dispersion relation connects the central frequency $\Omega = 2\pi/\tau$ of the excited phonon wave packet with its corresponding wave vector $Q = 2\pi/\lambda$. (e) Experimental data of ultrafast x-ray diffraction from the unexcited sample shows the (002) substrate reflection (green). After excitation with short pulses (blue), peaks at $G \pm Q$ and $G \pm 2Q$ occur. These peaks originate from inelastic scattering by the induced phonon wave packet. For longer pump pulses (black), the scattering at $G \pm 2Q$ is suppressed. This evidences that a narrow band phonon wave packet without its higher harmonics was excited.

several sharp strain fronts [Fig. 1(c)], corresponding to the excitation of higher harmonics $n \cdot \Omega$. These harmonics are identified in ultrafast x-ray diffraction (UXRD) experiments from their wave vector Q according to the dispersion relation of longitudinal phonons [$\omega = v_L q$, plotted in Fig. 1(d)]. For small wave vectors, $v_L(q)$ is a constant describing the longitudinal sound velocity. The UXRD data in Fig. 1(e) were obtained with an ultrathin SRO transducer layer ($d = 15$ nm). The green curve displays the relative diffraction intensity before the four pump pulses ($\tau = 11$ ps) reach the sample. The peak at G corresponds to the reciprocal lattice vector (002) of the STO substrate. When the 100 ps x-ray pulse was probing the sample shortly after the generation of the wave packet, additional diffraction intensity at $G \pm n \cdot Q = n \cdot 0.071$ nm^{-1} was detected (blue curve). The diffraction intensity is a direct measure of the spectral energy distribution of the imprinted coherent phonon modes [27]. When we increased the width of the pump pulses from $\Delta\tau_{\text{FWHM}} = 0.9$ to 3.4 ps, the diffraction of higher orders of Q was suppressed and we observed only the additional scattering from $G \pm Q$ (black curve) as suggested by the wave vector diagram in Fig. 1(a). High-frequency components of an oscillator can be excited only by stimuli which contain these frequencies.

To demonstrate second harmonic generation (SHG) of monochromatic phonon wave packets, we repeated the UXRD experiment with a 70 nm SRO transducer, which absorbs more optical energy. We used only two long laser pulses ($\tau = 17.7$ ps and $\Delta\tau_{\text{FHWM}} = 5.3$ ps) while keeping the total incident laser fluence constant. This doubles the local atomic displacement and quadruples the acoustic energy density $\mathcal{E} = E/V$ of the wave packet in the volume V—defined by the beam area and the length of the wave packet. This increased the up-conversion efficiency of phonons at the expense of monochromaticity according to the higher wave packet localization in space.

Figure 2(a) shows the fundamental phonon peak around $Q = 0.044$ nm^{-1} which was observed in the UXRD experiment when the x-rays probed the sample immediately after excitation. For time delays around 200 ps, a tiny peak at $2Q = 0.088$ nm^{-1} occurred. This rising SH is enhanced in Fig. 2(b), where the measured diffraction signal is multiplied by q^2 for better visibility. Figure 2(c) quantifies the transient change of the peak area Σ_i in the vicinity of 0.044 and 0.088 nm^{-1} [28]. $\Sigma_i \sim \mathcal{E}_i$ is proportional to the energy density $\mathcal{E}_i \sim \int \rho_E(q,t)dq$ of the phonons around $q = iQ$, obtained from integrating the spectral energy density $\rho_E(q,t)$ over the bandwidth of the fundamental ($i = 1$) and the SH ($i = 2$), respectively [27].

The signal Σ_1 of the excited fundamental mode (red diamonds) increased immediately after excitation, followed by a nearly exponential decay. Σ_2 describing the SH (cyan dots) was delayed by approximately 200 ps. Thus, the SH was not directly excited by the laser pulses but was only generated by the propagation of phonons in the anharmonic lattice of STO. The delay was longer than the 100 ps time
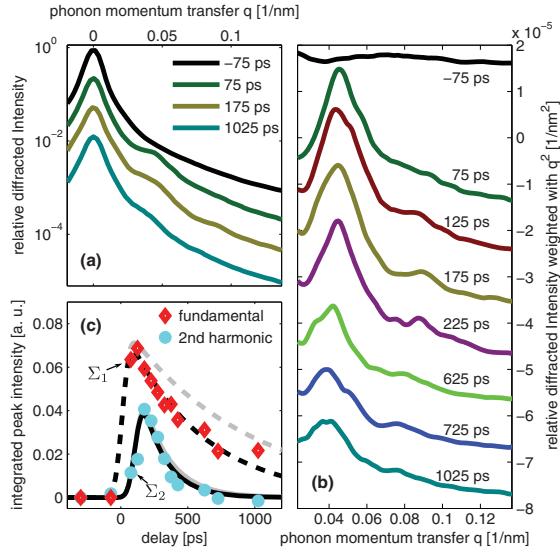
FIG. 2 (color). Transient x-ray diffraction from photoexcited phonons and their SH. (a) X-ray diffraction signals around the (002) lattice plane of the STO substrate. (b) Diffraction signals on the right shoulder of the STO substrate peak weighted by q^2 for better visualization. The peak around $Q = 0.044$ nm^{-1} after time zero reflects the optically excited coherent phonon wave packet with the central wave vector Q. After a delay of 200 ps, additional diffraction intensity around $2Q$ heralds the SH of Q generated via anharmonic phonon phonon interaction. (c) The gray (black) lines quantify the transient change of the integrated peak intensities of the fundamental and its second harmonic with (and without) a correction for the x-ray absorption.

resolution of this synchrotron experiment [37] and is a direct evidence for the SHG of phonons. Although the SH is continuously generated, it reaches its maximum very fast, since the damping of phonons scales with the square of the frequency.

The SH phonons damped out faster than the fundamental as expected for the frequency dependence of the damping rate $\Gamma \sim \omega^2$ [27]. The gray lines in Fig. 2(c) show the damping of both phonons corrected for effects of x-ray absorption in STO [27]. The corrected exponential decay times for the fundamental and the SH are 1056 and 300 ps, respectively, in good agreement with the literature values [27,38].

To confirm our result and to explore the SHG of phonons in the same sample in more detail, we performed broadband time-domain Brillouin-scattering (TDBS) experiments, which measure a substantial fraction of the phonon spectrum from 0.035 to 0.06 nm^{-1} in STO [23]. We set the pulse separation to $\tau = 30$ ps to let the SH phonon emerge at $2Q = 0.052$ nm^{-1}, in the center of the spectrum accessible by TDBS. The black line in Fig. 3(a) shows the time-dependent optical reflectivity change at $\lambda = 580$ nm which corresponds to this wave vector. The reflectivity increases in two steps from the two-pulse heating of SRO. We define the time zero as 7.5 ps after the maximum of the second pump pulse, confirmed by optical cross-correlation. The amplitude
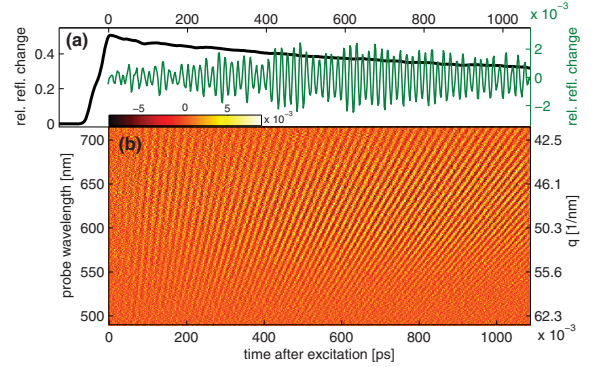

FIG. 3 (color). SHG of phonons observed by TDBS. (a) Transient relative reflectivity change at 580 nm (black line). The stepwise increase indicates the laser excitation of the metal film terminating at $t = 0$. Superimposed reflectivity oscillations (green line) originate from the SH phonons. The oscillation amplitude grows with the number of phonons up-converted to their SH. (b) Measured reflectivity oscillations across the white light probe spectrum. For each wavelength, the oscillation amplitude measures the occupation of a certain phonon q.

of the small superimposed oscillations with the phonon period 2Ω are a measure of how many second-harmonic phonons are present in the sample [23,39]. The rising oscillation amplitude indicates the nonlinear phonon interaction generating the SH of Q. The green line in Fig. 3(a) shows almost no SH phonons just after the two pump pulses with a pulse width of $\Delta\tau_{\mathrm{FWHM}} = 15$ ps. The maximum number of these phonons is observed after approximately 600 ps. In the UXRD data of Fig. 2(c), the maximum is observed earlier, because the phonons with larger wave vector $Q = 0.088$ nm^{-1} suffer a much stronger damping.

The broadband detection scheme allowed us to evaluate the spectral content of this SH phonon wave packet even more precisely. The relatively broad wave vector spectrum that extends over a large fraction of the visible range [Fig. 3(b)] results from the spatial confinement of the excited strain wave to two oscillation cycles [23]. We extracted the oscillation amplitude $a(q, t)$ of the relative reflectivity change as a function of the time delay for each probe wavelength λ corresponding to the different wave vectors q which compose the wave packet in the vicinity of $2Q$ [28–36,40].

In these experiments, the spectral energy density of the acoustic wave packet $\rho_E(q, t)$ is proportional [39] to the square of the reflectivity modulations $a(q, t)^2$ divided by q^2: $\rho_E \sim a(q, t)^2/q^2$. The experimentally derived energy proportional quantity $a(q, t)^2/q^2$ is plotted in Fig. 4(a) as contour lines and compared to the transiently changing spectral energy density $\rho_E(q, t)$ calculated on the basis of a Fermi-Pasta-Ulam (FPU) α-β chain with an empirical damping term. The FPU chain is widely used in theory to investigate phonons in the nonlinear lattice as well as heat transport in 1D [41–44]. In fact, we simulated a chain of oscillators with masses describing SRO and STO
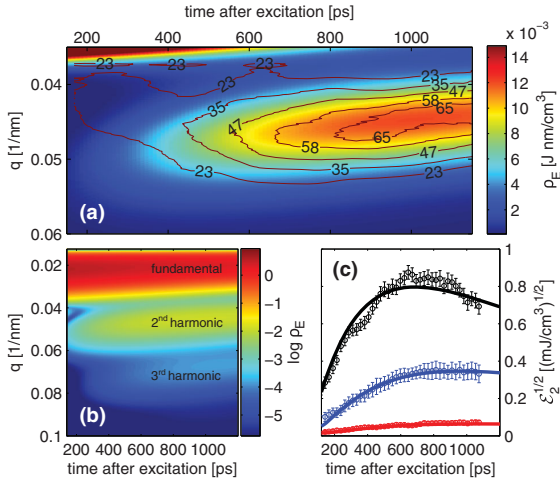
FIG. 4 (color). Comparing SHG experiments to the theory. (a) The color code shows the calculated transient change of the spectral energy density ρ_E around the SH of the excited phonons. The square of the measured relative reflectivity oscillation amplitude divided by q^2 in units of 10^{-7} nm^{-2} is overlaid as contour lines. (b) Calculated ρ_E over a broader range of wave vectors in the log scale. The photoexcited fundamental is transformed into the second and third harmonics. (c) visualizes the measured transient energy density change of the SH for different initial energy densities $\mathcal{E}_1$ (red = 13, blue = 67, and black = 235 nJ/cm^3) of the wave packet and compares this with theoretical calculations (solid lines). The wave vector for the highest energy density was $q = 0.03$ nm^{-1}, somewhat larger than the $q = 0.025$ nm^{-1}.

unit cells connected by anharmonic springs, where the second-order elastic constants along the [001] direction were derived from the speed of sound determined by time-resolved measurements [19,24,28]. From the comparison of the experimental data to the simulation, we found a third-order elastic constant describing the lattice anharmonicity in STO $C_{111} = -3.9 \times 10^{12}$ N/m^2 consistent with single-pulse time-resolved Brillouin scattering experiments [19]. It is 20% smaller than the value measured by megahertz acoustics at a frequency which is 3 orders of magnitude smaller [45]. In the calculation, the first few oscillators representing the opaque SRO film experience quasi-instantaneous [46] forces which describe the ultrafast heating by the two laser pulses. The force amplitude is known from previous UXRD measurements of the ultrafast lattice dynamics of SRO films [24].

Figure 4(b) shows $\rho_E(q, t)$ on a logarithmic scale over a broader wave vector range. The fundamental mode at 0.025 nm^{-1} is indeed excited at $t = 0$ ps, and subsequently phonons at the second and third harmonics are generated. The second harmonic is generated earlier than the third harmonic. This is an intrinsic feature of this linear chain calculation. By considering only the third order of the lattice potential as the nonlinear term, only three phonon

processes are allowed [47,48], and the third harmonic can only be generated via two sequential scattering processes. By observing the very weak third-harmonic generation, one could get information about the importance of higher orders of the lattice potential.

A pronounced feature of the measured data is the slow shift of the spectral distribution towards smaller wave vectors. The physical origin is uncovered by the simulations which show that the compressive strain front travels faster than the expansive strain. Since the wave packet contains only two strain cycles, this leads to a slightly increasing central wavelength of the wave packet [19,28]. This effect is much less pronounced for wave packets with more cycles.

Finally, the solid lines in Fig. 4(c) show the square root of the energy density $\mathcal{E}_2$ of the generated SH as a function of time for three different initial energy densities $\mathcal{E}_1$ of the excited fundamental mode. The initial linear increase and the linear dependence $\sqrt{\mathcal{E}_2} \sim \mathcal{E}_1$ are characteristic for this second-order nonlinear process of sum frequency generation or three-phonon scattering in general [48]. The corresponding experimental data obtained from integrating $a(q, t)^2/q^2$ over the same wave vector range show excellent agreement. Both the experimental and simulated energy density in Fig. 4(c) take into account that, for the same total energy deposited, the energy density is larger for higher wave vectors. To achieve the highest energy density, it was necessary to increase the wave vector to $q = 0.03$ nm^{-1} in order to avoid multishot damage of the sample.

Conclusion.—With the generation of the SH of a certain well-defined phonon wave packet, we have demonstrated a first conceptually simple experiment that monitors an elementary process of nanoscale nonlinear phononics in real time. The observed damping of the fundamental and SH to other modes is proportional to the square of the wave vector. We strongly believe that these experiments stimulate a series of new experiments ranging from simple extensions such as difference-frequency mixing to more complex experiments which are analogs of four-wave mixing, well known in experimental photonics. Future investigations may address the coupling of optical phonons to acoustic phonons and extend the phase-matching considerations by including also transverse polarisation of phonons and by going to larger wave vectors where the dispersion relation is bending over. Improvements of the signal-to-noise ratio may eventually permit studies on the single quantum level. A similar stimulus may be expected for theory. The Fermi-Pasta-Ulam chain can well predict effects related to longitudinal phonons. Modeling anharmonic phonon propagation and interaction in three dimensions including longitudinal and transverse phonon polarization in detail remains a major challenge. Exploring the physical nature of phonon damping processes and describing soft mode behavior in the vicinity of structural phase transitions by simulations and analytical theories can now be compared in detail to experimental results on a microscopic level.

*bargheer@uni-potsdam.de
http://www.udkm.physik.uni-potsdam.de

[1] M. E. Siemens, Q. Li, R. Yang, K. A. Nelson, E. H. Anderson, M. M. Murnane, and H. C. Kapteyn, Nat. Mater. **9**, 26 (2010).

[2] M. N. Luckyanova, J. Garg, K. Esfarjani, A. Jandl, M. T. Bulsara, A. J. Schmidt, A. J. Minnich, S. Chen, M. S. Dresselhaus, Z. Ren, E. A. Fitzgerald, and G. Chen, Science **338**, 936 (2012).

[3] N. Li, J. Ren, L. Wang, G. Zhang, P. Hänggi, and B. Li, Rev. Mod. Phys. **84**, 1045 (2012).

[4] M.-H. Bae, Z. Li, Z. Aksamija, P. N. Martin, F. Xiong, Z.-Y. Ong, I. Knezevic, and E. Pop, Nat. Commun. **4**, 1734 (2013).

[5] M. Maldovan, Phys. Rev. Lett. **110**, 025902 (2013).

[6] J. Ravichandran, A. K. Yadav, R. Cheaito, P. B. Rossen, A. Soukiassian, S. J. Suresha, J. C. Duda, B. M. Foley, C.-H. Lee, Y. Zhu, A. W. Lichtenberger, J. E. Moore, D. A. Muller, D. G. Schlom, P. E. Hopkins, A. Majumdar, R. Ramesh, and M. A. Zurbuchen, Nat. Mater. **13**, 168 (2014).

[7] R. Venkatasubramanian, E. Siivola, T. Colpitts, and B. O'Quinn, Nature (London) **413**, 597 (2001).

[8] B. Poudel, Q. Hao, Y. Ma, Y. Lan, A. Minnich, B. Yu, X. Yan, D. Wang, A. Muto, D. Vashaee, X. Chen, J. Liu, M. S. Dresselhaus, G. Chen, and Z. Ren, Science **320**, 634 (2008).

[9] K. Biswas, J. He, I. D. Blum, C.-I. Wu, T. P. Hogan, D. N. Seidman, V. P. Dravid, and M. G. Kanatzidis, Nature (London) **489**, 414 (2012).

[10] B. Li, L. Wang, and G. Casati, Phys. Rev. Lett. **93**, 184301 (2004).

[11] A. Shukla, M. Calandra, M. d'Astuto, M. Lazzeri, F. Mauri, C. Bellin, M. Krisch, J. Karpinski, S. M. Kazakov, J. Jun, D. Daghero, and K. Parlinski, Phys. Rev. Lett. **90**, 095506 (2003).

[12] O. Delaire, J. Ma, K. Marty, A. F. May, M. A. McGuire, M.-H. Du, D. J. Singh, A. Podlesnyak, G. Ehlers, M. D. Lumsden, and B. C. Sales, Nat. Mater. **10**, 614 (2011).

[13] J. W. L. Pang, W. J. L. Buyers, A. Chernatynskiy, M. D. Lumsden, B. C. Larson, and S. R. Phillpot, Phys. Rev. Lett. **110**, 157401 (2013).

[14] J. Chen, M. Trigo, S. Fahy, D. Murray, Y. M. Sheu, T. Graber, R. Henning, Y. J. Chien, C. Uher, and D. A. Reis, Appl. Phys. Lett. **102**, 181903 (2013).

[15] M. Trigo, M. Fuchs, J. Chen, M. P. Jiang, M. Cammarata, S. Fahy, D. M. Fritz, K. Gaffney, S. Ghimire, A. Higginbotham, S. L. Johnson, M. E. Kozina, J. Larsson, H. Lemke, A. M. Lindenberg, G. Ndabashimiye, F. Quirin, K. Sokolowski-Tinten, C. Uher, G. Wang *et al.*, Nat. Phys. **9**, 790 (2013).

[16] M. Först, C. Manzoni, S. Kaiser, Y. Tomioka, Y. Tokura, R. Merlin, and A. Cavalleri, Nat. Phys. **7**, 854 (2011).

[17] F. Rollins, Appl. Phys. Lett. **2**, 147 (1963).

[18] P. J. S. van Capel and J. I. Dijkhuis, Appl. Phys. Lett. **88**, 151910 (2006).

[19] A. Bojahr, M. Herzog, D. Schick, I. Vrejoiu, and M. Bargheer, Phys. Rev. B **86**, 144306 (2012).

[20] O. L. Muskens and J. I. Dijkhuis, Phys. Rev. Lett. **89**, 285504 (2002).

[21] W. Singhsomroje and H. J. Maris, Phys. Rev. B **69**, 174303 (2004).

[22] E. Péronne and B. Perrin, Ultrasonics **44**, e1203 (2006).

[23] A. Bojahr, M. Herzog, S. Mitzscherling, L. Maerten, D. Schick, J. Goldshteyn, W. Leitenberger, R. Shayduk, P. Gaal, and M. Bargheer, Opt. Express **21**, 21188 (2013).

[24] D. Schick, M. Herzog, A. Bojahr, W. Leitenberger, A. Hertwig, R. Shayduk, and M. Bargheer, Struct. Dyn. **1**, 064501 (2014).

[25] C. Klieber, E. Peronne, K. Katayama, J. Choi, M. Yamaguchi, T. Pezeril, and K. A. Nelson, Appl. Phys. Lett. **98**, 211908 (2011).

[26] M. Herzog, A. Bojahr, J. Goldshteyn, W. Leitenberger, I. Vrejoiu, D. Khakhulin, M. Wulff, R. Shayduk, P. Gaal, and M. Bargheer, Appl. Phys. Lett. **100**, 094101 (2012).

[27] R. Shayduk, M. Herzog, A. Bojahr, D. Schick, P. Gaal, W. Leitenberger, H. Navirian, M. Sander, J. Goldshteyn, I. Vrejoiu, and M. Bargheer, Phys. Rev. B **87**, 184301 (2013).

[28] See Supplemental Material at http://link.aps.org/supplemental/10.1103/PhysRevLett.115.195502 for details of the experimental setups, the data analysis and theory, which includes Refs. [29–36].

[29] N. Li and B. Li, Europhys. Lett. **78**, 34001 (2007).

[30] C. Alabiso, M. Casartelli, and P. Marenzoni, J. Stat. Phys. **79**, 451 (1995).

[31] J. Liu, S. Liu, N. Li, B. Li, and C. Wu, Phys. Rev. E **91**, 042910 (2015).

[32] C. Herring, Phys. Rev. **95**, 954 (1954).

[33] H. J. Maris, Phys. Acoust. **8**, 279(1971).

[34] H. Y. Hao and H. J. Maris, Phys. Rev. B **64**, 064302 (2001).

[35] A. N. Cleland, *Foundations of Nanomechanics: From Solid-State Theory to Device Applications*, Advanced Texts in Physics and Astronomy (Springer, Berlin, 2003).

[36] G. P. Berman and F. M. Izrailev, Chaos **15**, 015104 (2005).

[37] P. Gaal, D. Schick, M. Herzog, A. Bojahr, R. Shayduk, J. Goldshteyn, H. A. Navirian, W. Leitenberger, I. Vrejoiu, D. Khakhulin, M. Wulff, and M. Bargheer, J. Synchrotron Radiat. **21**, 380 (2014).

[38] L. Maerten, A. Bojahr, M. Gohlke, M. Rössle, and M. Bargheer, Phys. Rev. Lett. **114**, 047401 (2015).

[39] C. Thomsen, H. T. Grahn, H. J. Maris, and J. Tauc, Phys. Rev. B **34**, 4129 (1986).

[40] M. Bradler, P. Baum, and E. Riedle, Appl. Phys. B **97**, 561 (2009).

[41] S. Lepri, R. Livi, and A. Politi, Phys. Rev. Lett. **78**, 1896 (1997).

[42] B. Gershgorin, Y. V. Lvov, and D. Cai, Phys. Rev. Lett. **95**, 264302 (2005).

[43] N. Li, P. Tong, and B. Li, Europhys. Lett. **75**, 49 (2006).

[44] S. Liu, J. Liu, P. Hänggi, C. Wu, and B. Li, Phys. Rev. B **90**, 174304 (2014).

[45] E. L. Meeks and R. T. Arnold, Phys. Rev. B **1**, 982 (1970).

[46] A. Bojahr, D. Schick, L. Maerten, M. Herzog, I. Vrejoiu, C. von Korff Schmising, C. J. Milne, S. L. Johnson, and M. Bargheer, Phys. Rev. B **85**, 224302 (2012).

[47] R. L. Bivins, N. Metropolis, and J. R. Pasta, J. Comput. Phys. **12**, 65 (1973).

[48] D. Sholl, Phys. Lett. A **149**, 253 (1990).

Article XII – Supplemental Material

Supplement Material: Second Harmonic Generation of Nanoscale Phonon Wave Packets

A. Bojahr[1], M. Gohlke[1] W. Leitenberger[1], J. Pudell[1], M. Reinhardt[2],

A. von Reppert[1], M. Roessle[1], M. Sander[1], P. Gaal[2], and M. Bargheer

[1] *Institut für Physik & Astronomie, Universität Potsdam,*

Karl-Liebknecht-Str. 24-25, 14476 Potsdam, Germany and

[2] *Helmholtz Zentrum Berlin, Albert-Einstein-Str. 15, 12489 Berlin, Germany*[*]

(Dated: October 29, 2015)

————

[*] bargheer@uni-potsdam.de; http://www.udkm.physik.uni-potsdam.de

I. TIME RESOLVED X-RAY DIFFRACTION

A. Experimental Setup

For the time resolved x-ray diffraction experiments we used the ID09B beamline at the European Synchrotron Radiation Facility (ESRF) in Grenoble (France). Here a femtosecond laser system with 1 kHz repetition rate is synchronized to the storage ring. By adjusting the grating compressor of the laser system we were able to change the temporal width of the produced laser pulses. A combination of two interferometers was used to create 2 or 4 identical laser pulses with a defined temporal displacement τ. The transient change of diffracted x-ray light in dependence of the diffraction angle θ was then used to obtain information about the transient occupation of coherent phonons in the sample. The wavevector of these phonons is given by

$$q = \frac{4\pi}{\lambda_x} |\sin\theta - \sin\theta_0| \tag{1}$$

where $\lambda_x = 0.08\,\text{nm}$ is the wavelength of the x-ray probe light and $\theta_0 = 12.22°$ the diffraction angle of the (002) reciprocal lattice point.
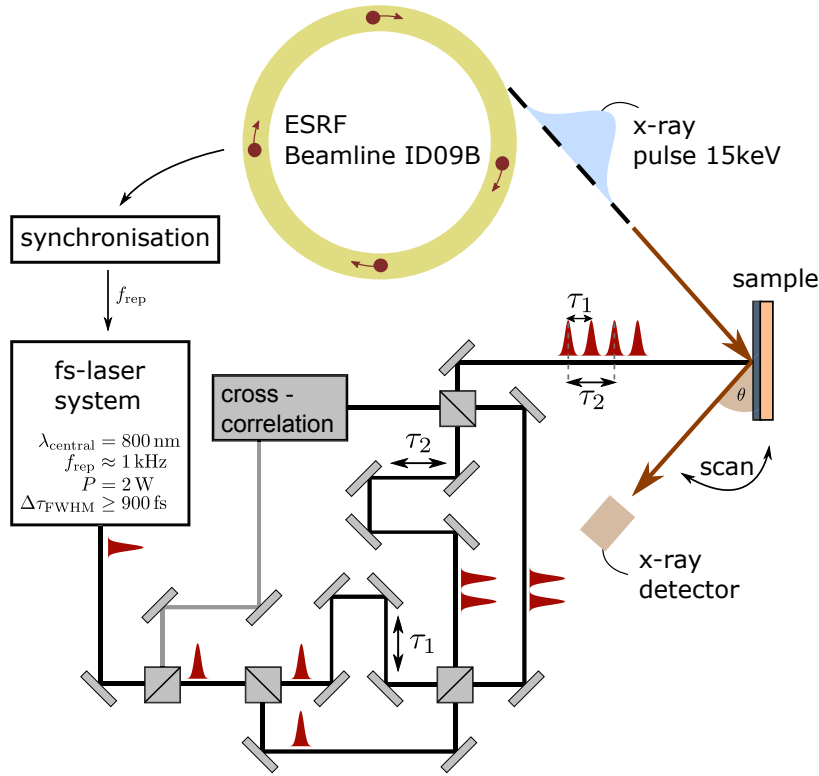
FIG. 1. **Experimental setup of the time-resolved x-ray diffraction** A femtosecond laser system produces 800 nm pump pulses with a repetition rate of $f_{\text{rep}} \approx 1\,\text{kHz}$ for the excitation of the sample, synchronised to the synchrotron bunch clock. The laser pulse length can be defined by an adjustable grating compressor inside the laser system. Two serial interferometers divide and recombine the incident laser pulse into 4 collinear pulses. Their temporal delay τ is set by adjusting the interferometer arms: $\tau = \tau_1 = \tau_2/2$. This pulse train finally generates a propagating phonon wavepacket with central frequency $\Omega = 2\pi/\tau$ in the SrTiO$_3$ substrate of the sample. A delayed hard x-ray pulse from the synchrotron probes the spectral content of the excited coherent acoustic phonons in the sample.

B. Evaluation of the sums Σ_i

To determine the integral diffraction intensities Σ_i of the fundamental ($i = 1$) and second harmonic ($i = 2$) we used the monochromatic nature of the excited wavepacket. We used smooth functions to fit the background contributions to the signal

which mainly stem from the wings of the substrate peak. For the fundamental we used a Lorentzian profile fitting the right wing of the substrate peak. For the second harmonic a third order polynomial fit proved to be more useful to substract the background farther away from the substrate peak. After the automated subtraction of the fitting function from the original datasets, we integrated over the individual peaks to obtain Σ_1 and Σ_2 for each time delay.

II.   TIME RESOLVED OPTICAL BRILLOUIN SCATTERING

A.   Experimental Setup

For the optical Brillouin scattering experiments we used a lasersystem with a repetition rate of 5 kHz and a central wavelength of 800 nm. The minimal pulselength is 100 fs. The laser output is split into a pump and a probe beam. We used a grating compressor to add chirp to the pump pulses which changes the pulsewidth to $\Delta \tau_{\text{FWHM}} = 15$ ps at the sample. These pump pulses are sent into an interferometer setup similar to the one used in the x-ray experiments (Fig. 1). Here two distinct pulses with a temporal separation of $\tau = 30$ ps are generated. These two pulses are used to excite a spot of the SrRuO$_3$ film with 210 μm diameter. The probe pulse was focussed into a sapphire plate to generate a supercontinuum laser pulse which has mainly spectral
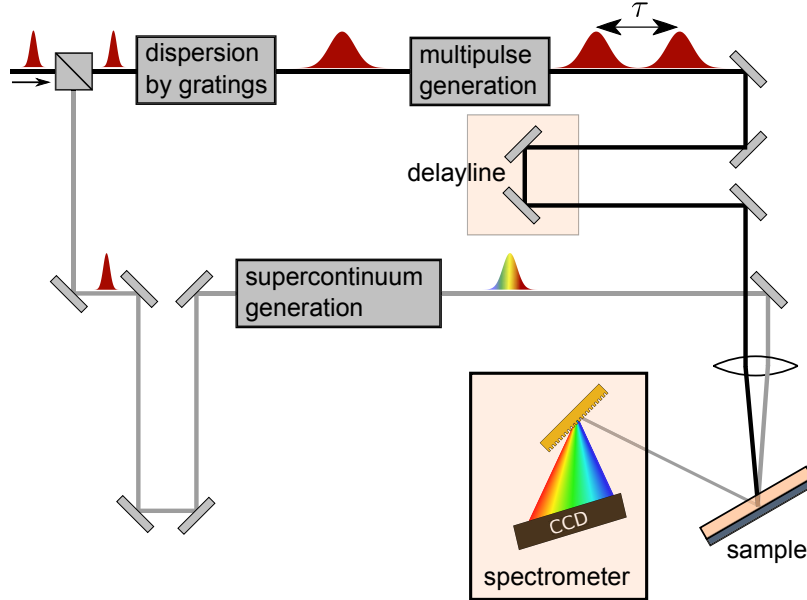
FIG. 2. **Experimental setup of the time-resolved optical Brillouin scattering**

components from $450 - 800$ nm.[1] We focused this broadband probe pulse onto a spot size of about 50 μm on the sample. The all optical experiments were conducted through the backside of the polished 1 mm thick substrate. This has the advantage that Brillouin backscattered photons from phonons in the substrate are not attenuated by the metallic film.

B.   Extraction of the Brillouin oscillations

In time-resolved Brillouin scattering experiment the wavelength dependent relative reflectivity change is measured as function of the time delay between pump and probe pulses. This quantity is given by the change of the reflected intensity between the pumped and the unpumped sample $I_p - I_u$ divided by the reflected intensity I_u of the unpumped sample. In case of a small reflection at the SrTiO$_3$/SrRuO$_3$ interface ($|r_u|^2 \ll 1$) we can describe the complex reflection coefficient r_p of the pumped sample as a sum of the unpumped r_u, the small changes due to layer heating Δr_l and the reflection from induced phonons Δr_p,

$$\frac{I_p - I_u}{I_u} = \frac{|r_p|^2 - |r_u|^2}{|r_u|^2} = \frac{|r_u + \Delta r_l + \Delta r_p|^2 - |r_u|^2}{|r_u|^2} \tag{2}$$

Here we neglect any change of the transmitted light fields after reflection from the soundwave because only a small part ($\approx 10^{-5}$) will be reflected. To first order approximation the transmitted field equals the incoming field and $|\Delta r_p|^2 \approx 0$. Eq. 2 can be written as,

$$\frac{I_p - I_u}{I_u} = \underbrace{\frac{|r_u + \Delta r_l|^2}{|r_u|^2} - 1}_{S_L} + \underbrace{\frac{2|r_u + \Delta r_l|\Delta r_p \cos(\phi)}{|r_u|^2}}_{S_H} \tag{3}$$

Here S_L is the slowly varying part of the signal. $\Delta r_l(t)$ changes mainly due to the heat transport from the layer into the substrate. S_H oscillates with the high frequency ω of the probed phonon mode ($\phi = \omega t$). The probed phonon oscillation period (tens of ps) is much shorter then the typical timescale of the heat transport (several ns). Thus we can determine S_L by smoothing our measured signal $\frac{I_p - I_u}{I_u}$ with an appropriate gaussian function broader then the phonon oscillation period but much smaller then heat transport timescale. The difference of $\frac{I_p - I_u}{I_u}$ and S_L yields S_H. The amplitude of the oscillating quantity

$$O(t) = \frac{S_H}{\sqrt{S_L + 1}} = 2\frac{|\Delta r_p(t)|}{|r_u|}\cos(\phi) = a(t)\cos(\phi) \tag{4}$$

is independent of transient changes of $\Delta r_l(t)$. It depends only on $|r_p|$ which is a measure of the occupation of the probed phonon wavevector q. By using a short-time Fourier transform (STFT) we can calculate the amplitude $a(t)$ of the quantity $O(t)$ which we finally used as a measure of exited coherent phonons.

III. THEORY

A. monoatomic linear chain with anharmonic springs

For the numeric simulations we used an one dimensional linear chain of masses coupled with anharmonic springs. Each mass represents one unit cell of the material SrRuO$_3$ or SrTiO$_3$ where the distance between masses is given by the lattice constants c_M along the [001] direction.

$$m_M \ddot{x}_i = k_M[(x_{i+1} - x_i) - (x_i - x_{i-1})] + \alpha_M[(x_{i+1} - x_i)^2 - (x_i - x_{i-1})^2]$$
$$+ \beta_M[(x_{i+1} - x_i)^3 - (x_i - x_{i-1})^3] + m_M\gamma_M[(\dot{x}_{i+1} - \dot{x}_i) - (\dot{x}_i - \dot{x}_{i-1})] + F_i(t) \tag{5}$$

The parameters k_M and α_M are the spring constants and the first order anharmonicities corresponding to the cubic contributions of the interatomic lattice potentials, respectively. β_M describes the quartic potential contribution and is in these calculations a small value which ensures the numerical stability. In literature this model is know as the Fermi-Pasta-Ulam (FPU) α-β-chain. Although first calculations were realized in the 1950s, the FPU-chain is still under theoretical investigations. Many interesting phenomena can be studied in this model, such as the mode coupling of phonons[2] or heat-transfer[3,4]. Several groups introduced the concept of renormalized phonons[5–8] of a heated FPU-chain, in which the mode coupling effectively changes the phonon dispersion relation. Recently, the damping of harmonic waves excited on a heated nonlinear lattice was investigated.[9] However, to model the dynamics observed in the present experiment we excluded thermal excitation in the chain and used effective k_M and α_M to simulate the mode coupling between the excited wave and its harmonics at a given temperature. For this work the value of α_M is crucial because it determines the cross section of three phonon scattering processes, whereas β_M is not essential and kept very small. We used an additional phenomenological damping γ_M of phonons which describes the coupling of coherent phonons to the thermal bath. It mimics the q^2 dependence of the Herring process in cubic crystals.[10,11] The final term $F_i(t)$ of eq. (5) represents the external force on a the unit cell i with mass m_M exerted by the laser heating, which is nonzero only for SrRuO$_3$. To calculate the forces F_i we used the thermoelastic model.[12]

Fig. 3 shows the spatiotemporal form of the wavepacket resulting from the simulation for an excitation with two laser pulses. In the co-propagating frame or reference we see that the fundamental wavepacket decreases in amplitude and broadens in real space, as the compressive strain travels faster than the tensile strain. At the same time, a small fraction of the wavepacket is converted to the second harmonic.
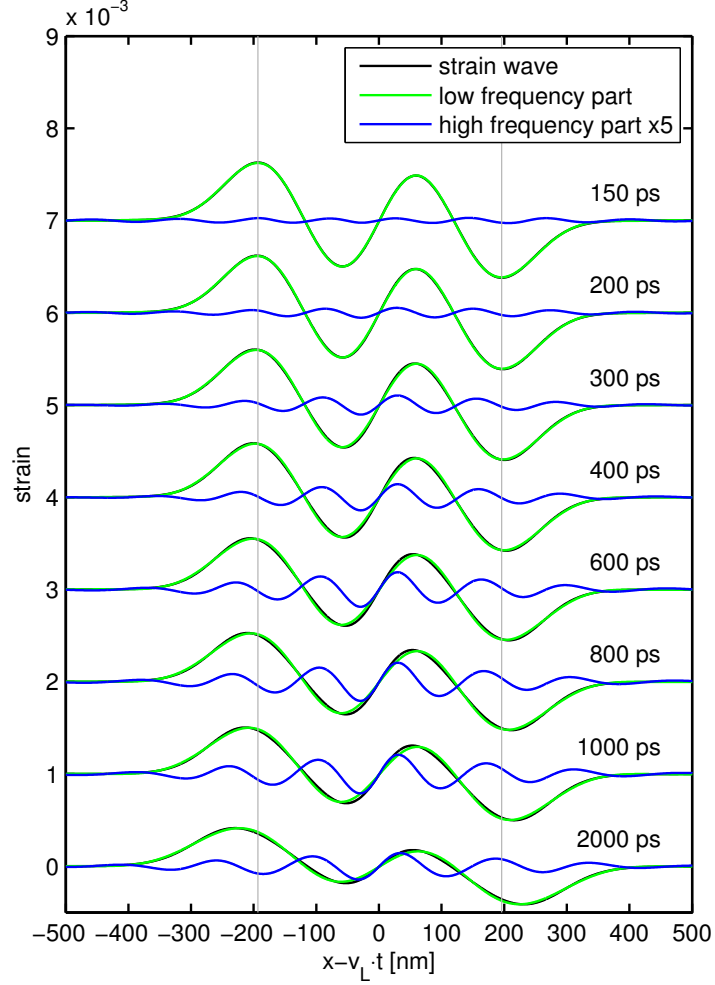
FIG. 3. **Transient change of wavepacket's spectral components** The strain wavepacket (black) is shown for different propagation times as calculated in the numerical simulation. The green curve shows the low frequency component mainly containing the excited wavevector whereas the blue curve represents the high frequency components of the wavepacket scaled with a factor of five. The vertical grey lines highlight the spatial broadening of the wavepacket.

B.   Relation between elastic constants and the FPU-chain parameters

Comparing the continuum approximation of eq. (5) using $\beta_M = 0$:

$$\frac{\partial^2}{\partial t^2}u(x,t) = \frac{k_M c_M^2}{m_M}\frac{\partial^2}{\partial x^2}u(x,t) + \gamma_M c_M^2 \frac{\partial}{\partial t}\frac{\partial^2}{\partial x^2}u(x,t) + \frac{2\alpha_M c_M^3}{m_M}\frac{\partial}{\partial x}u(x,t)\frac{\partial^2}{\partial x^2}u(x,t) + \frac{k_M c_M^4}{12 m_M}\frac{\partial^4}{\partial x^4}u(x,t) \qquad (6)$$

with the standard partial differential equation of nonlinear elastic theory for wave propagation along the [001] direction in a cubic crystal (eq. 4 in the paper of Hao and Maris[13]), we can deduce the second order elastic constant $C_{11} = \frac{k_M}{c_M}$ as well as the third order elastic constant $C_{111} = 2\alpha_M - 3\frac{k_M}{c_M}$ in dependence of the FPU-chain parameters.

C. Normal modes and their energy

In order to calculate the energy density $\rho_E(q,t)$ from the simulations we consider the linear chain as a coupled system of harmonic oscillators described by the conjugated variables amplitude A_q and momentum P_q of normal modes.[14] In a harmonic system these modes do not influence each other. They are uncoupled. Adding a small third order anharmonicity to the system leads in this picture to weakly coupled modes.[15] Here A_q and P_q are defined by,

$$A_q(t) := \frac{1}{\sqrt{N}} \sum_{n,\text{sub}} x_n(t) e^{-iqna} \tag{7}$$

$$P_q(t) := \frac{1}{\sqrt{N}} \sum_{n,\text{sub}} m\dot{x}_n(t) e^{iqna} \tag{8}$$

The sum extends over all oscillators n of the SrTiO$_3$ substrate with mass m whereas q represents the phonon wavevector. The number of all substrate oscillators is given by N. Neglecting the very small coupling energy of the "normal" modes we can write the total energy E as a sum of "normal" mode energies E_q which depend on A_q and P_q,

$$E = \sum_q E_q = \sum_q \left(\frac{1}{2m} P_q P_q^* + \frac{1}{2} m\omega_q^2 A_q A_q^* \right) \tag{9}$$

E_q, the energy per mode q, belongs to an excitation area a^2 with a the lattice constant of the cubic SrTiO$_3$ crystal ($a = 3.905\,\text{Å}$). Consequently we define the energy per excited Volume $V = a^2 l$ and wavevector interval as

$$\rho_E(q,t) = \frac{E_q(t)}{V\Delta q}, \tag{10}$$

where $\Delta q = 2\pi/Na$ is given by the distance between two neighboring wavevectors q. We define the length $l = N\lambda = Nv\tau$ of the wavepacket via its number N of cycles and wavelength λ or alternatively sound-velocity v and pulse delay τ.

[1] M. Bradler, P. Baum, and E. Riedle, Applied Physics B **97**, 561 (2009).
[2] D. Sholl, Physics Letters A **149**, 253 (1990).
[3] S. Lepri, R. Livi, and A. Politi, Phys. Rev. Lett. **78**, 1896 (1997).
[4] N. Li and B. Li, EPL (Europhysics Letters) **78**, 34001 (2007).
[5] C. Alabiso, M. Casartelli, and P. Marenzoni, Journal of Statistical Physics **79**, 451 (1995).
[6] B. Gershgorin, Y. V. Lvov, and D. Cai, Phys. Rev. Lett. **95**, 264302 (2005).
[7] N. Li, P. Tong, and B. Li, EPL (Europhysics Letters) **75**, 49 (2006).
[8] J. Liu, S. Liu, N. Li, B. Li, and C. Wu, Phys. Rev. E **91**, 042910 (2015).
[9] S. Liu, J. Liu, P. Hänggi, C. Wu, and B. Li, Phys. Rev. B **90**, 174304 (2014).
[10] C. Herring, Phys. Rev. **95**, 954 (1954).
[11] H. J. Maris, in *Principles and Methods*, Physical Acoustics, Vol. 8, edited by W. P. MASON and R. N. THURSTON (Academic Press, 1971) pp. 279 – 345.
[12] C. Thomsen, H. T. Grahn, H. J. Maris, and J. Tauc, Phys. Rev. B **34**, 4129 (1986).
[13] H. Y. Hao and H. J. Maris, Phys. Rev. B **64**, 064302 (2001).
[14] A. N. Cleland, *Foundations of nanomechanics : from solid-state theory to device applications*, Advanced texts in physics and astronomy (Springer, Berlin, 2003).
[15] G. P. Berman and F. M. Izrailev, Chaos: An Interdisciplinary Journal of Nonlinear Science **15**, (2005).

Article XIII

Azobenzene–functionalized polyelectrolyte nanolayers as ultrafast optoacoustic transducers

Elena Pavlenko, Mathias Sander, Steffen Mitzscherling, **Jan-Etienne Pudell**, Flavio Zamponi, Matthias Rössle, André Bojahr and Matias Bargheer

We introduce azobenzene-functionalized polyelectrolyte multilayers as efficient, inexpensive optoacoustic transducers for hyper-sound strain waves in the GHz range. By picosecond transient reflectivity measurements we study the creation of nanoscale strain waves, their reflection from interfaces, damping by scattering from nanoparticles and propagation in soft and hard adjacent materials like polymer layers, quartz and mica. The amplitude of the generated strain $\varepsilon 5 \times 10^{-4}$ is calibrated by ultrafast X-ray diffraction.

Nanoscale

PAPER

Azobenzene – functionalized polyelectrolyte nanolayers as ultrafast optoacoustic transducers

E. S. Pavlenko,[a] M. Sander,[a] S. Mitzscherling,[b] J. Pudell,[a] F. Zamponi,[a] M. Rössle,[a] A. Bojahr[a] and M. Bargheer*[a,c]

We introduce azobenzene-functionalized polyelectrolyte multilayers as efficient, inexpensive optoacoustic transducers for hyper-sound strain waves in the GHz range. By picosecond transient reflectivity measurements we study the creation of nanoscale strain waves, their reflection from interfaces, damping by scattering from nanoparticles and propagation in soft and hard adjacent materials like polymer layers, quartz and mica. The amplitude of the generated strain $\varepsilon \sim 5 \times 10^{-4}$ is calibrated by ultrafast X-ray diffraction.

Introduction

Optomechanical transducers are widely used in condensed matter. One application is to generate strain waves in order to study mechanical, thermo-elastic, opto-acoustic, magneto-acoustic and other properties of materials.[1–5] In the field of picosecond-acoustics, the ultrashort period of the excited waves allows for investigations on the nanometer length scale. Yet for soft matter, studying objects on the nano-scale by such hyper-sound waves is not well developed, although it has been successfully used for imaging of cells.[6–8] Standard materials like titanium, aluminum or chromium, which are used as opto-mechanical transducers for many solids,[9,10] often are not suitable for soft matter samples. They may require additional treatment due to hydrophobicity, are not biocompatible and even if these technical problems are solved, they suffer from large acoustic impedance mismatches. Therefore, soft matter transducers will be advantageous to study soft matter objects. Several polymers and photosensitive molecules have been investigated regarding their opto-mechanical properties.[11–13] Azobenzene (Azo) is the most thoroughly investigated photo-sensitive molecule.[14–18] It undergoes *trans–cis* and reverse iso-merization when illuminated by ultraviolet (UV) and visible (Vis) light, respectively. This effect is used in several experimental realizations of Azo-containing molecular devices and machines.[19–23] In particular, various Azo-containing polyelectrolytes were investigated under periodic UV-Vis illumination.[24,25] A partially irreversible expansion followed by reversible contraction–expansion under appropriate illumination was observed.[25] Polyelectrolyte multilayers form particularly robust, electrostatically bound thin films which can be deposited on various soft matter surfaces.[24] The film thickness is controlled *via* layer-by-layer deposition with nanometric precision.[26] Even though expansion and contraction of Azo-containing materials has been studied, there have been no reports on using nanoscale multilayers as optoacoustic transducers. Also the transient response of Azo-compound materials including the photo-induced volume change has not been studied on the picosecond time scale, on which molecular rearrangements take place.

In this work, we obtain quantitative information on the amplitude and phase of the strain waves generated in Azo-containing polyelectrolyte multilayers that transform the light energy of ultraviolet femtosecond pulses into hyper-sound waves. We investigate the propagation of the waves in polymers, crystalline mica, and quartz and observe the damping of these waves by scattering from nanoparticles. For a quantitative assessment of the strain amplitude, we used ultrafast X-ray diffraction (UXRD). Time-domain Brillouin scattering (TDBS)[27] was used to follow the strain propagation on the picosecond time scale in the all-optical experiments. We believe that these polyelectrolyte-nanolayer-transducers will allow for a new class of experiments using picosecond ultrasonics to investigate various structures down to nano-sized objects.

Methods

We produced various samples *via* spin-assisted layer-by-layer deposition.[28,29] With this technique, one can create structures with different, well-defined thicknesses on the nanometer length scale, and very smooth interfaces. In this experiment

[a]*Institute of Physics and Astronomy, University of Potsdam, Karl-Liebknecht-Str. 24-25, 14476 Potsdam, Germany. E-mail: bargheer@uni-potsdam.de*
[b]*Federal Institute for Materials Research and Testing, Unter den Eichen 87, 12205 Berlin, Germany*
[c]*Helmholtz-Zentrum Berlin, Albert-Einstein-Str. 15, 12489 Berlin, Germany*

the following polyelectrolytes have been used: poly(allylamine hydrochloride) (PAH) $M_w \sim 58\,000$ g mol^{-1}; poly(sodium 4-styrenesulfonate) (PSS) $M_w \sim 70\,000$ g mol^{-1}; poly(ethyleneimine) (PEI) 50 wt% aqueous solution, $M_w \sim 750\,000$ g mol^{-1}; poly[1-[4-(3-carboxy-4-hydroxyphenylazo)benzenesulfonamide]-1,2-ethanediyl, sodium salt] (PAzo).

All polyelectrolytes were purchased from Sigma-Aldrich Chemie Gmbh (Germany). PSS was dialyzed against ultra-purified water from an ELGA (PURELAB Classic) water purifier system before application. The other polymers were used as received, without further purification.

Aqueous polymer solutions were prepared with the following concentrations of polyelectrolytes: for PSS, PAH – 0.1% by weight, PEI – 1% by weight, PAzo – 0.1% by weight. The NaCl concentrations in the final solutions were 0.7 mol l^{-1} for PSS and PAH and 0.2 mol l^{-1} for PAzo; no NaCl was added to the PEI.

Gold nanorods (GNR), used in only one sample structure were synthesised by the method described by Nikoobakht *et al.*[30] to grow rods of the aspect ratio 3.25 indicated by a longitudinal plasmon resonance at 700 nm and verified by TEM images showing an average length of about 70 nm. The GNRs were coated with PSS in order to provide reliable bonding to the polymer surface.[31] To deposit the GNRs onto the sample, the surface was covered completely with GNR solution, left for 30 min and then washed with purified water.

Fig. 1(a) schematically summarizes the characteristic layering sequence of the samples.

Sample preparation

Fused silica discs (thickness 1.58 mm, diameter 24.5 mm) were used as substrates for optical experiments. The substrates were hydrophilized with a $H_2SO_4/(30\%\ H_2O_2)$ (3 : 1) (**warning:** hazardous acid) bath for 1 h, after which the substrates were washed excessively with pure water and dried in a nitrogen flow. In order to provide a reliable bonding of the polyelectrolytes to the substrate, a single layer of PEI polyelectrolyte was always deposited first, followed by washing. The thickness of one double layer of PSS/PAH is about 2.5 nm.[26] For PAzo/PAH this parameter is about 4.7 nm, as determined by AFM measurements. When films of dozens of double layers are constructed, the total thickness deviation is within 10% of the expected thickness. As a substrate for the ultrafast X-ray diffraction (UXRD) experiments we used a mica sheet (from Tedpella) with a thickness of approximately 4.5 µm, determined by spectroscopic ellipsometry. The polyelectrolyte structure has been deposited on mica in the same way as onto the quartz substrates, however without previous hydrophilization.

The main advantages of the proposed nanoscale transducers are the low cost of the layer-by-layer preparation and the ease with which it can be attached to almost any flat or curved surface.

Sample characterisation

The static all-optical characterization of the thin polyelectrolyte multilayers was carried out using a UV-Vis spectrophotometer
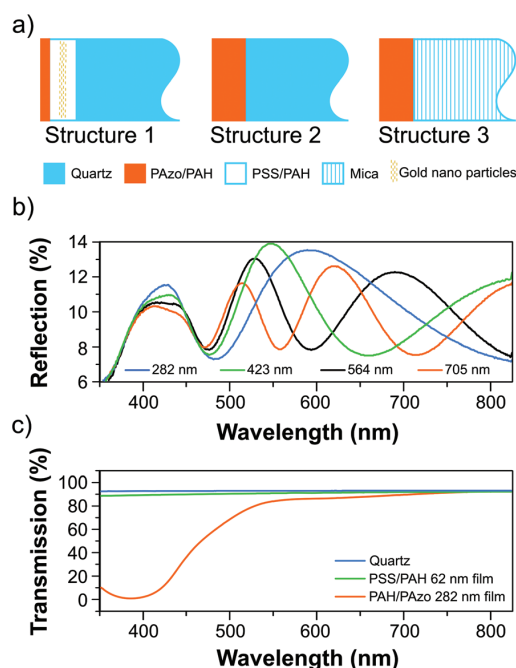

Fig. 1 (a) Schematic representation of the sample layering sequences. (b) Static reflection spectra of samples with PAzo/PAH films with different thicknesses on quartz. (c) Typical static transmission spectra of PAzo/PAH and PSS/PAH films on quartz compared to a bare substrate.

(VARIAN CARY 5000). Fig. 1(c) shows typical transmission spectra of a PAzo/PAH and a PSS/PAH multilayer as well as a quartz substrate. Static reflection spectra of films with the structure 2 for four different thicknesses $d_{\text{PAzo/PAH}}$ = 248, 423, 564, and 795 nm are plotted in Fig. 1(b). The interference of light reflected at the surface and at the polymer–substrate interface results in pronounced interference fringes as a function of the wavelength λ with minima at

$$2n_{\text{film}}d\cos(\beta) = m\lambda, \tag{1}$$

where β is the internal angle of incidence according to Snell's law in the film with refractive index $n_{\text{film}}(\lambda)$ and thickness d.

These measurements were cross-checked with spectroscopic ellipsometry (Sentech, SENresearch SE850E) and atomic force microscopy of purposely scratched films.

Ultrafast pump–probe spectroscopy

In order to establish the azobenzene-containing polymer as an opto-mechanical transducer for hyper-sound, we recorded transient optical reflectivity spectra with 140 fs time resolution based on a regeneratively amplified Ti:sapphire laser system from Spectra-Physics (MaiTai/Spitfire Pro) with a central wavelength of 795 nm. A small fraction of approximately 5 µJ was frequency-doubled in a BBO crystal. These pump-pulses with a wavelength of 398 nm were separated from the fundamental by a filter and focused onto the sample with a pump fluence of

about 1 mJ cm^{-2} to excite the azobenzene. Another 2 μJ of the laser energy were used to generate a white light continuum in a 1 mm-thick sapphire plate. These pulses probe the sample with an adjustable delay time t after excitation, and their reflection is recorded in a fiber spectrometer (Avantes). The pump and probe pulses are both p-polarized, and the pump beam was chopped at a rate of 125 Hz to measure the relative changes of the reflectance between the perturbed ($R_0 + \Delta R$) and unperturbed (R_0) sample.[32] Both pulses enter the sample from the front side (polymer structure side) at an angle of about $\alpha = 30°$ which yields the internal angle β according to Snell's law.

Ultrafast X-ray diffraction (UXRD)

Ultrafast X-ray diffraction measurements were performed with the diffractometer at the laser-driven plasma X-ray source (PXS) at the University of Potsdam.[33,34] The PXS provides a temporal resolution below 200 fs at an X-ray photon energy of 8.047 keV (Cu Kα). The X-ray and UV footprints on the sample have diameters of approximately 300 μm and 1 mm (FWHM), respectively. The fluence of the 398 nm pump light was 4 mJ cm^{-2}. An X-ray optic with a convergent beam is used with an X-ray area detector to map out the reciprocal space of the mica substrate.[35] Therefore, the specular and asymmetrically diffracted X-ray photons under the Bragg angle are detected simultaneously. The measurements were taken at a fixed sample angle omega, which is interpreted as a cut through the crystal truncation rod of the mica sheet.
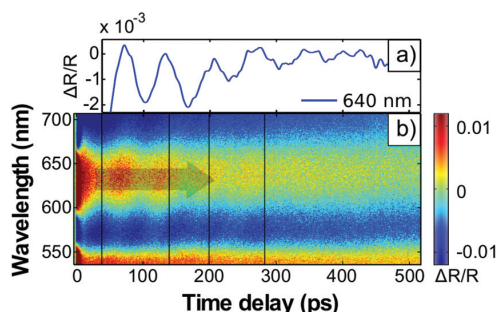

Fig. 2 (a) Relative change of the transient reflectivity $\Delta R(t)/R_0$ at $\lambda = 640$ nm measured for the sample structure 1 (see text). An exponential decay of the intensity is subtracted. (b) $\Delta R(t)/R_0$ over a broad spectral range.

Experimental results and discussion

All-optical generation and detection of propagating strain waves

As a first example of all-polymer hyper-sound-transduction, we designed and prepared samples on quartz substrates according to structure 1 (Fig. 1a) with a relatively thick PSS/PAH multilayer ($d_{PSS/PAH}$ = 630 nm). We incorporated gold nanoparticles in the middle of this PSS/PAH multilayer stack in order to scatter the hyper-sound waves and to exemplify the detection of impurities by nanoscale strain waves. The 80 nm thick composite layer contains a volume fraction of about 1% Au particles. On the top of the sample we added a thin PAzo/PAH multilayer (d_{PAzo1} = 141 nm) as the opto-mechanical transducer. The 398 nm pump pulses are exclusively absorbed in the PAzo/PAH multilayer, since PSS/PAH is transparent at this wavelength (Fig. 1(c)). Both layers are transparent for the white probe pulse spectrum. The transient reflectivity data $\Delta R(t)/R_0$ in Fig. 2(a) show pronounced oscillations as a function of the time delay. The wavelength-dependence of the oscillation period

$$T = \lambda/[2v_s n(\lambda)\cos(\beta)] \qquad (2)$$

is characteristic of time-domain Brillouin scattering (TDBS) from the hyper-sound waves in the PSS/PAH multilayer with the sound velocity v_s = 3.4 nm ps^{-1}. TDBS can be interpreted as interference of the probe light reflected at the surface and from the propagating strain pulse.[27] The refractive index $n(\lambda)$ of all materials was determined by ellipsometry (Table 1).

At t = 140 ps, the strain front launched from the surface reaches the incorporated nanoparticles residing at a depth of about 470 nm. The particles reduce the signal modulation by scattering the hyper-sound amplitude. The wavepacket components of the strain wave detected in Fig. 2 have a wavelength of about 250 nm compared to the GNR length of about 70 nm. Propagation of the entire strain front through the 80 nm composite layer of the nanoparticles takes about 60 ps, therefore the damping appears as a delayed feature (Fig. 2(a)). At t = 280 ps, the strain front reaches the quartz substrate and the TDBS signal essentially disappears. The remaining amplitude of the TDBS signal is caused by the reflection of the strain pulse at the polymer–quartz interface (see Discussion below).

The transient reflection shown in Fig. 2(a) also exhibits the characteristic static thin-film-interference (Fig. 1(b)) given by the total optical path length $s = n \times d_{film} = n_{PSS/PAH} \times D_{PSS/PAH}$ +

Table 1 Optical and acoustic properties of the materials used

Material	Density [kg m^{-3}]	Sound velocity [nm ps^{-1}]	Acoustic impedance Z [10^6 Ns m^{-3}]	Refractive index @ $\lambda = 600$ nm
PSS/PAH	940 (ref. 36)	3.4	3.1	1.47
PAzo/PAH	1000	3.4	3.4	1.71
Quartz	2200 (ref. 37)	5.8 (ref. 37)	12.7	1.45 (ref. 37)
Mica	2700	5.0 (ref. 38)	13.5	1.56

Values from the literature are indicated by citations. Sound velocities are measured values according to eqn (2). Refractive indices are measured by ellipsometry.

$n_{\text{PAzo1}} \times D_{\text{PAzo1}}$ of the total polymer multilayers. In structures with relatively thin PAzo/PAH layer, the total thickness is nearly unchanged since the expanding transducer contributes only little to the polymer film thickness.

Fig. 3(a) shows $\Delta R(t)/R_0$ of a 600 nm thick PAzo/PAH film on quartz. Again, we observe the TDBS-related oscillations. Their wavelength-dependent oscillation period $T(\lambda)$ is the same as for the sample structure 2, because the sound velocities in PSS/PAH and PAzo/PAH films match. The strain wave continuously expands the transducer layer until at $t = D_{\text{Azo2}}/\nu_{\text{poly}} = 180$ ps the strain front is reflected at the quartz interface.

Surprisingly, the shift of the thin-film-interference indicates a decreasing optical path length $s = n \times d_{\text{film}}$ although the transducer is expanding. A decreased refractive index n_{azo} of Azo-containing polymers for expanded films was already observed by Tanchak et al.[25] on much longer time scales. They observed a decrease of the refractive index of $\Delta n/n = -1\%$ for a relative thickness change of $\Delta d/d = +1.4\%$. This is consistent with our observations on ultrafast timescales: for an excitation fluence of $F = 4$ mJ cm^{-2} the average strain (relative thickness change) is about $\varepsilon = \Delta d/d \sim 5 \times 10^{-4}$, which is calibrated by ultrafast X-ray diffraction as described below. We can simulate the observed transient reflectivity data including the 20 nm

shift of thin-film interference pattern (interference maximum at 580 nm shifts to 560 nm) shown in Fig. 3a by assuming a relative refractive index change of $\Delta n/n = -2.6 \times 10^{-4}$ in the expanded polymer layer.

Fig. 3(b) shows the extracted oscillatory part of Fig. 3(a) by a Fourier-decomposition. In the data, one can very clearly observe the reflection of the strain wave at the quartz interface at 180 ps. Fig. 3(c) shows four snapshots of the motion at times, at which the main strain-front originating at the surface is in the center of the film, as it bounces between the interface and the surface. The linear chain model used for the illustration is further explained in the discussion of the ultrafast X-ray diffraction data. The green shaded area depicts the static strain profile generated by the stress profile assumed in the simulations according to the approximate penetration depth of about 500 nm for the intense excitation pulses with a wavelength of 400 nm. In the linear regime (Fig. 1c), the penetration depth is less than 250 nm. The lines in Fig. 3(c) indicate the superimposed propagating bipolar strain pulse. Adding the static (green shaded area) and propagating bipolar strain yield the total transient strain. Initially, it is essentially an expansion wave travelling from the surface to the substrate with a smaller leading compressive part.[39] The reflection of the bipolar strain pulse from the substrate – a material with larger acoustic impedance – conserves the sign. According to the acoustic impedance mismatch, a fraction of $(Z_{\text{poly}} - Z_{\text{Q}})/(Z_{\text{poly}} + Z_{\text{Q}}) = 60\%$ of the wave is reflected (Table 1). After the first reflection ($t = 180$ ps), the acoustic waveform propagates towards the laser probe-pulse. The refractive index change at the strain front now has the opposite sign, yielding a phase shift of π in the oscillation pattern. At $t = 360$ ps the acoustic pulse is reflected at the air interface which reverses the sign of the wave and of the propagation direction. Therefore, no phase shift is observed in the TDBS signal. The third reflection at $t = 540$ ps is so weak that the signal vanishes in the noise. In order to measure the 40% fraction of the strain pulse that propagates into the substrate, we designed a sample structure 2 with a thinner transducer of $d_{\text{PAzo/PAH}} = 282$ nm. Fig. 4 shows the oscillatory component of the transient reflection data. During the first 200 ps, the sound front bounces twice between the surface and the quartz interface, similar to the first 540 ps shown in Fig. 3(b) for the thicker PAzo layer. However, now due to the thinner sample, only about one full period of the
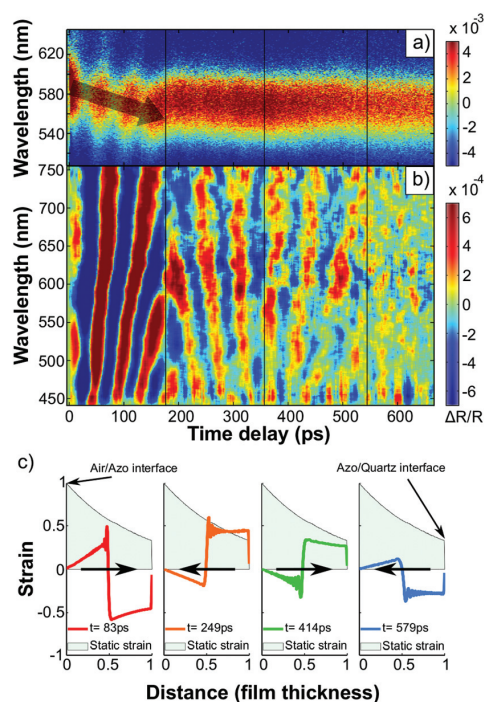
Fig. 3 (a) $\Delta R(t)/R_0$ of sample structure 2 with a 600 nm PAzo/PAH film on quartz. (b) Oscillatory component of $\Delta R(t)/R_0$. (c) Normalized simulated strain front within the PAzo/PAH at different time delays. The green shaded area corresponds to the static strain in the Azo layer resulting from the optical excitation.
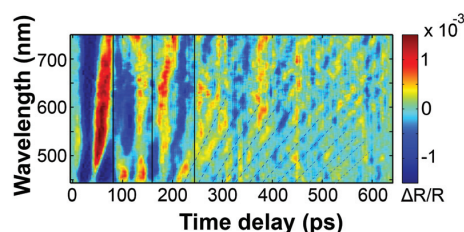

Fig. 4 Oscillatory component of $\Delta R(t)/R_0$ for a 282 nm thin PAzo/PAH multilayers on quartz (sample structure 2).

TDBS modulation occurs between two reflections. After 200 ps, the strain front passes the polymer–quartz interface and the signal modulation period shortens. This is consistent with eqn (2) for the sound velocity ν_Q = 5.8 nm ps^{-1} and refractive index n_Q of quartz. In fact, the strain created at the PAzo/air interface reaches the substrate already at $t = (D_{Azo3}/\nu_{poly})$ = 82 ps, but until 200 ps the fast oscillations are masked by the stronger signal modulation due to reflections of the strain wave in the transducer. We have recorded such transient reflection spectra also for approximately ten times thinner transducers. This results in equivalent signals, where the dynamics in the transducer film are only visible in the first 20 ps.

Calibration of transient strain by ultrafast X-ray diffraction (UXRD)

In order to calibrate the strain amplitude generated by the optical excitation of PAzo/PAH films we measured the strain after propagation into a crystalline medium, for which the lattice constant change can be measured in real time by ultrafast X-ray diffraction.[39] We prepared a film with $d_{PAzo/PAH}$ = 880 nm onto the 4.5 μm thin mica substrate. Fig. 5 shows the detected shift of the Bragg angle Θ, from which the transient strain can be calculated via $\varepsilon_{obs}(t) = \Delta c(t)/c = -\Delta \Theta \times \cot(\Theta)$, where c is the out-of-plane lattice constant of mica. The maximum compression of mica is observed at t = 260 ps, when the expansion wave created at the surface has travelled completely through the transducer. At this time, the wave front has propagated around 1.3 μm into the substrate. Therefore, the average strain within the first micrometer is about four times larger than the measured strain since the remaining 3.2 μm of the mica film are unchanged from their initial lattice constant. Hence the strain pulse detected in mica has an amplitude of about $\varepsilon = -5 \times 10^{-5}$. This is consistent with the simulation[40,41] of the strain in mica (dashed line in Fig. 5) based on a linear chain-model which we have previously tested against a large number of ultrafast X-ray diffraction experiments carried out on epitaxial metallic transducers.[40,41] The agreement of the simulation with the measured data confirms that the hyper-

sound-pulses created and propagating in these soft-matter materials can be well described by a linear chain model with the sound-velocity ν_{poly} = 3.4 nm ps^{-1} characteristic of hypersound in polymers.

From our model we predict that the corresponding expansion of the PAzo/PAH film at t = 260 ps measures $\varepsilon = 5 \times 10^{-4}$. The model simulates a linear chain of masses and springs, which are adjusted such, that the mass density and sound velocity of the materials are described correctly. The optical excitation is assumed to instantaneously generate a stress profile given by the absorption depth in the PAzo/PAH film. For calculating the strain in PAzo from the measured lattice deformation in mica, the model automatically takes into account three factors:[39,40] (i) 60% of the compressive sound has been reflected at the PAzo/quartz interface due to the acoustic impedance mismatch. (ii) The static expansion of the photoexcited PAzo layer adds to the coherent sound wave. (iii) The strain in mica is reduced by ratio 5/3.4 of the sound velocities as the pulse is stretched.

It is difficult to compare the efficiency of strain transduction to conventional metal transducers, but we shall shortly discuss a comparison to aluminum (Al). In our PAzo transducers, nearly all incident photons can be absorbed and converted to stress. Al transducers reflect about 90% of the incident fluence. The remaining fluence would be absorbed in about 10 nm. If we assume the energy to be distributed by rapid heat transport over 100 nm, the calculated temperature rise for an incident fluence of 4 mJ cm^{-2} is about 15 K, yielding a strain amplitude of $\varepsilon \sim 3 \times 10^{-4}$. This estimate is based on the specific heat and thermal expansion coefficient of Al. In fact, the strain level is very similar to the strain produced by the PAzo transducer. However, the two systems in fact have quite different properties. While the Al transducer would be more efficient for thinner transducers (high frequencies) as the energy density is higher due to the smaller penetration depth, the PAzo transducer can more easily be tuned to different frequencies, as the energy density varies only weakly for thicknesses between 20 and 500 nm. Moreover, the efficiency of sound transduction between Al and soft matter is significantly reduced by reflection according to the acoustic impedance mismatch.

Conclusions

In this paper, we have presented azobenzene containing polyelectrolyte multilayer films as transducers for picosecond ultrasonics, which is expected to boost the applicability of this method in soft materials and nanocomposites. The frequency spectrum of the generated strain can be tuned by the transducer thickness in the range of 1–100 GHz. We demonstrated the propagation of these nanoscale hyper-soundwaves through polyelectrolytes and their damping at nanometric metal inclusions. The good coupling efficiency of the hyper-sound pulses into various substrates demonstrates the potential for assembling nanometric hybrid devices. It also allowed us to
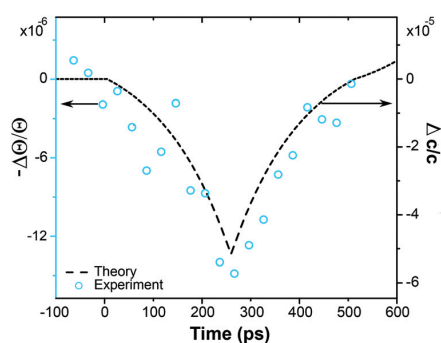
Fig. 5 The time dependence and amplitude of the measured change of the diffraction angle $\Delta \Theta$ (blue circles) agrees well with the average strain of the strained part (see text) of mica as calculated by the linear chain model (dashed line).

quantify the strain amplitude of the hyper-sound waves by ultrafast X-ray diffraction to be up to $\varepsilon = 5 \times 10^{-4}$. This transient strain is accompanied by a tiny refractive index change of about $\Delta n/n = 2.6 \times 10^{-4}$, which can nonetheless be easily detected by a substantial transient shift of the thin-film interference pattern. This will allow for all-optical sensing of the transducer dynamics in future applications.

Acknowledgements

References

1 O. Matsuda, M. C. Larciprete, R. Li Voti and O. B. Wright, *Ultrasonics*, 2015, **56**, 3–20.

2 H. A. Navirian, D. Schick, P. Gaal, W. Leitenberger, R. Shayduk and M. Bargheer, *Appl. Phys. Lett.*, 2014, **104**, 21906.

3 C. Thomsen, H. T. Grahn, H. J. Maris and J. Tauc, *Phys. Rev. B: Condens. Matter*, 1986, **34**, 4129.

4 O. B. Wright, *J. Appl. Phys.*, 1992, **71**, 1617.

5 J.-W. Kim, M. Vomir and J.-Y. Bigot, *Phys. Rev. Lett.*, 2012, **109**, 166601.

6 T. Dehoux, M. Abi Ghanem, O. F. Zouani, J.-M. Rampnoux, Y. Guillet, S. Dilhaire, M.-C. Durrieu and B. Audoin, *Sci. Rep.*, 2015, **5**, 8650.

7 A. Gadalla, T. Dehoux and B. Audoin, *Planta*, 2014, **239**, 1129–1137.

8 S. Danworaphong, M. Tomoda, Y. Matsumoto, O. Matsuda, T. Ohashi, H. Watanabe, M. Nagayama, K. Gohara, P. H. Otsuka and O. B. Wright, *Appl. Phys. Lett.*, 2015, **106**, 163701.

9 C. Rossignol, N. Chigarev, M. Ducousso, B. Audoin, G. Forget, F. Guillemot and M. C. Durrieu, *Appl. Phys. Lett.*, 2008, **93**, 123901.

10 G. Scarcelli and S. H. Yun, *Opt. Express*, 2012, **20**, 9197–9202.

11 A. S. Rury, S. Sorenson and J. M. Dawlaty, *J. Chem. Phys.*, 2016, **144**, 104701.

12 P. Ruello and V. E. Gusev, *Ultrasonics*, 2015, **56**, 21–35.

13 J. A. Rogers, A. A. Maznev, M. J. Banet and K. A. Nelson, *Annu. Rev. Mater. Sci.*, 2000, **30**, 117–157.

14 B.-Y. Choi, *Phys. Rev. Lett.*, 2006, **96**, 156106.

15 Q. Ferreira, P. A. Ribeiro, O. N. Oliveira and M. Raposo, *ACS Appl. Mater. Interfaces*, 2012, **4**, 1470–1477.

16 S. Pipolo, E. Benassi, G. Brancolini, M. Valášek, M. Mayor and S. Corni, *Theor. Chem. Acc.*, 2012, **131**, 1–14.

17 M. Quick, A. L. Dobryakov, M. Gerecke, C. Richter, F. Berndt, I. N. Ioffe, A. A. Granovsky, R. Mahrwald, N. P. Ernsting and S. A. Kovalenko, *J. Phys. Chem. B*, 2014, **118**, 8756–8771.

18 T. Hugel, N. B. Holland, A. Cattani, L. Moroder, M. Seitz and H. E. Gaub, *Science*, 2002, **296**, 1103–1106.

19 N. Liu, D. R. Dunphy, P. Atanassov, S. D. Bunge, Z. Chen, G. P. López, T. J. Boyle and C. J. Brinker, *Nano Lett.*, 2004, **4**, 551–554.

20 A. S. Kumar, T. Ye, T. Takami, B.-C. Yu, A. K. Flatt, J. M. Tour and P. S. Weiss, *Nano Lett.*, 2008, **8**, 1644–1648.

21 T. Muraoka, K. Kinbara and T. Aida, *Nature*, 2006, **440**, 512–515.

22 E. Merino and M. Ribagorda, *Beilstein J. Org. Chem.*, 2012, **8**, 1071–1090.

23 Y. Yu, M. Nakano and T. Ikeda, *Nature*, 2003, **425**, 145.

24 J. Han, D. Yan, W. Shi, J. Ma, H. Yan, M. Wei, D. G. Evans and X. Duan, *J. Phys. Chem. B*, 2010, **114**, 5678–5685.

25 O. M. Tanchak and C. J. Barrett, *Macromolecules*, 2005, **38**, 10566–10570.

26 M. Kiel, M. Klötzer, S. Mitzscherling and M. Bargheer, *Langmuir*, 2012, **28**, 4800–4804.

27 A. Bojahr, M. Herzog, S. Mitzscherling, L. Maerten, D. Schick, J. Goldshteyn, W. Leitenberger, R. Shayduk, P. Gaal and M. Bargheer, *Opt. Express*, 2013, **21**, 21188–21197.

28 M. Kiel, S. Mitzscherling, W. Leitenberger, S. Santer, B. Tiersch, T. K. Sievers, H. Möhwald and M. Bargheer, *Langmuir*, 2010, **26**, 18499–18502.

29 G. Decher and J. Schmitt, in *Trends in Colloid and Interface Science VI*, ed. C. Helm, M. Lösche and H. Möhwald, Steinkopff, 1992, pp. 160–164.

30 B. Nikoobakht and M. A. El-Sayed, *Chem. Mater.*, 2003, **15**, 1957–1962.

31 W. Ni, Z. Yang, H. Chen, L. Li and J. Wang, *J. Am. Chem. Soc.*, 2008, **130**, 6692–6693.

32 M. Kiel, H. Möhwald and M. Bargheer, *Phys. Rev. B: Condens. Matter*, 2011, **84**, 165121.

33 D. Schick, A. Bojahr, M. Herzog, C. von Korff Schmising, R. Shayduk, W. Leitenberger, P. Gaal and M. Bargheer, *Rev. Sci. Instrum.*, 2012, **83**, 25104.

34 F. Zamponi, Z. Ansari, C. v. Korff Schmising, P. Rothhardt, N. Zhavoronkov, M. Woerner, T. Elsaesser, M. Bargheer, T. Trobitzsch-Ryll and M. Haschke, *Appl. Phys. A*, 2009, **96**, 51–58.

35 D. Schick, R. Shayduk, A. Bojahr, M. Herzog, C. von Korff Schmising, P. Gaal and M. Bargheer, *J. Appl. Crystallogr.*, 2013, **46**, 1372–1377.

36 K. Haberska and T. Ruzgas, *Bioelectrochemistry*, 2009, **76**, 153–161.

37 C.-S. Zha, R. J. Hemley, H.-K. Mao, T. S. Duffy and C. Meade, *Phys. Rev. B: Condens. Matter*, 1994, **50**, 13105–13112.

38 D. J. Cebula, *Clay Miner.*, 1982, **17**, 195–200.

39 D. Schick, M. Herzog, A. Bojahr, W. Leitenberger, A. Hertwig, R. Shayduk and M. Bargheer, *Struct. Dyn.*, 2014, **1**, 64501.

40 D. Schick, A. Bojahr, M. Herzog, R. Shayduk, C. von Korff Schmising and M. Bargheer, *Comput. Phys. Commun.*, 2014, **185**, 651–660.

41 M. Herzog, D. Schick, P. Gaal, R. Shayduk, C. V. K. Schmising and M. Bargheer, *Appl. Phys. A*, 2012, **106**, 489–499.

Article XIV

Characterization of an ultrafast Bragg-switch for shortening hard x-ray pulses

Mathias Sander, Azize Koç, Christelle T. Kwamen, H. Michaels, Alexander von Reppert, **Jan-Etienne Pudell**, Flavio Zamponi, Matias Bargheer, Jan Sellmann, Jutta Schwarzkopf and Peter Gaal

We present a nanostructured device that functions as photoacoustic hard x-ray switch. The device is triggered by femtosecond laser pulses and allows for temporal gating of hard x-rays on picosecond (ps) timescales. It may be used for pulse picking or even pulse shortening in 3rd generation synchrotron sources. Previous approaches mainly suffered from insufficient switching contrasts due to excitation-induced thermal distortions. We present a new approach where thermal distortions are spatially separated from the functional switching layers in the structure. Our measurements yield a switching contrast of 14, which is sufficient for efficient hard x-ray pulse shortening. The optimized structure also allows for utilizing the switch at high repetition rates of up to 208 kHz.

Characterization of an ultrafast Bragg-Switch for shortening hard x-ray pulses

M. Sander,[1] A. Koc,[2] C. T. Kwamen,[2] H. Michaels,[3] A. v. Reppert,[1] J. Pudell,[1] F. Zamponi,[1] M. Bargheer,[1] J. Sellmann,[4] J. Schwarzkopf,[4] and P. Gaal[3]

[1]*Institute for Physics and Astronomy, Universität Potsdam, Karl-Liebknecht-Str. 24-25, 14476 Potsdam, Germany*
[2]*Helmholtz-Zentrum Berlin for Materials and Energy GmbH, Wilhelm-Conrad-Röntgen Campus, BESSY II, Albert-Einstein-Str. 15, 12489 Berlin Germany*
[3]*Institute for Solid State and Nanostructure Physics, Universität Hamburg, Jungiusstr. 11, 20355 Hamburg, Germany*
[4]*Institute for Crystal Growth, Berlin, Germany*

We present a nanostructured device that functions as photoacoustic hard x-ray switch. The device is triggered by femtosecond laser pulses and allows for temporal gating of hard x-rays on picosecond (ps) timescales. It may be used for pulse picking or even pulse shortening in 3rd generation synchrotron sources. Previous approaches mainly suffered from insufficient switching contrasts due to excitation-induced thermal distortions. We present a new approach where thermal distortions are spatially separated from the functional switching layers in the structure. Our measurements yield a switching contrast of 14, which is sufficient for efficient hard x-ray pulse shortening. The optimized structure also allows for utilizing the switch at high repetition rates of up to 208 kHz. *Published by AIP Publishing.* [http://dx.doi.org/10.1063/1.4967835]

I. INTRODUCTION

The controlled manipulation of x-ray radiation is a difficult task, especially in the hard x-ray regime (E_{photon} > 2 keV). This is due to the fact that x-rays penetrate the material rather than being reflected. In order to change the beam direction, one has to rely on total reflection at surfaces,[1] Fourier-optical elements such as zone-plates,[2,3] or at diffracting elements, e.g., Bragg mirrors in monochromators.[4,5] X-ray optics are therefore advanced devices placing high requirements on technological properties such as surface roughness, crystal quality, and structural perfection. In order to tailor the imaging characteristics of x-ray optical elements to environmental changes or to experimental requirements, adaptive optics are being developed. They are used in x-ray astronomy to compensate for atmospheric turbulence.[6] In large-scale research facilities, such as synchrotrons, adaptive x-ray optics are used to stabilize the x-ray beam from thermal drifting[7] or to optimize the imaging properties for the requirements at the experimental station.[8] Existing adaptive optics are typically based on slow physical processes like gravitational or thermal deformation. More advanced attempts rely on piezoelectric effects[9] or on MEMS-devices.[10]

Here, we demonstrate a different approach to build active x-ray optical elements by optical excitation. As an example, we introduce a switchable mirror where the reflectivity is modulated on picosecond timescales. We call this device the PicoSwitch. It utilizes modulation of the lattice parameter, and thus the x-ray diffraction efficiency, via controlled propagation of coherent acoustic phonon wavepackets. We employ this device to gate the x-ray pulse emitted from a synchrotron storage ring. The opening time of the gate is significantly shorter than the x-ray pulse duration. Hence, the PicoSwitch effectively reduces the duration of an x-ray pulse and therefore increases the temporal resolution in ultrafast x-ray diffraction (UXRD) experiments.

UXRD is an efficient technique to measure ultrafast dynamics of the crystal lattice.[11] Most experiments are performed at large scale facilities, e.g., synchrotrons. The newest generation of such large-scale radiation sources is free electron lasers (FELs). They provide significantly improved beam characteristics in terms of intensity, coherence, and pulse duration compared to 3rd generation synchrotron sources.[12] In the context of this article, we mention especially the pulse duration, which is reduced from typically 100 picoseconds (ps) at synchrotrons to sub-100 femtoseconds (fs) at FEL sources. Hence, synchrotrons provide a poor temporal resolution in UXRD measurements. The better performance of FELs is expressed by the brilliance (BR) parameter, which is around $10^{32} \frac{\text{photons}}{\text{s·mrad}^2 \cdot \text{mm}^2 \cdot 0.1\%\text{bw}}$ for FELs compared to $10^{25} \frac{\text{photons}}{\text{s·mrad}^2 \cdot \text{mm}^2 \cdot 0.1\%\text{bw}}$ for 3rd generation synchrotrons.[12] As an alternative to large-scale facilities, there exist lab-based table-top sources for hard x-rays. These plasma x-ray sources (PXS) provide hard x-ray bursts with a duration of less than 200 fs.[13] Disadvantages of the PXS are low photon count, large fluctuations, and high angular divergence,[14] which results in a low brilliance of only $1.1 \times 10^{15} \frac{\text{photons}}{\text{s·mrad}^2 \cdot \text{mm}^2 \cdot 0.1\%\text{bw}}$.[15] In particular, due to the high angular divergence of the generated x-ray beam, the diffraction angle can only be measured with low resolution at a PXS.

The PicoSwitch aims at improving a key characteristic of synchrotron sources, namely, the poor temporal resolution. We expect a reduction of the x-ray pulse duration down to 5 ps. Other pulse shortening schemes have been developed

and shown to reduce the pulse duration down to 200 fs.[16] However, these femtoslicing schemes are far more expensive in terms of equipment and experimental effort. The PicoSwitch requires only a mount for positioning and for aligning the incidence angle of the x-rays. It is an easy-to-use and economically reasonable tool that may be installed and removed in an UXRD setup upon request.

II. WORKING PRINCIPLE OF THE PICOSWITCH

The PicoSwitch is a photo-acoustic device that relies on the propagation of coherent acoustic phonon wavepackets.[17] These soundwaves are generated by ultrashort optical pulses impinging on a transducer. Former designs already showed an ultrafast lattice response, which resulted in shortening an incident x-ray pulse.[18] However, a synchrotron-based pump-probe experiment with a shortened pulse revealed an insufficient switching contrast,[19] which stems from thermal expansion of the transducer layer after optical excitation.

We demonstrate the PicoSwitch working principle with a simulation of the time dependent diffraction efficiency of sample I in Table I. The sample stack is shown in Figure 1(c) and consists of 46 nm transparent LaAlO$_3$ (LAO, green) on 77 nm metallic La$_{0.67}$Sr$_{0.33}$MnO$_3$ (LSMO, red) on transparent NdGaO$_3$ (NGO, blue) substrate. The PicoSwitch is excited by femtosecond (fs) laser pulses which are transmitted through the LAO cap layer to be absorbed in the LSMO transducer.

Absorption of the pump pulses leads to the excitation of coherent compression waves into the cap layer and into the substrate, respectively, as well as to expansion waves into the transducer itself. These coherent sound waves modulate the lattice parameter in the structure, thus shifting the x-ray diffraction efficiency in reciprocal space. The dynamics of the crystal lattice can be modeled with a linear chain of masses and springs.[20] The model yields transient strain matrices that are used to calculate the time-dependent x-ray diffraction efficiency[21] using dynamic x-ray diffraction theory.[22] Specifically, a strain induced expansion or compression of the crystal leads to a shift of diffraction efficiency η to lower or larger diffraction angles, respectively. In the following, we convert the diffraction angle to the out-of-plane reciprocal space coordinate q_z using the transformation $q_z = \frac{4\pi}{\lambda} \sin \theta$, where λ and θ denote the x-ray wavelength and diffraction angle, respectively. The position of the diffraction
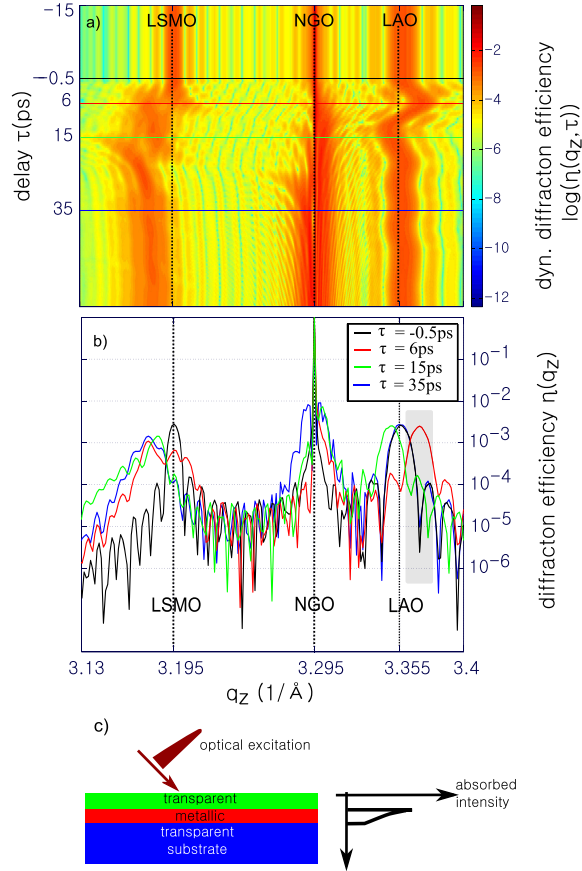

FIG. 1. (a) Simulation of the diffraction efficiency $\eta(q_z, \tau)$ of the sample I from Table I after excitation with an ultrashort optical pulse. (b) Transient diffraction efficiency vs. out-of-plane reciprocal space coordinate q_z at pump-probe delays of -0.5 ps (black), 6 ps (red), 13 ps (green), and 35 ps (blue), respectively. The curves indicate the time-dependent compression and expansion of the transparent cap layer at $q_z = 3.355$ Å^{-1} and of the metallic transducer layer at $q_z = 3.195$ Å^{-1}. (c) PicoSwitch sample structure and optical excitation profile.

efficiency η in reciprocal space coordinates is independent of the x-ray photon energy. We specifically investigate $\eta(q_z, \tau)$ at the Bragg peaks of the PicoSwitch structure.

The color plot in Figure 1(a) depicts the simulated diffraction efficiency of the PicoSwitch structure vs. pump-probe delay τ and out-of-plane reciprocal space coordinate q_z. Cross sections at different pump-probe delays are plotted in Figure 1(b). The black line shows a simulation where the sample is in thermal equilibrium, while the red, green, and blue curves depict the diffraction efficiency of 6 ps, 15 ps, and 35 ps after excitation, respectively. At $\tau = 0$, a compression wave is launched at the LSMO/LAO-interface and propagates into the dielectric LAO-layer. Hence, the red curve (6 ps delay) in Figure 1(b) shows an out-of-plane expanded and compressed LSMO- and LAO-layer, respectively. After reflection at the surface, the compression wave is converted into an expansion wave and propagates back into the structure. This leads to the expansion of the LAO-layer depicted in the green curve in Figure 1(b). Finally, the blue curve

TABLE I. Material properties of the PicoSwitch samples.

	Material	Lattice parameter (hkl)	d_{layer}	v_{sound}
I	LAO	3.791 Å (001)	46 nm	7.2 $\frac{nm}{ps}$
	LSMO	3.933 Å (001)	77 nm	7.8 $\frac{nm}{ps}$
	NGO	3.864 Å (110)	500 μm	7.8 $\frac{nm}{ps}$
II	STO	3.893 Å (001)	31.1 nm	7.8 $\frac{nm}{ps}$
	SRO	3.924 Å (001)	100 nm	6.3 $\frac{nm}{ps}$
	DSO	3.948 Å (110)	500 μm	6.8 $\frac{nm}{ps}$

(35 ps delay) shows a delay where all sound waves have propagated into the substrate. Acoustic impedance matching between the LAO cap layer and the LSMO transducer prevents multiple reflection of sound waves. At late times ($\tau > 35$ ps), the LSMO transducer is still expanded due to the deposited thermal energy from the pump pulse. However, the LAO cap layer is not strained in out-of-plane direction and the corresponding Bragg-peak returns to its initial q_z position. The layer will successively warm up via thermal diffusion from the laser excited-LSMO transducer and expands in consequence. This process is much slower compared to coherent phonon transport and occurs on long time-scales irrelevant for the switching process. It is important to note that the gate function is determined by the coherent compression wave that shifts diffraction efficiency to higher diffraction angles. Heating of the layer results in an expansion, thus shifting the diffraction efficiency to even lower diffraction angles. Hence, heat diffusion does not decrease the switching contrast even on long timescales.

The advantage of the new PicoSwitch compared to previous designs is the following: by spatially separating the excitation of the transducer from the switching in the transparent layer, one obtains high switching contrast even after depositing thermal energy in the sample. The best switching contrast is reached in the grey shaded area in Figure 1(b), i.e., in close proximity to the Bragg peak of the transparent LAO cap layer. Using the diffraction efficiency before (η_0) and after (η_∞) the propagation of coherent phonons, we define the q_z-dependent switching contrast $C_0(\eta)$ and $C_\infty(\eta)$

$$C_{0,\infty} = \frac{\eta_{max} - \eta_{0,\infty}}{\eta_{0,\infty}}, \tag{1}$$

where η_{max} is the maximum transient diffraction efficiency of the LAO layer.

Currently, the maximum diffraction efficiency is 5×10^{-3}, determined by the thickness of the transparent cap layer. The efficiency may be further improved, e.g., by using asymmetric diffraction geometries, different film thicknesses, or different material systems.

Based on simulations shown in Figures 1(a) and 1(b), we grew test samples for characterization of the new PicoSwitch design in UXRD experiments. The general structure of the PicoSwitch consisting of a transparent cap layer and a metallic transducer layer was realized with two different material systems. Samples were epitaxially grown by pulsed laser deposition (PLD).[23] Relevant material properties of both samples are listed in Table I.

III. EXPERIMENTAL METHOD

To fully characterize our pulse shortening device, we have to determine the time and reciprocal space dependent change of the diffraction efficiency $\eta(q_z, \tau)$. Knowledge of $\eta(q_z, \tau)$ provides characteristic parameters like switching time (FWHM) and switching contrast (Equation (1)). It is important to note that both a high temporal and angular resolution of the measurement are necessary to accurately determine $\eta(q_z, \tau)$.

We accomplish the characterization of our device by performing two measurements which make use of the advantages of different x-ray sources. First, we measure $\eta(q_z, \tau)$ with a high temporal resolution at the PXS at University Potsdam. The time resolution of 200 fs is clearly sufficient to determine the expected switching time of ≈ 5 ps. Second, we resolve the angular response of $\eta(q_z, \tau)$ in a correlation experiment similar to Ref. 18. This measurement was performed at the x-ray Pump-Probe (XPP) station of the KMC3-beamline at the Helmholtz-Zentrum for Materials and Energy. The PXS- and XPP-setups are shown in Figures 2(a) and 2(b), respectively, and have been described elsewhere in more detail.[13,24]

Both setups utilize femtosecond lasers for sample excitation and detect diffracted photons with a two-dimensional hybrid pixel area detector. The excitation fluence was 25 mJ/cm² and 40 mJ/cm² for the PXS and 13.6 mJ/cm² for the XPP measurement. Since the energy of an excitation pulse is 50 times larger in the PXS measurement, the focal area was reduced in the XPP-setup to achieve similar excitation intensities. In contrast, the XPP setup can measure at high repetition rates of up to 208 kHz. This leads to a large power density in the excited volume on the sample and to a
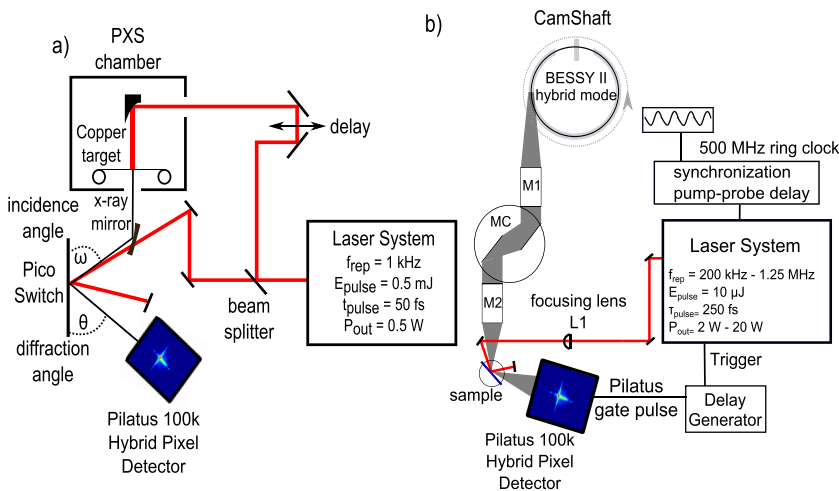

FIG. 2. (a) UXRD setup at the University of Potsdam using a Plasma x-ray Source for the generation of 150–200 fs x-ray bursts.[13] (b) XPP experimental station at the KMC3-beamline at BESSY II.[24]

TABLE II. Comparison of source parameters of the PXS and the XPP setup.

	PXS	XPP
X-ray pulse duration	<200 fs	<60 ps
Angular resolution	$0.15°$	$0.01°$
Photons on sample	$10^6 s^{-1}$	$10^8 s^{-1}$
X-ray photon energy	8047 eV	6500 eV
Optical pulse energy	0.5 mJ	10 μJ
Repetition frequency	1 kHz	208 kHz

stronger average heating of the crystal lattice compared to the PXS measurement. Specific issues for high-repetition UXRD experiments, such as average heating and sample deformation, are discussed in Refs. 24 and 25. Here, we would like to point out that the quasi-equilibrium steady state of the sample under excitation differs significantly between the PXS and the XPP measurement. Our data evaluation and model simulations account for these specific background effects by introducing a depth-dependent strain profile in our simulations. The characteristic source parameters for the PXS and the XPP setup are listed in Table II.

All UXRD measurements are performed in symmetric scattering geometry, i.e., the detector is held at twice the incidence angle ω of the x-ray beam to the sample surface. Such $\omega - 2\theta$-scans measure diffraction at lattice planes parallel to the sample surface and along the Crystal Truncation Rod (CTR) in reciprocal space.[26] We measure the second order diffraction, i.e., at the (002)-plane of the thin film materials, which shows the highest diffraction efficiency. This also holds for the 110-cut DSO substrate where we measure the (220) diffraction peak in symmetrical diffraction geometry. In principle, the switching contrast will be higher at higher diffraction orders. As mentioned before, we convert the diffraction angle θ to the reciprocal space coordinate q_z in order to directly compare measurements performed at PXS and XPP with different x-ray photon energies.

IV. RESULTS

Static diffraction efficiency $\eta(q_z)$ of samples I and II is shown in Figures 3(a) and 3(b). In sample I, the bright NGO substrate peak lies between the transparent LAO-peak at $q_z = 3.355\,\text{Å}^{-1}$ and the Bragg-peak of the metallic LSMO layer at $q_z = 3.195\,\text{Å}^{-1}$. In sample II, all three peaks appear in a q_z-range of less than $0.5\,\text{Å}^{-1}$, namely, at $q_z = 3.17\,\text{Å}^{-1}$ (DSO), $q_z = 3.236\,\text{Å}^{-1}$ (SRO), and $q_z = 3.264\,\text{Å}^{-1}$ (STO). This is in contrast to sample I where the peaks distribute over a range of $\approx 1.5\,\text{Å}^{-1}$.

The two-dimensional plots in Figures 3(c) and 3(d) depict the diffraction efficiency η vs. pump-probe delay τ and out-of-plane reciprocal space coordinate q_z, obtained by measurements at the PXS. The data were taken at an excitation fluence of $25\,\text{mJ/cm}^2$ (c) and $40\,\text{mJ/cm}^2$ (d), respectively. The initial peak position at $\tau < 0$ corresponds to data shown in Figures 3(a) and 3(b), respectively. The PicoSwitch was exposed to optical pump and x-ray probe beams for several weeks during our experiments. We did not observe any signs of long term degradation. Upon excitation at $\tau_0 = 0$, the LAO peak in Figure 3(c) shifts to larger q_z-values until $\tau_1 = 6.5\,\text{ps}$, indicating a compression of the out-of-plane lattice parameter. Upon reflection of the sound wave at the sample surface, the peak shift reverses its sign and the peak returns to its initial position at $\tau_2 = 13\,\text{ps}$. Compression of the LAO cap layer is only slightly visible due to the limited angular resolution of the measurement.

In contrast, the LSMO transducer peak shows an almost continuous shift to smaller q_z-values accompanied with a broadening until delay time τ_2. This indicates an expansion of the crystal lattice in out-of-plane direction. The substrate peak is almost unchanged except for a narrow sideband due to the propagating sound wave. The measured width of the substrate peak is of the same order as the width of cap layer and transducer peaks, respectively. Note that the measurement reproduces the dynamic diffraction efficiency simulated in Figure 1(a).
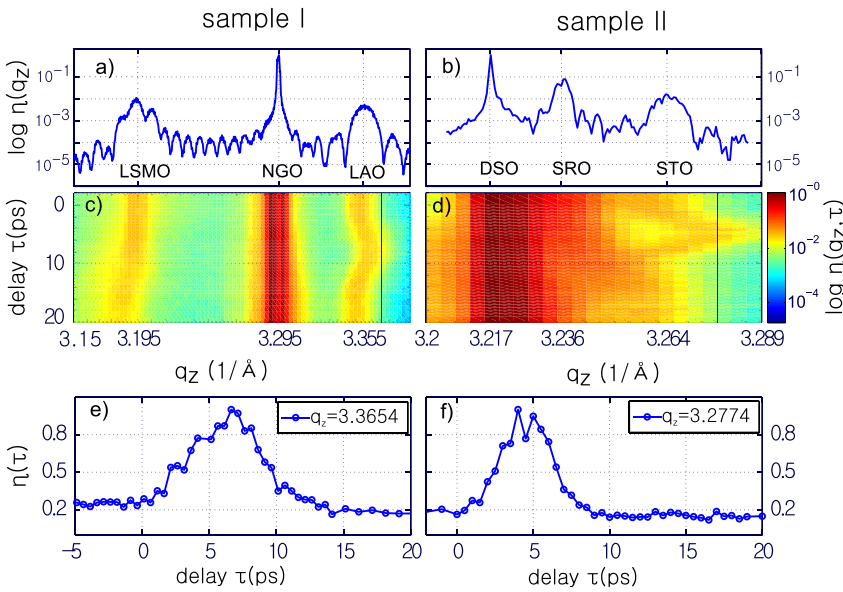
FIG. 3. Results of static and time-resolved x-ray diffraction measurements: (a) and (b): Static x-ray diffraction measurement from sample I and sample II. The data were measured at the XPP-beamline with high angular resolution. (c) (sample I) and (d) (sample II): Dynamic diffraction efficiency of the PicoSwitch measured at the PXS. Laser-excited propagating sound waves modulate the lattice parameter and lead to a shift of the Bragg peak positions. (e) and (f) Cross sections at $q_z = 3.365\,\text{Å}^{-1}$ (sample I) and $q_z = 3.277\,\text{Å}^{-1}$ (sample II) demonstrating the ultrafast modulation of the diffraction efficiency η.

Figure 3(d) shows a qualitatively similar behaviour for the STO- and SRO-peaks, respectively. Upon heating by the optical excitation pulse, the SRO-layer expands and the corresponding peak is covered by the DSO substrate peak in the diffraction image. This effect is especially strong at high repetition rates of the excitation laser, where the thermal background due to deposited heat in the metallic film is large.

The width of the substrate peaks in both measurements indicates the angular resolution of the PXS. Simulations of the sample structure shown in Figure 1 indicate a substrate peak width of $\approx 0.005\,\text{Å}^{-1}$. Due to the limited angular resolution, the PXS-measurements require large excitation fluences of $>20\,\text{mJ/cm}^2$.

Cross-sections at specific q_z-values of the normalized dynamic diffraction efficiency $\eta(\tau)$ of samples I and II are shown in Figures 3(e) and 3(f), respectively. The rise and fall of $\eta(\tau)$ constitute a temporal gate for diffraction of impinging x-ray photons. Both samples show comparable switching times.

In order to determine $\eta(\tau)$ with better angular resolution, we resort to the XPP-experimental station at HZB. Due to the insufficient temporal resolution at the synchrotron, we perform a correlation experiment which is already described in Ref. 18. It is important to note that we excite the sample with a repetition rate of 208 kHz. This has two important consequences. First, the high repetition rate results in a lower energy of the optical pump pulse, which limits the available excitation fluence. Second, accumulated heat in the sample may lead to strong distortions of the diffraction peaks such as peak broadening or a decrease in peak intensity. This must be compensated by reducing the footprint of the pump and probe pulses[25] and by careful adjustment of the spatial overlap.[24]

A measurement of the x-ray probe pulse at the XPP-beamline is shown in Figure 4(a). Data of the correlation experiment of the impinging x-ray pulse with the ultrafast PicoSwitch response are shown in Figure 4(b). Owing to the high repetition frequency, the experiment is performed at an excitation fluence of 13.6 mJ/cm², i.e., roughly half of the excitation fluence of the PXS measurement. Therefore, the switching gate differs from the data shown in Figure 3. The experiment was only performed on sample I, where the separation of the diffraction peaks in reciprocal space is larger than in sample II. The larger separation is necessary to circumvent heat-induced distortions of the diffraction peaks. For modeling the experimental data, we use the simulated sample response shown in the green solid line in Figure 4(b).

The magenta, dotted curve in Figure 4(b) depicts the result of the correlation experiment. It shows an asymmetric rise and fall of the diffracted intensity from the sample, similar to the incident x-ray pulse. Note that the latter is plotted against a real time axis t and not against the pump-probe delay τ. Therefore, the asymmetries appear inverted in Figure 4(b) compared to the incident x-ray beam shown in Figure 4(a). Numeric correlation of the simulated sample response with the incident x-ray pulse is shown in the blue solid curve in Figure 4(b).
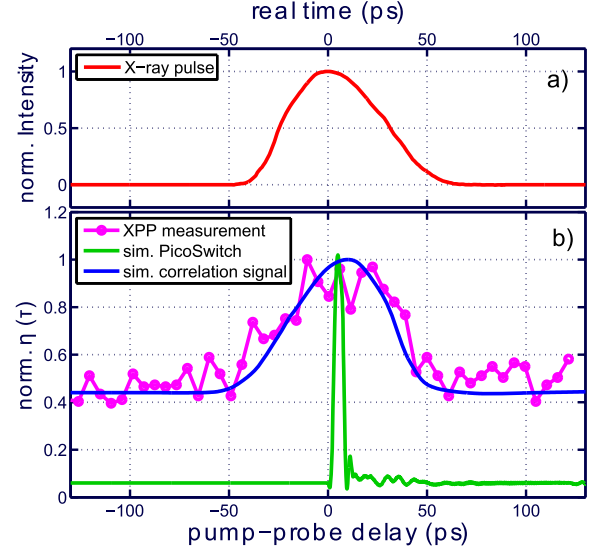

FIG. 4. (a) Time structure of the x-ray pulse at BESSY II in hybrid mode plotted vs. a real time axis t. The temporal shape was measured via laser-induced energy modulation of the relativistic electron bunch.[27] (b) Measured correlation of the BESSY x-ray pulse with the ultrafast response of sample I after optical excitation (magenta dotted curve). The blue solid line shows a simulated correlation signal using the measured BESSY x-ray pulse in (a). The green solid line shows the sample response used to calculate the correlation signal. All curves are plotted vs. the pump-probe delay time τ, which is inverted compared to the real time axis t.

V. DISCUSSION

Measurements of transient changes in the diffraction efficiency from the PicoSwitch samples shown in Figure 3 agree with model simulations as shown in Figure 1. In particular, we observe a compression and subsequent expansion of the transparent cap layer. At the same time, the transducer expands upon optical excitation. The extracted switching time τ_s perfectly agrees with the value expected from simulations of coherent phonon propagation in the samples. This value is given by $\tau_s = d_{layer}/v_{sound}$ and amounts to $\approx 8.1\,\text{ps}$ and $\approx 4.0\,\text{ps}$ for samples I and II, respectively. Deviations to the experimental value may stem from the limited angular resolution, background noise and from fluence-dependent effects.

The absorbed fluence was calibrated by comparing the measured angular shift of the LAO-peak to simulations described in Section II and determined to be 8 mJ/cm². We added a static background obtained a perfect agreement of simulation and experiment in Figure 4(b). The background stems from the low excitation fluence and from background scattering of the x-ray beam. The latter can be reduced by decreasing the divergence of the focused x-ray beam at the cost of x-ray flux.

The XPP-measurement shown in Figure 4 also demonstrates that the PicoSwitch can sustain high average powers and is thus suited for high-repetition UXRD setups. Decreasing the focal area with appropriate x-ray optics allows for stronger excitation fluences, which increases the switching contrast.

Due to the limited angular resolution, switching contrasts defined in Equation (1) cannot be determined through

measurements performed at the PXS. We will now estimate the switching contrast $C_{0,\infty}$ from data obtained by XPP measurements. The duration of a synchrotron x-ray pulse during our experiment was only $\tau_{fwhm} = 60$ ps. Hence, x-ray photons are diffracted from the PicoSwitch during the switching process and from background scattering while the switch is in the off-state. The latter process reduces the measured contrast proportional to the ratio D of the switching time τ_s and the pulse duration of the impinging x-ray pulse τ_{fwhm}. From Figure 4(b), we find $\Delta\eta = 0.45$. Using Equation (1), we extract a switching contrast of

$$C = \frac{\Delta\eta}{\eta_0} \cdot \frac{1}{D} = \frac{1 - 0.45}{0.45} \cdot \frac{58\,\text{ps}}{5\,\text{ps}} \approx 14. \qquad (2)$$

Our measured contrast is a factor of two larger compared to previous PicoSwitch designs.[19] By dropping the limiting noise floor, our calculations predict a switching contrast of $C_{0,\infty} = 27$. The PicoSwitch allows for even higher switching contrasts by increasing the excitation fluence. To the best of our knowledge, LSMO and SRO transducers may be excited with fluences up to $50\,\text{mJ/cm}^2$ at a repetition frequency of 1 kHz.

To quantify the effects of a finite switching contrast in a pump probe measurement, we show a simulation of a heavyside function which is sampled by the PicoSwitch probe pulse in Figure 5. The switching contrast was $C_{0,\infty} = 14$, as in the data shown in Figure 4. The switching background results in a temporal smearing of the pump probe signal. The ultrafast PicoSwitch gate results in a sharp drop of the pump probe signal around time zero. The amplitude of the drop is 30% of the total amplitude. The heavyside function is resolved with the temporal resolution of the gated probe pulse. The amplitude of the ultrafast response will be increased with better contrast ratios.

While we demonstrated ultrafast switching of hard x-rays on both samples, sample II is more vulnerable to thermal distortions induced by the optical excitation. This prevents efficient switching, especially at high repetition frequencies. Separation in reciprocal space of the diffraction peaks of the transducer and the transparent cap layer, respectively, renders the switch more stable with respect to thermally induced strain fields. However, both samples are
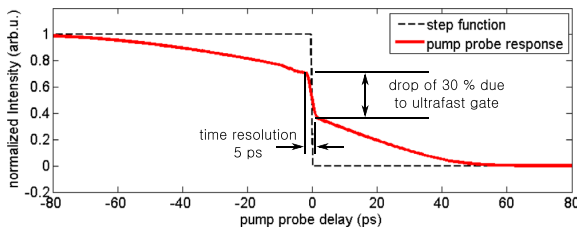

FIG. 5. Simulation of a Heavyside function (dashed) sampled by a shortend synchrotron pulse which was generated by the PicoSwitch. The pump probe response is shown in the red solid curve. The pump probe signal is smeared out over the duration of the incident x-ray pulse due to a finite switching contrast of $C_{0,\infty} = 14$. We assumed a FWHM duration of 120 ps of the incident pulse. The ultrafast gate of the probe pulse results in a 30% drop in amplitude. The ultrafast signal is therefore resolved with the time resolution of the switching gate.

suited for pulse switching at low repetition rates where thermal distortions are low.

Thermal diffusion leads to heating of the top layer of the PicoSwitch on nanosecond timescales. Ultrafast experiments resolving dynamics on the order of the x-ray pulse duration, e.g., by using gateable detectors, are not affected by heat diffusion. However, if the PicoSwitch is used as a beamline device which is exposed to the full bunch pattern, e.g., as pulse picker, dynamics on long timescales may become relevant. Heat diffusion dynamics depend on material properties and on experimental parameters, e.g., excitation fluence, repetition rate, and device cooling. Owing to the complexity of the issue, we will discuss thermally induced dynamics of PicoSwitch structures in a separate publication.

It is important to note that the PicoSwitch does not affect the divergence of the incident and reflected beam as long as the excitation area is at least twice as large as the footprint of the x-ray beam.

Finally, we compare reduction of the brilliance (BR) of two pulse shortening schemes, namely, Femtoslicing and the PicoSwitch. Both schemes reduce the brilliance by lowering the number of photons available for experiments. This reduction stems from a limited efficiency η, the reduction of the repetition rate $\Delta\nu = f_{short}/f_{incident}$, and the pulse shortening ratio $D = \tau_{short}/\tau_{incident}$. The PicoSwitch implemented at the XPP-station at BESSY II yields the following parameters: $\eta = 5 \times 10^{-3}$, $\Delta\nu = 208\,\text{kHz}/1.25\,\text{MHz} = 1/6$, and $D = 5\,\text{ps}/100\,\text{ps} = 1/20$. In total, BR is 4.16×10^{-5}. In comparison, Femtoslicing yields the following parameters: $\eta = 0.7$, $\Delta\nu = 1\,\text{kHz}/1.25\,\text{MHz} = 8 \times 10^{-4}$, and $D = 100\,\text{fs}/100\,\text{ps} = 1/1000$.[28,29] In total, Femtoslicing yields a BR of 5.6×10^{-7}. The BR is more important for Femtoslicing compared to the PicoSwitch because the repetition rate cannot be increased to more than few kHz due to limits in the bunch recovery time[30] and because the sliced pulse is much shorter than the incident pulse. To better compare brilliance between both pulse shortening schemes, we suggest to compare the peak brilliance, i.e., to normalize the BR to the duration of the shorted pulse. For Femtoslicing this yields $5.6 \times 10^{-7}/100\,\text{fs} = 5.6 \times 10^6$ compared to $4.16 \times 10^{-5}/5\,\text{ps} = 8.3 \times 10^6$ for the PicoSwitch. The peak brilliance is in the same order of magnitude in both schemes. The PicoSwitch main advantage is the high repetition frequency while Femtoslicing benefits from a better efficiency. For the reduced charge (low-α) mode, the same reasoning yields a BR of 0.01 and a peak brilliance of 2×10^9, assuming a pulse duration of 5 ps. Low-α-mode yields the highest brilliance; however, it is only available few weeks per year in normal 3rd generation synchrotrons.

VI. CONCLUSION

In conclusion, we demonstrated ultrafast switching of hard x-rays at high repetition frequencies using a photoacoustic Bragg-switch. The device, which we call the PicoSwitch, is suitable for shortening x-ray pulses emitted by 3rd generation synchrotron sources. Our characterization yields a switching contrast of $C_{0,\infty} = 14$. Comparison of coherent phonon and dynamic x-ray simulations shows that

the measured contrast is reduced by a static noise background which stems from the limited flux available during our experiment. With an improved background, our analysis yields $C_{0,\infty} = 27$, which is sufficient to increase the temporal resolution at synchrotron facilities to few ps. The contrast may be optimized even further by increasing the excitation fluence as demonstrated by measurements at a table-top plasma x-ray source. The device operates at high repetition frequencies up to 208 kHz. Our measurements of PicoSwitch structures present a next step towards ultrafast active x-ray optical elements.

ACKNOWLEDGMENTS

[1]A. Aquila, R. Sobierajski, C. Ozkan, V. Hjkov, T. Burian, J. Chalupsk, L. Juha, M. Strmer, S. Bajt, M. T. Klepka, P. Duewski, K. Morawiec, H. Ohashi, T. Koyama, K. Tono, Y. Inubushi, M. Yabashi, H. Sinn, T. Tschentscher, A. P. Mancuso, and J. Gaudin, "Fluence thresholds for grazing incidence hard X-ray mirrors," Appl. Phys. Lett. **106**(24), 241905 (2015).

[2]I. Mohacsi, I. Vartiainen, M. Guizar-Sicairos, P. Karvinen, V. A. Guzenko, E. Müller, C. M. Kewish, A. Somogyi, and C. David, "Fabrication and characterization of high-efficiency double-sided blazed X-ray optics," Opt. Lett. **41**(2), 281–284 (2016).

[3]S.-R. Wu, Y. Hwu, and G. Margaritondo, "Hard-X-ray zone plates: Recent progress," Materials **5**(10), 1752 (2012).

[4]S. Stoupin, F. Lenkszus, R. Laird, K. Goetze, K.-J. Kim, and Y. Shvyd'ko, "Adaptive angular control of high-resolution X-ray optics," Proc. SPIE **7803**, 780307 (2010).

[5]J. P. Quintana, M. Hart, D. Bilderback, C. Henderson, D. Richter, T. Setterston, J. White, D. Hauserman, M. Krumrey, and H. Schulte-Schrepping, "Adaptive silicon monochromators for high-power insertion devices. Tests at CHESS, ESRF and HASYLAB," J. Synchrotron. Rad. **2**(1), 1–5 (1995).

[6]G. R. Lemaitre, "Optical design and active optics methods in astronomy," Opt. Rev. **20**(2), 103–117 (2013).

[7]L. E. Berman and M. Hart, "Adaptive crystal optics for high power synchrotron sources," Nucl. Instrum. Methods Phys. Res. Sec. A **302**(3), 558–562 (1991).

[8]V. V. Yashchuk, G. Y. Morrison, M. A. Marcus, E. E. Domning, D. J. Merthe, F. Salmassi, and B. V. Smith, "Performance optimization of a bendable parabolic cylinder collimating X-ray mirror for the ALS micro-XAS beamline 10.3.2," J. Synchrotron. Rad. **22**(3), 666–674 (2015).

[9]T. Goto, H. Nakamori, T. Kimura, Y. Sano, Y. Kohmura, K. Tamasaku, M. Yabashi, T. Ishikawa, K. Yamauchi, and S. Matsuyama, "Hard X-ray nanofocusing using adaptive focusing optics based on piezoelectric deformable mirrors," Rev. Sci. Instrum. **86**(4), 043102 (2015).

[10]A. Brooks, A. Wirth, E. Lintz, and J. Cavaco, "Design and fabrication of a high precision X-ray deformable mirror," Proc. SPIE **9208**, 92080E (2014).

[11]A. Rousse, C. Rischel, and J.-C. Gauthier, "Femtosecond X-ray crystallography," Rev. Mod. Phys. **73**, 17–31 (2001).

[12]E. Weckert, "The potential of future light sources to explore the structure and function of matter," IUCrJ **2**(2), 230–245 (2015).

[13]F. Zamponi, Z. Ansari, C. Korff Schmising, P. Rothhardt, N. Zhavoronkov, M. Woerner, T. Elsaesser, M. Bargheer, T. Trobitzsch-Ryll, and M. Haschke, "Femtosecond hard X-ray plasma sources with a kilohertz repetition rate," Appl. Phys. A **96**, 51–58 (2009).

[14]D. Schick, A. Bojahr, M. Herzog, C. Von, K. Schmising, R. Shayduk, W. Leitenberger, P. Gaal, and M. Bargheer, "Normalization schemes for ultrafast X-ray diffraction using a table-top laser-driven plasma source," Rev. Sci. Instrum. **83**, 025104 (2012).

[15]D. Schick, R. Shayduk, A. Bojahr, M. Herzog, C. von Korff Schmising, P. Gaal, and M. Bargheer, "Ultrafast reciprocal-space mapping with a convergent beam," J. Appl. Crystallogr. **46**(5), 1372–1377 (2013).

[16]R. W. Schoenlein, S. Chattopadhyay, H. H. W. Chong, T. E. Glover, P. A. Heimann, C. V. Shank, A. A. Zholents, and M. S. Zolotorev, "Generation of femtosecond pulses of synchrotron radiation," Science **287**(5461), 2237–2240 (2000).

[17]M. Herzog, D. Schick, W. Leitenberger, R. Shayduk, R. M. van der Veen, C. J. Milne, S. L. Johnson, I. Vrejoiu, and M. Bargheer, "Tailoring interference and nonlinear manipulation of femtosecond X-rays," New J. Phys. **14**(1), 013004 (2012).

[18]P. Gaal, D. Schick, M. Herzog, A. Bojahr, R. Shayduk, J. Goldshteyn, H. A. Navirian, W. Leitenberger, I. Vrejoiu, D. Khakhulin, M. Wulff, and M. Bargheer, "Time-domain sampling of X-ray pulses using an ultrafast sample response," Appl. Phys. Lett. **101**(109), 243106–221115 (2012).

[19]P. Gaal, D. Schick, M. Herzog, A. Bojahr, R. Shayduk, J. Goldshteyn, W. Leitenberger, I. Vrejoiu, D. Khakhulin, M. Wulff, and M. Bargheer, "Ultrafast switching of hard X-rays," J. Synchrotron. Rad. **21**(21), 380–385 (2014).

[20]M. Herzog, D. Schick, P. Gaal, R. Shayduk, C. von Korff Schmising, and M. Bargheer, "Analysis of ultrafast X-ray diffraction data in a linear-chain model of the lattice dynamics," Appl. Phys. A **106**(3), 489–499 (2012).

[21]D. Schick, A. Bojahr, M. Herzog, C. von Korff Schmising, R. Shayduk, and M. Bargheer, "UDKM1DSIM—A simulation toolkit for 1D ultrafast dynamics in condensed matter," Comput. Phys. Commun. **185**(2), 651–660 (2014).

[22]B. E. Warren, *X-ray Diffraction*, Addison-Wesley Series in Metallurgy and Materials Engineering (Dover Publications, 1969).

[23]J. Sellmann, J. Schwarzkopf, A. Kwasniewski, M. Schmidbauer, D. Braun, and A. Duk, "Strained ferroelectric nanbo3 thin films: Impact of pulsed laser deposition growth conditions on structural properties," Thin Solid Films **570**, 107–113 (2014).

[24]M. Reinhardt, A. Koc, W. Leitenberger, P. Gaal, and M. Bargheer, "Optimized spatial overlap in optical pump - X-ray probe experiments with high repetition rate using laser-induced surface distortions," J. Synchrotron. Rad. **23**, 474 (2016).

[25]H. Navirian, R. Shayduk, W. Leitenberger, J. Goldshteyn, P. Gaal, and M. Bargheer, "Synchrotron-based ultrafast x-ray diffraction at high repetition rates," Rev. Sci. Instrum. **83**(6), 063303 (2012).

[26]V. Holy, U. Pietsch, and T. Baumbach, *High-Resolution X-ray Scattering from Thin Films and Multilayers*, 1st ed. (Springer Tracts in Modern Physics. Springer, 1999).

[27]K. Holldack, T. Quast, S. Khan, and R. Mitzner, "Bunch shape diagnostics using femtoslicing," in *Proceedings of EPAC* (2006), p. THPLS016.

[28]C. Stamm, T. Kachel, N. Pontius, R. Mitzner, T. Quast, K. Holldack, S. Khan, C. Lupulescu, E. F. Aziz, M. Wienstruk, H. A. Drr, and W. Eberhardt, "Femtosecond modification of electron localization and transfer of angular momentum in nickel," Nat. Mater. **6**, 740-743 (2007).

[29]T. Quast, A. Firsov, and K. Holldack, "Upgrade of the BESSY femtoslicing source," in *Proceedings of PAC07* (2007), p. TUMPMN016.

[30]K. Holldack, J. Bahrdt, A. Balzer, U. Bovensiepen, M. Brzhezinskaya, A. Erko, A. Eschenlohr, R. Follath, A. Firsov, W. Frentrup, L. L. Guyader, T. Kachel, P. Kuske, R. Mitzner, R. Müller, N. Pontius, T. Quast, I. Radu, J.-S. Schmidt, C. Schüßler-Langeheine, M. Sperling, C. Stamm, C. Trabant, and A. Föhlisch, "FemtoSpeX: a versatile optical pump–soft X-ray probe facility with 100fs X-ray pulses of variable polarization," J. Synchrotron. Rad. **21**(5), 1090–1104 (2014).
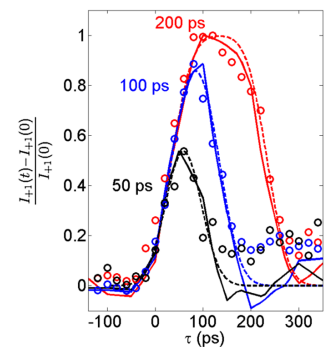
Article XV

Spatiotemporal coherent control of thermal excitations in solids

Mathias Sander, Marc Herzog, **Jan-Etienne Pudell**, Matias Bargheer, Norbert Weinkauf, Martin Pedersen, Gemma Elizabeth Newby, Jan Sellmann, Jutta Schwarzkopf, Valentin Besse, Vasily V. Temnov and Peter Gaal

X-ray reflectivity measurements of femtosecond laser-induced transient gratings (TG) are applied to demonstrate the spatiotemporal coherent control of thermally induced surface deformations on ultrafast time scales. Using grazing incidence x-ray diffraction we unambiguously measure the amplitude of transient surface deformations with sub-Åresolution. Understanding the dynamics of femtosecond TG excitations in terms of superposition of acoustic and thermal gratings makes it possible to develop new ways of coherent control in x-ray diffraction experiments. Being the dominant source of TG signal, the long-living thermal grating with spatial period Λ can be canceled by a second, time-delayed TG excitation shifted by $\Lambda/2$. The ultimate speed limits of such an ultrafast x-ray shutter are inferred from the detailed analysis of thermal and acoustic dynamics in TG experiments.

Spatiotemporal Coherent Control of Thermal Excitations in Solids

M. Sander,[1] M. Herzog,[1] J. E. Pudell,[1] M. Bargheer,[1,2] N. Weinkauf,[3] M. Pedersen,[4] G. Newby,[4] J. Sellmann,[5]
J. Schwarzkopf,[5] V. Besse,[6] V. V. Temnov,[6,7] and P. Gaal[3,2]

[1]*Institute for Physics and Astronomy, Universität Potsdam, Karl-Liebknecht-Straße 24-25, 14476 Potsdam, Germany*
[2]*Helmholtz-Zentrum Berlin for Materials and Energy GmbH, Wilhelm-Conrad-Röntgen Campus,
BESSY II, Albert-Einstein-Straße 15, 12489 Berlin Germany*
[3]*Institute for Solid State and Nanostructure Physics, Universität Hamburg, JungiusStraße 11, 20355 Hamburg, Germany*
[4]*European Synchrotron Radiation Facility ESRF, 71 Avenue des Martyrs 23800 Grenoble, France*
[5]*Institute for Crystal Growth, Max-Born-Straße 2, 12489 Berlin, Germany*
[6]*IMMM CNRS 6283, Université du Maine, 72085 Le Mans cedex, France*
[7]*Groupe d'Etude de la Matière Condensée (GEMaC), Université de Versailles-Saint Quentin en Yvelines,
CNRS UMR 8635, Université Paris-Sacley, 45 avenue des Etats-Unis, 78035 Versailles Cedex, France*

X-ray reflectivity measurements of femtosecond laser-induced transient gratings (TG) are applied to demonstrate the spatiotemporal coherent control of thermally induced surface deformations on ultrafast time scales. Using grazing incidence x-ray diffraction we unambiguously measure the amplitude of transient surface deformations with sub-Å resolution. Understanding the dynamics of femtosecond TG excitations in terms of superposition of acoustic and thermal gratings makes it possible to develop new ways of coherent control in x-ray diffraction experiments. Being the dominant source of TG signal, the long-living thermal grating with spatial period Λ can be canceled by a second, time-delayed TG excitation shifted by $\Lambda/2$. The ultimate speed limits of such an ultrafast x-ray shutter are inferred from the detailed analysis of thermal and acoustic dynamics in TG experiments.

Ultrafast photoacoustics [1,2] allows for the application of strain to a crystal lattice on ultrashort time and length scales. Numerous studies have investigated coherent and incoherent phonon dynamics and the coupling of lattice deformations to electronic [3], optical [4], magnetic [5–7], or plasmonic [8,9] degrees of freedom. Strain-induced phenomena may be used to discover new material properties and develop new applications, for example, the modification of optical and electronic properties in semiconductor nanostructures [10]. Surface acoustic waves (SAWs) are often employed as a source of lattice strain. They can be generated [11] and controlled [12] optically via the excitation of transient gratings (TGs) [13,14]. Recently, these TG excitations have been used to probe heat transport in suspended thin films [15] and magnetoelastic coupling in thin nickel films [16–18]. Optical excitation of a solid generates not only coherent sound waves but also incoherent thermal strain. Coherent excitations can be controlled in amplitude and phase by series of light pulses in the time domain, which is labeled temporal coherent control [19]. The main fraction of the deposited optical energy is stored in incoherent excitations of the lattice, i.e., heat [20,21], which can consequently not be controlled by a temporal sequence of light pulses. This thermal lattice excitation often generates a background, which makes is difficult to precisely observe the coherent acoustic signal in purely optical experiments.

In this Letter we demonstrate, for the first time, the coherent control of incoherent, thermal transient gratings. We apply spatiotemporal coherent control showing that the spatial part of coherent control adds a new degree of freedom to control the amplitude and the phase of a thermally deformed surface. This is clearly a new approach that introduces the concept of spatial coherent control to the dynamics of incoherent excitations on ultrafast time scales, a phenomenon impossible to achieve with temporal coherent control only. We also demonstrate the control of a transient thermal grating on a time scale faster than the oscillation of the simultaneously excited coherent acoustic modes. Our new quantitative method allows for decomposing the coherent and incoherent dynamics in the sample by measuring the amplitude of the surface excursion with sub-Å precision and ≈ 70 ps temporal resolution. The modification of x-ray diffraction intensity from laser-generated TGs is exploited to implement an ultrafast hard x-ray shutter. Whereas our data confirm the generation of Rayleigh SAWs and surface skimming longitudinal waves (SSLW) [16], the most intriguing results deal with coherent control of the *incoherent, thermal* transient grating. The latter becomes possible by using a second time-delayed and spatially phase-shifted TG excitation.

The optical TG excitation and experimental setup are shown in Fig. 1(a). The sample was a 60-nm strontium titanate (STO) on 150-nm strontium ruthenate (SRO) thin film system grown on dysprosium scandate (DSO) [22]. The energy of the pump laser is absorbed only in the SRO film, which has a penetration depth of 44 nm [23], i.e., shorter than the film thickness. The photoacoustic properties

075901-1

of these materials are well understood. In particular, we studied nanoscale heat diffusion [21], thermoelastic effects [24], and coherent phonon dynamics [25–29] in SRO, STO, and similar materials. We assign a characteristic wave vector $|\vec{q}_\parallel| = 2\pi/\Lambda$ to the optically generated surface distortion with periodicity Λ. $\vec{q}_\parallel$ is directed in the plane of the sample and in the diffraction plane of the incident x-ray beam. The periodic distortion results in a momentum transfer to the reflected x-ray beam, $\vec{k}_{\text{out}} - \vec{k}_{\text{in}} = \vec{q}_\perp \pm \vec{q}_\parallel$. We emphasize the conceptional difference to inelastic x-ray diffraction by phonons [30]: instead of a specific reciprocal lattice vector $\vec{G}$, $\vec{q}_\perp$ denotes the recoil momentum due to specular reflection. It is directed perpendicular to the sample surface and of continuous magnitude $\vec{q}_\perp = 2k_{\text{in}}\sin\alpha_i$. The Ewald construction of the scattering vector is shown in Fig. 1(b). It reveals that the x-ray photons diffracted by the periodic surface excursion (PSE) exhibit an exit angle $\alpha_f \neq \alpha_i$. Indeed, a typical detector image presented in Fig. 1(a) shows a first-order diffraction spot (orange solid line) above the specular total reflection (black solid line). Figure 1(c) shows a differential x-ray reflectivity measurement $R(\tau, \alpha_i) - R(-\infty, \alpha_i)$ at a pump-probe delay of $\tau = 500$ ps around the critical angle α_c of total reflection. Evaluation of the scattering condition for a spatial period of $\Lambda = 8.8$ μm yields the blue and black dashed curves, which are in excellent agreement with the angular position of the specular and $\pm$1st-order reflection, respectively. Having established the capability of picosecond x-ray reflectivity measurements to detect a PSE and to quantify its spatial periodicity, we now investigate the dynamics of impulsively excited PSEs. The black symbols in Fig. 2(a) represent the time-dependent intensity of the first-order diffraction peak $I_{+1}(\tau)$ at $\alpha_i = 0.16°$ after TG excitation with a period of $\Lambda = 4.4$ μm and an incident
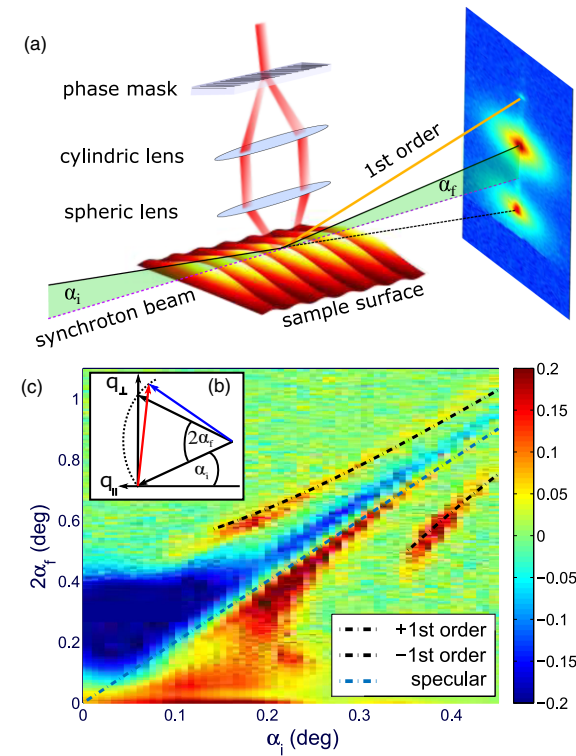

FIG. 1. (a) Experimental setup. 70 ps x-ray pulses are delivered from the synchrotron storage ring of the European Synchrotron Radiation Facility (ESRF). $\pm$1st diffraction orders of an ultrashort laser pulse are imaged onto the surface of the sample using a cylindrical and spherical lens in $4f$ geometry and generate a spatially periodic distortion at the surface. The x-ray pulses impinge the sample at grazing incidence angles and diffract in a specular beam and $\pm$1st diffraction orders. A fraction of the direct beam is also visible at the bottom of the detector image. (b) Ewald construction of the scattering vector (red arrow). (c) Difference of x-ray reflectivity measurement at a pump-probe delay τ of 500 ps and a characteristic wave vector $\vec{q}_\parallel = 2\pi/\Lambda$, where $\Lambda = 8.8$ μm. The measured specular reflection as well as $\pm$1st order correspond to the theoretically expected positions (black and blue dashed lines).
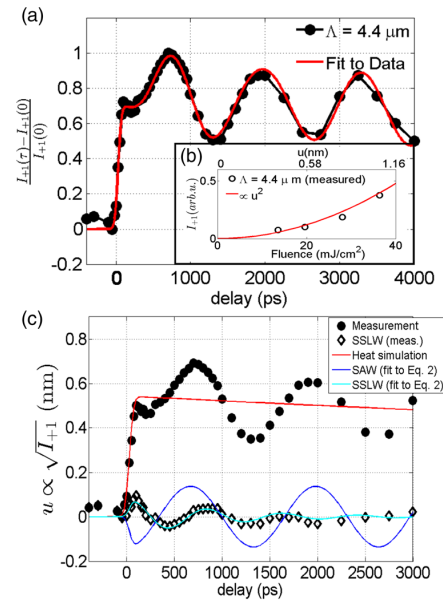

FIG. 2. (a) Time-resolved relative diffracted intensity in the +1st order I_{+1} (black dots) and fit to the data using Eq. (2) (red solid line). The TG period was $\Lambda = 4.4$ μm. (b) Calculated diffraction efficiency (symbols) versus surface amplitude u. The diffraction model is described in the Supplemental Material [38]. The red solid line shows a quadratic surface amplitude dependence. (c) Square root of the measured intensity $\sqrt{I_{+1}}$, which corresponds to the surface distortion (black dots). The y scale is converted to a surface distortion amplitude with the empirical calibration factor $0.02[\%/(\text{mJ}/\text{cm}^2)]$. The simulated thermal background, the SAW, and the SSLW are shown in the red, blue, and light blue solid lines, respectively. The black diamonds show the measured data after subtraction of thermal background and SAW.

fluence of 19.6 mJ/cm^2. Note that $\alpha_i < \alpha_c$; i.e., only the evanescent field of the incident x-ray beam penetrates the sample, and the main part of the beam is diffracted from the surface [31]. Upon TG excitation ($\tau = 0$), we observe a steplike increase of the diffracted intensity. The initial step, which occurs with the temporal resolution of the experiment, is followed by a signal decrease that lasts for 150 ps. Subsequently we observe oscillations of the diffracted intensity with a period of $T_{SAW} = 1310$ ps. Because of the short x-ray penetration depth in our surface diffraction experiment, we rely on kinematic theory [32–35] and find the following expression for the diffracted intensity from a PSE under grazing incidence below the critical angle $\alpha_i < \alpha_c$:

$$I_1 = \left| \int_{\parallel} e^{-i[q_{\parallel} \cdot r_{\parallel} + (\Delta\varphi/2)\sin(\frac{2\pi}{\Lambda} r_{\parallel})]} dr_{\parallel} \right|^2 = \left| J_1\left(\frac{\Delta\varphi}{2}\right) \right|^2. \quad (1)$$

$J_1(\Delta\varphi/2)$ is the first-order Bessel function and $\Delta\varphi$ denotes the phase difference between x-ray wave fields reflected from the maximum and the minimum of the PSE. For small arguments $\Delta\varphi/2$, I_1 is proportional to the square of the time-dependent surface amplitude $u(\tau)$, as evidenced by Fig. 2(b). Hence, in the limit of small deformations, the x-ray intensity diffracted from the PSE is directly proportional to the squared surface amplitude $I_{+1} \propto u(\tau)^2$. A quantitative comparison of experimental data with theoretical models [20,36,37] shows that an optical excitation fluence of 1 mJ/cm^2 results in a lattice strain of $0.2 \pm 0.05\%$. We derive the calibration factor in the Supplemental Material [38]. With our excitation fluence of 19.6 mJ/cm^2 and a thickness of 150 nm of the absorbing SRO layer, we determine the maximum surface amplitude to 0.57 nm. The y scale of Fig. 2(c) is an absolute scale that quantifies the surface distortion in nanometers.

Impulsive optical excitation of an absorbing medium with a spatially periodic intensity distribution results in a time-dependent surface deformation $u(\tau)$ of the form $u(\tau) = u_h \exp(-\alpha_h\tau) + u_c(\tau)$, where the first term accounts for the thermal grating. The coherent part u_c is the sum of SAW and SSLW contributions, respectively [16]:

$$u_c(\tau) = u_{SAW} \cos(\omega_{SAW}\tau + \varphi_{SAW})$$
$$+ u_{SSLW} \cos(\omega_{SSLW}\tau + \varphi_{SSLW}) \exp(-\alpha_{SSLW}\tau). \quad (2)$$

With the diffraction model outlined above, we can interpret all components that result from the decomposition of the measured surface amplitude $u(\tau)$ shown in the black dotted curve in Fig. 2(c). To model the thermal background $u_h(\tau)$ of the surface amplitude, we numerically solve the two-dimensional heat diffusion equation for one period of the PSE with periodic boundary conditions. The initial temperature profile into the depth of the absorbing SRO thin film is determined by the optical penetration depth and decays exponentially. We choose the in-plane and out-of-plane thermal conductance of SRO and DSO in order to reproduce the slow decay of the incoherent signal contribution (see Supplemental

Material [38]). By subtracting the simulated thermal background [red solid line in Fig. 2(c)], we obtain the coherent part of the time-dependent surface amplitude, which we decompose in two modes by fitting Eq. (2) to our data. The blue solid line in Fig. 2(c) represents the amplitude u_{SAW} of the Rayleigh wave propagating parallel to the surface. Further subtraction of the Rayleigh wave from the coherent signal reveals a strongly damped mode with a decay constant of 500 ps and a period of $T_{SSLW} = 800$ ps shown by the black diamonds (measurement) and the light blue solid curve (fit to data) in Fig. 2(c). We assign this feature to the SSLW that is generated by the optical excitation and propagates into the substrate. The results in Fig. 2 clearly demonstrate the ability to decompose the full surface dynamics into individual coherent acoustic and incoherent thermal components.

In the following we address the incoherent thermal background to fully control the surface deformation in a coherent control scheme. In particular, our experiment entails controlling the lateral heat flow in the sample by a series of consecutive TG excitations with defined time delay τ_{12}. In addition, we control the spatial phase $\Theta = 2\pi\Delta x/\Lambda$ by adjusting the angle of incidence of the second pulse on the transmission phase mask (see Supplemental Material [38]). Δx denotes the distance between the maxima of first and second TG excitation. Examples for $\Theta = \pi$ and $\Theta = 0$ are shown in Figs. 3(a) and 3(b), where the PSE is eliminated and enhanced, respectively. An experimental demonstration of this novel spatiotemporal TG coherent control is shown in Fig. 3(c), where the first-order diffracted intensity at a delay $\tau = \tau_{12} + 150$ ps is plotted as a function of spatial phase Θ. The delay between
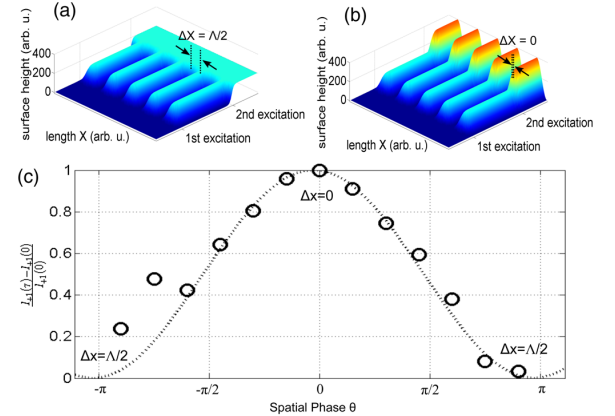

FIG. 3. Coherent control of a *thermal* transient grating using two TG excitations. (a),(b) The first excitation generates a thermal grating at $\tau = 0$. The second excitation at $\tau_{12} = 200$ ps creates another thermal grating shifted by $\Delta x = \Lambda/2$ (a) and $\Delta x = 0$ (b), thus canceling (enhancing) the first grating. (c) Diffracted intensity I_{+1} at a pump-probe delay of $\tau = \tau_{12} + 150$ ps versus the spatial phase Θ. The second TG excitation impinges the sample at a delay of $\tau_{12} = 200$ ps.

the first and second TG excitation τ_{12} is 200 ps. The experimental data follow the expected $(1 + \cos\Theta)$ dependence (dashed line) and thus evidence spatial coherent control of a thermal grating on ultrafast time scales.

Finally, we demonstrate coherent control of the thermal grating along the temporal degree of freedom by keeping the spatial phase $\Theta = \pm\pi$ constant and by changing the time delay τ_{12} between the first and second TG excitation. We restrict the experiment to pump-probe delays much shorter than the period of the coherent modes, i.e., $\tau_{12} \ll T_{SAW}, T_{SSLW}$. Hence the temporal phase difference of the coherent modes launched by either TG excitation nearly vanishes. The total spatiotemporal phase difference results in complete destructive interference of *both* the thermal grating and of the coherent acoustic waves because the spatial alignment introduces a phase shift of π.

The above considerations are fully confirmed by the experimental data (symbols) shown in Fig. 4(a), which evidence an almost complete elimination of the first-order diffraction efficiency by the second TG excitation for time delays $\tau_{12} = 50, 100, 200$ ps. In particular, all traces reveal that the transient PSE opens a temporal gate for incident x-ray photons that is spanned by the first and second TG excitation. The duration of the gate can be controlled by τ_{12} even to durations shorter than the incident x-ray pulse. However, the measured gate width cannot be shorter than the duration of the x-ray probe pulse [26,28], although individual x-ray pulses are truncated by the gate. This reduces the signal strength and decreases the signal-to-noise ratio in this measurement. To prove that the recorded data shown in Fig. 4(a) evidence the coherent superposition of two time-delayed laser-induced surface gratings, we construct the corresponding gate function by summation of two replica of the measured transients for a single-TG
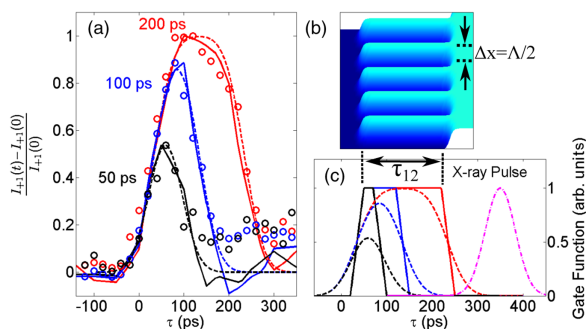
excitation such as shown in Fig. 2 with appropriate relative sign and time delay. For a spatial phase $\Theta = \pm\pi$, the second TG excitation reduces the amplitude of the surface deformation, which we incorporate by a negative sign of the second surface amplitude response. We further add the relative time delay τ_{12} to the second transient. This approach, which is explained in more detail in the Supplemental Material [38], is solely based on experimentally measured transients and yields the solid lines in Fig. 4(a). We observe a very good agreement between the measured and the constructed gate functions. The dashed lines in Fig. 4(a) result from a convolution of gate functions shown in Fig. 4(c) with a Gaussian-shaped x-ray probe pulse. This simple model also yields very good representation of the experimental data.

In conclusion, we demonstrated full control over a thermally excited incoherent surface deformation by introducing spatiotemporal coherent control in ultrafast laser-induced TG experiments. Our new approach allows for a separation of the coherent and incoherent response of the optically generated lattice excitation. We show that the incoherent thermal grating can be controlled on a time scale significantly shorter than the oscillation period of the coherent modes, which we exploit to implement an ultrafast shutter in grazing incidence x-ray diffraction geometry. The presented concept is not limited to thin metallic transducers deposited on dielectric substrates: it will work on any optically opaque bulk sample. However, the ultimate speed of an x-ray shutter will be determined by the acoustic propagation time through the depth of the laser-generated stress. With the demonstrated outstanding subangstrom spatial precision and a sub-100-ps instrumental time resolution, we are looking forward toward applying an ultrafast x-ray gating technique to resolve the dynamics of strain- and heat-induced phenomena in solids and nanostructures.

FIG. 4.   Spatiotemporal control of the thermal and coherent surface grating. The relative delay between first and second TG excitation τ_{12} is 200 ps (red), 100 ps (blue), and 50 ps (black), respectively. (a) Schematic view of the transient surface distortion. (b) Construction of the gate function (dashed lines) by convolution of the incident x-ray pulse (pink dash-dotted line) with the gate that is spanned by two TG excitations. (c) Comparison of measurement (symbols) and theoretical gate functions (solid and dashed lines).

[1] C. Thomsen, H. T. Grahn, H. J. Maris, and J. Tauc, Phys. Rev. B **34**, 4129 (1986).

[2] P. Ruello and V. E. Gusev, Ultrasonics **56**, 21 (2015).

[3] M. Wei, J. B. Kinzel, F. J. R. Schlein, M. Heigl, D. Rudolph, S. Morktter, M. Dblinger, M. Bichler, G. Abstreiter, J. J. Finley, G. Koblmller, A. Wixforth, and H. J. Krenner, Nano Lett. **14**, 2256 (2014).

[4] D. J. Singh, Q. Xu, and K. P. Ong, Appl. Phys. Lett. **104**, 011910 (2014).

[5] A. V. Scherbakov, A. S. Salasyuk, A. V. Akimov, X. Liu, M. Bombeck, C. Bruggemann, D. R. Yakovlev, V. F. Sapega, J. K. Furdyna, and M. Bayer, Phys. Rev. Lett. **105**, 117204 (2010).

[6] J.-W. Kim, M. Vomir, and J.-Y. Bigot, Phys. Rev. Lett. **109**, 166601 (2012).

[7] L. Thevenard, E. Peronne, C. Gourdon, C. Testelin, M. Cubukcu, E. Charron, S. Vincent, A. Lemaitre, and B. Perrin, Phys. Rev. B **82**, 104422 (2010).

[8] V. V. Temnov, C. Klieber, K. A. Nelson, T. Thomay, V. Knittel, A. Leitenstorfer, D. Makarov, M. Albrecht, and R. Bratschitsch, Nat. Commun. **4**, 1468 (2013).

[9] V. V. Temnov, I. Razdolski, T. Pezeril, D. Makarov, D. Seletskiy, A. Melnikov, and K. A. Nelson, J. Opt. **18**, 093002 (2016).

[10] Y. Wang, Y. Chen, H. Li, X. Li, H. Chen, H. Su, Y. Lin, Y. Xu, G. Song, and X. Feng, ACS Nano **10**, 8199 (2016).

[11] J. A. Rogers, A. A. Maznev, M. J. Banet, and K. A. Nelson, Annu. Rev. Mater. Sci. **30**, 117 (2000).

[12] M. Fayer, IEEE J. Quantum Electron. **22**, 1437 (1986).

[13] A. Vega-Flick, J. K. Eliason, A. A. Maznev, A. Khanolkar, M. Abi Ghanem, N. Boechler, J. J. Alvarado-Gil, and K. A. Nelson, Rev. Sci. Instrum. **86**, 123101 (2015).

[14] Y.-c. Shen and P. Hess, J. Appl. Phys. **82**, 4758 (1997).

[15] A. Vega-Flick, R. A. Duncan, J. K. Eliason, J. Cuffe, J. A. Johnson, J.-P. M. Peraud, L. Zeng, Z. Lu, A. A. Maznev, E. N. Wang, J. J. Alvarado-Gil, M. Sledzinska, C. M. Sotomayor Torres, G. Chen, and K. A. Nelson, AIP Adv. **6**, 121903 (2016).

[16] J. Janušonis, C L. Chang, T. Jansma, A. Gatilova, V. S. Vlasov, A. M. Lomonosov, V. V. Temnov, and R. I. Tobey, Phys. Rev. B **94**, 024415 (2016).

[17] J. Janusonis, T. Jansma, C. L. Chang, Q. Liu, A. Gatilova, A. M. Lomonosov, V. Shalagatskyi, T. Pezeril, V. V. Temnov, and R. I. Tobey, Sci. Rep. **6**, 29143 (2016).

[18] C. L. Chang, A. M. Lomonosov, J. Janusonis, V. S. Vlasov, V. V. Temnov, and R. I. Tobey, Phys. Rev. B **95**, 060409(R) (2017).

[19] V. Blanchet, C. Nicole, M. A. Bouchene, and B. Girard, Phys. Rev. Lett. **78**, 2716 (1997).

[20] M. Herzog, D. Schick, P. Gaal, R. Shayduk, C. von Korff Schmising, and M. Bargheer, Appl. Phys. A **106**, 489 (2012).

[21] R. Shayduk, H. A. Navirian, W. Leitenberger, J. Goldshteyn, I. Vrejoiu, M. Weinelt, P. Gaal, M. Herzog, C. von Korff Schmising, and M. Bargheer, New J. Phys. **13**, 093032 (2011).

[22] J. Sellmann, J. Schwarzkopf, A. Kwasniewski, M. Schmidbauer, D. Braun, and A. Duk, Thin Solid Films A **570**, 107 (2014).

[23] D. Schick, M. Herzog, A. Bojahr, W. Leitenberger, A. Hertwig, R. Shayduk, and M. Bargheer, Structural Dynamics **1**, 064501 (2014).

[24] H. A. Navirian, D. Schick, P. Gaal, W. Leitenberger, R. Shayduk, and M. Bargheer, Appl. Phys. Lett. **104**, 021906 (2014).

[25] R. Shayduk, M. Herzog, A. Bojahr, D. Schick, P. Gaal, W. Leitenberger, H. Navirian, M. Sander, J. Goldshteyn, I. Vrejoiu, and M. Bargheer, Phys. Rev. B **87**, 184301 (2013).

[26] P. Gaal, D. Schick, M. Herzog, A. Bojahr, R. Shayduk, J. Goldshteyn, H. A. Navirian, W. Leitenberger, I. Vrejoiu, D. Khakhulin, M. Wulff, and M. Bargheer, Appl. Phys. Lett. **101**, 243106 (2012).

[27] P. Gaal, D. Schick, M. Herzog, A. Bojahr, R. Shayduk, J. Goldshteyn, W. Leitenberger, I. Vrejoiu, D. Khakhulin, M. Wulff, and M. Bargheer, J. Synchrotron Radiat. **21**, 380 (2014).

[28] M. Sander, A. Koc, C. T. Kwamen, H. Michaels, A. v. Reppert, J. Pudell, F. Zamponi, M. Bargheer, J. Sellmann, J. Schwarzkopf, and P. Gaal, J. Appl. Phys. **120**, 193101 (2016).

[29] M. Herzog, A. Bojahr, J. Goldshteyn, W. Leitenberger, I. Vrejoiu, D. Khakhulin, M. Wulff, R. Shayduk, P. Gaal, and M. Bargheer, Appl. Phys. Lett. **100**, 094101 (2012).

[30] A. Bojahr, M. Herzog, S. Mitzscherling, L. Maerten, D. Schick, J. Goldshteyn, W. Leitenberger, R. Shayduk, P. Gaal, and M. Bargheer, Opt. Express **21**, 21188 (2013).

[31] B. E. Warren, *X-Ray Diffraction* (Dover Publications, New York, 1969).

[32] A. Madsen, T. Seydel, M. Tolan, and G. Grübel, J. Synchrotron Radiat. **12**, 786 (2005).

[33] J.-D. Nicolas, T. Reusch, M. Osterhoff, M. Sprung, F. J. R. Schülein, H. J. Krenner, A. Wixforth, and T. Salditt, J. Appl. Crystallogr. **47**, 1596 (2014).

[34] D. Irzhak and D. Roshchupkin, J. Appl. Phys. **115**, 244903 (2014).

[35] D. V. Roshchupkin, A. I. Erko, L. Ortega, and D. V. Irzhak, Appl. Phys. A **94**, 477 (2009).

[36] M. Herzog, D. Schick, W. Leitenberger, R. Shayduk, R. M. van der Veen, C. J. Milne, S. L. Johnson, I. Vrejoiu, and M. Bargheer, New J. Phys. **14**, 013004 (2012).

[37] D. Schick, A. Bojahr, M. Herzog, R. Shayduk, C. von Korff Schmising, and M. Bargheer, Comput. Phys. Commun. **185**, 651 (2014).

[38] See Supplemental Material at http://link.aps.org/supplemental/10.1103/PhysRevLett.119.075901 for the description of the experimental apparatus and the theory of x-ray diffraction on phase gratings.

Article XV – Supplemental Material

Supplemental Materials for Spatio-temporal coherent control of thermal excitations in solids

M. Sander,[1] M. Herzog,[1] J. E. Pudell,[1] M. Bargheer,[1,2] N. Weinkauf,[3] M. Pedersen,[4] G. Newby,[4] J. Sellmann,[5] J. Schwarzkopf,[5] V. Besse,[6] V. V. Temnov,[6,7] and P. Gaal[3,2]

[1]*Institute for Physics and Astronomy, Universität Potsdam,*
Karl-Liebknecht-Str. 24-25, 14476 Potsdam, Germany

[2]*Helmholtz-Zentrum Berlin for Materials and Energy GmbH,*
Wilhelm-Conrad-Röntgen Campus, BESSY II,
Albert-Einstein-Str. 15, 12489 Berlin Germany

[3]*Institute for Solid State and Nanostructure Physics,*
Universität Hamburg, Jungiusstr. 11, 20355 Hamburg, Germany

[4]*European Synchrotron Radiation Facility ESRF,*
71 Avenue des Martyrs 23800 Grenoble, France

[5]*Institute for Crystal Growth, Max-Born-Str. 2, 12489 Berlin, Germany*

[6]*IMMM CNRS 6283, Université du Maine, 72085 Le Mans cedex, France*

[7]*Groupe d'Etude de la Matière Condensée (GEMaC),*
Université de Versailles-Saint Quentin en Yvelines,
CNRS UMR 8635, Université Paris-Sacley,
45 avenue des Etats-Unis, 78035 Versailles Cedex, France

1

SUPPLEMENTAL MATERIAL

I. STRAIN CALIBRATION

Our measurement of the surface amplitude $u(\tau)$ relies on knowledge of the generated strain by an absorbed excitation laser pulse. We employ a linear chain of masses and springs[? ?] to model the propagation of coherent strain waves in our sample. The model yields a spatio-temporal strain map that is shown in Fig. S1 a). The total expansion is calculated by

$$u(\tau) = \sum_n < \frac{\Delta c(\tau)}{c_0} > |_n \cdot c_n \cdot N_n \tag{1}$$

where n denotes a sample layer, i.e., STO, SRO or DSO. $\frac{\Delta c(\tau)}{c_n}$ is the time-dependent strain calculated from the masses and springs model, c_n is the out-of-plane lattice parameter and N_n is the number of unitcells that compose the layer of material n. Lattice constants for the thin films are $3.905\,\mathring{A}$ for STO and $3.9045\,\mathring{A}$ for SRO. Other relevant parameters are given in Table I.

II. NUMERICAL SIMULATION

The heat transfer in our sample is is modeled using the heat diffusion equation,

$$\rho C \frac{\partial T}{\partial t} + \rho C \mathbf{u}.\nabla T + \nabla.\mathbf{q} = 0, \tag{2}$$

where ρ is the density, T is the temperature, C is the heat capacity, $\mathbf{u}$ is the field velocity,

$$\mathbf{q} = -\kappa \nabla T, \tag{3}$$

is the heat flux vector, κ is the thermal conductivity and ∇ is the differential operator defines for x and z direction. The convention used to name the space dimensions corresponds to the one shown in Fig.2. The sample is periodic in the x-dimension and the front and the back are isolated (i.e. there is no heat exchange at front and at the back).

The simulations have been done using COMSOL Multiphysics. The parameters used are defined in the Table I. The spatio-temporal temperature distribution in $SrRuO_3$ layer a few picoseconds after laser excitation is defined as

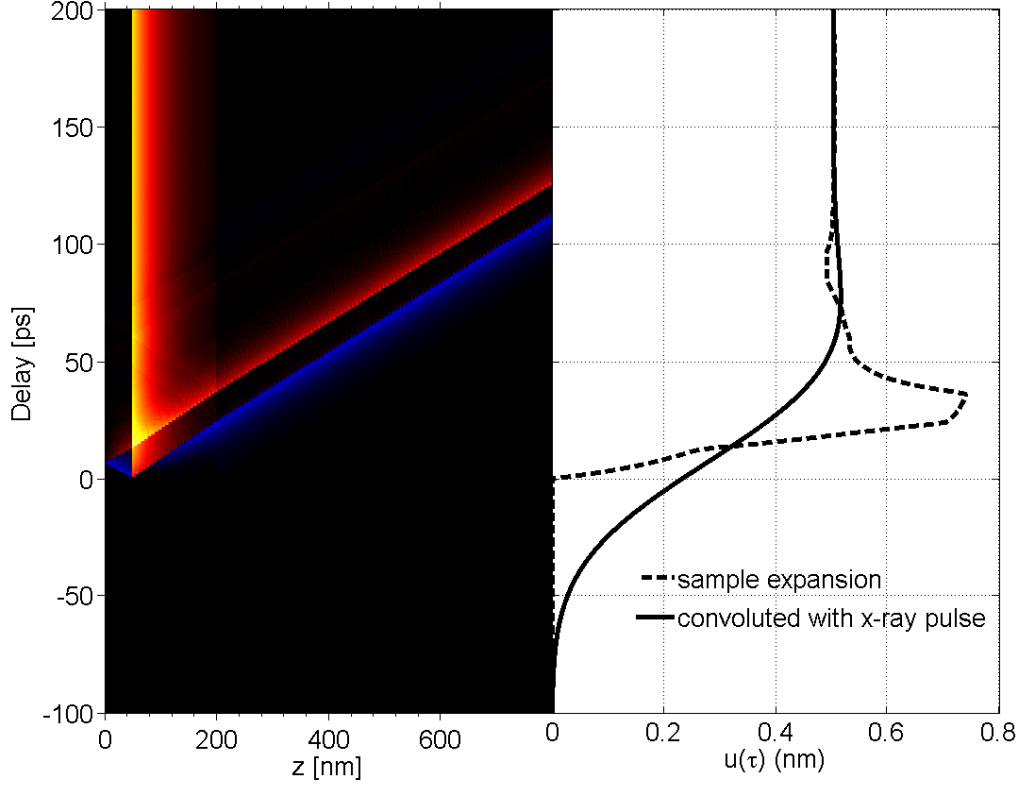$$T_2(x, z, t = 0) = T_0 + \Delta T \exp(-z/\delta_{p2})(\sin(2\pi x/\Lambda) + 1)/2, \tag{4}$$

2

FIG. 1: Supplemental Material, Fig. S3

where T_0 is the initial temperature, ΔT is the maximum temperature rise, δ_{p2} is the laser penetration depth in $SrRuO_3$ layer, Λ is the transient grating period. In order to optimize the computational time, we reduce the size of DSO layer from 500 μm to 3 μm. We did not observe any deviations with simulations assuming a thicker DSO layer. Using periodic boundary conditions we consider only one TG period sampled with 300 elements in x-direction. The z-axis is discretized with 20 elements for the STO, 60 elements for SRO and 75 elements for DSO layer, respectively. The time mesh is not equidistant; we used the generalized $-\alpha$ method available in COMSOL Multiphysics Modul in order to reduce the computation time. The initial time step equals to 0.1 ps and can change depending on the numerical convergence of the solution.

The data analysis was performed using Matlab. We calculate the thermal contribution
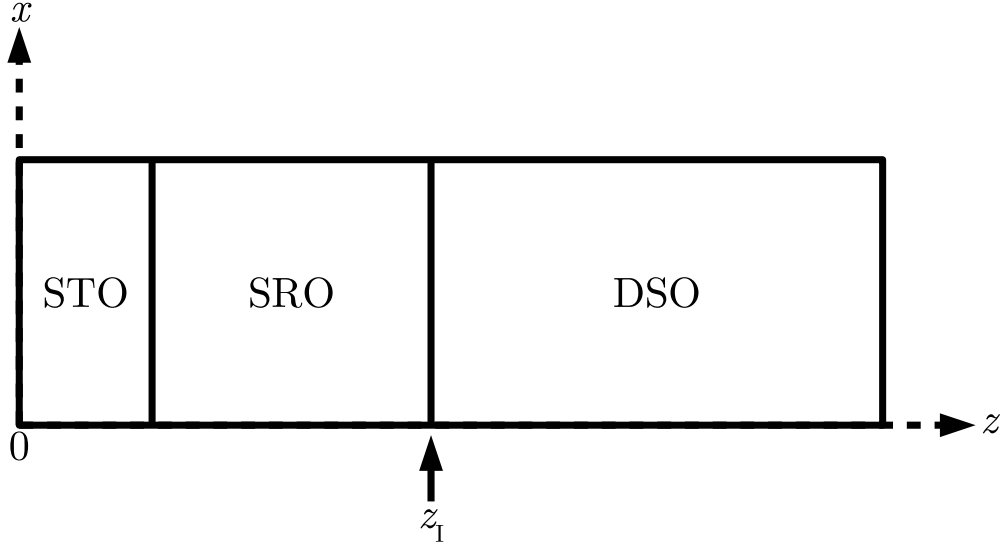
3

FIG. 2: Supplemental Material, Fig. S4 Illustration of the sample where STO corresponds to SrTiO$_3$ layer, SRO corresponds to SrRuO$_3$ and DSO corresponds to DyScO$_3$. This figure shows the convention for x and z direction used in the simulation. z_I corresponds to the interface between SRO's layer and STO's layer.

to the surface variation,

$$\Delta L\left(x,t\right) = \int_{z=0}^{z=L_1+L_2+L_3} \left[T\left(x,z,t\right) - T_0\right]\alpha(z)dz, \tag{5}$$

where α is the thermal expansion coefficient. Its value change as we consider the first, the second or the third layer. The thermal contribution to the surface variation is

$$u_{th}\left(t\right) = \Delta L(x_{\max}, t) - \Delta L(x_{\min}, t), \tag{6}$$

where $x_{\max}$ (respectively, $x_{\min}$) is the position along the x-dimension where the maximum (respectively, minimum) temperature is reach at z_I (i.e. the interface between the SRO and the DSO layers). We compare $u_{th}\left(t\right)$ to the experimental curve. The parameters used to fit the experimental curve are the SRO's heat capacity (C_2), SRO's and DSO's thermal conductivity (κ_2 and κ_3) and the Kapitza resistance (R_K (i.e. the interfacial thermal resistance). The best fitting is achieved with $C_2 = 460$ J/(kg.K), $\kappa_2 = 10$ W/(m.K)[?], $\kappa_3 = 30$ W/ (m.K) and $R_K = 5 \times 10^{-10}$.

4

Layer	Parameter	Value
Whole sample	Grating period	$\Lambda = 4.4\ \mu\mathrm{m}$
	Initial temperature	$T_0 = 293,15\ \mathrm{K}$
	Kapitza resistance	Fitting parameter
SrTiO$_3$ (1)	Thickness	$L_1 = 60\ \mathrm{nm}$
	Laser penetration depth	$\delta_{\mathrm{p}1} = \infty$
	Thermal expansion coefficient	$\alpha_1 = 1 \times 10^{-5}$
	Thermal conductivity	$\kappa_1 = 12\ \mathrm{W/(m.K)}$
	Density	$\rho_1 = 5.11 \times 10^3\ \mathrm{kg/m^3}$
	Heat capacity	$C_1 = 530\ \mathrm{J/(kg.K)}$
	Initial temperature distribution	$T_1(x, z, t = 0) = T_0$
SrRuO$_3$ (2)	Thickness	$L_2 = 150\ \mathrm{nm}$
	Laser penetration depth	$\delta_{\mathrm{p}2} = 46\ \mathrm{nm}$
	Thermal expansion coefficient	$\alpha_2 = 1.05 \times 10^{-5}$
	Thermal conductivity	Fitting parameter
	Density	$\rho_2 = 6.5 \times 10^3\ \mathrm{kg/m^3}$
	Heat capacity	Fitting parameter
	Initial temperature distribution	$T_2(x, z, t = 0)$ (see eq.(4))
DyScO$_3$ (3)	Thickness	$L_3 = 3\ \mu\mathrm{m}$
	Laser penetration depth	$\delta_{\mathrm{p}3} = \infty$
	Thermal expansion coefficient	$\alpha_3 = 8.4 \times 10^{-6}$
	Thermal conductivity	Fitting parameter
	Density	$\rho_3 = 6.9 \times 10^3\ \mathrm{kg/m^3}$
	Heat capacity	$C_3 = 650\ \mathrm{J/(kg.K)}$
	Initial temperature distribution	$T_3(x, z, t = 0) = T_0$

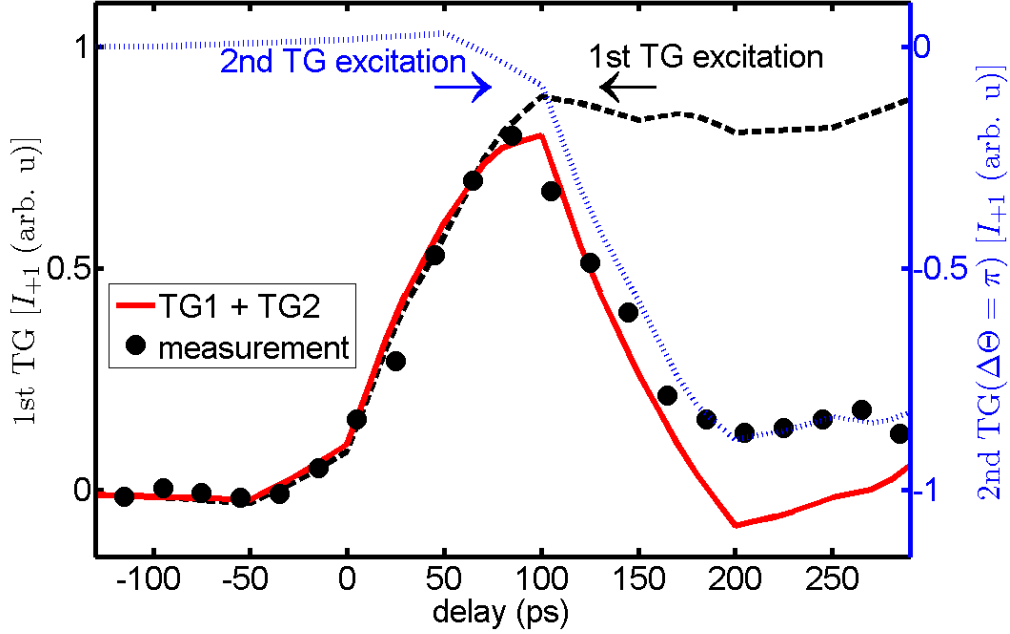TABLE I: Parameter's value used for the numerical simulation

5

FIG. 3: Supplemental Material, Fig. S2 Construction of a temporal gate from data shown in Fig.2a). The original data is shown in the black dashed line. To represent the second TG excitation (blue dotted line) the original data is time shifted by 100 ps and inverted to account for the phase shift of $\Delta\Theta = \pi$. The gate is obtained by adding TG1 and TG2 (red solid line). A measured temporal gate with an opening time of $\tau_{12} = 100$ ps is shown by the black dots.

III. TEMPORAL GATE FROM A TWO PULSE TG EXPERIMENT

Here we exemplify the construction of the temporal gate functions that are shown by the solid lines in Fig. 4c). The gate is modeled by combining replica of the measured transient diffracted intensity in the first order I_{+1} that is shown in Fig. 2a). The same data is depicted by the black dashed curve in Fig. S3. This transient depicts the sample response to a first TG excitation. To model the second TG excitation, which is shift by a spatial phase of $\Delta\Theta = \pi$ and a temporal delay of τ_{12}=100 ps, we transform the same measured transient via $I_{+1}^2(\tau + \tau_{12}) = -I_{+1}^1(\tau)$, where the subscripts $1, 2$ denote the first and second TG excitation, respectively. The spatial phase is incorporated by the minus sign, which means that the second TG-excitaton I_{+1}^2 reduces the surface excursion. I_{+1}^2 is shown by the blue dotted curve in Fig. S3. The temporal gate (red solid line) is simply the sum of both TG

6

excitations, i.e., $I^1_{+1} + I^2_{+1}$. The black dots in Fig. S3 depicts a measurement of a temporal gate with an opening time of $100\,\mathrm{ps}$ showing very good agreement with the temporal gate constructed from measured transients.

7

Article XVI

Quantitative disentanglement of coherent and incoherent laser-induced surface deformations by time-resolved x-ray reflectivity

Mathias Sander, **Jan-Etienne Pudell**, Marc Herzog, Matias Bargheer, Roman Bauer, Valentin Besse, Vasily V. Temnov and Peter Gaal

We present time-resolved x-ray reflectivity measurements on laser excited coherent and incoherent surface deformations of thin metallic films. Based on a kinematical diffraction model, we derive the surface amplitude from the diffracted x-ray intensity and resolve transient surface excursions with sub-Å spatial precision and 70 ps temporal resolution. The analysis allows for decomposition of the surface amplitude into multiple coherent acoustic modes and a substantial contribution from incoherent phonons which constitute the sample heating.

Quantitative disentanglement of coherent and incoherent laser-induced surface deformations by time-resolved x-ray reflectivity (EP) Editor's Pick

M. Sander,[1] J.-E. Pudell,[1] M. Herzog,[1] M. Bargheer,[1,2] R. Bauer,[3] V. Besse,[4] V. Temnov,[5] and P. Gaal[3,a]

[1]*Institut für Physik und Astronomie, Universität Potsdam, Karl-Liebknecht-Str. 24-25, 14476 Potsdam, Germany*
[2]*Helmholtz-Zentrum Berlin für Materialien und Energie GmbH, Wilhelm-Conrad-Röntgen Campus, BESSY II, Albert-Einstein-Str. 15, 12489 Berlin, Germany*
[3]*Institut für Nanostruktur und Festkörperphysik, Universität Hamburg, Jungiusstr. 11c, 20355, Germany*
[4]*IMMM CNRS 6283, Université du Maine, 72085 Le Mans cedex, France*
[5]*Institute of Molecules and Materials of Le Mans, CNRS UMR 6283, 72085 Le Mans, France*

We present time-resolved x-ray reflectivity measurements on laser excited coherent and incoherent surface deformations of thin metallic films. Based on a kinematical diffraction model, we derive the surface amplitude from the diffracted x-ray intensity and resolve transient surface excursions with sub-Å spatial precision and 70 ps temporal resolution. The analysis allows for decomposition of the surface amplitude into multiple coherent acoustic modes and a substantial contribution from incoherent phonons which constitute the sample heating. *Published by AIP Publishing.*
https://doi.org/10.1063/1.5004522

Ultrafast photoacoustics[1] has become an established method to probe the interaction of optical,[2] electronic,[3] and magnetic[4] properties with the crystal lattice in solids. It employs strain pulses that are generated by absorption of femtosecond light pulses in an optoacoustic transducer.[5] Subsequent lattice dynamics can be probed either optically or by ultrafast x-ray diffraction.[6] Nowadays, tailored longitudinal strain waves can be generated and monitored using time-resolved optical and x-ray techniques.[1,7,8] Mode selective excitation of coherent acoustic surface modes can be achieved with a Transient Grating (TG) technique.[9] In addition to Rayleigh-like Surface Acoustic Waves (SAWs), this method also excites so-called Surface Skimming Longitudinal Waves (SSLWs).[10,11] However, in any photoacoustic experiment, the main fraction of the deposited optical energy is stored in incoherent phonon excitations.[12,13] The absolute magnitude of the coherent and incoherent excitation is hard to determine from purely optical experiments. In this paper, we perform a full decomposition of optically excited coherent acoustic surface and longitudinal waves which propagate with their respective group velocities and the concomitant thermal phonons which move only by diffusion. Our method allows for measuring the absolute deformation of a solid surface using time-resolved x-ray reflectivity (TR-XRR). This method can resolve surface deformation with sub-Å spatial and 70 ps temporal resolution.

The experiments were performed at the ID09 beamline of the European Synchrotron Radiation Facility (ESRF) in Grenoble, France. The beamline is equipped with a commercial Ti:Sapphire laser amplifier (Coherent Legend) which delivers 800 nm optical pulses with a duration of 600 fs at a repetition rate of 1 kHz. The laser is synchronized to the storage ring to allow for tuning the pump-probe delay with a precision of better than 5 ps.

The optical excitation pulses are coupled into the transient grating (TG) setup shown in Fig. 1 to produce +1 and −1 diffraction order from a series of transmission phase gratings with various spatial periods Λ'. Both diffracted beams are imaged onto the sample surface using a cylindrical (CL) and spherical (SL) lens in 4*f*-geometry with focal lengths $f_{CL} = 75$ mm and $f_{SL} = 150$ mm, respectively. Interference of
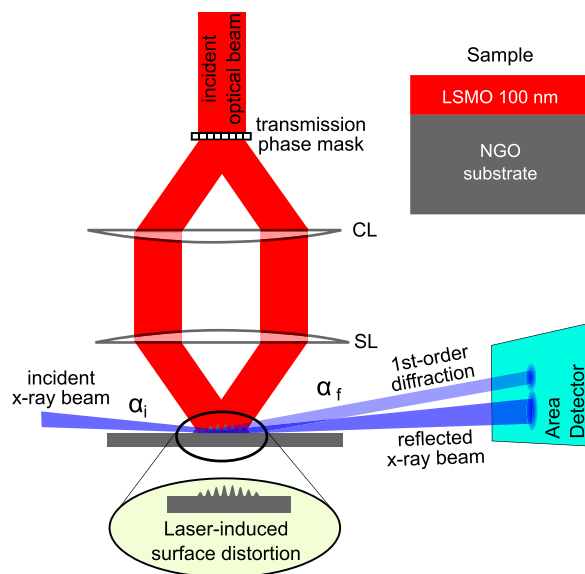

FIG. 1. Experimental setup installed at the ID09 beamline at the ESRF: Transient optical gratings are generated by splitting the output of a femtosecond laser system using a transmission phase mask and combining +1 and −1 order of the optical beam on the sample surface with a cylindrical (CL) and spherical (SL) lens in 4*f*-geometry. The surface is probed with 70 ps x-ray pulse impinging the sample at grazing incidence angle α_i. The specular beam is reflected at the exit angle α_f and the first order diffraction at $\alpha_f + \delta\alpha$. We measure TR-XRR in a pump-probe scheme. A schematic of the LSMO/NGO sample structure is shown at the top.

[a)]Electronic mail: pgaal@physnet.uni-hamburg.de

| **111**, 261903-1 |

both beams at the sample surface results in a spatial light intensity distribution with spatial period $\Lambda = \Lambda' f_{SL}/f_{CL}$ which is determined by the phase grating period and the optical magnification of the setup. We define the associated wavevector $q_{\parallel} = 2\pi/\Lambda$ which lies within both the sample surface and the x-ray diffraction plane. The optical setup results in a laser profile envelope at the sample surface with full-width at half maximum of 30 μm and 4 mm.

The sample is probed by 70 ps x-ray pulses with a photon energy of 15 keV ($\lambda_{\text{x-ray}} = 0.8266$ Å) which impinge the surface with a wavevector $\vec{k}_i$ at an incidence angle of $\alpha_i = 0.15°$, i.e., below the critical angle of total reflection. The x-ray footprint on the sample in our experiment was 10 μm × 1 mm, thus assuring overlap in a homogeneously excited sample area. The area detector image shows two pronounced peaks. The first peak originates from specular reflection of the incident beam at the sample surface $\vec{k}_f = \vec{k}_i + \vec{q}_{\perp}$, where $\vec{q}_{\perp} = 2\vec{k}_i \sin(\alpha_i)$ is the recoil momentum due to total reflection. The second peak is offset by an angle $\delta\alpha$ which results from the momentum transfer $\vec{q}_{\parallel}$ according to the laser-induced surface distortion. Hence, we call this peak the first-order diffraction from the laser-induced transient surface grating. In the following, we investigate the temporal evolution of this first order peak.

The investigated sample consists of 100 nm Lanthanum Strontium Manganate (LSMO) on a Neodym Gallate (NGO) substrate. It was grown by pulsed laser deposition.[14] The substrate is transparent at the wavelength of the excitation laser. Hence, the optical pump pulses are absorbed exclusively in the metallic LSMO film.

Experimental data of the LSMO/NGO sample for an absorbed pump fluence of 28 mJ/cm^2 are shown in Fig. 2(a). The plot depicts the intensity change of the +1st-order diffraction vs. pump-probe delay $(I(\tau) - I_0)/I_0 = \Delta I/I_0$. Upon optical excitation, we observe an instantaneous rise of the
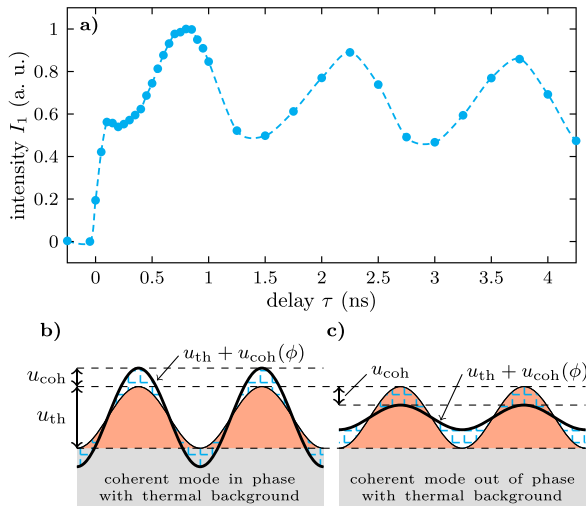

FIG. 2. (a) TR-XRR measurement of laser-generated transient surface deformations of a LSMO/NGO sample excited with 28 mJ/cm^2. The dotted line is a guide to the eye. (b) and (c) Visualization of coherent and incoherent surface dynamics: the surface amplitude is modulated by constructive and destructive interference, respectively, of the periodic thermal grating and the propagating acoustic modes.

diffracted intensity within the temporal resolution of the experiment. The initial rise is followed by a slight intensity decay which lasts for approximately 150 ps. The decay is followed by a signal increase which peaks at a pump-probe delay of approximately 800 ps and subsequently oscillates around an intensity offset with constant amplitude.

The time dependence of a similar TR-XRR measurement on a different sample was recently discussed in detail.[8] Briefly, the time-resolved data can be identified to be due to a periodic surface excursion with time-dependent amplitude $u(\tau)$ described by

$$u(\tau) = u_{th} \cdot e^{-\alpha_{th}\tau} + u_{SAW} \cdot \cos(\omega_{SAW}\tau + \varphi_{SAW}) + u_{SSLW} \cdot \cos(\omega_{SSLW}\tau + \varphi_{SSLW}) \cdot e^{-\alpha_{SSLW}\tau}. \quad (1)$$

Absorption of the ultrashort light pulse in the sample results in two fundamentally different processes. First, the sample is heated locally in the excitation area, which results in a periodic thermal expansion of the surface with amplitude u_{th}.[15] In addition, the impulsive optical excitation launches coherent strain waves which propagate parallel and perpendicular to the sample surface[7,16,17] and consist of two independent modes with surface displacement amplitudes $u_{SAW/SSLW}$, frequencies $\omega_{SAW/SSLW}$, and phases $\varphi_{SAW/SSLW}$, respectively. The thermal grating decays on a timescale $1/\alpha_{th} \approx 100$ ns by in-plane thermal diffusion, a process which is much slower than the measurement range in our experiment. The SSLW mode is strongly damped with decay constant α_{SSLW}, whereas the SAW mode exhibits no decay within our measurement window. A visualization of this decomposition is depicted in Figs. 2(b) and 2(c). Figure 2(b) depicts constructive spatial interference of the coherent modes with the thermal grating. Figure 2(c) shows a situation where the thermal grating and the coherent modes are spatially in the opposite phase. Hence, both excitations interfere destructively. The interplay of coherent and incoherent excitations can be exploited for spatio-temporal control of the surface excursion.[8]

Here, we explicitly analyze the TR-XRR probing mechanism to derive a diffraction model which relates the diffracted intensity $I(\tau)$ to the amplitude u of the surface excursion. A spatial period of the distorted sample is shown in Fig. 3(a). An x-ray beam impinges the sample at an incidence angle α_i in the bottom (point A) and on the top (point B) of the distortion and is reflected with an exit angle α_f. After reflection from A, the beam travels an additional path length X_1, while the other beam travels an additional path X_2 before reflection from point B. The total path difference results in a relative phase of both beams of $\Delta\phi = \frac{2\pi}{\lambda_{x-ray}} \cdot (X_2 - X_1)$. $\Delta\phi$ can be calculated using the following set of equations:

$$X_1 = \sqrt{u^2 + (\Lambda/2)^2} \cdot \cos(\gamma), \quad (2)$$

$$X_2 = \sqrt{u^2 + (\Lambda/2)^2} \cdot \sin(\eta), \quad (3)$$

$$\gamma = \alpha_f - \tan^{-1}(2u/\Lambda), \quad (4)$$

$$\eta = \pi/2 - \alpha_i - \tan^{-1}(2u/\Lambda), \quad (5)$$

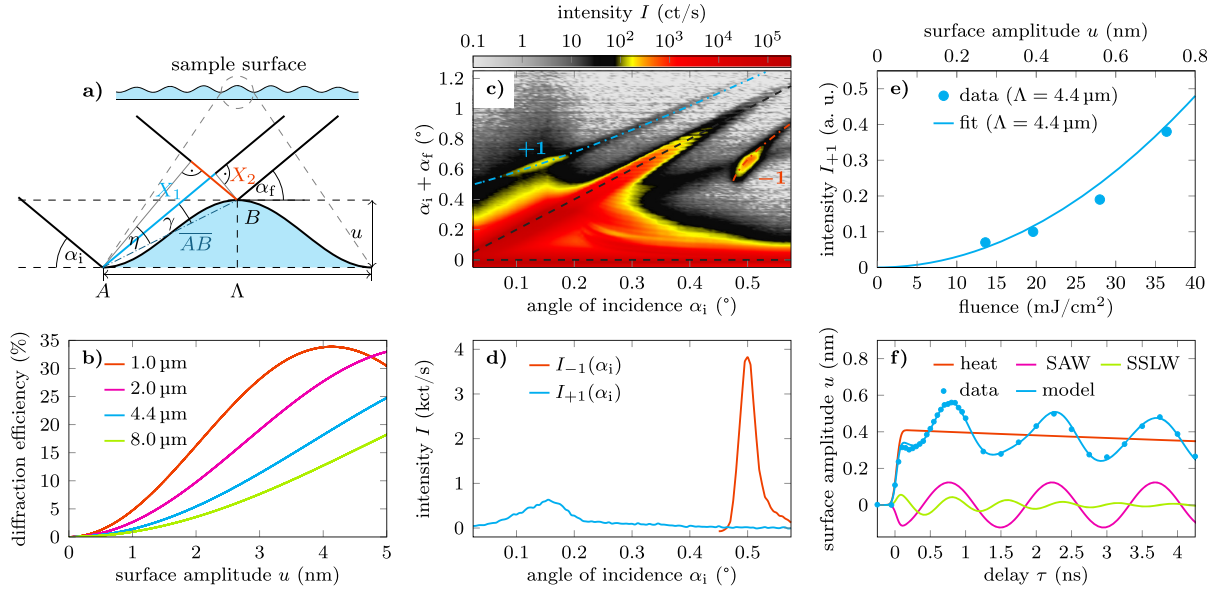and the grating equation for constructive interference:

FIG. 3. (a) Schematic for the diffraction model given by Eqs. (2)–(5). (b) Relative diffraction efficiency vs. surface excursion for grating periods of $\Lambda = 8.0\,\mu m$ (green), $4.4\,\mu m$ (blue), $2.0\,\mu m$ (magenta), and $1.0\,\mu m$ (orange). (c) Angle-resolved diffracted intensity vs. incidence angle α_i. The specular reflection (black dashed line) and $+1$st order diffraction from the surface grating (blue and red dashed lines) are indicated. (d) Intensity along the $+1$st and -1st diffraction order, i.e., along the colored dashed lines in (c). (e) Diffracted intensity (symbols) vs. absorbed pump fluence (bottom) and surface amplitude (top). The solid line shows a quadratic dependence of the diffracted intensity as expected from Eq. (9). (f) Decomposition of the diffraction data for an absorbed pump fluence of 28 mJ/cm^2. The amplitude of the individual components is given in the absolute scale.

$$\eta \lambda_{\text{x-ray}} = \Lambda (\cos(\alpha_f) - \cos(\alpha_i)). \qquad (6)$$

From kinematical theory of surface diffraction,[18,19] we find the following expression for the diffraction intensity of n-th order from a periodically distorted surface for incidence angles below the critical angle $\alpha_i < \alpha_c$, i.e., from a pure phase grating,

$$I_n = \left| \frac{1}{r_0} \int_{\parallel} e^{-i\left(n q_{\parallel} r_{\parallel} + \frac{\Delta\varphi}{2}\sin\left(\frac{2\pi}{\Lambda} r_{\parallel}\right)\right)} dr_{\parallel} \right|^2, \qquad (7)$$

$$= \left| J_n \left(\frac{\Delta\varphi}{2} \right) \right|^2, \qquad (8)$$

where $r_{\parallel}$ is the spatial coordinate along the surface grating, r_0 is a normalization constant, and J_n is the n-th Bessel function. The argument of the Bessel function is the modulation of the phase difference due to variation of the grating surface amplitude $\Delta\varphi = \Delta\phi - n\pi$, where $n\pi$ is the phase shift due to n-th order diffraction. For all practical purposes, we can assume that the surface amplitude is much smaller than the period of the surface grating, i.e., $u \ll \Lambda/2$ and therefore $\sqrt{u^2 + (\Lambda/2)^2} \approx \frac{\Lambda}{2}\left(1 + \frac{2u^2}{\Lambda^2}\right)$ and $\tan^{-1}\left(\frac{2u}{\Lambda}\right) \simeq \tan\left(\frac{2u}{\Lambda}\right) \simeq \frac{2u}{\Lambda}$. For grazing incidence $\alpha_i \leq \alpha_c$, the phase difference $\Delta\varphi$ is approximately given by

$$\Delta\varphi = -2\pi \frac{u}{\lambda_{\text{x-ray}}} \alpha_i \left[1 + \sqrt{1 + \frac{2n\lambda_{\text{x-ray}}}{\Lambda \alpha_i^2}} \right]. \qquad (9)$$

The results of the diffraction model laid out by Eqs. (2)–(8) are presented in Fig. 3(b). We plot the normalized diffracted first-order intensity I_1 vs. the surface excursion u for spatial grating periods $\Lambda = 8.0\,\mu m$ (pink), $4.4\,\mu m$ (blue), $2.0\,\mu m$ (green), and $1.0\,\mu m$ (red). The diffraction efficiency increases with increasing surface excursion and with decreasing spatial period Λ. The maximum diffraction efficiency is 33%, i.e., the maximum of the Bessel function shown in Fig. 3(b). Experimental data are shown in Fig. 3(c) which depicts the diffracted intensity from the sample vs. incidence angle α_i. The specular reflection and the ± 1st-order diffraction are marked by dashed lines. Integrated intensity of the $+1$st (blue) and -1st diffraction order is shown in Fig. 3(d). The integration was performed along the colored dashed lines in panel 3(c).

The fluence dependence of the $+1$st diffraction order intensity from a laser-generated surface grating with spatial period $\Lambda = 4.4\,\mu m$ is depicted in Fig. 3(e). The symbols indicate the measured maximum diffracted intensity at 800 ps time delay vs. absorbed pump fluence. The total surface excursion at this time delay is the sum of a thermal grating and coherent sound waves with an out-of-plane polarization component [see Fig. 2(b)]. Using recent time-resolved x-ray diffraction data from a similar LSMO sample,[20] a calibration factor for the laser-generated layer strain under the given circumstances can be estimated to be approx. 0.02% per mJ/cm^2.[21] Taking into account the LSMO layer thickness of 100 nm, the experimental fluence can thus be converted to a total surface excursion which is given at the top abscissa of Fig. 3(e). The solid line shows results from our diffraction model presented in Eqs. (2)–(5). The experimental data show the expected quadratic dependence as derived from Eq. (9).

The time-resolved surface dynamics upon transient grating excitation is shown in Fig. 3(f). By taking the square root of the diffracted intensity, i.e., data shown in Fig. 2(a), we

depict the surface excursion on an absolute length scale. Experimental data (symbols) are decomposed into a slowly decaying thermal grating (red), a Rayleigh-like SAW mode (magenta), and a SSLW-mode (green), respectively. The solid blue line shows the time-dependent surface dynamics given as described by Eq. (1), showing excellent agreement with the experimental curve.

In conclusion, we measure the absolute amplitude of the surface excursion of a laser-induced transient grating on a solid surface by time-resolved x-ray reflectivity. Ultrafast optical excitation generates incoherent thermal surface distortions and coherent acoustic surface waves. The measured dynamics at the surface allow for a decomposition of the surface amplitude in a thermal background and two coherent acoustic modes: a Rayleigh-like surface acoustic wave and a surface skimming longitudinal wave. Our method can be applied to decompose coherent and incoherent surface dynamics with sub-Å precision and with a temporal resolution better than 100 ps.

[1]P. Ruello and V. E. Gusev, Ultrasonics **56**, 21 (2015).
[2]M. Weiß, J. B. Kinzel, F. J. R. Schülein, M. Heigl, D. Rudolph, S. Morkötter, M. Döblinger, M. Bichler, G. Abstreiter, J. J. Finley, G. Koblmüller, A. Wixforth, and H. J. Krenner, Nano Lett. **14**, 2256 (2014).
[3]Y. Wang, Y. Chen, H. Li, X. Li, H. Chen, H. Su, Y. Lin, Y. Xu, G. Song, and X. Feng, ACS Nano **10**, 8199 (2016).
[4]J.-W. Kim, M. Vomir, and J.-Y. Bigot, Phys. Rev. Lett. **109**, 166601 (2012).

[5]C. Thomsen, H. T. Grahn, H. J. Maris, and J. Tauc, Phys. Rev. B **34**, 4129 (1986).
[6]C. Rose-Petruck, R. Jimenez, T. Guo, A. Cavalleri, C. W. Siders, F. Rksi, J. A. Squier, B. C. Walker, K. R. Wilson, and C. P. J. Barty, Nature **398**, 310 (1999).
[7]M. Herzog, A. Bojahr, J. Goldshteyn, W. Leitenberger, I. Vrejoiu, D. Khakhulin, M. Wulff, R. Shayduk, P. Gaal, and M. Bargheer, Appl. Phys. Lett. **100**, 094101 (2012).
[8]M. Sander, M. Herzog, J. E. Pudell, M. Bargheer, N. Weinkauf, M. Pedersen, G. Newby, J. Sellmann, J. Schwarzkopf, V. Besse, V. V. Temnov, and P. Gaal, Phys. Rev. Lett. **119**, 075901 (2017).
[9]J. A. Rogers, A. A. Maznev, M. J. Banet, and K. A. Nelson, Annu. Rev. Mater. Sci. **30**, 117 (2000).
[10]J. Janusonis, T. Jansma, C. L. Chang, Q. Liu, A. Gatilova, A. M. Lomonosov, V. Shalagatskyi, T. Pezeril, V. V. Temnov, and R. Tobey, Sci. Rep. **6**, 29143 (2016).
[11]J. Janušonis, C. L. Chang, T. Jansma, A. Gatilova, V. S. Vlasov, A. M. Lomonosov, V. V. Temnov, and R. I. Tobey, Phys. Rev. B **94**, 024415 (2016).
[12]M. Herzog, D. Schick, P. Gaal, R. Shayduk, C. von Korff Schmising, and M. Bargheer, Appl. Phys. A **106**, 489 (2012).
[13]R. Shayduk, H. A. Navirian, W. Leitenberger, J. Goldshteyn, I. Vrejoiu, M. Weinelt, P. Gaal, M. Herzog, C. V. Korff Schmising, and M. Bargheer, New J. Phys. **13**, 093032 (2011).
[14]J. Sellmann, J. Schwarzkopf, A. Kwasniewski, M. Schmidbauer, D. Braun, and A. Duk, Thin Solid Films **570**(Part A), 107 (2014).
[15]M. Reinhardt, A. Koc, W. Leitenberger, P. Gaal, and M. Bargheer, J. Synchrotron Radiat. **23**(2), 474 (2016).
[16]A. Bojahr, M. Herzog, S. Mitzscherling, L. Maerten, D. Schick, J. Goldshteyn, W. Leitenberger, R. Shayduk, P. Gaal, and M. Bargheer, Opt. Express **21**, 21188 (2013).
[17]R. Shayduk, M. Herzog, A. Bojahr, D. Schick, P. Gaal, W. Leitenberger, H. Navirian, M. Sander, J. Goldshteyn, I. Vrejoiu, and M. Bargheer, Phys. Rev. B **87**, 184301 (2013).
[18]A. Madsen, T. Seydel, M. Tolan, and G. Grübel, J. Synchrotron Radiat. **12**, 786 (2005).
[19]J.-D. Nicolas, T. Reusch, M. Osterhoff, M. Sprung, F. J. R. Schülein, H. J. Krenner, A. Wixforth, and T. Salditt, J. Appl. Crystallogr. **47**, 1596 (2014).
[20]A. Bojahr, M. Herzog, D. Schick, I. Vrejoiu, and M. Bargheer, Phys. Rev. B **86**, 144306 (2012).
[21]Note that the calibration factor given in Ref. 20 refers to the incident fluence instead of the absorbed fluence and accounts only for the thermal component. At 800 ps the in-phase coherent modes require an enhanced calibration factor of 0.02% per mJ/cm^2 which is applied in Fig. 3(e).

Article XVII

Full spatiotemporal control of laser-excited periodic surface deformations

Jan-Etienne Pudell, Mathias Sander, Roman Bauer, Matias Bargheer, Marc Herzog, and Peter Gaal

We demonstrate full control of acoustic and thermal periodic deformations at solid surfaces down to subnanosecond time scales and few-micrometer length scales via independent variation of the temporal and spatial phase of two optical transient grating (TG) excitations. For this purpose, we introduce an experimental setup that exerts control of the spatial phase of subsequent time-delayed TG excitations depending on their polarization state. Specific exemplary coherent control cases are discussed theoretically and corresponding experimental data are presented in which time-resolved x-ray reflectivity measures the spatiotemporal surface distortion of nanolayered heterostructures. Finally, we discuss examples where the application of our method may enable the control of functional material properties via tailored spatiotemporal strain fields.

Full Spatiotemporal Control of Laser-Excited Periodic Surface Deformations

J.-E. Pudell,[1] M. Sander,[2] R. Bauer,[3] M. Bargheer,[1,4] M. Herzog,[1,*] and P. Gaal[3,†]

[1]*Institut für Physik und Astronomie, Universität Potsdam, 14476 Potsdam, Germany*

[2]*European Synchrotron Radiation Facility (ESRF), 23800 Grenoble, France*

[3]*Institut für Nanostruktur und Festkörperphysik, Universität Hamburg, 20355 Hamburg, Germany*

[4]*Helmholtz-Zentrum Berlin für Materialien und Energie GmbH, Wilhelm-Conrad-Röntgen Campus, BESSY II, 12489 Berlin, Germany*

We demonstrate full control of acoustic and thermal periodic deformations at solid surfaces down to subnanosecond time scales and few-micrometer length scales via independent variation of the temporal and spatial phase of two optical transient grating (TG) excitations. For this purpose, we introduce an experimental setup that exerts control of the spatial phase of subsequent time-delayed TG excitations depending on their polarization state. Specific exemplary coherent control cases are discussed theoretically and corresponding experimental data are presented in which time-resolved x-ray reflectivity measures the spatiotemporal surface distortion of nanolayered heterostructures. Finally, we discuss examples where the application of our method may enable the control of functional material properties via tailored spatiotemporal strain fields.

I. INTRODUCTION

Ultrashort strain pulses can be generated by absorption of femtosecond or picosecond optical light pulses in solids and nanostructures [1,2]. This photoacoustic generation is employed to study properties of phonons in solids [3,4] or the interaction of lattice strain with optic [5], electronic [6], or magnetic [7,8] degrees of freedom. The various interaction channels suggest that lattice strain may be used as a functional tool to control and trigger specific processes and functions in materials. Recently, the control and enhancement of quantum entanglement using tailored surface acoustic waves was suggested [9]. In fact, thanks to their customizable short length and time scales down to a few nanometers and picoseconds, respectively, optically generated strain pulses may be particularly suited for selective excitation of nanostructures. However, a high level of control of the shape, frequency, lifetime, etc., of lattice strain is necessary before strain pulses can be used as functional tools for device operation. The control is typically gained by tailoring the temporal excitation sequence [10–13]. We recently demonstrated strain control on subnanosecond time scales by exploiting spatial variation of transient grating excitation sequences [14]. This method is not only limited to the control of coherent strain pulses but

also applies to thermal deformations. In particular, the control of thermal deformations can be applied on the same time scale as the control of coherent excitations. Hence, thermal strain, which is often regarded as an undesired side effect to optical excitations, can now be used to trigger specific material functions.

In this article, we present a comprehensive discussion of spatiotemporal control of acoustic and thermal excitations in solids. Our method relies on shaping the temporal and spatial sequence of optical excitations using the so-called transient grating (TG) technique. In particular, our experimental TG setup allows for easy tuning of the relative spatial phase of subsequent TG excitations. The periodic surface deformation (PSD) of the sample upon optical excitation is detected using time-resolved x-ray reflectivity (TRXRR) [15]. The article provides a detailed discussion of spatiotemporal coherent control with particular focus on important limiting cases in Sec. II. Also, the quantitative probing of PSDs by diffraction of x rays in x-ray reflection geometry is briefly explained. The optical setup for generating and controlling PSDs is presented in Sec. III. In Sec. IV, we discuss results of spatiotemporal coherent control measurements on thermal and acoustic PSDs in nanoscopic heterostructures. We analyze and decompose the experimental data by comparison to an empirical modeling. Section V exemplifies how the strain-control capabilities our method may be exploited in order to control functional material properties. Finally, Sec. VI summarizes and emphasizes the main results.

---

*marc.herzog@uni-potsdam.de

†pgaal@physnet.uni-hamburg.de

II. COHERENT CONTROL OF PERIODIC SURFACE DEFORMATIONS

Classical coherent control can be performed on any oscillator or wavelike harmonic excitation due to the superposition principle. Without restriction of the general validity, we restrict our considerations to an impulsive and displacive excitation of modes by an ultrashort excitation pulse [16]; i.e., the dynamics of the involved modes is much slower than the excitation pulse duration and the coherent oscillation occurs around a displaced equilibrium. The oscillation amplitude of such an impulsively excited harmonic oscillator can either be suppressed or doubled by a second identical excitation with a relative time delay τ of a half-period (relative phase $\phi = \pi$) or a full period ($\phi = 2\pi$), respectively. This type of coherent control has been successfully applied to various phenomena such as phonons [17–20], magnons [21–23], phonon-polaritons [24], and surface acoustic waves (SAWs) [14,25–27]. In displacive excitations, coherent control is limited to the oscillatory motion, i.e., the coherent part of the system response. The displacement from the equilibrium ground state, which for optical excitations corresponds to a heating of the sample due to the absorbed optical energy, is typically ignored in the coherent control experiments, although it may contain most of the absorbed energy [28].

In addition to the temporal coherence exploited in earlier coherent control experiments, an impulsive TG excitation also possesses a spatial coherence in the form of a sinusoidal intensity variation with spatial period Λ, which is typically oriented parallel to the sample surface. Assuming a linear response of the sample, the absorption of optical energy thus generates a spatially periodic energy density along the sample surface with periodicity Λ. The depth profile of the absorbed energy density is dictated by either the optical properties of the sample or the sample dimensions. In the following, we consider a thermoelastic excitation; i.e., the absorbed energy density results in a mechanical stress that eventually gives rise to a thermal transient grating (TTG). Given the impulsive excitation with ultrashort laser pulses, the thermoelastic stress also launches coherent counterpropagating SAWs, resulting in a standing SAW in the optically excited area. Both excitations can be associated with the characteristic wave vector $|\vec{q}_{\parallel}| = 2\pi/\Lambda$. The spatial coherence introduces an additional coherent control coordinate given by the spatial phase of the TG excitation [14]. Hence, a second TG excitation with a spatial phase φ_x relative to the first TG excitation can be employed to control the relative spatial phase ϕ_{th} of the corresponding TTGs. Choosing $\phi_{\text{th}} = 2n\pi$ or $\phi_{\text{th}} = (2n-1)\pi$ either amplifies or suppresses the TTG, respectively. Here, the relative spatial phase of the TG excitation patterns directly determines the relative spatial phase of the TTGs, i.e., $\phi_{\text{th}} = \varphi_x$. The coherent SAW, however, is controlled via the spatiotemporal phase $\phi_{\text{SAW}} = \varphi_x + \varphi_t = \varphi_x + v_{\text{SAW}}|\vec{q}_{\parallel}|\tau$, where v_{SAW} is the phase velocity of the excited SAW and τ is the temporal delay between the two TG excitation pulses. Similar to the TTG, the SAW can be amplified ($\phi_{\text{SAW}} = 2n\pi$) or suppressed [$\phi_{\text{SAW}} = (2n-1)\pi$]. According to the definition of ϕ_{SAW}, a change in the relative spatial phase φ_x implies an adopted time delay τ if the interference of the SAWs is to be kept unchanged. In summary, we introduce two experimental coherent control coordinates φ_x and φ_t given by the relative spatial phase and the relative time delay of two consecutive TG excitations in order to control the thermal and coherent PSD via the spatiotemporal phases ϕ_{th} and ϕ_{SAW}.

In this article, we employ these coherent control coordinates to disentangle four extreme cases of coherent control, which are depicted in Fig. 1:

A. Constructive interference of TTGs and constructive interference of two standing SAWs: $\varphi_x = 0$, $\varphi_t = 0 \rightarrow \phi_{\text{th}} = 0$, $\phi_{\text{SAW}} = 0$ [Fig. 1(a)].

B. Destructive interference of TTGs and destructive interference of two standing SAWs: $\varphi_x = \pi$, $\varphi_t = 0 \rightarrow \phi_{\text{th}} = \pi$, $\phi_{\text{SAW}} = \pi$ [Fig. 1(b)].

C. Constructive interference of TTGs and destructive interference of two standing SAWs: $\varphi_x = 0$, $\varphi_t = \pi \rightarrow \phi_{\text{th}} = 0$, $\phi_{\text{SAW}} = \pi$ [Fig. 1(c)].

D. Destructive interference of TTGs and constructive interference of two standing SAWs: $\varphi_x = \pi$, $\varphi_t = \pi \rightarrow \phi_{\text{th}} = \pi$, $\phi_{\text{SAW}} = 2\pi \equiv 0$ [Fig. 1(d)].

Note that, while there is no SAW oscillation present in cases B and C, the SAW modulates the surface deformation of a TTG or a flat surface in cases A and D, respectively, as indicated by the blue shading in Figs. 1(a)–1(d). As discussed below, TRXRR can unambiguously distinguish these situations as they manifest differently in the experimental data. Note that we assume two identical excitations in accordance with a time-independent TTG. The amplitude of the second TG excitation may of course be adapted to compensate for a potential decay of the first excitation during the time delay τ.

In the following, we briefly discuss the detection of dynamics triggered by the TG excitation. Typically, experiments employ an optical laser pulse that is diffracted from the excited modes via photothermal or photoelastic effects [29,30]. Alternatively, PSDs can be detected using x-ray diffraction and photoemission electron microscopy techniques [31–33]. We have recently shown that the PSD associated with the excited quasistatic and transient modes may also be probed by TRXRR [14,15]. This method is exclusively sensitive to the surface displacement and can detect deformations of only a few nanometers [14]. Thermally induced expansion can be
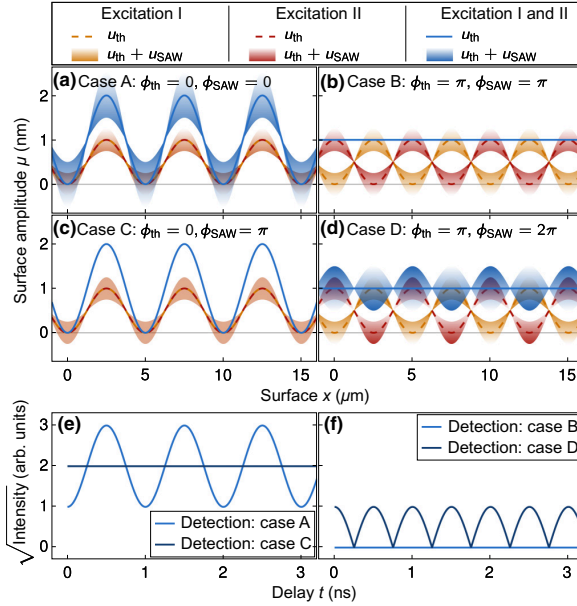
FIG. 1. Spatiotemporal coherent surface control with two tailored excitations: yellow and red dashed lines depict quasistatic TTGs of the individual excitations I and II, respectively. The gradient of the colored shaded areas represents the temporal evolution of the standing SAW on the TTG over a half-period. Blue lines and blue colored areas represent the combined excitation (excitation I & II). (a) Case A: constructive interference of two TTGs and constructive interference of two standing SAWs. Note that both excitations have the same spatiotemporal phase; therefore, the shaded area is orange. (b) Case B: destructive interference of two TTGs and destructive interference of two standing SAWs. (c) Case C: constructive interference of two TTGs and destructive interference of two standing SAWs. Note that both excitations have the same spatial phase and opposite temporal phase; therefore, the shaded area is orange without a color gradient. (d) Case D: destructive interference of two TTGs and constructive interference of two standing SAWs. (e),(f) Square root of the diffracted intensity from the combined excitation for (e) cases A and C and (f) cases B and D. Note that, for x rays, the square root of the intensity is proportional to the surface modulation amplitude.

unambiguously disentangled from coherent elastic effects via the characteristic time scale of the surface deformation [15], thus yielding a complete picture of the surface dynamics. For the TRXRR probe, the Laue condition, i.e., momentum conservation, must be fulfilled:

$$\vec{k}_{\pm 1} = \vec{k}_{\mathrm{in}} + \vec{q}_\perp \pm \vec{q}_\parallel, \tag{1}$$

where $\vec{k}_{\mathrm{in}}$ and $\vec{q}_\perp$ are the wave vector of the incident probe photons and the recoil momentum due to reflection at the surface, respectively. We restrict our considerations to first-order diffraction from the PSD, although diffraction to

higher orders is also present, even if a perfect sinusoidal PSD is monitored [15]. Note that Eq. (1) is independent of the spatial phase of the TG; i.e., the phase of the PSD cannot be inferred from the diffracted intensity *per se*. The intensity of the diffracted x-ray probe pulse is proportional to $\Delta u^2(t)$, i.e., to the squared difference between the minimum and maximum surface deformation [15]. Thus, the square root of the diffracted intensity measures the magnitude of the total surface modulation amplitude, i.e., $\sqrt{I(t)} = |\Delta u(t)| = |\Delta u_{\mathrm{th}} + \Delta u_{\mathrm{SAW}} \cos(\omega t)|$, where $\omega = v_{\mathrm{SAW}} |q_\parallel|$ is the frequency of the SAW.

First, consider the case where a strong TTG is modulated by a SAW with relatively small amplitude, i.e., $\Delta u_{\mathrm{SAW}} < \Delta u_{\mathrm{th}}$. Excluding thermal diffusion within the TTG, $\Delta u(t) > 0$ holds for all times and the measured signal directly reveals the SAW's frequency and its relative phase with respect to the TTG as depicted in Fig. 1(e). However, if $\Delta u_{\mathrm{SAW}} > \Delta u_{\mathrm{th}}$, the detection signal is altered. The extreme case is shown in Fig. 1(d), where the SAW modulates a flat surface (case D), i.e., $\Delta u_{\mathrm{th}} = 0$ (note that $u_{\mathrm{th}} \neq 0$ may hold). Here, the time-dependent intensity is proportional to $\Delta u^2(t) = [\Delta u_{\mathrm{SAW}} \cos(\omega t)]^2 = \Delta u_{\mathrm{SAW}}^2 [1 + \cos(2\omega t)]/2$. Therefore, the diffracted probe intensity shows twice the frequency of the SAW as presented in Fig. 1(f). The effect of the TTG is analogous to a spatial local oscillator, which allows us to infer the spatiotemporal phase of the coherent SAW from the diffracted probe pulse after TG excitation.

III. EXPERIMENTAL METHODS

A detailed view of our optical experimental setup is shown in Figs. 2(a)–2(e). The general layout of the TG setup is described elsewhere [14,34]. Our particular setup is designed for optical pump TRXRR probe measurements at the ID09 beamline at the European Synchrotron Radiation Facility (ESRF). Taking into account the specific conditions at the beamline, we optimize the optical setup for small size, stability, and tunability. Therefore, we use two 50-mm-wide acylindrical lenses with a focal length of 40 mm to image the +1st and −1st diffraction order from a transmission phase mask onto the sample surface. Interference of the +1 and −1 beam at the sample surface results in a sinusoidal modulation of the optical intensity. Grating, lenses, and sample are mounted in 4f geometry. We optionally introduce an additional cylindrical lens with a focal length of 75.6 mm in the perpendicular plane. This lens is mounted with variable distance to the sample to generate higher excitation fluences.

To generate two replica of an ultrashort optical pump pulse with perpendicular polarization for coherent control, we use a Michelson interferometer [cf. Fig. 2(b)] with a polarizing beamsplitter (PBS). The relative intensity of the pulses can be tuned by a half-wave plate (HWP) in front of the PBS. Each arm of the Michelson
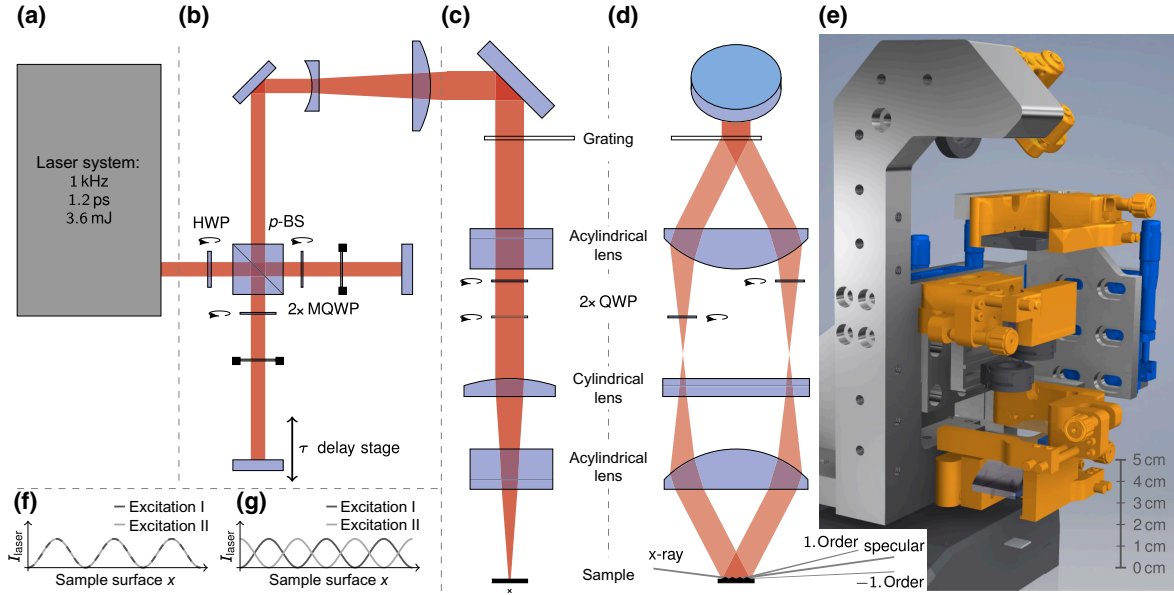
FIG. 2. Optical setup. (a) The output of a 1-kHz laser system is coupled to a Michelson interferometer (b), where *s*- and *p*-polarized replicas of the pump pulse are generated. (c) Side view of the TG setup. (d) Front view of the beam path of the +1st and −1st diffraction order. (e) Three-dimensional (3D) view of the TG setup with the optomechanical components. (f),(g) The created relative spatial phase of the interference grating for parallel and perpendicular setting of the QWPs.

interferometer includes a quarter-wave plate, which we refer to as Michelson-quarter-wave plates (MQWP) in Fig. 2b. Due to the double passage of the beams, the MQWP effectively rotates the linear polarization by 90°. Thus, the output of the interferometer yields one *s*- and one *p*-polarized optical pump pulse. The pulses have a variable relative time delay τ that is defined by the difference of the path lengths of the Michelson interferometer arms. Both pulses are subsequently coupled into the TG setup, where they essentially are diffracted into ±1st-order beams by the phase mask. Zero-order and higher-order diffraction intensities are minimized by the specific design of the transmission phase mask.

In addition to simple TG excitation, our setup allows for selecting the spatial phase of the TG to perform spatiotemporal coherent control. We use the fact that the spatial phase of the TG at the sample surface depends on the relative temporal phase of the interfering optical beams. For example, interference gratings generated by two optical beams of either parallel or antiparallel polarization have an opposite spatial phase with respect to each other [35]. Note that, in the antiparallel case, the electric fields of +1st- and −1st-order beams have a relative temporal phase of π, i.e., exactly the same value as the relative spatial phase shift of the generated TG. As explained below, we employ quarter-wave plates (QWP) and different polarizations to impose a relative spatial phase shift between two consecutive TG excitations.

After collimation by the first acylindrical lens, each beam propagates through a QWP. The QWPs are oriented either with the fast or slow axis aligned with the polarization of the laser pulses. If the QWPs have identical orientation, there is no relative temporal phase offset between the ±1st-order beams as they both traverse the QWPs at either the fast or the slow axis. Note that both consecutive *s*- and *p*-polarized laser pulses generate TGs with an identical spatial phase, i.e., $\varphi_x = 0$. Hence, with a parallel setting of the QWPs, one can generate cases A and C, discussed in Sec. II.

If the QWPs are oriented perpendicular to each other, the +1st- and −1st-order beams experience a relative temporal phase shift of $\pm \pi/2$, which directly translates into a spatial phase offset of $\pm \pi/2$ of the TG excitations. The opposite sign of the temporal phase shift holds for the *s*- and *p*-polarized beams, respectively. The magnitude of the spatial phase difference between the *s*- and *p*-polarized TG is therefore equal to π, i.e., $\varphi_x = \pi$. Hence, with a perpendicular setting of the QWPs, one readily obtains cases B and D, discussed in Sec. II, where the PSD due to the TTG is relieved by the second TG excitation.

The experimental results presented and discussed in the next section are obtained on a 30-nm-thick metallic SrRuO$_3$ (SRO) film epitaxially grown by pulsed laser deposition on a (110)-oriented DyScO$_3$ (DSO) substrate. The sample is excited with TG excitations, each having a spatial period $\Lambda = 2.4$ μm and an incident pump fluence

of 18 mJ/cm^2 for the central fringes of the TG [36]. We employ a commercial Ti:sapphire laser amplifier (Coherent Legend Elite), which delivers 800-nm pulses with a duration of 1.2 ps and a pulse energy of 3.6 mJ. The laser repetition rate is 1 kHz, synchronized to the synchrotron. The shortest grating period Λ inscribed in the sample is ultimately limited by the laser wavelength. By frequency doubling or tripling of the fundamental frequency, one can reduce the period to less than 300 nm. The generation of transient gratings with periods less than 100 nm has been demonstrated by using high-energy radiation from free-electron laser sources [37,38]. Thus, our method can be employed truly on nanometer length scales.

Monochromatized 15-keV x-ray probe pulses are selected from the synchrotron pulse train by a high-speed chopper at the same frequency. The pump-probe delay can be changed electronically by the laser synchronization unit. In the experiment presented here, the total temporal resolution is limited to 75 ps, mainly due to the duration of the x-ray probe pulses. In principle, the experimental time resolution is also limited by the rather large wave-front tilt between the exciting laser and probing x-ray pulses; however, in the present case, this is only a minor limitation (approximately 10 ps). Diffracted x-ray photons are captured on an area detector (Rayonics MX170-HS) [39,40]. For the evaluation, the intensity I_{-1st} of the -1st diffraction order is integrated in a region of interest on the area detector. The recorded intensity is normalized to a static diffraction background I_n to reduce influences of beam instabilities and thermal drifts of the sample and setup. In order to extract the surface modulation amplitude Δu, we take the square root of the diffracted intensity after subtracting a scattering background I_{bg} by averaging all unpumped detected intensities of the -1st diffraction order. This results in

$$\Delta u \propto \sqrt{\left| \frac{I_{-1st} - I_{bg}}{I_n} \right|} \, \text{sgn}\left(I_{-1st} - I_{bg} \right), \quad (2)$$

where the absolute function circumvents imaginary results and the sgn function projects these values on the negative axis for the surface modulation amplitude Δu.

IV. RESULTS AND DISCUSSION

First, we briefly discuss the transient response of the sample surface to a single TG excitation. As derived in earlier studies [15], the surface modulation amplitude Δu is proportional to the square root of the diffracted intensity. The transient amplitude of the laser-generated PSD inferred from the the x-ray intensity diffracted into -1st-order is shown by the blue bullets in Fig. 3(a). It features a steplike rise followed by oscillations on top of a slowly decaying thermal offset. The surface excursion field can
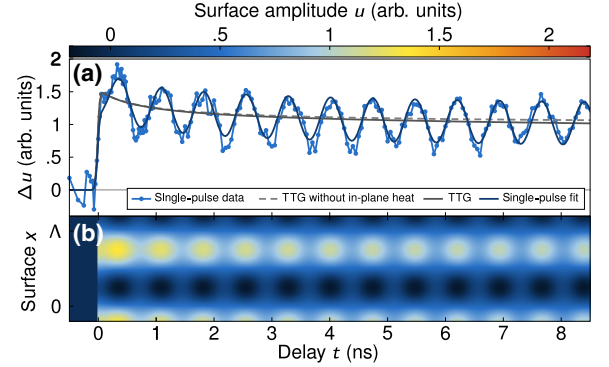

FIG. 3. Single-pulse excitation. (a) Time-dependent surface modulation amplitude $\Delta u(t)$ measured with TRXRR. The data (blue bullets) are modeled by calculating the spatiotemporal surface deformation field $u(x, t)$ [cf. Eq. (3)]. The dark blue solid line shows the time dependence of the Fourier component $(\mathcal{F}u)(q_\parallel, t)$ at the characteristic wave vector $q_\parallel$. The surface modulation amplitude of only the thermal distortion $(\mathcal{F}u_{th})(q_\parallel, t)$ due to the TTG is shown by the gray lines with (solid) and without (dashed) in-plane heat diffusion. (b) Illustration of the spatiotemporal surface deformation field $u(x, t)$ calculated using Eq. (3).

thus be precisely modeled by

$$u = \Theta(t)\left[u_{th}(x, t, \varphi_x) + u_{SAW}(x, t, \varphi_x, \varphi_t) \right], \quad (3)$$

where u_{th} is the slowly decaying amplitude of the TTG and u_{SAW} is the amplitude of the coherent surface acoustic mode, defined as

$$u_{th} = \frac{u_{th,0}(t)}{2} e^{-\alpha_x q_\parallel^2 t} \left[1 + \sin\left(q_\parallel x - \varphi_x \right) \right], \quad (4)$$

$$u_{SAW} = -\frac{u_{SAW,0}}{2} \sin\left(q_\parallel x - \varphi_x \right) \cos(\omega t - \varphi_t). \quad (5)$$

The rise time τ_{rise} of the TTG is dictated by the ratio of the thickness (or the optical penetration depth if the latter is much shorter) and sound velocity of the laser-excited film. Typical time scales of thin-film expansion are a few tens of picoseconds or even down to a few picoseconds for very thin films [41]. In the present case, τ_{rise} is much shorter than all other involved dynamics and thus approximated by the Heaviside function $\Theta(t)$ in Eq. (3). In fact, τ_{rise} defines the fundamental limit for coherent control of the TTG (cases B and D), which can thus be truly applied down to picosecond time scales as demonstrated in Sander *et al.* [15]. The concept of spatiotemporal coherent control is generally applicable to an arbitrary number of coherent modes [14,15,42], but in the present case the data only exhibit a single Rayleigh-like SAW mode. We can thus restrict our model to only include this single coherent mode. Note that the first TG

excitation always defines the zero phase φ_x and φ_t, respectively. In order to mimic the sensitivity of the x-ray probe beam to only the modulation of the PSD, we extract the transient wave-vector-dependent surface modulation amplitude $\Delta u(q, t) = (\mathcal{F}u)(q, t)$ by Fourier transformation of the spatiotemporal surface deformation field $u(x, t)$ depicted in Fig. 3(b). We then evaluate the surface modulation amplitude $\Delta u(q_\parallel, t)$ at the characteristic wave vector $q_\parallel$. The dark blue solid line in Fig. 3(a) shows the temporal behavior convoluted with the experimental temporal resolution of 75 ps.

The slowly decaying signal shown in Fig. 3(a) is caused by the PSD associated with the TTG that slowly decays due to thermal diffusion. This decay clearly exhibits a fast component decaying within the first 2 ns and a much slower component. The latter is due to in-plane thermal diffusion between hot and cold areas of the TTG. An analytical solution of the in-plane thermal diffusion for a sinusoidal thermal grating yields the exponential term in Eq. (4), which implies a decay time of $(\alpha_x q_\parallel^2)^{-1} = 210$ ns [43,44]. Here, the homogeneous in-plane diffusivity $\alpha_x = 0.8$ mm^2/s is used for a substrate temperature of 323 K [45]. The initial fast decay originates from different thermal expansion coefficients of the metallic SRO film and the insulating DSO substrate. In fact, SRO expands stronger upon heating than DSO [46,47]. Thus, as heat diffuses along the out-of-plane direction from the excited areas in the SRO film into the substrate, the total surface excursion is reduced. In order to verify this, we model the out-of-plane heat transport by solving the one-dimensional heat diffusion equation with a finite-element method [48,49] by accounting for all relevant thermophysical properties of the materials. The experimental data are reproduced without including additional thermal resistance at the interface due to the nearly perfect acoustic impedance match between the involved materials and the high structural quality of the sample. The simulation yields the surface distortion $u_{\mathrm{th},0}(t)$ used as input for Eq. (4). The surface modulation amplitude due to combined out-of-plane and in-plane thermal diffusion is shown as a gray solid line in Fig. 3(a). If in-plane thermal diffusion is neglected ($\alpha_x = 0$), the grey dashed line is obtained, which proves that the initial fast decay is indeed governed by the out-of-plane thermal transport. The very good agreement between experiment and calculation evidences that the presented method can be a powerful tool to investigate multidirectional thermal transport in nanoscopic heterostructures. We do not observe deviations from linear behavior of our sample even up to very large excitation densities [50]. This aspect is particularly important for the multipulse excitation discussed in the next paragraph.

With the well-calibrated single-pulse excitation, we finally demonstrate full spatiotemporal control of transient and quasistatic PSDs via double-pulse TG excitation. By employing two consecutive TG excitations, we set the spatiotemporal phase of the excitation to the four different cases introduced in Sec. II. The corresponding dynamic surface excursion measured by TRXRR for these four cases is shown in Figs. 4(a)–4(d), respectively. As predicted above, the spatial phase setting $\varphi_x = 0$, selected by a parallel alignment of the QWPs in the optical setup, results in an increase of the PSD (cases A and C) due to an enhancement of the TTG. In contrast, the 90° rotation of only one QWP suppresses the PSD and relieves the TTG completely (cases B and D). The phase of the SAW is controlled by both the spatial and temporal phase φ_x and φ_t, respectively. For any setting of the spatial phase, one can either suppress (cases C and B) or enhance (cases A and D) the SAW mode by choosing the correct time delay τ of the second TG excitation. Note, in particular, the comparison of cases A and B, where $\tau = 0.73$ ns is identical. Still, not only the timing τ alone determines the amplitude of the SAW after the second excitation, as explained in Sec. II.

The possibility of suppressing the coherent mode (cases B and C) offers a precise tool for investigations of the multidirectional thermal transport in nanoscale heterostructures without undesired coherent signals yet ensuring sufficient time resolution given by the ultrashort laser and x-ray pulses. In case C, we clearly observe the multicomponent relaxation due to in-plane and out-of-plane heat diffusion, which is discussed above for single-pulse excitation. However, here, the signal of thermal origin is not masked by the coherent signal. The finite decaying intensity after the second TG excitation in case B [Fig. 4(b)] evidences that the TTG is not immediately suppressed by the second excitation. This is caused by the partial decay of the first TTG between the two excitations due to fast out-of-plane heat diffusion, which results in the observed imbalance of both TTGs. All observations are accurately reproduced by our modeling introduced above. Altogether, the sensitivity to thermal transport in layered heterostructures can be greatly enhanced with spatiotemporal coherent control using TG excitations.

A qualitative difference from the other recorded signals is observed in case D shown in Fig. 4(d), where the TTG is suppressed and the SAW is enhanced. Here, we observe a coherent oscillation exhibiting twice the frequency of the excited SAW. Recall that the data represent the variations of the 1st-order diffracted x-ray intensity. If a true second harmonic of the fundamental SAW is present, Eq. (1) implies that the corresponding 1st order of the second harmonic would be diffracted toward larger angles. In other words, the 1st-order diffraction angle cannot contain signatures of a second harmonic SAW. Again, we model the transient diffracted x-ray intensity caused by the spatiotemporal sample surface dynamics in analogy to the single-pulse excitation data analysis [cf. Eqs. (3)–(5)]. Note that our model is a purely linear response
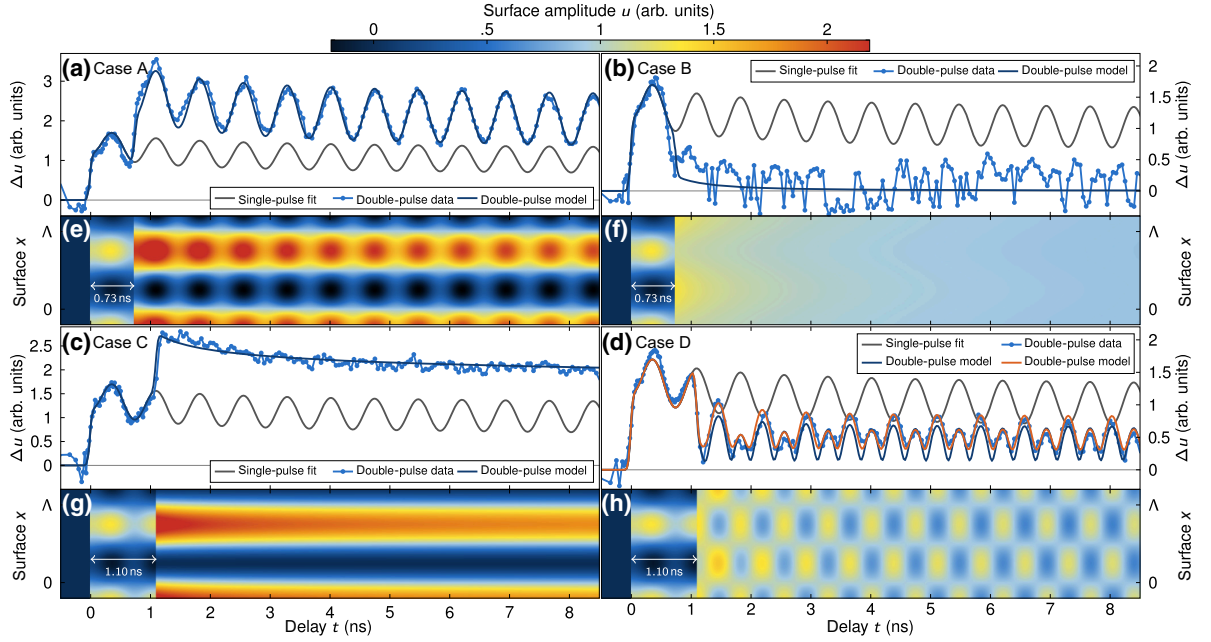
FIG. 4.   Double-pulse excitation: (a),(e) case A; (b),(f) case B; (c),(g) case C; (d),(h) case D. The single-pulse responses as modeled in Fig. 3 are shown in gray for comparison in (a)–(d). Symbols show the TRXRR measurements and dark blue solid lines show the transient surface modulation amplitude $\Delta u(q_\parallel, t)$ for the characteristic wave vector $q_\parallel$ of the spatiotemporal surface deformation field shown in (e)–(h) derived from Eq. (3). All calculated traces are convoluted with a 75-ps Gaussian to match the temporal resolution of the experiment. The orange line in (d) represents the best fit to the double-pulse data by allowing for an amplitude and phase variation of the second excitation pulses.

model and thus does not support higher harmonics of the employed modes. Assuming the time delay τ chosen in the experiment and two identical TG excitations, we obtain the dark blue curve in Fig. 4(d). Obviously, our modeling correctly yields the doubled frequency. As indicated above, this is due to the detection process, which measures different oscillation frequencies from the same acoustic mode with and without the additional TTG that acts as a spatial local oscillator. Note that the amplitudes of the even and odd oscillation maxima are different, which can be traced back to the heat diffusion dynamics of the first TTG between the two TG excitations breaking the symmetry. As case B reveals, the two TTGs converge in amplitude after a few nanoseconds. In case D (dark blue line), this is manifested in the equilibration of the even and odd oscillation maxima on the same time scale. However, this equilibration of oscillation amplitudes is not fully featured in the experimental data, which indicates an asymmetry in the TG excitation strengths. Also, the level around which the signal oscillates is larger. Indeed, the data are accurately reproduced [orange line in Fig. 4(d)] if we assume a 9% larger amplitude and a slight detuning of the spatial phase of 3% for the second excitation pulse. Such errors may stem from slight deviations from optimal laser beam and QWP alignments.

V. STRAIN CONTROL IN FUNCTIONAL MATERIALS

In the following paragraph, we outline possible interaction channels between the excited deformation and functional properties of the crystal. In particular, we describe strain-induced changes of the free energy density via magnetoelastic effects and changes of the electronic band energy via deformation potential coupling. Finally, we briefly introduce active optical elements that use dynamic strain fields to manipulate x-ray pulses emitted by synchrotron storage rings.

If strain is used as a functional tool, it is important to recall that the interaction of lattice deformations with a material strongly depends on the symmetry, i.e., on the specific component of the strain tensor ε. The strain fields corresponding to TTG and coherent Rayleigh-like SAWs are composed of both compressive or tensile (e.g., ε_{xx}, ε_{zz}) and shear (e.g., ε_{xz}) components. The TRXRR method detects the absolute surface deformation, i.e., the integrated out-of-plane expansion of the excited volume. However, knowing one component of the strain tensor of a Rayleigh wave allows us to infer all the other components as well [51]. In our coherent control scheme, all strain components of the coherent mode are customizable as well as

the in-plane and shear components of the TTG. Only the out-of-plane component of the thermal grating is given by the initially absorbed energy density profile.

In multiferroic materials, a dynamic strain wave modifies the free energy density due to elastic deformations of the lattice. As an example, we discuss ferromagnetic materials, where the magnetoelastic interaction modulates the free magnetic energy density f_{mag} [52]. In a static case, f_{mag} is composed of the Zeeman energy, which depends on an external magnetic field, and of static anisotropy components such as magnetocrystalline, shape, and magnetoelastic anisotropy [53]. The interplay of these terms results in a direction and magnitude of the macroscopic magnetization $\vec{M}$. Their dynamics can be induced through time-dependent changes of free magnetic energy f_{mag}. Prominent examples are ferromagnetic resonance (FMR) measurements [54], which act on the Zeeman energy or all-optical switching [55], where laser-induced heating leads to changes of the shape anisotropy. In complete analogy, an acoustic wave dynamically changes f_{mag} via the magnetoelastic energy term [52].

Although magnetoelastic interaction is well known, magnetoacoustics has only been investigated quite recently [8,56,57]. Since then, strain-induced magentization dynamics of nanoparticles excited specifically by Rayleigh waves has gained strong interest [58,59]. These efforts are driven by the potential of strain-induced dynamics, i.e., energy efficiency, mode selectivity, and the ability to tailor the excitation to nanosize dimensions. Several of these recent experiments use optical generation of strain waves, thus pushing magnetoelastic excitations to picosecond time scales [34,42,60]. The strain control scheme described in this article not only allows us to selectively excite magnetization dynamics, but also enables control of these excitations on picosecond time scales. In particular, this is not only limited to the coherent strain but rather extends to thermal strain, while maintaining the high temporal resolution.

The second interaction channel we discuss is the deformation potential coupling of electrons with acoustic phonons. The deformation of the crystal lattice by an acoustic lattice distortion leads to an energy shift $\Delta E = a\varepsilon$ of the extremal points of the electron bands, where a is the deformation potential, which typically has a value of about 10 eV at the Γ point of tetrahedral semiconductors such as Si or GaAs [61]. Hence, already a small dynamic strain of the order of 10^{-3} up to 10^{-2} leads to changes of the conduction and valence bands of 10–100 meV. Strain-induced changes of the electronic structure affect charge transport and optical properties [62,63] and provide control of recombination dynamics in nanostructures [6,64]. Strain control of optical properties of nanostructures is a promising candidate for applications in quantum computation and quantum information technology [65,66]. The realization of such applications depends on the ability to

control the lattice strain, ideally on short to ultrashort time scales. While the two examples given above may require probing mechanisms other than TRXRR (e.g., magneto-optical probing, optical and/or x-ray dichroism, or valence spectroscopies), the method presented in this paper may pave the way for these future applications.

Finally, we discuss a specific application developed by our group, where strain-induced deformations are used to realize active ultrafast x-ray optics. The devices are optimized for installation at synchrotron beamlines. A prominent example is the picosecond Bragg switch (PicoSwitch), which shortens an incident synchrotron x-ray pulse to a duration of a few picoseconds [67]. The coherent control of TTGs similar to case B (cf. Sec. II) allows for controlling diffraction of an incident x-ray pulse into the ± 1st diffraction order of the TTG. In particular, our approach allows us to turn the diffraction on and off on sub-nanosecond time scales. Thus, TTGs could be employed to pick individual x-ray pulses from a synchrotron pulse train for subsequent pump-probe experiments. Furthermore, the device may also be employed as a variable beam splitter in order to, e.g., distribute x-ray pulses among multiple beamlines. This may be particularly interesting at x-ray free-electron laser (XFEL) facilities, where currently only one experimental station is operational at a time. With such an approach, several instruments could be supplied with XFEL pulses in parallel. The main challenge for this device is to achieve high diffraction efficiencies. Our previous studies suggest that a maximum efficiency of more than 30% could be reached [14,15,68].

VI. CONCLUSION

In conclusion, we demonstrate spatiotemporal control of acoustic and thermal deformations of solid surfaces. The optical setup allows for generation of transient surface gratings with a variable spatial phase. Hence, a thermal deformation can either be enhanced or suppressed by a temporal sequence of excitation pulses on time scales much shorter than the deformation lifetime. In addition, we show that the suppression of the coherent signal facilitates investigations of multidirectional thermal transport in nanolayered heterostructures with high time resolution. We believe that our method presents an important step toward developing strain as a functional tool for solids and nanostructures. As examples, we discuss the magnetoelastic interaction in ferromagnetic materials. While numerous recent studies have demonstrated the ability to manipulate the macroscopic magnetization with coherent strain pulses, our present scheme paves the way for controlled strain-induced preparation of a ferromagnetic state. Strain control may also be applied to manipulate electronic states in bulk and low-dimensional semiconductors. Finally, we discuss active optical elements, which are a new kind of

strain-based device for ultrafast x-ray beam manipulation at synchrotrons.

[1] C. Thomsen, H. T. Grahn, H. J. Maris, and J. Tauc, Surface generation and detection of phonons by picosecond light pulses, Phys. Rev. B **34,** 4129 (1986).

[2] P. Ruello and V. E. Gusev, Physical mechanisms of coherent acoustic phonons generation by ultrafast laser action, Ultrasonics **56,** 21 (2015).

[3] R. Shayduk, M. Herzog, A. Bojahr, D. Schick, P. Gaal, W. Leitenberger, H. Navirian, M. Sander, J. Goldshteyn, I. Vrejoiu, and M. Bargheer, Direct time-domain sampling of subterahertz coherent acoustic phonon spectra in SrTiO₃ using ultrafast x-ray diffraction, Phys. Rev. B **87,** 184301 (2013).

[4] A. Bojahr, M. Gohlke, W. Leitenberger, J. Pudell, M. Reinhardt, A. von Reppert, M. Roessle, M. Sander, P. Gaal, and M. Bargheer, Second Harmonic Generation of Nanoscale Phonon Wave Packets, Phys. Rev. Lett. **115,** 195502 (2015).

[5] D. J. Singh, Q. Xu, and K. P. Ong, Strain effects on the band gap and optical properties of perovskite SrSnO₃ and BaSnO₃, Appl. Phys. Lett. **104,** 011910 (2014).

[6] M. Weiß, J. B. Kinzel, F. J. R. Schülein, M. Heigl, D. Rudolph, S. Morkötter, M. Döblinger, M. Bichler, G. Abstreiter, J. J. Finley, G. Koblmüller, A. Wixforth, and H. J. Krenner, Dynamic acoustic control of individual optically active quantum dot-like emission centers in heterostructure nanowires, Nano Lett. **14,** 2256 (2014).

[7] A. V. Scherbakov, A. S. Salasyuk, A. V. Akimov, X. Liu, M. Bombeck, C. Brüggemann, D. R. Yakovlev, V. F. Sapega, J. K. Furdyna, and M. Bayer, Coherent Magnetization Precession in Ferromagnetic (Ga,Mn)As Induced by Picosecond Acoustic Pulses, Phys. Rev. Lett. **105,** 117204 (2010).

[8] J.-W. Kim, M. Vomir, and J.-Y. Bigot, Ultrafast Magnetoacoustics in Nickel Films, Phys. Rev. Lett. **109,** 166601 (2012).

[9] R. Blattmann, H. J. Krenner, S. Kohler, and P. Hänggi, Entanglement creation in a quantum-dot–nanocavity system by fourier-synthesized acoustic pulses, Phys. Rev. A **89,** 012327 (2014).

[10] K. A. Nelson, R. J. D. Miller, D. R. Lutz, and M. D. Fayer, Optical generation of tunable ultrasonic waves, J. Appl. Phys. **53,** 1144 (1982).

[11] C. Klieber, E. Peronne, K. Katayama, J. Choi, M. Yamaguchi, T. Pezeril, and K. A. Nelson, Narrow-band acoustic attenuation measurements in vitreous silica at frequencies between 20 and 40 GHz, Appl. Phys. Lett. **98,** 211908 (2011).

[12] M. Herzog, A. Bojahr, J. Goldshteyn, W. Leitenberger, I. Vrejoiu, D. Khakhulin, M. Wulff, R. Shayduk, P. Gaal, and M. Bargheer, Detecting optically synthesized quasi-monochromatic sub-terahertz phonon wavepackets by ultrafast x-ray diffraction, Appl. Phys. Lett. **100,** 094101 (2012).

[13] F. J. R. Schülein, E. Zallo, P. Atkinson, O. G. Schmidt, R. Trotta, A. Rastelli, A. Wixforth, and H. J. Krenner, Fourier synthesis of radiofrequency nanomechanical pulses with different shapes, Nat. Nanotechnol. **10,** 512 EP (2015).

[14] M. Sander, M. Herzog, J. E. Pudell, M. Bargheer, N. Weinkauf, M. Pedersen, G. Newby, J. Sellmann, J. Schwarzkopf, V. Besse, V. V. Temnov, and P. Gaal, Spatiotemporal Coherent Control of Thermal Excitations in Solids, Phys. Rev. Lett. **119,** 075901 (2017).

[15] M. Sander, J.-E. Pudell, M. Herzog, M. Bargheer, R. Bauer, V. Besse, V. Temnov, and P. Gaal, Quantitative disentanglement of coherent and incoherent laser-induced surface deformations by time-resolved x-ray reflectivity, Appl. Phys. Lett. **111,** 261903 (2017).

[16] M. Bargheer, N. Zhavoronkov, Y. Gritsai, J. C. Woo, D. S. Kim, M. Woerner, and T. Elsaesser, Coherent atomic motions in a nanostructure studied by femtosecond x-ray diffraction, Science **306,** 1771 (2004).

[17] A. M. Lindenberg, I. Kang, S. L. Johnson, R. W. Falcone, P. A. Heimann, Z. Chang, R. W. Lee, and J. S. Wark, Coherent control of phonons probed by time-resolved x-ray diffraction, Opt. Lett. **27,** 869 (2002).

[18] O. Synnergren, T. N. Hansen, S. Canton, H. Enquist, P. Sondhauss, A. Srivastava, and J. Larsson, Coherent phonon control, Appl. Phys. Lett. **90,** 171929 (2007).

[19] P. Beaud, S. L. Johnson, A. Streun, R. Abela, D. Abramsohn, D. Grolimund, F. Krasniqi, T. Schmidt, V. Schlott, and G. Ingold, Spatiotemporal Stability of a Femtosecond Hard–X-ray Undulator Source Studied by Control of Coherent Optical Phonons, Phys. Rev. Lett. **99,** 174801 (2007).

[20] Y.-H. Cheng, F. Y. Gao, S. W. Teitelbaum, and K. A. Nelson, Coherent control of optical phonons in bismuth, Phys. Rev. B **96,** 134302 (2017).

[21] Q. Zhang, A. V. Nurmikko, A. Anguelouch, G. Xiao, and A. Gupta, Coherent Magnetization Rotation and Phase Control by Ultrashort Optical Pulses in CrO₂ Thin Films, Phys. Rev. Lett. **89,** 177402 (2002).

[22] T. Kampfrath, A. Sell, G. Klatt, A. Pashkin, S. Mährlein, T. Dekorsy, M. Wolf, M. Fiebig, A. Leitenstorfer, and R. Huber, Coherent terahertz control of antiferromagnetic spin waves, Nat. Photonics **5,** 31 (2010).

[23] J. Nishitani, T. Nagashima, and M. Hangyo, Terahertz radiation from antiferromagnetic MnO excited by optical laser pulses, Appl. Phys. Lett. **103,** 081907 (2013).

[24] D. W. Ward, J. D. Beers, T. Feurer, E. R. Statz, N. S. Stoyanov, and K. A. Nelson, Coherent control of

phonon-polaritons in a terahertz resonator fabricated with femtosecond laser machining, Opt. Lett. **29**, 2671 (2004).

[25] D. H. Hurley, R. Lewis, O. B. Wright, and O. Matsuda, Coherent control of gigahertz surface acoustic and bulk phonons using ultrafast optical pulses, Appl. Phys. Lett. **93**, 113101 (2008).

[26] Q. Li, K. Hoogeboom-Pot, D. Nardi, M. M. Murnane, H. C. Kapteyn, M. E. Siemens, E. H. Anderson, O. Hellwig, E. Dobisz, B. Gurney, R. Yang, and K. A. Nelson, Generation and control of ultrashort-wavelength two-dimensional surface acoustic waves at nanoscale interfaces, Phys. Rev. B **85**, 195431 (2012).

[27] H. F. Yang, F. Garcia-Sanchez, X. K. Hu, S. Sievers, T. Böhnert, J. D. Costa, M. Tarequzzaman, R. Ferreira, M. Bieler, and H. W. Schumacher, Excitation and coherent control of magnetization dynamics in magnetic tunnel junctions using acoustic pulses, Appl. Phys. Lett. **113**, 072403 (2018).

[28] M. Herzog, D. Schick, P. Gaal, R. Shayduk, C. V. Korff Schmising, M. Bargheer, Analysis of ultrafast X-ray diffraction data in a linear-chain model of the lattice dynamics, Appl. Phys. A **106**, 489 (2012).

[29] A. A. Maznev, A. Mazurenko, L. Zhuoyun, and M. Gostein, Laser-based surface acoustic wave spectrometer for industrial applications, Rev. Sci. Instrum. **74**, 667 (2003).

[30] A. Vega-Flick, J. K. Eliason, A. A. Maznev, A. Khanolkar, M. Abi Ghanem, N. Boechler, J. J. Alvarado-Gil, and K. A. Nelson, Laser-induced transient grating setup with continuously tunable period, Rev. Sci. Instrum. **86**, 123101 (2015).

[31] W. Sauer, M. Streibl, T. H. Metzger, A. G. C. Haubrich, S. Manus, A. Wixforth, J. Peisl, A. Mazuelas, J. Härtwig, and J. Baruchel, X-ray imaging and diffraction from surface phonons on GaAs, Appl. Phys. Lett. **75**, 1709 (1999).

[32] J.-D. Nicolas, T. Reusch, M. Osterhoff, M. Sprung, F. J. R. Schülein, H. J. Krenner, A. Wixforth, and T. Salditt, Time-resolved coherent x-ray diffraction imaging of surface acoustic waves, J. Appl. Crystallogr. **47**, 1596 (2014).

[33] M. Foerster, N. Statuto, B. Casals, A. Hernández-Mínguez, S. Finizio, A. Mandziak, L. Aballe, J. M. Hernàndez Ferràs, and F. Macià, Quantification of propagating and standing surface acoustic waves by stroboscopic x-ray photoemission electron microscopy, J. Synchrotron Radiat. **26**, 184 (2019).

[34] J. Janušonis, T. Jansma, C. L. Chang, Q. Liu, A. Gatilova, A. M. Lomonosov, V. Shalagatskyi, T. Pezeril, V. V. Temnov, and R. I. Tobey, Transient grating spectroscopy in magnetic thin films: Simultaneous detection of elastic and magnetic dynamics, Sci. Rep. **6**, 29143 (2016).

[35] F. Lagugné Labarthet, T. Buffeteau, and C. Sourisseau, Azopolymer holographic diffraction gratings: Time dependent analyses of the diffraction efficiency, birefringence, and surface modulation induced by two linearly polarized interfering beams, J. Phys. Chem. B **103**, 6690 (1999).

[36] The incident laser power per TG excitation is 970 mW at a 1-kHz repetition rate. The footprint of the noninterfering laser beams at the sample surface (elliptical Gaussian) is 4.0×3.4 mm^2 (major and minor $1/e$ diameter). Assuming a homogeneous distribution of the laser pulse energy over an ellipse, having the above size yields a pump fluence

of 9 mJ/cm^2. Because of the interference of the crossing laser beams, the TG fringes at the center of the elliptical Gaussian have twice that fluence in the maximum.

[37] A. A. Maznev *et al.*, Generation of coherent phonons by coherent extreme ultraviolet radiation in a transient grating experiment, Appl. Phys. Lett. **113**, 221905 (2018).

[38] C. Svetina *et al.*, Towards x-ray transient grating spectroscopy, Opt. Lett. **44**, 574 (2019).

[39] M. Wulff, A. Plech, L. Eybert, R. Randler, F. Schotte, and P. Anfinrud, The realization of sub-nanosecond pump and probe experiments at the ESRF, Faraday Discuss. **122**, 13 (2003).

[40] M. Cammarata, L. Eybert, F. Ewald, W. Reichenbach, M. Wulff, P. Anfinrud, F. Schotte, A. Plech, Q. Kong, M. Lorenc, B. Lindenau, J. Räbiger, and S. Polachowski, Chopper system for time resolved experiments with synchrotron radiation, Rev. Sci. Instrum. **80**, 015101 (2009).

[41] D. Schick, M. Herzog, A. Bojahr, W. Leitenberger, A. Hertwig, R. Shayduk, and M. Bargheer, Ultrafast lattice response of photoexcited thin films studied by x-ray diffraction, Struct. Dyn. **1**, 064501 (2014).

[42] C. L. Chang, A. M. Lomonosov, J. Janusonis, V. S. Vlasov, V. V. Temnov, and R. I. Tobey, Parametric frequency mixing in a magnetoelastically driven linear ferromagnetic-resonance oscillator, Phys. Rev. B **95**, 060409(R) (2017).

[43] O. W. Käding, H. Skurk, A. A. Maznev, and E. Matthias, Transient thermal gratings at surfaces for thermal characterization of bulk materials and thin films, Appl. Phys. A **61**, 253 (1995).

[44] J. A. Johnson, A. A. Maznev, M. T. Bulsara, E. A. Fitzgerald, T. C. Harman, S. Calawa, C. J. Vineis, G. Turner, and K. A. Nelson, Phase-controlled, heterodyne laser-induced transient grating measurements of thermal transport properties in opaque material, J. Appl. Phys. **111**, 023503 (2012).

[45] J. Hidde, C. Guguschev, S. Ganschow, and D. Klimm, Thermal conductivity of rare-earth scandates in comparison to other oxidic substrate crystals, J. Alloys Compd. **738**, 415 (2018).

[46] S. Yamanaka, T. Maekawa, H. Muta, T. Matsuda, S.-I. Kobayashi, and K. Kurosaki, Thermophysical properties of SrHfO3 and SrRuO3, J. Solid State Chem. **177**, 3484 (2004).

[47] R. Uecker, B. Velickov, D. Klimm, R. Bertram, M. Bernhagen, M. Rabe, M. Albrecht, R. Fornari, and D. Schlom, Properties of rare-earth scandate single crystals (Re = Nd–Dy), J. Cryst. Growth **310**, 2649 (2008).

[48] R. Shayduk, H. Navirian, W. Leitenberger, J. Goldshteyn, I. Vrejoiu, M. Weinelt, P. Gaal, M. Herzog, C. V. K. Schmising, and M. Bargheer, Nanoscale heat transport studied by high-resolution time-resolved x-ray diffraction, New J. Phys. **13**, 093032 (2011).

[49] D. Schick, A. Bojahr, M. Herzog, R. Shayduk, C. von Korff Schmising, and M. Bargheer, udkm1Dsim − A simulation toolkit for 1D ultrafast dynamics in condensed matter, Comput. Phys. Commun. **185**, 651 (2014).

[50] M. Herzog, D. Schick, W. Leitenberger, R. Shayduk, R. M. van der Veen, C. J. Milne, S. L. Johnson, I. Vrejoiu, and M. Bargheer, Tailoring interference and nonlinear

manipulation of femtosecond x-rays, New J. Phys. **14,** 013004 (2012).

[51] P. Haas, Surface acoustic waves in materials science, Phys. Today **55,** 42 (2002).

[52] D. Sander, A. Enders, and J. Kirschner, Stress and magnetic properties of surfaces and ultrathin films, J. Magn. Magn. Mater. **200,** 439 (1999).

[53] R. C. O'Handley, *Modern magnetic materials: Principles and applications* (John Wiley, New York, 2000).

[54] M. Farle, Ferromagnetic resonance of ultrathin metallic layers, Rep. Prog. Phys. **61,** 755 (1998).

[55] A. Kirilyuk, A. V. Kimel, and T. Rasing, Ultrafast optical manipulation of magnetic order, Rev. Mod. Phys. **82,** 2731 (2010).

[56] M. Deb, E. Popova, M. Hehn, N. Keller, S. Mangin, and G. Malinowski, Picosecond acoustic-excitation-driven ultrafast magnetization dynamics in dielectric bi-substituted yttrium iron garnet, Phys. Rev. B **98,** 174407 (2018).

[57] S. P. Zeuschner, T. Parpiiev, T. Pezeril, A. Hillion, K. Dumesnil, A. Anane, J. Pudell, L. Willig, M. Rössle, M. Herzog, A. von Reppert, and M. Bargheer, Tracking picosecond strain pulses in heterostructures that exhibit giant magnetostriction, Struct. Dyn. **6,** 024302 (2019).

[58] Y. Yahagi, B. Harteneck, S. Cabrini, and H. Schmidt, Controlling nanomagnet magnetization dynamics via magnetoelastic coupling, Phys. Rev. B **90,** 140405(R) (2014).

[59] J. Tejada, E. M. Chudnovsky, R. Zarzuela, N. Statuto, J. C. de la Rosa, P. V. Santos, and A. Hernández-Mínguez, Switching of magnetic moments of nanoparticles by surface acoustic waves, Europhys. Lett. **118,** 37005 (2017).

[60] C. L. Chang, R. R. Tamming, T. J. Broomhall, J. Janusonis, P. W. Fry, R. I. Tobey, and T. J. Hayward, Selective

Excitation of Localized Spin-Wave Modes by Optically Pumped Surface Acoustic Waves, Phys. Rev. Appl. **10,** 034068 (2018).

[61] A. Blacha, H. Presting, and M. Cardona, Deformation potentials of $k = 0$ states of tetrahedral semiconductors, Phys. Stat. Sol. (b) **126,** 11 (1984).

[62] Y. Wang, Y. Chen, H. Li, X. Li, H. Chen, Y. Su, Y. Lin, Y. Xu, G. Song, and X. Feng, Buckling-based method for measuring the strain–photonic coupling effect of GaAs nanoribbons, ACS Nano **10,** 8199 (2016).

[63] O. D. D. Couto, Jr., S. Lazic, F. Iikawa, J. A. H. Stotz, U. Jahn, R. Hey, and P. V. Santos, Photon anti-bunching in acoustically pumped quantum dots, Nat. Photonics **3,** 645 EP (2009).

[64] M. M. de Lima and P. V. Santos, Modulation of photonic structures by surface acoustic waves, Rep. Prog. Phys. **68,** 1639 (2005).

[65] C. H. W. Barnes, J. M. Shilton, and A. M. Robinson, Quantum computation using electrons trapped by surface acoustic waves, Phys. Rev. B **62,** 8410 (2000).

[66] M. J. A. Schuetz, E. M. Kessler, G. Giedke, L. M. K. Vandersypen, M. D. Lukin, and J. I. Cirac, Universal Quantum Transducers Based on Surface Acoustic Waves, Phys. Rev. X **5,** 031031 (2015).

[67] M. Sander, R. Bauer, V. Kabanova, M. Levantino, M. Wulff, D. Pfuetzenreuter, J. Schwarzkopf, and P. Gaal, Demonstration of a picosecond Bragg switch for hard x-rays in a synchrotron-based pump–probe experiment, J. Synchrotron Radiat. **26,** 1253 (2019).

[68] S. Vadilonga, I. Zizak, D. Roshchupkin, A. Petsiuk, I. Dolbnya, K. Sawhney, and A. Erko, Pulse picker for synchrotron radiation driven by a surface acoustic wave, Opt. Lett. **42,** 1915 (2017).

Conclusion

In this thesis based on 17 publications I summarize my contributions to the research field of ultrafast structural dynamics. It covers the complex interplay between electron, magnon, and phonon subsystems and the resulting lattice strain after laser excitation.

In article I we present a perspective on the ultrafast coupling between electron and phonons in metal heterostructures. The optical excitation of a 6 nm gold layer on top of a 12 nm nickel layer leads to a rapid heating of the nickel lattice while the gold lattice initially remains cold. This was observed with ultrafast x-ray diffraction (UXRD) measuring time-resolved the lattice constant of gold and nickel: The covered nickel layer directly expands after the optical excitation whereas the gold layer is compressed by the expansion of the nickel layer. The observed heat transfer from nickel to the gold lattice is found to be very slow, on a time scale of 100 ps. The reason for this is that the optically introduced energy is rapidly coupled with the nickel lattice. The large lattice heat capacity of nickel results in low temperature gradients between the gold lattice and the nickel and therefore leads to the observed slow thermal transport of heat to the gold lattice.

In article II the ultrafast transport by hot electrons through a material with weak electron–phonon coupling is investigated with UXRD. From an optically excited 5 nm platinum layer electrons travel through a 100 nm copper layer and couple to the lattice in a 20 nm nickel layer. The layer-specific UXRD probe allows to track the energy transport, which can be modeled by a diffusive two-temperature model considering the increased heat conductivity of hot electrons. We found that the transport by hot electrons considering the electron–phonon coupling leads to a linear rise time of the relative temperature, i.e. $T_{\mathrm{rise}}^{\mathrm{e}} = 10\% T_{\mathrm{max}}^{\mathrm{e}}$.

The ultrafast heat transport is of great interest in nanoscale metal multilayers in the context of optically induced demagnetization, remagnetization, and switching. In articles V– X we discuss the interplay of lattice and magnetism.

In article VI the lattice dynamics of the rare earth metal holmium are discussed. In the paramagnetic (PM) phase the optical excitation results in an exponentially decreasing stress profile driving the strain wave. The experiments using a burried strain detection layer show that the stress profile closely matches the optical penetration depth. In the antiferromagnetic (AFM) phase the optical excitation induces an additional negative thermal expansion (NTE) with quasi-instantaneous contractive stress and a second contractive stress contribution that increases on a 12 ps time scale attributed to the spin disordering time scale. A numerical modeling using the UDKM1DSIM toolbox was required to extract the time scales of the observed ultrafast NTE. This model was used to describe the positive and negative stress produced by the excited phonon and spins in holmium. In article VII an extended model is presented. It considers saturation effects at the phase transition within the magnetic transducer and fits the UXRD data sets of the rare earth metal dysprosium.

Another topic of this thesis is the coherent control of excitations. Temporally delayed excitations allow the enhancement or suppression of acoustic excitations to trigger material specific properties in order to use them as a new excitation or use such samples as ultrafast switch. In article XVII a setup to excite two spatiotemporal shifted transient gratings on the sample surface is introduced. This setup allows the excitation of a spatiotemporal shifted pair of thermal and acoustic periodic surface deformations. The resulting excitations are measured by time-resolved x-ray reflectivity (TR-XRR) and can be used as an ultrafast x-ray switch.

Within the course of this thesis I rebuilt the optical path and implemented upgrades of the existing laser-driven table-top UXRD setup. These upgrades allow us to achieve an enhancement of the x-ray flux and reduce the maintenance time of the setup. This enables the study of single digit nanometer thin films with UXRD. The extension of the UXRD setup with a magneto-optic Kerr effect (MOKE) and optical reflectivity setup enable in-situ and operando studies of the energy flux in magnetic materials in the future.

The combination of these three techniques deliver promising results enriching the discussion about the coupling of different subsystems in materials. These experiments prove the applicability of the N-temperature model (NTM) and give insights in the energy flux after optical excitation.

From a physical point of view, the interplay between different dimensions is interesting. Here, measurements of the in-plane and out-of plane dynamics of thin films and nano cubes could give answers to the coupling between the in-plane and out-of plane stresses and strains.

To perform theses studies x-ray free-electron lasers (XFELs) are an interesting tool providing ultrashort pulses with high x-ray flux. This enables studies on thinner samples that show faster dynamics. Furthermore, inelastic scattering techniques are available, which can monitor the excited phonon population momentum- and frequency-resolved [121].

Bibliography

[1] D. G. Schlom, L.-Q. Chen, C. J. Fennie, V. Gopalan, D. A. Muller, X. Pan, R. Ramesh and R. Uecker: "Elastic strain engineering of ferroic oxides", *MRS Bulletin* 39, 118 (2014)

[2] L. W. Martin and A. M. Rappe: "Thin-film ferroelectric materials and their applications", *Nature Reviews Materials* 2, 16087 (2016)

[3] J. Coey, Ariando and W. Pickett: "Magnetism at the edge: New phenomena at oxide interfaces", *MRS Bulletin* 38, 1040 (2013)

[4] E. Dagotto: "Complexity in Strongly Correlated Electronic Systems", *Science* 309, 257 (2005)

[5] J. Zhang and R. Averitt: "Dynamics and Control in Complex Transition Metal Oxides", *Annual Review of Materials Research* 44, 19 (2014)

[6] N. A. Spaldin: *Ferroelectric Materials and Their Applications* (Cambridge University Press, 2010), 1st edition

[7] N. A. Spaldin: *Magnetic Materials: Fundamentals and Applications* (Cambridge University Press, 2010), 2nd edition

[8] D. Weller, O. Mosendz, G. Parker, S. Pisana and T. S. Santos: "L10 FePtX-Y media for heat-assisted magnetic recording", *physica status solidi (a)* 210, 1245 (2013)

[9] D. Weller, G. Parker, O. Mosendz, A. Lyberatos, D. Mitin, N. Y. Safonova and M. Albrecht: "Review Article: FePt heat assisted magnetic recording media", *Journal of Vacuum Science & Technology B, Nanotechnology and Microelectronics: Materials, Processing, Measurement, and Phenomena* 34, 060801 (2016)

[10] J. Zhu and Y. Wang: "Microwave Assisted Magnetic Recording Utilizing Perpendicular Spin Torque Oscillator With Switchable Perpendicular Electrodes", *IEEE Transactions on Magnetics* 46, 751 (2010)

[11] C. M. Wolff, P. Caprioglio, M. Stolterfoht and D. Neher: "Nonradiative Recombination in Perovskite Solar Cells: The Role of Interfaces", *Advanced Materials* 1902762 (2019)

[12] B. K. Tanner: "High resolution X-ray diffraction and topography for crystal characterization", *Journal of Crystal Growth* 99, 1315 (1990)

[13] B. Warren: *X-ray Diffraction* Addison-Wesley series in metallurgy and materials engineering (Dover Publications, 1990)

[14] R. Schoenlein, T. Elsaesser, K. Holldack, Z. Huang, H. Kapteyn, M. Murnane and M. Woerner: "Recent advances in ultrafast X-ray sources", *Philosophical Transactions of the Royal Society A: Mathematical, Physical and Engineering Sciences* 377, 20180384 (2019)

[15] W. C. Röntgen: *Über eine neue Art von Strahlen* (Stahel, Würzburg, 1896), 2nd edition

[16] B. L. Henke, E. M. Gullikson and J. C. Davis: "X-ray interactions: photoabsorption, scattering,

transmission, and reflection at E=50-30000 eV, Z=1-92", *Atomic Data and Nuclear Data Tables* 54, 181 (1993)

[17] V. Holy, T. Baumbach and U. Pietsch: *High-Resolution X-Ray Scattering from Thin Films and Multilayers*, volume 149 of *Springer Tracts in Modern Physics*(Springer, Berlin and Heidelberg, 1999)

[18] L. J. P. Ament, M. van Veenendaal, T. P. Devereaux, J. P. Hill and J. van den Brink: "Resonant inelastic x-ray scattering studies of elementary excitations", *Phys. Chem. Chem. Phys.* 83, 705 (2011)

[19] J. Als-Nielsen and Des McMorrow: *Elements of modern X-ray physics* (Wiley, Chichester, 2011), second edition edition

[20] A. McPherson, G. Gibson, H. Jara, U. Johann, T. S. Luk, I. A. McIntyre, K. Boyer and C. K. Rhodes: "Studies of multiphoton production of vacuum-ultraviolet radiation in the rare gases", *Journal of the Optical Society of America B* 4, 595 (1987)

[21] X. F. Li, A. L'Huillier, M. Ferray, L. A. Lompré and G. Mainfray: "Multiple-harmonic generation in rare gases at high laser intensity", *Phys. Rev. A* 39, 5751 (1989)

[22] M. M. Murnane, H. C. Kapteyn, M. D. Rosen and R. W. Falcone: "Ultrafast X-ray Pulses from Laser-Produced Plasmas", *Science* 251, 531 (1991)

[23] M. Bargheer, N. Zhavoronkov, Y. Gritsai, J. C. Woo, D. S. Kim, M. Woerner and T. Elsaesser: "Coherent atomic motions in a nanostructure studied by femtosecond X-ray diffraction", *Science* 306, 1771 (2004)

[24] M. Bargheer, N. Zhavoronkov, M. Woerner and T. Elsaesser: "Recent progress in ultrafast X-ray diffraction", *Chemphyschem : a European journal of chemical physics and physical chemistry* 7, 783 (2006)

[25] M. Bargheer: "Atombewegung im Röntgenkino - Die Femtosekunden-Röntgenbeugung entschlüsselt ultraschnelle Gitterdynamik", *Physik Journal* 6, 1 (2007)

[26] F. Zamponi et al.: "Femtosecond hard X-ray plasma sources with a kilohertz repetition rate", *Applied Physics A* 96, 51 (2009)

[27] J. Weisshaupt, V. Juvé, M. Holtz, S. Ku, M. Woerner, T. Elsaesser, S. Ališauskas, A. Pugžlys and A. Baltuška: "High-brightness table-top hard X-ray source driven by sub-100-femtosecond mid-infrared pulses", *Nature Photonics* 8, 927 (2014)

[28] N. Zhavoronkov, Y. Gritsai, M. Bargheer, M. Woerner, T. Elsaesser, F. Zamponi, I. Uschmann and E. Förster: "Microfocus Cu K? source for femtosecond x-ray science", *Optics Letters* 30, 1737 (2005)

[29] N. Zhavoronkov, Y. Gritsai, M. Bargheer, M. Woerner and T. Elsaesser: "Generation of ultrashort K_α radiation from quasipoint interaction area of femtosecond pulses with thin foils", *Applied Physics Letters* 86, 244107 (2005)

[30] M. Bargheer, N. Zhavoronkov, R. Bruch, H. Legall, H. Stiel, M. Woerner and T. Elsaesser: "Comparison of focusing optics for femtosecond X-ray diffraction", *Applied Physics B* 80, 715 (2005)

[31] Schoenlein, Chattopadhyay, Chong, Glover, Heimann, Shank, Zholents and Zolotorev: "Generation of femtosecond pulses of synchrotron radiation", *Science* 287, 2237 (2000)

[32] S. Khan, K. Holldack, T. Kachel, R. Mitzner and T. Quast: "Femtosecond Undulator Radiation from Sliced Electron Bunches", *Physical Review Letters* 97, 074801 (2006)

[33] D. Schick et al.: "Analysis of the halo background in femtosecond slicing experiments", *Journal of Synchrotron Radiation* 23, 700 (2016)

[34] P. Gaal et al.: "Ultrafast switching of hard X-rays", *Journal of synchrotron radiation* 21, 380 (2014)

[35] M. Sander, R. Bauer, V. Kabanova, M. Levantino, M. Wulff, D. Pfuetzenreuter, J. Schwarzkopf and P. Gaal: "Demonstration of a picosecond Bragg switch for hard X-rays in a synchrotron-based pump–probe experiment", *Journal of Synchrotron Radiation* 26, 1253 (2019)

[36] S. Vadilonga, I. Zizak, D. Roshchupkin, A. Petsiuk, I. Dolbnya, K. Sawhney and A. Erko: "Pulse picker for synchrotron radiation driven by a surface acoustic wave", *Opt. Lett.* 42, 1915 (2017)

[37] R. Shayduk and P. Gaal: "Transition regime in the ultrafast laser heating of solids" (2020)

[38] C. Bostedt et al.: "Linac Coherent Light Source: The first five years", *Rev. Mod. Phys.* 88, 015007 (2016)

[39] S. Huang et al.: "Generating Single-Spike Hard X-Ray Pulses with Nonlinear Bunch Compression in Free-Electron Lasers", *Physical Review Letters* 119, 154801 (2017)

[40] M. Chergui and A. H. Zewail: "Electron and X-Ray Methods of Ultrafast Structural Dynamics: Advances and Applications", *ChemPhysChem* 10, 28 (2009)

[41] A. Rousse, C. Rischel and J.-C. Gauthier: "Femtosecond x-ray crystallography", *Rev. Mod. Phys.* 73, 17 (2001)

[42] F. Schotte, M. Lim, T. A. Jackson, A. V. Smirnov, J. Soman, J. S. Olson, G. N. Phillips, M. Wulff and P. A. Anfinrud: "Watching a Protein as it Functions with 150-ps Time-Resolved X-ray Crystallography", *Science* 300, 1944 (2003)

[43] N. Thielemann-Kühn, D. Schick, N. Pontius, C. Trabant, R. Mitzner, K. Holldack, H. Zabel, A. Föhlisch and C. Schüßler-Langeheine: "Ultrafast and Energy-Efficient Quenching of Spin Order: Antiferromagnetism Beats Ferromagnetism", *Phys. Rev. Lett.* 119, 197202 (2017)

[44] D. Schick, A. Bojahr, M. Herzog, P. Gaal, I. Vrejoiu and M. Bargheer: "Following strain-induced mosaicity changes of ferroelectric thin films by ultrafast reciprocal space mapping", *Physical review letters* 110, 095502 (2013)

[45] T. Barron, J. Collins and G. White: "Thermal expansion of solids at low temperatures", *Advances in Physics* 29, 609 (1980)

[46] G. K. White: "Phase transitions and the thermal expansion of holmium", *Journal of Physics: Condensed Matter* 1, 6987 (1989)

[47] G. Ernst, C. Broholm, G. R. Kowach and A. P. Ramirez: "Phonon density of states and negative thermal expansion in ZrW2O8", *Nature* 396, 147 (1998)

[48] S. Khmelevskyi, I. Turek and P. Mohn: "Large negative magnetic contribution to the thermal expansion in iron-platinum alloys: quantitative theory of the Invar effect", *Physical review letters* 91, 037201 (2003)

[49] C. v. Korff Schmising et al.: "Ultrafast magnetostriction and phonon-mediated stress in a photoexcited ferromagnet", *Physical Review B* 78 (2008)

[50] M. Nicoul, U. Shymanovich, A. Tarasevitch, D. von der Linde and K. Sokolowski-Tinten: "Picosec-

ond acoustic response of a laser-heated gold-film studied with time-resolved x-ray diffraction", *Applied Physics Letters* 98, 191902 (2011)

[51] J. Chen, L. Fan, Y. Ren, Z. Pan, J. Deng, R. Yu and X. Xing: "Unusual transformation from strong negative to positive thermal expansion in PbTiO3-BiFeO3 perovskite", *Physical review letters* 110, 115901 (2013)

[52] R. M. van der Veen, O.-H. Kwon, A. Tissot, A. Hauser and A. H. Zewail: "Single-nanoparticle phase transitions visualized by four-dimensional electron microscopy", *Nature chemistry* 5, 395 (2013)

[53] D. J. Singh, Q. Xu and K. P. Ong: "Strain effects on the band gap and optical properties of perovskite $SrSnO_3$ and $BaSnO_3$", *Applied Physics Letters* 104, 011910 (2014)

[54] M. Weiß et al.: "Dynamic acoustic control of individual optically active quantum dot-like emission centers in heterostructure nanowires", *Nano Letters* 14, 2256 (2014)

[55] A. V. Scherbakov et al.: "Coherent magnetization precession in ferromagnetic (Ga,Mn)As induced by picosecond acoustic pulses", *Physical Review Letters* 105, 117204 (2010)

[56] J.-W. Kim, M. Vomir and J.-Y. Bigot: "Ultrafast magnetoacoustics in nickel films", *Physical Review Letters* 109, 166601 (2012)

[57] M. Deb, E. Popova, M. Hehn, N. Keller, S. Mangin and G. Malinowski: "Picosecond acoustic-excitation-driven ultrafast magnetization dynamics in dielectric Bi-substituted yttrium iron garnet", *Physical Review B* 98, 444 (2018)

[58] M. Deb, E. Popova, M. Hehn, N. Keller, S. Petit-Watelot, M. Bargheer, S. Mangin and G. Malinowski: "Femtosecond Laser-Excitation-Driven High Frequency Standing Spin Waves in Nanoscale Dielectric Thin Films of Iron Garnets", *Phys. Rev. Lett.* 123, 027202 (2019)

[59] A. Koç: "Ultrafast x-ray studies on the non-equilibrium of the magnetic and phononic system in heavy rare-earths" doctoralthesis, Universität Potsdam (2018)

[60] R. Gross and A. Marx: *Festkörperphysik* (de Gruyter, Berlin, 2014), 2nd edition

[61] J.-C. Diels and W. Rudolph: *Ultrashort Laser Pulse Phenomena : Fundamentals, Techniques, and Applications on a Femtosecond Time Scale* (Elsevier, Amsterdam, 2006), 2nd edition

[62] R. Menzel: *Phontonics – Linear and Nonlinear Interactions of Laser Light and Matter* (Springer, Berlin, 2007), 2nd edition

[63] T. G. Mayerhöfer, H. Mutschke and J. Popp: "Employing Theories Far beyond Their Limits—The Case of the (Boguer-) Beer–Lambert Law", *ChemPhysChem* 17, 1948 (2016)

[64] M. Bass, E. W. Van Stryland, D. R. Williams and W. L. Wolfe: "Volume I: Fundamentals, Techniques, and Design" in *Handbook of Optics,* (McGraw-Hill, Inc., New York, NY, USA, 2010), 2nd edition

[65] A. Khorsand, M. Savoini, A. Kirilyuk and T. Rasing: "Optical excitation of thin magnetic layers in multilayer structures", *Nature materials* 13, 101 (2014)

[66] A. Eschenlohr et al.: "Reply to Optical excitation of thin magnetic layers in multilayer structures", *Nature materials* 13, 102 (2014)

[67] Abelès, Florin: "La théorie générale des couches minces", *Journal de Physique et Le Radium* 11, 307 (1950)

[68] P. Lissberger: "The Relationship between Optical Absorptance and Electric Field of the Radiation in Multilayer Thin Films", *Optica Acta: International Journal of Optics* 28, 187 (1981)

[69] H. Ishida and K. Ohta: "Matrix Formalism for Calculation of Electric Field Intensity of Light in Stratified Multilayered Films", *Applied Optics* 29, 1952 (1990)

[70] K. Ohta and H. Ishida: "Matrix Formalism for Calculation of the Light Beam Intensity in Stratified Multilayered Films, and its Use in the Analysis of Emission Spectra", *Applied Optics* 29, 2466 (1990)

[71] L. Le Guyader, A. Kleibert, F. Nolting, L. Joly, P. M. Derlet, R. V. Pisarev, A. Kirilyuk, T. Rasing and A. V. Kimel: "Dynamics of Laser-Induced Spin Reorientation in $Co/SmFeO_3$ Heterostructure", *Physical Review B* 87, 054437 (2013)

[72] L. D. Landau and E. M. Lifshitz: "Electrodynamics of Continuous Media" in *Course of Theoretical Physics*, volume 8 (Pergamon Press, Oxford, 1960), 2nd edition

[73] J. D. Jackson: *Classical Electrodynamics* (John Wiley & Sons, New York, 1998), 3rd edition

[74] P. M. Oppeneer: "Magneto-Optical Kerr Spectra" in K. H. J. Buschow (Editor), *Handbook of Magnetic Materials*, volume 13, chapter 3, 229–422 (Elsevier, Amsterdam, 2001), 1st edition

[75] P. S. Pershan: "Magneto-Optical Effects", *Journal of Applied Physics* 38, 1482 (1967)

[76] G. Jellison Jr.: "Data analysis for spectroscopic ellipsometry", *Thin Solid Films* 234, 416 (1993)

[77] M. N. Polyanskiy: "Refractive index database" https://refractiveindex.info

[78] J. Humlíček: "Polarized Light and Ellipsometry" in *Handbook of Optics* (Springer, Berlin, 2005), 1st edition

[79] L. G. Parratt: "Surface Studies of Solids by Total Reflection of X-Rays", *Phys. Rev.* 95, 359 (1954)

[80] J. Daillant and A. Gibaud: *X-ray and Neutron Reflectivity – Principles and Applications* (Springer, Berlin, 2009), 1st edition

[81] N. Ashcroft and N. Mermin: *Solid State Physics* (Harcourt College, Orlando, 1976)

[82] X. Wang, S. Nie, J. Li, R. Clinite, J. E. Clark and J. Cao: "Temperature dependence of electron-phonon thermalization and its correlation to ultrafast magnetism", *Physical Review B* 81 (2010)

[83] D. G. Cahill et al.: "Nanoscale thermal transport. II. 2003–2012", *Applied Physics Reviews* 1, 011305 (2014)

[84] D. Schick, A. Bojahr, M. Herzog, R. Shayduk, C. von Korff Schmising and M. Bargheer: "UDKM1DSIM – A Simulation Toolkit for 1D Ultrafast Dynamics in Condensed Matter", *Computer Physics Communications* 185, 651 (2014)

[85] B. C. Rethfeld: "Mikroskopische Prozesse bei der Wechselwirkung von Festkörpern mit Laser-pulsen im Subpikosekundenbereich" doctoralthesis, Technische Universität Carolo-Wilhelmina zu Braunschweig (1999)

[86] X. Y. Wang, D. M. Riffe, Y.-S. Lee and M. C. Downer: "Time-resolved electron-temperature measurement in a highly excited gold target using femtosecond thermionic emission", *Physical Review B* 50, 8016 (1994)

[87] L. D. Landau and E. M. Lifshitz: "Theory of Elasticity" in *Course of Theoretical Physics*, volume 7 (Pergamon Press, Oxford, 1959), 2nd edition

[88] S. Anisimov and B. Kapeliovich: "Electron emission from metal surfaces exposed to ultrashort laser pulses", *The Journal of Experimental and Theoretical Physics* 66, 375 (1974)

[89] M. Bonn, D. N. Denzler, S. Funk, M. Wolf, S.-S. Wellershoff and J. Hohlfeld: "Ultrafast electron dynamics at metal surfaces: Competition between electron-phonon coupling and hot-electron transport", *Physical Review B* 61, 1101 (2000)

[90] J. Hohlfeld, J. Müller, S.-S. Wellershoff and E. Matthias: "Time-resolved thermoreflectivity of thin gold films and its dependence on film thickness", *Applied Physics B* 64, 387 (1997)

[91] G. D. Barrera, J. A. O. Bruno, T. H. K. Barron and N. L. Allan: "Negative thermal expansion", *Journal of Physics: Condensed Matter* 17, R217 (2005)

[92] E. Grüneisen: "Theorie des festen Zustandes einatomiger Elemente", *Annalen der Physik* 344, 257 (1912)

[93] E. Grüneisen: *Zustand des festen Körpers* (Springer, Berlin, 1926)

[94] P. Ruello and V. E. Gusev: "Physical mechanisms of coherent acoustic phonons generation by ultrafast laser action", *Ultrasonics* 56, 21 (2015)

[95] C. Thomsen, H. T. Grahn, H. J. Maris and J. Tauc: "Surface generation and detection of phonons by picosecond light pulses", *Physical Review B* 34, 4129 (1986)

[96] R. S. Krishnan, R. Srinivasan, S. Devanarayanan and B. R. Pamplin: *Thermal Expansion of Crystals: International Series in The Science of The Solid State* (Elsevier Science, Burlington, 1979)

[97] A. Bojahr: "Hypersound interaction studied by time-resolved inelastic light and x-ray scattering" doctoralthesis, Universität Potsdam (2016)

[98] M. Sander: "Ultrafast tailored strain fields in nanostructures" doctoralthesis, Universität Potsdam (2018)

[99] D. Royer and E. Dieulesaint: *Elastic Waves in Solids II – Generation, Acousto-optic Interaction, Applications* (Springer, Berlin, 2000), 1st edition

[100] J. Janušonis, C. L. Chang, T. Jansma, A. Gatilova, V. S. Vlasov, A. M. Lomonosov, V. V. Temnov and R. I. Tobey: "Ultrafast magnetoelastic probing of surface acoustic transients", *Phys. Rev. B* 94, 024415 (2016)

[101] G. P. Berman and F. M. Izrailev: "The Fermi-Pasta-Ulam problem: Fifty years of progress", *Chaos: An Interdisciplinary Journal of Nonlinear Science* 15, 015104 (2005)

[102] C. Herring: "Role of Low-Energy Phonons in Thermal Conduction", *Phys. Rev.* 95, 954 (1954)

[103] M. Mattern: "Hyperschall und akustische Solitonen in Dysprosiumscandat" Bachelor's thesis, University of Potsdam, Potsdam (2019)

[104] O. L. Muskens and J. I. Dijkhuis: "High Amplitude, Ultrashort, Longitudinal Strain Solitons in Sapphire", *Phys. Rev. Lett.* 89, 285504 (2002)

[105] B. Auld: *Acoustic fields and waves in solids* (John Wiley & Sons, New York, 1973), 1st edition

[106] A. von Reppert: "Ultrafast Magnetostriction in Dysprosium studied by Femtosecond X-Ray diffraction" Master's thesis, University of Potsdam, Potsdam (2015)

[107] L. Rayleigh: "On Waves Propagated along the Plane Surface of an Elastic Solid", *Proceedings of*

the London Mathematical Society s1-17, 4 (1885)

[108] D. Schick, R. Shayduk, A. Bojahr, M. Herzog, C. von Korff Schmising, P. Gaal and M. Bargheer: "Ultrafast reciprocal-space mapping with a convergent beam", *Journal of Applied Crystallography* 46, 1372 (2013)

[109] U. Pietsch, V. Holý and T. Baumbach: *High-Resolution X-Ray Scattering: From Thin Films to Lateral Nanostructures* Advanced texts in physics (Springer, New York, NY, 2004), 2nd edition

[110] M. Kozina et al.: "Measurement of transient atomic displacements in thin films with picosecond and femtometer resolution", *Structural dynamics* 1, 034301 (2014)

[111] D. Schick, A. Bojahr, M. Herzog, C. von Korff Schmising, R. Shayduk, W. Leitenberger, P. Gaal and M. Bargheer: "Normalization schemes for ultrafast x-ray diffraction using a table-top laser-driven plasma source", *The Review of scientific instruments* 83, 025104 (2012)

[112] M. Herzog, D. Schick, W. Leitenberger, R. Shayduk, R. M. van der Veen, C. J. Milne, S. L. Johnson, I. Vrejoiu and M. Bargheer: "Tailoring interference and nonlinear manipulation of femtosecond x-rays", *New Journal of Physics* 14, 013004 (2012)

[113] C. von Korff Schmising et al.: "Femtosecond X-ray diffraction from nanolayered oxides", *Physics Procedia* 3, 333 (2010)

[114] L. Willig: "LabWare UDKM" https://github.com/LisaWillig (2019)

[115] L. Willig: "Ultrafast Magneto-Optical Studies of Remagnetisation Dynamics in Transition Metals" doctoralthesis, Universität Potsdam (2019)

[116] W. Fullagar, M. Harbst, S. Canton, J. Uhlig, M. Walczak, C. G. Wahlström and V. Sundström: "A broadband laser plasma x-ray source for application in ultrafast chemical structure dynamics", *Review of Scientific Instruments* 78 (2007)

[117] M. Silies, S. Linden, H. Witte and H. Zacharias: "The dependence of the Fe K$_\alpha$ yield on the chirp of the femtosecond exciting laser pulse", *Applied Physics B* 87, 623 (2007)

[118] L. Miaja-Avila, G. C. O'Neil, J. Uhlig, C. L. Cromer, M. L. Dowell, R. Jimenez, A. S. Hoover, K. L. Silverman and J. N. Ullom: "Laser plasma x-ray source for ultrafast time-resolved x-ray absorption spectroscopy", *Structural dynamics* 2 (2015)

[119] L. Willig, A. von Reppert, M. Deb, F. Ganss, O. Hellwig and M. Bargheer: "Finite-size effects in ultrafast remagnetization dynamics of FePt", *Physical Review B* 100, 224408 (2019)

[120] H. F. Ding, S. Pütter, H. P. Oepen and J. Kirschner: "Experimental method for separating longitudinal and polar Kerr signals", *Journal of Magnetism and Magnetic Materials* 212, 5 (2000)

[121] M. Trigo et al.: "Fourier-transform inelastic X-ray scattering from time- and momentum-dependent phonon-phonon correlations", *Nature Physics* 9, 790 (2013)

Acknowledgment

First I want to thank my supervisor Matias Bargheer for giving me the opportunity to realize and implement the ideas during this thesis, for encouraging me to do fascinating research, for generating new ideas and to interpret surprising experimental data in the right way.

Many thanks also to all of my colleagues and former colleagues of the ULTRAFAST DYNAMICS IN CONDENSED MATTER group for several excursions, beamtimes and great physical and non-physical discussions during our coffee breaks. Special thanks also to my colleagues of the PXS lab: Flavio Zamponi, Matthias Rössle, Marc Herzog and in particular to Alexander von Reppert, with whom I enjoyed several long nights measuring great UXRD data sets.

Many thanks also to Elko Hannemann for the machining and realization of many constructions, which are used for beamtimes and at the PXS setup.

I would like to thank Lisa Willig and Felix Stete for helpful design discussions which lead to optical attractive publications. A special thanks also to Marc Herzog and Lisa Willig for the late night sushi sessions. A special thanks goes to Lisa Willig with whom I developed the MOKE and optical reflectivity setup and the beam stabilization.

Special thanks goes also to Matthias Sander, Peter Gaal und Marc Herzog for awesome beamtimes at the id09 beamline at the ESRF.

Last but not least I want to thank my family and my friends.

Declaration of Authorship

I hereby declare that this thesis was written independently and without assistance except where otherwise indicated. Third parties other than the referenced sources and aids were not used. This thesis was not previously presented to another examination board or audit authority and has not been published.

_____

Jan-Etienne Pudell   Potsdam, November 27, 2020